Habilitation à diriger des recherches

devant l'Université Paris-Sud

Instability dynamics in jets and plumes

---

par

Lutz Lesshafft

Laboratoire d'Hydrodynamique
CNRS / École polytechnique
Palaiseau, France

présenté le 16 novembre 2018 devant le jury composé de

Carlo Cossu	rapporteur
Taraneh Le Chenadec	
Frédéric Moisy	
Caroline Nore	
Benoît Pier	président
Jan Pralits	rapporteur
Jean-Christophe Robinet	rapporteur

Contents

1 Introduction

1.1 My research activities

The study of instability dynamics in jets, already the topic of my Ph.D. thesis [L65], has remained the focus of my research over the last nine years. My postdoctoral work (2007–2008) was concerned with sedimentation from river outflows and from near-coastal turbidity currents, and occasional collaborations with Eckart Meiburg's group at UC Santa Barbara on these topics continue [L20], but these studies are not included in the present manuscript for the sake of a coherent presentation of my main line of research.

My interests lie in the conceptual description of instability dynamics in jets and in jet-like open shear flows, based on a variety of methodological approaches befitting the different aspects of flow behaviour that these flows can exhibit. These aspects include oscillator and amplifier behaviour, laminar deterministic and turbulent stochastic dynamics, primary as well as secondary instability phenomena. The methodology employed for their characterisation relies on local and global formulations, modal and non-modal perturbation growth, statistical state dynamics, and Floquet theory. In all instances, the objective in my research is to uncover physical mechanisms and to identify the most appropriate framework for a conceptual modelling of the flow dynamics.

This first section of the manuscript provides a short overview of the flow phenomena that have been treated in my past research projects since 2009, and how these have been approached from a methodological point of view. A brief chronological account is attempted in §1.2, offering a deliberately subjective perspective on the context in which our current understanding of jet instability has evolved. This context is presented in broad strokes; references to the literature outside of jet studies are given sparingly and only in so far as they influenced my own direction of research.

1.2 Trends in jet instability over the last ten years

Global eigenmode analysis Scientific development, even within one discipline as close-knit as open flow instability, does not usually advance in lockstep. When I took my position at LadHyX in 2009, global eigenmode analysis (or "BiGlobal" in the diction of [57]) was the fashion of the time. This framework, which is based on the computation of temporal eigenmodes of the linear operator formulated for a non-parallel base flow, had been introduced already in the late 1980s (see the review by Theofilis [57]), yet its application to jet flows remained virgin territory. The Ph.D. work of Nichols [44], Coenen [12] and myself [L65] on jet instability was still entirely built on the *local* analysis of laminar steady base flows, even though all these works were concerned with self-sustained global oscillations in low-density jets. Our studies demonstrated that such oscillator behaviour is well characterised by the onset of absolute instability

above a critical ambient-to-jet density ratio, although the general validity of such a critical value was challenged [13], and by means of adjoint-based optimisation indeed was shown not to exist [L6].

Meanwhile, the success of linear global eigenmode analysis of flows exhibiting self-sustained oscillations generated great enthusiasm in the instability community. Noack *et al.* [46], Barkley [3] and Sipp & Lebedev [55] had demonstrated that linear global instability in a laminar cylinder wake sets in at $Re = 47$, in perfect agreement with experimental observations. Marquet *et al.* [35] showed how adjoint-based sensitivity analysis of global eigenmodes can be leveraged for passive control design, and Giannetti & Luchini [20] proposed a global "wavemaker" definition that served as a basis for the physical discussion of instability mechanisms. Global eigenmode analysis, base flow sensitivity and the "wavemaker" formalism provided the blueprint for instability studies over many years.

The study of jets has benefited from this global toolbox with significant delay: linear global eigenspectra of supersonic jets were finally presented by Nichols & Lele [45], and for subsonic settings by Garnaud *et al.* [L10]. Both of these studies were carried out in parameter regimes where jets behave as *amplifiers* of external noise, as opposed to their *oscillator* behaviour in the presence of strong density gradients. Linear global spectra of jets in their oscillator regime, at low Reynolds number and high density ratio, have been published only very recently [L16],[L18].

Input-output analysis For several years, global eigenmode analysis was the standard tool of choice for the study of oscillator- as well as amplifier-type flow configurations. On the one hand, the qualitative characterisation of amplifier flows as being *stable* from this point of view is certainly a matter of poor semantics; on the other hand, decaying eigenmodes are not particularly useful objects for a quantitative analysis of amplifying flow behaviour. The least stable eigenmodes describe the asymptotic perturbation dynamics at long times after an initial perturbation, and in an amplifier flow that asymptotic limit is ultimately zero[1]. Short-time growth is *non-modal* and can be characterised by the gain of the optimal initial perturbation, as done for jets in references [45] and [L10].

In the context of local theory, it had been established long ago that amplifier behaviour is consistently described in the *frequency domain* (the "spatial problem", see Michalke [37]). A non-modal formalism in the frequency domain, suitable for non-parallel flow instability problems, had been introduced by Trefethen *et al.* [59], but it was only hesitantly accepted in the global instability community, following its application to boundary layers [34, 42, 24]. Based on singular value decomposition (SVD)

[1] "But this long run is a misleading guide to current affairs. In the long run we are all dead. [Scientists] set themselves too easy, too useless a task if in tempestuous seasons they can only tell us that when the storm is past the ocean is flat again." Keynes [27].

of the resolvent operator, this analysis method is known under many names in the literature: optimal forcing, frequency response, resolvent or input-output analysis — the latter will be used throughout this manuscript. Garnaud *et al.* [L11] performed such input-output analysis of jet flows, both in incompressible and in compressible settings (see [L46] for compressible jets with acoustic radiation). These studies used laminar steady solutions as well as turbulent mean flows as base flows, even though the theoretical justification for mean flow analysis seemed unclear at the time.

Linear wavepackets in turbulent mean flow Frequency-domain analysis of linear perturbation wavepackets in turbulent jet mean flows has been pursued at Pprime and at Caltech over the last ten years, motivated by the prospect of obtaining dynamical models for the prediction and the control of jet noise.

The classical framework of flow instability analysis is based on the linearisation of governing equations about a steady flow state, which provides a consistent description of small-amplitude perturbation dynamics. In practice, however, such a steady solution is often replaced with a time-averaged mean flow; the motivation may be simply that a mean flow is more readily available, or that a laminar steady state poorly represents the spatial features of a turbulent flow. In the case of a turbulent jet at high Reynolds number, the mean flow spreads much more rapidly than the corresponding laminar steady state, and it seems inappropriate to model perturbations as if they evolved in a nearly parallel base flow.

A large body of literature suggests that the dominant large-scale fluctuations in turbulent jets behave like linear instability waves developing in the jet mean flow [26]. Such instability waves, or indeed "wavepackets", have in the past been modelled by local spatial theory [56] and by PSE [21]. Application of resolvent-based input-output analysis to an experimental mean flow at high Reynolds number, and validation of the results against unsteady flow measurements, was the proposition of the "Cool Jazz" project (2013–2016). Cool Jazz was funded by the Agence Nationale de la Recherche, and associated researchers at LadHyX, Pprime and Limsi. Towards the end of this project, it was realised that the analogy between spectral POD modes of the turbulent jet and linear input-output modes has a clear mathematical foundation. The theory of statistical state dynamics, pioneered by Farrell & Ioannou [16], provides the adequate formalism for the analysis of mean flow and "jittering" wavepackets [9] as *statistical* objects. The implications of this description for turbulent shear flows are currently being explored by various research teams [5, 8], particularly for the case of jets [L57][58, 53][L22].

Instability and control of periodic flows The above developments indicate that trends are driven to a large extent by available methodology. The current Ph.D. work of Léopold Shaabani Ardali aims to extend the established techniques for non-modal

instability analysis and optimal control to the class of periodic base flows. Similar efforts are currently being conducted by other research groups [50, 43]. A pulsed jet is chosen as the object of our study; subject to axisymmetric harmonic forcing, such a jet forms ring vortices at the forcing frequency. Secondary instabilities arise in the form of vortex pairing, which may be analysed by way of Floquet theory. Additional non-axisymmetric forcing is known to give rise to the phenomenon of "bifurcation" [49]. Optimisation of such active control requires strategies different from singular value decomposition, as it is used in the case of steady base flows.

Tools developed in this context may prove useful in a wide array of applications, such as periodic flow in turbo engines, behind flapping wings, and in blood vessels.

1.3 Organisation of this manuscript

Results of my research on jets and plumes from the past nine years are summarised in the following sections, grouped into the three categories

1. Extrinsically driven oscillations (§2), described by input-output relations developed around a steady base flow,

2. Intrinsic oscillations (§3), described by modal instabilities of a steady base flow,

3. Secondary instabilities (§4), described by the modal and non-modal evolution of perturbations in a periodic base flow.

Perspectives on the application of these concepts, to reacting flows and to jet noise predictions in complex settings, are given in §5. Publications and conference presentations that I have co-authored are listed in §6, followed by general literature references. The publications that are discussed in the body of the manuscript are provided in the appendix.

2 Extrinsically driven oscillations in jets

The amplifier behaviour of jets, i.e. their linear response to external perturbation input, in the absence of strong density variations, was the topic of Xavier Garnaud's Ph.D. work [19]. Laminar steady states as well as turbulent mean states were considered, both under incompressible and under compressible conditions. These studies were continued by Onofrio Semeraro, during his postdoc project 2013–2016, who used experimental mean flows and compared quantitatively the linear flow response to experimentally measured spectral POD modes.

Note that all flow configurations in this section represent jets that are of the same chemical composition and the same temperature as the ambient fluid. If furthermore the incompressible limit $Ma = 0$ is considered, the density is strictly constant in these flows; however, at non-zero Mach number, small density variations arise from compressibility effects. In the following, these configurations (incompressible as well as compressible) will be denoted as *homogeneous* jets, in order to distinguish them from the *inhomogeneous* settings investigated in §3, which involve strong density variations between the jet interior and the ambient atmosphere.

2.1 Linear eigenmodes of homogeneous jets

[L9] X. Garnaud, L. Lesshafft, P. Schmid & J.-M. Chomaz (2012): A relaxation method for large eigenvalue problems, with an application to flow stability analysis. *J. Comp. Phys.* vol. 231, p. 3912–3927

[L10] X. Garnaud, L. Lesshafft, P. Schmid & P. Huerre (2013): Modal and transient dynamics of jet flows. *Phys. Fluids* vol. 25, art. 044103

Motivation Xavier Garnaud's investigation of the forcing response in jets set out from the hypothesis that a *slightly damped eigenmode* exists, which would be easily excited by low-amplitude forcing input. This conception, suggested by Huerre & Monkewitz [23], would be consistent with the typical observation of a "preferred mode" in amplifier jets, characterised by a distinct maximum of perturbation amplitude in a turbulent jet around a Strouhal number of 0.3 [14].

Methodology The computation of converged global jet eigenmodes in *compressible* settings turned out to be fraught with technical difficulties. Due to high-order finite-difference schemes and large flow domains, which were used in order to capture the acoustic field, the need for matrix inversion as part of the classical shift-invert technique led to computational resource requirements that appeared to be too restrictive.

A new computational method, named the "shift and relax" technique [L9] was developed for these compressible eigenmode calculations. The method is matrix-free and

only requires the memory needed for time-stepping of an augmented system. Akin to the "selective frequency damping" [1], a set of auxiliary filter equations is added to the regular system of linear flow equations, and a coupling is prescribed in such a way that eigenmodes are damped with increasing distance from a chosen shift value. The resulting eigenmode calculations are rather time-intensive, but very light on memory, such that they can be run on workstations.

Incompressible problems were discretised on an unstructured grid with finite elements (FreeFEM++), and eigenmode spectra were efficiently found with standard ARPACK and SLEPc routines. These calculations are easily performed on a single processor.

Results Stable spectra were obtained in all cases, mostly characterised by a more or less flat branch of eigenvalues. The spectrum for a laminar incompressible jet at $Re = 1000$ is shown in figure 1: modes plotted as black crosses form an 'arc branch' [L19], brought about by spurious feedback from the outflow boundary (see §3.3.2). The modes shown as red plus signs were linked to the limited accuracy of the numerical scheme, which allows the resolution of global amplitude variations over not more than 15 decades [L10].

Eigenvalues of a laminar compressible jet, computed with the "shift and relax" technique, are shown in figure 2. The base flow, at $Re = 100$ and $Ma = 0.75$, was obtained using selective frequency damping. The eigenvalues again form a branch that is likely to arise from spurious boundary feedback. Eigenmode perturbations of vorticity are represented in figure 3, corresponding to the labels in figure 2. These structures have the typical appearance of Kelvin-Helmholtz wavepackets that originate at the nozzle ($x = 0$), coupled with Tollmien–Schlichting waves in the boundary layers of the inflow pipe.

None of the computed spectra exhibited a slightly stable discrete eigenmode that could convincingly be interpreted as the origin of the "preferred mode" flow response to low-amplitude forcing. It had become clear that temporal eigenmodes are not an adequate basis for the description of extrinsically driven flow oscillations.

2.2 Deterministic input-output analysis of incompressible jets

[L11] X. Garnaud, L. Lesshafft, P. Schmid & P. Huerre (2013): The preferred mode of incompressible jets: linear frequency response analysis. *J. Fluid Mech.*, vol. 716, p. 189–202

Motivation Extrinsically driven flow oscillations in a jet are to be expressed in a modal basis that genuinely reflects their input-output character, and ideally, such a basis would be orthogonal. These are the properties of *singular value decomposition*

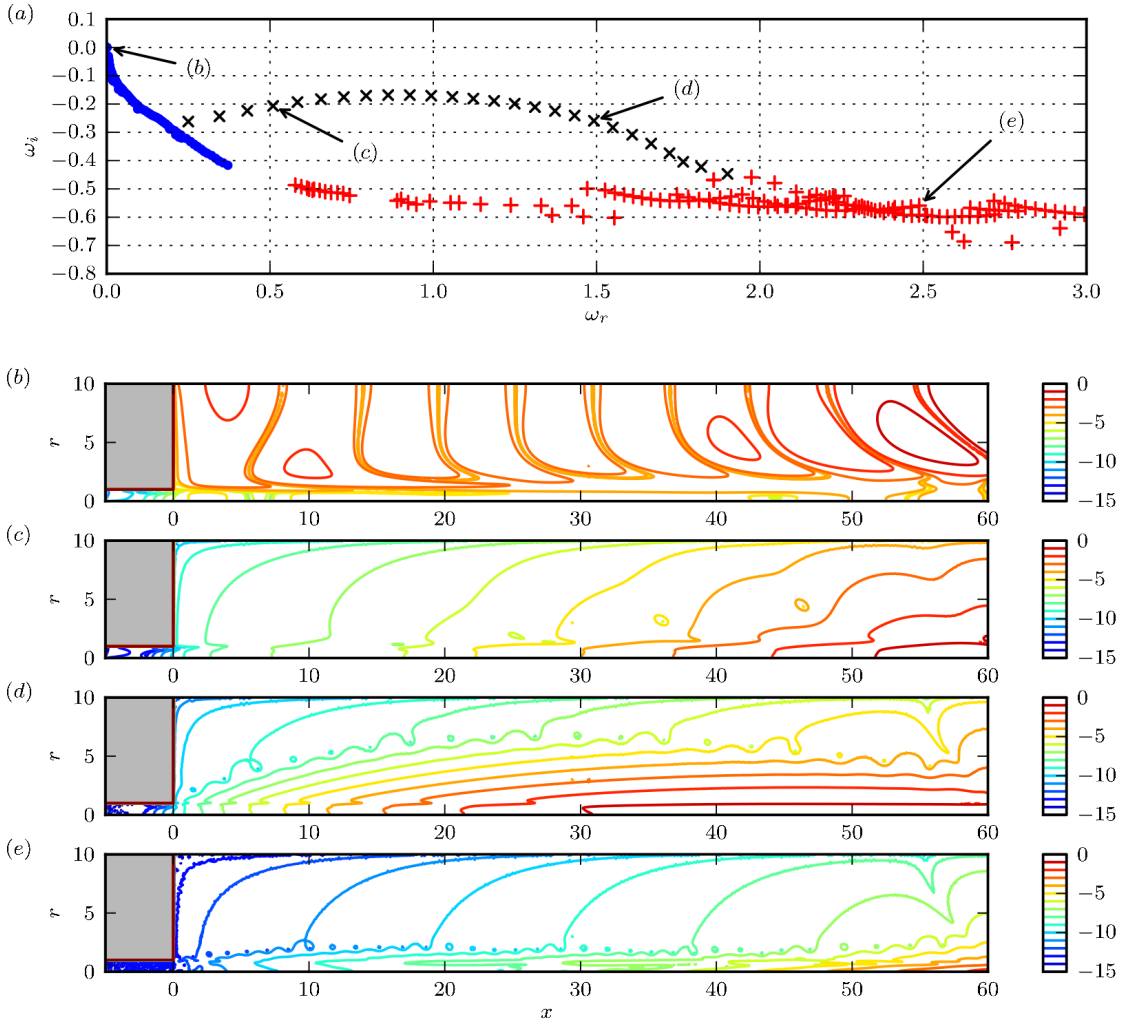

Figure 1: Eigenmodes of axisymmetric perturbations in a laminar incompressible jet at $Re = 1000$. a) Eigenvalues; b)-e) modulus of axial velocity perturbations, $\log_{10}|u|$, of individual modes, as labeled in (a). From reference [L10].

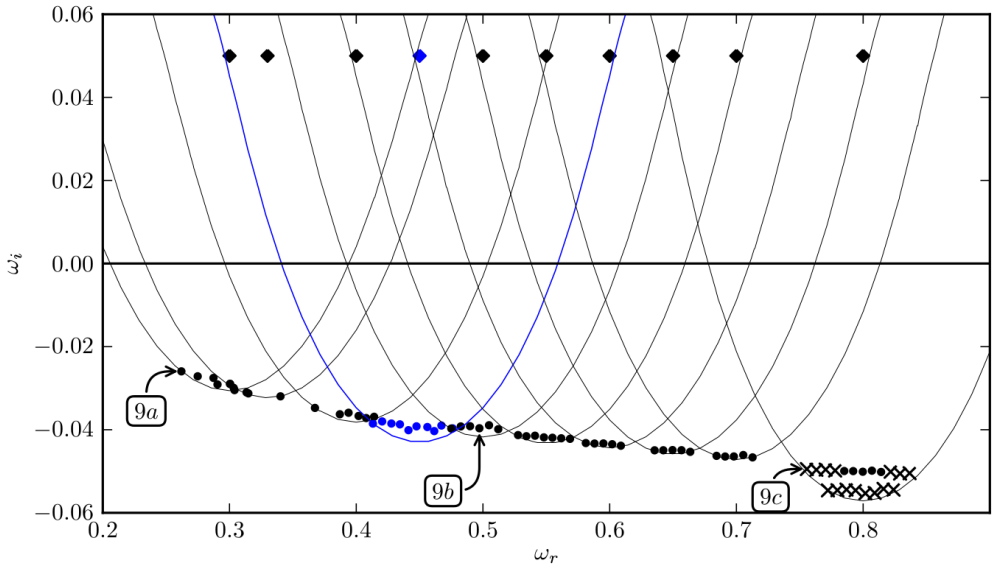

Figure 2: Eigenvalues of axisymmetric perturbations in an isothermal jet at $Re = 100$ and $Ma = 0.75$, computed using the "shift and relax" method. Diamond markers indicate shift values. From reference [L9].

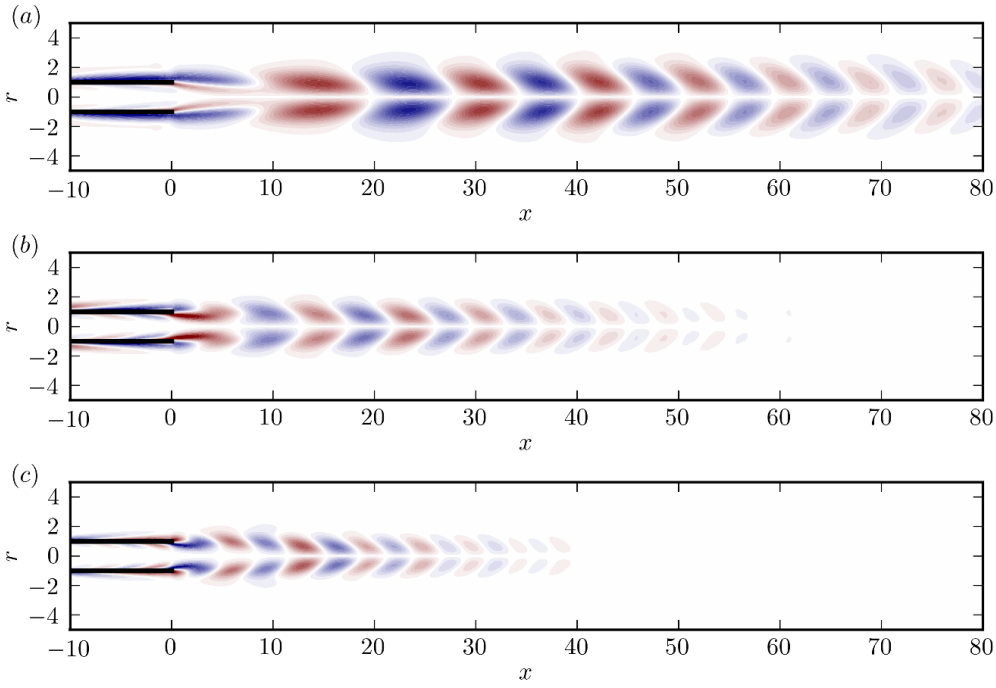

Figure 3: Real part of the vorticity perturbations of typical eigenmodes, labeled in figure 2. From reference [L9].

(SVD). Following the eigenspectrum analysis described in the previous section, Xavier Garnaud proceeded to apply an SVD-based formalism to an incompressible jet, in order to test if the "preferred mode" at $St \approx 0.3$ could be captured and characterised in this way.

Methodology SVD-based input-output analysis has been introduced for flow instability problems by Trefethen *et al.* [59], and has been applied to a number of *parallel* flow situations in the following years. The application of such a formalism to *non-parallel* problems has been demonstrated, to my knowledge, for the first time by Alizard *et al.* [2] for a separated boundary layer, using a reduced-order eigenmode representation of the linear flow system. Monokrousos *et al.* [42] computed leading singular modes in a Blasius boundary layer without the need for eigenmode expansion. In the context of Xavier Garnaud's PhD thesis, our goal was to use the same formalism on jet flows.

The governing equations are linearised around a steady base flow. These equations include a source term f that represents a volume force, as a model for external perturbation input. After a temporal Fourier transform, the linear system is written as

$$(-i\omega B + L)\hat{q} = \hat{f}. \tag{1}$$

The operator $(-i\omega B + L)^{-1}$ that maps any given forcing $\hat{f}e^{-i\omega t}$ onto its time-asymptotic linear flow response $\hat{q}e^{-i\omega t}$ is called the *resolvent* operator [52]. Its matrix SVD representation, $(-i\omega B + L)^{-1} = U\Sigma V^H$, associates each column vector v_i of matrix V with a real gain value σ_i and a column vector u_i of matrix U. The sets of v_i and u_i are both orthonormal among themselves. It follows that the pair (v_i, u_i) with highest associated gain σ_i represents the *optimal forcing* and *response* structures of frequency ω. The resolvent operator can be tweaked prior to the SVD in order to account for specific gain definitions and forcing restrictions.

For any given frequency, a discrete resolvent matrix was constructed with FreeFEM++, using similar tools as in the incompressible eigenmode computations described in §2.1. Singular value decomposition was performed on regular workstations, with routines from the MUMPS and SLEPc libraries, called from Python.

Results An analytical model of a turbulent jet mean flow [41] was chosen as a base flow, with a straight pipe section upstream of the nozzle, and the Reynolds number was fixed at $Re = 1000$ for the linear perturbation computations. Forcing input was restricted to the interior of the pipe, the rationale being that stochastic random fluctuations enter the flow from the nozzle, whereas no volume forces are present in the free jet. The jet was treated as a purely linear flow system, for lack of clear ideas on how to model the effect of nonlinearity, especially in the face of the incoherent nature of turbulent fluctuations.

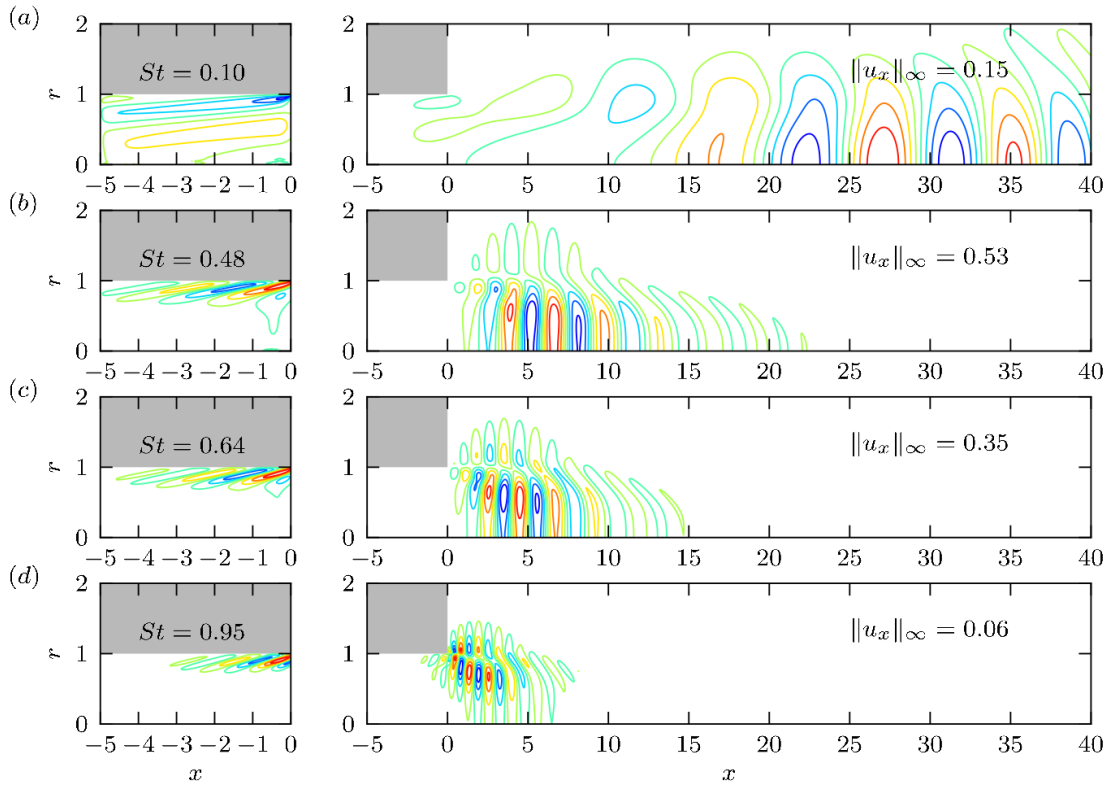

Figure 4: Input-output analysis of an incompressible turbulent jet mean flow: spatial structures associated with optimal body forcing at different Strouhal numbers, indicated in the figures. Left column: axial component of optimal forcing; right column: axial velocity of associated flow response. From reference [L11].

Optimal forcing in this base flow, at all frequencies, takes the shape of tilted vortical structures near the pipe wall, with maximum amplitude at the nozzle exit. These structures, shown on the left side in figure 4, are suggestive of the Orr-mechanism in boundary layers, which give rise to strong energy growth over short convection distances. The ensuing flow response, shown on the right side in figure 4, clearly represents a free-jet wavepacket that grows and eventually decays due to shear instability. It was demonstrated that the initial spatial growth of perturbation amplitude in the response wavepacket corresponds well to the local growth rate of a spatial shear instability mode. The maximum input-output energy gain was achieved at a Strouhal number around $St_D = 0.45$, in decent agreement with typical measurements of the "preferred mode" in turbulent jets.

2.3 Deterministic input-output analysis of compressible jets

[L46] X. Garnaud, R. Sandberg & L. Lesshafft (2013): Global response to forcing in a subsonic jet: instability wavepackets and acoustic radiation. *AIAA Paper* 2013-2232

[L15] O. Semeraro, L. Lesshafft, V. Jaunet & P. Jordan (2016): Modeling of coherent structures in a turbulent jet as global linear instability wavepackets: theory and experiment. *Int. J. Heat Fluid Flow* vol. 62, p. 24–32

Methodology As the resolvent matrix of highly-resolved compressible flow systems is unpractically large, a direct-adjoint time-stepping strategy [31] was chosen for the computations presented in this section. Jet noise analysis was one objective of these studies from the outset; we therefore opted for high-order finite-difference discretisation on orthogonal grids. Accurate adjoint time-stepping is achieved by a modular construction technique [18]. These compressible computations require significantly more resources than the incompressible studies presented in the preceding sections, and they were all run on the HPC platforms of TGCC and CINES.

Results In two separate studies, we investigated optimal forcing and associated linear response structures in the mean flow of turbulent compressible jets. The mean flow used by Garnaud *et al.* [L46] was provided by Richard Sandberg, obtained by direct numerical simulation of a jet issuing from a long straight pipe, at $Re = 3691$ and $Ma = 0.84$, and with significant co-flow. The study by Semeraro *et al.* [L15] used an experimentally measured mean flow at $Re = 10^6$ and $Ma = 0.9$, without co-flow, made available by Peter Jordan and his group.

Following the same conceptions as in the incompressible analysis of section 2.2, forcing input was again restricted to the interior of the pipe. Both compressible studies led to similar results. A clear peak in the energy gain is found, at $St_D = 0.8$ in the co-flowing configuration [L46] and at $St_D = 0.4$ in the case of [L15]. Optimal forcing structures as well as flow response wavepackets resemble those identified in the incompressible case, except for the added presence of acoustic waves in both.

Garnaud *et al.* [L46] compared the linear response wavepackets to Fourier modes extracted from the DNS by Richard Sandberg and found good agreement in the near-nozzle region of the free jet. More strikingly, the *acoustic far field* from the DNS is well reproduced, displaying beam-like radiation patterns, as shown in figure 5. Only at the highest frequency $\omega = 4$ (or $St_D = 1.27$), the linear flow response in figure 5c exhibits a strong upstream lobe, which is absent in the DNS Fourier mode.

An additional point of interest in the analysis of the experimental base flow [L15] lies in the use of a spatially distributed *turbulent viscosity*, deduced from Reynolds stress measurements. Including this in the linear model has the predictable effect of

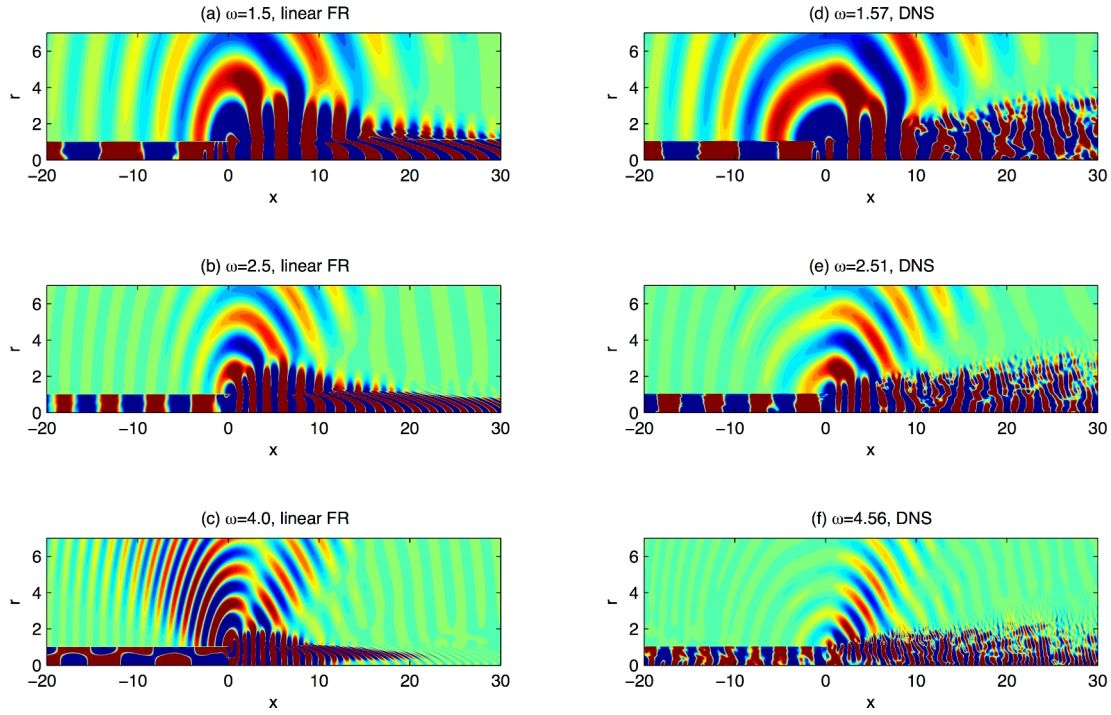

Figure 5: Comparison between the linear flow response to optimal forcing (left column) and Fourier modes extracted from DNS data (right column): density fluctuations at various frequencies $\omega = \pi St_D$. Contour values are chosen such as to visualise the acoustic field. From reference [L46].

lowering the global energy gain and shortening the streamwise extent of the response wavepackets.

2.4 Stochastic input-output analysis of compressible jets

[L57] O. Semeraro, V. Jaunet, P. Jordan, A.V.G. Cavalieri & L. Lesshafft (2016): Stochastic and harmonic optimal forcing in subsonic jets. *AIAA Paper* 2016-2935

[L22] L. Lesshafft, O. Semeraro, V. Jaunet, A.V.G. Cavalieri & P. Jordan (2018): Resolvent-based modelling of coherent wavepackets in a turbulent jet. ArXiv preprint 1810.09340, submitted to *Phys. Rev. Fluids*

An important step forward in jet instability research has been made over the last two years, following the realisation that optimal linear input-output structures are closely related to *spectral POD* modes of the fluctuations in turbulent jets. This term is used in the sense of reference [47], denoting eigenmodes of the cross-spectral density

tensor, and thereby characterising two-point statistics in frequency-space. The theoretical basis for this relation is partially described by Dergham *et al.* [15], Hwang & Cossu [24] and Beneddine *et al.* [5]. More complete developments are given in references [L57], [58] and [L22].

Motivation While it had been acknowledged for a while, and the evidence reviewed in detail by Jordan & Colonius [26], that coherent structures in fully turbulent jets strongly resemble linear instability wavepackets developing in the *mean flow*, the theoretical justification for this analogy remained elusive until very recently. PSE calculations of perturbations in mean flows had been shown to reproduce spectral POD modes, or at least filtered power-spectral density distributions [21, 54], with high accuracy over several jet diameters downstream of the nozzle. Our own linear response wavepackets, obtained from fully global input-output analysis (see the previous section), promised to allow even more accurate predictions. Beneddine *et al.* [L14] had just demonstrated very good agreement between global response wavepackets and spectral POD modes in turbulent flow over a backward-facing step. Based on the argument that the anonymous forcing term $\hat{f}$ in the linear input-output relation (1) can be interpreted as a representation of turbulent Reynolds stress fluctuations, they had worked out that such agreement may be expected in flow regimes where the largest singular value is much greater than the second-largest ("gain separation").

Furthermore, together with André Cavalieri and Peter Jordan, we elaborated an approach to jet turbulence based on the dynamics of covariances [16], in parallel with colleagues at Caltech and Stanford. It is easily demonstrated that spectral POD modes and the singular modes of the mean-flow resolvent are indeed identical under the strongly idealising hypothesis that the Reynolds stress fluctuations consist of white noise [L57],[58]. This assumption, however, is not required in cases of large gain separation. Jets with thin initial shear layers represent such a case.

The overarching question of our stochastic jet analysis is therefore: can the dominant coherent structures in jet turbulence be accurately modelled by linear input-output analysis, which requires the turbulent mean flow as the only *a priori* information?

Methodology The stochastic input-output analysis requires the same computational tools as the deterministic studies discussed in section 2.3. A hierarchical set of orthogonal forcing input and response output structures was computed, for the resolvent operator that stems from linearisation of the flow equations around the mean flow. As developed in [L57], and more fully in [L22], the deterministic resolvent operator provides the relation between the cross-spectral densities of the forcing (the Reynolds stresses) and of the response (the turbulent fluctuations).

The acquisition of experimental reference data for a spatially resolved representa-

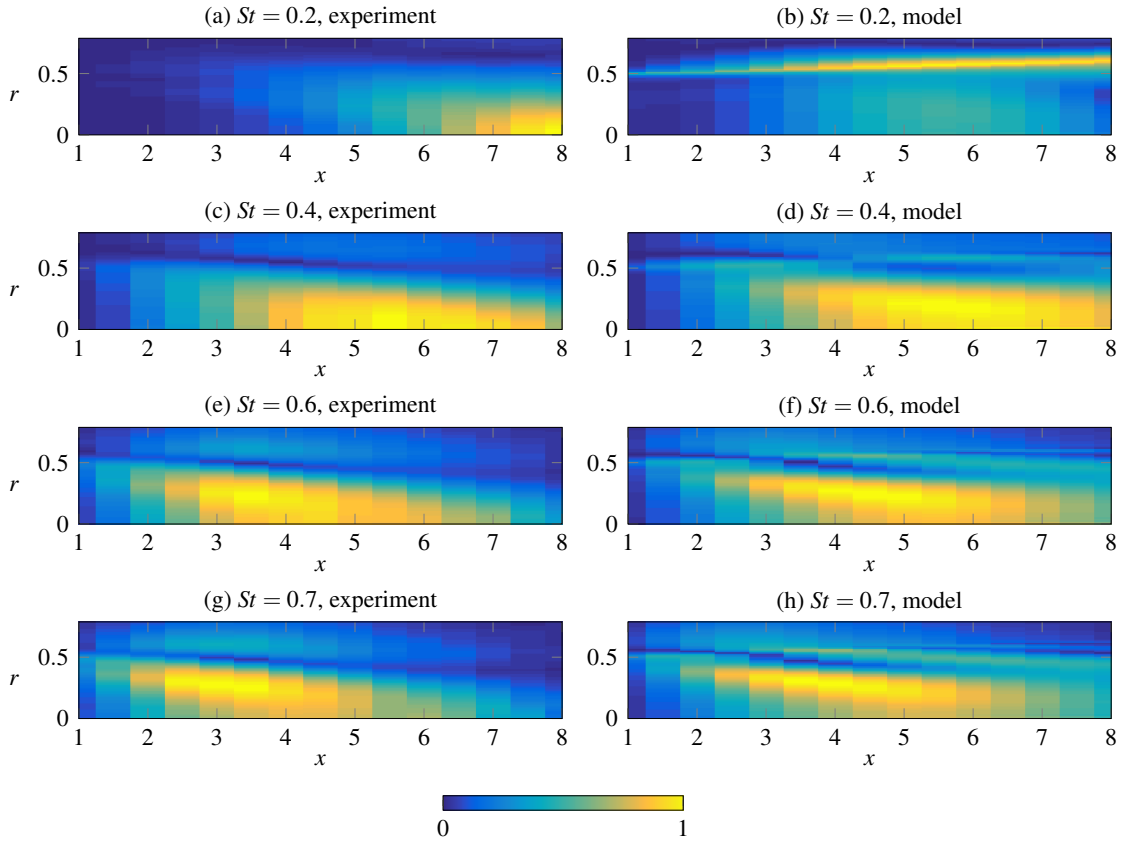

Figure 6: Comparison between the leading spectral POD modes extracted from experiments (left column) and from the linear model, based on the first five output modes (right column). Absolute values of axial velocity fluctuations are shown in linear scale. Taken from [L22].

tion of two-point correlations is an ambitious undertaking. Vincent Jaunet and Peter Jordan at the Pprime Institute performed synchronised dual-plane TR-PIV measurements in a jet at $Ma = 0.4$ and $Re = 460\,000$, gathering correlated data in cross-stream planes at 15 different streamwise locations. About 20 terabytes of image data were recorded [25].

A model cross-spectral density matrix was then constructed, at various Strouhal numbers, from the five leading linear output modes, under the strong assumption that the forcing is given by spatially uncorrelated noise. Eigenvectors of this linear model matrix provide our prediction for spectral POD modes of the turbulent jet.

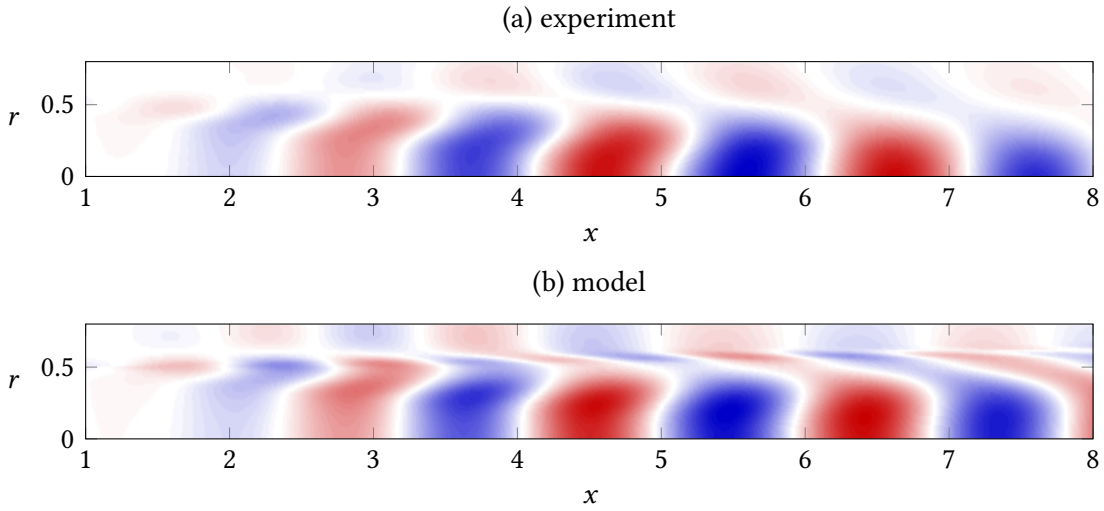

Figure 7: Real parts of spectral POD (experiment and model) at the dominant Strouhal number, corresponding to figures 6c and 6d. The data is interpolated between measurement locations in x. Taken from [L22].

Results The mean flow of the jet experiment was used as a basis for linearisation, and its careful inter- and extrapolation onto the numerical mesh was an important step towards clean analysis results. Frequency-resolved wavepackets corresponding to the dominant coherent structures (leading spectral POD modes) in the experimental data are compared to their numerical counterparts, computed as the leading eigenvectors of the model cross-spectral density matrix, in figure 6. Except at the lowest Strouhal number (figures 6a and 6b), the agreement between the two is remarkable. Figure 7 gives a more detailed comparison at the most amplified Strouhal number $St_D = 0.4$ (the "preferred mode" [14]), showing the real part of axial velocity fluctuations. The data had to be interpolated between the 15 measurement positions in x for this plot.

It can be noted that the computed wavepackets extend slightly further in the streamwise direction than the experimental ones; including the effect of turbulent dissipation would help to improve the agreement further. However, at present it is not obvious how such turbulent dissipation is best modelled. The principal limitation of the analysis at this point lies in the assumption of perfectly uncorrelated Reynolds stress fluctuations ("white noise forcing"). Current efforts, together with our collaborators, aim at a more realistic characterisation of the Reynolds stress statistics.

3 Intrinsically driven oscillations in jets and plumes

If the density of a jet is significantly lower than that of the ambient fluid at rest, a spontaneous onset of synchronised flow oscillations may be observed. Such oscillator behaviour, characterised as a global instability, has been observed experimentally in situations where the density variations were either due to heating [40] or due to the mixing of air with helium [28, 22, 61]. In all these studies, intrinsic oscillations appear in the form of a regular roll-up of axisymmetric ring vortices.

The link between these oscillations and absolute instability, a *local* concept, was the subject of my Ph.D. thesis [L65]. My more recent research, which will be presented in the present section, focused on a *global* characterisation of the linear instability behind intrinsic oscillations in jets.

The Ph.D. thesis of Chakravarthy covered both local and global instability in circular *plumes*. These flows differ from jets in the one important aspect, that their momentum is generated by buoyancy. The question to what extent the instability dynamics of plumes are determined by buoyancy was largely unexplored before Chakravarthy's analysis.

Motivation The earlier local instability studies of jets necessarily relied on the assumption of slow streamwise flow variations. In jets, this assumption is questionable, because the region near the nozzle exit, where local instability is most pronounced, presents strong shear layer growth. Also, the nozzle itself represents a geometrical singularity in the flow, which may be very important for global pressure feedback effects [L24]. The objective of linear global instability analysis was to fully account for the non-parallelism of the base flow, and to characterise the mechanisms by which light jets may become globally unstable.

A second important question concerned the role of buoyancy as an instability mechanism in jets and plumes. In previous local jet instability studies, buoyancy, if it was at all included in the governing equations, had been found to be unimportant for the instability dynamics. Would it become an important ingredient in plumes?

Methodology Light jets and plumes were treated as two branches of one family of flows, arising from the injection of low-density fluid into a higher-density ambient through a circular orifice. Light jets are then characterised by a low Richardson number, which measures the effect of buoyant acceleration with respect to the injected momentum, whereas plumes are characterised by a high Richardson number. The same set of equations was used for both flow regimes: the so-called low-Mach-number approximation of the compressible Navier–Stokes equations [36] fully accounts for the dynamic effects of density variations, but it does not allow density to increase due to compressibility by pressure. This corresponds in fact to the limit of *zero* Mach number.

For all global calculations, the linearised low-Mach-number equations were discretised by finite elements in the FreeFEM++ environment, by extending the code originally developed by Xavier Garnaud for incompressible homogeneous jets (see §2.1). The parameters in the equations were the Richardson number, the density ratio $S = \rho_{jet}/\rho_\infty$ and the Reynolds number; the inflow condition introduced the boundary layer thickness at the orifice as an additional parameter.

The identification of *physical mechanisms* is an essential element of the global instability studies presented in this section. In some cases, such mechanisms may be inferred in an *ad hoc* fashion from an inspection of the eigenmode structures, if plausible narratives about the cause-and-effect relationship between different perturbation quantities may be constructed. (In the context of instability, which always relies on positive feedback effects, the relation between cause and effect is analogous to the relation between hen and egg.) However, a more universal formal approach for the identification of instability mechanisms in eigenmodes has been proposed in an unpublished article [L67]. This formalism is briefly outlined in section §3.3, together with a study on spurious eigenmodes that are regularly encountered in global spectra of open shear flows, owing to unphysical pressure feedback from imperfectly transparent outflow conditions.

3.1 Linear global instability of weakly buoyant jets

[L16] W. Coenen, L. Lesshafft, X. Garnaud & A. Sevilla (2017): Global instability of low-density jets. *J. Fluid Mech.* vol. 820, p. 187–207

The choice of parameter values for this study was guided by the helium jet experiments by Hallberg & Strykowski [22]: laminar jets with Reynolds number values $Re_D \leqslant 1000$ and with density ratios $0.143 \leqslant S \leqslant 0.5$ were considered. The jet exits from a straight pipe, included in the numerical domain, with a shear layer momentum thickness θ_0 between 2.8% and 6.7% of the nozzle diameter.

In settings corresponding to pure helium injected into air, $S = 0.143$, an isolated eigenvalue was found to dominate the spectrum. Convergence tests demonstrated that this was indeed the only eigenvalue in our calculations that was independent of the computational domain size (see figure 8). Through systematic variations of the Reynolds number and of the nozzle-exit shear layer thickness, the neutral curve of this dominant eigenmode was traced, as shown in figure 9, and could thus be compared to the experimental results [22].

While the general trend of the experimental neutral curve is well captured by our linear calculations, and decent agreement is found between measured and computed Strouhal numbers (indicated by text labels in figure 9), a quite significant offset in the critical Reynolds number remains. In order to find an explanation for this discrepancy, the numerical model was extended to include the effects of buoyancy as well as

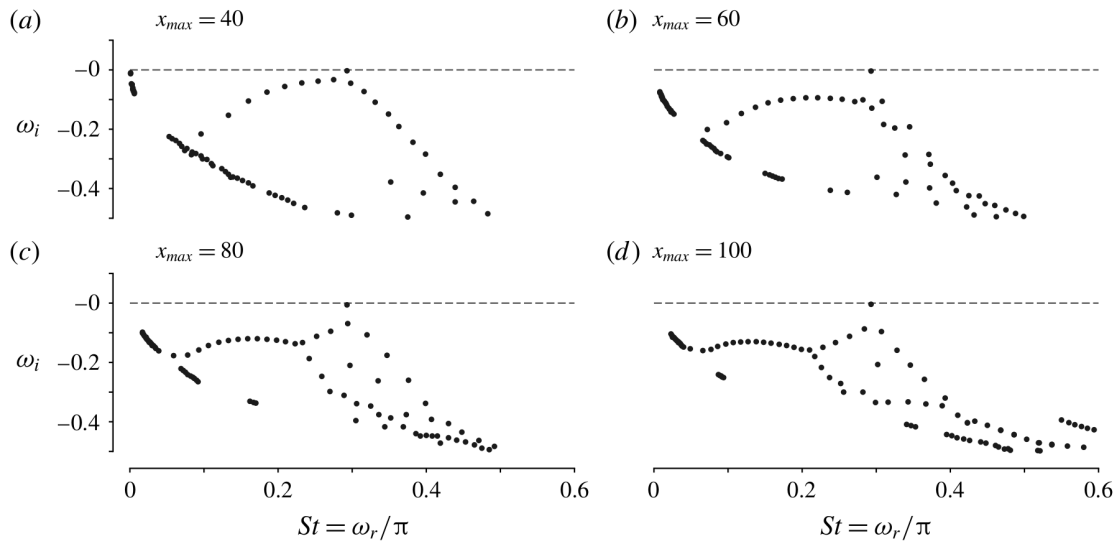

Figure 8: Spectrum of a jet at $Re = 360$, $S = 0.143$ and $D/\theta_0 = 24.3$, computed on numerical domains of different streamwise length x_{max}. From reference [L16].

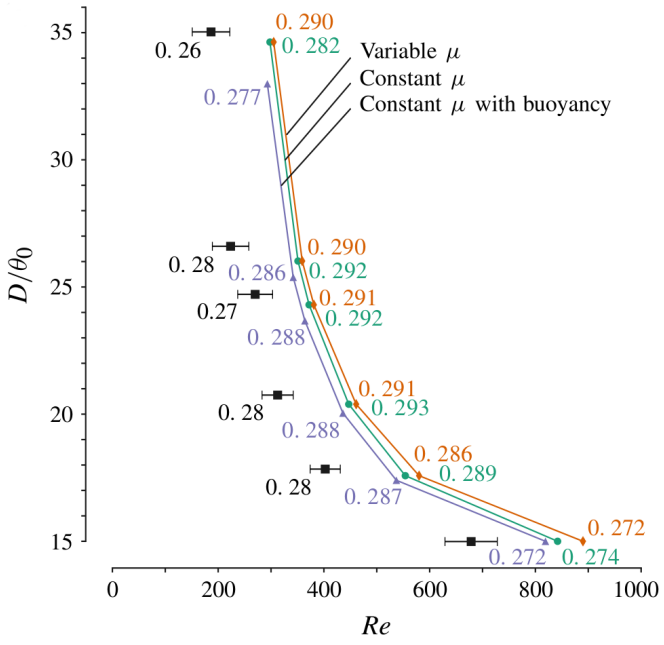

Figure 9: Comparison of neutral curves obtained from linear analysis (colour) with those obtained experimentally (black squares and error bars) by Hallberg & Strykowski [22] for pure helium jets. Numbers indicate the Strouhal values of dominant jet oscillations. From reference [L16].

viscosity variations, but both effects are seen to be rather negligible.

The onset of linear global instability was successfully linked to the presence of absolute instability near the nozzle. Both the structural sensitivity [20] and the sensitivity to base flow variations [35] was computed, but neither one of these provided clear indications about the physical mechanisms that are involved in the global destabilisation of the jet. This discussion was revisited in the investigation of plumes (see §3.2).

At the highest Reynolds number, $Re = 1000$, no isolated eigenvalue could be detected, and the entire spectrum was found to be strongly dependent on the length of the computational domain. This observation, consistent with our earlier homogeneous jet calculations [L10], motivated a more detailed investigation of the effect of domain truncation (see §3.3.2).

3.2 Linear local and global instability of strongly buoyant plumes

[L13] R.V.K. Chakravarthy, L. Lesshafft & P. Huerre (2015): Local linear stability of laminar axisymmetric plumes. *J. Fluid Mech.* vol. 780, p. 344–369

[L12] L. Lesshafft (2015): Linear global stability of a confined plume. *Theor. Appl. Mech. Lett.* vol. 5, p. 126–128

[L18] R.V.K. Chakravarthy, L. Lesshafft & P. Huerre (2018): Global stability of buoyant jets and plumes. *J. Fluid Mech.* vol. 835, p. 654–673

In 2013, at the beginning of Chakravarthy's Ph.D. project, the literature on linear instability of plumes was limited to a few local studies, mostly from the 1980s. Temporal and spatial analyses had been performed for self-similar base flows in parameter regimes that were numerically accessible at the time. Prandtl numbers for these self-similar profiles were limited to values 1 and 2. Yet several experiments and numerical simulations had established the presence of intrinsic oscillations, in the form of axisymmetric vortex formation.

The first step towards a linear description of self-sustained oscillations in plumes had to be made in terms of *local* theory. Our first article [L13] describes a numerical procedure for the construction of self-similar plume profiles, under the Boussinesq approximation, for arbitrary Prandtl and Grashof number values, which were then used for temporal and spatio-temporal instability analysis. New instability mechanisms were described, both for axisymmetric and for helical modes, based on the interplay between vorticity and temperature perturbations in the self-similar plume far from its source. Absolute instability in such profiles was shown to occur for helical, but never for axisymmetric perturbations. The absolute helical mode is characterised by a very long wavelength, small frequency and small positive growth rate.

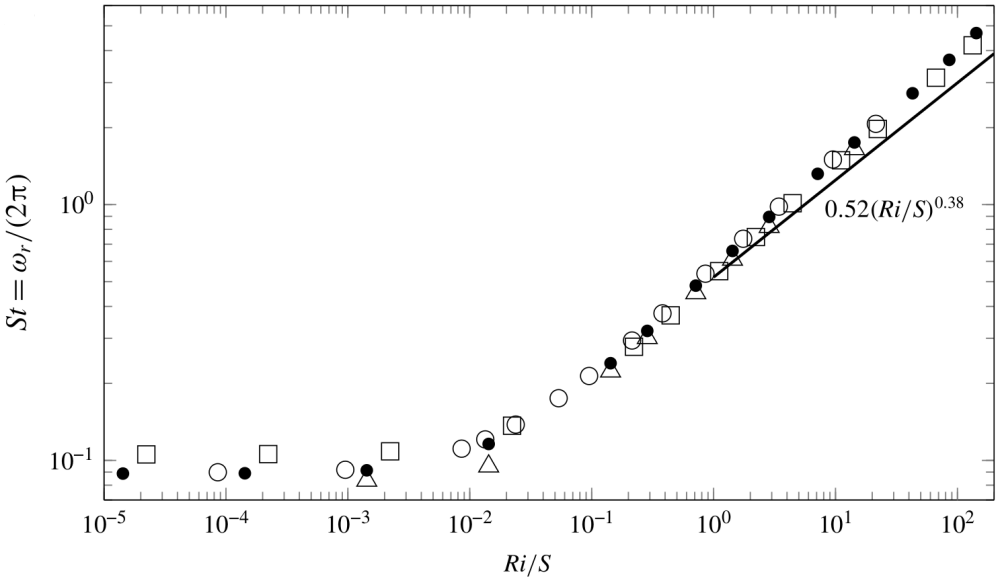

Figure 10: Strouhal number of the dominant global eigenvalue, as a function of Ri/S. Legend: (•) $Re = 200$, $S = 7$; (◦) $Re = 500$, $S = 7$; (□) $Re = 200$, $S = 4.5$; (△) $Re = 200$, $S = 7$, with parabolic inlet velocity profile. Solid line: power law from the Cetegen & Kasper [10] experiments, rescaled to match the present definition of Ri. From reference [L18].

These local results, valid in the self-similar regime, do not explain the observed intrinsic plume oscillations, which are consistently reported to be axisymmetric. A *global* eigenmode analysis was therefore undertaken, for laminar base flows that include the buoyancy source region, obtained by Newton–Raphson iteration of the low-Mach-number flow equations. This set of equations does not invoke the Boussinesq approximation, and is valid for arbitrarily high density variations. The principal influence parameters in this study were the density ratio, in this study defined as $S = \rho_\infty/\rho_{plume}$ (reciprocally to our previous definition), and the Richardson number Ri. A low value of Ri denotes a base flow which is dominated by the injected momentum, and therefore is classified as a *jet*, whereas a high value of Ri denotes a flow that is dominated by the effect of the buoyancy force, characteristic of a *plume*.

The global spectra of these non-self-similar base flows revealed the presence of several strongly growing eigenmodes in the high-Ri plume regime, distinct from the instability already documented for low-Ri jets (§ 3.1). Across the entire interval of investigated Richardson number values, $10^{-4} \leqslant Ri \leqslant 10^3$, only *axisymmetric* perturbations were found to exhibit global instability, fully consistent with empirical observations. All globally unstable base flows were shown to be absolutely unstable at the inflow, but convectively unstable in the downstream self-similar flow region. The ab-

solute instability of helical perturbations turned out to be too weak in order to trigger global instability.

The first significant result of Chakravarthy's global stability analysis was the precise recovery of the experimental scaling law, given by Cetegen & Kasper [10], that relates the Strouhal number of flow oscillations to the ratio Ri/S. This scaling is shown in figure 10: symbols represent the Strouhal number of the dominant instability mode in various flow configurations, and a solid line indicates the power law reported from experiments [10]. This result has been corroborated in a parallel study by Bharadwaj & Das [6].

Another significant result was the formal demonstration that global instability in the plume regime is underpinned by the effect of *buoyancy*, whereas in the jet regime it is caused by the *baroclinic torque*. This analysis of physical mechanisms was based on the formalism developed by Marquet & Lesshafft [L67] (see §3.3.1), slipped into our publication [L18] in the guise of a sensitivity analysis.

A short study of internal plumes, confined inside a cylindrical box with solid, isothermal walls, indicated that global instability in such a configuration is driven by non-local feedback between a cooled top and a heated bottom boundary [L12]. Despite the absence of absolute instability, global instability was observed in such a setting. The critical Rayleigh number for the onset of nonlinear oscillations, determined to be $Ra_c = 3.85 \times 10^7$ in direct numerical simulations [32], was recovered as $Ra_c = 3.80 \times 10^7$ for the threshold of linear global instability; the nonlinear and linear frequencies at this threshold were found to match within 0.5%.

3.3 Interpretation of instability mechanisms

3.3.1 A refined definition of the global wavemaker

[L67] O. Marquet & L. Lesshafft (2015): Identifying the active flow regions that drive linear and nonlinear instabilities. arXiv:1508.07620

The "wavemaker" (Monkewitz [38]) associated with a global instability mode, as a notional concept, denotes the flow region where oscillations are *generated*, as opposed to the flow region where they may reach their amplitude maximum after further *amplification*. In the context of weakly non-parallel flows, the wavemaker has been identified with the location of a saddle point in the analytic continuation of the absolute frequency as a function of the streamwise coordinate [11]. In the context of global eigenmode analysis, the wavemaker definitions by Luchini *et al.* [20, 33], based on the structural sensitivity of a given eigenmode, has been widely used for the discussion of instability dynamics.

Olivier Marquet and myself proposed a similar but different definition of the wavemaker [L67]. The definition starts from the simple observation that the linear operator

L of a given eigenvalue problem

$$\omega B q = L q \tag{2}$$

has a unique diagonal representation $L = BQ\Omega Q^{-1}$, and that the matrix $Q^\dagger$ formed by the adjoint eigenvectors satisfies $Q^{-1} = Q^{\dagger,H}B$. The diagonal eigenvalue matrix Ω is then uniquely related to L as

$$\Omega = Q^{\dagger,H} L Q. \tag{3}$$

Suppose one can formulate a *physically meaningful* decomposition of the linear operator, $L = L_1 + L_2 + \cdots + L_n$, a given eigenvalue ω_1 with associated direct and adjoint eigenvectors q_1 and $q_1^\dagger$ is precisely determined by

$$\omega_1 = q_1^{\dagger,H} L q_1 = q_1^{\dagger,H}(L_1 + L_2 + \cdots + L_n) q_1, \tag{4}$$

such that the contribution of each component L_i to the eigenvalue ω_1 is quantified as $q_1^{\dagger,H} L_i q_1$.

The decomposition of the operator L can be performed to denote spatial locations, individual terms in the flow equations, or both. Contributions of different flow regions, as well as different physical mechanisms, to the frequency and the growth rate of an eigenmode may therefore be quantified. The original paper [L67] demonstrated this concept for the Ginzburg–Landau equation and for the 2D cylinder wake, both in linear and nonlinear contexts. It was shown for these examples that the ensuing wavemaker definition is consistent with those given by Chomaz *et al.*[11] and by Luchini *et al.* [20, 33]. In contrast to those established definitions, however, our formalism provides a straightforward framework for a discussion of physical mechanisms, in so far as they can be related to individual terms in the flow equations. Its potential has since been tested in several flow configurations, including the plume study discussed in the previous section, the dynamics of a spring-mounted cylinder [L59](c), and the instability of a premixed flame [L58](a). A new submission of the manuscript [L67] is in preparation.

3.3.2 Spurious feedback from boundary conditions

[L19] L. Lesshafft (2018): Artificial eigenmodes in truncated flow domains. *Theor. Comp. Fluid Dyn.*, vol. 32, p. 245-262.

The prominent branch of evenly spaced eigenmodes, which has been found to dominate most jet and plume spectra, is in fact regularly encountered in the global spectral analysis of open shear flows. We have named it the "arc branch" [L19]. The arc branch has in several instances been discussed as the spectral manifestation of amplifier flow behaviour, but such a conception is problematic — first, because amplifier behaviour is appropriately described by the *pseudospectrum*, which does not require the presence

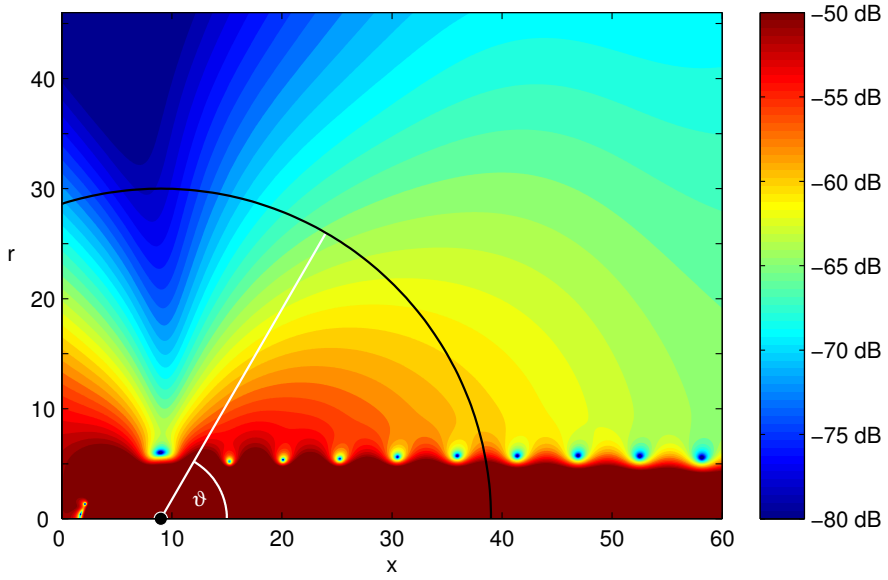

Figure 11: Isocontours of the pressure amplitude in the acoustic far field of a jet with $S = 0.3$. The apparent sound source on the jet axis is located at $x = 9$. The directivity pattern in figure 12 is extracted along the arc of radius 30. From reference [L5].

of such eigenmodes, second, because the arc branch is notoriously dependent on the computational domain size. The nature of these modes craved an explanation.

It was demonstrated that arc branch modes in jets arise from the coupling of downstream-propagating shear instability waves and upstream-reaching pressure feedback [L19]. The latter originates as a spurious effect at the numerical outflow, and it provokes perturbations at the numerical inflow, where shear instabilities can be triggered. The study shows that explicit inflow-outflow coupling in a Ginzburg–Landau model produces an arc branch very similar to the one found in open shear flows. It is further confirmed that arc branch modes of a parallel jet depend on the presence of spurious forcing of a local k^+ instability wave at the inflow, caused by pressure signals that appear to be generated at the outflow. Absorbing layers, or sponge zones, are suggested and tested as a technical means to reduce the effect of spurious pressure feedback from artificial domain boundaries.

3.4 Acoustic radiation from oscillating hot jets

[L5] L. Lesshafft, P. Huerre & P. Sagaut (2010): Aerodynamic sound generation by global modes in hot jets. *J. Fluid Mech.* vol. 647, p. 473–489

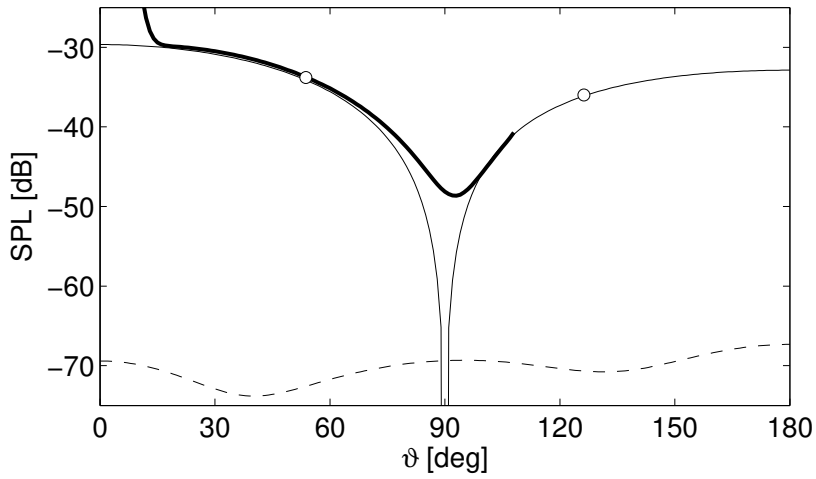

Figure 12: Directivity of the acoustic far field, comparison between direct numerical simulation and Lighthill solution. Thick solid line: directly computed sound; thin solid line: Lighthill solution from enthalpy-flux term alone; dashed line: combined radiation from all other terms. The absolute SPL level is not adjusted, but follows directly from the data analysis. From reference [L5].

Jet instability studies are in large measure motivated by the problem of jet noise. The noise that is emitted by the regular formation of vortex rings in a hot jet is available from the direct numerical simulations performed during my Ph.D., and it is accessible for an investigation into the underlying acoustic source mechanisms.

A configuration with Reynolds number $Re = 1000$, Mach number $Ma = 0.1$ and density ratio $S = 0.3$ is chosen as the baseline case (density ratios 0.1 and 0.2 are also considered. The acoustic far field, extracted from the DNS and shown in figure 11, is found to be of dipole character: the pressure amplitude varies with the observation angle ϑ (measured from the jet axis) as $\hat{p} \propto \cos\vartheta$.

In order to identify the acoustic source mechanisms, far-field solutions of the Lighthill equation are constructed, under the Fraunhofer approximation and under the assumption of radially compact, axisymmetric near-field source distributions. These solutions permit the isolation of contributions from individual source terms to the total acoustic far field. The source distributions are evaluated from the numerical simulation data.

A first attempt [L65], based on the original source terms of the Lighthill equation, gave unsatisfactory results, because (i) the Lighthill equation only contains monopole and quadrupole sources, (ii) as a result, the acoustic extinction angle was inaccurately reproduced and (iii) the dominant source term was found to be the apparent 'entropy' fluctuation, which does not lead to a clear physical interpretation in the presence of

strong density variations. Instead, Lilley's [30] reformulation of the Lighthill source terms was employed with success. Dipole components appear explicitly in this formulation, and it was shown that the dominant contribution by far arises from the dipole source related to the axial flux of enthalpy in the oscillating jet. This isolated component is compared to the total sound field in figure 12 (solid lines). In this highly synchronised flow case, the acoustic source region is quite compact in the axial direction, and antenna effects are therefore not pronounced.

4 Secondary global instabilities of incompressible jets

Moving onwards from linear analysis of primary instabilities in steady jet base flows, the study project of Léopold Shaabani Ardali's Ph.D. work targets the *secondary* instability of axisymmetric vortex streets in a jet. Two particularly striking instances of secondary instability phenomena are considered:

a) **vortex pairing** as a self-sustained process,

b) **jet bifurcation** [49] as an extrinsically forced process.

Both scenarios, as observed in experiments and in numerical simulations, appear to be of a fundamentally nonlinear nature, yet we approach them in a linear framework. Vortex pairing, arising from inherent mechanisms, is formalised as a modal Floquet problem and complemented by an analysis of transient growth. Jet bifurcation, relying on subharmonic actuation at the nozzle, is investigated as a non-modal optimal forcing problem. The analysis in both cases is based on a *time-periodic* base flow, represented by the axisymmetric T-periodic vortex street resulting from T-periodic forcing of the primary instability at the inlet.

4.1 Vortex pairing as a Floquet instability

[L17] L. Shaabani-Ardali, D. Sipp & L. Lesshafft (2017): Time-delayed feedback technique for suppressing instabilities in time-periodic flow. *Phys. Rev. Fluids* vol. 2, no. 113904

[L21] L. Shaabani Ardali, D. Sipp & L. Lesshafft (2018): Vortex pairing in jets as a global Floquet instability: modal and transient dynamics. *J. Fluid Mech.*, in press

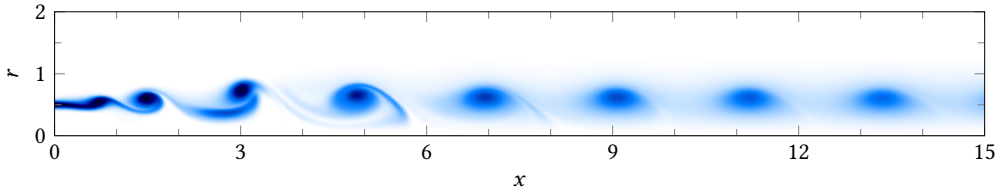

Figure 13: Vortex pairing in a harmonically forced jet, for $St_D = 0.6$, $Re = 2000$ and an inflow forcing amplitude $A = 0.05$. From [L21].

Motivation Vortex pairing, visualised in figure 13 has long been described as a secondary instability of a regular vortex street, both in plane shear layers and in jets. The underlying vortex street arises from the primary shear instability, typically in response to harmonic forcing at the nozzle. If this primary forcing is T-periodic, characterised by the *fundamental* Strouhal number $St_D = D/TU_j$ based on jet diameter and exit velocity, the pairing process is $2T$-periodic, and therefore a *subharmonic* instability is expected. Much work in the 1980s and 1990s was directed at the conditions under which subharmonic perturbations can grow in vortex streets, principally based on the resonance criterion formulated by Monkewitz [39]; it was even suspected that the global feedback mechanism behind vortex pairing underpinned the development of jet turbulence [29]. Yet no quantitative *global* stability analysis of the vortex pairing phenomenon had ever been undertaken.

Our study analyses the instability properties of a spatially developing T-periodic vortex street, as it arises due to harmonic forcing at the inflow, in the framework of Floquet theory [17].

Methodology Prior to performing instability analysis, the T-periodic base flow is obtained from nonlinear DNS. However, as this base flow may be unstable with respect to pairing, all non-T-periodic perturbations must be artificially stabilised. Harmonic modulations of the inlet jet velocity are imposed, with Strouhal number St_D and forcing amplitude A, such that the time-dependent inflow condition is prescribed as $U(r, z = 0, t) = [1 + A\sin(2\pi St_D t)]\tilde{U}(r)$. Similar to the technique of *selected frequency damping*, commonly applied in order to compute unstable *steady* base flows, Léopold Shaabani Ardali devised a method based on *time-delay control* [L17], which damps differences between the flow states at times t and $t - T$, and which is maximally efficient for eliminating subharmonic fluctuations. By the time of submission of this first article, we realised that this technique constitutes a special case of the delayed feedback control method described by Pyragas [48], used in the context of low-dimensional chaotic systems.

Floquet instability is characterised by the presence of Floquet multipliers μ_i with an absolute value larger than unity, denoting modal perturbation growth over one

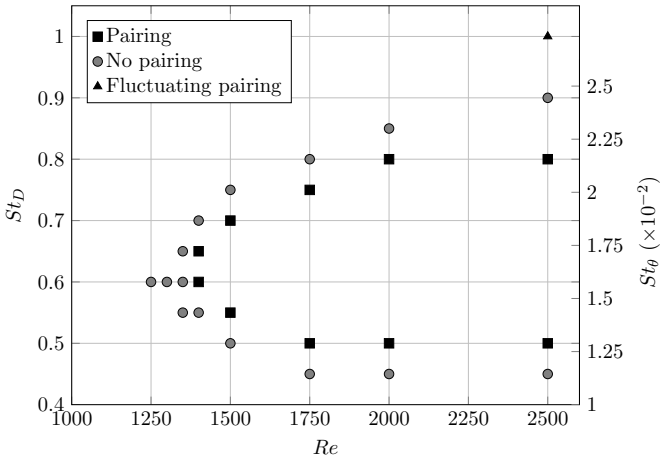

Figure 14: Occurrence of vortex pairing in direct numerical simulations, for an inflow forcing amplitude $A = 0.05$. From reference [L21].

flow period T. These multipliers are found as the eigenvalues of the linear time-shift operator Φ that propagates a small perturbation from time 0 to T. The eigenvalues are computed by projecting Φ onto an orthonormal basis of a Krylov subspace, using only linear time-stepping of the linearised flow equations. The linear time-stepping is implemented in FreeFEM++, and a block-Arnoldi algorithm [51] is employed in order to construct the orthonormal Krylov basis with maximum efficiency.

The possibility of transient perturbation growth in the time-periodic base flow is again explored by means of singular value decomposition, as described by Barkley *et al.* [4]. A special twist of the numerical procedure permits us to construct the leading singular modes solely based on the same Krylov basis that is already available from the modal analysis, without the need for further time-stepping. In particular, contrary to the procedure given by Barkley *et al.* [4], no adjoint time-stepping is required.

Results The study starts out from a parametric survey of the spontaneous occurrence of vortex pairing in direct numerical simulations, in the absence of artificial stabilisation. Simulations of the nonlinear flow development are performed with the Nek5000 code, restricted to an axisymmetric geometry. Both the Strouhal and the Reynolds number are varied systematically, for three different values $A = 0.01$, 0.05 and 0.1. As a result of the inflow modulations and the primary jet instability, the shear layer rolls up into a regular street of ring vortices, with a passage Strouhal number equal to St_D. Self-sustained vortex pairing is observed in these simulations in a specific region of the St_D/Re plane, delineated by a "neutral curve", which depends on A. Figure 14 shows these empirical results for the standard forcing amplitude values $A = 0.05$.

The first question is whether the occurrence of self-sustained vortex pairing is linked to the presence of a linear instability of the T-periodic (i.e. unpaired) base flow. Using the time-delay stabilisation technique [L17], which only involves adding a control force that depends linearly on the difference of the flow state at times t and $t - T$, strictly T-periodic flows are computed. Modal Floquet analysis is performed for $A = 0.05$, along two paths in the St_D/Re plane, once varying Re at constant $St_D = 0.6$ and once varying St_D at constant $Re = 2000$. Along both paths, unstable eigenvalues are found to arise precisely over the parameter regime where vortex pairing occurs in the DNS. Furthermore, these unstable eigenvalues are real and negative; in other words, their complex phase is π. This characterises the associated perturbation mode as being *subharmonic* with respect to the T-periodic forcing, as one would expect for the vortex pairing instability. It is concluded that vortex pairing, as a $2T$-periodic limit cycle, is indeed the result of a subharmonic Floquet instability.

However, the transition from an unstable unpaired towards a paired state, in typical simulations, exhibits stronger growth and different spatial distributions than what the modal analysis predicts. In order to better describe the transient dynamics by which this bifurcation takes place, the *optimal perturbation* for transient growth is computed. Non-modal analysis predicts strong transient growth of perturbations close to the jet inlet, in good agreement with DNS observations. At $St_D = 0.6$ and $Re = 2000$, a modally unstable setting, the optimal perturbation provides an amplitude gain of five orders of magnitude over the purely modal growth.

4.2 Optimal forcing of jet bifurcation

[L23] L. Shaabani-Ardali, L. Lesshafft & D. Sipp: Optimal triggering of jet bifurcation. In preparation for *J. Fluid Mech.*

Motivation The phenomenon of jet bifurcation is chosen as a particularly interesting effect of active flow control exploiting a secondary instability of a periodic flow. Under suitable actuation at the inflow, a jet splits into two separate streams of vortex rings in a zipper-like fashion (see figure 15). The actuation is composed of an axisymmetric component of Strouhal number St_D and an added helical subharmonic component of $St_D/2$. While the axisymmetric component sets up the basic T-periodic vortex street, as in the previous section, the helical component imparts a left/right displacement to each vortex ring, which is amplified as the vortices propagate downstream. The rather drastic split-up of the fundamental vortex street occurs once the subharmonic perturbation reaches nonlinear amplitude levels, but we suspect that linear instability mechanisms acting within the periodic base flow provide the necessary amplification that leads up to the parting of the streams.

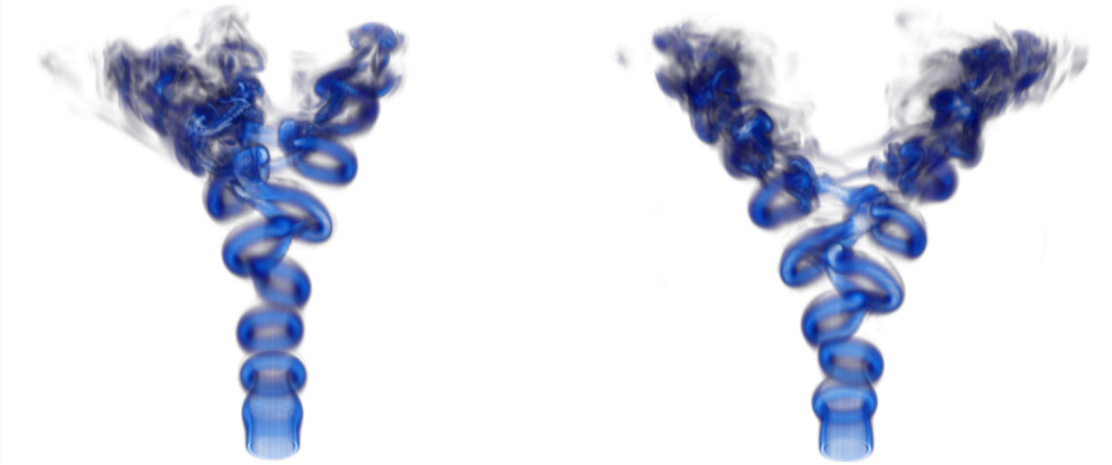

(a) nozzle flapping (b) optimal forcing

Figure 15: Direct numerical simulation of jet bifurcation at $St_D = 0.5$ and $Re = 2000$, snapshots of vorticity contours. (a) "traditional" subharmonic forcing in the form of nozzle flapping; (b) optimal subharmonic forcing, as identified by linear analysis. From [L23].

The unstable vortex dynamics can be worked out qualitatively by three-fingered hand-wringing, as explained by Reynolds *et al.* [49]. Yet the quantitative analysis requires global input-output computations, similar to those discussed in §2.2, adapted to time-periodic base flows. Hitherto unexplored, optimal forcing strategies for jet bifurcation can then be identified.

Methodology The base flow computations are performed in the same way as described in the previous section, using the Nek5000 code for nonlinear axisymmetric DNS, with added stabilisation of non-T-periodic components [L17]. These computations fully account for the axisymmetric forcing that leads to the formation of the basic vortex street. The evolution of *linear* helical subharmonic perturbations within this axisymmetric and T-periodic base flow is calculated via linear time-stepping in FreeFEM++.

Continuous subharmonic forcing is applied only in the inlet plane $z = 0$, by prescribing helical perturbations in all three velocity components as a boundary condition. Radial distributions are chosen in the form of Bessel functions (J_0, J_1 and J_2), combined such as to respect the compatibility conditions on the axis and as to ensure that the velocity field is divergence-free. Linear time-stepping is performed for a large number of such boundary conditions, which form an orthogonal basis for inflow velocity perturbations, until the long-time asymptotic flow response is obtained for each of

them. Coefficients for the optimal superposition of forcing basis functions are readily obtained for any given objective in the linear flow response.

Results The objective of optimal triggering of jet bifurcation is formalised in two ways: first, we aim to maximise the standard L_2 norm of subharmonic velocity perturbations in the flow response to unit-L_2-norm forcing. This represents an integral measure of subharmonic kinetic energy gain in the flow domain. Second, we consider a specifically tailored norm of the flow response that measures the *radial displacement* of base flow vortices, which corresponds more directly to the intended effect of triggering bifurcation of the vortex street. It is found however that both formulations lead to nearly identical shapes of the optimal forcing.

In previous numerical simulations of jet bifurcation, for instance by [60], the shape of helical inflow forcing was prescribed such as to represent a low-amplitude left/right flapping of the jet nozzle. Using our optimised forcing distribution in three-dimensional DNS, it is found that the splitting of the vortex street is more vigorous, and achievable over a larger range of St_D, than with simple nozzle flapping. Figure 15 compares snapshots from simulations, at $St_D = 0.5$ and $Re = 2000$, with flapping and with optimal forcing. The injected kinetic energy of the subharmonic velocity perturbations is identical in both cases.

5 Perspectives

5.1 Flame instability

Flames constitute a family of flows that are similar to jets and plumes in many respects, with the added ingredient of chemical reaction and heat release. Unsteadiness in combustion processes, due to instability phenomena, is a cause for loss of performance, increased pollution, and structural damage of combustion engines. These phenomena involve multi-physics and multi-scale mechanisms, through the coupling of heat release, gas flow and acoustics.

Over the past three years, I have attempted linear analysis of several flame configurations. Together with postdoc Onofrio Semeraro, building on the Ph.D. work of Mathieu Blanchard at LadHyX, we first investigated the instability of a premixed "M-flame" in an annular burner [7], by means of modal as well as input-output analysis [L58]. The annular burner consists of a pipe, from where the premixed fuel-air stream exits into a large combustion chamber, and a thin cylindrical rod, concentrically fixed inside the pipe. A flame of the M-type attaches to the exterior rim of the inflow pipe and to the interior rim of the rod. Mesh and base flow (methane volume fraction) in the flame region are shown in figure 16. An Arrhenius law is used to model the reaction rate [7].

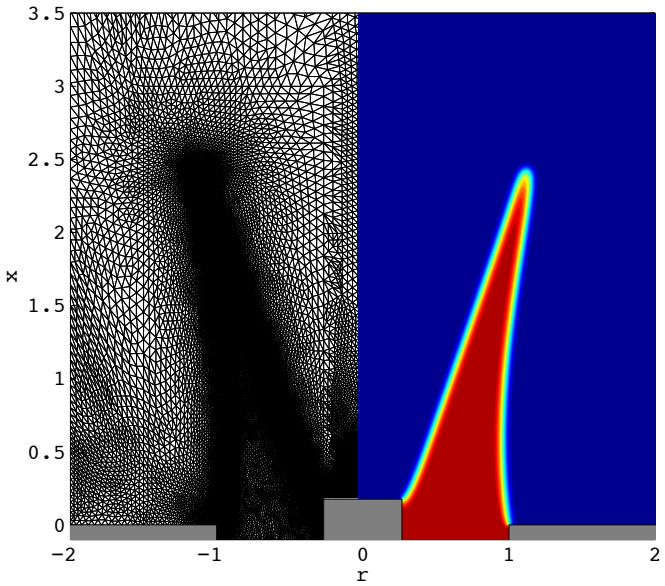

Figure 16: Geometry, mesh and base flow (methane volume fraction) of an M-flame. The base flow is taken from [7] and interpolated onto the FEM mesh.

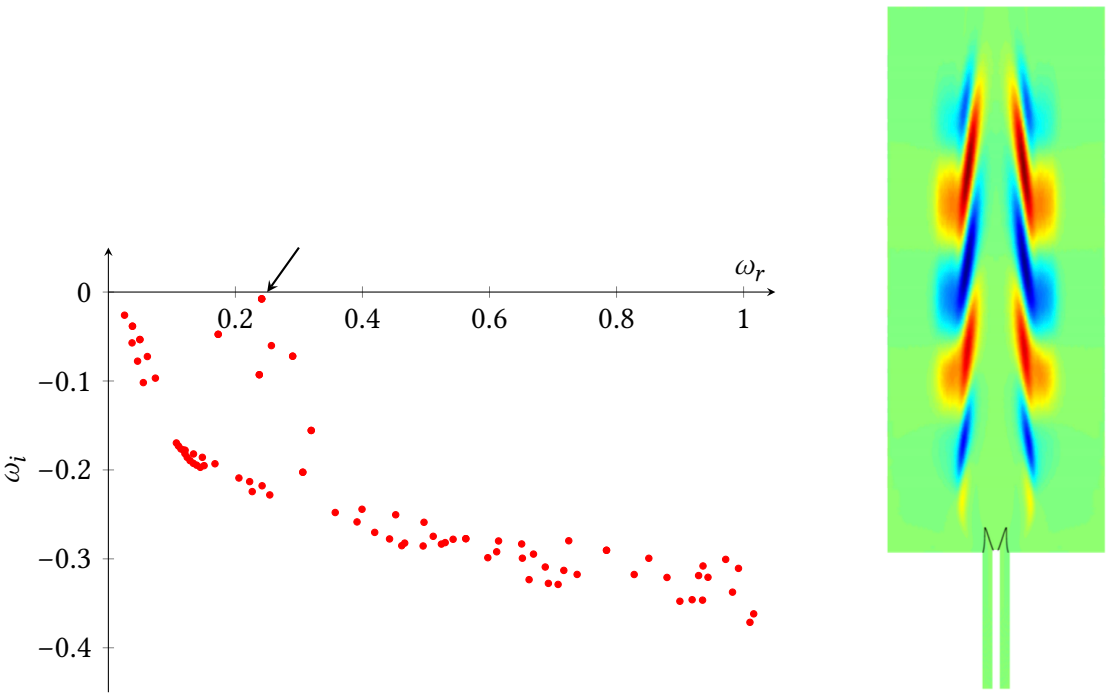

Figure 17: Left: eigenvalue spectrum of the M-flame (axisymmetric perturbations only). Right: Snapshot of temperature fluctuations associated with the least stable mode. The flame front is drawn as a black line.

Experiments indicate that this flame configuration does not exhibit self-excited behaviour, but that it is highly receptive to incoming perturbations. Our linear analysis reproduces this receptivity in a narrow frequency band, where the energy gain between flow response and applied forcing peaks sharply. This behaviour is the result of a resonance, caused by a slightly stable eigenmode of the flame spectrum displayed in figure 17. This eigenmode is accessible to a detailed analysis of its intrinsic mechanisms, by way of the wavemaker in the sense of section 3.3.1. It is thus found that the instability is dominated by simple shear mechanisms, which act mainly outside the flame region and give rise to strong oscillations ("puffing") in the plume. Fluctuations of reaction rate and heat release only play a passive part in driving this instability. The role of combustion in this context, as it turns out, is only to set up the basic shear flow state through buoyancy.

We carried out similar calculations for laminar "V-flames" and turbulent swirl flames, with base flows provided by Kilian Oberleithner at TU Berlin. All these analyses suffer from severe uncertainty about the appropriate chemistry modelling, and from the unavailability of accurate density and temperature fields. Our current efforts, led by Léopold Shaabani Ardali and myself, are concentrated on a simple premixed conical flame of a Bunsen burner, for which the base flow is contributed by our partners Bénédicte Cuenot and Laurent Gicqel at CERFACS, computed in direct numerical simulations with the AVBP code.

5.2 Semi-empirical modelling of noise from installed jets in flight

Following up on the mostly fundamental research within the ANR Cool Jazz project, our new project "DARETOMODEL" in the H2020 CleanSky2 program is a step higher up on the TR-scale. This project is led by Peter Jordan (Institut Pprime), with Anurag Agarwal (University of Cambridge), Jérôme Huber (Airbus) and myself as partners.

The objective is to construct low-rank models for the prediction of noise radiated from engine jets, in the presence of a wing, and with co-flow as in flight conditions. The noise source is to be modelled as a stochastic wavepacket, with an amplitude envelope function obtained from parabolised Navier–Stokes computations. The associated sound field may then be constructed from the Green's function, which can be modified in order to account for the effect of a wing surface and co-flow. An important unanswered question in this context is how turbulence may realistically be modelled in the form of non-white forcing of a linear system, and if the concept of turbulent viscosity may be adapted in order to capture a portion of turbulence effects on coherent perturbation statistics.

6 Publications and Conferences

6.1 Journal publications

[L1] L. Lesshafft, P. Huerre, P. Sagaut & M. Terracol, 2006:
Nonlinear global modes in hot jets
J. Fluid Mech., vol. 554 (50^{th} anniversary volume), 393–409

[L2] L. Lesshafft & P. Huerre, 2007:
Linear impulse response in hot round jets
Phys. Fluids, vol. 19, no. 024102

[L3] L. Lesshafft, P. Huerre & P. Sagaut, 2007:
Frequency selection in globally unstable round jets
Phys. Fluids, vol. 19, no. 054108

[L4] B. Selvam, L. Talon, L. Lesshafft & E. Meiburg, 2009:
Convective/absolute instability in miscible core–annular flow. Part 2. Numerical simulations and nonlinear global modes
J. Fluid Mech., vol. 618, 323–348

[L5] L. Lesshafft, P. Huerre & P. Sagaut, 2010:
Aerodynamic sound generation by global modes in hot jets
J. Fluid Mech., vol. 647, 473–48

[L6] L. Lesshafft & O. Marquet, 2010:
Optimal velocity and density profiles for the onset of absolute instability in jets
J. Fluid Mech., vol. 662, 398–408

[L7] L. Lesshafft, E. Meiburg, B. Kneller & A. Marsden, 2011:
Towards inverse modeling of turbidity currents: the inverse lock-exchange problem
Comput. Geosci., vol. 37, 521–529

[L8] L. Lesshafft, B. Hall, E. Meiburg & B. Kneller, 2011:
Deep-water sediment wave formation: linear stability analysis of coupled flow/bed interaction
J. Fluid Mech., vol. 680, 435–458

[L9] X. Garnaud, L. Lesshafft, P. Schmid & J.-M. Chomaz, 2012:
A relaxation method for large eigenvalue problems, with an application to flow stability analysis
J. Comput. Phys., vol. 231(10), 3912–3927

[L10] X. Garnaud, L. Lesshafft, P. Schmid & P. Huerre, 2013:
Modal and transient dynamics of jet flows
Phys. Fluids, vol. 25, no. 044103

[L11] X. Garnaud, L. Lesshafft, P. Schmid & P. Huerre, 2013:
The preferred mode of incompressible jets: linear frequency response analysis
J. Fluid Mech., vol. 716, 189–202

[L12] L. Lesshafft, 2015:
Linear global stability of a confined plume
Theor. Appl. Mech. Lett., vol. 5, p. 126-128

[L13] R. Chakravarthy, L. Lesshafft & P. Huerre, 2015:
Local linear stability of laminar axisymmetric plumes
J. Fluid Mech., vol. 780, p. 344-369

[L14] S. Beneddine, D. Sipp, A. Arnault, J. Dandois & L. Lesshafft, 2016:
Conditions for validity of mean flow stability analysis
J. Fluid Mech., vol. 798, p. 485-504

[L15] O. Semeraro, L. Lesshafft, V. Jaunet & P. Jordan, 2016:
Modeling of coherent structures in a turbulent jet as global linear instability wavepackets: theory and experiment
Int. J. Heat Fluid Flow, vol. 62A, p. 24-32

[L16] W. Coenen, L. Lesshafft, X. Garnaud & A. Sevilla, 2017:
Global instability of low-density jets
J. Fluid Mech., vol. 820, p. 187-207

[L17] L. Shaabani Ardali, D. Sipp & L. Lesshafft, 2017:
Time-delayed feedback technique for suppressing instabilities in time-periodic flow
Phys. Rev. Fluids, vol. 2, 113904

[L18] R. Chakravarthy, L. Lesshafft & P. Huerre, 2018:
Global stability of buoyant jets and plumes
J. Fluid Mech., vol. 835, p. 654-673

[L19] L. Lesshafft, 2018:
Artificial eigenmodes in truncated flow domains
Theor. Comp. Fluid Dyn., vol. 32, p. 245-262

[L20] N. Konopliv, L. Lesshafft & E. Meiburg, 2018:
The influence of shear on double-diffusive and settling-driven instabilities
J. Fluid Mech., vol. 849, p. 902-926

[L21] L. Shaabani Ardali, D. Sipp & L. Lesshafft 2018:
Vortex pairing in jets as a global Floquet instability: modal and transient dynamics
J. Fluid Mech., in press

[L22] L. Lesshafft, O. Semeraro, V. Jaunet, A.V.G. Cavalieri & P. Jordan:
Resolvent-based modelling of coherent wavepackets in a turbulent jet
arXiv 1810.09340, submitted to *Phys. Rev. Fluids*

[L23] L. Shaabani Ardali, L. Lesshafft & D. Sipp:
Optimal triggering of jet bifurcation
in preparation for *J. Fluid Mech.*

6.2 Conference presentations

[L24] L. Lesshafft, P. Huerre, P. Sagaut & M. Terracol:
Global modes in hot jets, absolute/convective instabilities and acoustic feedback
AIAA Paper 2005-3040, presented at the 11^{th} AIAA Aeroacoustics Conference
May 2005, Monterey, California

[L25] L. Lesshafft, P. Huerre, P. Sagaut & M. Terracol:
Global modes in hot jets and their acoustic far field
58^{th} annual meeting of the APS Division of Fluid Dynamics
November 2005, Chicago, Illinois

[L26] L. Lesshafft, P. Huerre & P. Sagaut:
Sound radiation from instability waves in subsonic jets: entropy sound and superdirectivity
59^{th} annual meeting of the APS Division of Fluid Dynamics
November 2006, Tampa, Florida

[L27] L. Lesshafft, E. Meiburg & B. Kneller:
Sediment deposition from buoyant river plumes
60^{th} annual meeting of the APS Division of Fluid Dynamics
November 2007, Salt Lake City, Utah

[L28] L. Lesshafft, E. Meiburg & B. Kneller:
Numerical modelling of sediment deposition from buoyant river plumes
Euromech Coll. 501 "Mixing of coastal, estuarine and riverine shallow flows"
June 2008, Ancona, Italie

[L29] a) L. Lesshafft, B. Hall, E. Meiburg & B. Kneller:
Sediment waves: coupled flow/sediment-bed instability in turbidity currents
b) L. Lesshafft, P. Huerre & P. Sagaut:
Sound radiation from self-sustained oscillations in a hot jet
7^{th} Euromech Fluid Mechanics Conference (EFMC7)
September 2008, Manchester, UK

[L30] a) L. Lesshafft, E. Meiburg & B. Kneller:
Inverse modeling: reconstructing the initial conditions of a turbidity current
b) B. Hall, L. Lesshafft, E. Meiburg & B. Kneller:
Sediment wave formation by turbidity currents: a Navier-Stokes based linear stability analysis
61^{st} annual meeting of the APS Division of Fluid Dynamics
November 2008, San Antonio, Texas

[L31] a) L. Lesshafft, E. Meiburg & B. Kneller:
Inverse modeling of sediment deposition from turbidity currents
b) L. Lesshafft, B. Hall, E. Meiburg & B. Kneller:
Linear instabilities in a turbidity current boundary layer
CSDMS Workshop "Modeling of turbidity currents and related gravity currents"
June 2009, Santa Barbara, California

[L32] a) L. Lesshafft, B. Hall, E. Meiburg & B. Kneller:
Sediment wave formation by unstable internal waves in a turbidity current boundary layer
b) P. Burns, L. Lesshafft & E. Meiburg:
Instability Phenomena in Stratified, Particle-laden Flow
62^{nd} annual meeting of the APS Division of Fluid Dynamics
November 2009, Minneapolis, Minnesota

[L33] L. Lesshafft, E. Meiburg & B. Kneller:
Sediment deposition from turbidity currents: inverse modeling and instability phenomena
Hydrodynamique des Lacs et Approximation de St Venant
January 2010, Paris, France

[L34] L. Lesshafft, B. Hall, E. Meiburg & B. Kneller:
Hydrodynamic instabilities in a turbidity current boundary layer as a mechanism for sediment wave formation
Deep-water circulation: processes & products
Juin 2010, Baiona, Spain

[L35] L. Lesshafft & O. Marquet:
Sensitivity-based optimization of jet profiles for the onset of absolute instability
8^{th} Euromech Fluid Mechanics Conference (EFMC8)
September 2010, Bad Reichenhall, Germany

[L36] X. Garnaud, L. Lesshafft, P. Schmid & P. Huerre:
Global modes of compressible subsonic jets
63^{th} annual meeting of the APS Division of Fluid Dynamics
November 2010, Long Beach, California

[L37] X. Garnaud, L. Lesshafft & P. Huerre:
Global linear stability of a model subsonic jet
AIAA Paper 2011-3608, presented at the 41^{st} AIAA Fluid Dynamics Conference
June 2011, Honolulu, Hawaii

[L38] L. Lesshafft, B. Hall, E. Meiburg & B. Kneller:
Hydrodynamic instabilities in turbidity currents as mechanisms for bed-form creation
7th Int. Symp. on Stratified Flows
August 2011, Rome, Italy

[L39] L. Lesshafft, X. Garnaud, P. Huerre & P. Schmid:
Global stability of subsonic jets
ERCOFTAC Workshop
September 2011, Toledo, Spain

[L40] X. Garnaud, L. Lesshafft, P. Schmid &P. Huerre :
Stabilité globale d'un jet laminaire subsonique
20^{e} Congrès Français de Mécanique
August 2011, Besançon, France

[L41] L. Lesshafft, X. Garnaud, P. Huerre & P. Schmid:
Linear forcing response of subsonic jets
64^{th} annual meeting of the APS Division of Fluid Dynamics
November 2011, Baltimore, Maryland

[L42] X. Garnaud, L. Lesshafft, P. Schmid & P. Huerre:
Linear mechanisms of the sensitivity of jets to external forcing
23^{rd} ICTAM, August 2012, Beijing, China

[L43] a) X. Garnaud, L. Lesshafft, P. Schmid & P. Huerre:
Global frequency response in subsonic jets
b) X. Garnaud, L. Lesshafft, P. Schmid & P. Huerre:
Global instability of jets: limitations of a modal approach
9th Euromech Fluid Mechanics Conference
September 2012, Rome, Italy

[L44] X. Garnaud, L. Lesshafft, P. Schmid & P. Huerre:
Preferred modes in jets: comparison between different measures of receptivity
65^{th} annual meeting of the APS Division of Fluid Dynamics
November 2012, San Diego, California

[L45] S. Derebail, X. Garnaud, L. Lesshafft, P. Schmid & P. Huerre:
Instabilités dans les jets et les panaches
16^{e} Rencontre du Non-linéaire, March 2013, Paris, France

[L46] X. Garnaud, R. Sandberg & L. Lesshafft:
Global response to forcing in a subsonic jet: instability wavepackets and acoustic radiation
AIAA Paper 2013-2232
19th AIAA/CEAS Aeroacoustics Conference
May 2013, Berlin, Germany

[L47] X. Garnaud, L. Lesshafft & P. Huerre:
Global flow response of a RANS jet to inflow forcing
Euromech Colloquium "Trends in Open Shear Flow Instability",
June 2013, École polytechnique, France

[L48] W. Coenen, A. Sevilla & L. Lesshafft:
The influence of the density ratio on the linear frequency response of low-density jets
66^{th} annual meeting of the APS Division of Fluid Dynamics
November 2013, Pittsburgh, Pennsylvania

[L49] a) L. Lesshafft & O. Marquet:
"Wavemakers" — how do we identify what drives an eigenmode?
b) O. Marquet & L. Lesshafft:
Global stability of three-dimensional wake flows developing behind

rectangular flat plates
Interdisciplinary Fluids Meeting, Madingley Hall, Cambridge, July 2014.

[L50] L. Lesshafft, W. Coenen, X. Garnaud & A. Sevilla:
Modal instability analysis of light jets
IUTAM-ABCM Symposium on Laminar-Turbulent Transition, Rio de Janeiro, September 2014.

[L51] a) L. Lesshafft, R.V.K. Chakravarthy & P. Huerre:
Local and global instability of free and confined plumes
b) O. Semeraro & L. Lesshafft:
Optimal forcing of subsonic jets
c) W. Coenen, L. Lesshafft, X. Garnaud & A. Sevilla:
Modal instability analysis of low-density jets
d) O. Marquet & L. Lesshafft:
Steady and unsteady three-dimensional bifurcations in separated flow
10th European Fluid Mechanics Conference, Copenhagen, September 2014.

[L52] a) O. Semeraro, L. Lesshafft & R. Sandberg:
Wavepackets in subsonic jets using optimal forcing
b) W. Coenen, L. Lesshafft, X. Garnaud & A. Sevilla:
Global mode and frequency response analysis of low-density jets
c) R.V.K. Chakravarthy, L. Lesshafft & P. Huerre:
Local stability of axisymmetric plumes
59th meeting of the American Physical Society, San Francisco, November 2014.

[L53] L. Lesshafft & O. Marquet:
Unsteady wavemakers: how to identify instability mechanisms in propagating nonlinear wavefronts
11th ERCOFTAC SIG 33 Workshop on Progress in Transition Modelling and Control, Jersey, 2015

[L54] a) O. Marquet & L. Lesshafft:
Is the frequency of finite-amplitude time- periodic instabilities selected by the mean flow or the eddies interaction?
b) L. Lesshafft & O. Marquet:
How to characterize the instability source in linear and nonlinear global modes
c) O. Semeraro, L. Lesshafft, V. Jaunet, P. Jordan & R. Sandberg:
Coherent structures in turbulent jets: a numerical-experimental analysis
Bifurcations and Instabilities in Fluid Dynamics, Paris, 2015

[L55] L. Lesshafft & O. Marquet:
Endogeneity analysis of linear and nonlinear global modes
ERCOFTAC Symposium on Global Flow Instability and Control, Crete, 2015

[L56] a) R.V.K. Chakravarthy, L. Lesshafft & P. Huerre:
Effect of Buoyancy on the Instability of Light Jets and Plumes
b) O. Semeraro, L. Lesshafft & R. Sandberg:
Can jet noise be predicted using linear instability wavepackets?
c) L. Lesshafft, O. Semeraro, V. Jaunet & P. Jordan:
Modeling of coherent structures in a turbulent jet as global linear instability wavepackets: theory and experiment
Proceedings of the 5th International Conference on Jets, Wakes and Separated Flows, Stockholm, 2015

[L57] O. Semeraro, V. Jaunet, P. Jordan, A. Cavalieri & L. Lesshafft:
Stochastic and harmonic optimal forcing in subsonic jets
AIAA Paper 2016-2935
22th AIAA/CEAS Aeroacoustics Conference, Lyon, 2016

[L58] a) L. Lesshafft, M. Blanchard & O. Semeraro:
Instability response of a premixed M-flame to harmonic and stochastic forcing
b) S. Beneddine, D. Sipp, A. Arnault, J. Dandois & L. Lesshafft:
Conditions of validity for mean flow stability analysis and application to a turbulent backward-facing step case
c) L. Shaabani Ardali, L. Lesshafft & D. Sipp:
Vortex pairing in a jet as an unstable Floquet mode
d) O. Marquet & L. Lesshafft:
Identifying the frequency selection of fluid/solid modes when the interaction is large
e) O. Semeraro, V. Jaunet, P. Jordan & L. Lesshafft:
Stochastic and deterministic optimal forcing in subsonic jets: an experimental and numerical analysis
11th European Fluid Mechanics Conference, Sevilla, 2016

[L59] a) P. Huerre, R.V.K. Chakravarthy & L. Lesshafft:
Local and global instability of buoyant jets and plumes
b) S. Beneddine, A. Arnault, R. Yegavian, D. Sipp, J. Dandois, B. Leclaire & L. Lesshafft:
Stability analysis of the mean field to determine coherent structures in a turbulent backward-facing step flow
c) O. Marquet & L. Lesshafft:

A new formalism for identifying wavemaker regions of linear instabilities: application to a spring-mounted cylinder
XXIV International Congress of Theoretical and Applied Mechanics, Montréal, 2016

[L60] a) L. Shaabani Ardali, L. Lesshafft & D. Sipp:
Vortex pairing and Floquet instability
b) L. Lesshafft, O. Semeraro, V. Jaunet, A. Cavalieri & P. Jordan:
Modelling of large-scale dynamics in a stochastically driven jet
Euromech Colloquium and IUTAM Symposium "Jet Noise Modelling and Control", Palaiseau, 2016

[L61] a) L. Lesshafft, R.V.K. Chakravarthy & P. Huerre:
The multifold effects of density on the instability of jets, plumes and premixed flames
b) L. Shaabani Ardali, D. Sipp & L. Lesshafft:
Subharmonic instability mechanisms of the bifurcation phenomenon in harmonically forced jets
12th ERCOFTAC SIG 33 Workshop on Progress in Flow Instability, Transition and Control, Siena, 2017

[L62] a) L. Lesshafft, O. Semeraro, V. Jaunet, P. Jordan & A.V.G. Cavalieri:
Modelling of coherent structures in turbulent jets at high Reynolds number by mean flow instability analysis
b) L. Shaabani Ardali, D. Sipp & L. Lesshafft:
Optimal forcing for jet bifurcation
16th European Turbulence Conference, Stockholm, 2017

[L63] a) L. Lesshafft, O. Semeraro, V. Jaunet, P. Jordan & A.V.G. Cavalieri:
Success and open questions in the modelling of jet turbulence through Statistical State Dynamics
b) L. Shaabani Ardali, D. Sipp & L. Lesshafft:
Mixing enhancement through optimally controlled jet bifurcation
13th ERCOFTAC SIG 33 Workshop on Progress in Flow Instability, Transition and Control, Paraty, 2018

[L64] a) L. Lesshafft, L. Shaabani Ardali, O. Semeraro, V. Jaunet, P. Jordan, A.V.G. Cavalieri, B. Cuenot & L. Gicquel:
Recovering the transfer function of a turbulent jet and a laminar flame from linear mean flow analysis
b) L. Shaabani Ardali, L. Lesshafft & D. Sipp:
Triggering symmetry-breaking secondary instabilities in pulsed jets and

flames
12th European Fluid Mechanics Conference, Vienna, 2018

6.3 Other

[L65] L. Lesshafft, 2006:
Nonlinear global modes and sound generation in hot jets
Ph.D. thesis, École Polytechnique, defended 11/12/2006

[L66] L. Lesshafft, 2012:
Le génome du bananier épluché
L'Express.fr, 13/07/2012

[L67] O. Marquet & L. Lesshafft, 2015:
Identifying the active flow regions that drive linear and nonlinear instabilities
arXiv:1508.07620

[L68] L. Lesshafft, 2015:
Preface to a Festschrift for Patrick Huerre
Eur. J. Mech. B/Fluids, vol. 49, p. 299–300

[L69] L. Lesshafft, P. Jordan & A. Agarwal 2018:
Foreword
C. R. Mecanique, vol. 346, p. 887–889

References

[1] E. Åkervik, L. Brandt, D.S. Henningson, J. Hœpffner, O. Marxen & P. Schlatter, 2006. **Steady solutions of the navier-stokes equations by selective frequency damping**. *Phys. Fluids*, vol. 18, art. 068102.

[2] F. Alizard, S. Cherubini & J.-C. Robinet, 2009. **Sensitivity and optimal forcing response in separated boundary layer flows**. *Phys. Fluids*, vol. 21, art. 064108.

[3] D. Barkley, 2006. **Linear analysis of the cylinder wake mean flow**. *Europhys. Lett.*, vol. 75, p. 750.

[4] D. Barkley, H.M. Blackburn & S.J. Sherwin, 2008. **Direct optimal growth analysis for timesteppers**. *Int. J. Num. Meth. Fluids*, vol. 57, p. 1435–1458.

[5] S. Beneddine, R. Yegavian, D. Sipp & B. Leclaire, 2017. **Unsteady flow dynamics reconstruction from mean flow and point sensors: an experimental study**. *J. Fluid Mech.*, vol. 824, p. 174–201.

[6] K.K. Bharadwaj & D. Das, 2017. **Global instability analysis and experiments on buoyant plumes**. *J. Fluid Mech.*, vol. 832, p. 97–145.

[7] M. Blanchard, T. Schuller, D. Sipp & P.J. Schmid, 2015. **Response analysis of a laminar premixed M-flame to flow perturbations using a linearized compressible Navier–Stokes solver**. *Phys. Fluids*, vol. 27, art. 043602.

[8] E. Boujo & F. Gallaire, 2015. **Sensitivity and open-loop control of stochastic response in a noise amplifier flow: the backward-facing step**. *J. Fluid Mech.*, vol. 762, p. 361–392.

[9] A.V.G. Cavalieri, D. Rodríguez, P. Jordan, T. Colonius & Y. Gervais, 2013. **Wavepackets in the velocity field of turbulent jets**. *J. Fluid Mech.*, vol. 730, p. 559–592.

[10] B.M. Cetegen & K.D. Kasper, 1996. **Experiments on the oscillatory behavior of buoyant plumes of helium and helium-air mixtures**. *Phys. Fluids*, vol. 8, p. 2974–2984.

[11] J.-M. Chomaz, P. Huerre & L.G. Redekopp, 1991. **A frequency selection criterion in spatially developing flows**. *Stud. Appl. Math.*, vol. 84, p. 119–144.

[12] W. Coenen, 2010. **Absolute instability in the near field of low-density jets**. PhD thesis, Universidad Carlos III de Madrid.

[13] W. Coenen, A. Sevilla & A.L. Sánchez, 2008. **Absolute instability of light jets emerging from circular injector tubes**. *Phys. Fluids*, vol. 20, art. 074104.

[14] S.C. Crow & F.H. Champagne, 1971. **Orderly structure in jet turbulence**. *J. Fluid Mech.*, vol. 48, p. 547–591.

[15] G. Dergham, D. Sipp & J.-C. Robinet, 2013. **Stochastic dynamics and model reduction of amplifier flows: the backward facing step flow**. *J. Fluid Mech.*, vol. 719, p. 406–430.

[16] B.F. Farrell & P.J. Ioannou, 2014. **Statistical State Dynamics: a new perspective on turbulence in shear flow**. arXiv:1412.8290.

[17] G. Floquet, 1883. **Sur les équations différentielles linéaires à coefficients périodiques**. In *Annales scientifiques de l'École Normale Supérieure*, vol. 12, p. 47–88.

[18] M. Fosas de Pando, D. Sipp & P.J. Schmid, 2012. **Efficient evaluation of the direct and adjoint linearized dynamics from compressible flow solvers**. *J. Comput. Phys.*, vol. 231, p. 7739–7755.

[19] X. Garnaud, 2012. **Modes, transient dynamics and forced response of circular jets**. PhD thesis, École polytechnique.

[20] F. Giannetti & P. Luchini, 2007. **Structural sensitivity of the first instability of the cylinder wake**. *J. Fluid Mech.*, vol. 581, p. 167–197.

[21] K. Gudmundsson & T. Colonius, 2011. **Instability wave models for the near-field fluctuations of turbulent jets**. *J. Fluid Mech.*, vol. 689, p. 97–128.

[22] M.P. Hallberg & P.J. Strykowski, 2006. **On the universality of global modes in low-density axisymmetric jets**. *J. Fluid Mech.*, vol. 569, p. 493–507.

[23] P. Huerre & P.A. Monkewitz, 1990. **Local and global instabilities in spatially developing flows**. *Annu. Rev. Fluid Mech.*, vol. 22, p. 473–537.

[24] Y. Hwang & C. Cossu, 2010. **Amplification of coherent streaks in the turbulent Couette flow: an input–output analysis at low Reynolds number**. *J. Fluid Mech.*, vol. 643, p. 333–348.

[25] V. Jaunet, P. Jordan & A.V.G. Cavalieri, 2017. **Two-point coherence of wave packets in turbulent jets**. *Phys. Rev. Fluids*, vol. 2, art. 024604.

[26] P. Jordan & T. Colonius, 2013. **Wave packets and turbulent jet noise**. *Annu. Rev. Fluid Mech.*, vol. 45, p. 173–195.

[27] J.M. Keynes, 1924. *A tract on monetary reform.* MacMillan & Co., London.

[28] D. Kyle & K.R. Sreenivasan, 1993. **The instability and breakdown of a round variable-density jet**. *J. Fluid Mech.*, vol. 249, p. 619–664.

[29] J. Laufer & P.A. Monkewitz, 1980. **On turbulent jet flows: a new perspective**. *AIAA Paper* 80-0962.

[30] G. M. Lilley, 1974. **On the noise from jets**. *AGARD-CP*, vol. 131, p. 13.1–13.12.

[31] J.-C. Loiseau, M.A. Bucci, S. Cherubini & J.-C. Robinet, to appear. **Time-stepping and Krylov methods for large-scale instability problems**. In A. Gelfgat, editor, *Computational Modeling of Bifurcations and Instabilities in Fluid Mechanics*, Springer Verlag.

[32] J.M. Lopez & F. Marques, 2013. **Instability of plumes driven by localized heating**. *J. Fluid Mech.*, vol. 736, p. 616–640.

[33] P. Luchini, F. Giannetti & J. Pralits, 2008. **Structural sensitivity of linear and nonlinear global modes**. *AIAA Paper* 2008-4227.

[34] O. Marquet & D. Sipp, 2010. **Global sustained perturbations in a backward-facing step flow**. In *Seventh IUTAM Symposium on Laminar-Turbulent Transition*, IUTAM Bookseries, vol. 18, p. 525–528.

[35] O. Marquet, D. Sipp & L. Jacquin, 2008. **Sensitivity analysis and passive control of cylinder flow**. *J. Fluid Mech.*, vol. 615, p. 221–252.

[36] P.A. McMurtry, J.J. Riley & R.W. Metcalfe, 1989. **Effects of heat release on the large-scale structure in turbulent mixing layers**. *J. Fluid Mech.*, vol. 199, p. 297–332.

[37] A. Michalke, 1965. **On spatially growing disturbances in an inviscid shear layer**. *J. Fluid Mech.*, vol. 23, p. 521–544.

[38] P. Monkewitz, 1990. **The role of absolute and convective instability in predicting the behavior of fluid systems**. *Eur. J. Mech. B/Fluids*, vol. 9, p. 395–413.

[39] P.A. Monkewitz, 1988. **Subharmonic resonance, pairing and shredding in the mixing layer**. *J. Fluid Mech.*, vol. 188, p. 223–252.

[40] P.A. Monkewitz, D.W. Bechert, B. Barsikow & B. Lehmann, 1990. **Self-excited oscillations and mixing in a heated round jet**. *J. Fluid Mech.*, vol. 213, p. 611–639.

[41] P.A. Monkewitz & K. Sohn, 1988. **Absolute instability in hot jets**. *AIAA J.*, vol. 26, p. 911–916.

[42] A. Monokrousos, E. Åkervik, L. Brandt & D.S. Henningson, 2010. **Global three-dimensional optimal disturbances in the blasius boundary-layer flow using time-steppers**. *J. Fluid Mech.*, vol. 650, p. 181–214.

[43] M. Morzyński, W. Szeliga & B. Noack, 2018. **Unstable periodically forced Navier–Stokes solutions - towards nonlinear first-principle reduced-order modeling of actuator performance**. arXiv:1804.08113.

[44] J.W. Nichols, 2005. **Simulation and stability analysis of jet diffusion flames**. PhD thesis, University of Washington.

[45] J.W. Nichols & S.K. Lele, 2011. **Global modes and transient response of a cold supersonic jet**. *J. Fluid Mech.*, vol. 669, p. 225–241.

[46] B. Noack, K. Afanasiev, M. Morzynski, G. Tadmor & F. Thiele, 2003. **A hierarchy of low-dimensional models for the transient and post-transient cylinder wake**. *J. Fluid Mech.*, vol. 497, p. 335–363.

[47] C. Picard & J. Delville, 2000. **Pressure velocity coupling in a subsonic round jet**. *Int. J. Heat Fluid Flow*, vol. 21, p. 359–364.

[48] K. Pyragas, 1988. **Continuous control of chaos by self-controlling feedback**. *Phys. Lett. A*, vol. 170, p. 421.

[49] W.C. Reynolds, D.E. Parekh, P.J. Juvet & M.J. Lee, 2003. **Bifurcating and blooming jets**. *Annu. Rev. Fluid Mech.*, vol. 35, p. 295–315.

[50] G. Rocco, T.A. Zaki, X. Mao, H. Blackburn & S.J. Sherwin, 2015. **Floquet and transient growth stability analysis of a flow through a compressor passage**. *Aerosp. Sci. Technol.*, vol. 44, p. 116–124.

[51] Y. Saad, 2001. *Numerical Methods for Large Eigenvalue Problems: Revised Edition.* SIAM.

[52] P.J. Schmid & D.S. Henningson, 2001. *Stability and transition in shear flows*, volume 142 of *Applied Mathematical Sciences.* Springer Verlag.

[53] O.T. Schmidt, A. Towne, G. Rigas, T. Colonius & G.A. Brès, 2018. **Spectral analysis of jet turbulence**. *J. Fluid Mech.*, vol. 855, p. 953–982.

[54] A. Sinha, D. Rodríguez, G.A. Brès & T. Colonius, 2014. **Wavepacket models for supersonic jet noise**. *J. Fluid Mech.*, vol. 742, p. 71–95.

[55] D. Sipp & A. Lebedev, 2007. **Global stability of base and mean flows: a general approach and its applications to cylinder and open cavity flows**. *J. Fluid Mech.*, vol. 593, p. 333–358.

[56] T. Suzuki & T. Colonius, 2006. **Instability waves in a subsonic round jet detected using a near-field phased microphone array**. *J. Fluid Mech.*, vol. 565, p. 197–226.

[57] V. Theofilis, 2003. **Advances in global linear instability analysis of nonparallel and three-dimensional flows**. *Prog. Aerosp. Sci.*, vol. 39, p. 249–315.

[58] A. Towne, O.T. Schmidt & T. Colonius, 2018. **Spectral proper orthogonal decomposition and its relationship to dynamic mode decomposition and resolvent analysis**. *J. Fluid Mech.*, vol. 847, p. 821–867.

[59] L.N. Trefethen, A.E. Trefethen, S.C. Reddy & T.A. Driscoll, 1993. **Hydrodynamic stability without eigenvalues**. *Science*, vol. 261, p. 578–584.

[60] A. Tyliszczak & B.J. Geurts, 2014. **Parametric analysis of excited round jets - numerical study**. *Flow Turbulence Combust.*, vol. 93, p. 221–247.

[61] Y. Zhu, V. Gupta & L. Li, 2017. **Onset of global instability in low-density jets**. *J. Fluid Mech.*, vol. 828.

7 Appendix: Collection of articles

The articles discussed in §§2–4 are provided in this appendix. A continuous pagination is omitted for formatting reasons; articles can be accessed directly via these hyperlinks:

[L5] L. Lesshafft, P. Huerre & P. Sagaut, 2010:
Aerodynamic sound generation by global modes in hot jets
J. Fluid Mech., vol. 647, 473–48

[L6] L. Lesshafft & O. Marquet, 2010:
Optimal velocity and density profiles for the onset of absolute instability in jets
J. Fluid Mech., vol. 662, 398–408

[L9] X. Garnaud, L. Lesshafft, P. Schmid & J.-M. Chomaz, 2012:
A relaxation method for large eigenvalue problems, with an application to flow stability analysis
J. Comput. Phys., vol. 231(10), 3912–3927

[L10] X. Garnaud, L. Lesshafft, P. Schmid & P. Huerre, 2013:
Modal and transient dynamics of jet flows
Phys. Fluids, vol. 25, no. 044103

[L11] X. Garnaud, L. Lesshafft, P. Schmid & P. Huerre, 2013:
The preferred mode of incompressible jets: linear frequency response analysis
J. Fluid Mech., vol. 716, 189–202

[L46] X. Garnaud, R. Sandberg & L. Lesshafft:
Global response to forcing in a subsonic jet: instability wavepackets and acoustic radiation
AIAA Paper 2013-2232
19th AIAA/CEAS Aeroacoustics Conference, Berlin, 2013

[L12] L. Lesshafft, 2015:
Linear global stability of a confined plume
Theor. Appl. Mech. Lett., vol. 5, p. 126-128

[L13] R. Chakravarthy, L. Lesshafft & P. Huerre, 2015:
Local linear stability of laminar axisymmetric plumes
J. Fluid Mech., vol. 780, p. 344-369

[L67] O. Marquet & L. Lesshafft, 2015:
Identifying the active flow regions that drive linear and nonlinear instabilities
arXiv:1508.07620

[L15] O. Semeraro, L. Lesshafft, V. Jaunet & P. Jordan, 2016:
Modeling of coherent structures in a turbulent jet as global linear instability wavepackets: theory and experiment
Int. J. Heat Fluid Flow, vol. 62A, p. 24-32

[L57] O. Semeraro, V. Jaunet, P. Jordan, A. Cavalieri & L. Lesshafft:
Stochastic and harmonic optimal forcing in subsonic jets
AIAA Paper 2016-2935
22th AIAA/CEAS Aeroacoustics Conference, Lyon, 2016

[L16] W. Coenen, L. Lesshafft, X. Garnaud & A. Sevilla, 2017:
Global instability of low-density jets
J. Fluid Mech., vol. 820, p. 187-207

[L17] L. Shaabani Ardali, D. Sipp & L. Lesshafft, 2017:
Time-delayed feedback technique for suppressing instabilities in time-periodic flow
Phys. Rev. Fluids, vol. 2, 113904

[L18] R. Chakravarthy, L. Lesshafft & P. Huerre, 2018:
Global stability of buoyant jets and plumes
J. Fluid Mech., vol. 835, p. 654-673

[L19] L. Lesshafft, 2018:
Artificial eigenmodes in truncated flow domains
Theor. Comp. Fluid Dyn., vol. 32, p. 245-262

[L21] L. Shaabani Ardali, D. Sipp & L. Lesshafft 2018:
Vortex pairing in jets as a global Floquet instability: modal and transient dynamics
J. Fluid Mech., in press

[L22] L. Lesshafft, O. Semeraro, V. Jaunet, A.V.G. Cavalieri & P. Jordan:
Resolvent-based modelling of coherent wavepackets in a turbulent jet
arXiv 1810.09340, submitted to *Phys. Rev. Fluids*

Aerodynamic sound generation by global modes in hot jets

By LUTZ LESSHAFFT[1], PATRICK HUERRE[1] AND PIERRE SAGAUT[2]

[1]Laboratoire d'Hydrodynamique, CNRS – École Polytechnique,
91128 Palaiseau, France,
[3]D'Alembert Institute, Université Pierre et Marie Curie (Paris 6),
Boite 162, 4 place Jussieu, 75252 Paris Cedex 05, France

(Received November 16, 2009)

The acoustic field generated by the synchronized vortex street in self-excited hot subsonic jets is investigated via direct numerical simulation of the compressible equations of motion in an axisymmetric geometry. The simulation simultaneously resolves both the aerodynamic near field and the acoustic far field. Self-sustained near field oscillations in the present flow configurations have been described as *nonlinear global modes* in an earlier study. The associated acoustic far field is found to be that of a compact dipole, emanating from the location of vortex roll-up. A far field solution of the axisymmetric Lighthill equation is derived, based on the source term formulation of Lilley (1974). With near field source distributions obtained from the direct numerical simulations, the Lighthill solution is in good agreement with the far field simulation results. Fluctuations of the *enthalpy flux* within the jet are identified as the dominant aeroacoustic source. Superdirective effects are found to be negligible.

1. Introduction

Subsonic jets, if they are sufficiently hot compared to the ambient air, may bifurcate to a regime of intrinsic self-sustained oscillations that give rise to a street of highly regular ring vortices. This oscillator-type behaviour in hot jets has first been observed experimentally by Monkewitz, Bechert, Barsikow & Lehmann (1990). Recent numerical studies (Lesshafft, Huerre, Sagaut & Terracol 2006; Lesshafft, Huerre & Sagaut 2007) have demonstrated that these oscillations are due to an absolute instability of the jet profile near the nozzle, and that they may be described theoretically as a *nonlinear global mode*.

The present study examines the acoustic far field that is radiated from the self-sustained vortex street in globally unstable hot jets. The thick shear layer configurations treated in Lesshafft *et al.* (2006), with ambient-to-jet temperature ratios $S = 0.1$, 0.2 and 0.3, are chosen for this investigation. Although only the aerodynamic near field dynamics have been addressed in our previous publications, the computational domain of the DNS already encompassed a large portion of the acoustic far field. These far field results are now used to analyze the directivity pattern and the physical sound generation mechanisms that dominate the acoustic radiation from the global mode in a hot jet.

Numerical simulations in which the acoustic field is computed from first principles have become known as direct noise calculations (DNC). Mitchell, Lele & Moin (1999) were the first to apply this approach to the jet noise problem. Their study focused on

the sound generated by the pairing of large-scale vortices in forced isothermal jets. As in the present paper, the simulations of Mitchell *et al.* (1999) were carried out in an axisymmetric setting, which hindered the onset of turbulence, and thus allowed a study of the isolated aeroacoustic behaviour of large-scale near field dynamics. Freund (2001) performed direct numerical simulations resolving the acoustic field of a three-dimensional turbulent isothermal jet at low Reynolds number, which gave results in good agreement with experimental measurements. The low Reynolds number restriction was relaxed by Bogey, Bailly & Juvé (2003) through the use of LES subgrid modelling. In subsequent papers (Bogey & Bailly 2004, 2005), these authors investigated the influence of numerical boundary conditions and various subgrid models, as well as Mach and Reynolds number effects. A list of further LES studies that directly resolve the acoustic field of turbulent jets is given in Bodony & Lele (2006). Only few among these include the effect of jet heating: the simulations of Andersson, Eriksson & Davidson (2005) successfully reproduced experimental acoustic measurements of Jordan, Gervais, Valière & Foulon (2002) in a subsonic hot jet when the nozzle geometry was included. Shur, Spalart & Strelets (2005) achieved good agreement with the reference experiments of Tanna (1977) and Viswanathan (2004) in hot jet simulations in both subsonic and supersonic settings.

The large majority of numerical jet noise studies, as reviewed by Wang, Freund & Lele (2006), relies on hybrid methods. Based on jet near-field data obtained from RANS or LES calculations, the acoustic far field is calculated according to an acoustic analogy. The common objective of these investigations is to validate the predictive capabilities of acoustic analogies or boundary integral methods, by comparison with available acoustic data from experiments or direct calculations. In some instances, computed near-field data have also been used to investigate the acoustic source mechanisms underlying the far-field spectrum and directivity pattern: Mitchell *et al.* (1999) compared the relative importance of individual source terms, in the sense of Lighthill's equation, in forced laminar jets. Their results demonstrated that streamwise variations of the source strength, even in regions of very low amplitude, greatly influence the far-field sound directivity. Freund's (2001) analysis of DNS data for a *turbulent* unheated jet identified large-scale structures as the dominant noise sources. The spatial distribution of the structures takes the form of a wave packet, similar to what instability theory would predict for a laminar setting.

The numerical analysis of acoustic source mechanisms in *hot* jets, despite their practical importance, has received little attention in recent literature. Fortuné & Gervais (1999) proposed a prediction scheme for temperature-related turbulence noise, on the basis of the k-ϵ model. In LES studies by Bodony & Lele (2005) of hot turbulent jets in the high subsonic and supersonic régime, the sound field was computed directly. In the framework of Lighthill's acoustic analogy, cancellation effects between Reynolds stress and so-called entropy contributions were documented. Similar cancellation effects at a high subsonic Mach number were reported by Lew, Blaisdell & Lyrintzis (2007), by means of a hybrid numerical approach. Lew *et al.* (2007) concluded from their results that the sound field of a hot jet at low Mach number is strongly dominated by radiation from entropy-related sources.

The present study investigates sound generation mechanisms due to large-scale instability structures (global modes) in self-excited hot jets at low Mach number. The numerical approach is similar to that of Mitchell *et al.* (1999): the axisymmetric equations of motion are resolved directly in the near and far field. This axisymmetric restriction prevents the development of small-scale turbulence; it is justified by the experimental observations of Monkewitz *et al.* (1990). Lighthill's equation is used not to *predict* the far field sound, but as an *analytical* tool, in order to identify dominant source mechanisms. To this end, the aeroacoustic source terms of the Lighthill equation are recast in

the formulation proposed by Lilley (1974, 1996). Lighthill's original formulation includes one monopole source term that is commonly linked to entropy fluctuations in the near field, although it is known to contain both isentropic and non-isentropic components (see for instance A. Michalke's note in Lilley 1974). This source term will be referred to as the "excess density" (Dowling 1992) in the following. Lilley's formulation decomposes the excess density term into explicit monopole and dipole sources, and it allows for a less ambiguous interpretation of the sound-producing physical mechanisms, as will be demonstrated in this paper. Freund (2003) achieved an improved interpretation of his 2001 simulation results based on Lilley's source decomposition. Similarly, Bodony & Lele (2008) used Lilley's formalism for a refined analysis of some of their earlier results (Bodony & Lele 2005), including one case of a transonic hot jet.

Laufer & Yen (1983) measured the acoustic radiation due to regular vortex pairing events in forced isothermal jets at low Mach number. The acoustic field was found to exhibit a *superdirective* beaming pattern, with maximum intensity I at the radiation angle $\vartheta = 0$ in the downstream direction of the jet:

$$I(\vartheta) \propto \exp\left[-A(1 - Ma_{cv}\cos\vartheta)^2\right], \quad A = 45, \tag{1.1}$$

where the Mach number Ma_{cv} is formed with the vortex convection velocity. This result has been confirmed in only one experimental configuration by Fleury, Bailly & Juvé (2005). According to the discussion of Laufer & Yen (1983), such strong beaming behaviour seemed unlikely to arise from an acoustically compact source region: the near field fluctuation amplitudes associated with vortex pairing were measured to vary as a Gauß function in the streamwise direction, with a half-width an order of magnitude smaller than the acoustic wavelength. However, the theoretical analyses of Huerre & Crighton (1983) and Crighton & Huerre (1990) have demonstrated that a perfectly Gaussian shape of the near field wave packet indeed results in an antenna factor of the form (1.1). More generally, these authors surmised that any extended wave packet, depending on its precise envelope shape, may emit a superdirective sound field. The nonlinear global modes in hot jets described in Lesshafft *et al.* (2006, 2007) may be represented as such extended wave packets. As their spatial amplitude and phase modulations are precisely known from the numerical simulations, the approach of Huerre & Crighton (1983) will be applied in the present study to the case of a globally unstable hot jet. It is hoped that this analysis will further elucidate the conditions for superdirective sound radiation from low Mach number jets.

The paper is organized as follows: the flow parameters are defined, and the numerical methods used in the direct computations are outlined in §2.1. Simulation results in the acoustic far field are presented in §2.2. In §3, the solution procedure for the Lighthill equation is laid out. This formalism is then applied to three hot jet configurations in §4, and the main conclusions are summarized in §5.

2. Direct noise computation of a hot jet

2.1. *Flow configuration and numerical method*

The flow model and the numerical solution techniques employed in the simulation have been presented in Lesshafft *et al.* (2006) and are documented in full detail in Lesshafft (2006): the problem is formulated in axisymmetric coordinates x and r; the conservative flow variables $\boldsymbol{q} = (\rho, \rho u, \rho v, \rho E)$ are decomposed into a steady baseflow component $\boldsymbol{q}_b$ and an unsteady perturbation component $\boldsymbol{q}'$. The symbol ρ denotes density, u and v are the axial and radial velocity components, and E is the total energy. The baseflow $\boldsymbol{q}_b(x, r)$

is obtained by numerical integration of the compressible boundary layer equations, starting from an analytical jet velocity profile ('profile 2' of Michalke 1984) at the upstream boundary $x = 0$ of the computational domain. The temporal evolution of perturbations $\boldsymbol{q}'(x, r, t)$ within this baseflow is then computed according to the compressible equations of continuity, momentum and energy, closed by the equation of state for a perfect gas.†

All quantities are made non-dimensional with respect to the jet radius R and the jet centreline values of density ρ_c, velocity U_c and temperature T_c in the potential core. The three flow configurations investigated in this study are defined by the following parameters:

$$\begin{array}{ll} R/\theta = 10, & S = 0.1,\ 0.2,\ 0.3, \\ Re = 1000, & Ma_c = 0.1, \\ Pr = 1, & \gamma = 1.4. \end{array} \tag{2.1}$$

As defined in Lesshafft *et al.* (2006), Re, Ma_c and Pr are the Reynolds, Mach and Prandtl numbers, θ is the momentum shear layer thickness of the inlet velocity profile, $S = T_\infty/T_c$ is the ambient-to-jet temperature ratio and γ is the ratio of specific heats. Note that the Mach number Ma_c is defined with respect to the speed of sound on the centreline. It is easily converted to the more conventional definition $Ma_\infty = U_c/c_\infty = S^{-1/2}Ma_c$. The three temperature ratios $S = 0.1$, 0.2 and 0.3 then yield Mach numbers $Ma_\infty = 0.32$, 0.22 and 0.18.

Among the three jet configurations (2.1), the $S = 0.3$ case will be discussed in full detail, because it is trusted to be the least affected by inaccuracies due to the numerical boundary treatment. Results for the two other cases, $S = 0.1$ and 0.2, are summarized in §4.2 in oder to test the validity of the main conclusions for a range of globally unstable temperature ratios and Mach numbers. In the following, throughout the end of §4.1, the discussion will focus on the $S = 0.3$ case.

The long-time response of a jet to an initial pulse perturbation is computed on an orthogonal grid that discretizes the physical domain $0 \leqslant r \leqslant 46$ and $0 \leqslant x \leqslant 80$ into 349×801 grid points. Outside this region, all perturbations are attenuated by artificial damping and strong grid stretching in sponge zones extending over $46 < r \leqslant 200$ and $80 < x \leqslant 105$. First-order characteristic boundary conditions given by Giles (1990) are applied at the upstream numerical boundary in order to minimize acoustic reflections and spurious coupling of acoustic and vortical waves in the jet shear layer. Inside the physical region of the computational domain, spatial derivatives in the governing equations are evaluated using a sixth-order explicit finite difference scheme, and the solution is time-advanced via a third-order Runge–Kutta algorithm.

2.2. *Direct numerical simulation results*

As discussed in §5 of Lesshafft *et al.* (2006), the near field dynamics of jets with parameters (2.1) are characterized by self-sustained oscillations that give rise to a highly regular roll-up of the jet shear layer into evenly spaced ring vortices. In theoretical terms, this periodic flow state is described as a nonlinear global mode. The *global frequency* of vortex roll-up at $S = 0.3$ has been determined to be $\omega_g = 0.728$ in the numerical simulations ('mode 1' in Lesshafft *et al.* 2006). It has been discussed that the $S = 0.3$ configuration represents the critical case for the marginal onset of global instability, and that the asymptotic approach of the final oscillating state is extremely slow as a consequence. For the present investigation, the computations have been continued over an additional

† Note that there is a typographical error in equation (2.4*b*) of Lesshafft *et al.* (2006), which has been corrected in Lesshafft (2006).

number of approximately 30 oscillation periods, and the global frequency has further converged to a value of $\omega_g = 0.722$.

Only configurations with $R/\theta = 10$ are chosen for the present investigation because the observed global mode structure is unaffected by vortex pairing; in simulations with thinner initial shear layers $R/\theta > 10$ (Lesshafft *et al.* 2007), a secondary instability of the vortex street leads to regular "leap-frogging" of neighbouring vortices. These events modify the spatial envelope of the fundamental global mode oscillations and at the same time radiate a subharmonic sound field. An investigation of sound generation mechanisms due to vortex pairing is not the subject of this paper. The restriction to globally unstable configurations without vortex pairing further limits the parameter regime to low values of the Mach number and temperature ratio (see figure 10 of Lesshafft & Huerre 2007).

In the present flow examples, the acoustic field may be regarded as monochromatic: the near field is free of random fluctuations, and, as in the low Mach number cases of Mitchell *et al.* (1999), harmonic components in the far field are negligible when compared to the fundamental sound component ($\omega_g = 0.722$ for $S = 0.3$). The acoustic wavelength is then $\lambda_a = 2\pi c_\infty/\omega_g = 47.7$, which approximately corresponds to the radial extent of the physical domain in the simulation. In the following, the acoustic field is investigated in terms of the temporal Fourier coefficient of pressure fluctuations, defined as

$$\hat{p}(\boldsymbol{x};\omega) = \int p'(\boldsymbol{x},t)\, e^{i\omega t}\, \mathrm{d}t\,. \tag{2.2}$$

Isocontours of $|\hat{p}(\boldsymbol{x};\omega_g)|$ are shown in figure 1: the acoustic field is composed of two lobes, with an extinction angle at about 90° from the jet axis. The apparent source location at $x = 9$ corresponds to the streamwise station of vortex roll-up (compare to figure 7*a* of Lesshafft *et al.* 2006). The decibel levels in figure 1 are scaled with respect to the maximum near field pressure amplitude. Due to weak reflections from the downstream sponge region, the isocontours in the acoustic field at $x > 60$ are slightly distorted and not shown in figure 1. For a quantitative examination of the acoustic directivity pattern, values of $|\hat{p}|$ are interpolated along an arc of radius $\xi = 30$ around the apparent source location. Figure 2 reveals that the directivity pattern observed in the numerical simulation closely corresponds to that of a compact dipole $\hat{p} \propto \cos\vartheta$, the radiation angle ϑ being measured relative to the downstream jet axis (see figure 1).

The isocontour diagram in figure 1 suggests that the transition from the aerodynamic near field to the acoustic far field takes place over a length scale much shorter than the acoustic wavelength. This observation is confirmed in figure 3, which displays the variation of $|\hat{p}|$, measured at an angle $\vartheta = 60°$, as a function of distance ξ from the apparent sound source location. Outside the near field of the jet, for $\xi \gtrsim 8$, the slope of the pressure amplitude quickly adjusts to the characteristic decay rate $|\hat{p}| \propto \xi^{-1}$ of the acoustic far field.

3. Integration of the Lighthill equation

3.1. *Source term decompositions of Lighthill (1952) and Lilley (1974)*

Lighthill (1952) derived an exact inhomogeneous wave equation for acoustic fluctuations by combining the continuity and momentum equations. In Cartesian coordinates x_i, the Lighthill equation for pressure fluctuations reads (see for instance Crighton 1975):

$$\frac{1}{c_\infty^2}\frac{\partial^2 p'}{\partial t^2} - \frac{\partial^2 p'}{\partial x_i^2} = \frac{\partial^2 S_{ij}}{\partial x_i \partial x_j} - \frac{\partial^2 \rho_e}{\partial t^2}\,, \tag{3.1}$$

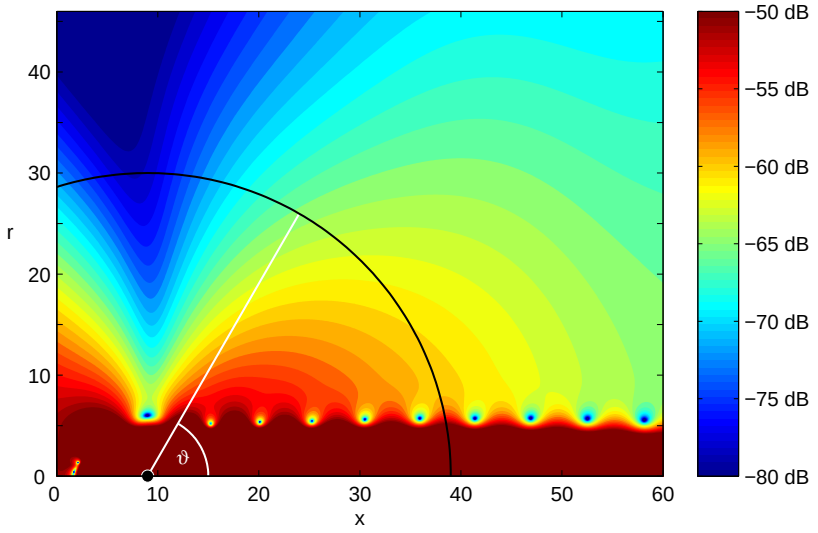

FIGURE 1. Isocontours of the pressure amplitude $|\hat{p}(r, x; \omega_g)|$ in the acoustic far field of a jet with $S = 0.3$. The apparent sound source on the jet axis is located at $x = 9$. The directivity pattern in figures 2 and 5 is extracted along the black arc of radius 30.

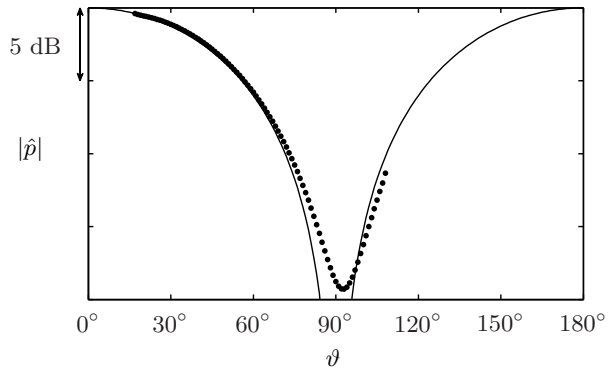

FIGURE 2. (•) Pressure amplitude as a function of radiation angle ϑ, interpolated along the arc indicated in figure 1; (—) directivity of a compact dipole $\hat{p} \propto \cos\vartheta$.

where c_∞ denotes the speed of sound in the far field. The stress tensor

$$S_{ij} = \rho u_i u_j - \tau_{ij} \tag{3.2}$$

is composed of Reynolds stresses and viscous terms, while the "excess density"

$$\rho_e = \rho' - p'/c_\infty^2 \tag{3.3}$$

is related to thermodynamic fluctuations. Primes in the above equations denote fluctuations around a steady flow state (see §2.1).

One possible way to proceed is to solve for the acoustic pressure p' via numerical time integration of equation (3.1), simultaneously with a DNS of the near field, from which the right-hand-side terms are evaluated at each time step. The individual contribution of each source term to the acoustic far field can then be examined separately. This strategy

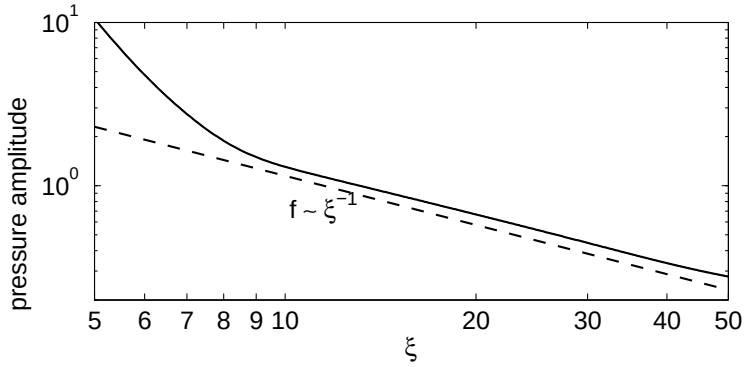

FIGURE 3. Solid line: pressure amplitude $|\hat{p}|$ as a function of observer distance ξ, measured along the radiation angle $\vartheta = 60°$. Dashed line: algebraic decay $\propto \xi^{-1}$ as expected in the acoustic far field.

has been applied, for instance, by Freund (2001) and Boersma (2005). Alternatively, a solution for the acoustic pressure field can be sought in terms of a Green's function to the wave operator, that is to be evaluated for the source terms of the Lighthill equation (3.1). The latter approach has been applied to the present jet configuration in a preliminary study (chapter 5 in Lesshafft 2006). The results clearly identify the excess density as the dominant acoustic source, and the sound field computed from this source term satisfactorily reproduces the directivity pattern displayed in figure 2.

However, the interpretation of the results in Lesshafft (2006) remains inconclusive: first, the analysis shows that the excess density formally produces a *monopole* source distribution. The overall dipole character of the directly computed far field can still be retrieved, but the process requires a very accurate representation of phase variations in the source distribution, and therefore it is quite susceptible to numerical imprecisions. As a result, the extinction angle (near $\vartheta = 90°$ in figure 2) in the Lighthill analysis of Lesshafft (2006) is shifted by 15° when compared to the simulation results. Second, it is difficult to interpret the physical nature of the sound-generating mechanisms represented by the excess density. Formally, $\rho_e = \rho' - p'/c_\infty^2$ appears to represent non-isentropic fluctuations, but this interpretation does not apply to flows with variable speed of sound, such as hot jets. For a better characterization of the relevant acoustic source mechanism in the case on hand, the observed sound radiation must be associated with a component of the excess density that explicitly produces a dipole field.

The following investigation will be based on an alternative formulation of equation (3.1), derived by Lilley (1974, 1996). By combining the momentum and *energy* equations (instead of using the continuity equation, as done by Lighthill 1952), Lilley obtained a wave equation for pressure fluctuations, equivalent to equation (3.1), where the excess density source term is replaced by

$$\frac{\partial^2 \rho_e}{\partial t^2} = \frac{1}{c_\infty^2}\frac{\partial^2}{\partial t^2} K(\boldsymbol{x},t) - \frac{1}{c_\infty}\frac{\partial^2}{\partial t \partial x_i} H_i(\boldsymbol{x},t) - \frac{1}{c_\infty}\frac{\partial^2}{\partial t \partial x_i} D_i(\boldsymbol{x},t)\,. \tag{3.4}$$

Note that this is *not* what is commonly known as "Lilley's equation" (derived in the same 1974 publication), which involves third-order derivatives and provides an improved separation of sound generation and propagation effects. The individual source terms in

equation (3.4) are

$$K(\boldsymbol{x},t) = \frac{\gamma-1}{2}\rho|\boldsymbol{u}|^2\,, \tag{3.5}$$

$$H_i(\boldsymbol{x},t) = \frac{\gamma-1}{c_\infty}\rho u_i(h_\infty - h_s)\,, \tag{3.6}$$

$$D_i(\boldsymbol{x},t) = \frac{\gamma-1}{c_\infty}(\tau_{ij}u_j - q_i)\,. \tag{3.7}$$

The first two components, K and H_i, represent fluctuations of the kinetic energy and of the total enthalpy flux, respectively. All diffusive effects, due to $\boldsymbol{\tau}$ and the heat flux $\boldsymbol{q} = -\nabla T/[(\gamma-1)Ma_c^2RePr]$, are contained in D_i. The stagnation enthalpy is defined as $h_s = h + |\boldsymbol{u}|^2/2$, with the local enthalpy h (see Lilley 1996). The far-field enthalpy is found as $h_\infty = c_\infty^2/(\gamma-1)$. In terms of conservative variables, as used in the present direct numerical simulations (see §2.1), expression (3.6) can be rewritten as

$$H_i(\boldsymbol{x},t) = c_\infty\rho u_i - \frac{\gamma-1}{c_\infty}\left(\rho E + p\right)u_i\,. \tag{3.8}$$

The spatial derivatives in equation (3.4) characterize the kinetic energy term as a monopole source, whereas the enthalpy- and diffusion-related terms are dipole sources. With respect to generalized acoustic analogy formulations in recent literature, the dipole sources in equation (3.4) may be recovered as special cases of the source terms identified by Goldstein (2003, the η_i' term in his equation 3.5) and by Morfey & Wright (2007, the p_{ij} term in their equation 3.22).

3.2. *Far field solution*

The Lighthill equation (3.1) as well as Lilley's decomposition (3.4) follow from exact manipulations of the governing flow equations. An approximate solution for pressure fluctuations in the far field is given by Lilley (1996), and may be rewritten in our notation as

$$\begin{aligned} p'(\boldsymbol{\xi},t) = {} & \frac{1}{4\pi\xi c_\infty^2}\frac{\xi_i\xi_j}{\xi^2}\frac{\partial^2}{\partial t^2}\int S_{ij}(\boldsymbol{x},t')\mathrm{d}^3\boldsymbol{x} - \frac{1}{4\pi\xi c_\infty^2}\frac{\partial^2}{\partial t^2}\int K(\boldsymbol{x},t')\mathrm{d}^3\boldsymbol{x} \\ & -\frac{1}{4\pi\xi c_\infty^2}\frac{\xi_i}{\xi}\frac{\partial^2}{\partial t^2}\int H_i(\boldsymbol{x},t')\mathrm{d}^3\boldsymbol{x} - \frac{1}{4\pi\xi c_\infty^2}\frac{\xi_i}{\xi}\frac{\partial^2}{\partial t^2}\int D_i(\boldsymbol{x},t')\mathrm{d}^3\boldsymbol{x}\,. \end{aligned} \tag{3.9}$$

The acoustic signal observed at the far field location $\boldsymbol{\xi}$ at time t has been emitted from location $\boldsymbol{x}$ in the source region at the retarded time

$$t' = t - \frac{|\boldsymbol{x}-\boldsymbol{\xi}|}{c_\infty} \approx t - \frac{\xi}{c_\infty} + \frac{\boldsymbol{x}\cdot\boldsymbol{\xi}}{\xi c_\infty}\,. \tag{3.10}$$

With the approximation (3.10), and with the temporal and spatio-temporal Fourier transforms defined as

$$\hat{f}(\boldsymbol{x},\omega) = \int f(\boldsymbol{x},t)\,e^{i\omega t}\mathrm{d}t\,, \quad \tilde{f}(\boldsymbol{k},\omega) = \iint f(\boldsymbol{x},t)\,e^{i(\omega t-\boldsymbol{k}\cdot\boldsymbol{x})}\mathrm{d}^3\boldsymbol{x}\,\mathrm{d}t\,, \tag{3.11}$$

the temporal Fourier-transformed acoustic pressure is found to be

$$\hat{p}(\boldsymbol{\xi},\omega) = \frac{k_a^2}{4\pi\xi} e^{ik_a\xi} \int \left\{ -\frac{\xi_i\xi_j}{\xi^2}\hat{S}_{ij}(\boldsymbol{x},\omega) + \hat{K}(\boldsymbol{x},\omega) + \frac{\xi_i}{\xi}\hat{H}_i(\boldsymbol{x},\omega) + \frac{\xi_i}{\xi}\hat{D}_i(\boldsymbol{x},\omega) \right\} e^{-i\boldsymbol{k}_a\cdot\boldsymbol{x}}\, \mathrm{d}^3\boldsymbol{x} \tag{3.12}$$

$$= \frac{k_a^2}{4\pi\xi} e^{ik_a\xi} \left[-\frac{\xi_i\xi_j}{\xi^2}\tilde{S}_{ij}(\boldsymbol{k}_a,\omega) + \tilde{K}(\boldsymbol{k}_a,\omega) + \frac{\xi_i}{\xi}\tilde{H}_i(\boldsymbol{k}_a,\omega) + \frac{\xi_i}{\xi}\tilde{D}_i(\boldsymbol{k}_a,\omega) \right] \tag{3.13}$$

The acoustic wave vector is defined as $\boldsymbol{k}_a = \omega/c_\infty\, \mathbf{e}_\xi$, oriented in the observer direction. As pointed out by Crighton (1975), the acoustic radiation observed at a given far field location $\boldsymbol{\xi}$ is caused by a single spectral component of the source distribution: a plane wave of wavenumber k_a, travelling in the radiation direction.

3.3. *Axisymmetric and radially compact sources*

3.3.1. *Axial symmetry*

Under the assumption of an axisymmetric source term distribution consisting only of S_{ij}, equation (3.12) has been rewritten by Huerre & Crighton (1983) for the particular case of a Gaussian envelope function $S_{ij}(r,x) \propto \exp(-x^2/\sigma^2)$. Fleury (2006) gives a more general formulation, valid for arbitrary envelope shapes, and the excess density source term (equation 3.1) has been included in Lesshafft (2006).

In order to evaluate the spatial Fourier integrals in equation (3.12), source locations $\boldsymbol{x}$ are expressed in cylindrical coordinates (x,r,φ), while the observer location $\boldsymbol{\xi}$ in the axisymmetric far field is characterized by its spherical coordinates (ξ,ϑ). The resulting integral can be solved numerically in all three (x,r,φ) directions, as done by Mitchell *et al.* (1999). However, Huerre & Crighton (1983) have noted that the azimuthal integration admits closed-form solutions in terms of Bessel functions. After integration in φ, equation (3.12) becomes

$$\hat{p}(\xi,\vartheta,\omega) = \frac{k_a^2}{2\xi}\, e^{ik_a\xi} \iint D(x,r,\vartheta,\omega)\, e^{-ik_a x\cos\vartheta}\, r\,\mathrm{d}r\,\mathrm{d}x, \tag{3.14}$$

with the integrand given by

$$D(x,r,\vartheta,\omega) = I_{Sxx} + I_{Srx} + I_{Srr} + I_{S\varphi\varphi} + I_K + I_{Hx} + I_{Hr} + I_{Dx} + I_{Dr}\,, \tag{3.15}$$

$$I_{Sxx} = -J_0(\alpha r)\, \cos^2\vartheta\, \hat{S}_{xx}(x,r,\omega)\,, \tag{3.16}$$

$$I_{Srx} = -i2J_1(\alpha r)\, \sin\vartheta\, \cos\vartheta\, \hat{S}_{rx}(x,r,\omega)\,, \tag{3.17}$$

$$I_{Srr} = -0.5\,[J_0(\alpha r) - J_2(\alpha r)]\, \sin^2\vartheta\, \hat{S}_{rr}(x,r,\omega)\,, \tag{3.18}$$

$$I_{S\varphi\varphi} = -0.5\,[J_0(\alpha r) + J_2(\alpha r)]\, \sin^2\vartheta\, \hat{S}_{\varphi\varphi}(x,r,\omega)\,, \tag{3.19}$$

$$I_K = J_0(\alpha r)\, \hat{K}(x,r,\omega)\,, \tag{3.20}$$

$$I_{Hx} = J_0(\alpha r)\, \cos\vartheta\, \hat{H}_x(x,r,\omega)\,, \tag{3.21}$$

$$I_{Hr} = iJ_1(\alpha r)\, \sin\vartheta\, \hat{H}_r(x,r,\omega)\,, \tag{3.22}$$

$$I_{Dx} = J_0(\alpha r)\, \cos\vartheta\, \hat{D}_x(x,r,\omega)\,, \tag{3.23}$$

$$I_{Dr} = iJ_1(\alpha r)\, \sin\vartheta\, \hat{D}_r(x,r,\omega)\,. \tag{3.24}$$

The argument of the Bessel functions J_i is $\alpha r = -k_a r\sin\vartheta$. Equation (3.14) explicitly gives the far field pressure in terms of a spatial phase, a radial decay $\propto \xi^{-1}$, and a ϑ-dependent far field directivity function. The Bessel functions represent the effect of azimuthal interference, whereas factors composed of $\cos\vartheta$ and $\sin\vartheta$ produce quadrupole

or dipole directivities. Each source term contains an *antenna factor*, which depends on the spatial distribution $\hat{S}_{xx}(r,x,\omega),\ldots,\hat{D}_r(r,x,\omega)$ of the source strength. The influence of the antenna factor on the directivity pattern is commonly referred to as the *superdirective* effect, following the interpretation given by Crighton & Huerre (1990) of the experimental results of Laufer & Yen (1983, see section 1). For an analysis of the acoustic radiation from the present jet configuration, discussed in §2.2, the distributions $\hat{S}_{xx}(r,x,\omega),\ldots,\hat{D}_r(r,x,\omega)$ may be obtained directly from the numerical simulation.

3.3.2. *Radial compactness*

Following the approach of Huerre & Crighton (1983), the aeroacoustic source distributions in a jet may be assumed to be compact in the radial direction, but not necessarily so in the axial direction. For the present analysis, the source terms are modelled as being concentrated in the center of the shear layer at $r=1$ such that, for instance,

$$\hat{S}_{ij}(x,r,\omega) = \hat{S}^x_{ij}(x,\omega)\,\delta(r-1), \tag{3.25}$$

and therefore

$$\hat{S}^x_{ij}(x,\omega) = \int_0^\infty \hat{S}_{ij}(x,r,\omega)\,r\,\mathrm{d}r\,, \tag{3.26}$$

$$\tilde{S}^x_{ij}(k,\omega) = \int_{-\infty}^\infty \hat{S}^x_{ij}(x,\omega)\,e^{-ikx}\,\mathrm{d}x\,. \tag{3.27}$$

These integrals must be solved numerically. Radially compact representations of all other source terms and their Fourier transforms, marked by the superscript x in the following, are obtained accordingly.

Under the assumption of radial compactness of all aeroacoustic sources, equation (3.14) simplifies to

$$\hat{p}(\xi,\vartheta,\omega) = \frac{k_a^2}{2\xi}\,e^{ik_a\xi}\,D^x(\vartheta,\omega)\,, \tag{3.28}$$

with

$$D^x(\vartheta,\omega) = I^x_{Sxx} + I^x_{Srx} + I^x_{Srr} + I^x_{S\varphi\varphi} + I^x_K + I^x_{Hx} + I^x_{Hr} + I^x_{Dx} + I^x_{Dr}\,, \tag{3.29}$$

$$I^x_{Sxx} = -J_0(\alpha)\,\cos^2\vartheta\,\tilde{S}^x_{xx}(k_a\cos\vartheta,\omega)\,, \tag{3.30}$$

$$I^x_{Srx} = -i2J_1(\alpha)\,\sin\vartheta\,\cos\vartheta\,\tilde{S}^x_{rx}(k_a\cos\vartheta,\omega)\,, \tag{3.31}$$

$$I^x_{Srr} = -0.5\,[J_0(\alpha)-J_2(\alpha)]\,\sin^2\vartheta\,\tilde{S}^x_{rr}(k_a\cos\vartheta,\omega)\,, \tag{3.32}$$

$$I^x_{S\varphi\varphi} = -0.5\,[J_0(\alpha)+J_2(\alpha)]\,\sin^2\vartheta\,\tilde{S}^x_{\varphi\varphi}(k_a\cos\vartheta,\omega)\,, \tag{3.33}$$

$$I^x_K = J_0(\alpha)\,\tilde{K}^x(k_a\cos\vartheta,\omega)\,, \tag{3.34}$$

$$I^x_{Hx} = J_0(\alpha)\,\cos\vartheta\,\tilde{H}^x_x(k_a\cos\vartheta,\omega)\,, \tag{3.35}$$

$$I^x_{Hr} = iJ_1(\alpha)\,\sin\vartheta\,\tilde{H}^x_r(k_a\cos\vartheta,\omega)\,, \tag{3.36}$$

$$I^x_{Dx} = J_0(\alpha)\,\cos\vartheta\,\tilde{D}^x_x(k_a\cos\vartheta,\omega)\,, \tag{3.37}$$

$$I^x_{Dr} = iJ_1(\alpha)\,\sin\vartheta\,\tilde{D}^x_r(k_a\cos\vartheta,\omega)\,. \tag{3.38}$$

The Bessel functions now take the argument $\alpha=-k_a\sin\vartheta$. At low Mach numbers, where $k_a\ll 1$, variations of the Bessel functions are negligible. A factor $J_0(\alpha)\approx 1$ is associated with source terms that are nearly unaffected by azimuthal interference, whereas a factor $J_1(\alpha)\approx 0$ signifies almost complete cancellation of a source with its image across the jet axis. The antenna factor due to each source term distribution is given explicitly by its one-dimensional Fourier transform along x. From the argument $k=k_a\cos\vartheta$, it is seen

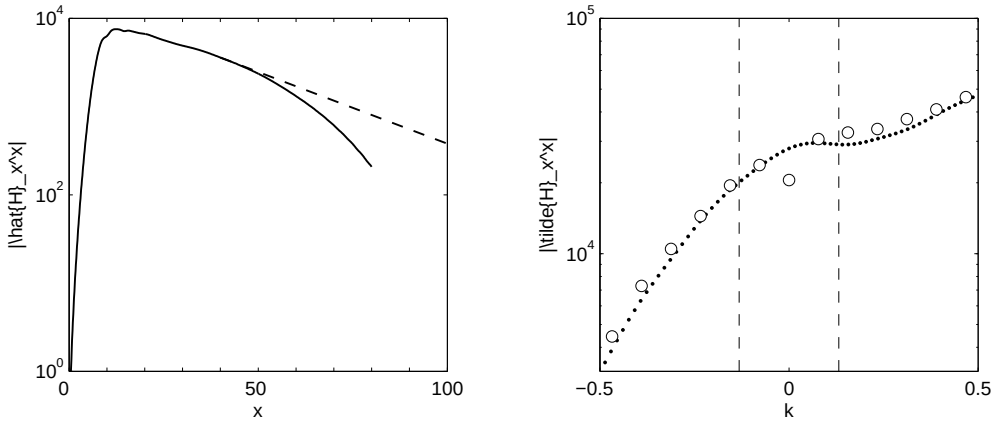

(a) (b)

FIGURE 4. a) Jet with $S = 0.3$: amplitude of the radially compact enthalpy-flux source term $|\hat{H}_x^x|$ as a function of x. Solid line: original DNS data, dashed line: extrapolated exponential decay over the interval $40 \leqslant x \leqslant 400$. b) Corresponding discrete Fourier spectra near $k = 0$; white circles: based on original DNS data, black dots: based on extrapolated amplitude envelope. Dashed lines indicate the acoustically relevant interval $-k_a \leqslant k \leqslant k_a$.

again that only the interval $-k_a \leqslant k \leqslant k_a$ of the spectrum radiates sound into the far field.

4. Acoustic source term analysis for hot jets

4.1. *Marginal globally unstable case* $S = 0.3$

The far field pressure solution (3.28) is first evaluated for the jet configuration with $S = 0.3$. All source term distributions $\hat{S}_{ij}$, $\hat{K}$, $\hat{H}_i$ and $\hat{D}_i$, as defined in equations (3.2, 3.5–3.7, 3.11), are extracted from the direct numerical simulation as functions of r and x. The temporal Fourier transform (3.11) of all sources is evaluated for $\omega = \omega_g$ during runtime over one cycle period. Under the assumption of radial compactness, the one-dimensional distributions $\hat{S}_{ij}^x$, $\hat{K}^x$, $\hat{H}_i^x$ and $\hat{D}_i^x$ are obtained according to equation (3.26) by numerical integration in r. Evaluation of the far field pressure solution (3.28) then involves a discrete Fourier transform in x.

As an example, the streamwise variation of the enthalpy-flux source envelope $|\hat{H}_x^x(x, \omega_g)|$ is presented in figure 4a as a solid line. It displays a sharp front near the upstream boundary and a slow decay downstream of the vortex roll-up location around $x = 9$. Accelerated decay is observed near the end of the numerical domain, but the source amplitude at the downstream end $x = 80$ is still two orders of magnitude larger than at the upstream boundary. As a result, the truncation of the spatial domain may produce significant errors in the spatial Fourier transform. The corresponding discrete spectrum $|\tilde{H}_x^x(k, \omega_g)|$ near $k = 0$ is displayed in figure 4b as white circles. Its peak, not shown in the diagram, is found at $k_{max} = 1.28$, with a value of $|\tilde{H}_x^x(k_{max}, \omega_g)| = 2.5 \times 10^6$. Since the streamwise physical extent of the numerical domain, $0 \leqslant x \leqslant 80$, is less than twice the acoustic wavelength, only three points of the spectrum can be obtained within the radiating interval $-k_a \leqslant k \leqslant k_a$. A discussion of the directivity pattern based on only three data points is unsatisfactory; it is therefore desirable to first achieve a higher spectral resolution of the spatial Fourier transform.

Mitchell *et al.* (1999) faced the same problem in their computations of the acoustic

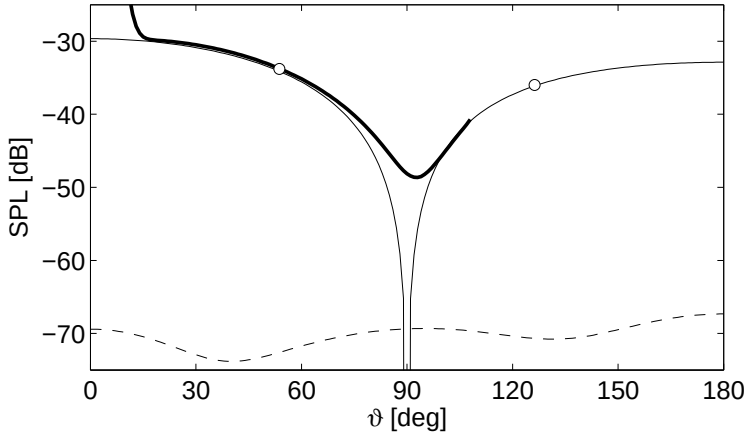

FIGURE 5. Jet with $S = 0.3$: directivity of the acoustic far field, comparison between direct numerical simulation and Lighthill solution. (—) Directly computed sound; (∘) Lighthill solution due to H_x^x without streamwise extrapolation. Lighthill solution from extrapolated sources: (—) enthalpy-flux term H_x^x alone, (- - -) combined radiation from all other terms.

field in forced isothermal jets. These authors suggest to extrapolate the source term distributions, prior to evaluating the Lighthill solution, over a sufficiently long downstream region beyond the end of the computational domain. Following this idea, the source terms in the present calculations are taken to develop exponentially as

$$f(x) = f(x_0)\, e^{ik_x(x-x_0)} \quad \text{with} \quad k_x = -i\frac{f'(x_0)}{f(x_0)}\,, \tag{4.1}$$

from $x_0 = 40$ down to $x = 400$. The extrapolated source envelope $|\hat{H}_x(x, \omega_g)|$ is shown as a dashed line in figure 4a. Over the interval $20 \leqslant x \leqslant 50$, the amplitude decay of the original distribution may indeed be well approximated by an exponential function. Black dots in figure 4b represent the discrete Fourier spectrum $|\tilde{H}_x^x(k, \omega_g)|$ of the extrapolated source distribution. They align well with the previously obtained data points (white circles) in the vicinity of the radiating interval, which now is resolved by 17 points. In particular, the extrapolation procedure is found to appropriately correct the apparent error, due to domain truncation, in the $k = 0$ component of the original spectrum.

The Lighthill solution obtained from extrapolated source distributions in the $S = 0.3$ jet, according to equation (3.28), is compared to the DNS results in figure 5. The thick line represents directly computed sound pressure levels, measured along the arc in figure 1. At angles less than 18°, the arc crosses the hydrodynamic near field. The thin line interpolates the Lighthill solution due to the extrapolated H_x^x term, whereas results based on the non-extrapolated H_x^x distribution are shown as white circles. The combined acoustic radiation from all other source terms, as obtained from equation (3.28), is represented by a dashed line. Sound pressure levels are computed as $\mathrm{SPL} = 20\log_{10}(\xi|\hat{p}|/p_{\mathrm{ref}})$, thereby eliminating the ξ^{-1} decay of the acoustic pressure amplitude. The dB scaling takes the near field pressure maximum $p_{\mathrm{ref}} = \max_{\boldsymbol{x}} |\hat{p}(\boldsymbol{x}, \omega_g)|$ as a common reference value for *all* curves.

Figure 5 demonstrates that the dipole strength of the directly computed acoustic field is very well retrieved by the Lighthill prediction for dipole radiation due to the axial enthalpy-flux term H_x^x. Over the interval $20° \leqslant \vartheta \leqslant 60°$, both curves coincide within 0.5 dB accuracy. Without source extrapolation, the one point obtained within the down-

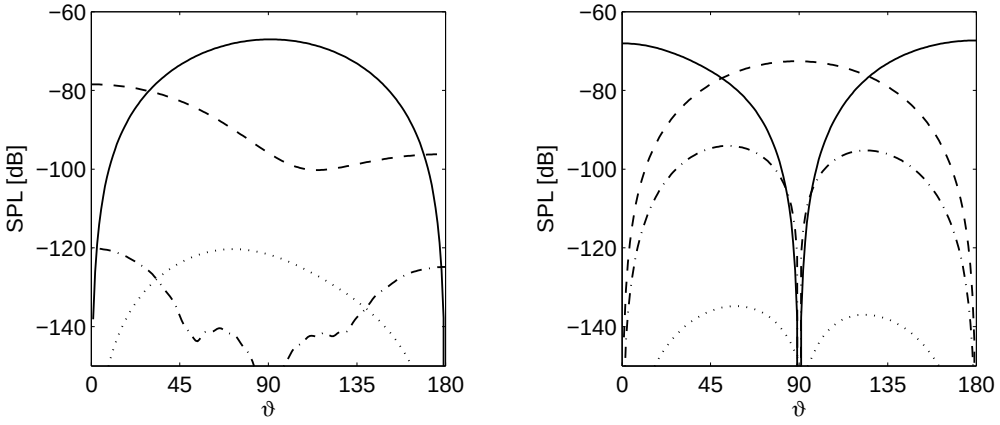

FIGURE 6. Jet with $S = 0.3$: individual far field contributions from all source terms except H_x^x. a) Excess density components: (—) H_r^x; (- - -) K^x; (- · -) D_x^x; (· · ·) D_r^x. b) Reynolds and viscous stresses: (—) S_{xx}^x; (- - -) S_{rr}^x; (- · -) S_{rx}^x; (· · ·) $S_{\varphi\varphi}^x$.

stream lobe, at $\vartheta = 54°$, matches the simulation result with a precision of 0.1 dB. Furthermore, the separation of individual source term contributions clearly indicates that the radiation due to H_x^x strongly dominates the acoustic field in the present jet configuration: the combined radiation from all other aeroacoustic sources together does not exceed -68 dB at any angle. Near $\vartheta = 90°$, where this low-level radiation may in principle be detected, the far field simulation results are likely to be affected by spurious numerical effects, most notably due to unphysical acoustic reflections at the domain boundaries.

The results presented in figure 5 are quite robust with respect to details of the extrapolation (4.1). A choice of x_0 anywhere in the interval $20 \leqslant x \leqslant 60$ locally changes the SPL values associated with H_x^x by not more than 0.5 dB.

Individual contributions of all other source terms are documented in figure 6. Acoustic emission from dissipative effects (D_x^x and D_r^x, dash-dotted and dotted lines in figure 6a) scales with the Reynolds number, and in the present case it is found to be negligible even when compared to the low-level radiation from the radial enthalpy flux H_r^x and the kinetic energy fluctuations K^x. While the fluctuation amplitude of H_r^x in the jet is comparable to that of the axial enthalpy flux H_x^x, its acoustic radiation is much less significant in an axisymmetric setting, due to the azimuthal interference given by $J_1(\alpha)$ in equation (3.36). Acoustic radiation from Reynolds stresses S_{xx}^x and S_{rr}^x (solid and dashed lines in figure 6b) is similar in strength to that from H_r^x and K^x, while the effects of S_{rx}^x and $S_{\varphi\varphi}^x$ are negligible. Although viscous stresses are included in the S_{ij} terms (equation 3.2), their contribution is found to be insignificant.

The Lighthill solution in figure 5 indicates a difference of only 3 dB between the upstream and downstream acoustic amplitude. This difference characterizes the weak superdirective quality of the acoustic field; it is caused by the antenna factor, *i.e.* by the variation of spectral density $\tilde{H}_x^x$ between $-k_a$ and $+k_a$. In comparison to the beam-like directivity pattern (1.1) measured by Laufer & Yen (1983), superdirectivity in the present configuration can be said to be negligible.

According to Crighton & Huerre (1990), superdirective radiation in the particular form of equation (1.1) would occur if the spectrum in figure 4b took the shape of a narrow Gauß function, centred at the carrier wavenumber $k_{\max} = 1.28$ and extending down to

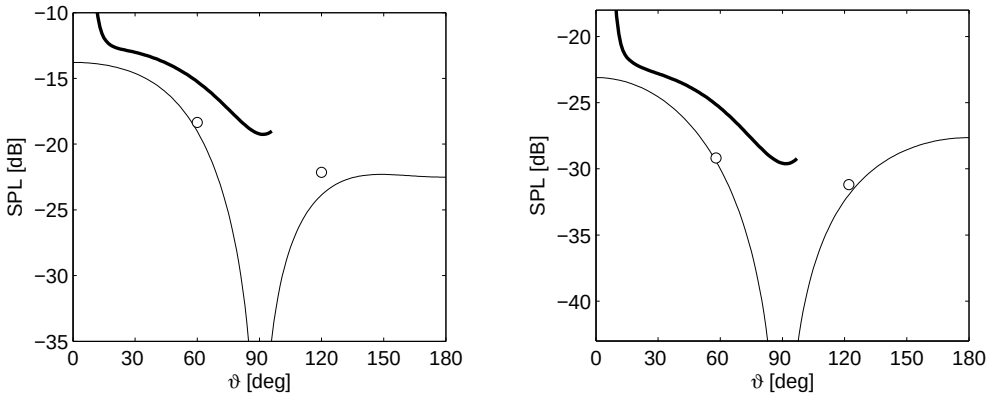

(a) $S = 0.1$ (b) $S = 0.2$

FIGURE 7. Supercritically hot jets with a) $S = 0.1$, b) $S = 0.2$. Directivity of the acoustic far field, comparison between direct numerical simulation and Lighthill solution. Directly computed sound (—); Lighthill solution due to enthalpy flux source term H_x^x without extrapolation (∘) and with extrapolation (—). Other sources are negligible (see text).

the acoustic range $|k| < k_a$. In the low Mach number limit ($k_{\max} \gg k_a$), this assumption indeed necessitates a perfectly Gaussian source distribution ($\propto \exp(x^2)$) in physical space over a large streamwise interval. Instead, it has been found that the source amplitude in the present configuration decays exponentially ($\propto \exp(x)$), as in the isothermal jet simulations of Mitchell *et al.* (1999). Crighton & Huerre (1990) have demonstrated that an exponential source envelope cannot give rise to a superdirective factor as measured by Laufer & Yen (1983).

A recent study by Obrist (2009) generalizes the analysis of Crighton & Huerre (1990) to two-dimensional wavepackets that are non-compact in both spatial directions. It is found that a finite cross-stream extent of the acoustic source region may strengthen the superdirective character of the far field. Whether the assumption of radial compactness is valid in the present context may be assessed by solving equation (3.14) with the two-dimensional source distribution $\hat{H}_x(r, x, \omega_g)$. It is difficult to define a consistent extrapolation procedure in two dimensions, therefore the non-compact solution may only be computed for radiation angles $\vartheta = 54°$ and $126°$. At both angles, the results are found to match the compact solution (white circles in figure 5) within 0.005 dB accuracy.

4.2. *Supercritically heated jets:* $S = 0.1$ *and* $S = 0.2$

The analysis carried out for the $S = 0.3$ jet in the preceeding section is now applied to the configurations with $S = 0.1$ and 0.2 (see §2.1). The global frequencies, as reported in Lesshafft *et al.* (2006), are $\omega_g = 0.493$ and 0.658, respectively, and the acoustic wavelengths therefore are $\lambda_a = 40.3$ and 42.7. The main results of the analysis are shown in figure 7: thick lines trace the acoustic directivity measured in the far field of the direct numerical simulations, thin lines and circle symbols represent the Lighthill solution due to the axial enthalpy flux source term H_x^x with and without streamwise extrapolation. As in the $S = 0.3$ jet, acoustic emission from all other source terms is found to be negligible in comparison. Their combined radiation, not shown in figure 7, is below -45 dB ($S = 0.1$) and -64 dB ($S = 0.2$). Sound pressure levels in both cases are again scaled with the respective maximum values of $|\hat{p}(\boldsymbol{x}, \omega_g)|$ in the near field.

Agreement between the directly computed acoustic field and the Lighthill solution for these two configurations is less accurate than in the $S = 0.3$ case. In both parts of figure

7, simulation and prediction results are seperated by almost 2 dB at $\vartheta = 20°$ and 5 dB at $\vartheta = 60°$. However, the overall dipole character is well retrieved in both cases, and the agreement may be regarded as sufficiently close in order to allow for a qualitative discussion. It can therefore be concluded that axial enthalpy flux fluctuations are the dominant acoustic source mechanism in globally unstable hot jets also at temperature ratios $S = 0.1$ and 0.2. The resulting acoustic field is that of a dipole, with maximum intensity in the upstream and downstream directions. Amplitude modulations due to the axial non-compactness of the source distribution are found to be moderately small, and the apparent source location corresponds to the region of vortex roll-up ($x = 3$ for $S = 0.1$ and $x = 4$ for $S = 0.2$). It is noted again that the acoustic radiation due to vortex pairing, as a secondary instability of the global mode structure, is not considered in the present study.

Direct numerical simulation results for the supercritical cases $S = 0.1$ and 0.2 are much more affected by numerical inaccuracies than the marginally unstable case $S = 0.3$. These inaccuracies stem primarily from the numerical treatment of the upstream boundary conditions (see §2.1). As discussed in Lesshafft *et al.* (2006, 2007), the location of vortex roll-up moves closer to the upstream domain boundary as the flow becomes more supercritical with decreasing values of S. This results in stronger spurious reflections, because the acoustic waves now propagate almost parallel to the upstream boundary, whereas the numerical treatment assumes nearly perpendicular incidence of acoustic waves. Spurious reflections increase the acoustic energy contained in the numerical domain. Unphysical interaction between acoustic and vortical perturbations at the upstream boundary must also be expected to increase as perturbation amplitudes reach nonlinear levels close to the inlet. It has been noted in Lesshafft *et al.* (2006, 2007) that the influence of the numerical boundary treatment on the near field dynamics is stronger for low values of S.

5. Conclusion

The near and far fields of three globally unstable hot jets have been resolved in direct numerical simulations of the axisymmetric Navier–Stokes equations. The three configurations have temperature ratios $S = 0.1$, 0.2 and 0.3, and associated Mach number values $Ma_\infty = 0.32$, 0.22 and 0.18. Results have been discussed in depth for the marginally unstable configuration with temperature ratio $S = 0.3$: the nonlinear global mode in the near field, described by Lesshafft *et al.* (2006), radiates into the far field as a compact acoustic dipole, with maximum amplitude along the jet axis. A solution to the Lighthill equation, including source terms due to fluctuations of enthalpy flux, kinetic energy, Reynolds stresses and dissipative effects (Lilley 1974, 1996), has been formulated for an axisymmetric geometry, with and without the assumption of radially compact source distributions. In order to retrieve the directly computed far field directivity pattern, the source distributions used in the Lighthill analysis have been extrapolated far beyond the downstream boundary of the computational domain used in the simulation. For the reference configuration with temperature ratio $S = 0.3$, the resulting Lighthill solution matches the directly computed acoustic field within 0.5 dB accuracy over a large range of the radiation angle. The decomposition of source terms has demonstrated that the global mode acoustic field is strongly dominated by dipole radiation due to *axial enthalpy flux* fluctuations.

The Lighthill analysis has been extended to the supercritical regime of strongly heated jets, with temperature ratios $S = 0.1$ and 0.2. Although the numerical simulation data obtained for these two configurations are not of the same high quality as in the $S =$

0.3 case, and the agreement with the Lighthill solution for the acoustic field is less accurate as a consequence, the analysis supports the same principal conclusion: the source mechanism related to the axial enthalpy flux strongly dominates the overall acoustic radiation, giving rise to a dipole directivity in the far field. Comparison between figures 5 and 7 demonstrates that the acoustic intensity increases with stronger heating.

Antenna effects, which could potentially yield a *superdirective* radiation pattern, are not found to be significant in the present configurations. At $S = 0.3$, the antenna factor only causes a 3 dB difference between the $\vartheta = 0°$ and the $\vartheta = 180°$ directions. The absence of superdirectivity is due to the spatial shape of the global mode wave packet: its k-spectrum is very different from a Gaussian shape (see figure 4b), and it presents only weak variations over the radiating interval $-k_a \leqslant k \leqslant k_a$. Higher values of the Mach number will probably favor superdirectivity; if Ma is increased, the radiating window is enlarged and may contain regions of large variations in spectral density. An extension of the present study to externally forced jets in the high subsonic Mach number regime will be the focus of future investigations.

It is a pleasure to dedicate this study to Steve Davis in recognition of his many fundamental contributions to fluid mechanics. Steve is a source of inspiration to all of us, from both a scientific and personal point of view.

We are very grateful to Professor Marvin Goldstein for his suggestion to employ Lilley's source term decomposition in the present study.

Financial support for this work was provided by ONERA and by the EADS Foundation.

REFERENCES

Andersson, N., Eriksson, L. E. & Davidson, L. 2005 Large-eddy simulation of subsonic turbulent jets and their radiated sound. *AIAA J.* **43** (9), 1899–1912.

Bodony, D. J. & Lele, S. K. 2005 On using large-eddy simulation for the prediction of noise from cold and heated turbulent jets. *Phys. Fluids* **17** (085103).

Bodony, D. J. & Lele, S. K. 2006 Review of the current status of jet noise predictions using large-eddy simulation. *AIAA Paper* **2006-0468**.

Bodony, D. J. & Lele, S. K. 2008 On using large-eddy simulation for the prediction of noise from cold and heated turbulent jets. *J. Fluid Mech.* **617**, 231–253.

Boersma, B. 2005 Large eddy simulation of the sound field of a round turbulent jet. *Theoret. Comput. Fluid Dynamics* **19**, 161–170.

Bogey, C. & Bailly, C. 2004 Investigation of subsonic jet noise using LES: Mach and Reynolds number effects. *AIAA Paper* **2004-3023**.

Bogey, C. & Bailly, C. 2005 Effects of inflow conditions and forcing on subsonic jet flows and noise. *AIAA J.* **43** (5), 1000–1007.

Bogey, C., Bailly, C. & Juvé, D. 2003 Noise investigation of a high subsonic, moderate Reynolds number jet using a compressible large eddy simulation. *Theoret. Comput. Fluid Dynamics* **16**, 273–297.

Crighton, D. 1975 Basic principles of aerodynamic noise generation. *Prog. Aerospace Sci.* **16**, 31–96.

Crighton, D. & Huerre, P. 1990 Shear-layer pressure fluctuations and superdirective acoustic sources. *J. Fluid Mech.* **220**, 355–368.

Dowling, A. 1992 Thermoacoustic sources and instabilities. In *Modern Methods in Analytical Acoustics*, pp. 378–405. Springer.

Fleury, V. 2006 Superdirectivité, bruit d'appariement et autres contributions au bruit de jet subsonique. PhD thesis, École Centrale de Lyon, France.

Fleury, V., Bailly, C. & Juvé, D. 2005 Shear-layer acoustic radiation in an excited subsonic jet: experimental study. *C. R. Mecanique* **333**, 746–753.

Fortuné, V. & Gervais, Y. 1999 Numerical investigation of the noise radiated from hot subsonic turbulent jets. *AIAA J.* **37** (9), 1055–1061.

Freund, J. 2001 Noise sources in a low-Reynolds-number turbulent jet at Mach 0.9. *J. Fluid Mech.* **438**, 277–305.

Freund, J. 2003 Noise source turbulence statistics and the noise from a Mach 0.9 jet. *Phys. Fluids* **15** (6), 1788–1799.

Giles, M. 1990 Nonreflecting boundary conditions for Euler equation calculations. *AIAA J.* **28**, 2050–2058.

Goldstein, M. E. 2003 A generalized acoustic analogy. *J. Fluid Mech.* **488**, 315–333.

Huerre, P. & Crighton, D. 1983 Sound generation by instability waves in a low Mach number flow. *AIAA Paper* **83-0661**.

Jordan, P., Gervais, Y., Valière, J.-C. & Foulon, H. 2002 Results from acoustic field measurements. *Tech. Rep.* G4RD-CT2000-00313. Laboratoire d'Etudes Aérodynamiques, Université de Poitiers, France.

Laufer, J. & Yen, T.-C. 1983 Noise generation by a low-Mach-number jet. *J. Fluid Mech.* **134**, 1–31.

Lesshafft, L. 2006 Nonlinear global modes and sound generation in hot jets. PhD thesis, École Polytechnique, Palaiseau, France.

Lesshafft, L. & Huerre, P. 2007 Linear impulse response in hot round jets. *Phys. Fluids* **19** (024102).

Lesshafft, L., Huerre, P. & Sagaut, P. 2007 Frequency selection in globally unstable round jets. *Phys. Fluids* **19** (054108).

Lesshafft, L., Huerre, P., Sagaut, P. & Terracol, M. 2006 Nonlinear global modes in hot jets. *J. Fluid Mech.* **554**, 393–409.

Lew, P.-T., Blaisdell, G. A. & Lyrintzis, A. S. 2007 Investigation of noise sources in turbulent hot jets using large-eddy simulation data. *AIAA Paper* **2007-0016**.

Lighthill, M. 1952 On sound generated aerodynamically – I. General theory. *Proc. Roy. Soc. London, Series A* **201** (1107), 564–587.

Lilley, G. M. 1974 On the noise from jets. *AGARD-CP* **131**, 13.1 – 13.12.

Lilley, G. M. 1996 The radiated noise from isotropic turbulence with application to the theory of jet noise. *J. Sound Vib.* **190**, 463–476.

Michalke, A. 1984 Survey on jet instability theory. *Prog. Aerospace Sci.* **21**, 159–199.

Mitchell, B., Lele, S. & Moin, P. 1999 Direct computation of the sound generated by vortex pairing in an axisymmetric jet. *J. Fluid Mech.* **383**, 113–142.

Monkewitz, P., Bechert, D., Barsikow, B. & Lehmann, B. 1990 Self-excited oscillations and mixing in a heated round jet. *J. Fluid Mech.* **213**, 611–639.

Morfey, C. L. & Wright, M. 2007 Extensions of Lighthill's acoustic analogy with application to computational aeroacoustics. *Proc. R. Soc. A* **463**, 2101–2127.

Obrist, D. 2009 Directivity of acoustic emissions from wave packets to the far-field. *J. Fluid Mech.* In press.

Shur, M., Spalart, P. R. & Strelets, M. K. 2005 Noise prediction for increasingly complex jets. part I: methods and tests. *Inter. J. Aeroacoustics* **4** (3–4), 213–266.

Tanna, H. K. 1977 An experimental study of jet noise. part I: turbulent mixing noise. *J. Sound Vib.* **50** (3), 405–428.

Viswanathan, K. 2004 Aeroacoustics of hot jets. *J. Fluid Mech.* **516**, 39–82.

Wang, M., Freund, J. B. & Lele, S. K. 2006 Computational prediction of flow-generated sound. *Annu. Rev. Fluid Mech.* **38**, 483–512.

Optimal velocity and density profiles for the onset of absolute instability in jets

By LUTZ LESSHAFFT[1] AND OLIVIER MARQUET[2]

[1]Laboratoire d'Hydrodynamique, CNRS – École Polytechnique, 91128 Palaiseau, France
[2]ONERA DAFE, 8 rue des Vertugadins, 92190 Meudon, France

(Received July 31, 2010)

The absolute/convective character of the linear instability of axisymmetric jets is investigated for a wide range of parallel velocity and density profiles. An adjoint-based sensitivity analysis is carried out in order to maximize the absolute growth rate of jet profiles with and without density variations. It is demonstrated that jets without counterflow may display absolute instability at density ratios well above the previously assumed threshold $\rho_{jet}/\rho_\infty = 0.72$, and even in homogeneous settings. Absolute instability is promoted by a strong velocity gradient in the low-velocity region of the shear layer, as well as by a step-like density variation near the location of maximum shear. A new efficient algorithm for the computation of the absolute instability mode is presented.

1. Introduction

The spontaneous onset of self-excited oscillations in low-density axisymmetric jets has been linked to the presence of absolute instability in the unperturbed underlying baseflow since their first experimental observation by Monkewitz *et al.* (1990). Numerous experimental and numerical studies have confirmed this hypothesis (*e.g.* Hallberg *et al.* 2007; Lesshafft *et al.* 2007, and references therein). One important implication of this association is that linear stability theory may predict the range of parameters, and in particular the ratio of jet density over ambient density, over which self-excited oscillations may occur in real jets.

Monkewitz & Sohn (1988) were the first to investigate the absolute/convective instability properties of low-density jets. For a specific family of analytical velocity and density profiles, designed to match experimental measurements, a transition from convective to absolute instability was found to be possible when the density ratio $S = \rho_{jet}/\rho_\infty$ fell below the critical value $S_{crit} = 0.72$. This value was obtained for the inviscid, zero-Mach-number case, and for a velocity profile with a thin shear layer of momentum thickness $\theta_u = 0.042$, nondimensionalized with the jet radius, as it may be found in the potential core region close to the nozzle exit. Lower Reynolds and higher Mach numbers, as well as thicker shear layers, were shown to require stronger density differences in order to admit absolute instability. Furthermore, for baseflow profiles typical of the potential core, absolute instability was always found to occur first for axisymmetric perturbations. Later linear instability studies by Jendoubi & Strykowski (1994) and Lesshafft & Huerre (2007) corroborated the validity of all the above observations for a different family of analytical profiles, introduced by Michalke (1971). The critical density ratio for this profile family was determined to be $S_{crit} = 0.713$, for a momentum thickness of $\theta_u = 0.039$. It has since been generally assumed that these critical values are approximately valid regardless of the precise functional shape of the velocity profile, which would then be sufficiently

characterized by its momentum thickness. The density profile in all these studies follows directly from the velocity profile via the Crocco–Busemann relation.

Coenen *et al.* (2008) integrated the boundary layer equations in order to obtain velocity profiles of low-density jets issuing from a straight pipe. Their computations account for the growth of a laminar boundary layer inside the pipe; at the nozzle exit, the density profile is prescribed as a step function. The analysis of Coenen *et al.* (2008) showed that absolute instability in such configurations may set in at a density ratio $S = 0.9$, for velocity profiles with a fairly thick shear layer $\theta_u = 0.1$. This remarkable result clearly demonstrates that the restriction to the previously studied analytical velocity profile shapes, and to density profiles governed by the Crocco–Busemann relation, is inadequate for determining a general upper bound for the density ratio of absolutely unstable jets.

The principal objective of the present study is to assess whether such an upper bound of S for the onset of absolute instability can be established. Towards this end, many limiting assumptions about the shape of velocity and density profiles will be successively relaxed. A sensitivity-based optimization procedure is employed to identify profile shapes that display absolute instability at a minimal density difference. The methodology is similar to that of Bottaro *et al.* (2003) and Hwang & Choi (2006). All previous jet instability studies, including that of Coenen *et al.* (2008), indicate that absolute instability can be expected to first arise for axisymmetric perturbations, at infinite Reynolds number and zero Mach number. The present investigation is therefore limited to those settings. The effects of jet swirl and of counterflow in the outer stream, which both may also give rise to absolute instability (Gallaire & Chomaz 2003; Jendoubi & Strykowski 1994), are excluded from the analysis.

The governing equations and numerical methods are presented in §2. In particular, the adjoint-based sensitivity analysis is laid out, and a novel efficient algorithm for calculating the absolute instability mode is introduced. Section 3 offers a parametric study of an analytical profile family, where velocity and density are no longer linked by the Crocco–Busemann law. In §4, the restriction to analytical profile shapes is dropped. Free optimization yields baseflow profiles that require a minimal density difference in order to be absolutely unstable. An argument for the early onset of absolute instability is derived from the shape of the eigenmodes.

2. Numerical model

2.1. *Direct and adjoint temporal dispersion relations*

The linear stability analysis in the present study is restricted to axisymmetric disturbances in inviscid jets at zero Mach number. Perturbations of the streamwise velocity u', radial velocity v' and pressure p' are assumed to take the form of normal modes $[u', v', p'](x, r, t) = [U(r), V(r), P(r)] \exp(i\omega t - ikx)$, where x and r are the streamwise and radial coordinates, ω is the complex circular frequency and k is the complex wavenumber. A parallel baseflow is defined by the velocity and density profiles $u_b(r)$ and $\rho_b(r)$. All quantities are made nondimensional with respect to the jet radius and the velocity and density values on the jet axis at $r = 0$. In the inviscid, zero-Mach-number limit, the linear perturbation equations given in Lesshafft & Huerre (2007) reduce to

$$ku_b U - iV\partial_r u_b + k\rho_b^{-1} P = \omega U\,, \tag{2.1}$$

$$ku_b V - i\rho_b^{-1}\partial_r P = \omega V\,, \tag{2.2}$$

$$\partial_r V + r^{-1} V + ikU = 0\,, \tag{2.3}$$

with boundary conditions $\partial_r U = V = \partial_r P = 0$ on the jet axis. Note that density perturbations at zero Mach number are decoupled from the velocity and pressure perturbations, and do not need to be solved for. Equations (2.1–2.3) are discretized using Chebyshev collocation, with 200 collocation points distributed over the interval $0 \leqslant r \leqslant r_{max} = 100$, according to the same mapping function as used in Lesshafft & Huerre (2007). The equations are then cast in the form of the discrete temporal eigenvalue problem $\mathbf{A}\mathbf{q} = \omega\mathbf{B}\mathbf{q}$, where the eigenvector $\mathbf{q} = (\mathbf{U}, \mathbf{V}, \mathbf{P})^T$ and the eigenvalue ω are associated with a prescribed value of k. This generalized eigenvalue problem is solved via an Arnoldi algorithm.

The adjoint eigenvector $\mathbf{q}^+$ associated with the direct eigenvector $\mathbf{q}$ for a given value of ω is found as a solution of the discrete adjoint eigenvalue problem $\mathbf{A}^H\mathbf{q}^+ = \omega^+\mathbf{B}^H\mathbf{q}^+$, with $\omega^+ = \bar{\omega}$. The superscript H denotes the conjugate transpose, an overbar denotes the complex conjugate. Note that $\mathbf{q}, \mathbf{q}^+$ in the following always represent associated pairs with $\omega^+ = \bar{\omega}$, and that $\mathbf{q}^+$ is assumed to be normalized such that $\mathbf{q}^{+H}\mathbf{B}\mathbf{q} = 1$. The adjoint eigenvector can therefore be obtained by solving the linear system $(\mathbf{A}^H - \bar{\omega}\mathbf{B}^H)\mathbf{q}^+ = 0$, which is regularized with the normalization condition.

2.2. *Sensitivities*

Knowledge of $\mathbf{q}^+$ allows to explicitly compute how small variations of the matrix $\mathbf{A}$ translate to small variations in ω. The perturbed direct problem

$$(\mathbf{A} + \delta\mathbf{A})(\mathbf{q} + \delta\mathbf{q}) = (\omega + \delta\omega)\mathbf{B}(\mathbf{q} + \delta\mathbf{q}) \tag{2.4}$$

is linearized and multiplied with $\mathbf{q}^+$ to give

$$\mathbf{q}^{+H}(\mathbf{A} - \omega\mathbf{B})\delta\mathbf{q} + \mathbf{q}^{+H}(\delta\mathbf{A} - \delta\omega\mathbf{B})\mathbf{q} = 0\,. \tag{2.5}$$

The first term in (2.5) is identically zero because $\mathbf{q}^{+H}(\mathbf{A}-\omega\mathbf{B}) = 0$; the second term yields $\delta\omega = \mathbf{q}^{+H}\delta\mathbf{A}\mathbf{q}$. In the context of this study, variations $\delta\mathbf{A}$ may arise from variations of the discrete baseflow vectors $(\mathbf{u}_b, \boldsymbol{\rho}_b)$ and of the wavenumber k. The associated gradients of the complex frequency are

$$\frac{\partial\omega}{\partial\mathbf{u}_b} = \mathbf{q}^{+H}\frac{\partial\mathbf{A}}{\partial\mathbf{u}_b}\mathbf{q}\,, \quad \frac{\partial\omega}{\partial\boldsymbol{\rho}_b} = \mathbf{q}^{+H}\frac{\partial\mathbf{A}}{\partial\boldsymbol{\rho}_b}\mathbf{q}\,, \quad \frac{\partial\omega}{\partial k} = \mathbf{q}^{+H}\frac{\partial\mathbf{A}}{\partial k}\mathbf{q}\,. \tag{2.6}$$

The partial derivatives of $\mathbf{A}$ are obtained by differentiation of the left-hand sides of (2.1–2.3). The gradient vectors $\partial\omega/\partial\mathbf{u}_b$ and $\partial\omega/\partial\boldsymbol{\rho}_b$ in (2.6) reflect the sensitivity of ω to baseflow variations at the collocation points; their numerical values are inherently dependent on the grid spacing. For the purpose of §4, it is preferable to define sensitivity vectors $\mathbf{s}_u, \mathbf{s}_\rho$ as discrete representations of continuous, grid-independent functions $s_u(r), s_\rho(r)$ over the interval $0 \leqslant r \leqslant r_{max}$, such that

$$\delta\omega = \int_0^{r_{max}} \left[s_u(r)\,\delta u_b(r) + s_\rho(r)\,\delta\rho_b(r)\right] \mathrm{d}r \approx \mathbf{s}_u^T\,\mathbf{M}\,\delta\mathbf{u}_b + \mathbf{s}_\rho^T\,\mathbf{M}\,\delta\boldsymbol{\rho}_b\,. \tag{2.7}$$

With a suitable diagonal metric $\mathbf{M}$, the grid-independent sensitivity values at the collocation points are then recovered as

$$\mathbf{s}_u = \mathbf{M}^{-1}\frac{\partial\omega}{\partial\mathbf{u}_b}\,, \quad \mathbf{s}_\rho = \mathbf{M}^{-1}\frac{\partial\omega}{\partial\boldsymbol{\rho}_b}\,. \tag{2.8}$$

The present formalism is entirely based on the *discrete* direct and adjoint dispersion relations. Continuous formulations of similar problems are given by Bottaro *et al.* (2003) and Hwang & Choi (2006). Both approaches are expected to give identical results.

2.3. *Absolute eigenmode*

The scalar quantity $\partial\omega/\partial k = v_g$ is the group velocity of the direct eigenmode. The absolute instability mode is characterized by a zero group velocity. The possibility to obtain v_g directly from (2.6) leads to a new procedure for the computation of the absolute eigenmode for a given baseflow. Starting from an initial guess k^* for the absolute wavenumber, the associated frequency and group velocity are computed by solving the direct and adjoint dispersion relations. A secant method is then employed to drive $v_g(k^*)$ towards zero, and to thereby converge to the true absolute wavenumber k_0 and frequency ω_0. This procedure is found to be highly efficient in the present calculations. The secant method gives a fast rate of convergence, because the group velocity is a nearly linear function of k in the vicinity of k_0. Each iteration involves the solution of one eigenvalue problem via an Arnoldi algorithm, which takes a fraction of a second even for excessive spatial resolutions, and the solution of a linear system for the adjoint eigenvector.

However, this algorithm does not guarantee that the final (k_0, ω_0) pair represents a pinch point between a k^+ and a k^- branch, according to the Briggs–Bers criterion (Huerre & Monkewitz 1990). The validity of this requirement has been verified for all final results presented in this paper via a detailed inspection of the spatial branches, as demonstrated in Lesshafft & Huerre (2007).

3. Absolute/convective transition for hyperbolic-tangent baseflow profiles

In the search for optimal velocity and density profiles that favour the onset of absolute instability at small density differences, a parametric study of analytical profile shapes is attempted first. Following the approach of Srinivasan *et al.* (2010), the familiar hyperbolic-tangent profiles of Michalke (1971) are extended in such a way that mixing layer thickness parameters b_u and b_ρ may be prescribed independently for the baseflow velocity u_b and density ρ_b. Furthermore, an offset d between the radial positions of both mixing layers is introduced. In a first step, let the baseflow be given by

$$\tilde{u}_b(r) = \frac{1}{2}\left(1 + \tanh\left[\frac{1}{4b_u}\left(\frac{1}{r} - r\right)\right]\right), \tag{3.1}$$

$$\tilde{\rho}_b(r) = \left\{S + \frac{1-S}{2}\left(1 + \tanh\left[\frac{1}{4b_\rho}\left(\frac{1}{r-d} - r + d\right)\right]\right)\right\}^{-1}. \tag{3.2}$$

With the implicit definition of the jet radius in the above formulation, the parameter b_u precisely represents the momentum shear layer thickness. However, since non-analytical profile shapes will be considered in §4, an explicit definition of the jet radius as a reference length scale will be used consistently throughout this study. The length scale is adjusted in such a way that the non-dimensional volume flux of the baseflow is that of a plug profile with radius 1, $\int_0^\infty u_b(r)\, r\, \mathrm{d}r = 0.5$. The profiles (3.1, 3.2) are rescaled as

$$u_b(r) = \tilde{u}_b(\alpha r)\,, \quad \rho_b(r) = \tilde{\rho}_b(\alpha r)\,, \quad \text{with} \quad \alpha^2 = 2\int_0^\infty \tilde{u}_b(r)\, r\, \mathrm{d}r\,. \tag{3.3}$$

The momentum shear layer thickness of the rescaled baseflow is $\theta_u = b_u/\alpha$.

3.1. *Parametric mapping*

The effect of variations in b_ρ and d on the absolute/convective transition is systematically investigated for a fixed velocity profile parameter $b_u = 0.05$ (corresponding to $R/\theta = 20$ in Lesshafft & Huerre 2007). Figure 1 displays contours of the critical density ratio S_{crit},

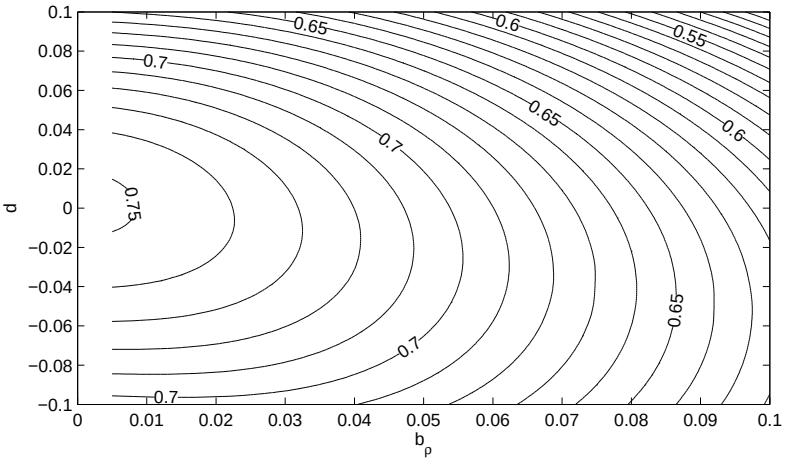

FIGURE 1. Critical density ratio S_{crit} for absolute/convective transition of hyperbolic-tangent profiles (3.1, 3.2) with $b_u = 0.05$, as a function of b_ρ and d.

at which the transition from convective to absolute instability takes place, as a function of b_ρ and d. The value of S_{crit} for each parameter combination has been determined iteratively by use of a secant method, ensuring that $\omega_{0,i}(S_{crit}) = 0$. Baseflows with a given combination (b_u, b_ρ, d) are absolutely unstable for all $S < S_{crit}$ and convectively unstable for all $S > S_{crit}$.

Figure 1 clearly demonstrates that thin density mixing layers favour the onset of absolute instability. In the absence of radial offset, $d = 0$, the critical density ratio increases monotonically with smaller values of b_ρ. The smallest value considered here is $b_\rho = 0.005$, but it may be estimated by extrapolation that a discontinuous step profile for the temperature would yield an asymptotic critical ratio $S \approx 0.751$ for $b_u = 0.05$ and $d = 0$. The optimal radial offset at a given value of b_ρ is found to be slightly negative. However, the increase in the critical density ratio that can be achieved by choosing $d \neq 0$ is rather insignificant, especially at small values of b_ρ. The general trends exposed in figure 1 for $b_u = 0.05$ are found to also hold for values $b_u = 0.1$ and 0.025.

3.2. *Parametric optimization*

In order to identify the optimal parameter combination (b_u, b_ρ, d) that yields the highest possible value S_{crit} for absolute/convective transition, one might proceed to extensively sample the four-dimensional parameter space, as done in the above section for one specific value of b_u. A more efficient approach may be derived from the sensitivity analysis of §2. The gradient of the complex frequency ω with respect to b_u, b_ρ, S and d at any given point in the parameter space is easily constructed via the chain rule:

$$\frac{\partial\omega}{\partial b_u} = \frac{\partial\omega}{\partial\mathbf{u}_b}\frac{\partial\mathbf{u}_b}{\partial b_u}\,, \quad \frac{\partial\omega}{\partial b_\rho} = \frac{\partial\omega}{\partial\boldsymbol{\rho}_b}\frac{\partial\boldsymbol{\rho}_b}{\partial b_\rho}\,, \quad \frac{\partial\omega}{\partial S} = \frac{\partial\omega}{\partial\boldsymbol{\rho}_b}\frac{\partial\boldsymbol{\rho}_b}{\partial S}\,, \quad \frac{\partial\omega}{\partial d} = \frac{\partial\omega}{\partial\boldsymbol{\rho}_b}\frac{\partial\boldsymbol{\rho}_b}{\partial d}\,. \tag{3.4}$$

The gradients $\partial\omega/\partial\mathbf{u}_b$ and $\partial\omega/\partial\boldsymbol{\rho}_b$ are obtained from (2.6), the partial derivatives of $\mathbf{u}_b$ and $\boldsymbol{\rho}_b$ follow directly from (3.1,3.2).

The optimization algorithm starts with the computation of (ω_0, k_0) for a given parameter combination (b_u, b_ρ, S, d). The gradient of the temporal growth rate $\omega_i = \Im(\omega)$ in the parameter space is evaluated according to the imaginary parts of (3.4). The parameters b_u, b_ρ and d are then varied in the direction of the positive gradient, such that ω_i is increased, whereas S is varied in such a way that ω_i is driven towards zero. The abso-

lute frequency/wavenumber pair is computed for the new baseflow, and the procedure is repeated until all four parameters are converged. The final value of S represents the highest possible value at which absolute/convective transition can be achieved with a baseflow of the form (3.1,3.2).

As may be expected from the results presented in figure 1, the optimization drives the temperature mixing layer thickness to ever smaller values. In order to maintain an appropriate discrete resolution of the continuous temperature profile, a finite lower bound must be imposed for b_ρ. With two different restrictions $b_\rho \geqslant 0.005$ and $b_\rho \geqslant 0.0025$, the optimized critical temperature ratio is found to be

$$S_{crit} = 0.7514 \quad \text{for} \quad b_u = 0.04935, \quad b_\rho = 0.005, \quad d = 0.0017, \quad \text{and} \tag{3.5}$$

$$S_{crit} = 0.7520 \quad \text{for} \quad b_u = 0.04929, \quad b_\rho = 0.0025, \quad d = 0.0021\,. \tag{3.6}$$

The value $b_u = 0.05$, used for the parametric study presented in figure 1, therefore is very near the optimal setting. The above optimization results are found to be insensitive to the choice of initial parameters, and in all likelihood represent the global optimum.

The threshold value $S_{crit} = 0.752$, above which absolute instability is impossible for the present family of baseflow profiles, is to be compared to the value $S_{crit} = 0.713$ that has been determined in previous studies of hyperbolic-tangent profiles restricted by the Crocco–Busemann law. The difference between these two values is not very significant, and it certainly does not explain the results of Coenen *et al.* (2008), who found absolute instability at $S = 0.9$.

4. Absolute/convective transition for shape-optimized profiles

For a more general investigation of optimal conditions for the onset of absolute instability in jets, the limiting assumption of any parametrized analytical shape for the velocity and density profiles is now relaxed. Each discretization point in both profiles now represents one degree of freedom. A minimal set of constraints is imposed in order to ensure that the baseflow retains the basic characteristics of a jet with prescribed density ratio S:

(a) $0 \leqslant u_b \leqslant 1$ and $1 \leqslant \rho_b \leqslant S^{-1}$ for all r,
(b) only one inflection point in u_b and in ρ_b,
(c) $\partial_r u_b = \partial_r \rho_b = 0$ at $r = 0$ and at r_{max}.

Conditions b) and c) also imply that both profiles vary monotonically in r.

Within these limits, the profile shapes with the maximum absolute growth rate for a given value of S are sought via successive baseflow modifications $\mathbf{u}_b^{n+1} = \mathbf{u}_b^n + \delta\mathbf{u}_b$ and $\boldsymbol{\rho}_b^{n+1} = \boldsymbol{\rho}_b^n + \delta\boldsymbol{\rho}_b$. This iterative process constitutes the *outer* optimization procedure. In each step, variations $\delta\mathbf{u}_b$ and $\delta\boldsymbol{\rho}_b$ of the current baseflow vectors $\mathbf{u}_b^n$ and $\boldsymbol{\rho}_b^n$ are obtained by solving an *inner* optimization problem: optimal variations are sought that maximize the increase of the temporal growth rate, given by the imaginary part of (2.7), while at the same time the modified profiles $\mathbf{u}_b^{n+1}$ and $\boldsymbol{\rho}_b^{n+1}$ must obey all the above constraints. This constrained optimization problem is solved using an SQP method, as implemented in the Matlab routine `fmincon`. Bounds for $\delta\mathbf{u}_b$ and $\delta\boldsymbol{\rho}_b$ follow from (a). The single-inflection-point condition is formally expressed as a linear inequality constraint, by requiring the second derivative of $\mathbf{u}_b^n + \delta\mathbf{u}_b$ to be non-positive for $r < r_{ip} - \varepsilon$, and non-negative for $r > r_{ip} + \varepsilon$, where r_{ip} is the current position of the inflection point. This position is allowed to change by a distance ε in the updated profile $\mathbf{u}_b^{n+1}$. A similar constraint is imposed on the density variations. Condition (c) yields Neumann boundary conditions for $\delta\mathbf{u}_b$ and $\delta\boldsymbol{\rho}_b$. In addition, the norm of the variations is prescribed as a nonlinear constraint $\delta\mathbf{u}_b^T\,\mathbf{M}\,\delta\mathbf{u}_b = \delta\boldsymbol{\rho}_b^T\,\mathbf{M}\,\delta\boldsymbol{\rho}_b = 0.01$ for well-posedness.

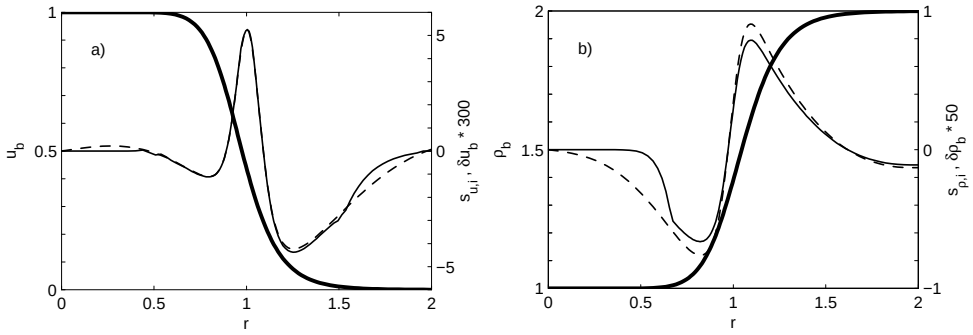

FIGURE 2. Baseflow profiles (3.1,3.2) with parameters $b_u = b_\rho = 0.1$, $d = 0$, $S = 0.5$, constrained optimal variations, and sensitivities of the absolute growth rate. *a)* ▬, velocity u_b; —, variation δu_b; - -, sensitivity $s_{u,i} = \Im(s_u)$; *b)* ▬, density ρ_b; —, variation $\delta\rho_b$; - -, sensitivity $s_{\rho,i} = \Im(s_\rho)$.

Figure 2 illustrates the approach for a hyperbolic-tangent baseflow (3.1,3.2). The baseflow profiles (thick lines) are shown together with their sensitivity distributions (dashed lines) and optimal variations (thin solid lines, note the ordinate scaling). The sensitivity values represent the gradient of the temporal growth rate with respect to unconstrained baseflow changes. The optimal variations are seen to closely follow the gradient direction, except in regions where such baseflow modifications would violate the constraints.

Once the optimal variations have been applied to the baseflow, a filter procedure $\tilde{f}(r_i) = 0.25f(r_{i-1}) + 0.5f(r_i) + 0.25f(r_{i+1})$ is performed on $\mathbf{u}_b^{n+1}$ and $\boldsymbol{\rho}_b^{n+1}$, in order to ensure that the profiles remain sufficiently smooth for an accurate computation of their radial derivatives. The absolute frequency and wavenumber of the new baseflow are then recalculated, and new variations are computed for the next outer optimization step.

4.1. *Optimized velocity profile of a homogeneous jet*

The case of a homogeneous jet is considered first. Keeping $\rho_b \equiv 1$ fixed, the baseflow velocity profile is optimized, starting from a hyperbolic-tangent profile (3.1) with $b_u = 0.1$ and $\omega_0 = 1.21 - 0.19i$, $k_0 = 1.07 - 1.63i$. Successive modification of the velocity profile yields a steady increase of the absolute growth rate, which finally takes on positive values — *i.e.* the homogeneous jet becomes absolutely unstable.

The profile shape with zero absolute growth rate ($\omega_0 = 1.21$, $k_0 = 1.11 - 1.99i$) is presented in figure 3a as a thick line. Most notably, this profile is characterized by an asymmetry of the shear layer, which is partitioned into an inner region with low shear and an outer region with high shear. As the optimization is pursued further, this asymmetry becomes increasingly pronounced: the thin line in figure 3a represents the final result, with $\omega_{0,i} = 0.06$. This optimal profile is of a nearly piece-wise linear shape, slightly smoothed by numerical filtering, with a sharp outer gradient. Without the single-inflection-point constraint, a concave shape would form in the inner region. The momentum shear layer thickness changes during the optimization process from $\theta_u = 0.10$ (initial profile with $b_u = 0.1$) to values of 0.09 ($\omega_{0,i} = 0$) and 0.16 ($\omega_{0,i} = 0.06$).

The optimization procedure converges to virtually identical final results from different starting conditions. This is demonstrated by the circle symbols in figure 3a, which represent the optimal result reached from an initial analytical profile with $b_u = 0.05$ (one out of two collocation points is shown).

As neither density inhomogeneities nor counterflow are present in the current config-

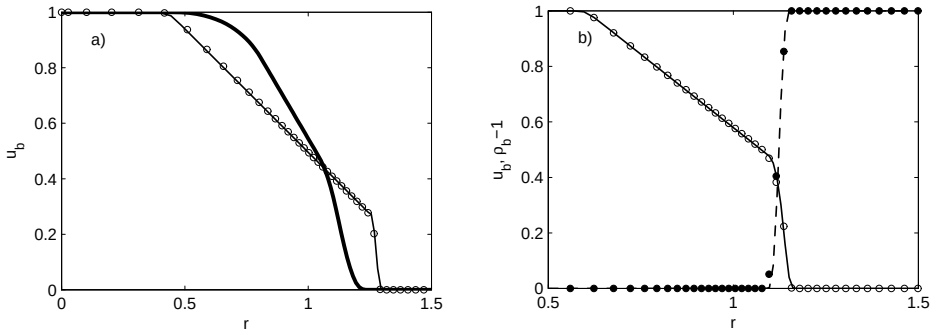

FIGURE 3. *a)* Velocity profiles of a homogeneous jet at two stages of the optimization, starting from (3.1) with $b_u = 0.1$: ▬, marginally unstable profile ($\omega_{0,i} = 0$); —, optimal profile ($\omega_{0,i} = 0.06$). Circles: optimal profile reached from (3.1) with $b_u = 0.05$. *b)* Optimal baseflow profiles for a low-density jet with $S = 0.5$, starting from $b_u = b_\rho = 0.1$: —, velocity u_b; - -, density ρ_b. Circles: optimal profiles reached from (3.1,3.2) with $b_u = b_\rho = 0.05$ (one out of two collocation points is plotted).

uration, the onset of absolute instability remains unexplained in light of the existing literature. An interpretation is attempted by examining the absolute eigenmode. Figure 4 displays the eigenfunctions of streamwise velocity $|U(r)|$ and pressure $|P(r)|$ for the marginally absolutely unstable profile as solid lines. These are compared to the corresponding eigenfunctions, shown as dashed lines, of the analytical profile (3.1) with $b_u = 0.1$. The pressure eigenfunctions (figure 4*a*) are very similar in both cases; they peak on the jet axis and decay monotonically in the radial direction. This shape is characteristic of the *jet column* mode, as opposed to the shear layer mode in a round jet (Jendoubi & Strykowski 1994). The velocity eigenfunctions (figure 4*b*) also share similar features; in particular, the location of the maximum amplitude in both cases coincides precisely with the maximum baseflow velocity gradient ($r = 1.12$ and $r = 0.95$, respectively). During the optimization procedure, this location continuously shifts into the region of low baseflow velocity. In analogy to configurations with counterflow, it may be surmised that a lower baseflow velocity around the peak location of the velocity eigenfunction leads to a lower group velocity of the instability mode, and thereby favours absolute instability.

4.2. *Optimized velocity and density profiles of a low-density jet*

When low-density jets are considered, the baseflow profiles of velocity and density may be varied separately or simultaneously. Starting from the analytical configuration displayed in figure 2, the baseflow density is first optimized alone, while the velocity profile is kept fixed. During the optimization, the baseflow density steadily evolves towards a step profile, with the maximum gradient always in the close vicinity of the maximum shear location. The absolute growth rate increases continuously with the steepening of the density profile. This observation is consistent with the results obtained for analytical profile shapes in §3.

Varying the baseflow velocity while keeping the analytical density profile fixed leads to a piece-wise linear velocity profile similar to the one shown in figure 3a. The presence of density variations increases the absolute growth rate, but it does not seem to alter in any significant way the trends discussed in §4.1.

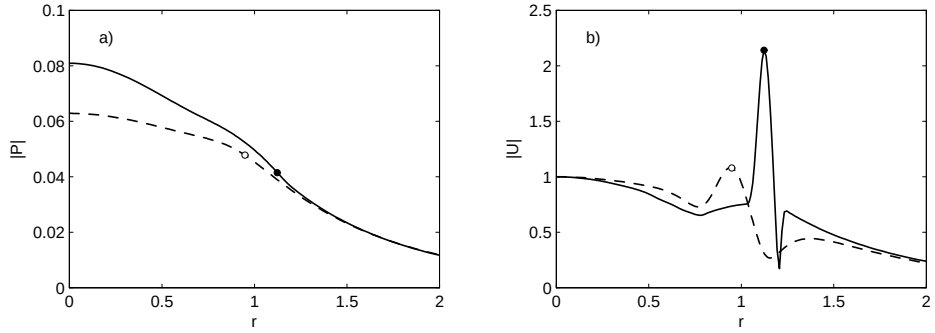

FIGURE 4. Eigenfunctions of the absolute mode in two homogeneous jets. ——, marginally AU profile (cf. figure 3a); - -, tanh-profile with $b_u = 0.1$. *a*) Pressure $|P(r)|$; *b*) streamwise velocity $|U(r)|$. Circles mark the respective locations of the maximum baseflow velocity gradient. All eigenfunctions are normalized with respect to the value of $|U|$ at $r = 0$.

Finally, u_b and ρ_b are allowed to evolve simultaneously, again starting from the analytical profiles given in figure 2. The final result is presented in figure 3b. The velocity profile (solid line) again takes on a piece-wise linear shape, within the requirement of smooth discretization as enforced by the filter procedure, whereas the density distribution (dashed line) approaches a step profile. The maximum of the density gradient occurs at $r = 1.12$, close to the location of maximum shear at $r = 1.14$. These optimal profile shapes are again reached from various starting conditions: the circle symbols in figure 3b represent a nearly identical optimization result, obtained from an initial hyperbolic-tangent profile with $b_u = b_\rho = 0.05$, $d = 0$ and $S = 0.5$. The absolute growth rate of the optimal baseflow is $\omega_{0,i} = 0.225$, the shear layer momentum thickness is $\theta_u = 0.095$. For comparison, the highest absolute growth rate that can be achieved with the analytical profile shapes (3.1,3.2) at $S = 0.5$ is determined as $\omega_{0,i} = 0.172$, for a much thinner shear layer $\theta_u \approx b_u = 0.036$ and with $b_\rho \to 0$, $d = 0$.

5. Conclusions

The onset of absolute instability in low-density jets has been investigated for a large variety of velocity and density profile shapes. The primary aim of this study was to determine whether a universal upper bound of the density ratio exists, above which absolute instability, in the absence of swirl or counterflow, would be impossible. The investigation is restricted to axisymmetric disturbances in inviscid, zero-Mach-number settings, and density ratios $S > 1$ (heavy jets) are not considered.

First, a classical family of hyperbolic-tangent baseflow profiles was extended to allow for independently prescribed values of the velocity and density mixing layer thickness, as well as for a radial offset between the two. The results of §3 have shown that only a modest increase of S_{crit} from 0.713 to 0.752 can be achieved within the remaining restriction to hyperbolic-tangent profile shapes. In §4, velocity and density profiles were iteratively modified, according to the sensitivity of the absolute growth rate $\omega_{0,i}$, such as to maximize $\omega_{0,i}$ for a given density ratio. The most important result from this investigation is that certain velocity profiles may exhibit absolute instability even in the homogeneous case $S = 1$. The precise shape of these profiles, as identified in §4, is certainly not encountered in typical laboratory jets. Yet their most characteristic feature, an asymmetry of the shear

layer that shifts the maximum shear into the low-velocity region, may be expected to be present in common jet flows immediately downstream of the nozzle. In particular, the velocity profiles of Coenen *et al.* (2008), which largely motivated the present study, prominently display such asymmetric shear layers.

An interpretation of how shear layer asymmetry may promote absolute instability is based on the observation that the peak of the velocity eigenfunction coincides with the location of maximum baseflow shear. It is argued that the group velocity of this mode is likely to decrease as its amplitude peak shifts into a region of low baseflow velocity.

Density profiles that optimally favour absolute instability have consistently been found to take the form of a step function. The step occurs very near the location of maximum shear.

All results presented herein lead to the conclusion that low-density jets may in principle display absolute instability at *any* density ratio. Furthermore, the momentum thickness of the velocity profile has been seen to be an inadequate measure for the instability characteristics. Whether a given baseflow is absolutely or convectively unstable depends critically on the precise shape of the velocity and density profiles.

We gratefully acknowledge the work of Emily Obert, who carried out the calculations presented in figure 1 during her stay at LadHyX, with support from the MIT–France program. Valuable discussions with Yongyun Hwang and Fulvio Martinelli have greatly contributed to this study. We thank Peter Schmid and Patrick Huerre for their helpful comments on this manuscript.

REFERENCES

Bottaro, A., Corbett, P. & Luchini, P. 2003 The effect of base flow variation on flow stability. *J. Fluid Mech.* **476**, 293–302.

Coenen, W., Sevilla, A. & Sánchez, A. 2008 Absolute instability of light jets emerging from circular injector tubes. *Phys. Fluids* **20**, 074104.

Gallaire, F. & Chomaz, J.-M. 2003 Mode selection in swirling jet experiments: a linear stability analysis. *J. Fluid Mech.* **494**, 223–253.

Hallberg, M., Srinivasan, V., Gorse, P. & Strykowski, P. 2007 Suppression of global modes in low-density axisymmetric jets using coflow. *Phys. Fluids* **19**, 014102.

Huerre, P. & Monkewitz, P. 1990 Local and global instabilities in spatially developing flows. *Annu. Rev. Fluid Mech.* **22**, 473–537.

Hwang, Y. & Choi, H. 2006 Control of absolute instability by basic-flow modification in a parallel wake at low Reynolds number. *J. Fluid Mech.* **560**, 465–475.

Jendoubi, S. & Strykowski, P. 1994 Absolute and convective instability of axisymmetric jets with external flow. *Phys. Fluids* **6**, 3000–3009.

Lesshafft, L. & Huerre, P. 2007 Linear impulse response in hot round jets. *Phys. Fluids* **19**, 024102.

Lesshafft, L., Huerre, P. & Sagaut, P. 2007 Frequency selection in globally unstable round jets. *Phys. Fluids* **19**, 054108.

Michalke, A. 1971 Instabilität eines kompressiblen runden Freistrahls unter Berücksichtigung des Einflusses der Strahlgrenzschichtdicke. *Z. Flugwiss.* **19**, 319–328.

Monkewitz, P., Bechert, D., Barsikow, B. & Lehmann, B. 1990 Self-excited oscillations and mixing in a heated round jet. *J. Fluid Mech.* **213**, 611–639.

Monkewitz, P. & Sohn, K. 1988 Absolute instability in hot jets. *AIAA J.* **26**, 911–916.

Srinivasan, V., Hallberg, M. P. & Strykowski, P. J. 2010 Viscous linear stability of axisymmetric low-density jets: Parameters influencing absolute instability. *Phys. Fluids* **22** (2), 024103.

A relaxation method for large eigenvalue problems, with an application to flow stability analysis

X. Garnaud, L. Lesshafft, P.J. Schmid, J.-M. Chomaz[a]

[a] *Laboratoire d'Hydrodynamique, Ecole Polytechnique – CNRS, Palaiseau, France*

Abstract

Linear stability analysis of fluid flows usually involves the numerical solution of large eigenvalue problems. We present a spectral transformation allowing the computation of the least stable eigenmodes in a prescribed frequency range, based on the filtering of the linearized equations of motion. This "shift-relax" method has the advantage of low memory requirements and is therefore suitable for large two- or three-dimensional problems. For demonstration purposes, this new method is applied to compute eigenmodes of a compressible jet.

Keywords: eigenvalue solver, spectral transformation, Krylov method, matrix-free, global modes

1. Introduction

The stability of fluid flow is a fundamental question in fluid dynamics, which has significant implications on the design, operation and control of flow devices. Consequently, hydrodynamic stability theory has taken a central role in fluid dynamics research, and remarkable progress has been made over the past decades. Early investigations of generic flow configurations, such as channel flows or boundary layers, have recently given way to more complex two- and three-dimensional geometries and more complex flow physics. The resulting eigenvalue problems from simple configurations were sufficiently small to allow their solution by direct techniques (such as the QR-algorithm). For more complex stability problems, however, direct techniques no longer provide a feasible solution; iterative eigenvalue algorithms have to be employed to compute a subset of the full spectrum that effectively describes the essential dynamics of small disturbances superposed on a steady base flow. Many of these algorithms for large-scale eigenvalue problems have been developed within the linear-algebra community and are readily available through several public domain libraries [12]. Among them, the two most commonly used in fluid-flow problems are the Arnoldi [16] and the Krylov-Schur [23] algorithms. These methods can, in principle, extract any portion of the full spectrum through the repeated application of a restarting step. In practice, however, only the dominant modes (i.e. those associated with the eigenvalues of largest magnitude) can be computed in many applications; yet, these modes may not provide relevant information about the physics of the problem and, in some cases, may even be spurious. As far as the asymptotic stability behavior is concerned, the least stable modes (i.e., the modes with the largest exponential growth rate) are far more important. They can be computed by coupling an iterative eigenvalue algorithm to a time-stepping routine for the linearized equations of motion (abbreviated by the linear operator L) over a given time interval Δt[10]. This way, the iterative eigenvalue solver will efficiently extract the modes that are most amplified over a time interval Δt, that is to say, it extracts the least stable modes of L. The propagation time Δt, in general, affects the speed of convergence of the iterative solver, but does not influence which modes the solver will converge to.

This technique is generally sufficient for bounded flows that are governed by a limited number of (or even a single) dominant instability mechanism, since the associated spectrum consists of eigenvalues that are well separated. In this case, the principal eigenvalues are easy to isolate by the iterative algorithm. When multiple and competing mechanisms are at play, the spectrum is far more complicated, and physically relevant modes are more difficult to extract. In particular, eigenvalue clusters near the neutral axis, stemming from

continuous branches or even numerical artifacts, pose a great challenge to the convergence of the iterative algorithm. Even though unstable modes may still be extracted, the stable part of the spectrum quickly moves beyond the reach of the iterative algorithm; in this case, a different strategy is called for.

The region of convergence may be manipulated and adjusted by a rational transformation of the complex eigenvalue plane. The "shift-invert" method [16] allows the computation of the modes whose eigenvalues are closest to a complex shift parameter σ. But at each iteration of the eigenvalue solver, the method requires the solution of a linear system of the form $(L-\sigma \mathrm{I})x = b$. Most studies accomplish the latter solution using a direct LU decomposition which has to be performed once at the start and is used for all successive iterations, until the shift parameter σ is changed to access different parts of the spectrum. A variant of the shift-invert method, known as the Cayley transformation, yields better convergence, if an iterative solution of the linear system is chosen [18].

The LU decomposition is based on a matrix representation of the linear stability operator. Some global stability investigations used spectral discretization methods which resulted in a dense matrix of moderate size [2]. Later studies took advantage of a sparse representation, in particular, when the operator arises from a finite-element or finite-difference discretization [5]. In this case, the number of non-zero elements is proportional to the number of degrees of freedom N, making a sparse matrix representation convenient to handle computationally. Highly efficient multi-frontal LU solvers for large-scale sparse matrices are readily available (see e.g. [9, 3, 4]), but the sparsity of the output matrices is not always guaranteed. Even though the bandwidth of the factorization is not greater than that of the original matrix [11, p.152], all elements between the upper and lower band may be non-zero. Computing and storing the decomposition thus results in substantial memory requirements. For example, for the discretization of a two-dimensional problem with N degrees of freedom on a structured mesh, the bandwidth scales with $N^{1/2}$, in which case the LU decomposition would contain up to $\mathcal{O}(N^{3/2})$ non-zero elements. In three dimensions, as the bandwidth increases to $N^{2/3}$, the memory requirements go up as $N^{5/3}$. For a discretization of the compressible Navier-Stokes equations on a two-dimensional domain with 256×512 points using a finite-differences scheme with a six-points stencil, one can estimate that storing the LU decomposition requires about 80 GB of memory (work space requirements during the decomposition tend to be even larger), thus illustrating the limitation of this method for larger-scale problems. In some cases, appropriate reordering of the matrix entries can somewhat alleviate the problem by improving the sparsity of the factorization; this approach, however, does not provide a viable and extendable solution for large-scale problems.

An alternative that avoids the computation of the LU decomposition of the operator L consists of iterative algorithms [24] to solve the linear system arising from the shift-invert or Cayley transformation. Together with ILU-type preconditioners, this approach has been applied to incompressible [15] and compressible flows [18]; in [22], the authors use un-preconditioned iterative solvers for the computation of unstable modes in plasma flows. These methods yield a reduction of computational costs associated with the solution of the linear system, but they do not provide the same level of versatility as direct methods do. Indeed, if one chooses the shift parameter σ close to the spectrum of L, then $(L - \sigma Id)$ becomes ill-conditioned. In this case, the cost of preconditioning as well as the number of iterations for the linear solver to converge have to be assessed critically. In contrast, if σ is selected farther from the spectrum, the iterative linear solver is more likely to converge with a "cheap" preconditioner, but at the same time the focusing effect of the shift-invert transformation is rather weak; consequently, it may not be possible to extract the desired modes.

The present paper presents a method for selectively extracting modal information from a linear operator L without relying on the (iterative or direct) solution of a linear system. This approach has been inspired both by the "shift-invert" technique for the solution of eigenvalue problems [16] and by the selective frequency damping method of [1] for the computation of unstable steady flow. Similar to the latter method, we propose to use a relaxation procedure to selectively stabilize parts of the spectrum away from a chosen frequency shift, after which a standard Krylov method is employed to obtain the least stable modes of the relaxed system. Although the spectral transformation involved in the present "shift-relax" technique is somewhat less flexible than the "shift-invert" technique, its low memory requirement and ease of implementation make it suitable and attractive for large-scale stability computations of two- or three-dimensional flows.

2. Description of the method

2.1. Definition of the problem

Let the dynamics of the problem under consideration be governed by a set of non-linear equations of the form

$$\dot{\boldsymbol{q}} = F(\boldsymbol{q}), \tag{1}$$

where $\boldsymbol{q}$ is the state vector and F denotes a discrete integro-differential operator with appropriate boundary conditions. For simplicity, only finite-dimensional operators (which arise after spatial discretization) will be considered in this paper. We assume that this operator has a fixed point $\boldsymbol{q}_0$, such that $F(\boldsymbol{q}_0) = 0$. If this *base state* is stable to finite-amplitude perturbations, it can be computed by integrating the dynamical system (1) over a sufficiently long time. Algorithms such as the Newton-Krylov method [10] or Selective Frequency Damping (SFD) [1] can be used to obtain a base state even in unstable situations. The SFD method relies on low-pass filtering of the equations of motion in order to suppress high-frequency instabilities. The present method generalizes this approach in order to compute modes of a linear operator in a selected frequency band.

Let $L = \nabla_{\boldsymbol{q}} F(\boldsymbol{q}_0)$ be the linearization of F about the steady base state $\boldsymbol{q}_0$. Based on the decomposition $\boldsymbol{q} = \boldsymbol{q}_0 + \boldsymbol{q}'$, the dynamics of small perturbations $\boldsymbol{q}'$ is governed by the linear system

$$\dot{\boldsymbol{q}}' = L\boldsymbol{q}'. \tag{2}$$

Temporal modes of (2) are sought in the form

$$\boldsymbol{q}'(\boldsymbol{x}; t) = \widetilde{\boldsymbol{q}}(\boldsymbol{x}) \exp(-\mathrm{i}\omega t),$$

such that the spatial structure $\widetilde{\boldsymbol{q}}$ satisfies

$$-\mathrm{i}\omega\widetilde{\boldsymbol{q}} = L\widetilde{\boldsymbol{q}}. \tag{3}$$

A *complex* eigenfrequency ω is associated with the eigenmode $\widetilde{\boldsymbol{q}}$.

If an iterative solver is used to compute the least stable modes of (3) using an iterative eigenvalue solver, it is of advantage to consider the operator that takes a state $\boldsymbol{q}'(0)$ as an initial condition for (2) and returns the state $\boldsymbol{q}'(\Delta t)$ after a given time Δt. This operator is referred to as the *propagator* and can be formally written as

$$P = \exp(\Delta t L).$$

Krylov-based iterative eigenvalue solvers identify a subset of the eigenvalues $\lambda = \lambda_r + \mathrm{i}\lambda_i$ with the largest absolute value $|\lambda|$ (in the following, the subscript $_r$ and $_i$ respectively denote the real and imaginary parts of a complex number). Modes of P with the largest $|\lambda|$ are identical to modes of L with the largest *growth rate* ω_i. Even though the explicit computation of the matrix P would be an onerous task, its application to vectors can be easily performed by a standard time marching method; this makes the use of P appropriate for an iterative solver.

For some flows however, it may be interesting to investigate modes that belong to different frequency ranges, as these may correspond to different physical mechanisms (see for example the case of the flow around a leading edge [19] or that of supersonic jet flows [20]). In this case the objective is to compute the least stable modes with a real frequency ω_r close to a given value ω_0. The present method achieves this goal by applying a bandpass temporal filter to the propagator, such that modes with real frequency ω_r far from the target frequency $\omega_{0,r}$ are attenuated.

2.2. Filtering

In this section we recall standard filtering results applied to a signal $\boldsymbol{y}(t)$ with $t \in \mathbb{R}$. Its Fourier transform reads

$$\boldsymbol{y}(t) = \int_{-\infty}^{\infty} \hat{\boldsymbol{y}}(\omega) \exp(-\mathrm{i}\omega t)\, \mathrm{d}\omega.$$

We proceed by damping out the components of $\boldsymbol{y}(t)$ with frequencies far from a given value ω_0 using a standard first-order bandpass filter whose transfer function is given by

$$H(\omega) = \frac{1}{1 - \mathrm{i}\dfrac{\omega - \omega_0}{\tau}}. \tag{4}$$

The filtered signal $\bar{\boldsymbol{y}}(t)$ is then given by the convolution

$$\bar{\boldsymbol{y}}(t) = \int_{-\infty}^{\infty} H(\omega)\hat{\boldsymbol{y}}(\omega)\exp(-\mathrm{i}\omega t)\,\mathrm{d}\omega,$$

which satisfies the filtered ordinary differential equation

$$\dot{\bar{\boldsymbol{y}}} = -\mathrm{i}\omega_0\bar{\boldsymbol{y}} - \tau(\bar{\boldsymbol{y}} - \boldsymbol{y}). \tag{5}$$

The above bandpass filter is centered about the target frequency ω_0 and has a half width at half maximum of $\sqrt{3}\tau$.

The presented analysis applies to signals defined for all times. If one wants to use the differential equation (5) to filter a signal defined only for $t \geq 0$, initial conditions have to be specified. The overall frequency selection effect, however, will prevail independent of initial conditions, if the differential equations have been sufficiently advanced in time. In this way, the differential equation (5) provides a way to filter a signal without having to store its entire history.

2.3. Selective frequency damping of a linear dynamical system

Following [1], let us consider the following linear dynamical system:

$$\dot{\boldsymbol{q}}' = L\boldsymbol{q}' - \chi(\boldsymbol{q}' - \overline{\boldsymbol{q}}'), \tag{6a}$$

$$\dot{\overline{\boldsymbol{q}}}' = -\mathrm{i}\omega_0\overline{\boldsymbol{q}}' - \tau(\overline{\boldsymbol{q}}' - \boldsymbol{q}'). \tag{6b}$$

Equation (6b) represents a differential equation corresponding to the bandpass filter introduced above. The signal $\overline{\boldsymbol{q}}'$ is therefore a filtered version of $\boldsymbol{q}'$, in which frequency components far from the target frequency ω_0 are damped.

The right-hand side of (6a) is a sum of two terms. The first one represents the linear operator, while the second part acts as a proportional controller that drives the variable $\boldsymbol{q}$ towards its filtered counterpart $\overline{\boldsymbol{q}}$.

The SFD procedure of [1] applies the same filtering with $\omega_0 = 0$ to a non-linear operator instead of L in (6). In this case, any fixed point of F corresponds to a fixed point of the extended system, the filtered state $\overline{\boldsymbol{q}}'$ being then equal to the full state. However, the stability of the fixed point of the extended system is modified and trajectories differ. Our shift-relax (SR) approach relies on the observation that the frequency selection procedure not only preserves the fixed points of non-linear operators, but also the eigenmodes of linear systems, as will be demonstrated next.

In order to study the relationship between the spectra associated with the original linear dynamical system (2) and the SR extension (6), we introduce the composite filtered operator $\mathcal{F}$ defined as

$$\mathcal{F} \equiv \left(\begin{array}{c|c} L - \chi\mathrm{Id} & \chi\mathrm{Id} \\ \hline \tau\mathrm{Id} & (-\mathrm{i}\omega_0 - \tau)\mathrm{Id} \end{array}\right) \tag{7}$$

such that (6) can be rewritten as

$$\begin{pmatrix} \dot{\boldsymbol{q}}' \\ \dot{\overline{\boldsymbol{q}}}' \end{pmatrix} = \mathcal{F}\begin{pmatrix} \boldsymbol{q}' \\ \overline{\boldsymbol{q}}' \end{pmatrix}.$$

If the state vector $\boldsymbol{q}'$ contains N elements, then a $2N$-dimensional eigenvector of $\mathcal{F}$ associated with the complex eigen-frequency Ω, i.e.

$$\mathcal{F}\widetilde{\boldsymbol{Q}} = -\mathrm{i}\Omega\widetilde{\boldsymbol{Q}},$$

can be decomposed into two N-dimensional components, $\widetilde{\boldsymbol{Q}} = (\widetilde{\boldsymbol{q}}, \widetilde{\widetilde{\boldsymbol{q}}})^T$. According to (6b), these two components are related by

$$\widetilde{\widetilde{\boldsymbol{q}}} = \frac{1}{1 - \mathrm{i}\dfrac{\Omega - \omega_0}{\tau}} \widetilde{\boldsymbol{q}}.$$

Consistent with the design of the filter, the scalar factor between $\widetilde{\widetilde{\boldsymbol{q}}}$ and $\widetilde{\boldsymbol{q}}$ can be related to the transfer function (4). We can substitute this result back into (6a) to obtain

$$L\widetilde{\boldsymbol{q}} = -\mathrm{i}\omega(\Omega)\widetilde{\boldsymbol{q}} \tag{8}$$

with

$$\omega(\Omega) = \Omega + \mathrm{i}\chi \left(1 - \frac{1}{1 - \mathrm{i}\dfrac{\Omega - \omega_0}{\tau}} \right). \tag{9}$$

Equation (8) shows that $\widetilde{\boldsymbol{q}}$, i.e. the vector corresponding to the first N elements of $\widetilde{\boldsymbol{Q}}$, is an eigenvector of L. This justifies the use of the SR system (6) as a spectral transformation, as the modes of L can be recovered from those of $\mathcal{F}$.

Equation (9) characterizes the mapping between the spectra of L and $\mathcal{F}$. For any eigenvector $\widetilde{\boldsymbol{Q}} = (\widetilde{\boldsymbol{q}}, \widetilde{\widetilde{\boldsymbol{q}}})^T$ of $\mathcal{F}$ with complex frequency Ω, $\widetilde{\boldsymbol{q}}$ is an eigenvector of L with complex frequency $\omega(\Omega)$ given by (9). This latter equation can be re-arranged as a second-order polynomial in Ω where ω appears as a parameter. This shows that two values of Ω correspond to a single value of ω, which is consistent with the fact that the dimension of $\mathcal{F}$ is twice the dimension of L.

Proceeding with the analysis of the mapping between the spectra of the original operator L and its SR extension $\mathcal{F}$, let us introduce the following scaled variables

$$(\omega', \Omega', \chi') = \frac{1}{\tau}(\omega - \omega_0, \Omega - \omega_0, \chi).$$

Equation (9) can then be simplified as follows

$$\omega' = \Omega' + \mathrm{i}\chi' \left(1 - \frac{1}{1 - \mathrm{i}\Omega'} \right). \tag{10}$$

It therefore appears that after a shift of origin (given by the parameter ω_0) and a scaling (given by the factor τ) of the complex-frequency plane, the transformation can be studied in terms of one single parameter $\chi' = \chi/\tau$.

Effect of χ'. The parameter χ' measures the gain of the proportional controller relative to the frequency scale τ. The analysis (given in detail in Appendix A) shows how χ' influences the spectral transformation. We observe that the transformation is self-similar with respect to two transformations of ω' and Ω' : first, by different shifts of origins of these two variables and, second, by a scaling by the factor ${\chi'}^{-1/2}$. The shift of origin for Ω' has no influence on the frequency selection effect of the filter, as it changes neither the order in which modes will be extracted nor the separation between the eigenvalues of the filtered propagator. The scaling is more relevant, but its effect on the transformation is the same as that of τ. Acting on χ' therefore adds no additional flexibility to the method. In an effort to keep the scaling of the complex plane and the shift of origin as two parameters, we choose $\chi' = 1$ throughout our study and only use ω_0 and τ as changing parameters.

Study of the transformation for $\chi' = 1$. For a given value of ω', (10) is a second-order polynomial in Ω'. As mentioned previously, this results in two solution branches, for which an analytic expression can easily be obtained. We note that the distinction between the two branches is not unique, as it depends on the location of the branch cut for the square root function with complex arguments. In the following representation we chose the common branch cut for negative real arguments of the square root.

Figure 1a, b illustrates the mapping between the original spectral plane ω' and the two associated values of $\Omega'_{1,2}$ by the SR transformation, respectively indicated by blue and black lines, together with the transformation of several sample values of ω' represented by colored symbols. These values are chosen arbitrarily for illustration purposes. The solid and dashed lines in figure 1b are, respectively, the images of iso-ω'_i- and iso-ω'_r-lines in the ω'-plane represented in figure 1a. The mapping (with the chosen branch cut) defines two regions of the complex Ω'-plane. Values of Ω' inside the unit circle centered at $\Omega' = -\mathrm{i}$ correspond to the first root Ω'_1 while values outside the circle correspond to the second root Ω'_2. Accordingly, the sample values represented by colored symbols in figure 1a has two images in the Ω'-plane. We notice, however, that neither the mapping $\omega' \to \Omega'_1$ nor the mapping $\omega' \to \Omega'_2$ is continuous.

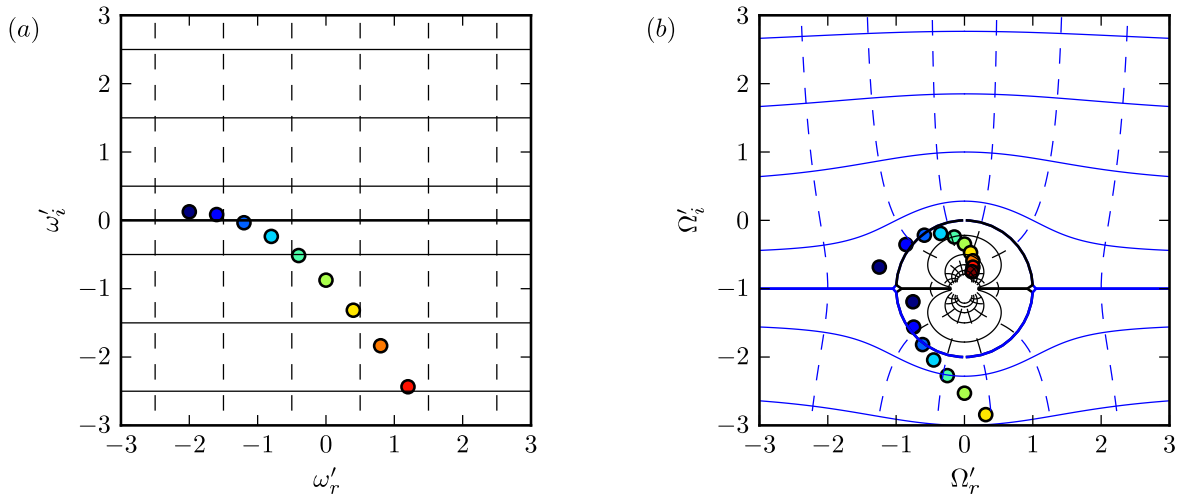

Figure 1: Mapping between the original spectral plane ω' (a) and its SR-transformed image Ω' (b). The colored symbols correspond to sample values.

The images of the sample values in figure 1b suggest another distinction between the two images of ω'. We respectively define Ω'^+ and Ω'^- as the images of ω' such that the following relation involving the transformed growth rates is satisfied

$$\Omega'^-_i(\omega') \leq -1 \leq \Omega'^+_i(\omega').$$

See Appendix A for a proof. As τ is real and positive, the above distinction between the two branches results in

$$\Omega^-_i \leq \omega_{0,i} - \tau \leq \Omega^+_i,$$

expressed in terms of the non-scaled variables.

The least stable modes of the SR operator $\mathcal{F}$ (given in (7)) will then be extracted by applying an eigenvalue solver to the filtered propagator

$$\mathcal{P} = \exp(\mathrm{i}\Delta t \mathcal{F}) \tag{11}$$

as motivated in § 2.1. This will extract the least stable modes of the filtered operator $\mathcal{F}$. Consequently, we can restrict our attention to the Ω'^+ branch. Furthermore, as only the growth rate rather than the frequency decides which modes will be extracted, the relevant features of the transformation can be studied in terms of the single-valued real function $\omega' \to \Omega'^+_i$. This function is represented in figure 2.

Three regions of the ω'-plane can be identified:

- For $1 \lesssim \omega'_i$, the transformed growth rate Ω'^+_i behaves similar to the un-transformed growth rate ω'_i. No significant dependency with ω'_r is observed, indicating that no noticeable frequency selection occurs.

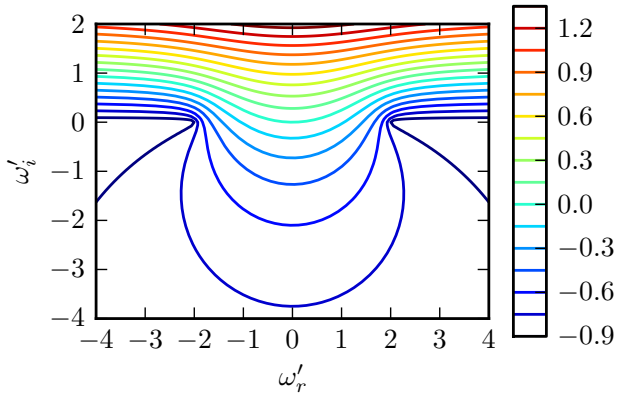

Figure 2: Imaginary part of the eigenvalue of the SR operator $\Omega_i'^{+}(\omega')$ as a function of the eigenvalue ω' of the origin for $\chi' = 1$.

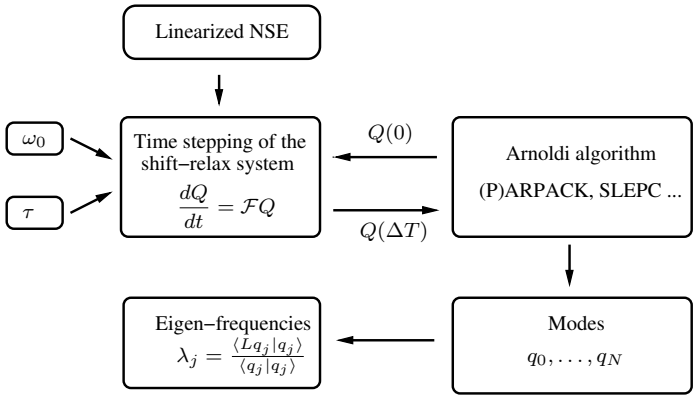

Figure 3: Practical implementation of the method

- For $-2 \lesssim \omega_i' \lesssim 1$, the value of $\Omega_i'^{+}(\omega')$ exhibits strong dependency on the real frequency ω_r'. Along a line of constant ω_i, the value of $\Omega_i'^{+}(\omega')$ reaches a maximum for $\omega_r = 0$, confirming that the filter plays the expected role of stabilizing modes with real frequencies far from $\omega_{0,r}$.
- For $\omega_i' \lesssim -2$, $\Omega_i'^{+}(\omega')$ is approximately constant. The dynamics of the SR system is dominated by the control term in (6a) which conceals the dynamics of the linear operator L.

The above representation allows to determine the behavior of the proposed method. For $\omega_i \gtrsim \omega_{0,i} + \tau$, the spectral transformation produces results similar to that of the propagator approach (see § 2.1 and [10]). The frequency selection effect is insignificant in this region. Strong frequency selection is achieved in the range of frequencies $\omega_{0,i} - 2\tau \lesssim \omega_i \lesssim \omega_{0,i} + \tau$, as the effect of the bandpass filter is clearly present. Modes with real frequencies outside a bandwidth of order τ centered around $\omega_{0,r}$ are damped. In this range of growth rates, modes with real frequencies close to $\omega_{0,r}$ will be extracted first. All modes with a growth rate $\omega_i \lesssim \omega_{0,i} - 2\tau$ will map to essentially the same growth rate for the SR operator. These modes will be difficult to distinguish with an iterative eigenvalue solver.

2.4. Numerical considerations

Implementation. A practical implementation of the present method requires only few additions to a standard DNS code. These are summarized in figure 3. First, a routine evaluating the linearized Navier-Stokes operator is needed. The linearization may be carried out by hand, as done in the examples given in this paper, or numerically "on the fly" from a non-linear routine, as done in [14].

Next, the eigenvalue extraction is performed. Several libraries for both sequential and parallel implementations may be used for this task. The Krylov-Schur solver provided in the SLEPc library [23] is used here to extract the eigenmodes of the SR operator, with 60 Krylov vectors. Better convergence behavior has been observed compared to the Implicitly Restarted Arnoldi Method (IRAM), which is more frequently used for the computation of modes in fluid flow problems[16]. In [22], the authors report good results using the "harmonic extraction" solver of SLEPc for frequency selection. For our cases, this method has not produced the desired outcome.

Finally, only minor changes in order to integrate the filtering procedure into a standard time-stepping routine are necessary. The algorithm for the time stepping of the SR dynamical system is exemplified using an explicit Euler scheme as outlined below. The variables q_1 and q_2, respectively, represent the state and its filtered counterpart, L is the linear flow operator, and δt is a discrete time step.

1: $t \leftarrow 0$
2: **while** $t \leq \Delta t$ **do**
3: $\quad r_1 \leftarrow L(q_1)$
4: $\quad r_1 \leftarrow r_1 - \chi * (q_1 - q_2)$
5: $\quad r_2 \leftarrow \mathrm{i}\omega_0 * q_2 - \chi * (q_2 - q_1)$
6: $\quad q_1 \leftarrow q_1 + \delta t * r_1$
7: $\quad q_2 \leftarrow q_1 + \delta t * r_2$
8: $\quad t \leftarrow t + \delta t$
9: **end while**

The algorithm differs from standard time stepping by the additional lines 4, 5 and 7. These correspond to a small number of operations compared to the application of the operator L, in particular, when high-order schemes are employed; the SR computations are therefore only slightly slower than regular time-stepping, and they can be just as efficiently parallelized.

Memory requirements. The memory requirement of the present method is twice that of a standard propagator technique, as the dimension of the phase space is doubled due to the presence of the filtered variables. If the eigenvalue solver and the time stepper respectively require ncv and nts vectors of size N (the number of degrees of freedom associated with the discretization of the equations) as workspace, most of the memory requirement will originate from the storage of these $2N(ncv + nts)$ values. For the discretization of the compressible Navier-Stokes equations mentioned in the introduction with $ncv = 60$, $nts = 20$ and double precision complex arithmetics, the program would require $2 \times 5 \times 256 \times 512 \times 80 \times 16$ B ≈ 1.6 GB of memory, which is substantially less than the 80 GB required for the sparse LU decomposition alone.

Effect of the propagation time. The effect of the propagation time on the SR operator is the same as for the classical propagator method [10]. The actual value of the propagation time Δt should not influence which subset of modes will be extracted. The propagation time will however affects the convergence of the eigenvalue solver. If Δt is small, only a few time marching steps are required in each iteration; nonetheless, a large number of iterations will be necessary in order to reach a desired accuracy. It will also require a large number of restarts, which ultimately may affect robustness. On the other hand, if Δt is too large, each iteration will be rather costly since it consists of many time steps, and the method will make less use of the orthogonalization step. A balance has to be found between the computational time needed to propagate the solution forward in time, the cost associated with the eigenvalue solver and the robustness of the restarting procedure.

Time stepping accuracy. Numerical time stepping methods such as Euler and Runge-Kutta schemes correspond to an approximation of the exponential matrix propagator by a matching polynomial. Such an approximation preserves the modes: it therefore introduces no error on the computed modes. In practical applications, the time step δt of the time-stepping routine is much smaller than the characteristic time scale of modes one wishes to compute. As a consequence, the spectrum transformation introduced by numerical time stepping will be nearly exponential in the range of eigenfrequencies of interest, such that the rules derived earlier for the choice of parameters remain valid.

Eigenvalue recovery. As explained in § 2.3, recovering the eigenvectors of L is straightforward, as they correspond to the first N components of the eigenvectors of the SR propagator. The eigenfrequency ω associated with an eigenvector $\boldsymbol{q}$ of L may conveniently be obtained by computing the Rayleigh quotient

$$-\mathrm{i}\omega = \frac{\langle \boldsymbol{q}|L\boldsymbol{q}\rangle}{\langle \boldsymbol{q}|\boldsymbol{q}\rangle}. \tag{12}$$

Alternatively, the eigenvalue Ω of the SR operator may be computed from the eigenvalue λ of the SR propagator via

$$\Omega = \frac{\log(\lambda)}{-\mathrm{i}\Delta t}, \tag{13}$$

and (9). Method (12) has three advantages over the latter method. First, as the logarithm is multivalued, the above formula yields the imaginary part only if one knows the Riemann sheet Ω lies on, i.e. for example that $0 \leq \Omega_r \leq 2\pi/\Delta t$. Second, the numerical time stepping makes (13) inexact: as discussed in § 2.4, the transformation introduced by time-stepping is not exactly exponential but rather a polynomial approximation. This problem does not arise for the Rayleigh quotient (12). Finally, (12) minimizes the residual $\|L\boldsymbol{q} + \mathrm{i}\omega\boldsymbol{q}\|/\|\boldsymbol{q}\|$, the norm being that corresponding to the inner product in (12). This inner product may include weights that select specific flow quantities of regions. In all computation presented in § 3 and 4, the l^2 inner product on the state vector components is chosen as it is the one used in the Krylov–Schur algorithm.

3. Application to the local and global stability analysis of a compressible jet

3.1. Governing equations for local and global computations

We consider a compressible jet of radius R, with characteristic velocity U_0, density ρ_0 and temperature T_0 measured on the centerline, discharging into a fluid at rest with density ρ_∞ and temperature T_∞. These same quantities are used to make the problem non-dimensional. In a cylindrical coordinate system (x, r, θ), the nonlinear governing equations are expressed in terms of the conservative flow variables $\boldsymbol{q} = (\rho, \rho u_x, \rho u_r, \rho u_\theta, \rho E)^T$, where ρ is the density, $\boldsymbol{u} = u_x\boldsymbol{e}_x + u_r\boldsymbol{e}_r + u_\theta\boldsymbol{e}_\theta$ is the flow velocity, and E denotes the total energy [25]. The Reynolds, Mach and Prandtl numbers are defined as

$$\mathrm{Re} = \frac{U_0 R \rho_0}{\mu}, \qquad \mathrm{Ma} = \frac{U_0}{c_0}, \qquad \mathrm{Pr} = \frac{\mu C_p}{\kappa} = 1, \tag{14}$$

with c_0 the reference speed of sound on the jet axis, C_p the ambient specific heat at constant pressure, μ the dynamic viscosity and κ the thermal conductivity of the fluid. The fluid properties C_p, μ and κ are assumed to be constant throughout the flow.

For the purpose of a stability analysis, the flow variables $\boldsymbol{q}$ are decomposed into a steady axisymmetric base flow $\boldsymbol{q}^b$ and unsteady perturbations $\boldsymbol{q}'$, such that $\boldsymbol{q}(x, r, \theta, t) = \boldsymbol{q}^b(x, r) + \boldsymbol{q}'(x, r, \theta, t)$. The governing equations are then linearized around $\boldsymbol{q}^b$, and a normal mode ansatz for $\boldsymbol{q}'$ allows to characterize the temporal growth or decay of perturbation eigenmodes of the linear system. Both local (§ 3.2) and global (§ 3.3 and 4) normal modes will be considered in the following. Local theory assumes the flow to be infinite, parallel and uniform in the $x-$ direction. In this case, perturbations are Fourier-transformed in x, leaving only r as an eigendirection. Global theory, by contrast, considers spatially developing base flows, and accounts for boundary conditions at the inlet and outlet. In the global framework, both r and x are thus eigendirections, which leads to a system size that precludes the use of direct eigenvalue solvers.

3.2. Validation: direct computation of local temporal eigenmodes

A validation of the present SR propagator method is conducted by computing the eigenmodes of a *parallel* jet of infinite streamwise extent. This test case represents the local stability problem, as it has been widely

used to describe the stability properties of slowly varying flows [13]. The base flow is prescribed as

$$u_x^b = \frac{1}{2}\left\{1 + \tanh\left[2\left(r - \frac{1}{r}\right)\right]\right\}, \tag{15a}$$

$$u_r^b = u_\theta^b = 0, \tag{15b}$$

$$T^b = S + (1-S)u_x^b + \frac{\gamma-1}{2}\mathrm{Ma}^2 u_x^b(1-u_x^b), \tag{15c}$$

$$\rho^b = {T^b}^{-1}, \tag{15d}$$

from which we obtain the total energy $\rho^b E^b = \gamma^{-1}(\gamma-1)^{-1}Ma^{-2} + \rho^b {u_x^b}^2/2$, with uniform pressure $p^b = (\gamma \mathrm{Ma}^2)^{-1}$. The ratio of specific heats is taken as $\gamma = 1.4$, and $S = T_\infty/T_0$ denotes the ambient-to-jet temperature ratio. A hot jet with $S = 0.5$ is chosen for the present configuration, along with the parameters $\mathrm{Re} = 500$, $\mathrm{Ma} = 0.4$ and $\mathrm{Pr} = 1$.

Azimuthal periodicity and streamwise invariance justify a normal mode ansatz of the form

$$\boldsymbol{q}'(x,r,\theta,t) = \widetilde{\boldsymbol{q}}(r)\exp\left[\mathrm{i}(kx + m\theta - \omega t)\right] + cc, \tag{16}$$

where cc stands for the complex conjugate. Within the framework of a temporal stability analysis, the complex frequency ω is sought as a function of prescribed streamwise and azimuthal wave-numbers $k \in \mathbb{R}^+$ and $m \in \mathbb{Z}$.

One-dimensional reference solution. Upon substitution of the base flow (15) and normal mode perturbations (16) into the linearized equations of motion, only the radial coordinate direction needs to be discretized. We use a compact finite-difference scheme [17] for the spatial discretization and impose homogeneous Dirichlet boundary conditions at $r = 150$, leading to the discrete local temporal eigenvalue problem of the form

$$\mathbf{A}(k,m)\widetilde{\boldsymbol{q}} = \omega \mathbf{B}\widetilde{\boldsymbol{q}}\,. \tag{17}$$

All eigenmodes $(\omega, \widetilde{\boldsymbol{q}})$ are then computed via a QR-algorithm. The most relevant part of the spectrum for values $k = m = 1$ is shown in figure 4*a*. Three families of eigenmodes may be distinguished based on their frequency ω_r, their growth rate ω_i, and their spatial distributions of azimuthal vorticity (figure 4*b*) and dilatation $\boldsymbol{\nabla}\cdot\boldsymbol{u}$ (figure 4*c*).

Vortical perturbations localized in the fluid at rest outside the jet form the classical continuous spectrum of unbounded shear flows [26] with near-zero real frequency. Due to the finite size of the numerical domain, continuous branches results in densely clustered discrete modes in the discretized problem. These are represented by blue symbols that line up close to the $\omega_r = 0$ axis in figure 4*a*. Acoustic waves in the freestream form two continuous branches, both plotted in red in figure 4*a*. These are characterized by very slow temporal decay ($\omega_i \approx 0$) and frequencies in the continuous ranges $\omega_r \leq -k\sqrt{S}/\mathrm{Ma}$ and $\omega_r \geq k\sqrt{S}/\mathrm{Ma}$. These cut-off frequency $\pm k\sqrt{S}/\mathrm{Ma}$ corresponds to cylindrical acoustic waves traveling parallel to the jet axis at the speed of sound c_∞ in the outer flow. Real parts of vorticity and dilatation fields are shown in figures 4*b, c* as a function of r for particular modes (vortical mode with $\omega = 2.24.10^{-6} - 1.49.10^{-3}\mathrm{i}$ in blue and acoustic mode with $\omega = 2.03 - 1.91.10^{-3}\mathrm{i}$ in red). A fourth branch of modes is represented by green symbols in figure 4*a*. This branch consists of discrete modes with a single unstable one marked by a cross. The spatial structure of the unstable eigenmode is plotted in green in figures 4*b, c*. This mode displays strong vorticity perturbations inside the jet shear-layer around $r = 1$, and nearly no dilatation perturbation. As the discrete modes (green symbols in figure 4*a*) have real frequencies below the acoustic cut-off value (i.e. a subsonic phase velocity), no sound is radiated by these modes.

3.3. Local eigenmodes via the SR method on a two-dimensional periodic domain

In order to demonstrate the use of the SR technique, it is applied to reproduce a selected part of the spectrum shown in figure 4*a*. Local modes may be computed as global eigenmodes on a two-dimensional (x,r) domain,

$$\boldsymbol{q}'(x,r,\theta,t) = \widetilde{\boldsymbol{q}}(x,r)\exp\left[\mathrm{i}(m\theta - \omega t)\right]\,, \tag{18}$$

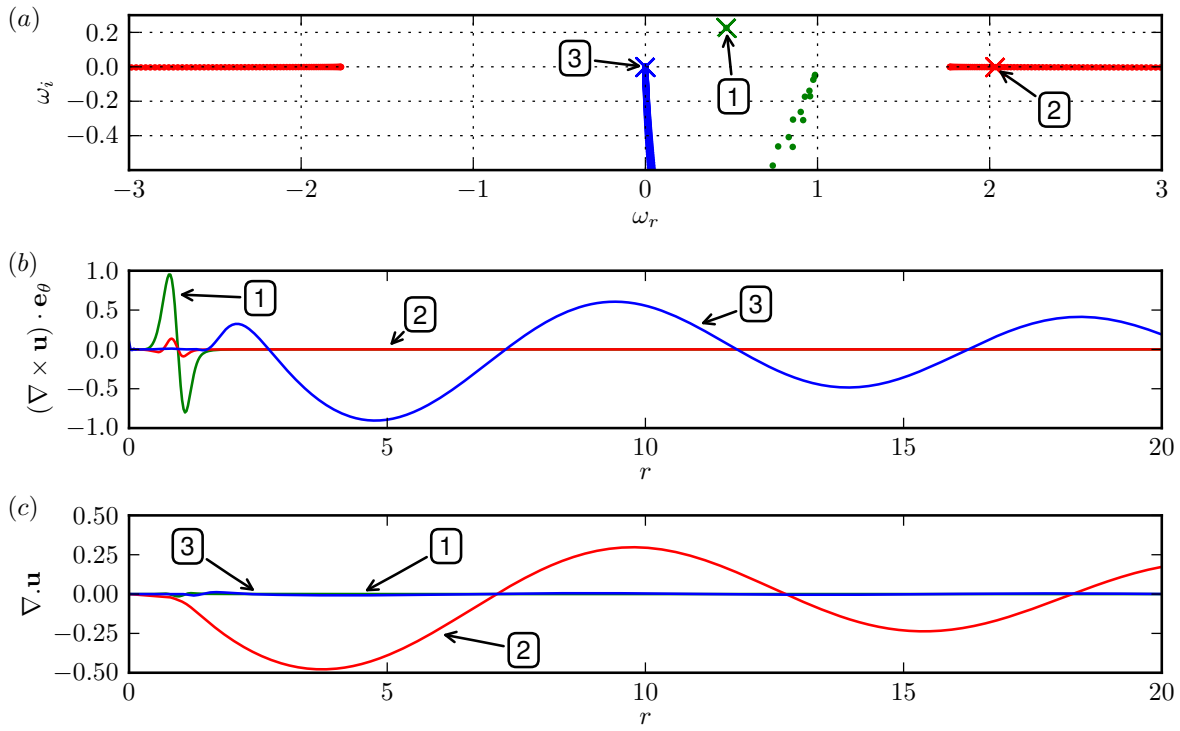

Figure 4: Temporal spectrum directly computed with the QR algorithm for the parallel base flow given by (15) for Re = 500, Ma = 0.4 and Pr = 1, and for waves number $k = 1$ and $m = 1$. (a) The eigenvalue spectrum is displayed in terms of real frequency ω_r' and temporal growth rate ω_i' of the modes. Blue symbols correspond to vortical modes in the outer flow; red symbols to acoustic modes in the outer flow and green ones to shear-layer modes. (b) The real part of vorticity eigenfunction for three selected modes (indicated by large color crosses in (a)) (Green: $\omega = 0.471+0.226$i, label 1 in (a); red: $\omega = 2.03-1.91.10^{-3}$i, label 2 in ($a$); Blue: $\omega = 2.24.10^{-6} - 1.49.10^{-3}$i, label 3 in ($a$)). ($c$) The real part of dilatation eigenfunction is represented for the same modes as in (b).

with periodic boundary conditions in x and with a streamwise extent $0 \leq x \leq 2\pi/k$. Using a two-dimensional discretization allows the use of the same code here (for a parallel base flow) and in § 4 (for non-parallel base flow), except for different boundary conditions. The base flow in the present case is still parallel, given by (15). The objective is to compute a number of least stable discrete eigenmodes of the shear-layer type (green symbols in figure 4a).

If a standard Krylov technique were to be applied to the propagator of the linear equations of motion alone, only the single unstable shear-layer mode could be extracted, all other discrete modes being masked by the less stable acoustic (red in figure 4) or vortical (blue) branches. The SR technique allows to stabilize all modes outside a region of interest of the spectrum, and thereby may give access to otherwise masked parts of the spectrum, in particular here by stabilizing the continuous branches.

The extended linear system (6) is discretized on an orthogonal grid, resolving the domain $0 \leq r \leq 15$, $0 \leq x \leq 2\pi/k$ with 30×256 points. Explicit 5^{th}-order centered finite differences in combination with a spatial filtering scheme [6] are used for the spatial derivatives. The spatial filter merely suppresses numerical instabilities of the finite-difference scheme; it is unrelated to the temporal filtering employed by the SR method. Matrix-free time stepping of the extended linear equations is performed using a 3^{rd}-order Runge–Kutta algorithm. For the purpose of validation against the results of § 3.2, only modes with a streamwise wavenumber $k = 1$ are sought, and higher harmonics of the periodic domain are continuously filtered out during the time stepping, by means of an FFT in x.

Choice of transformation parameters. In order to focus on the green branch represented in figure 4*a*, appropriate parameter values for χ, τ and ω_0 must be chosen. As discussed in § 2.2, a value of $\chi' = 1$ is maintained, such that $\chi = \tau$. The frequency shift ω_0 selects the region of interest in the frequency plane; a choice of $\omega_0 = 1 + 0.2\mathrm{i}$ has been found to be suitable. The parameter τ determines the width of the bandpass filter. It should be chosen sufficiently small to efficiently damp undesired modes (here, the blue and red branches) but large enough such that the modes of interest achieve growth rates $\omega_i \gtrsim \omega_{0,i} - 2\tau$, as discussed in § 2.3. A value of $\tau = 0.5$, yielding $\chi = 0.5$, represents a good compromise for the present case. The propagation time is set to $\Delta t = 0.5$.

Results. Ten eigenvalues obtained with the SR method are shown as black circles in figure 5, alongside the reference solution (identical to figure 4*a*). The agreement is excellent, with relative errors smaller than 10^{-4} on both the eigenvalues and the eigenmodes (in L^∞ norm). The spectral transformation with the present choice of parameters successfully selects the least stable shear-layer modes. Contour lines in figure 5 indicate the transformed growth rate $\Omega_i(\omega)$ that governs the mode selection by the SR method.

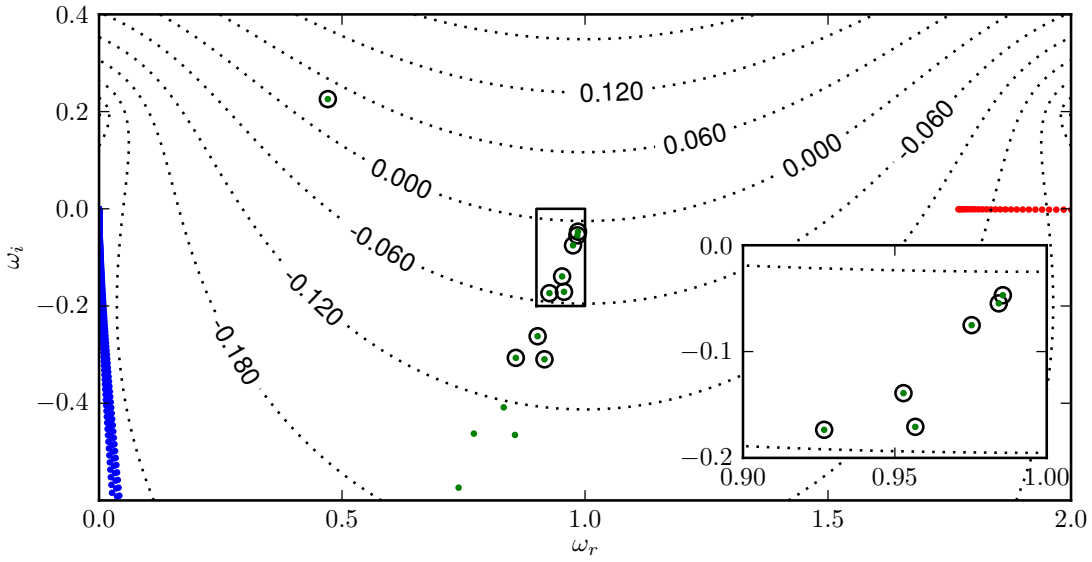

Figure 5: Application of the SR method to the computation of local modes of a compressible jet flow for the same parameter settings as in figure 4. The spectrum from figure 4*a* is reproduced with the same conventions. The ten modes computed with the SR method are denoted by black circles. The dotted lines represent isocontours of the growth rate Ω_i^+ of the filtered propagator, based on parameters $\omega_0 = 1 + 0.2\mathrm{i}$ and $\tau = \chi = 0.5$, confirming that the computed eigenvalues correspond to the largest Ω_i^+. The insert on the bottom right of the figure shows a close-up view on the region marked by a black rectangle

4. Application: global eigenmodes of a compressible jet

4.1. Non-parallel base flow

The SR method is now applied to compute global modes (18) of a non-parallel jet. The geometry of the computational domain is represented in figure 6. The jet exits from an idealized nozzle, modeled as an infinitely thin adiabatic wall at $r = 1$ and $x \leq 0$. Only the upper half-plane $r > 0$ is resolved in the calculations, and appropriate symmetry conditions for axisymmetric flow are imposed on the jet axis $r = 0$. In order to control the jet profile at $x = 0$ (diffusive effects inside the pipe can be particularly important at low Reynolds and high Mach numbers), velocity and temperature profiles are imposed at $x = x_0$, close to the jet nozzle. The Navier–Stokes equations are solved downstream of x_0 (domain II in figure 6*a*), with local

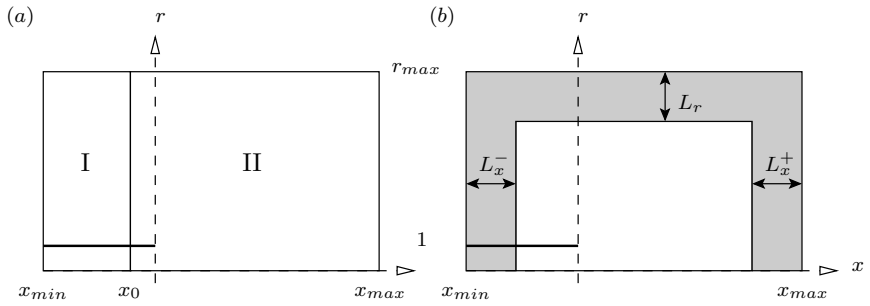

Figure 6: Computational domains for (a) base flow and (b) global mode computations. The parameter values for these computations are: $x_{min} = -200$, $x_{max} = 300$, $r_{max} = 250$, $x_0 = -2$, $L_x^+ = L_x^- = L_r = 150$. The base flow is taken to be parallel in region I, whereas the Navier–Stokes equations are solved in region II.

one-dimensional (LODI) boundary conditions [21] on the numerical boundaries at x_{min}, x_{max} and r_{max}. The same explicit finite-difference scheme as described in § 3.3 is used. A steady solution of the nonlinear Navier–Stokes equations, computed via the SFD method of [1] for Re = 100, Ma = 0.75, Pr = 1 and $S = 1$ is taken as a base flow. A parallel flow region is added upstream of x_0 (domain I in figure 6a) to extend the base flow to the domain used for the linear stability calculations. Axial velocity and angular vorticity distributions of the spatially spreading base flow are shown in figure 7a, b. The momentum thickness

$$\theta(x) = \int_0^{\alpha} \frac{\rho^b(r,x)u^b(r,x)}{\rho^b(0,x)u^b(0,x)} \left(1 - \frac{u^b(r,x)}{u^b(0,x)}\right) r\mathrm{d}r, \quad \alpha = \begin{cases} 1 & x \leq 0 \\ \infty & x > 0 \end{cases}$$

is displayed in figure 7c, and selected axial velocity profiles are shown in figure 7d.

Temporal eigenmodes of the linearized Navier–Stokes equations, commonly referred to as "global modes", are computed on the domain displayed in figure 6b. Non-reflecting boundary conditions given by [7] are employed at the inflow, outflow and upper boundary. Furthermore, perturbation quantities are artificially attenuated in sponge layers [8], indicated by the outer gray regions in figure 6b, in order to further minimize spurious reflections. Only axisymmetric modes ($m = 0$) are computed, and symmetry conditions on the jet axis are imposed accordingly. The numerical domain spanned by $-200 \leq x \leq 300$ and $0 \leq r \leq 250$ is discretized with 1024×512 grid points.

Five eigenvalues were requested for each of nine shift parameters ω_0 with $0.3 \leq \omega_{0,r} \leq 0.75$ and $\omega_{0,i} = 0.05$, represented by black diamonds in figure 8a. Note that SLEPc may return more than the requested number of eigenvalues. Parameters $\tau = \chi = \Delta t = 0.1$ were used in all calculations. The resulting eigenfrequencies are represented in figure 8a in the complex ω- plane and form a discrete branch of solutions. For each value of ω_0, one isocontour of the growth rate Ω_i^+ of the filtered propagator is drawn, corresponding to the growth rate of the most stable mode computed with each particular shift; no eigenfrequency other than those computed should lie above these parabola-shaped curves.

For $\omega_0 = 0.8 + 0.05\mathrm{i}$, five eigenvalues were first requested, as for the other values of the frequency shift. The computation was then continued to yield a total of fifteen modes. This portion of the spectrum is displayed in more detail in figure 8c, together with iso-contours of the growth rate of the filtered propagator. The first five modes that have been found are marked by red circles. Among the additional requested modes, several are found to lie on a separate, slightly more attenuated branch. The spatial structure of the real part of vorticity perturbations associated with three eigenmodes of the upper branch, marked by labels in figure 8, are displayed in figure 9. Perturbations are concentrated in the jet shear layer region, suggesting an inflectional instability mechanism. The time evolution of these modes show that the vortical structures represented in figure 9 propagate downstream at a phase velocity of about half the jet centerline velocity; as a consequence, their typical axial wavelength decreases with increasing real frequency. Modes belonging to the more attenuated branch, which is only detected in figure 8 for the shift $\omega_0 = 0.8 + 0.05\mathrm{i}$, display a very similar structure (not shown).

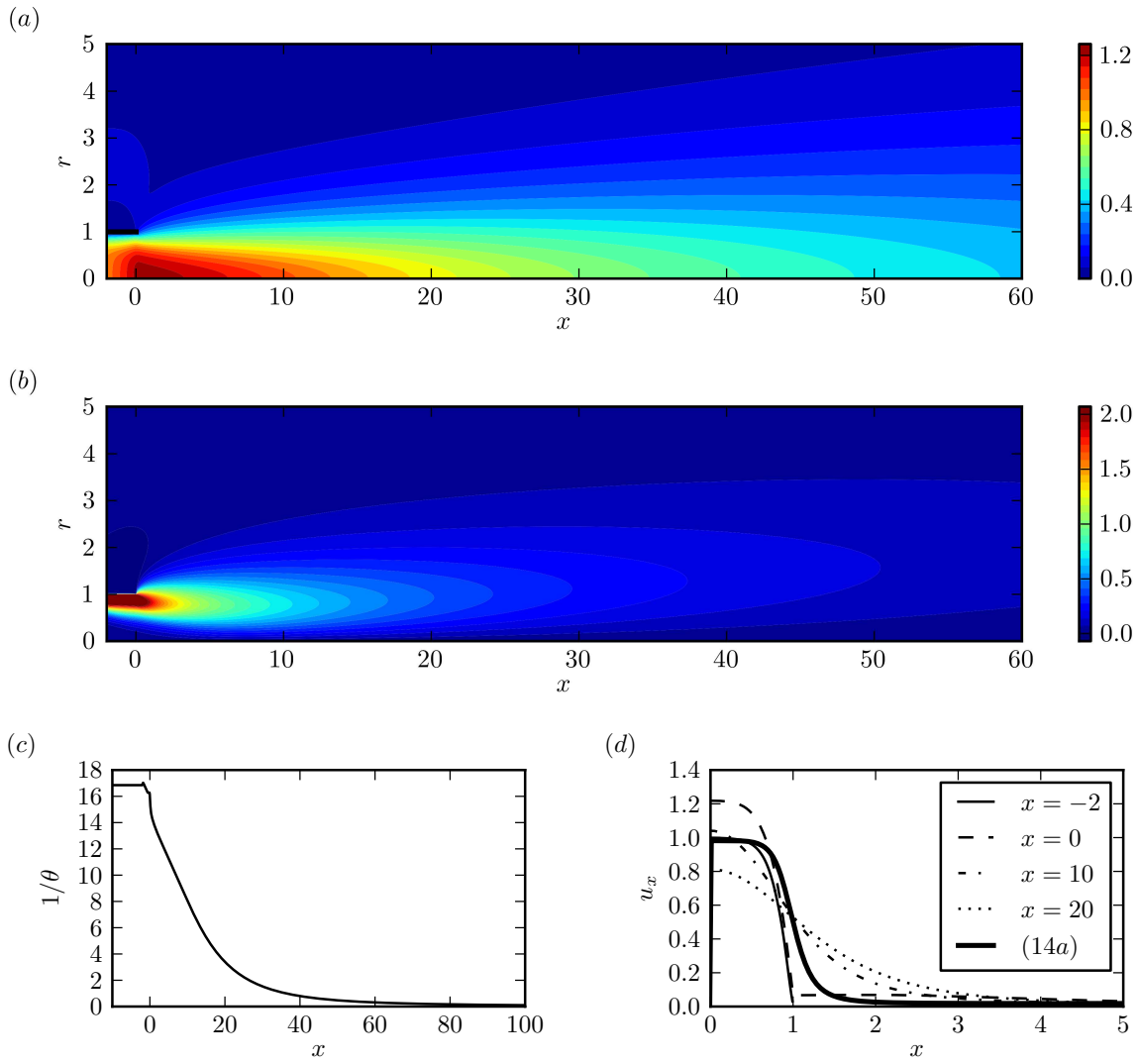

Figure 7: Base flow for the global linear stability study of a spatially developing jet with Re = 100, Ma = 0.75, Pr = 1 and $S = 1$ (unheated). The axial velocity and angular vorticity distributions are respectively displayed in (a) and (b). Only a portion of the computational domain is shown. The evolution of the momentum thickness θ is represented in (c). In (d), axial velocity profiles are at various locations are shown together with the profile used in § 3.2 and 3.3.

Fifteen modes were computed for a large frequency shift $\omega_0 = 5.1$. These are represented in figure 8*b* by red and green symbols. Their dilatation fields, shown in figure 10, characterize these modes as being of acoustic nature. Comparing the real and imaginary parts (not shown) of the dilatation fields in the pipe, it appears that some modes correspond to acoustic waves propagating downstream inside the duct and being scattered at the nozzle exit (green symbols in figure 8*b*). Others correspond to acoustic waves emanating from a location close to the nozzle exit (red symbols in figure 8*b*). These modes propagate upstream in the inlet duct.

One should keep in mind that free-stream vortical modes with near zero decay rates are also present in the spectrum, similar as in the local analysis of § 3.2. Without shifting and relaxing of the propagator, all modes shown in figure 8 would be masked by those least stable modes. In practice, however, the computation of these modes is challenging, as the separation between eigenvalues is very weak (on the order of $1/\left[\mathrm{Re}(x_{max} - x_{min})\right]$). No result could be converged with sufficient accuracy for this family of modes, and they are not shown.

4.2. Convergence

Convergence of the eigenvectors through the iterations of the Krylov-Schur algorithm is usually monitored in terms of a residual associated with the operator the algorithm is applied to, i.e the SR propagator in the present case. Denoting by $\boldsymbol{Q}_{j,p}$ the estimated p^{th} leading eigenvector after the j^{th} restart of the Krylov-Schur algorithm, and by $\lambda_{j,p}$ the corresponding eigenvalue, the residual is estimated

$$e_{j,p} = \frac{\|\exp(\Delta t \mathcal{F})\boldsymbol{Q}_{j,p} - \lambda_{j,p}\boldsymbol{Q}_{j,p}\|}{\|\boldsymbol{Q}_{j,p}\|},$$

and $\boldsymbol{Q}_{j,p}$ is accepted as converged if the estimation is smaller than a user-chosen tolerance ϵ. A typical evolution of the estimation of this residual is displayed in figure 11*a*. Non-monotonous convergence is observed, consistent with the fact that, in the present case for which the operator L is non-Hermitian, the filtered propagator is non-Hermitian as well. For $\omega_0 = 0.45 + 0.05\mathrm{i}$, computations were performed with values $\epsilon = 10^{-3}$ ($\times$ in figure 11*b*), 10^{-4} ($\circ$) and 10^{-5} ($+$). Five modes were requested in each computation. The resulting spectra are shown in figure 11*b*. Significant scattering of the computed eigenvalues is noticed for $\epsilon = 10^{-3}$. The absolute scattering being of the same order of magnitude in the real and imaginary directions, relative errors in the real part of the eigenfrequency are much smaller than in the growth rate. The scattering of eigenvalues becomes less important as requested accuracy increases. With $\epsilon = 10^{-4}$ and $\epsilon = 10^{-5}$ eigenvalues seem to converge to a line trend, and eigenvalues in the overlapping region from the two shift values $\omega_0 = 0.45 + 0.05\mathrm{i}$ and $0.5 + 0.05\mathrm{i}$ are in reasonably good agreement, as shown in figure 11*c*. However, this measure of convergence depends on the spectral transformation used, in particular here on Δt and τ. A more meaningful measure of accuracy may be defined based on the original operator L:

$$e'_{j,p} = \frac{\|L\boldsymbol{q}_{j,p} + \mathrm{i}\omega_{j,p}\boldsymbol{q}_{j,p}\|}{\|\boldsymbol{q}_{j,p}\|} \quad \text{with } \boldsymbol{Q}_{j,p} = (\boldsymbol{q}_{j,p}, \overline{\boldsymbol{q}}_{j,p})^T$$

These residuals are computed after convergence (denoted by $j = \infty$), and are displayed in figure 11*d*. A first observation is that the values differ significantly from the values of the $e_{\infty,p} \approx \epsilon$ discussed earlier, measured with respect to the SR propagator. Furthermore, the values of $e'_{\infty,p}$ decrease only slowly with ϵ; values on the order of 3%, 2% and 1% are found for $\epsilon = 10^{-3}$, 10^{-4} and 10^{-5} respectively. This saturation seems to be due to the spatial filtering which is applied during time-stepping in order to maintain stability. It introduces a slight modification of the propagator which is not taken into account when the Rayleigh quotient (12) is taken.

In order to achieve residuals $e' \leq 2.2\%$, values of ϵ ranging from 10^{-4} to 10^{-7} had to be used for the computations presented in the previous section, depending on the shift ω_0 (larger values of $\omega_{0,r}$ requiring smaller values of ϵ in the present case).

5. Conclusion

A new numerical procedure for the solution of large eigenvalue problems has been presented. A relaxation technique using a first-order temporal bandpass filter is coupled to to the linearized equations of motion, such that the least stable eigenmodes of the filtered system lie in a prescribed frequency band of interest centered around a shift frequency. These modes are then recovered through propagation over a finite time interval, using standard eigenvalue extraction techniques. This "shift-relax" transformation therefore requires no solution of linear systems, which are computationally expensive or even untractable for global stability problems involving two- or three-dimensional flows. Although not as flexible as the classical "shift-invert" transformation or its variants, the present method has the advantage of considerably lower memory requirement, making it suitable for the analysis of complex two- or three-dimensional flow geometries. Another advantage lies in the ease of implementation: only a simple filter equation needs to be added to an existing simulation code in order to perform eigenmode extraction. No matrix needs to be built, and no preconditioning is required. Finally, the algorithm can be parallelized as efficiently as a regular time stepper, as the filter is local in space.

Acknowledgments

This work was supported by DGA grant number 2009.60.034.00.470.75.01. The authors are thankful to Miguel Fosas and Patrick Huerre for their comments.

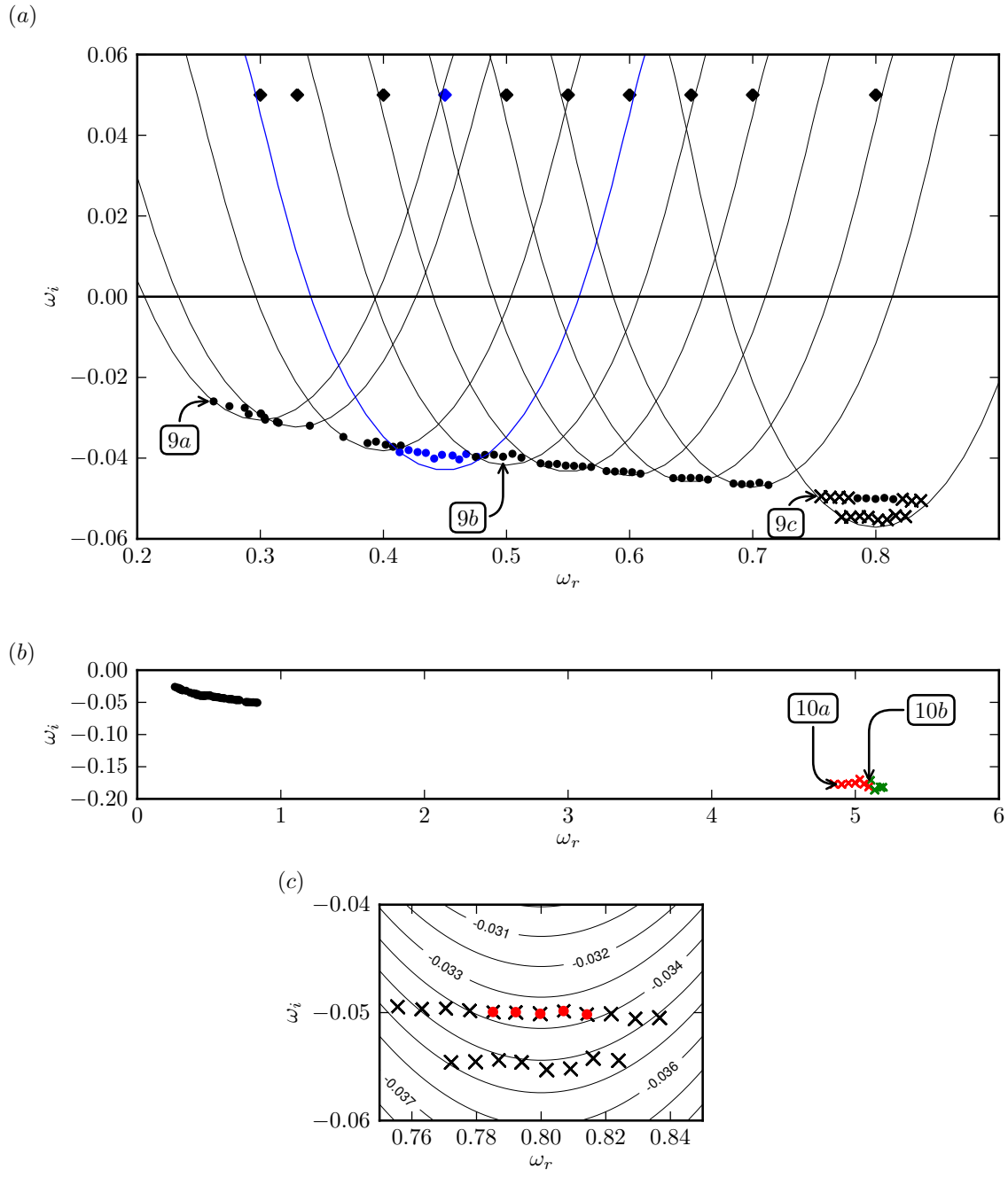

Figure 8: Eigenvalues of axisymmetric modes in an isothermal jet at Re = 100, Ma = 0.75 and Pr = 1 computed using the SR method. Tolerance was set to $\epsilon = 10^{-4}$ for $\omega_{0,r} \leq 0.5$, $\epsilon = 10^{-5}$ for $0.5 < \omega_{0,r} \leq 0.8$ and $\epsilon = 10^{-7}$ for $\omega_{0,r} = 5.1$. (*a*) Low frequency shear layer modes. Shift positions are indicated by diamonds. For each shift, an isocontour of the filtered propagator growth rate is represented; its value corresponds to the least amplified mode computed by the Krylov-Schur solver. For $\omega_0 = 0.45 + 0.05\mathrm{i}$, the shift, the modes and the isocontour are represented in blue. (*b*) Low frequency vortical modes are shown together with higher frequency acoustic modes. (*c*) Close-up on the 15 modes computed for $\omega_0 = 0.8 + 0.05\mathrm{i}$, showing the existence of two branches: dots correspond to the first five modes computed, crosses correspond to the next ten. Labels correspond to the modes for which the vorticity or dilatation field is displayed in figure 9 and 10.

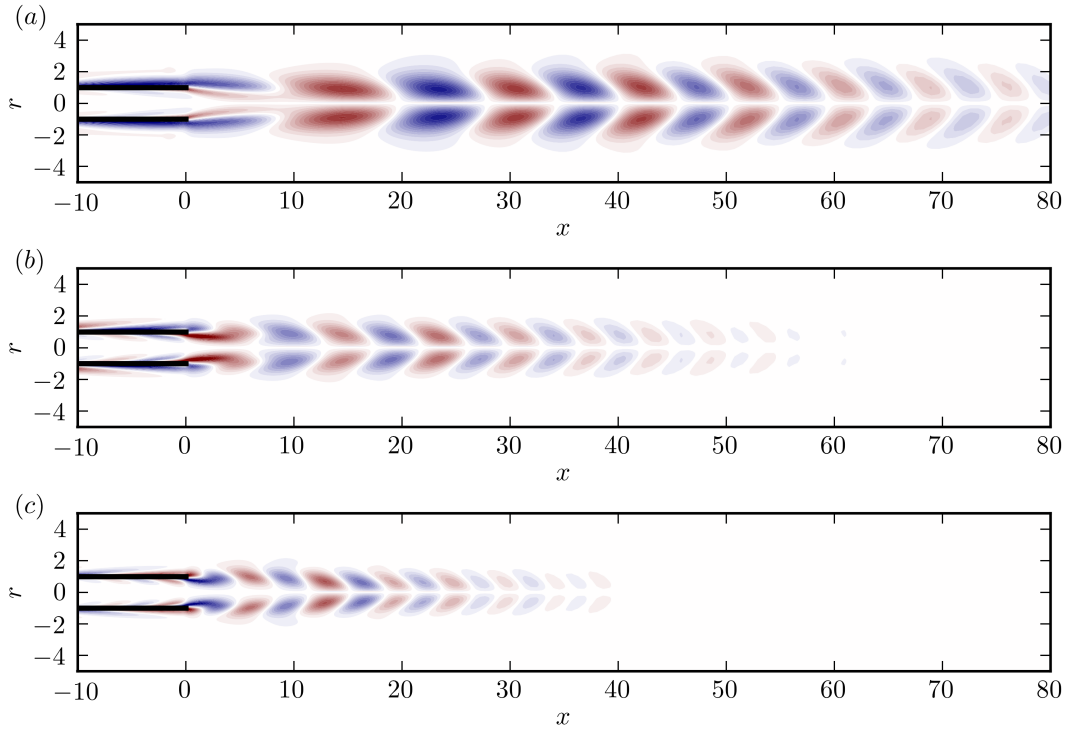

Figure 9: Real part of the vorticity fields of typical eigenmodes, labeled in figure 8*a*, in an isothermal jet at Re = 100, Ma = 0.75 and Pr = 1. (*a*) $\omega = 0.26 - 0.026\mathrm{i}$. (*b*) $\omega = 0.50 - 0.040\mathrm{i}$. (*c*) $\omega = 0.71 - 0.047\mathrm{i}$.

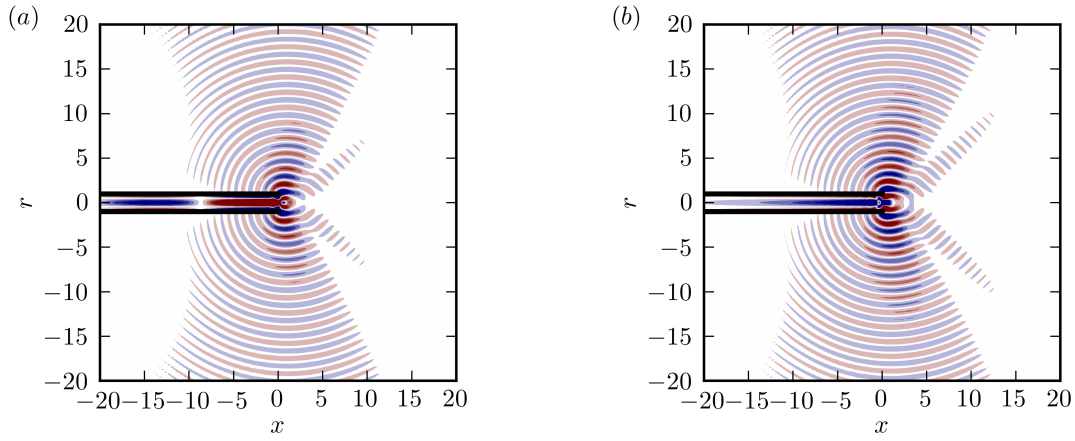

Figure 10: Real part of the dilatation fields of typical eigenmodes, labeled in figure 8*a*, in an isothermal jet at Re = 100, Ma = 0.75 and Pr = 1. (*a*) $\omega = 4.9 - 0.17\mathrm{i}$. (*b*) $\omega = 5.1 - 0.18\mathrm{i}$.

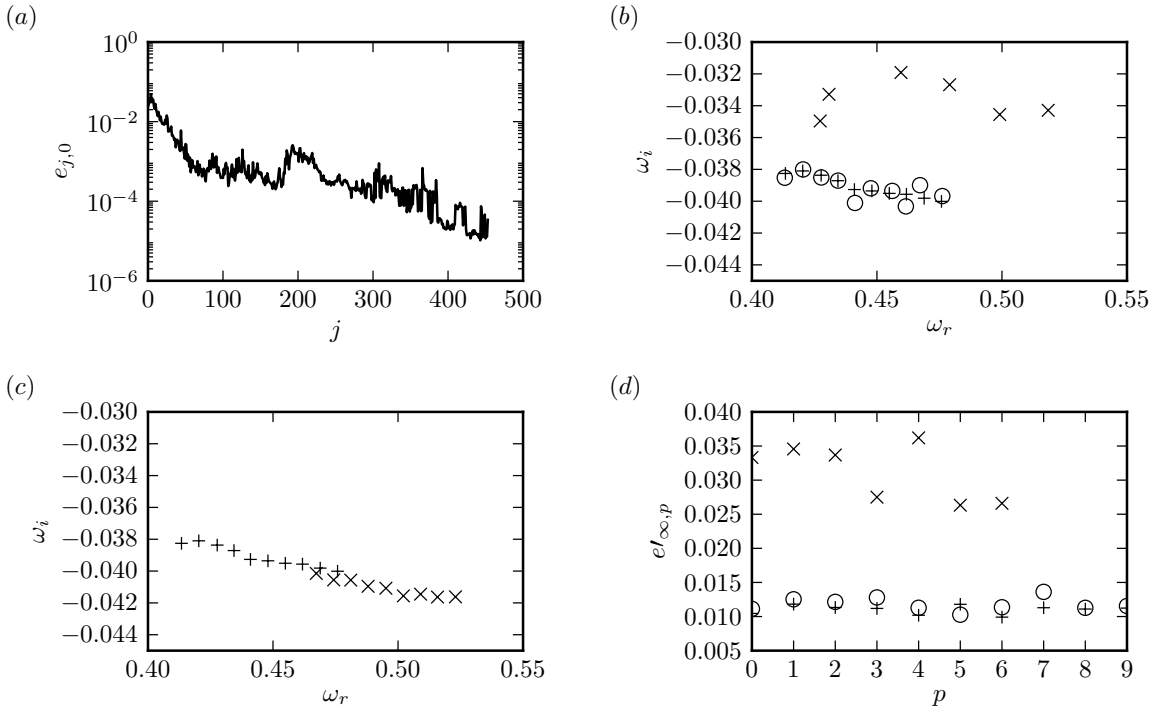

Figure 11: Convergence features. (a) A typical evolution of the estimated residual of the leading eigenvalue with the number of restarts. (b) Spectra computed with $\omega_0 = 0.45 + 0.05\mathrm{i}$ and $\epsilon = 10^{-3}$, 10^{-4} and 10^{-5} (respectively represented by $\times$, $\circ$ and $+$ symbols). 5 modes were requested. (c) Spectra computed for $\epsilon = 10^{-5}$ with $\omega_0 = 0.45 + 0.05\mathrm{i}$ and $0.5 + 0.05\mathrm{i}$ are shown. (d) Residual based for the computations of (b).

Appendix A. Distinction between the two transformed eigenvalues

The eigenvalue transformation is given in terms of the scaled variables by (10). Let us introduce

$$\widetilde{\Omega} = \frac{\Omega' + \mathrm{i}}{\sqrt{\chi'}}, \qquad \widetilde{\omega} = \frac{\omega' + \mathrm{i}(1-\chi')}{\sqrt{\chi'}}.$$

Equation (10) then reads

$$\widetilde{\Omega}^2 - \widetilde{\omega}\widetilde{\Omega} + 1 = 0. \tag{A.1}$$

The solutions of this second-order polynomial are given by

$$\widetilde{\Omega} = \frac{1}{2}\left(\widetilde{\omega} \pm \sqrt{\widetilde{\omega}^2 - 4}\right).$$

Let $\alpha = \sqrt{\widetilde{\omega}^2 - 4}$. One of these roots has a positive imaginary part and the other one a negative one if $|\widetilde{\omega}_i| \leq |\alpha_i|$. In order to prove that this condition holds, real and imaginary parts are introduced in the definition of α:

$$(\alpha_r^2 - \alpha_i^2) + 2\alpha_r\alpha_i\mathrm{i} = (\widetilde{\omega}_r^2 - \widetilde{\omega}_i^2) - 4 + 2\widetilde{\omega}_r\widetilde{\omega}_i\mathrm{i}$$

so

$$\widetilde{\omega}_r\widetilde{\omega}_i = \alpha_r\alpha_i \qquad \alpha_r^2 - \alpha_i^2 = \widetilde{\omega}_r^2 - \widetilde{\omega}_i^2 - 4.$$

The variable α_i can then be written as

$$\alpha_i^2 = \widetilde{\omega}_i^2 + 4 - (\widetilde{\omega}_r^2 - \alpha_r^2) = \widetilde{\omega}_i^2 + 4 - \left(\frac{\alpha_i^2}{\widetilde{\omega}_i^2} - 1\right)\alpha_r^2$$

which finally gives

$$\alpha_i^2 = \frac{\widetilde{\omega}_i^2 + 4 + \alpha_r^2}{1 + \dfrac{\alpha_r^2}{\widetilde{\omega}_i^2}} = \widetilde{\omega}_i^2\frac{\widetilde{\omega}_i^2 + 4 + \alpha_r^2}{\widetilde{\omega}_i^2 + \alpha_r^2} \geq \widetilde{\omega}_i^2.$$

Let $\widetilde{\Omega}^+$ denote the root of (A.1) with a positive imaginary part and $\widetilde{\Omega}^-$ the one with the negative imaginary part. In terms of the primed variables, this corresponds to

$$\Omega'^-_i \leq -1 \leq \Omega'^+_i.$$

References

[1] E. Akervik, L. Brandt, D.S. Henningson, J. Hoepffner, O. Marxen, and P. Schlatter. Steady solutions of the Navier-Stokes equations by selective frequency damping. *Phys. Fluids*, 18(6):068102, 2006.

[2] E. Akervik, U. Ehrenstein, F. Gallaire, and D.S. Henningson. Global two-dimensional stability measures of the flat plate boundary-layer flow. *Eur. J. Mech. B-Fluid*, 27(5):501–513, 2008.

[3] P.R. Amestoy, I.S. Duff, and J.Y. L'Excellent. Multifrontal parallel distributed symmetric and unsymmetric solvers. *Comput. Method. Appl. M.*, 184(2-4):501–520, 2000.

[4] S. Balay, K. Buschelman, V. Eijkhout, W.D. Gropp, D. Kaushik, M.G. Knepley, L. Curfman McInnes, B.F. Smith, and H. Zhang. PETSc users manual. Technical Report ANL-95/11 - Revision 3.0.0, Argonne National Laboratory, 2008. Available at http://www.mcs.anl.gov/petsc/petsc-as/.

[5] A. Barbagallo, D. Sipp, and P.J. Schmid. Closed-loop control of an open cavity flow using reduced-order models. *J. Fluid Mech.*, 641:1–50, 2009.

[6] J. Berland, C. Bogey, O. Marsden, and C. Bailly. High-order, low dispersive and low dissipative explicit schemes for multiple-scale and boundary problems. *J. Comput. Phys.*, 224(2):637–662, 2007.

[7] C. Bogey and C. Bailly. Three-dimensional non-reflective boundary conditions for acoustic simulations: far field formulation and validation test cases. *Acta Acust.*, 88:463–471, 2002.

[8] T. Colonius. Modeling artificial boundary conditions for compressible flow. *Annu. Rev. Fluid Mech.*, 36(1):315–345, 2004.

[9] T.A. Davis. UMFPACK version 5.5.0 user guide. Technical report, 2009. Available at http://www.cise.ufl.edu/research/sparse/umfpack/.

[10] W.S. Edwards, L.S. Tuckerman, R.A. Friesner, and D.C. Sorensen. Krylov methods for the incompressible Navier-Stokes equations. *J. Comput. Phys.*, 110(1):82–102, 1994.

[11] G.H. Golub and C.F. Van Loan. *Matrix computations, third edition.* The John Hopkins University Press, 1996.

[12] V. Hernandez, J.E. Roman, A. Tomas, and V. Vidal. A survey of software for sparse eigenvalue problems. Technical Report STR-6, Universidad Politcnica de Valencia, 2006. Available at http://www.grycap.upv.es/slepc.

[13] P. Huerre and P.A. Monkewitz. Local and global instabilities in spatially developing flows. *Annu. Rev. Fluid Mech.*, 22:473–537, 1990.

[14] D. A. Knoll and D. E. Keyes. Jacobian-free Newton-Krylov methods: a survey of approaches and applications. *J. Comput. Phys.*, 193(2):357–397, January 2004.

[15] R.B. Lehoucq and A.G. Salinger. Large-Scale eigenvalue calculations for stability analysis of steady flows on massively parallel computers. *Inter. J. Numer. Meth. Fl.*, 36:309–327, 1999.

[16] R.B. Lehoucq, D.C. Sorensen, and C. Yang. *ARPACK Users' Guide: Solution of Large-Scale Eigenvalue Problems with Implicitly Restarted Arnoldi Methods.* SIAM, 1998.

[17] S.K. Lele. Compact finite difference schemes with spectral-like resolution. *J. Comput. Phys.*, 103(1):16–42, 1992.

[18] C.J. Mack and P.J. Schmid. A preconditioned krylov technique for global hydrodynamic stability analysis of large-scale compressible flows. *J. Comput. Phys.*, 229(3):541–560, 2010.

[19] C.J. Mack, P.J. Schmid, and J.L. Sesterhenn. Global stability of swept flow around a parabolic body: connecting attachment-line and crossflow modes. *J. Fluid Mech.*, 611:205–214, 2008.

[20] J.W. Nichols and S.K. Lele. Global modes and transient response of a cold supersonic jet. *J. Fluid Mech.*, 669:225–241, January 2011.

[21] T.J. Poinsot and S.K. Lele. Boundary conditions for direct simulations of compressible viscous flows. *J. Comput. Phys.*, 101(1):104–129, 1992.

[22] J.E. Roman, M. Kammerer, F. Merz, and F. Jenko. Fast eigenvalue calculations in a massively parallel plasma turbulence code. *Parallel Comput.*, 36(5-6):339–358, 2010. Parallel Matrix Algorithms and Applications.

[23] J.E. Roman, E. Romero, and A. Tomas. SLEPc users manual. Technical Report DSIC-II/24/02, Universidad Politecnica de Valencia, 2010. Available at http://www.grycap.upv.es/slepc.

[24] Y. Saad. *Iterative methods for sparse linear systems, second edition.* SIAM, 2003.

[25] R.D. Sandberg. Governing equations for a new compressible Navier-Stokes solver in general cylindrical coordinates. Technical Report AFM-07/07, University of Southampton, 2007. Available at http://eprints.soton.ac.uk/49523/.

[26] P.J. Schmid and D.S. Henningson. *Stability and Transition in Shear Flows*. Springer, 2001.

Modal and transient dynamics of jet flows

X. Garnaud,[1, a)] L. Lesshafft,[1] P.J. Schmid,[1] and P. Huerre[1]
LadHyX, Ecole Polytechnique – CNRS, 91128 Palaiseau, France.

The linear stability dynamics of incompressible and compressible isothermal jets are investigated by means of their optimal initial perturbations and of their temporal eigenmodes. The transient growth analysis of optimal perturbations is robust and allows physical interpretation of the salient instability mechanisms. In contrast, the modal representation appears to be inadequate, as neither the computed eigenvalue spectrum nor the eigenmode shapes allow a characterization of the flow dynamics in these settings. More surprisingly, numerical issues also prevent the reconstruction of the dynamics from a basis of computed eigenmodes. An investigation of simple model problems reveals inherent problems of this modal approach in the context of a stable convection-dominated configuration. In particular, eigenmodes may exhibit an exponential growth in the streamwise direction even in regions where the flow is locally stable.

I. INTRODUCTION

Jets are known to sustain large-scale perturbation structures, both in the laminar and turbulent flow regime. These structures are commonly interpreted as wavepackets developing within a laminar steady base state, or a turbulent mean flow, due to inflectional instability mechanisms. The spatial shape of the wavepacket envelope then depends on the downstream development of the base or mean flow. In order to fully account for the effects of non-parallelism, the present study seeks to identify wavepacket structures in the form of temporal eigenmodes of the linearized equations of motion in a two-dimensional domain. Linear "global modes" of this kind have been investigated for a large variety of flow configurations in recent years; examples include vortex shedding in the cylinder wake[1] or in a three-dimensional jet in crossflow[2], and the flapping of a separated boundary layer[3]. Weakly nonlinear flow dynamics may in some cases be described by a combination of several dominant global modes[4,5]; furthermore, passive[6] as well as active[7] control strategies for the suppression of flow oscillations have been devised based on the knowledge of the global mode spectrum. However, Barbagallo *et al.*[8] showed that a model reduction based on eigenmodes successfully captures the unstable structures but fails to represent the stable dynamics.

All of the above examples represent oscillator-type flows, where intrinsic flow oscillations observed in the nonlinear regime are found to be linked to the presence of at least one unstable linear global mode. In open shear flows, global instability is typically associated with the presence of a locally absolutely unstable flow region[9], although feedback mechanisms may also be responsible for the flow destabilization. In contrast, amplifier-type flows are characterized by a stable global eigenspectrum. Consistent with the notion of local convective instability, non-normal interaction of stable global modes may give rise to transient perturbation growth[10], but ultimately all perturbations decay in time. Jets, unless sufficiently hot[11,12], are prominent examples of amplifier-type flows. Crow & Champagne[13] measured the flow response in low-Mach number turbulent jets as a function of the forcing frequency, and found maximum amplification to occur at a Strouhal number of 0.3. This approximate value for the *preferred mode* has been confirmed in numerous later studies to be remarkably universal over a large range of operating conditions, even in the supersonic regime[14]. Huerre & Monkewitz[9] hypothesized that the preferred mode was the manifestation of a "slightly damped oscillator" character of the flow, i.e. that the strong flow response may be interpreted as a resonance of the least stable global mode in the presence of external

[a)] Electronic mail: garnaud@ladhyx.polytechnique.fr

forcing. Such an eigenmode has been identified by Cooper & Crighton[15] by extending the dispersion relation of the local shear-layer mode into the complex X-plane. The authors report a Strouhal number based on the diameter of 0.44 for this mode, in agreement with experimental observations[16]. This analysis is based on the hypothesis of the contribution of one single local mode to the global response and of a slow streamwise development of the flow.

Motivated by these results, the first objective of the present study is to compute the global spectrum of subsonic jets. A laminar steady state as well as a turbulent mean flow are considered in the incompressible limit, and the turbulent mean flow is further investigated in the compressible setting at a Mach number of 0.75.

Stable global spectra have been successfully computed for supersonic jets by Nichols & Lele[17,18]. In weakly non-parallel laminar settings, these calculations required extremely large numerical domains, extending over up to 800 jet radii in the downstream direction, in order to capture the wavepacket maximum and reach convergence. In turbulent mean flows obtained from Reynolds averaged calculations, the dominant modes were sufficiently localized near the nozzle to be accurately resolved on much shorter domains. However, difficulties with the computation of stable global modes have been reported for a variety of flow configurations. Barkley *et al.*[19] obtained easily converged modes that are localized within the recirculation bubbles behind a backward-facing step, but no convergence was achieved for a family of stable modes exhibiting spatial growth far downstream of the step; these modes therefore were not further explored. Similar problems were encountered in planar wakes with surface tension[20,21]. In a flat plate boundary layer[22], all modes are stable and spatially growing. Convergence with respect to the domain length was achieved in this case through the use of carefully designed boundary conditions, based on the local dispersion relation. Amplitudes at the in- and outflow differed by two orders of magnitude. Much larger variations occurred in the analysis of a Batchelor vortex by Heaton *et al.*[23]; amplitude differences on the order of 10^6 were found to prevent convergence. The second and principal objective of the present paper is to expose the root cause for such computational problems of stable global modes, and to delineate circumstances under which convergence may be impossible to achieve.

It has been shown that individual eigenmodes may carry a limited physical meaning in the context of amplifier flows and that non-modal stability analyses are more suitable[24,25] to represent instability features in this case. An eigenmode representation of the dynamics can however be used to carry out these analyses, and previous studies have shown that this provides a robust means of analyzing non-normal effects[22,26] as well as of performing control[7] for weakly unstable flows. Optimal perturbations are therefore computed in order to characterize transient growth phenomena in jets. Results obtained using both an adjoint method[27] and a modal representation of the propagator[28] are discussed.

The significance and challenges of a modal representation of the dynamics for advection dominated flows is first investigated by means of model systems in § II. The flow configuration of a round jet with a solid nozzle is then presented in § III, together with the numerical procedure and the different base flows that are investigated. The results of optimal perturbation (§ IV) and eigenmode (§ V) computations are then presented. Although most of the discussion is established in the context of incompressible flows, compressibility effects are also mentioned. Conclusions are offered in § VII.

II. MODEL PROBLEMS: EIGENMODES OF ADVECTIVE SYSTEMS

Reddy & Trefethen[29] investigated the features of the spectrum and pseudo-spectrum of a 1D convection-diffusion problem with homogeneous Dirichlet conditions at the inflow and outflow, a well posed Sturm-Liouville type of problem. The eigenmodes exhibit an exponential spatial growth, and a boundary layer forms at the outflow. In contrast in the model under consideration in Cossu & Chomaz[30] eigenmodes have a Gaussian envelope. The two models presented below aim at reproducing some of the features of a flow where instability mechanisms act in an upstream region, creating structures that are convected

downstream by a neutrally stable flow. These models show features similar to the problem considered by Reddy & Trefethen and provide an understanding of the relationship between the decay rate of a mode, its spatial structure and local instability features.

A. Advection equation with upstream boundary forcing

The simplest possible model for the evolution of perturbations in an advection-dominated flow is given by a pure advection equation with one spatial direction x and a constant advection velocity $U_0 > 0$. The system is forced by an unsteady upstream boundary condition with its own dynamics,

$$\frac{\partial \psi}{\partial t}(x,t) + U_0 \frac{\partial \psi}{\partial x}(x,t) = 0 \qquad x > 0, \tag{1a}$$

$$\psi(0,t) = \psi_0(t), \tag{1b}$$

$$\dot{\psi}_0(t) = -a\psi_0(t) \qquad a \in \mathbb{C}. \tag{1c}$$

The dynamics of this system are imposed by the linear ordinary differential equation (1c). The system (1) only has one single mode of the form $\psi(x,t) = \widetilde{\psi}(x)\exp(-\mathrm{i}\omega t)$, with eigenvector $\widetilde{\psi}(x)$ and eigenvalue ω given by

$$\widetilde{\psi}(x) = \exp\left(\frac{a}{U_0}x\right), \qquad \omega = -\mathrm{i}a. \tag{2}$$

If the system is stable, $a_r \geq 0$ (subscripts $_r$ and $_i$ denote, respectively, the real and imaginary parts of complex scalars and vectors), the amplitude of the mode grows exponentially in x and diverges as $x \to \infty$. A lower advection velocity U_0 leads to stronger spatial growth of $\widetilde{\psi}(x)$.

It is quite clear from this simple example how a temporally decaying source of perturbations under pure advection gives rise to a spatially growing structure, since all perturbations generated at a later time must be exponentially smaller than those generated earlier. Furthermore, this model also serves to exemplify the occurrence of spurious numerical modes. If (1) is discretized using a first-order upwind scheme on a uniform mesh, the mode (2) is recovered independently of the size of the numerical domain, but a second eigenvalue is found as $-1/h$, where h is the grid spacing. The corresponding spatial structure is localized at the outflow discretization point. If a general non-uniform mesh with n points is used, then n distinct modes exist, localized anywhere on the grid. In this particular example, $n-1$ of them have no physical meaning because they do not correspond to modes of the continuous problem. In a more general case where no *a priori* knowledge about the modal structure is available, care must be taken with numerically computed modes. Although the discretization method is suitable for transient problems, it is possible that even the least stable modes computed numerically may have no physical meaning.

B. Unforced advection–diffusion–reaction equation

It may be argued that the above model is indeed too simple for a comparison with jet dynamics, since information can only propagate downstream. This property, however, is not the cause for the exponential spatial growth. A similar reasoning can be applied to the linear advection–diffusion–reaction equation (also referred to as linear Ginzburg–Landau equation) , given as

$$\frac{\partial \psi}{\partial t} + U_0 \frac{\partial \psi}{\partial x} = -a(x)\psi + \frac{\partial^2 \psi}{\partial x^2} \qquad x > 0, \tag{3a}$$

$$\psi(0,t) = 0. \tag{3b}$$

In this generalized form, with the extra term $a(x)\psi$, (3a) is often referred to as the linear Ginzburg–Landau equation in the literature. At each individual location x, the system is known[31] to be locally stable if $a(x)>0$, convectively unstable if $-U_0^2/4 < a(x) < 0$ and absolutely unstable if $a(x)< -U_0^2/4$.

Cossu & Chomaz[30] considered solutions of a problem of the form (3a) that are bounded in $\mathbb{R}$, and assumed the instability parameter $a(x)$ to be of a parabolic shape $a(x) = \alpha x^2 + \beta$, with $\alpha > 0$, such that the spatial and temporal growth rates tend to $-\infty$ as $x \to \pm\infty$. Eigenmode shapes are recovered analytically, and they are found to decay as $\exp(-x^2)$ for large x.

On the contrary, if a reaches a *finite* value a_∞ as $x \to \infty$, perturbations do not experience arbitrarily strong spatial or temporal decay. For a demonstration of the spatial behavior, this limiting value a_∞ can be taken as 0 without loss of generality, as it only affects the temporal eigenvalue but not the corresponding eigenfunction. In order to model a situation where instability mechanisms are active around a given position, while passive convection and diffusion of perturbations is dominant throughout the rest of the domain, let the instability parameter $a(x)$ be of the form

$$a(x) = a_0(\mathrm{i} - 1)\mathrm{e}^{-(x-2)^2}, \quad a_0 > 0. \tag{4}$$

In order to numerically solve (3)–(4) on the interval $[0, x_{max}]$, a boundary condition has to be imposed at the outflow $x = x_{max}$. While a homogeneous Dirichlet boundary condition can be imposed for $a(x) = \alpha x^2 + \beta$ with $\alpha > 0$, this would result in the formation of a boundary layer at the outflow in our present case[32]. In order to take into account convective effects at the outflow, $\psi''(x_{max}) = 0$ is imposed. This "convective outflow"-type boundary condition neglects viscous effects at $x = x_{max}$. Results are qualitatively similar when imposing a homogeneous Neumann boundary condition, but the truncation effect is stronger.

Figure 1 shows the effect of the different parameters on the spectrum as well as on the leading eigenmode $\psi^{(0)}$. Figure 1(a) shows that, for $a_0 = 1$, the system changes from globally unstable to stable as U_0 is increased. At low values of U_0, the leading eigenmode reaches a maximum around $x = 2$ and decays exponentially downstream (figure 1(b)). As U_0 increases, the temporal decay of the mode becomes stronger, and the spatial maximum eventually disappears: exponential growth is observed essentially throughout the entire domain. As observed previously[22], the spatial growth rate of the global mode corresponds to the local spatial growth rate at the global frequency.

For $U_0 = 4$ and $U_0 = 5$, the largest values of U_0 considered in figure 1(a, b), the overall shape of the spectrum completely changes. Figure 1(b) shows that in these cases, exponential growth occurs throughout the domain, and the amplitude of the mode varies by a factor of 10^{16} between $x = 0$ and the outlet at $x = 25$: the modes, and in particular the region $1 < x < 3$ where instability mechanisms act, cannot be resolved numerically. This phenomenon can also be seen as the length of the domain is increased for fixed U_0 and a_0. The same behavior is observed for $a(x) \in \mathbb{R}$, in which case the spectrum should lie on the imaginary axis, indicating that none of these computed modes actually correspond to modes of the continuous problem. Figure 1(c) shows that the eigenvalues returned by the eigensolver for $U_0 = 5$ approximately lie on the 10^{-14} contour of the pseudospectrum of the discrete operator which, in this case, does not provide a good approximation to the spectrum. In situations where the amplitude of the mode cannot be represented throughout the domain, even the QZ algorithm fails to compute an accurate approximation to the discrete spectrum.

The relative effect of the instability parameter and of the advection velocity is summarized in figure 1(d), where the spatial growth rate of the leading eigenmode is represented as a function of the two parameters U_0 and a_0. From this growth rate, it is possible to evaluate the maximum domain length for which the computation is possible using double precision arithmetic. The dashed lines displayed in figure 1(d) correspond to values of (a_0, U_0) for which the numerical truncation errors prevented the computation.

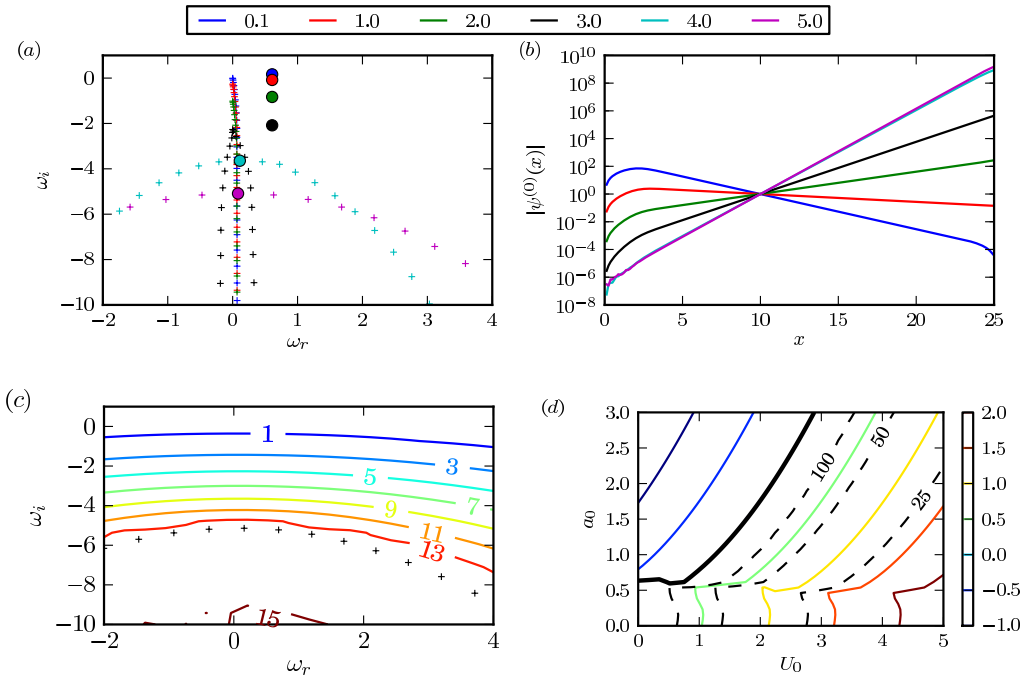

FIG. 1. (color online) (a, b): effect of U_0 on the leading eigenmodes for the advection–diffusion–reaction model (for $x_{max} = 25$ and $a_0 = 1$). The least stable part of the eigenvalue spectrum is shown in (a), and the leading eigenmode for each value of U_0 (represented in (a) by circles) are displayed in (b). (c): spectrum (+ symbols) and iso-contours of the pseudo-spectrum for $x_{max} = 25$, $U_0 = 5$ and $a_0 = 1$ (logarithmic scale). (d): Spatial growth rate of the leading global mode (measured as $\psi^{(0)\prime}(10)/\psi^{(0)}(10)$) as a function of parameters a_0 and U_0. The solid contour represents the limit between growing and decaying modes, the dashed lines gives the maximum value of the advection parameter for which computation is possible in a domain of a given length (indicated on the curve).

C. Conclusions from model problems

The above examples have shown that the spatial behavior to be seen in § V A for the eigenmodes of the Navier–Stokes equations is not inconsistent, and that it does not correspond to a spatial instability within a local framework. In the case where the flow dynamics are dominated by convection and diffusion effects, the downstream evolution of the modes results from two opposing mechanisms: the local stability of the flow tends to decrease the amplitude of the mode in the streamwise direction, but the advection of the globally stable structures has the opposite effect. In the case of a parabolic profile for a, the local stability eventually dominates for large x and the global modes decay to 0. On the contrary for $a \to a_0$ as $x \to \infty$ the local stability is not necessarily strong enough to prevent exponential spatial growth. The second model pointed out that, when convective effects dominate as $x \to \infty$, the size of the computational domain should be small enough that the amplitude of the mode can be resolved throughout the domain, otherwise numerical accuracy becomes problematic as the 10^{-15}-pseudospectrum can extend far from the spectrum[29]. The following section will present details on how this affects the computation and the convergence of modes for the Navier–Stokes system.

III. SETUP OF THE JET PROBLEM

A. Flow configuration

a. Incompressible setting

A cylindrical jet of a Newtonian fluid with viscosity ν^*, of radius R^* and exit velocity U_0^* is considered. The two latter quantities are used to make lengths and velocities non-dimensional. The outer fluid is at rest. The Reynolds number is taken as

$$\mathrm{Re} = \frac{U_0^* R^*}{\nu^*} = 10^3.$$

Frequencies f^* will be reported in terms of the non-dimensional circular frequency ω, related to the Strouhal number St as

$$\mathrm{St} = \frac{2 f^* R^*}{U_0^*} = \frac{\omega}{\pi}.$$

The axisymmetric flow domain, described in terms of cylindrical coordinates r, θ and x, is represented in figure 2(a). The steady solution of the non-linear Navier–Stokes equations (see § III B) is assumed to be axisymmetric. This assumption is no longer made for the perturbations, but in a linear context all perturbation quantities can be decomposed into independent Fourier-modes in θ, by introducing the azimuthal wavenumber $m \in \mathbb{N}$. Consequently, only the two-dimensional (r, x) plane needs to be discretized for both non-linear and linear calculations.

The boundary of the computational domain Ω consists of Γ_i, Γ_w,Γ_t,Γ_o and Γ_a, corresponding to the inlet, a solid wall, the outer radial boundary, the outflow and the jet axis. The inflow velocity is imposed on Γ_i, a no-slip condition on Γ_w, and stress-free boundary conditions are applied on Γ_t[33]:

$$\frac{1}{\mathrm{Re}} \frac{\partial \boldsymbol{u}}{\partial \boldsymbol{n}} - p\boldsymbol{n} = 0,$$

where $\boldsymbol{n}$ is the outgoing normal at the boundary (cf. equation 10.67 in Ref. 33). Compatibility conditions on Γ_a ensure a smooth solution on the axis[34]. Unless stated otherwise, stress-free boundary conditions are imposed at the outflow Γ_o.

The length of the pipe included in the numerical domain is set to $x_p = 5$, and it has been verified that setting the domain height to $r_{max} = 10$ does not affect the results of all incompressible calculations.

b. Compressible setting

In addition to the flow parameters introduced above, the compressible setting is characterized by density and temperature scales ρ_∞^* and T_∞^*, defined as the respective values in the outer fluid at rest. Natural choices for the Mach and Prandtl numbers are

$$\mathrm{Ma} = \frac{U_0^*}{c_\infty^*}, \qquad \mathrm{Pr} = \frac{\mu^* C_P^*}{\kappa^*},$$

where $c_\infty^* = \sqrt{\gamma r^* T_\infty^*}$ denotes the ambient speed of sound and C_p the specific heat at constant pressure.

In order to capture the acoustic radiation, the typical extent of the numerical domain has to be of the same order in the axial and radial direction. High resolution Finite Differences (FD) on a rectilinear grid are used to treat such a large problem. Consequently, the geometry (schematically displayed in figure 2(b)) is slightly different than in the incompressible case. In compressible studies, the jet pipe is modeled as an infinitely thin adiabatic wall located

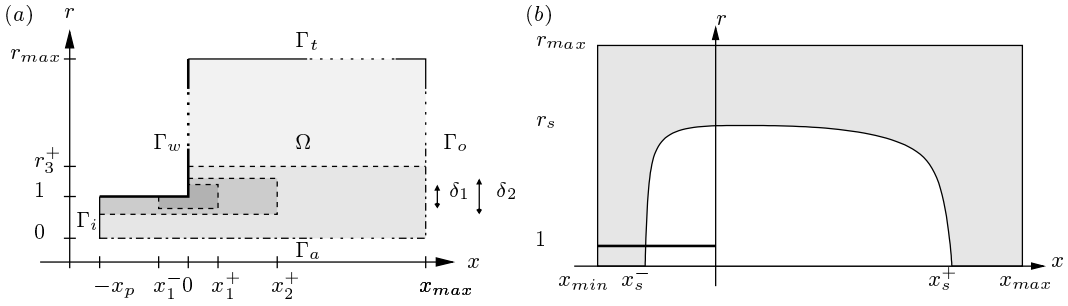

FIG. 2. Flow configuration for (a) incompressible and (b) compressible computations . The incompressible Navier–Stokes equations are solved on the 2D domain Ω using a Finite Element formulation, with an inflow boundary condition (BC) on Γ_i (thin solid line), a no slip BC on Γ_w (thick solid line), a stress-free BC on Γ_o (dashed line) and compatibility conditions on the axis Γ_a (dash-dot line). No sponge layers are used in this case. The compressible Navier–Stokes equations are discretized using high order Finite Differences (FD) on the rectangular domain represented in (b). The shaded regions correspond to sponge layers, and the presence of an infinitely thin adiabatic wall for $r = 1$ and $x \leq 0$ is taken into account by means of appropriate FD schemes.

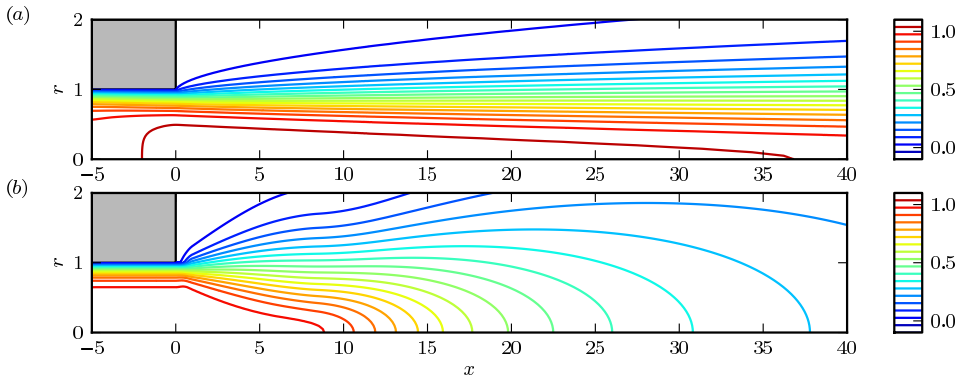

FIG. 3. Axial velocity field of the two base flows. (a) : laminar base flow, computed as a steady solution of the Navier–Stokes equations. (b) : turbulent mean flow, adapted from an analytical model[36].

at $r = 1$ and $x \leq 0$. Its presence is taken care of by using appropriate FD schemes. The treatment of the far field boundary conditions depends on the type of study performed. As will be shown later, the eigenmodes of the linearized Navier–Stokes equations are not spatially localized, so an accurate treatment of the outer boundaries is needed. To limit as much as possible the reflection of vortical or acoustic waves, the non-reflecting boundary conditions described by Bogey and Bailly[35] are used together with sponge layers. This is not required for the computation of the optimal perturbations which have a limited spatial extent. In the latter case, the sponge layers alone suffice to ensure that the solution decays to zero at the outer boundaries without affecting the flow in the physical region.

B. Base flows

Two types of base flows are investigated in this study: a laminar steady-state solution of the Navier–Stokes equations, and a parametric model of a turbulent mean flow. The incompressible analysis is performed on both these base flows, whereas only the turbulent case is considered in the compressible study.

a. Laminar steady state

A steady flow state is computed as an exact solution of the Navier–Stokes equations (see §III C). The inflow velocity is prescribed on Γ_i as

$$u_x(-x_p, r) = \tanh\left(5(1-r)\right) \qquad u_r(-x_p, r) = 0 \qquad u_\theta(-x_p, r) = 0.$$

This profile has a momentum thickness

$$\delta = \int_0^1 r u_x(1-u_x)\,\mathrm{d}r \approx \frac{1}{20}.$$

Stress-free boundary conditions are employed at the outflow Γ_o. The resulting base flow is weakly non-parallel, as seen in figure 3(a). A slight growth of the boundary layer in the pipe leads to an increase in the centerline velocity between $x = -x_p$ and 0, so that the exit centerline velocity is 1.06 at $x = 0$.

b. Turbulent mean flow

Based on experimental measurements, Monkewitz & Sohn[36] proposed a model for the turbulent mean flow of compressible jets. The flow field comprises two regions: a potential core extending over a distance of eight jet radii downstream of the nozzle, and an adjoining self-similar region with Gaussian profile shapes. This model is extended in our study by a parallel flow region inside the pipe, which smoothly connects to the free jet over the interval $0 \leq x \leq 1$. The full model is described in detail in Garnaud *et al.*[37]. The resulting streamwise velocity field is displayed in figure 3(b) for the zero-Mach-number case. The formulation does take into account compressibility effects, and finite-Mach-number configurations are used for the compressible analysis. The inflow momentum thickness is prescribed as $\delta^{-1} \approx 23$, similar to the laminar case.

Following Hussein & Reynolds[38], the stability of turbulent flows can be analyzed using a triple decomposition of the flow field into a mean flow, coherent perturbations and fine-scale turbulence. Using this decomposition, turbulent scales affect the motion of instability waves through Reynolds stresses, for which a closure model needs to be provided[39,40]. For turbulent jet flows, successful stability analyses[41,42] have been performed while neglecting the effect of Reynolds stresses, and this approach is also followed here as a first approximation. Local stability analyses show that perturbations with low azimuthal wavenumber m are amplified in the potential core region, whereas the self-similar downstream region of the base flow is unstable only to helical $m = 1$ perturbations.

C. Numerical methods

a. Incompressible setting

The incompressible Navier–Stokes equations are discretized using P2-P1 Finite Elements (FE), and the zero-divergence condition for the flow velocity is enforced by a penalty method[43]. The incompressible laminar steady flow is computed using Newton's method and the FreeFEM++ software[43]. A direct solver[44] is used for linear systems. Given this steady state or a model turbulent mean flow (see § III B b), the linearized Navier–Stokes equations that govern the evolution of perturbations may be written as

$$B\frac{\partial \boldsymbol{q}}{\partial t} = L\boldsymbol{q} \tag{5}$$

where $\boldsymbol{q}$ is the state vector, containing the values of all degrees of freedom of the velocity and pressure fields. Equation (5) is discretized using FreeFEM++ and the resulting sparse

matrices are exported for the linear analysis. The solution of all the problems in § IV and § V A relies on the software libraries PETSc[45], SLEPc[46] and MUMPS[44]. Eigenvalue problems arising in § V A are non-Hermitian, so the Krylov-Schur method is used. In order to compute the least stable eigenmodes the "shift-invert"[47] spectral transformation is applied using a direct linear solver.

In the study of optimal perturbations the amplitude of a perturbation needs to be measured. The square root of the perturbation kinetic energy integrated over the entire domain Ω is used for incompressible flows. This results in a pseudo-norm, as pressure is not taken into account. For the problem to be well posed, the amplitude of the initial condition needs to be measured in terms of a norm. The initial disturbance is therefore assumed to consist only of a velocity perturbation. Let $\boldsymbol{q}_u$ be a vector containing only velocity-related degrees of freedom, and P be a matrix that associates $\boldsymbol{q}_u$ to a state vector where pressure-related degrees of freedom are zero. Conversely, the operator $P^\dagger$ removes these degrees of freedom from a full state vector $\boldsymbol{q}$. The pseudo-norm is then obtained as

$$\|\boldsymbol{q}\|^2 = \boldsymbol{q}_u^\dagger Q_u \boldsymbol{q}_u = \boldsymbol{q}^\dagger P Q_u P^\dagger \boldsymbol{q} = \boldsymbol{q}^\dagger Q \boldsymbol{q} \tag{6}$$

where Q_u is a Hermitian definite matrix.

The computation of optimal perturbations described in § IV requires (i) a direct time stepper, (ii) an adjoint time stepper and (iii) an eigenvalue solver. The linear equations of motion are marched forward in time using the Crank-Nicolson method (steps (i) and (ii)). A discrete adjoint is used for step (ii), based on the Hermitian transpose of the discretization matrices. Finally, as the eigenvalue problem to be solved is Hermitian, the Lanczos method is used.

b. Compressible setting

The linearized compressible Navier–Stokes equations are spatially discretized using a finite-difference scheme designed for aero-acoustic studies[48]. The resulting discretization matrix is sparse, but with an important number of nonzero elements, in particular due to the stencil of the cross derivative terms which involves here 121 discretization points. Another consequence of the large FD stencils is that the bandwidth of the sparse discretization matrices becomes relevant, leading to excessive memory requirements for direct solvers. Iterative solvers could be used instead[49], but these methods are very sensitive to the design of an efficient preconditioner and robustness may be an issue. In order to circumvent these problems, all of the analysis is performed using an algorithm based on time stepping of linear equations (an explicit third order Runge-Kutta method is used here). In such a framework, the structure of the discretization matrices is not needed, therefore a matrix-free approach is used. Compressible eigenmodes are computed by use of a relaxation method[50], which is based on the application of a bandpass frequency filter to the equations of motion. This method allows to solve very large eigenvalue problems with low memory requirements. However, our experience shows that the relaxation method in general does not reach the machine-precision accuracy that is possible with the shift-invert method.

The adjoint Navier–Stokes operator is needed for the computation of optimal perturbations (§ IV). A discrete adjoint formulation is chosen, following the memory-efficient approach of Fosas *et al.*[51]. The norm used is that of Hanifi *et al.*[52]. Care is taken with the selective spatial filter so that the discrete propagator of the adjoint equations is the adjoint of the discrete direct propagator up to machine precision.

IV. TRANSIENT GROWTH OF PERTURBATIONS

The initial condition $\boldsymbol{q}(0)$ that is most amplified over a finite time interval T is referred to as the *optimal perturbation* for T. Reddy & Henningson[32] established the notion of optimal perturbations in order to characterize the transient (short-term) linear dynamics of flow

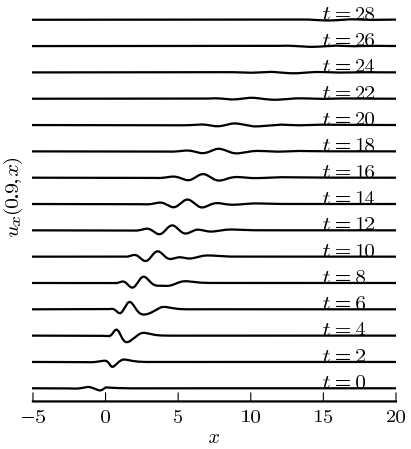

FIG. 4. Spatio-temporal evolution of the optimal initial condition for $m = 0$ and $T = 10$ for the turbulent jet mean profile in the incompressible case. The value of the axial velocity along the line $r = 0.9$ is represented at various time steps, as indicated next to the curve.

systems. Let the amplification factor be defined as

$$G_m(T) = \max_{\boldsymbol{q}(0)} \frac{\|\boldsymbol{q}(T)\|}{\|\boldsymbol{q}(0)\|} \,. \tag{7}$$

Furthermore, let $\mathcal{P}_T$ be the propagator, i.e. the linear operator that advances an initial condition over the time interval T according to equation (5). The optimal gain $G_m(T)$ is found as the leading eigenvalue of the operator $Q_u^{-1} P \mathcal{P}_T^\dagger Q \mathcal{P}_T P^\dagger$, and the associated eigenvector represents the optimal perturbation. The eigenvalue problem is solved using the Lanczos method, as implemented in the SLEPc library. The operators $\mathcal{P}_T$ and $\mathcal{P}_T^\dagger$ are applied using the time steppers described in § III C, and Q_u^{-1} is determined using a Cholesky decomposition (in the case of a finite-difference discretization, this decomposition is easily performed by hand).

A. Incompressible flow

In the incompressible setting, the length of the computational domain is chosen as $x_{max} = 40$, and stress-free boundary conditions are employed at the outflow. The convergence of the results with respect to the spatial and temporal discretizations has been verified by using (i) a halved time-step and (ii) a finer mesh where the cell size in the near-nozzle region is divided by more than 3. For both the laminar and the turbulent base flows, and for all azimuthal wave numbers and time horizons, the optimal perturbation is found in the form of structures localized in the boundary layer upstream of the nozzle, and the perturbations are amplified as they travel downstream. A typical example is shown in figure 4, which displays the evolution of the optimal perturbation of the turbulent jet for $m = 0$ and $T = 10$, along the line $r = 0.9$.

The optimal gain as a function of time horizon T is displayed in figure 5 for both base flows. In the case of the laminar base flow, this amplification factor grows monotonically with T as long as the perturbation is contained inside the numerical domain. Very large amplitudes are reached, comparable to similar computations in the supersonic regime by Nichols & Lele[17]. In the case of the turbulent base flow (figure 5(b)), the gain reaches a maximum for a finite time horizon $T_{opt,m}$. This maximum is particularly pronounced for axisymmetric perturbations ($m = 0$), with $T_{opt,0} \approx 10$. This interval roughly corresponds

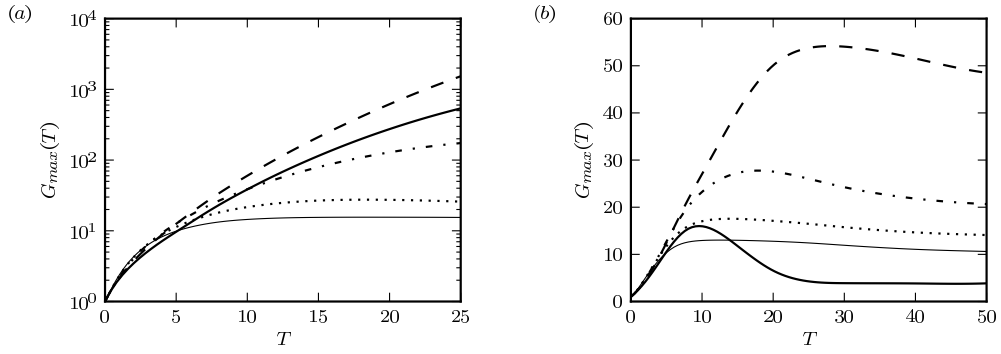

FIG. 5. Gains associated with the optimal perturbations for (a) the laminar and (b) the model base flows.Thick solid line : $m = 0$, dashed line : $m = 1$, dash-dotted line : $m = 2$, dotted line : $m = 3$ and thin solid line $m = 4$.

to the advection time of the initial perturbation across the potential core. Downstream of the potential core, axisymmetric perturbations decay as they travel on. Non-axisymmetric perturbations may still experience further growth beyond the potential core, and the decay of $G_m(T)$ with T is slower as a consequence. This observation is consistent with the fact that ~~bell-shaped~~ profiles in the self-similar regime may be unstable for $m \neq 0$ but not for axisymmetric perturbations[53]. Both the laminar and the turbulent settings display the largest gains for helical perturbations $m = 1$. It may be conjectured that a *lift-up* mechanism[54] is responsible for the strong growth of helical perturbations, since such a mechanism can only exist at azimuthal wavenumbers $m \neq 0$. However, no firm evidence of lift-up effects can be reported at present.

B. Effects of compressibility

Corresponding results of optimal perturbations of the turbulent mean flow at $Ma = 0.75$ are displayed in figure 6. The qualitative behavior of $G_{max}(T)$ (shown in figure 6(a)) is similar to that obtained for incompressible flows (figure 5(b)), and the amplification levels are comparable, although perturbations are not measured in the same norm. The spatial shape of optimal perturbations for short time horizons also resembles those found in the incompressible setting. Figures 6(b, c) show the optimal perturbation for $T = 12$: vortical structures in the pipe boundary layer are amplified as they travel through the jet shear layer. However, compressibility allows a different scenario at longer time horizons $T \gtrsim 25$, as shown in figures 6(d, e): the optimal initial condition takes the form of a spherical acoustic pulse that *contracts* and hits the nozzle at a finite time. A vortical wavepacket is thus created at the nozzle, which is amplified while it propagates through the potential core. This result illustrates that acoustic waves can be very efficiently converted into vortical perturbations at the nozzle tip[55–57].

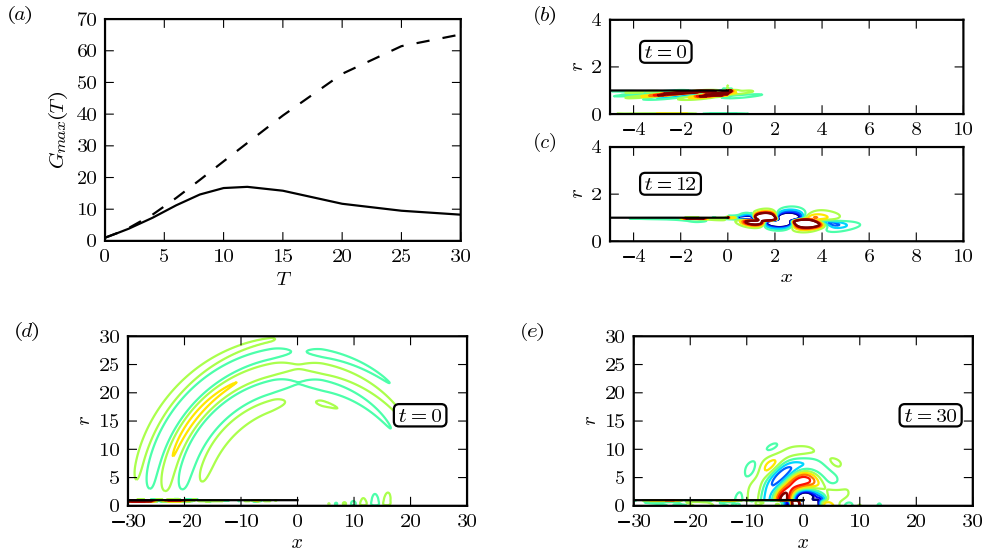

FIG. 6. (a) Optimal perturbations for the model subsonic jet at Ma $= 0.75$ for $m = 0$ (solid line) and $m = 1$ (dashed line). (b, c) : Azimuthal vorticity field for the optimal initial condition for $m = 0$ and $T = 12$, and the corresponding perturbation at $t = 12$. (d, e) : Dilatation field for the optimal initial condition for $m = 0$ and $T = 30$, and the corresponding perturbation at $t = 30$.

V. MODAL ANALYSIS

A. Incompressible global modes

a. Spectrum of the laminar base state

Eigenmodes of the linear equations (5) are sought in the form $\boldsymbol{q}(t) = \widetilde{\boldsymbol{q}} \exp(-\mathrm{i}\omega t)$, such that $\widetilde{\boldsymbol{q}}$ and ω satisfy the generalized eigenvalue problem

$$-\mathrm{i}\omega B\widetilde{\boldsymbol{q}} = L\widetilde{\boldsymbol{q}}. \tag{8}$$

Stress-free boundary conditions are used at the outflow Γ_o, and eigenmodes are computed for $x_{max} = 60$ with various shift parameters. The resulting spectra for the laminar base flow are shown in figure 7(a).

All eigenvalues have a negative growth rate $\omega_i \leq 0$ and therefore are stable. This finding is consistent with local instability results from the literature, which have shown isothermal jets to be convectively unstable[36], except in rare circumstances[58].

Several families of modes can be identified from figure 7(a). A first branch of modes, starting at the origin, is represented as circles (blue online). The least stable of these modes correspond to vortical structures in the free-stream, as displayed in figure 7(b). The wavelength of these nearly stationary modes scales with the size of the numerical domain. As the growth rate decreases along this branch, the branch is distorted and the mode structure tends to be localized more towards the jet shear-layer. This is an effect of the finite extent of the numerical domain that has been observed in other studies[26,59]. A second branch is represented by $\times$ symbols (black online). These eigenmodes are localized inside the shear layer. At the lowest frequencies, an exponential spatial growth in the streamwise direction is observed throughout the computational domain, as shown in figure 7(c). This behavior is similar to what was observed in the model problems of § II, and by this analogy we attribute the exponential spatial growth to the temporal decay of these modes. At higher frequencies (figure 7(d)), spatial growth is still found downstream of the nozzle, but the mode reaches a maximum amplitude within the computational domain. The maximum growth rate along

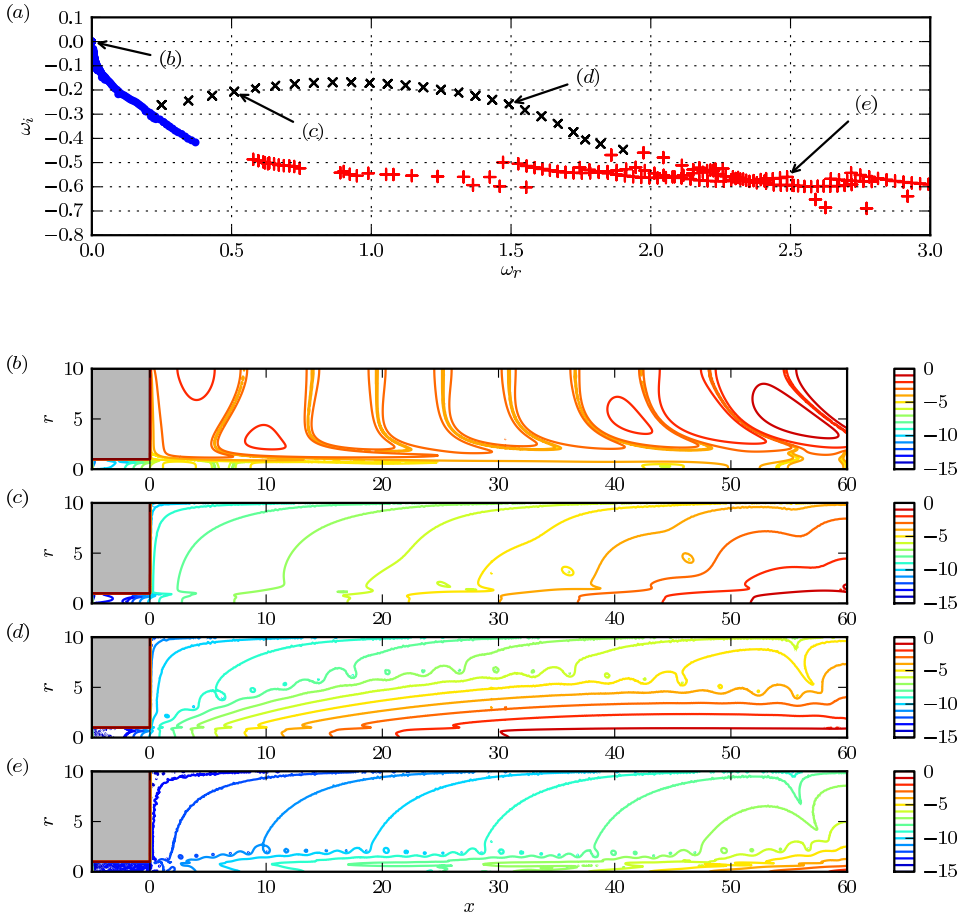

FIG. 7. Global modes computed for $m = 0$ on the laminar base flow. (a): eigenfrequency spectrum. (b, c, d, e): axial velocity magnitude of four selected modes, in logarithmic scale, as indicated in (a).

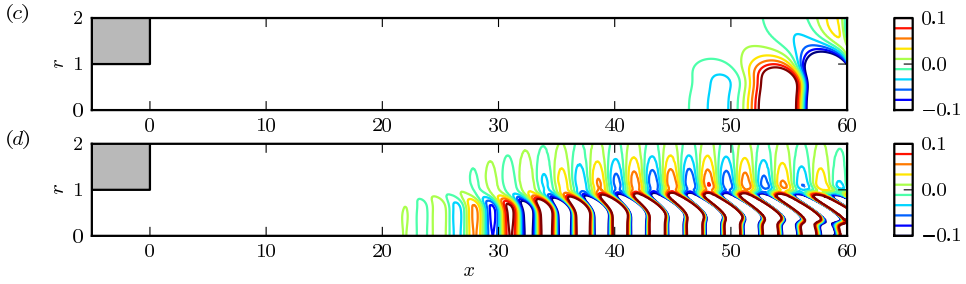

FIG. 8. Axial velocity for global modes (c) and (d) of figure 7, in linear scale.

this branch occurs around the frequency ($\omega_r \approx 1$) for which the location of maximum amplitude of the mode enters the computational domain, suggesting that the maximum in ω_i is an artifact of the finite domain size. Domain truncation effects are investigated in the following section. The phase velocity of all modes along this branch corresponds approximately to half the jet velocity on the centerline; modes at higher frequency therefore display shorter wavelengths, as can be seen in figure 8.

A third family of modes is found, represented by plus signs (red online) in figure 7(a).

None of these eigenvalues are recovered identically with different shift parameters, indicating a lack of convergence. However, these modes have been computed by the eigenvalue solver with the specified convergence criterion, namely $\|L\boldsymbol{q} + \mathrm{i}\omega\boldsymbol{q}\| < 10^{-10}\|\boldsymbol{q}\|$. We attribute this class of modes to spurious effects arising from finite machine precision. The spatial structure of one such spurious mode is represented in figure 7(e).

All modes represented in figure 7 display very large amplitude variations throughout the free-jet region. If these variations are of the order of machine precision, the low-amplitude dynamics near the nozzle cannot be accurately resolved. The perturbation amplitudes shown in figures 7($b-d$) do not span more than ten orders of magnitude in the free-jet region, and appear to be well-converged. The spurious mode in figure 7(e), in contrast, varies over 14 orders of magnitude, and seems to be affected by the double-precision round-off error as a consequence. In fact, it may be surmised that its very existence is due to the round-off error; this conjecture will be further investigated in the next section. A similar observation has been made by Heaton *et al.*[23] in their modal stability analysis of the Batchelor vortex. Those authors report that modes with amplitude variations above a factor of 10^6, between the inlet and outlet of the computational domain, cannot be accurately resolved with their numerical method. With the present algorithm, this limiting factor is approximately 10^{14}.

b. Influence of domain truncation

All eigenmodes displayed in figure 7 reach their maximum amplitude at or near the downstream boundary of the numerical domain. It may therefore be expected that the position of this boundary, as well as the numerical treatment of the outflow condition, should affect the results. In order to evaluate this influence, different domain lengths between 40 and 100 radii have been tested. The results are compared in figure 9(a), which shows that the branches of eigenmodes computed are not domain-independent. A similar behavior has been obtained in the analysis of the Blasius boundary layer[22], and is attributed to the fact that the wavepackets travel throughout the domain. Most importantly, the maximum growth rate of the shear-layer branch shifts to lower frequencies as x_{max} is increased. An inspection of the associated spatial amplitude distributions reveals that this maximum growth rate occurs roughly at the frequency at which the mode maximum amplitude is first captured inside the numerical domain. At low real frequencies, the true amplitude maximum lies on the outflow boundary of the numerical domain, and the eigenvalues are strongly affected by truncation. With increasing real frequency, this amplitude maximum moves further upstream, and the influence of the domain truncation lessens. The mode shapes shown in figure 7 are consistent with this observation. If the trend with increasing domain size is extrapolated, one may expect that the growth rate of the shear-layer branch decreases monotonically with increasing frequency in an infinitely long domain.

While the spectra in figure 9(a) have been computed with stress-free outflow conditions, figure 9(b) displays corresponding results obtained with a "convective outflow" formulation[60]. Both boundary conditions are found to give very similar results. It is inferred from this comparison that the outflow boundary conditions do not have a significant impact on the eigenmode computations in this study.

It appears that the spurious branches become less and less stable as the domain length increases. This branch is interpreted as a consequence of finite precision arithmetic. Under the assumption of a quasi-parallel flow, let C_g be the group velocity of a spurious spatial instability wave forced by numerical noise in the vicinity of the jet pipe,

$$\psi_{sp} = \widehat{\psi}(r)\exp(\mathrm{i}(k_r + \mathrm{i}k_i)x)\exp(-\mathrm{i}\omega t) \tag{9}$$

where ω is the complex forcing frequency. This forced wave will be considered an eigenmode by the solver if the forcing amplitude is of the order of the numerical precision ϵ_m, i.e. if the amplitudes of this forced wave at the inlet and at the outlet are such that

$$\psi(x=0) \sim \epsilon_m \psi(x = x_{max}).$$

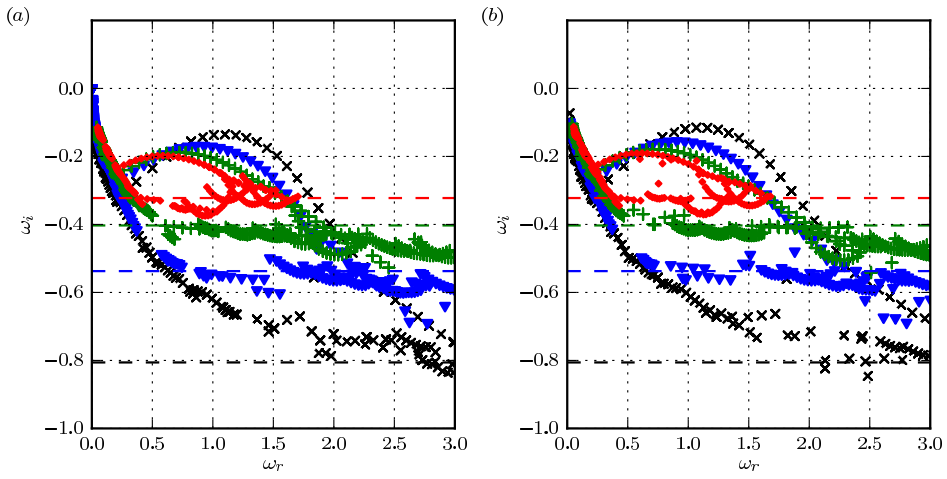

FIG. 9. Spectra computed for various domain lengths using stress-free (a) and convective outflow (b) boundary conditions at the outlet. Crosses : $x_{max} = 40$ (black online). Triangles : $x_{max} = 60$ (blue online). Plusses : $x_{max} = 80$ (green online). Circles : $x_{max} = 100$ (red online). The dashed lines corresponds to the estimated decay rate (11).

In this case, (9) gives $k_i = -\log(\epsilon_m)/x_{max}$. Let $\omega_i^t(k_r)$ be the local temporal growth rate associated with the axial wavenumber k_r. In the limit of long wavelengths, jet flow profiles are approximately marginally stable. Following an approach similar to that of the Gaster transformation[61], the global temporal decay rate ω_i can be related to the global spatial growth rate k_i by

$$\omega_i \approx C_g k_i + \omega_i^t(k_r) \approx C_g \frac{\log(\epsilon_m)}{x_{max}}. \tag{10}$$

As the group velocity C_g is of the order of the base flow velocity U_0, the decay rate associated with such pseudomodes can be estimated as

$$\sigma \equiv U_0 \frac{\log(\epsilon_m)}{x_{max}}. \tag{11}$$

Figure 9 shows that the above expression provides a reasonable estimate for the decay rate of the spurious modes. Since σ varies as $1/x_{max}$, this spurious branch will eventually become less stable than the other two branches as x_{max} increases, preventing their computation. It is thus impossible to obtain converged results for the spectra, at least using standard double precision arithmetic ($\epsilon_m = 10^{-15}$).

It appears that machine precision imposes severe constraints on global mode computations for convective flows such as jets. The streamwise extent of the numerical domain must be sufficiently large to capture the amplitude maximum of the mode, but the amplitude variations must also be within the range of machine precision. At the same time, spurious modes contaminate an increasingly large portion of the spectrum as the numerical domain length is increased.

c. Spectrum of the turbulent mean flow

One may intuitively expect that the much faster spreading of the turbulent mean flow, compared to the laminar base flow considered in the last section, will lead to global mode structures that decay spatially within a shorter distance from the nozzle. In view of the

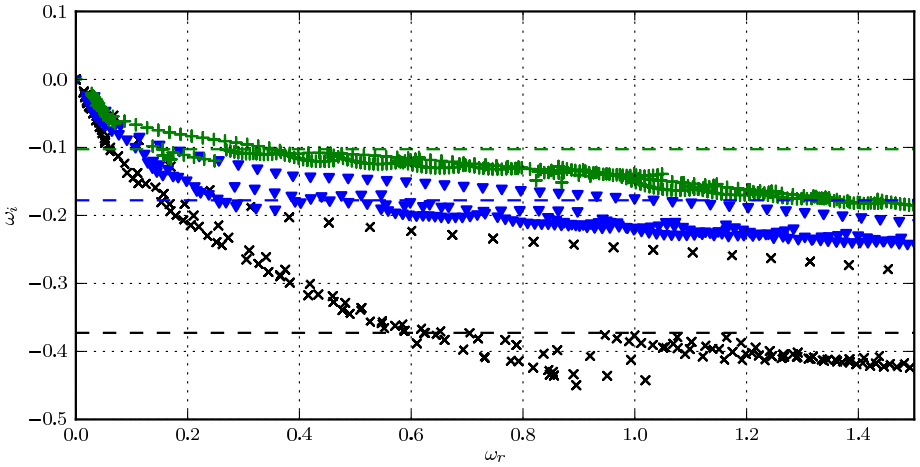

FIG. 10. Global spectra computed for $m = 0$ for the model base flow. Crosses : $x_{max} = 40$ (black online). Triangles : $x_{max} = 60$ (blue online). Plusses : $x_{max} = 80$ (green online). The dashed lines corresponds to the estimated decay rate of the spurious branch given by (11).

discussion in the preceeding section, such a behavior would be favorable for the numerical analysis. However, the mean flow spreading also implies a decreased advection velocity, which in turn strengthens the spatial growth due to the advection of stable structures.The estimate for the decay rate of spurious structures given by (11) can be modified to account for the significant variation of the base velocity on the jet axis, giving

$$\sigma' \equiv \log(\epsilon_m) \left(\int_0^{x_{max}} \frac{1}{u_x^0(0,x)} \, \mathrm{d}x \right)^{-1}. \tag{12}$$

The spectra displayed in figure 10 show that this estimate is also reasonably accurate. This implies an even more stringent constraint on the size of the computational domain than in the case of a nearly parallel flow.

Figure 11 displays selected global modes computed for $x_{max} = 60$: as for all the modes presented in figure 10, the exponential growth continues throughout the computational domain. Indeed, in light of the discussion of the model problems, there is no guarantee that a maximum will ever be reached: the maximum amplitude may well continue towards infinity. Against all expectations, it is found that the faster spreading of the present mean flow does not lead to more upstream-localized mode structures. Therefore the computation of the spectrum is *not* any more accessible than in the laminar base flow case.

B. Compressible eigenmodes

Eigenmodes have been computed for the model mean flow at Ma = 0.75. The computed spectrum is displayed in figure 12(a). Similar to the incompressible case, it is worth pointing out that the spectrum does not show any preferred frequency. The decay rates of the modes are however significantly less stable than in the incompressible case, by more than a factor of five. Although the solver used for this computation is less accurate than the one used for incompressible computations, the results displayed in figure 12 are converged with respect to the iterative eigenvalue solver. As a consequence of the very low decay rate, the spatial growth of eigenmodes is weaker than in the incompressible case, and at high frequencies the global modes decay right after the end of the jet pipe (see figure 12(b, c, d))

Several reasons may explain such a slow temporal decay. As it was seen in § IV, acoustic disturbances efficiently excite vortical structures, and, as the Mach number increases, the

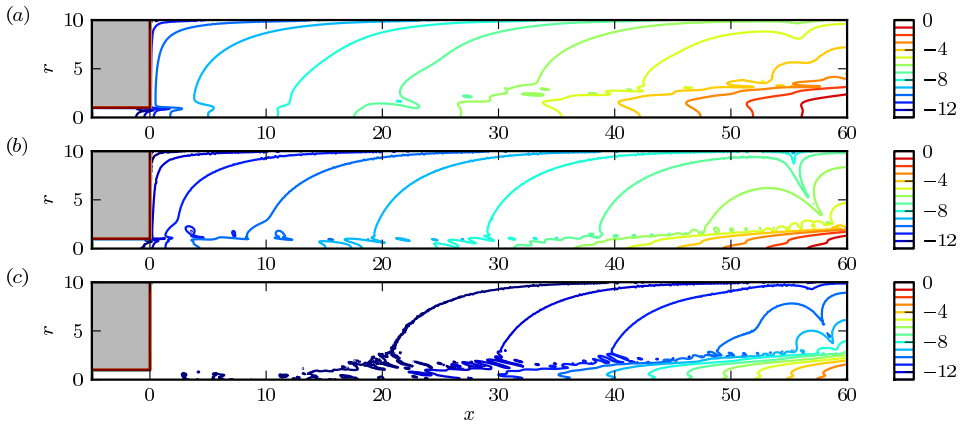

FIG. 11. Axial velocity fields of selected global modes computed for $m = 0$ for the model base flow with $x_{max} = 60$ and stress-free outflow boundary conditions (logarithmic scale). (a) : $\omega = 0.22 - 0.11\mathrm{i}$, (b) : $\omega = 1.0 - 0.17\mathrm{i}$, (c) : $\omega = 0.98 - 0.23\mathrm{i}$.

acoustic wavelength gets closer to the wavelength of vortical wavetrains, so that excitation can be efficient and lead to a feedback loop. The feedback could also be spurious: indeed, although the optimal perturbation results of § IV are quite insensitive to the treatment of the outer boundaries, this significantly affects the eigenmodes. In spite of the use of non-reflecting boundary conditions and very weak sponge regions, it is expected that an effect is still present here. Similarly, as the vorticity field grows in space due to the temporal stability, the acoustic field also grows exponentially with the distance to the acoustic sources. As a consequence, even for weakly damped modes, reflection can be significant in large numerical domains. Finally, the low decay rate may be related to the fact that the numerical dissipation is lower with the present FD formulation than with the FE discretization used for incompressible flows. Indeed, in situations where structures are convected outside of the numerical domain, dissipative effects can be important at large times.

VI. PROJECTION OF THE TRANSIENT DYNAMICS ONTO THE SPACE SPANNED BY EIGENMODES.

Optimal perturbations have been computed in § IV using a direct-adjoint technique. An alternative method is to approximate the propagator using a reduced-order basis consisting of the computed eigenmodes. This technique has, for example, been successfully used by Akervik *et al*[7] for the global analysis of an amplifier flow. Regardless of the relevance of the eigenmodes to describe the dynamics, such an analysis is expected to yield accurate results provided the eigenmodes are computed accurately. Figure 13 displays the optimal gains computed for the laminar incompressible jet with $m = 0$: the N least stable eigenmodes have been used for the computation, with N varying from 5 to 183[62]. It appears that even when all the computed eigenmodes are taken into account, the optimal gains are under-estimated by up to two orders of magnitude. Eigenmodes are therefore not relevant individually, which is already well known for amplifier flows, but also as a superposition to represent transient dynamics. A similar study on a stable lid-driven cavity flow (not shown here) yielded substantially better convergence towards transient energy gains when the number of included eigenmodes is increased. This further emphasized the role of advection in the representation of transient phenomena by global modes. The above finding is contrary to that of Akervik *et al*[7] and is related to the much stronger streamwise growth of eigenmodes in the present configuration. Indeed the optimal initial conditions consist of structures in the jet pipe. In this region, all eigenmodes have very small amplitudes and numerical inaccuracies

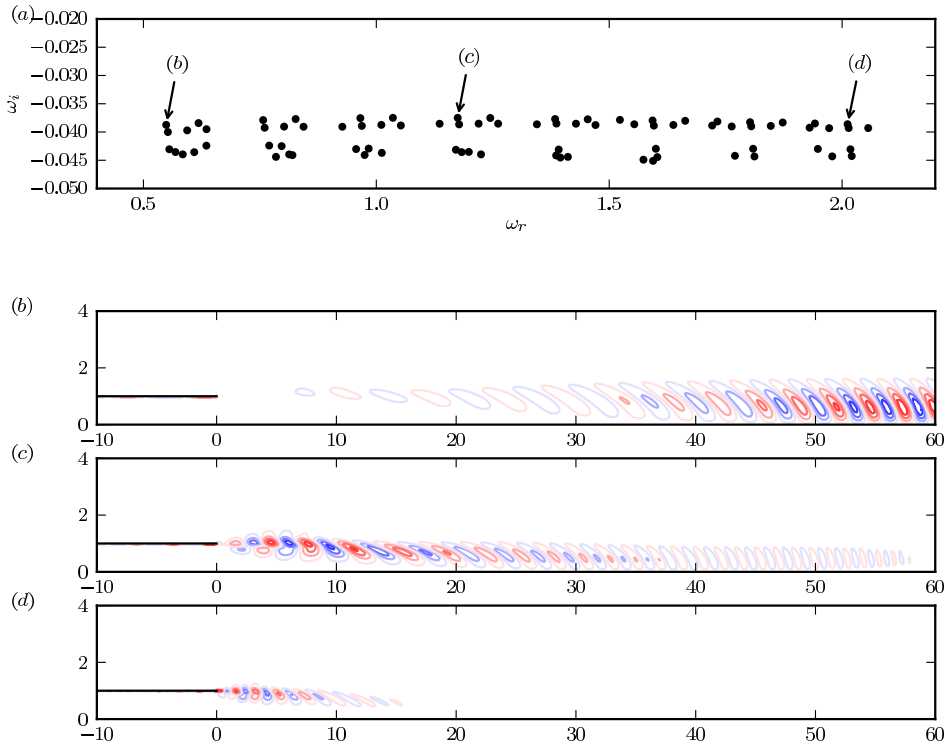

FIG. 12. Global modes computed for $m = 0$ on the model subsonic jet at Ma $= 0.75$. (a): eigenvalue spectrum. (b, c, d): azimuthal vorticity of three selected modes, as indicated in (a).

(due to both the eigenmode computation and the projection) become significant.

VII. CONCLUSIONS

The linear dynamics of perturbations in jet flows is the result of two mechanisms, advection by the base flow and shear layer instability. In order to investigate the effect of these two features on the modal and non-modal stability properties of the flow, two types of base flows have been considered. The first one is a laminar steady solution of the Navier–Stokes equation, for which both advection and instability remain approximately constant in the streamwise direction. A turbulent mean flow has also been used: in this case, instability is limited to a region of about eight radii downstream of the jet pipe, referred to as the potential core, where advection remains approximately constant. Further downstream the base flow velocity decreases significantly and the jet profiles become stable to axisymmetric perturbations.

An optimal perturbation analysis has been performed on these two base flows, revealing that vortical structures are amplified throughout the laminar jet, but only in the potential core for turbulent mean flows. In both cases the flow is globally stable.

In order to investigate the preferred frequency observed in jet experiments, a modal analysis has then been performed, but several difficulties were encountered. The eigenmodes, computed on a finite domain, exhibit an exponential growth in the streamwise direction. Intuitively, one might expect that eigenmodes should spatially decay in locally stable flow regions, and that therefore such a decay will eventually occur if the numerical domain is long enough in the streamwise direction. This is actually not the case, and longer computational domains in fact tend to aggravate the numerical difficulties.

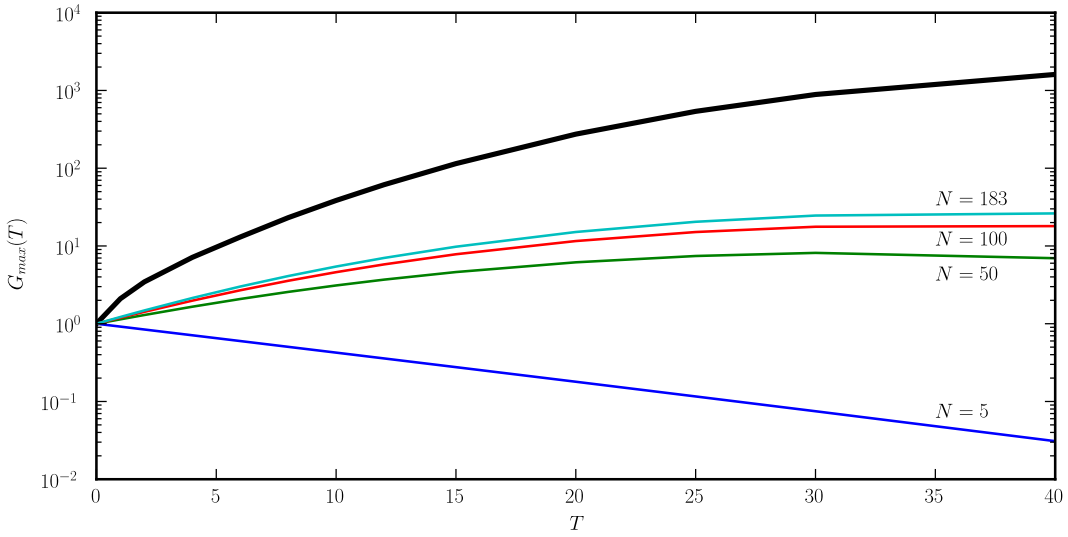

FIG. 13. Optimal transient amplification of axisymmetric perturbations for the laminar incompressible jet. Thick line: computation using the adjoint equations, as computed in § IV. Thin lines: optimal gains computed by projecting the dynamics onto the space spanned by the N least stable eigenmodes.

The cause of these problems has been discussed for model equations that mimic the advection and instability properties of jet flows. Indeed, when eigenmodes represent the advection of stable, temporally decaying structures, they grow exponentially in the streamwise direction. When computing such modes, difficulties therefore arise due to the domain truncation, the modeling of outflow boundary conditions and the finite precision of computer arithmetic.

Eigenmodes have been computed for jets in laminar and turbulent, compressible and incompressible settings, and results display the same properties as those obtained from the model problems. It has been shown that convergence of the spectrum of incompressible jets is inhibited by the presence of spurious pseudomodes which impose strict constraints on the size of the numerical domain.

As was shown with simple models, the exponential spatial growth of the stable modes is not an indication of a local spatial instability, it is merely a reflection of the fact that the eigenfrequency ω has a negative imaginary part. This has been further exemplified through the computation of eigenmodes for turbulent mean flows that grow even faster than those computed for a laminar base flow while the flow is stable downstream of the potential core for $m = 0$. The temporally stable structures observed in the modes, generated by a shear layer instability downstream of the nozzle, are convected downstream in a quasi-neutral flow resulting in an apparent spatial growth. For both mean flows the global decay rates of shear layer modes are of the same order of magnitude since the inflow shear layer thickness is similar. As the advection velocity is much smaller for the turbulent mean flow, the spatial growth is therefore larger.

For compressible flows, the computed eigenmodes are less stable than in the incompressible case. As a consequence, the local stability of shear layer structures dominates over the growth due to stable advection such that the exponential growth is not observed. However, this growth not only affects vortical structures but also acoustic waves. For acoustic perturbations the exponential growth due to the advection of stable structures eventually dominates over the algebraic decay: the acoustic waves radiated from a mode reach their maximum amplitude at the boundaries of the computational domain, which represents considerable challenges to avoid spurious reflections.

The present results found for jet flows are consistent with the literature on the stability of the Blasius boundary layer. The qualitative features of the eigenmodes are similar for jets and boundary layers, but the physical settings are quite different, and eigenmodes are much

less temporally stable for the boundary layer problem. Consequently, the spatial growth of boundary layer modes is weaker and numerical issues are less important than in the jet configuration.

All the numerical challenges faced in the modal analysis of jet flows cannot be attributed to a poor discretization and other numerical influence, since the numerical tools used in this study provided robust results for the transient flow analysis. As the numerical schemes employed for this study are linear, the transient simulations can be viewed as a superposition of all eigenmodes of the discrete problem. The issues are not related to the convective nature of the flow, since the transient analysis successfully and robustly reproduced the flow behavior; they rather lie with the description of stable convective dynamics by global modes, and their interpretation as coherent invariant structures.

ACKNOWLEDGMENTS

This work was supported by DGA grant number 2009.60.034.00.470.75.01 and by a fellowship from the EADS Foundation. Calculations were performed using HPC resources from GENCI (Grant 2012-026451). The authors thank F. Gallaire for his help.

[1]D. Barkley, "Linear analysis of the cylinder wake mean flow," Europhysics Letters **75**, 750–756 (2006) doi:10.1209/epl/i2006-10168-7.
[2]S. Bagheri, P. Schlatter, P. Schmid, and D. Henningson, "Global stability of a jet in crossflow," Journal of Fluid Mechanics **624**, 33 (2009) doi:10.1017/S0022112009006053.
[3]U. Ehrenstein and F. Gallaire, "Two-dimensional global low-frequency oscillations in a separating boundary-layer flow," Journal of Fluid Mechanics **614**, 315 (2008) doi:10.1017/S0022112008003285.
[4]P. Meliga, J. Chomaz, and D. Sipp, "Global mode interaction and pattern selection in the wake of a disk: a weakly nonlinear expansion," Journal of Fluid Mechanics **633**, 159 (2009) doi:10.1017/S0022112009007290.
[5]M. Navarro, L. Witkowski, L. Tuckerman, and P. L. Quéré, "Building a reduced model for nonlinear dynamics in Rayleigh-Bénard convection with counter-rotating disks," Physical Review E **81** (2010) doi: 10.1103/PhysRevE.81.036323.
[6]O. Marquet, D. Sipp, and L. Jacquin, "Sensitivity analysis and passive control of cylinder flow," Journal of Fluid Mechanics **615**, 221–252 (2008) doi:10.1017/S0022112008003662.
[7]E. Akervik, J. Hoepffner, U. Ehrenstein, and D. Henningson, "Optimal growth, model reduction and control in a separated boundary-layer flow using global eigenmodes," Journal of Fluid Mechanics **579**, 305 (2007) doi:10.1017/S0022112007005496 .
[8]A. Barbagallo, D. Sipp, and P. Schmid, "Inputoutput measures for model reduction and closed-loop control: application to global modes," Journal of Fluid Mechanics **685**, 23–53 (2011) doi:10.1017/jfm.2011.271.
[9]P. Huerre and P. Monkewitz, "Local and global instabilities in spatially developing flows," Annual Review of Fluid Mechanics **22**, 473–537 (1990) doi:10.1146/annurev.fl.22.010190.002353.
[10]J. Chomaz, "Global instabilities in spatially developing flows: Non-Normality and nonlinearity," Annual Review of Fluid Mechanics **37**, 357–392 (2005) doi:10.1146/annurev.fluid.37.061903.175810.
[11]L. Lesshafft, P. Huerre, P. Sagaut, and M. Terracol, "Nonlinear global modes in hot jets," Journal of Fluid Mechanics **554**, 393–409 (2006) doi:10.1017/S0022112006008974.
[12]L. Lesshafft, P. Huerre, and P. Sagaut, "Frequency selection in globally unstable round jets," Physics of Fluids **19**, 054108 (2007) doi:10.1063/1.2732247.
[13]S. Crow and F. Champagne, "Orderly structure in jet turbulence," Journal of Fluid Mechanics **48**, 547 (1971) doi:10.1017/S0022112071001745 .
[14]D. Bodony and S. Lele, "On using large-eddy simulation for the prediction of noise from cold and heated turbulent jets," Physics of Fluids **17**, 085103 (2005) doi:10.1063/1.2001689.
[15]A. Cooper and D. Crighton, "Global modes and superdirective acoustic radiation in low-speed axisymmetric jets," European Journal of Mechanics - B/Fluids **19**, 559–574 (2000) doi:10.1016/S0997-7546(00)90101-8.
[16]C. Moore, "The role of shear-layer instability waves in jet exhaust noise," Journal of Fluid Mechanics **80**, 321 (1977) doi:10.1017/S0022112077001700.
[17]J. Nichols and S. Lele, "Non-normal global modes of high-speed jets," International Journal of Spray and Combustion Dynamics **3**, 285–302 (2011) doi:10.1260/1756-8277.3.4.285.
[18]J. Nichols and S. Lele, "Global mode analysis of turbulent high-speed jets," Annual Research Briefs 2010 (Center for Turbulence Research, 2010).
[19]D. Barkley, M. Gomes, and R. Henderson, "Three-dimensional instability in flow over a backward-facing step," Journal of Fluid Mechanics **473** (2002) doi:10.1017/S002211200200232X.
[20]O. Tammisola, *Linear stability of plane wakes and liquid jets: global and local approach*, PhD thesis, KTH (2009).
[21]O. Tammisola, F. Lundell, and L. Soderberg, "Effect of surface tension on global modes of confined wake flows," Physics of Fluids **23**, 014108 (2011) doi:10.1063/1.3540686.

[22]U. Ehrenstein and F. Gallaire, "On two-dimensional temporal modes in spatially evolving open flows: the flat-plate boundary layer," Journal of Fluid Mechanics **536**, 209–218 (2005) doi: 10.1017/S0022112005005112.
[23]C. Heaton, J. Nichols, and P. Schmid, "Global linear stability of the non-parallel batchelor vortex," Journal of Fluid Mechanics **629**, 139 (2009) doi:10.1017/S0022112009006399.
[24]L. Trefethen, A. Trefethen, S. Reddy, and T. Driscoll, "Hydrodynamic stability without eigenvalues," Science **261**, 578–584 (1993) doi:10.1126/science.261.5121.578.
[25]P. Schmid, "Nonmodal stability theory," Annual Review of Fluid Mechanics **39**, 129–162 (2007) doi: 10.1146/annurev.fluid.38.050304.092139.
[26]E. Akervik, U. Ehrenstein, F. Gallaire, and D. Henningson, "Global two-dimensional stability measures of the flat plate boundary-layer flow," European Journal of Mechanics - B/Fluids **27**, 501–513 (2008) doi:10.1016/j.euromechflu.2007.09.004.
[27]B. Farrell and A. Moore, "An adjoint method for obtaining the most rapidly growing perturbation to oceanic flows," Journal of Physical Oceanography **22**, 338–349 (1992) doi:10.1175/1520-0485(1992)022¡0338:AAMFOT¿2.0.CO.
[28]K. Butler and B. Farrell, "Three-dimensional optimal perturbations in viscous shear flow," Physics of Fluids A: Fluid Dynamics **4**, 1637 (1992) doi:10.1063/1.858386.
[29]S. Reddy and L. Trefethen, "Pseudospectra of the Convection-Diffusion operator," SIAM Journal on Applied Mathematics **54**, 1634 (1994).
[30]C. Cossu and J. Chomaz, "Global measures of local convective instabilities," Physical Review Letters **78**, 4387–4390 (1997) doi:10.1103/PhysRevLett.78.4387.
[31]P. Huerre and P. Monkewitz, "Absolute and convective instabilities in free shear layers," Journal of Fluid Mechanics **159**, 151–168 (1985) doi:10.1017/S0022112085003147.
[32]S. Reddy and D. Henningson, "Energy growth in viscous channel flows," Journal of Fluid Mechanics **252**, 209–238 (1993) doi:10.1017/S0022112093003738.
[33]E. Dick, "Introduction to finite element methods in computational fluid dynamics," in *Computational Fluid Dynamics*, edited by J. Wendt (Springer Berlin Heidelberg, 2009) pp. 235–274 doi:10.1007/978-3-540-85056-4˙10.
[34]T. Matsushima and P. Marcus, "A spectral method for polar coordinates," Journal of Computational Physics **120**, 365–374 (1995) doi:10.1006/jcph.1995.1171.
[35]C. Bogey and C. Bailly, "Three-dimensional non-reflective boundary conditions for acoustic simulations: far field formulation and validation test cases," Acta Acustica **88**, 463–471 (2002).
[36]P. Monkewitz and K. Sohn, "Absolute instability in hot jets," AIAA Journal **26**, 911–916 (1988) doi: 10.2514/3.9990.
[37]X. Garnaud, L. Lesshafft, and P. Huerre, "Global linear stability of a model subsonic jet," AIAA paper 2011-3608 (2011).
[38]W. Reynolds and A. Hussain, "The mechanics of an organized wave in turbulent shear flow. part 3. theoretical models and comparisons with experiments," Journal of Fluid Mechanics **54**, 263 (1972) doi: 10.1017/S0022112072000679.
[39]V. Kitsios, L. Cordier, J. Bonnet, A. Ooi, and J. Soria, "Development of a nonlinear eddy-viscosity closure for the triple-decomposition stability analysis of a turbulent channel," Journal of Fluid Mechanics **664**, 74–107 (2010) doi:10.1017/S0022112010003617 .
[40]J. Crouch, A. Garbaruk, and D. Magidov, "Predicting the onset of flow unsteadiness based on global instability," Journal of Computational Physics **224**, 924–940 (2007) doi:10.1016/j.jcp.2006.10.035.
[41]D. Crighton and M. Gaster, "Stability of slowly diverging jet flow," Journal of Fluid Mechanics **77**, 397 (1976) doi:10.1017/S0022112076002176.
[42]K. Gudmundsson and T. Colonius, "Instability wave models for the near-field fluctuations of turbulent jets," Journal of Fluid Mechanics **689**, 97–128 (2011) doi:10.1017/jfm.2011.401.
[43]F. Hecht, "Freefem++ manual, third edition, version 3.16-1," Tech. Rep. (2011) université Pierre et Marie Curie, Paris, France.
[44]P. Amestoy, I. Duff, and J. L'Excellent, "Multifrontal parallel distributed symmetric and unsymmetric solvers," Computational Methods in Applied Mathematics **184**, 501–520 (2000).
[45]S. Balay, K. Buschelman, V. Eijkhout, W. Gropp, D. Kaushik, M. Knepley, L. C. McInnes, B. Smith, and H. Zhang, "PETSc users manual," Tech. Rep. ANL-95/11 - Revision 3.0.0 (Argonne National Laboratory, 2008) mathematics and Computer Science Division, Argonne National Laboratory, USA.
[46]V. Hernandez, J. Roman, and V. Vidal, "SLEPc: a scalable and flexible toolkit for the solution of eigenvalue problems," ACM Transactions on Mathematical Software **31**, 351362 (2005).
[47]R. Lehoucq, D. Sorensen, and C. Yang, *ARPACK Users' Guide: Solution of Large-Scale Eigenvalue Problems with Implicitly Restarted Arnoldi Methods* (SIAM, 1998).
[48]C. Bogey and C. Bailly, "A family of low dispersive and low dissipative explicit schemes for flow and noise computations," Journal of Computational Physics **194**, 194–214 (2004) doi:10.1016/j.jcp.2003.09.003.
[49]C. Mack and P. Schmid, "A preconditioned krylov technique for global hydrodynamic stability analysis of large-scale compressible flows," Journal of Computational Physics **229**, 541–560 (2010) doi: 10.1016/j.jcp.2009.09.019.
[50]X. Garnaud, L. Lesshafft, P. Schmid, and J. Chomaz, "A relaxation method for large eigenvalue problems, with an application to flow stability analysis," Journal of Computational Physics (2012) doi: 10.1016/j.jcp.2012.01.038, .

[51]M. Fosas de Pando, D. Sipp, and P. Schmid, "Efficient evaluation of the direct and adjoint linearized dynamics from compressible flow solvers," Journal of Computational Physics **231**, 7739–7755 (2012) doi: 10.1016/j.jcp.2012.06.038.
[52]A. Hanifi, P. Schmid, and D. Henningson, "Transient growth in compressible boundary layer flow," Physics of Fluids **8**, 826–837 (1996) doi:10.1063/1.868864.
[53]A. Michalke, "Survey on jet instability theory," Progress in Aerospace Science **21**, 159–199 (1984) doi: 10.1016/0376-0421(84)90005-8.
[54]M. Landahl, "A note on an algebraic instability of inviscid parallel shear flows," Journal of Fluid Mechanics **98**, 243 (1980) doi:10.1017/S0022112080000122.
[55]D. Jones and J. Morgan, "The instability of a vortex sheet on a subsonic stream under acoustic radiation," Mathematical Proceedings of the Cambridge Philosophical Society **72**, 465 (1972) doi: 10.1017/S0305004100047320.
[56]D. Crighton and F. Leppington, "Radiation properties of the semi-infinite vortex sheet: the initial-value problem," Journal of Fluid Mechanics **64**, 393 (1974) doi:10.1017/S0022112074002461.
[57]M. Barone and S. Lele, "Receptivity of the compressible mixing layer," Journal of Fluid Mechanics **540**, 301–335 (2005) doi:10.1017/S0022112005005884.
[58]L. Lesshafft, P. Huerre, and P. Sagaut, "Aerodynamic sound generation by global modes in hot jets," Journal of Fluid Mechanics **647**, 473–489 (2010) doi:10.1017/S0022112009993612.
[59]P. Schmid and D. Henningson, *Stability and Transition in Shear Flows* (Springer, New York, 2001) doi: 10.1115/1.1470687.
[60]I. Orlanski, "A simple boundary condition for unbounded hyperbolic flows," Journal of Computational Physics **21**, 251–269 (1976) doi:10.1016/0021-9991(76)90023-1.
[61]W. Criminale, T. Jackson, and R. Joslin, *Theory and computation of hydrodynamic stability* (Cambridge University Press, Cambridge, UK, 2003) doi:10.1017/CBO9780511550317.
[62]For $m = 0$ the linearized Navier–Stokes operator is real, so only eigenvalues with $\omega_r \geq 0$ need to be considered.

The preferred mode of incompressible jets: linear frequency response analysis

X. GARNAUD, L. LESSHAFFT, P.J. SCHMID AND P. HUERRE

Laboratoire d'Hydrodynamique (LadHyX), Ecole Polytechnique – CNRS, 91128 Palaiseau, France

(Received 23 November 2012)

The linear amplification of axisymmetric external forcing in incompressible jet flows is investigated within a fully non-parallel framework. Experimental and numerical studies have shown that isothermal jets preferably amplify external perturbations for Strouhal numbers in the range $0.25 \leq St_D \leq 0.5$, depending on the operating conditions. In the present study, the optimal forcing of an incompressible jet is computed as a function of the excitation frequency. This analysis characterizes the preferred amplification as a pseudo-resonance with a dominant Strouhal number of around 0.45. The flow response at this frequency takes the form of a vortical wavepacket that peaks inside the potential core. Its global structure is characterized by the cooperation of local shear-layer and jet-column modes.

1. Introduction

Large-scale coherent structures develop in the shear-layers of isothermal jet flows, for both laminar and turbulent regimes. These structures are not self-sustained, but are the consequence of strong amplification of incoming disturbances. Crow & Champagne (1971) performed experiments where the flow was forced with a controlled frequency; they showed that optimal excitation is achieved for a Strouhal number based on the jet diameter of about 0.3. The corresponding flow perturbations, referred to as the jet *preferred mode*, grow in amplitude starting at the nozzle until they undergo non-linear saturation.

A local analysis of jets (Michalke 1984) identifies shear-layer perturbations immediately downstream of the nozzle as the fastest growing instability modes, which would indicate that the preferred frequency scales with the initial shear-layer thickness. This also suggests that the mechanisms underlying the selection of the preferred frequency depend on the downstream flow development. Under the assumption of a slowly diverging base flow, Crighton & Gaster (1976) used a WKBJ approximation to describe the spatial development of the instability wave. Their results are in reasonable agreement with the experimental results of Crow & Champagne (1971) for the initial growth of the structures. This approach has subsequently been generalized through the use of the parabolized stability equations (Ray *et al.* 2009; Gudmundsson & Colonius 2011; Rodriguez *et al.* 2011). While this approach also relies on the assumption of a slow variation of the base flow in the streamwise direction, these results were found to yield good agreement with experiments of natural turbulent jets.

The optimal disturbance of flows subjected to time-harmonic linear perturbations has been described by Trefethen *et al.* (1993). This method was first applied to general non-parallel configurations using a projection of the flow dynamics onto a reduced space spanned by a set of eigenmodes (Alizard *et al.* 2009; Nichols & Lele 2010). In other studies

(Monokrousos *et al.* 2010; Marquet & Sipp 2010; Nichols & Lele 2011*b*; Sipp & Marquet 2012) the resolvent norm has been computed directly from the linearized Navier–Stokes operator, such that the entire non-normal flow behavior captured by the discretization is taken into account in the results. This approach is followed here to provide a better understanding of the preferred frequency selection and the associated spatial structures; in particular, the non-parallel nature of the flow, as well as the effects of a solid circular jet-pipe, are taken into account. The present analysis is mainly restricted to axisymmetric forcing and perturbations. Results for helical forcing are only briefly discussed.

After a description of the flow under consideration in § 2, two different models of the external forcing are described in § 4, together with the numerical method used. The results, presented in § 5, are then discussed and compared to classical local stability analysis.

2. Flow configuration

2.1. *Geometry*

A cylindrical jet of an incompressible Newtonian fluid of viscosity ν^*, with radius R^* and exit centerline velocity U_0^* is considered. The latter two quantities are used to make lengths and velocities non-dimensional. Frequencies f^* can be non-dimensionalized to yield either a circular frequency ω or a Strouhal number St based on the jet diameter. These parameters are related via $St = \omega/\pi$. Throughout the study, the Reynolds number is taken to be

$$Re = \frac{U_0^* R^*}{\nu^*} = 10^3.$$

The flow geometry, described in terms of the cylindrical coordinates r, θ and x, is represented in figure 1. The boundary of the computational domain Ω is decomposed into Γ_i, Γ_w,Γ_o and Γ_a respectively corresponding to the inlet, a solid wall, the outlet and the jet axis. No-slip boundary conditions are imposed on Γ_w, and stress-free boundary conditions are used on Γ_o (Dick 2009). Compatibility conditions, ensuring the smoothness of the computed fields are imposed on the axis $r = 0$ (Matsushima & Marcus 1995). At the inflow, homogeneous or inhomogeneous Dirichlet boundary conditions are imposed on the velocity as requested by the problem under consideration.

Two unstructured meshes with identical dimensions but different resolution are used for the finite element computations. The density of vertices in the domain is controlled by the distance between discretization points on the boundary of the computational domain as well as on interior boundaries (dashed lines in figure 1). This distance is denoted by h_4 for boundaries in the far field ($r > r_3^+$). It is smaller than h_3 for $r \leq r_3^+$, and respectively smaller than h_2 and h_1 in the inner regions defined by $x \leq x_2^+$ and $1-\delta_2/2 \leq r \leq 1+\delta_2/2$ and by $x_1^- \leq x \leq x_1^+$ and $1 - \delta_1/2 \leq r \leq 1 + \delta_1/2$. These subdomains are indicated by gray shaded areas in figure 1. The values of the h_i for both meshes are given in figure 1.

2.2. *Base state*

Linear stability analysis formally applies to base states that are steady solutions of the governing equations. However, several studies have found that linearization around a time-averaged mean flow yields better predictions of the nonlinear flow behaviour, in particular with regard to the frequency selection of intrinsic oscillations (Pier 2002; Barkley 2006). The present study employs the mean-flow model proposed by Monkewitz & Sohn (1988) for a turbulent free jet, displayed in figure 2. This model consists of a potential core, starting from a momentum thickness $\theta = 0.043$, and extending over eight radii

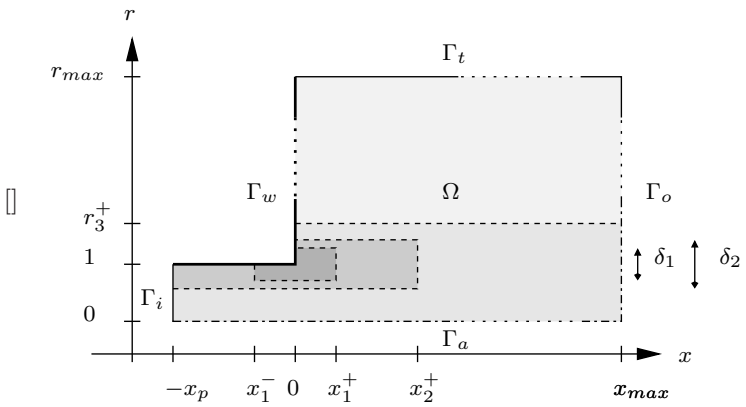

Mesh	#1	#2
h_1	0.035	0.01
h_2	0.035	0.035
h_3	0.07	0.05
h_4	0.2	0.2

FIGURE 1. Schematic representation of the numerical domain. The pipe length is set to $x_p = 5$, and it has been verified that setting $r_{max} = 10$ does not influence the results. Gray shaded areas correspond to subregions in which different grid resolutions are selected. Values of $x_1^- = -2$, $x_1^+ = 1$, $\delta_1 = 0.15$, $x_2^+ = 10$, $\delta_2 = 0.5$ and $r_3^+ = 2$ are used.

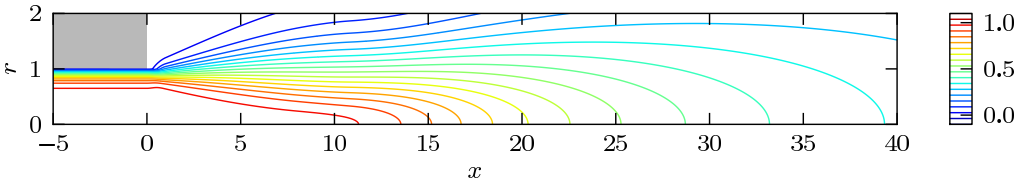

FIGURE 2. Axial velocity field for the model turbulent mean flow of Monkewitz & Sohn (1988).

downstream of the end of the jet pipe, followed by a self-similar region where the velocity profiles have an approximately Gaussian shape. A parallel pipe flow region has been added upstream, and a smooth transition is made for $0 \leq x \leq 1$, as described in Garnaud *et al.* (2011).

In the following, infinitesimal perturbations around the steady mean flow are considered, such that the flow field can be written as $(\boldsymbol{u}, p) = (\boldsymbol{U} + \epsilon \boldsymbol{u}', P + \epsilon p')$, where $(\boldsymbol{U}, P)$ denotes the base state displayed in figure 2.

3. Modal analyis

Monkewitz (1989) and Huerre & Monkewitz (1990) conjectured that the preferred mode observed in experiments corresponds to the resonance of the least stable eigenmode of the jet with incoming disturbances. This issue has been investigated by Cooper & Crighton (2000) by means of a WKBJ approximation. Upon making the assumptions that (i) the global mode has the shape of a local shear-layer mode at each location, and that (ii) the base flow development is slow, the authors found a weakly stable global mode at a Strouhal number of 0.44 which agrees well with experimental observations. In order to avoid such strong assumptions, eigenmodes can now be computed using the axisymmetric Navier–Stokes equations discretized on a two-dimensional domain. Such a modal analysis has for example been performed by Nichols & Lele (2011*a*) in the context of supersonic jets. This approach is followed in this section. Figure 3 displays the

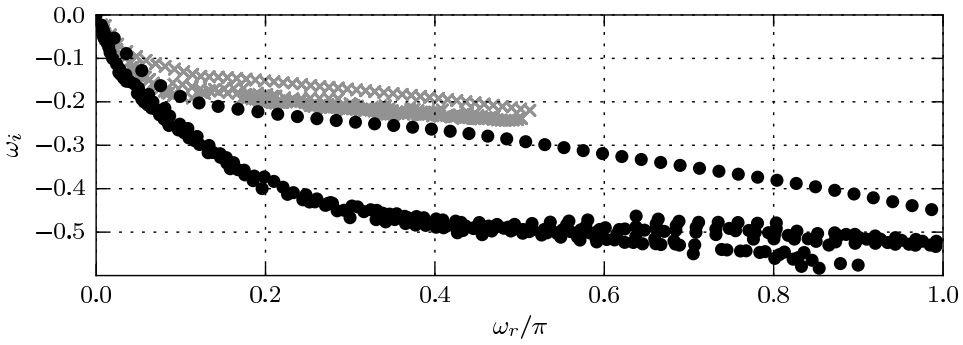

FIGURE 3. Eigenvalue spectra of the linearized Navier–Stokes equations ($L\boldsymbol{q} = \mathrm{i}\omega B\boldsymbol{q}$) computed for a domain of length $x_{max} = 40$ (black dots) and $x_{max} = 60$ (gray crosses).

spectrum obtained for the global eigenvalue problem

$$\begin{aligned} \boldsymbol{\nabla}\cdot\boldsymbol{u}' &= 0, \\ -\mathrm{i}\omega\boldsymbol{u}' + (\boldsymbol{U}\cdot\boldsymbol{\nabla})\boldsymbol{u}' + (\boldsymbol{u}'\cdot\boldsymbol{\nabla})\boldsymbol{U} &= -\boldsymbol{\nabla}p' + \frac{1}{Re}\boldsymbol{\nabla}^2\boldsymbol{u}' + \psi(\boldsymbol{x})\boldsymbol{f}', \end{aligned} \tag{3.1}$$

with homogeneous Dirichlet boundary conditions on $\Gamma_i \cup \Gamma_w$. All eigenmodes are stable, and three families of modes can be identified. First, low-frequency free-stream modes (eigenvalues close to the origin) correspond to standing vortical structures. These decay very slowly due to viscous effects. Second, a branch of shear-layer / jet-column modes is observed (upper branch in figure 3). Along this branch the decay rate $-\omega_i$ increases with frequency ω_r, and the spatial structure of the eigenmodes is characterized by an exponential growth throughout the computational domain. This growth can be understood as a consequence of the stable advection of nearly neutral shear-layer structures. Finally, the lower branch of eigenmodes in figure 3 corresponds in fact to pseudomodes that lie on the 10^{-10} contour of the pseudospectrum. Note that the actual spectrum is quite dependent on the size of the numerical domain, but that qualitative features are not. For more details, see Garnaud (2012).

The spectrum of the linearized Navier–Stokes equations therefore exhibits no isolated or least stable eigenmode that could explain the preferred mode through a resonance mechanism. In the next section, a pseudo-resonance analysis is carried out to investigate the origin of the preferred mode.

4. Response to harmonic forcing

4.1. *External forcing as a body force*

Following Monokrousos *et al.* (2010), Marquet & Sipp (2010) and Sipp & Marquet (2012), the external forcing can be modeled as a body force $\boldsymbol{f}(\boldsymbol{x}, t)$ acting on the momentum equation,

$$\frac{\partial\boldsymbol{u}}{\partial t} + (\boldsymbol{u}\cdot\boldsymbol{\nabla})\boldsymbol{u} = -\boldsymbol{\nabla}p + \frac{1}{Re}\boldsymbol{\nabla}^2\boldsymbol{u} + \psi(\boldsymbol{x})\boldsymbol{f},$$

while $\boldsymbol{\nabla}\cdot\boldsymbol{u} = 0$ is maintained throughout the flow. The weight function ψ is used to restrict the flow region where forcing is applied, and the forcing amplitude is assumed to be small: $\boldsymbol{f} = \epsilon\boldsymbol{f}'$. To leading order, the dynamics of perturbations are governed by the

linear system

$$\begin{aligned} \boldsymbol{\nabla}\cdot\boldsymbol{u}' &= 0, \\ \frac{\partial \boldsymbol{u}'}{\partial t} + (\boldsymbol{U}\cdot\boldsymbol{\nabla})\boldsymbol{u}' + (\boldsymbol{u}'\cdot\boldsymbol{\nabla})\boldsymbol{U} &= -\boldsymbol{\nabla}p' + \frac{1}{Re}\boldsymbol{\nabla}^2\boldsymbol{u}' + \psi(\boldsymbol{x})\boldsymbol{f}', \\ \boldsymbol{u}' &= 0, \qquad\qquad \Gamma_i \cup \Gamma_w \\ \frac{1}{Re}\frac{\partial \boldsymbol{u}'}{\partial n} - p'\boldsymbol{n} &= 0. \qquad\qquad \Gamma_t \cup \Gamma_o \end{aligned} \tag{4.1}$$

In a linear framework, all signals are decomposed in time into independent Fourier components. The forcing is therefore considered to be time-harmonic, $\boldsymbol{f}' = \widetilde{\boldsymbol{f}}\exp(-\mathrm{i}\omega t)$, prompting an asymptotic flow response $(\boldsymbol{u}', p') = (\widetilde{\boldsymbol{u}}, \widetilde{p})\exp(-\mathrm{i}\omega t)$ at the same frequency. The amplification of the externally applied forcing at a given frequency ω is measured in terms of the gain

$$G^{bf}_{opt}(\omega) = \max_{\widetilde{\boldsymbol{f}}} \left(\int_\Omega |\widetilde{\boldsymbol{u}}|^2 r\,\mathrm{d}r\,\mathrm{d}x\right) \Big/ \left(\int_\Omega |\widetilde{\boldsymbol{f}}|^2 r\,\mathrm{d}r\,\mathrm{d}x\right). \tag{4.2}$$

The optimal forcing $\widetilde{\boldsymbol{f}}_{opt}(\omega)$ realizes this maximum. For the results presented in §5.1, the forcing is assumed to be localized inside the pipe only, i.e. the weight function is defined as $\psi(\boldsymbol{x}) = 1$ for $x < 0$ and $\psi(\boldsymbol{x}) = 0$ for $x \geq 0$.

4.2. *External forcing as an inflow condition*

Rather than forcing the jet through a distributed body force in the pipe interior as in the previous section, one may model incoming perturbations in the form of an unsteady upstream boundary condition of the linearized Navier–Stokes equations:

$$\begin{aligned} \boldsymbol{\nabla}\cdot\boldsymbol{u}' &= 0, \\ \frac{\partial \boldsymbol{u}'}{\partial t} + (\boldsymbol{U}\cdot\boldsymbol{\nabla})\boldsymbol{u}' + (\boldsymbol{u}'\cdot\boldsymbol{\nabla})\boldsymbol{U} &= -\boldsymbol{\nabla}p' + \frac{1}{Re}\boldsymbol{\nabla}^2\boldsymbol{u}', \\ \boldsymbol{u}' &= 0, \qquad\qquad \Gamma_w \\ \frac{1}{Re}\frac{\partial \boldsymbol{u}'}{\partial n} - p'\boldsymbol{n} &= 0, \qquad\qquad \Gamma_t \cup \Gamma_o \\ \boldsymbol{u}' &= \boldsymbol{f}'. \qquad\qquad \Gamma_i \end{aligned} \tag{4.3}$$

Such a model corresponds more closely to the assumptions of local spatial stability, WKBJ and PSE approximations. In this case, the gain between a harmonic inflow forcing and the corresponding response is measured as

$$G^{bc}_{opt}(\omega) = \max_{\widetilde{\boldsymbol{f}}} \left(\int_\Omega |\widetilde{\boldsymbol{u}}|^2 r\,\mathrm{d}r\,\mathrm{d}x\right) \Big/ \left(\int_{\Gamma_i} |\widetilde{\boldsymbol{f}}|^2 r\,\mathrm{d}r\right). \tag{4.4}$$

4.3. *Numerical solution of the optimization problem*

The linear systems (4.1) and (4.3) are discretized by $P2$-$P1$ finite element using the software FreeFEM++ (Hecht 2011). Let $\boldsymbol{q}$ be the discrete state vector containing all degrees of freedom related to velocity and pressure fields. Both (4.1) and (4.3) can then be written in their semi-discretized form as

$$B\dot{\boldsymbol{q}} = L\boldsymbol{q} + B_f\boldsymbol{f}, \tag{4.5}$$

where $\boldsymbol{f}$ is the discrete forcing vector and L, B and B_f are sparse matrices resulting from the finite elements discretization of the linearized Navier–Stokes equations. Let

$\boldsymbol{f} = \widetilde{\boldsymbol{f}}\exp(-\mathrm{i}\omega t)$ and $\boldsymbol{q} = \widetilde{\boldsymbol{q}}\exp(-\mathrm{i}\omega t)$ be time-harmonic such that

$$-(L + \mathrm{i}\omega B)\widetilde{\boldsymbol{q}} = B_f \widetilde{\boldsymbol{f}}. \tag{4.6}$$

Perturbation amplitudes are measured in a pseudonorm $\|\boldsymbol{q}\|^2 = \boldsymbol{q}^\dagger Q \boldsymbol{q}$ that represents the discretization of the perturbation kinetic energy:

$$\|(\boldsymbol{u}', p')\|^2 = \int_\Omega |\boldsymbol{u}'|^2 r \,\mathrm{d}r \,\mathrm{d}x. \tag{4.7}$$

The norm of the forcing vector $\boldsymbol{f}$, which appears in the denominator of (4.2) and (4.4), is expressed accordingly in discrete form as $\|\boldsymbol{f}\|_f^2 = \boldsymbol{f}^\dagger Q_f \boldsymbol{f}$. Note that $\boldsymbol{f}$ does not contain pressure components, and that Q_f therefore is symmetric positive-definite, in contrast to Q, which is positive semi-definite. The discrete optimal forcing problem can be written as

$$G_{opt}^2(\omega) = \max \frac{\|\widetilde{\boldsymbol{q}}\|^2}{\|\widetilde{\boldsymbol{f}}\|_f^2}. \tag{4.8}$$

Monokrousos *et al.* (2010) formalized a similar optimal forcing problem by use of a constrained optimization approach involving Lagrange multipliers. For linear time-harmonic problems, a more concise formalism is possible. The formulation used here, similar to that of Sipp & Marquet (2012), is briefly outlined below. Substituting (4.6) into (4.8) gives

$$\begin{aligned} G_{opt}(\omega)^2 &= \max_{\widetilde{\boldsymbol{f}}} \frac{\|(L + \mathrm{i}\omega B)^{-1} B_f \widetilde{\boldsymbol{f}}\|^2}{\|\widetilde{\boldsymbol{f}}\|_f^2}, \\ &= \max_{\widetilde{\boldsymbol{f}}} \frac{\widetilde{\boldsymbol{f}}^\dagger B_f^\dagger {(L + \mathrm{i}\omega B)^{-1}}^\dagger Q^\dagger (L + \mathrm{i}\omega B)^{-1} B_f \widetilde{\boldsymbol{f}}}{\widetilde{\boldsymbol{f}}^\dagger Q_f \widetilde{\boldsymbol{f}}}. \end{aligned}$$

Let $M_f^\dagger M_f$ be the Cholesky decomposition of Q_f, and let $\widetilde{\boldsymbol{g}} = M_f \widetilde{\boldsymbol{f}}$, i.e. $\widetilde{\boldsymbol{f}} = M_f^{-1}\widetilde{\boldsymbol{g}}$. The optimal gain can then be rewritten as

$$G_{opt}(\omega)^2 = \max_{\widetilde{\boldsymbol{g}}} \frac{\widetilde{\boldsymbol{g}} {M_f^{-1}}^\dagger B_f^\dagger {(L + \mathrm{i}\omega B)^{-1}}^\dagger Q^\dagger (L + \mathrm{i}\omega B)^{-1} B_f M_f^{-1} \widetilde{\boldsymbol{g}}}{\widetilde{\boldsymbol{g}}^\dagger \widetilde{\boldsymbol{g}}}.$$

The right-hand side of the above expression is a Rayleigh quotient, and $G_{opt}(\omega)$ is therefore the leading eigenvalue of the associated Hermitian eigenvalue problem

$${M_f^{-1}}^\dagger B_f^\dagger {(L + \mathrm{i}\omega B)^{-1}}^\dagger Q^\dagger (L + \mathrm{i}\omega B)^{-1} B_f M_f^{-1} \widetilde{\boldsymbol{g}} = \lambda \widetilde{\boldsymbol{g}},$$

which can be re-written in terms of the forcing $\widetilde{\boldsymbol{f}}$ as

$$Q_f^{-1} B_f^\dagger {(L + \mathrm{i}\omega B)^{-1}}^\dagger Q^\dagger (L + \mathrm{i}\omega B)^{-1} B_f \widetilde{\boldsymbol{f}} = \lambda \widetilde{\boldsymbol{f}}. \tag{4.9}$$

The leading eigenvalue of (4.9) and its associated eigenvector, which respectively correspond to the optimal gain and optimal forcing, are computed by using the Lanczos solver implemented in SLEPc (Hernandez *et al.* 2005). The operator $(L + \mathrm{i}\omega B)^{-1}$ and its adjoint are applied by using the sparse linear algebra package MUMPS through its PETSc interface (Balay *et al.* 2008). Finally, the operator Q_f^{-1} is applied by using a Cholesky decomposition, if memory requirements permit, or otherwise by using an ILU-preconditioned conjugate gradient method.

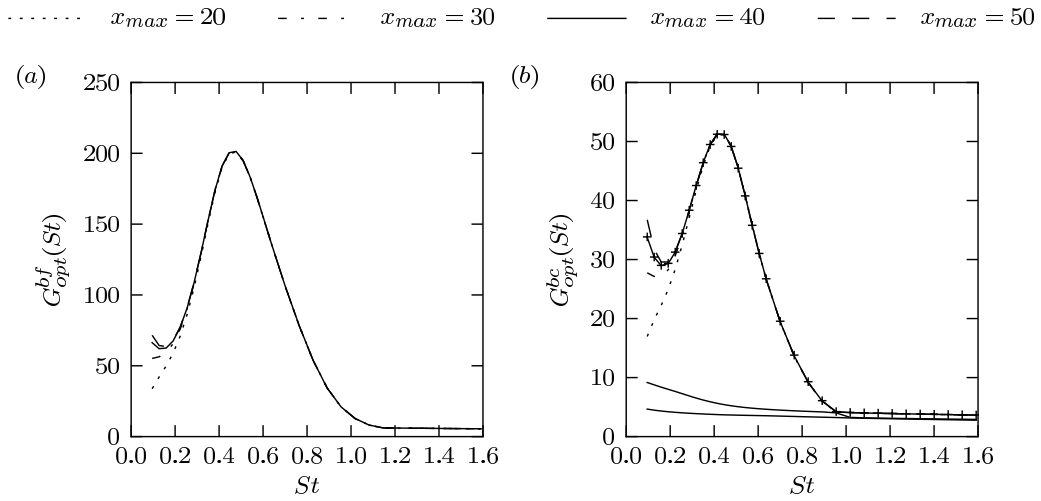

FIGURE 4. Optimal gain as a function of the Strouhal number for body (a) and boundary (b) forcing. The gains are computed for various domain lengths x_{max}. + symbols displayed in (b) correspond to gains computed for a finer mesh (mesh #2 in figure 1), showing convergence with respect to grid resolution. For boundary forcing on a domain of length $x_{max} = 40$, not only is the most amplified mode displayed but the three leading eigenvalues of (4.9) as well.

5. Results

5.1. *Optimal body forcing*

Optimal harmonic forcing by means of a distributed body force inside the jet pipe, as outlined in § 4.1, is computed first. The gain (4.2) is displayed in figure 4(a) as a function of the Strouhal number. Different line styles represent results obtained for various lengths of the computational domain, in order to assess the influence of domain truncation. Figure 5 displays the spatial distributions of axial velocity of forcing and flow response at selected Strouhal numbers, for a domain length $x_{max} = 40$. It is found from figure 4(a) that domain truncation only affects the gains at very low Strouhal numbers. The flow response structure in this regime extends far downstream, as can be seen in figure 5(a), and the truncation at the outflow therefore leads to a lower measure of the flow response norm. Neither the forcing distribution nor the captured part of the flow response appear to be significantly influenced by the downstream truncation. Similarly, it has been verified that a radial truncation at $r = 10$ has a negligible impact on the results.

The largest gain is observed at $St = 0.46$. The perturbations in the free jet exhibit a strong spatial growth in the shear-layer just downstream of the nozzle exit; their amplitude peaks near the end of the potential core at $r = 8$ (figure 5(b)). In the adjacent decaying part of the wavepacket, the radial amplitude distribution changes markedly, with its maximum now at the centreline. The wavepacket structure at higher frequencies displays similar characteristics, but the region of spatial growth is confined to an ever smaller distance from the nozzle.

The optimal distribution of the body force inside the pipe also exhibits consistent characteristics at all Strouhal numbers presented in figure 5. The amplitude is largest within the boundary layer at the pipe wall, and it is increasingly concentrated near the wall at higher Strouhal numbers. At the same time, the downstream spatial growth of the response increases with the Strouhal number, and its wavelength shortens. In all cases,

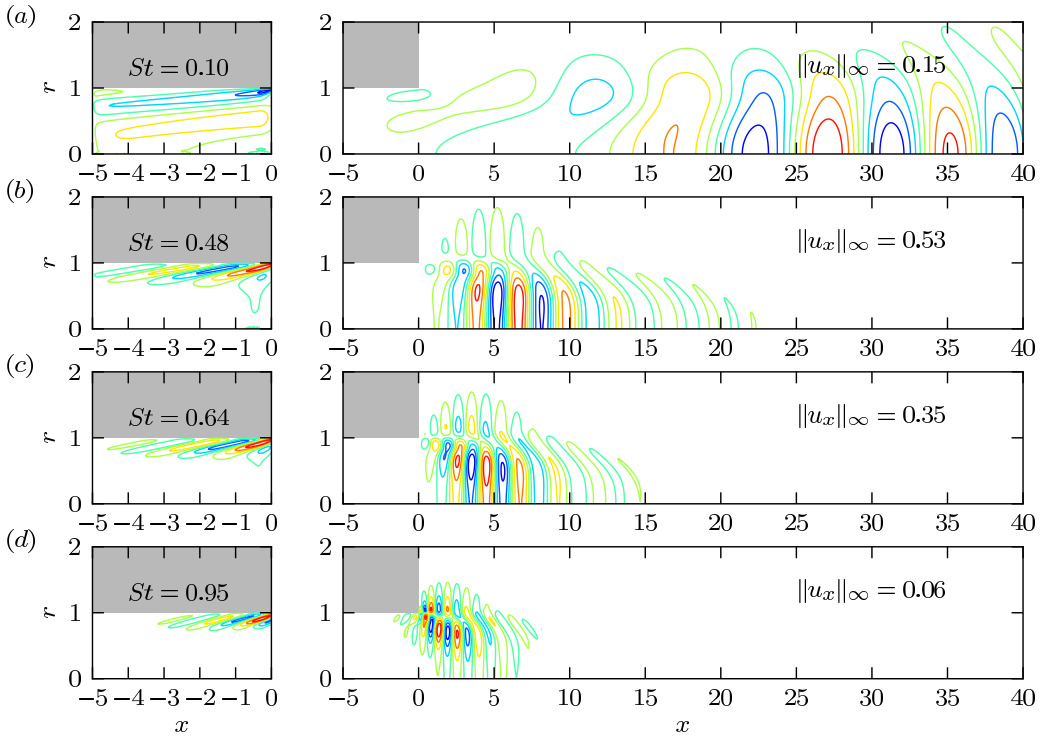

FIGURE 5. Spatial structures associated with the optimal body forcing at different Strouhal numbers, indicated in the figures. In the left column, the real parts of the axial component of the forcing is displayed. On the right, the figures show the axial component of the response velocity (real part). Computations were performed for $x_{max} = 40$.

the forcing structures are tilted upstream away from the wall, suggesting that the Orr mechanism contributes to the perturbation gain as in the case of boundary layer flow (Sipp & Marquet 2012).

Use of the L^2 norm as a measure of the amplification gain inevitably implies that spatially extended structures are given more weight than spatially localized structures, even though the latter may represent modes with high spatial amplification. This effect is undoubtedly responsible for the slight increase of G^{bf}_{opt} at very low Strouhal numbers. The infinity norm would provide a sensible and intuitive measure for the amplification of perturbations; unfortunately, this norm does not lend itself to the formulation of the optimization problem. It can however be determined *a posteriori* for the results obtained with the present approach. Values are given in figure 5 for the four cases represented. It is indeed found that the infinity norm follows the same trends as the gain defined by the L^2 norm, except for the increase at very low Strouhal numbers.

Figure 6(a) displays the maximum amplification curves obtained when the length of pipe included in the computational domain is increased from 5 to 10. It shows that this parameter affects the values of the gain but that the shape of the curve remains the same. In particular the optimal Strouhal number does not change, which confirms the relevance of the choice of geometric parameters used in this study. A more critical parameter in this analysis is the Reynolds number, as a model turbulent mean flow is used as a base state for the stability analysis so the choice is rather arbitrary: figure 6(b) indicates that the

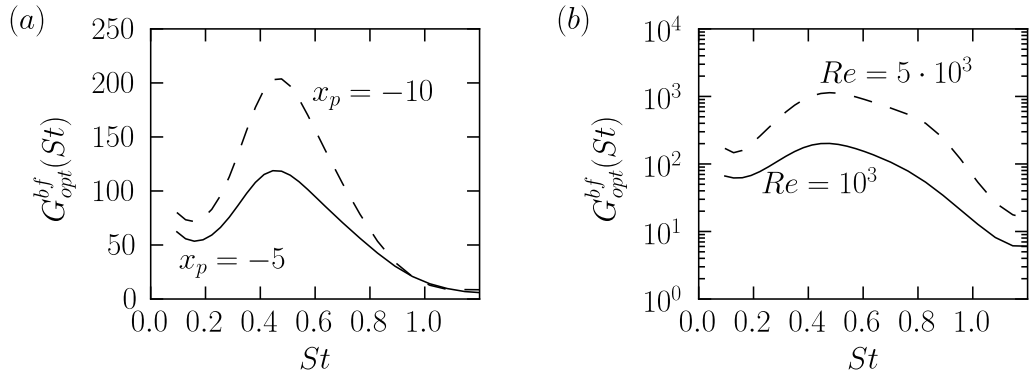

FIGURE 6. Optimal gains obtained for boundary forcing when (a) the length of pipe under included in the computational domain increases from 5 to 10, and (b) the Reynolds number increases from 10^3 to $5 \cdot 10^3$.

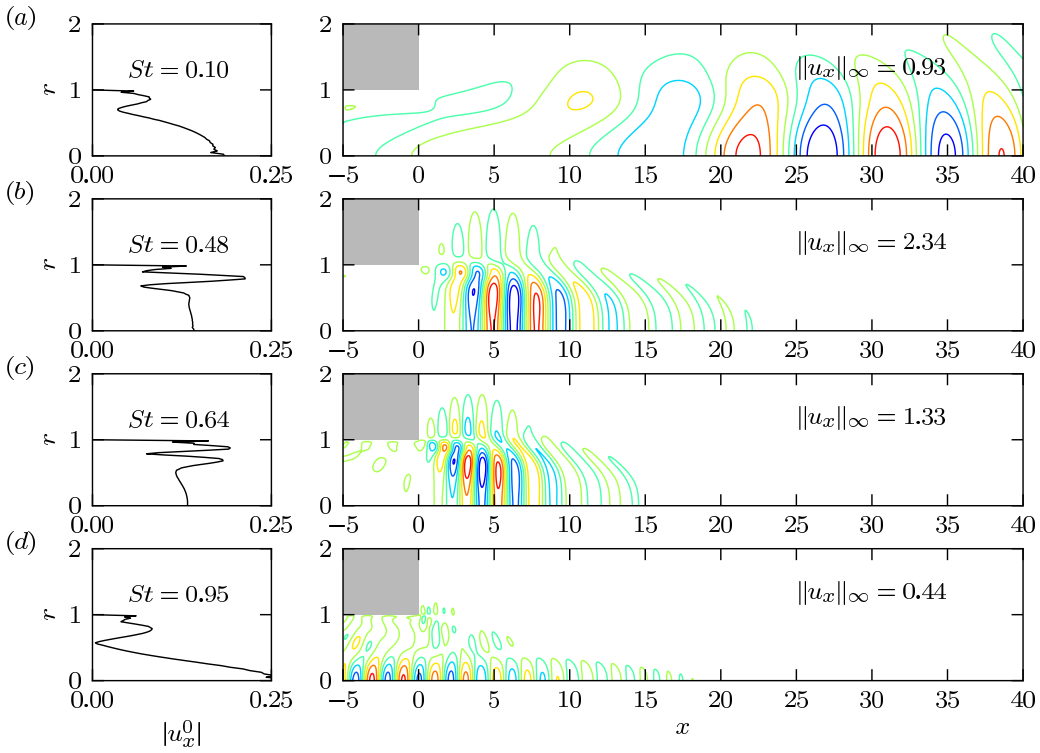

FIGURE 7. Spatial structures associated with the optimal boundary forcing at different Strouhal number, indicated in the figures. In the left column, the modulus of the inflow axial velocity component is displayed. On the right, the axial component of the response velocity is displayed (real part). Computations were performed for $x_{max} = 40$.

optimal excitation frequency remains the same when the Reynolds number is increased from 10^3 to $5 \cdot 10^3$.

5.2. *Optimal boundary forcing*

The perturbation gain obtained from the problem formulation based on forcing at the inflow boundary, as given in § 4.2, is presented in figure 4(b). The trends are very similar to those observed in the case of a distributed body force. The strongest amplification occurs at $St = 0.43$. Domain truncation has no influence, except at very low Strouhal numbers, and the results are converged with respect to mesh resolution. The radial distribution of the optimal forcing input is displayed in figure 7, alongside the flow response at the same four values of St as in the preceding section. The flow response wavepackets are indeed nearly identical to those of figure 5, except for the highest Strouhal number shown. The forcing distributions display some unexpected features. At low St, the amplitude maximum is located on the centreline, whereas in the intermediate frequency range the highest forcing amplitudes occur in the pipe boundary layer. The no-slip condition requires the forcing to be zero at $r = 1$, but the amplitude is expected to jump to a finite value over a distance of the order of the thickness of the Stokes boundary layer, which scales as $(\omega Re)^{-1/2}$ (Batchelor 1967). Both forcing and flow response are of a different character at the highest Strouhal number shown in figure 7. Perturbations are induced around the centreline; they experience weak growth inside the pipe and immediately decay as they enter the free jet. A closer inspection of the gain curves reveals that the high-St regime is dominated by a formerly sub-optimal branch of singular values. Two additional branches are displayed in figure 4(b). Although barely visible, one of these branches becomes dominant around $St \approx 1$. The perturbation distribution shown in figure 7(d) belongs to this distinct branch.

5.3. *Comparison with local instability results*

The structure of the response wavepackets in figures 5 and 7 is readily understood from well-known local instability characteristics of jet flows (Jendoubi & Strykowski 1994; Lesshafft 2007). Strong spatial growth takes place in the potential core region, where the shear-layer is thin compared to the instability wavelength. The perturbation amplitude of this local *shear-layer mode* is concentrated around $r = 1$. Downstream of the potential core, the shear-layer mode stabilizes, and the *jet-column mode* takes over as the least stable, spatial local eigenmode. The amplitude of the jet-column mode in the self-similar base-flow region peaks on the jet axis. The gradual streamwise transition from a shear-layer mode to a jet-column mode is visualized in figure 8 for the wavepacket shown in figure 5(b). The thick line represents the local growth rate of the wavepacket, computed as $\frac{1}{2}\partial_x(\log E)$ with $E(x)$ as the perturbation kinetic energy at each streamwise station x integrated in the radial direction. The thin solid and dashed lines trace the spatial growth rates of the local shear-layer and jet-column modes, respectively, as functions of x. The growth rate of the global wavepacket quickly adapts to that of the shear-layer mode near $x = 0$, and it follows its decrease throughout the unstable interval. Downstream of $x \approx 5$, the global wavepacket gradually adjusts to the growth rate of the jet-column mode.

Contrary to what one might initially expect, the forcing structures displayed in figures 5 and 7 bear little resemblance to the local instability modes of the parallel flow inside the pipe. In fact, the optimization algorithm aims at finding the inflow condition that optimally excites shear-layer structures such that the wave packet in the free jet is generated with a maximum amplitude. To this end, the inflow condition consists of a superposition of local instability modes in order to exploit spatial transient amplification mechanisms (Andersson *et al.* 1999).

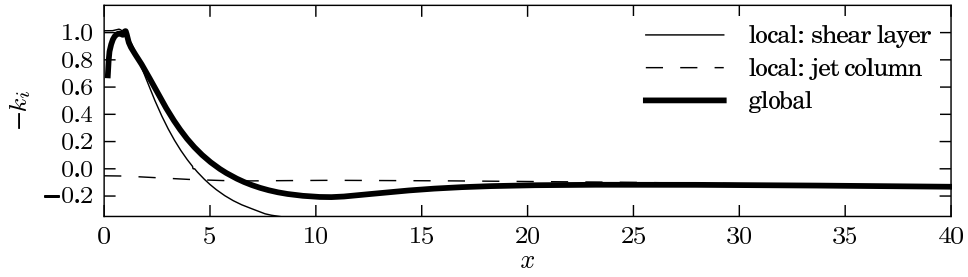

FIGURE 8. Spatial growth rate of the wavepacket envelope (thick line) corresponding to figure 5(b), compared to spatial growth rates of the local spatial shear-layer mode (thin line) and the jet-column mode (dashed line) at $St = 0.43$.

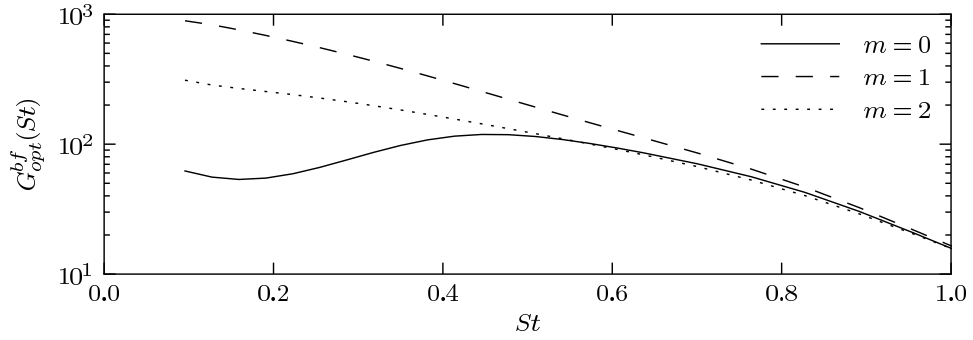

FIGURE 9. Optimal amplification of body forcing for various azimuthal wave-numbers m.

6. Conclusions

The linear dynamics of forced structures in a jet has been studied within a fully non-parallel framework, so that the effects of the base-flow spreading and of the presence of a solid jet pipe can be taken into account. Unlike approaches using the WKBJ or PSE approximations where the frequency and inflow disturbance profile are imposed to solve for the flow evolution downstream, the present method only seeks the optimal spatial distribution of time-harmonic forcing at a given frequency.

It has been demonstrated that there is no least damped global mode that can resonate in the presence of frequency forcing. The preferred frequency obtained in the present analysis is therefore due to a pseudo-resonance rather than to a resonance as conjectured by Monkewitz (1989) and Huerre & Monkewitz (1990). The analysis of Cooper & Crighton (2000) relies on a tangent approximation of the local dispersion relation so as to obtain a "global mode" with a Gaussian envelope. Such an assumption is unlikely to hold in a full WKB approach or in the global analysis followed here. For this reason, one should not expect to recover the "global modes" of Cooper & Crighton in the present analysis.

Whether external forcing is modeled as an inflow condition or a body force, the amplification of external forcing has been found to be largest for a Strouhal number around 0.45. This preferred frequency is in good agreement with experimental observation at low forcing intensity (Moore 1977; Crow & Champagne 1971). Note however that, as shown in the latter reference, the preferred frequency depends on the amplitude of excitation through non-linear effects. Around this optimal frequency, the excitation generates a

wavepacket that develops in the free-jet shear-layer. It is amplified through the potential core, where shear is important, and decays further downstream while it gets localized on the centreline. This behaviour is consistent with local stability results that show that, while shear-layer modes are spatially unstable in the potential core, the jet column mode becomes the least damped spatial eigenmode further downstream.

The shape of the optimal body forcing indicates that the Orr mechanism is at play to generate perturbations that grow in the jet pipe boundary layer and then optimally excite the free-jet wavepacket. The results are not very sensitive to the actual shape of the forcing term as similar results are obtained for body and boundary forcing. In both cases, a good agreement is found between the most amplified wavepacket and the experimentally observed preferred mode.

The framework of optimal forcing is therefore a suitable tool for the analysis of the non-modal instabilities developing in convection dominated amplifier flows.

Local spatial stability analysis indicates that helical perturbations, unlike axisymmetric ones, are spatially amplified downstream of the potential core, as shown e.g. by Batchelor & Gill (1962) and Michalke (1984). This is especially true in the low frequency range. Computations have been performed using the current framework for higher azimuthal wave numbers m. For $m \neq 0$, $G_{opt}(St)$ is a monotonically decreasing function of St, and the levels obtained at low frequencies are indeed larger for $m = 1, 2$ than for $m = 0$ (see figure 9). However this is not only due to a faster growth of the wave packet downstream of the nozzle, but also and most importantly to a spatial amplification over a longer streamwise distance, resulting in larger L^2 norms for the flow response. The growth of the wavepacket through the potential core is however similar for all values of m.

Experiments typically do not show a dominance of $m = 1$ helical modes in the self-similar region. Several reasons may explain this discrepancy between the results in figure 9 and observations, in particular the effects of turbulence and nonlinear saturation, which are not captured in the present analysis. In this light, the L^∞ norm might provide a more relevant and intuitive measure of the perturbation amplification. The use of such a formulation will be explored in future studies.

This work was supported by DGA grant number 2009.60.034.00.470.75.01 and by a fellowship from the EADS Foundation. Computational resources were provided by GENCI (Grant 2012-026451).

REFERENCES

Alizard, F., Cherubini, S. & Robinet, J.-C. 2009 Sensitivity and optimal forcing response in separated boundary layer flows. *Physics of Fluids* **21** (6), 064108.

Andersson, P., Berggren, M. & Henningson, D. S. 1999 Optimal disturbances and bypass transition in boundary layers. *Physics of Fluids* **11** (1), 134.

Balay, S., Buschelman, K., Eijkhout, V., Gropp, W. D., Kaushik, D., Knepley, M. G., McInnes, L. Curfman, Smith, B. F. & Zhang, H. 2008 PETSc users manual. *Tech. Rep.* ANL-95/11 - Revision 3.3.0. Argonne National Laboratory, available at http://www.mcs.anl.gov/petsc/petsc-as/.

Barkley, D 2006 Linear analysis of the cylinder wake mean flow. *Europhysics Letters* **75** (5), 750–756.

Batchelor, G. K. 1967 *An introduction to fluid dynamics*. Cambridge: Cambridge Univ. Press.

Batchelor, G. K. & Gill, A. E. 1962 Analysis of the stability of axisymmetric jets. *Journal of Fluid Mechanics* **14** (04), 529.

Cooper, A. J. & Crighton, D. G. 2000 Global modes and superdirective acoustic radiation in low-speed axisymmetric jets. *European Journal of Mechanics - B/Fluids* **19** (5), 559–574.

Crighton, D. G. & Gaster, M. 1976 Stability of slowly diverging jet flow. *Journal of Fluid Mechanics* **77** (02), 397.

Crow, S. C. & Champagne, F. H. 1971 Orderly structure in jet turbulence. *Journal of Fluid Mechanics* **48** (03), 547.

Dick, E. 2009 Introduction to finite element methods in computational fluid dynamics. In *Computational fluid dynamics: an introduction*, 3rd edn. Springer.

Garnaud, X. 2012 Modes, transient dynamics and forced response of circular jets. PhD thesis, Ecole Polytechnique.

Garnaud, X., Lesshafft, L. & Huerre, P 2011 Global linear stability of a model subsonic jet. *AIAA paper 2011-3608* .

Gudmundsson, K. & Colonius, T. 2011 Instability wave models for the near-field fluctuations of turbulent jets. *Journal of Fluid Mechanics* **689**, 97–128.

Hecht, F. 2011 Freefem++ manual, third edition, version 3.2. *Tech. Rep.*. Available at http://www.freefem.org/ff++.

Hernandez, V., Roman, J. E. & Vidal, V. 2005 SLEPc: a scalable and flexible toolkit for the solution of eigenvalue problems. *ACM Transactions on Mathematical Software* **31** (3), 351362.

Huerre, P. & Monkewitz, P. A. 1990 Local and global instabilities in spatially developing flows. *Annual Review of Fluid Mechanics* **22**, 473–537.

Jendoubi, S. & Strykowski, P. J. 1994 Absolute and convective instability of axisymmetric jets with external flow. *Physics of Fluids* **6** (9), 3000.

Lesshafft, L. 2007 Global modes and aerodynamic sound radiation in self-excited hot jets. PhD thesis, Ecole Polytechnique.

Marquet, Olivier & Sipp, Denis 2010 Global sustained perturbations in a backward-facing step flow. In *Seventh IUTAM Symposium on Laminar-Turbulent Transition* (ed. Philipp Schlatter & Dan S. Henningson), *IUTAM Bookseries*, vol. 18, pp. 525–528. Springer Netherlands.

Matsushima, T. & Marcus, P. S. 1995 A spectral method for polar coordinates. *Journal of Computational Physics* **120**, 365–374.

Michalke, A. 1984 Survey on jet instability theory. *Progress in Aerospace Science* **21**, 159–199.

Monkewitz, P. A. 1989 Feedback control of global oscillations in fluid systems. *AIAA Paper 89-0991* .

Monkewitz, P. A. & Sohn, K. 1988 Absolute instability in hot jets. *AIAA Journal* **26** (8), 911–916.

Monokrousos, A., Akervik, E., Brandt, L. & Henningson, D. S. 2010 Global three-dimensional optimal disturbances in the blasius boundary-layer flow using time-steppers. *Journal of Fluid Mechanics* **650**, 181.

Moore, C. J. 1977 The role of shear-layer instability waves in jet exhaust noise. *Journal of Fluid Mechanics* **80** (02), 321.

Nichols, J. W. & Lele, S. K. 2010 Global mode analysis of turbulent high-speed jets. Annual research briefs 2010. Center for Turbulence Research.

Nichols, J. W. & Lele, S. K. 2011*a* Global modes and transient response of a cold supersonic jet. *Journal of Fluid Mechanics* **669**, 225–241.

Nichols, J. W. & Lele, S. K. 2011*b* Non-normal global modes of high-speed jets. *International Journal of Spray and Combustion Dynamics* **3** (4), 285–302.

Pier, B. 2002 On the frequency selection of finite-amplitude vortex shedding in the cylinder wake. *Journal of Fluid Mechanics* **458**.

Ray, P. K., Cheung, L. C. & Lele, S. K. 2009 On the growth and propagation of linear instability waves in compressible turbulent jets. *Physics of Fluids* **21** (5), 054106.

Rodriguez, D., Samanta, A., Cavalieri, A.V.G, Colonius, T. & Jordan, P. 2011 Parabolized stability equation models for predicting large-scale mixing noise of turbulent round jets. In *Proceedings of the 17th AIAA/CEAS Aeroacoustics Conference*. Portland, Oregon.

Sipp, Denis & Marquet, Olivier 2012 Characterization of noise amplifiers with global singular modes: the case of the leading-edge flat-plate boundary layer. *Theoretical and Computational Fluid Dynamics* pp. 1–19.

Trefethen, L. N., Trefethen, A. E., Reddy, S. C. & Driscoll, T. A. 1993 Hydrodynamic stability without eigenvalues. *Science* **261** (5121), 578–584.

19th AIAA/CEAS Aeroacoustics Conference
May 27-29, 2013, Berlin, Germany

AIAA 2013-2232

Global response to forcing in a subsonic jet: instability wavepackets and acoustic radiation

Xavier Garnaud[1*]
Richard D. Sandberg[2†]
Lutz Lesshafft[1‡]

[1] *Laboratoire d'Hydrodynamique, CNRS – École Polytechnique, 91128 Palaiseau, France*

[2] *Faculty of Engineering and the Environment, University of Southampton, Southampton SO17 1BJ, UK*

The linear flow response of a turbulent subsonic jet to low-level harmonic forcing is investigated in a fully non-parallel framework. The analysis is carried out for the configuration studied by Sandberg *et al.*,[1,2] and the predictions are validated against their DNS data. The present formalism relies on a singular mode analysis of the linear global resolvent operator for a forced compressible flow. We obtain the optimal distribution of volume forces inside the jet pipe that gives rise to the maximal flow response. Two definitions of optimality are explored, one based on the integrated energy of the instability wavepacket in the near field, the other based on the radiated acoustic power. Both definitions give similar results for the flow response, overall in good qualitative agreement with the nonlinear DNS results. The approach opens a new perspective on the instability response of jets and the associated noise generation.

Nomenclature

r, θ, x	radial, azimuthal and axial coordinates
ρ, p, T, E	density, pressure, temperature and total energy
$\mathbf{u}$	velocity vector
$\mathbf{q}$	linear perturbations of conservative flow variables
$\mathbf{f}$	volume force acting on conservative flow variables
ω, St_D	angular frequency and Strouhal number; $St_D = \omega/\pi$
R	nozzle radius
U	bulk velocity of the pipe flow
ρ_∞	ambient density
Re, Ma	Reynolds and Mach number, defined with R, U, $\rho_\infty$and ambient viscosity and speed of sound
L	Navier-Stokes operator, linearized around the base flow
B	restriction operator for flow forcing
$\mathcal{E}, \mathcal{F}$	energy and acoustic power (pseudo-)norms
Subscript	
0	base flow quantity

I. Introduction

In so far as jet noise is attributable to the presence of coherent perturbation wavepackets inside the flow, the aeroacoustic generation mechanisms and far-field acoustic signature can be studied as a problem

*Research Engineer, xavier.garnaud@ladhyx.polytechnique.fr, currently: Altran Research, Vélizy-Villacoublay (France).
†Professor, sandberg@soton.ac.uk, AIAA senior member
‡CNRS Research Scientist, lesshafft@ladhyx.polytechnique.fr, corresponding author

of hydrodynamic instability. The assertion that dominant noise components in subsonic jets are related to instability wavepackets goes back at least to Mollo-Christensen,[3] and the subject has just been thoroughly reviewed by Jordan & Colonius[4] (see in particular their figure 1). Jet instability has been studied under this angle over many decades, using the best available approaches of the day from instability theory. Michalke[5] provided numerical solutions of the spatial instability problem for a compressible jet under the parallel flow assumption. Crighton & Gaster[6] used a WKB approximation in order to account to first order for slow streamwise changes of the base flow. The parabolized stability equations (PSE)[7] make very similar assumptions and in their linear form give comparable results. Linear[8,9] and nonlinear[10,11] PSE computations of instability wavepackets in jets and shear layers have recently been conducted, and the results show overall reasonable agreement with experimental and numerical near-field data. However, acoustic radiation in subsonic flows is not obtained directly by this method, and must be deduced from acoustic analogies or similar procedures. Local spatial analysis, its WKB extension, linear and nonlinear PSE: all these present tools for the solution of the *signalling problem*, i.e. the flow response to sustained localized forcing, on different approximation levels. Apart from nonlinearity, the main difference lies in the extent to which the non-parallelism of the base flow is taken into account.

In this paper, we present solutions of the fully non-parallel linear signalling problem in a subsonic jet. Such results are sought in the form of singular modes of the linear resolvent operator. The resolvent operator maps a time-harmonic body force distribution onto the associated time-harmonic flow response; its singular modes represent a hierarchy of force distributions that are ranked according to the ratio of flow response norm over forcing input norm, i.e. the amplification gain. The formalism therefore allows to trace the *frequency response* of the linear flow system, or synonymously, its pseudo-spectrum (although only real frequencies are considered in the present study). Refs. 12, 13 describe the full formalism for a parallel flow problem, and recently it has been used in global contexts to determine the frequency response of boundary layers[14,15] and incompressible jets.[16] Nichols & Lele[17] present some first results for a compressible supersonic jet, and Garnaud[18] fully documents the near-field and far-field frequency response of a subsonic jet. The latter study uses a parametric model for a base flow. The objective of the present paper is to use the same methodology on the turbulent mean flow computed by Sandberg *et al.*,[2] and to attempt a comparison with the unsteady DNS results. Differences and similarities between the fully global flow response and corresponding PSE solutions are briefly discussed.

II. Flow configuration

We use the turbulent mean flow obtained by Sandberg *et al.*[1,2] from a DNS of a jet with Reynolds number $Re = 3691$, based on jet radius. The jet issues from a long circular pipe at $Ma = 0.84$ into an ambient coflow with $Ma = 0.2$. The axial mean velocity, made non-dimensional with respect to the bulk velocity inside the pipe, is displayed in figure 1. Note that the inlet pipe, 40 jet radii long, is explicitly included in the computational domain as a solid structure of finite thickness. All computations discussed in the present paper, except PSE results, are resolved on a domain extending over $-40 \leq x \leq 80$ and $0 \leq r \leq 70$, whereas a domain of $-50 \leq x \leq 110$ and $0 \leq r \leq 80.5$ was resolved in the reference DNS. Absorbing sponge regions are used near the numerical boundaries in combination with non-reflecting boundary conditions,[19] in order to minimize acoustic reflections.

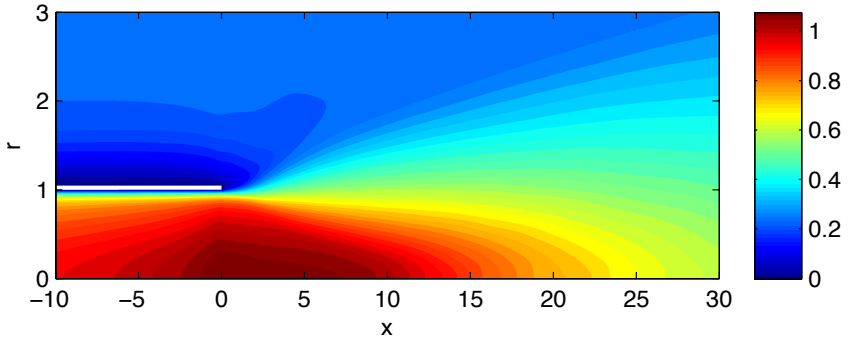

Figure 1. base flow: axial mean velocity, with jet Mach number $Ma_j = 0.84$ and coflow at $Ma = 0.2$. The entire flow domain extends over $-40 \leq x \leq 80$ and $0 \leq r \leq 70$.

III. Method

GLOBAL FREQUENCY RESPONSE: Flow perturbations at low amplitude in a given base flow (see section II) are assumed to be governed by the linearized compressible Navier–Stokes equations. These are written in conservative variables $(\rho, \rho\mathbf{u}, \rho E)$ and cylindrical coordinates (r, θ, x). All discussion in the following is restricted to axisymmetric perturbations, therefore all perturbations are independent of the azimuthal coordinate θ, and the azimuthal velocity component is strictly zero. Reference values for the dimensionless formulation are the nozzle radius R, the bulk velocity U inside the nozzle, and the ambient density ρ_∞. High-order explicit finite difference schemes[20] are used to resolve spatial derivatives on a rectilinear grid, and time-stepping is performed with a stability-preserving fourth-order Runge–Kutta algorithm. The equations and their numerical discretization are detailed in Ref. 18.

If the unforced linear system in discrete form is noted as $\dot{\mathbf{q}} = L\mathbf{q}$, then the long-time asymptotic flow response $\mathbf{q}$ to a time-harmonic volume forcing $\mathbf{f}$ at angular frequency ω obeys

$$-i\omega\tilde{\mathbf{q}} = L\tilde{\mathbf{q}} + B\tilde{\mathbf{f}}, \tag{1}$$

$$\text{where } \mathbf{q}(r,x,t) = \tilde{\mathbf{q}}(r,x)e^{-i\omega t} \text{ and } \mathbf{f}(r,x,t) = \tilde{\mathbf{f}}(r,x)e^{-i\omega t}, \tag{2}$$

and the matrix B may be used to impose a localization of the forcing. In the present case, B prescribes the forcing to be zero everywhere except inside the nozzle duct.

The resolvent operator $C(\omega) = -(L + i\omega\mathrm{Id})^{-1}B$ then relates forcing and flow response as

$$\tilde{\mathbf{q}} = C(\omega)\tilde{\mathbf{f}}. \tag{3}$$

We seek the forcing that yields the maximum flow response, in the sense that a chosen norm $\|\tilde{\mathbf{q}}\|^2 = \tilde{\mathbf{q}}^\dagger Q\tilde{\mathbf{q}}$ is maximized for a forcing of unity norm $\|\tilde{\mathbf{f}}\|^2 = \tilde{\mathbf{f}}^\dagger Q_f\tilde{\mathbf{f}} = 1$. The metric matrices Q and Q_f used to measure the response and the forcing need not be identical. In fact, only Q_f is required to be positive definite (a true norm), whereas Q may be positive semi-definite[18] (a pseudo-norm). The optimal forcing is defined by the Rayleigh quotient

$$\tilde{\mathbf{f}}_{opt} = \arg\max_{\tilde{f}} \frac{\tilde{\mathbf{f}}^\dagger C^\dagger Q C\tilde{\mathbf{f}}}{\tilde{\mathbf{f}}^\dagger Q_f\tilde{\mathbf{f}}}, \tag{4}$$

and can therefore be determined as the leading eigenvector of the operator $C^\dagger QC$, which is the right-singular vector of the resolvent. The corresponding eigenvalue σ (the leading singular value of $C(\omega)$) represents the gain that is achieved between the square of the norm of the forcing input and the square of the (pseudo-)norm of the flow response. If both norms are not identical, the definition of this gain may not be physically very meaningful, but even in this case, the variation of $\sigma(\omega)$ allows a quantitative comparison of the flow response at different frequencies.

Two distinct measures of the flow response will be used in the present study. The first is given by a true energy norm $\mathcal{E}$, discussed in Refs. 21, 22, which excludes the compression work associated with acoustic waves. The second is defined as the acoustic power $\mathcal{F}$ radiated across a control surface Σ. The latter is an example of a pseudo-norm with a positive semi-definite metric Q. These two measures are defined as

$$\mathcal{E} = \int_\Omega \left(\rho_0\tilde{\mathbf{u}}^2 + \frac{p_0}{\rho_0}|\tilde{\rho}|^2 + \frac{\rho_0^2}{\gamma^2(\gamma-1)Ma^4p_0}|\tilde{T}|^2\right) r\,\mathrm{d}r\,\mathrm{d}x\,, \tag{5}$$

$$\mathcal{F} = 0.5\int_\Sigma Ma|\tilde{p}|^2 r\,\mathrm{d}l. \tag{6}$$

The integration domain Ω is restricted to the physical portion of the numerical domain (excluding the sponge zones), and the surface Σ is taken to be a sphere of radius 20 around the origin (a circle in the (r,x) plane), excluding the nozzle duct. The forcing is *always* measured in terms of the norm $\mathcal{E}$.

The eigenvalue problem is solved using an iterative Lanczos method, which is particularly efficient for Hermitian operators. The numerical challenge lies in the repeated application of the inverse operator $(L + i\omega\mathrm{Id})^{-1}$, and its adjoint, at each iteration of the algorithm. One possibility is to explicitly construct the system matrix and invert it once,[17] but the massive memory requirements for this procedure are quite problematic. We chose a matrix-free approach, where the inversion is performed by time-marching the governing equations until an asymptotic state is reached. Special care is required in the backward-in-time

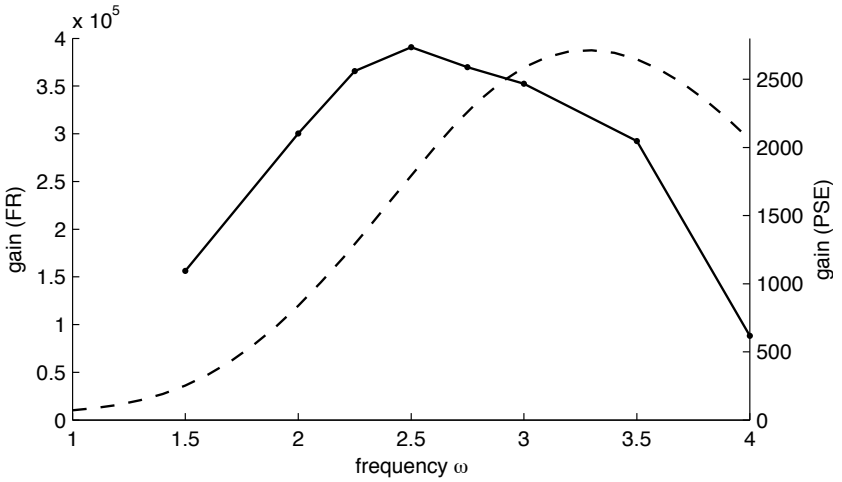

Figure 2. Maximum energy gain (equation 5) as a function of frequency. Solid line, left ordinate: Global linear frequency response; dashed line, right ordinate: linear PSE.

integration of the adjoint equations in order to preserve the perfectly Hermitian quality of the resolvent operator; this is found to be crucial for the accuracy of the Lanczos method. A Hermitian discrete operator can only be achieved by solving the adjoint version of the *discrete* direct problem, which is not trivial to construct in a matrix-free framework. The details of this procedure are discussed in Ref. 18, 23.

Parabolized stability equations: The compressible PSE are set up as given in Ref. 24; they are solved using Chebyshev collocation in r and an implicit Euler scheme in x. A stabilization technique[25] is added that allows arbitrarily small step sizes in the streamwise integration. All PSE calculations are initialized at the nozzle location $x = 0$ with the local k^+ shear-layer mode. The construction of the acoustic far-field by means of an acoustic analogy or a Kirchhoff surface method is not attempted here.

IV. Results

IV.A. Maximum energy response

Only results obtained by maximizing the perturbation energy $\mathcal{E}$ (Eq. 5) are discussed in this section. Results pertaining to maximum acoustic radiation $\mathcal{F}$ (Eq. 6) are presented in section IV.B.

Figure 2 shows the energy gain σ between the forcing input and the instability wavepacket as a function of frequency, as obtained from the frequency response analysis (solid line, left ordinate). The most amplified frequencies lie in the interval $2 \leq \omega \leq 3.5$, the maximum gain is found at $\omega = 2.5$. The decay of σ seems to be monotonic in both directions from the maximum. Compared to the DNS results, this band of preferred amplified frequencies is plausible: PSD measurements for axisymmetric pressure fluctuations in the DNS, taken near the nozzle at $r = 1$, $x = 2$, display a broad peak in the range $0.5 \leq St_D \leq 1$ (figure 4a in Ref. 1). The Strouhal number is related to the nondimensional angular frequency as $St_D = \omega/\pi$, therefore the dominant frequencies in the DNS near-field are found in the interval $\pi/2 \leq \omega \leq \pi$, in agreement with the present predictions.

Snapshots of the flow response wavepackets (axial momentum perturbations) for three frequencies, as obtained from the global frequency response analysis (FR), are presented in figures 3 *a,b,c.* Clearly, these wavepackets correspond to the shear-layer instability mode near the nozzle. In the downstream decaying part of the wavepacket, the perturbation shapes appear to gradually transition towards jet-column-type perturbations. In all cases, this transition occurs near the end of the potential core, around $x \approx 10$. Earlier studies of local instability modes[26] indicate that the shear-layer and jet-column modes cease to be distinct as the base flow approaches a self-similar bell-shaped velocity profile.

Note that the *linear* framework implies an arbitrary scaling of perturbation amplitudes. Contour levels are not specified in representations of linear results herein, as their absolute values are meaningless. The color scales in all figures are *linearly* varying between blue (minimum contour value) and red (maximum

contour value).

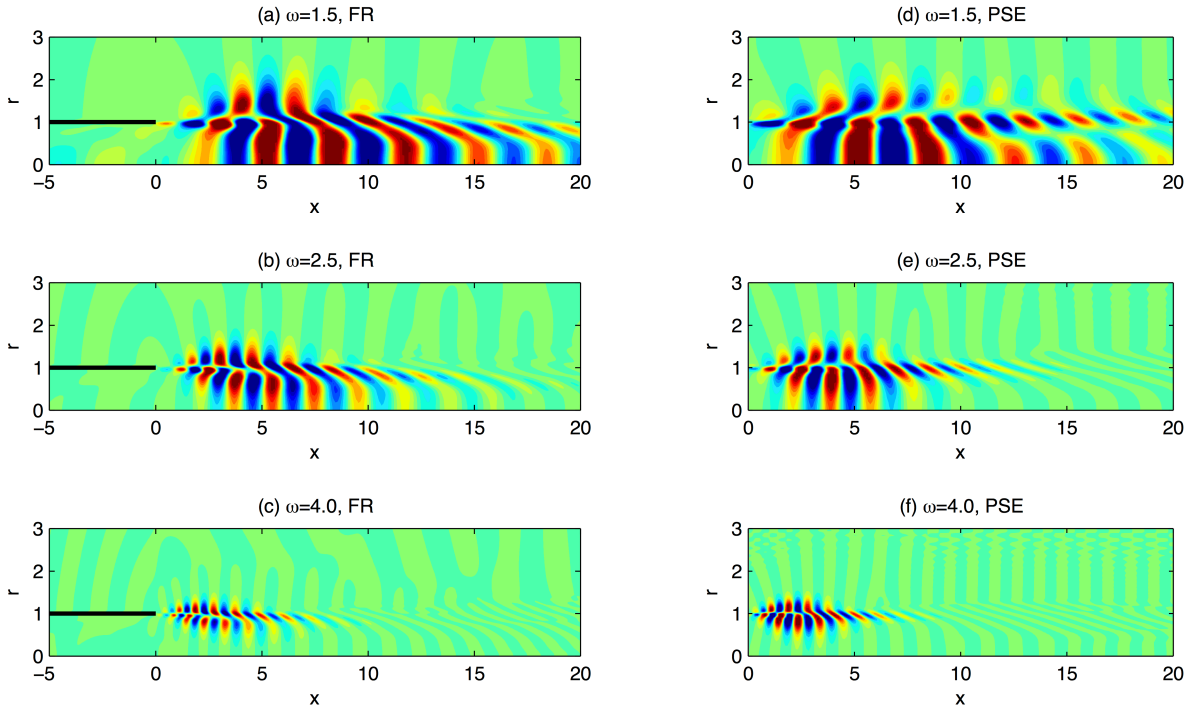

Figure 3. Flow response wavepackets (axial momentum perturbations $[\rho u_x]'$) at various forcing frequencies. (*a,b,c*): global frequency response; (*d,e,f*): PSE.

Corresponding results obtained from PSE calculations are also presented in figure 2 (dashed line, right ordinate) and in figures 3 *d,e,f*. The gain in this case is computed as the ratio of the energy norm (5) of the instability wavepacket over the input energy integrated along r at $x = 0$. The absolute values of σ measured this way are not commensurate with those obtained in the global framework, but their variation as a function of frequency is equally pertinent. Compared to the fully global frequency response (FR) analysis, the PSE gain variations are similar in shape, but noticeably shifted to higher frequencies; the maximum is reached at $\omega = 3.3$. The wavepacket shapes in figure 3 present some obvious differences between FR and PSE results. It is quite remarkable that these differences appear to be more pronounced in the downstream decaying region, where the slowly varying base flow assumption should be expected to be well justified. A close comparison with local eigenmode shapes in the downstream region may help to understand these differences, but such an analysis is yet to be performed. At present, it must be concluded that the simplifying assumptions of the PSE do affect the wavepacket shapes in a way that may be relevant for the sound generation. Visually, these effects appear to be stronger at low frequencies.

Optimal forcing distributions (axial momentum) identified from the singular value decomposition are shown in figure 4, for the same frequencies as considered in figure 3. Clearly, the forcing is localized in all cases within the boundary layer of the duct, immediately adjacent to the nozzle exit. The short wavelengths of the forcing structures are well resolved by the mesh ($\Delta x = 0.009$ and $\Delta r = 0.01$ at the nozzle lip). The observation that this is the region of maximum receptivity indicates that the pipe-flow eigenmodes do not couple efficiently with the shear-layer mode of the free jet, as otherwise the optimal forcing would rather excite a pipe mode. Indeed, a local analysis confirms that the flow inside the pipe is stable.

The global frequency response (FR) modes are finally compared to DNS results in figure 5. Density perturbations are visualized in the near field of the jet. FR results are to the left, DNS results at similar but not identical frequencies are shown to the right. These DNS results represent the axisymmetric spatial structures obtained from a Fourier transform of the time-resolved simulation; the data are identical to those used in Ref. 27. Full time-resolved data is not available in the entire domain, therefore only the hydrodynamic near field and the near acoustic field are represented. Furthermore, the currently available data from DNS and FR analysis do not exactly match in frequency. Yet the values are sufficiently close to allow a meaningful, albeit qualitative discussion.

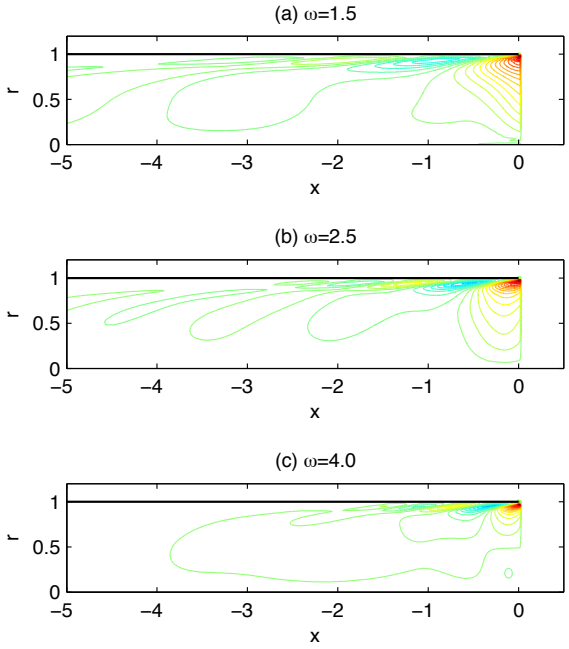

Figure 4. Optimal distribution of volume forces $\tilde{\mathbf{f}}$ (real part of axial momentum component) inside the pipe at three different frequencies. The spatial support of volume forces is restricted to the interior of the pipe ($x \leq 0$, $r < 1$). Optimality is defined with respect to the energy norm (5).

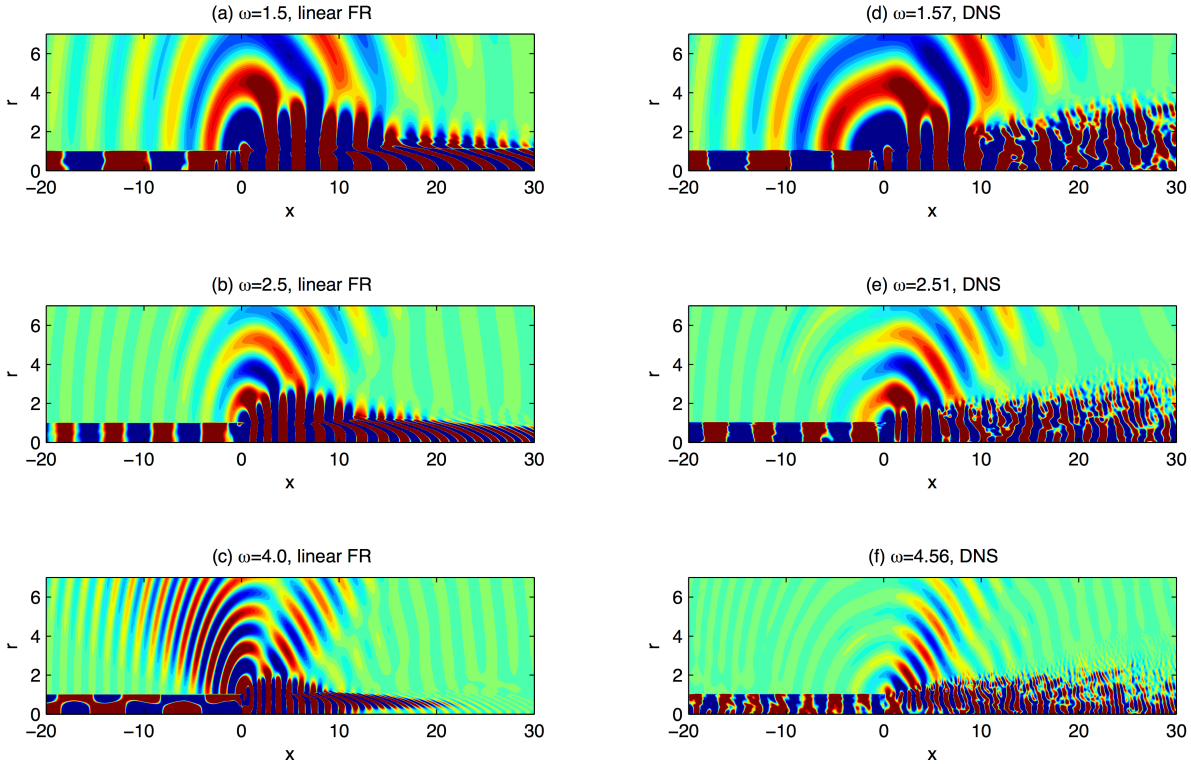

Figure 5. Comparison between global frequency response modes and temporal Fourier modes extracted from the DNS (axisymmetric perturbations). Density perturbations are shown. The data presented in (*d*,*e*,*f*) is identical to those of figures 9 (*a*,*d*,*g*) in Ref. 27.

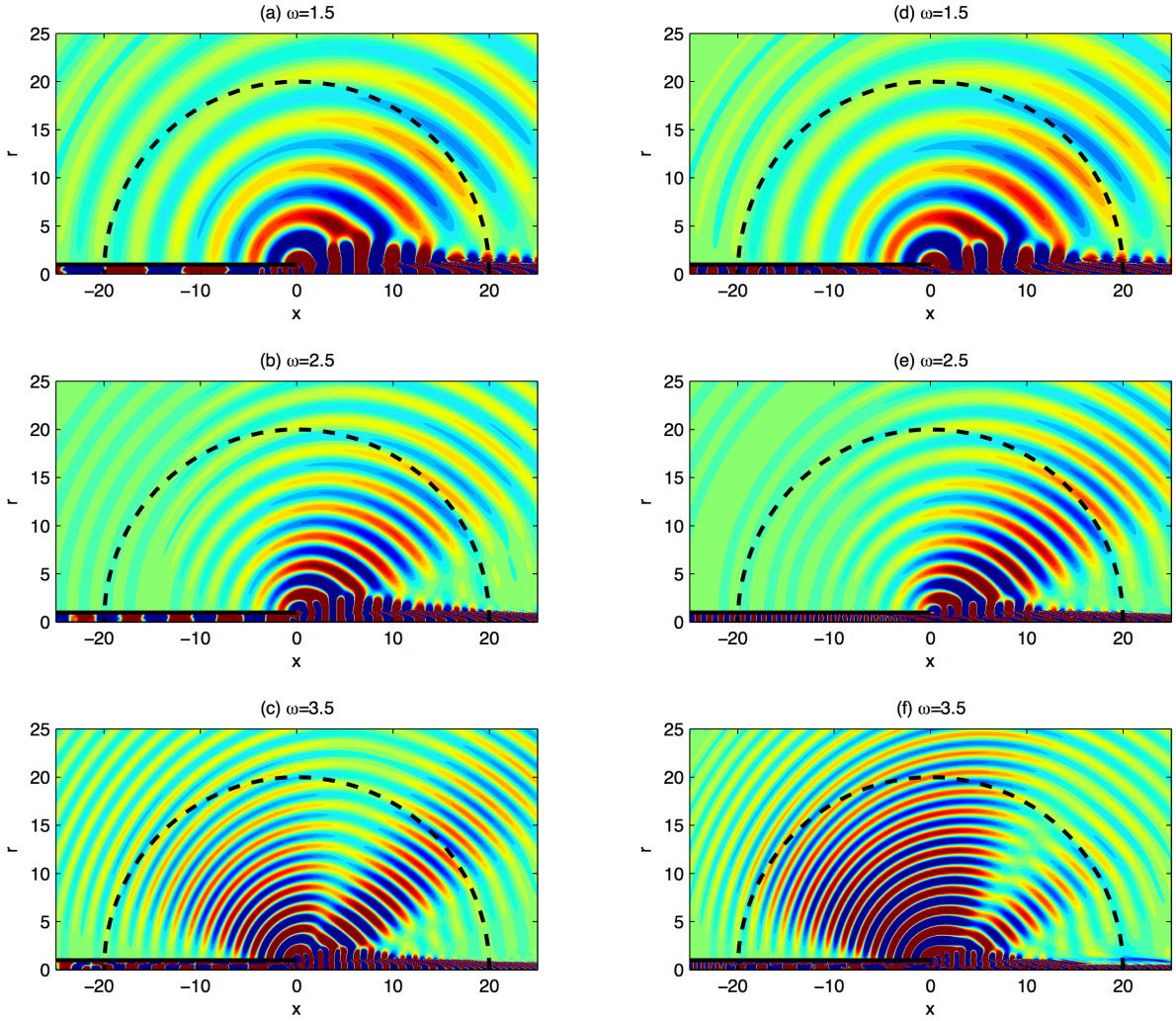

Figure 6. Snapshots of the far-field density fluctuations that are obtained as a part of the frequency response. *a,b,c*: optimization with respect to the integrated energy (5); *d,e,f*: optimization with respect to the radiated acoustic power (6). Contour levels are chosen as appropriate to visualize the acoustic far field. Dashed lines represent the limit of the physical flow region, coinciding with the contour Σ for the evaluation of acoustic power.

At frequencies $\omega = 1.5$ and 2.5, the resemblance between the FR optimal-response wavepacket and the corresponding DNS Fourier mode in figure 5 is rather striking. Coherent structures dominate the DNS fluctuations inside the potential core region, with a spatial structure very similar to the FR solution. Density fluctuations inside the pipe represent downstream-propagating acoustic waves in all cases. The acoustic near-field, which is remarkably coherent in all three DNS-extracted modes, appears to be accurately reproduced in the FR solutions. At the highest frequency, $\omega = 4.0$, a strong upstream radiation is observed, which is absent or small in the DNS data. Also, the acoustic waves inside the pipe at this frequency are of a different character than those found in the DNS.

Density fluctuations in the acoustic far field are visualized in figure 6 (the real part of the asymptotic flow response are shown, corresponding to a snapshot at an arbitrary temporal phase). Figures (*a,b,c*) represent the response to optimal forcing in a maximum-energy sense; figures (*d,e,f*) will be discussed in the next section. Only a portion of the numerical domain is shown, but the entire physical domain inside a semi-circle of radius 20 (dashed lines) is visible. Damping in the sponge regions is ramped up very slowly, and it barely affects perturbations in the region shown in figure 6. In all cases, all sound seems to emanate from the nozzle exit at $x = 0$. The spherical wavefronts are convected by the outer coflow (at $Ma = 0.2$). At frequencies $\omega = 1.5$ and 2.5, the far-field directivity is marked by a single-beam pattern. The angle of the

downstream beam with respect to the jet axis changes only slowly with frequency. At higher frequencies, visible in figure 6 only for $\omega = 4.0$, an additional upstream-oriented lobe appears.

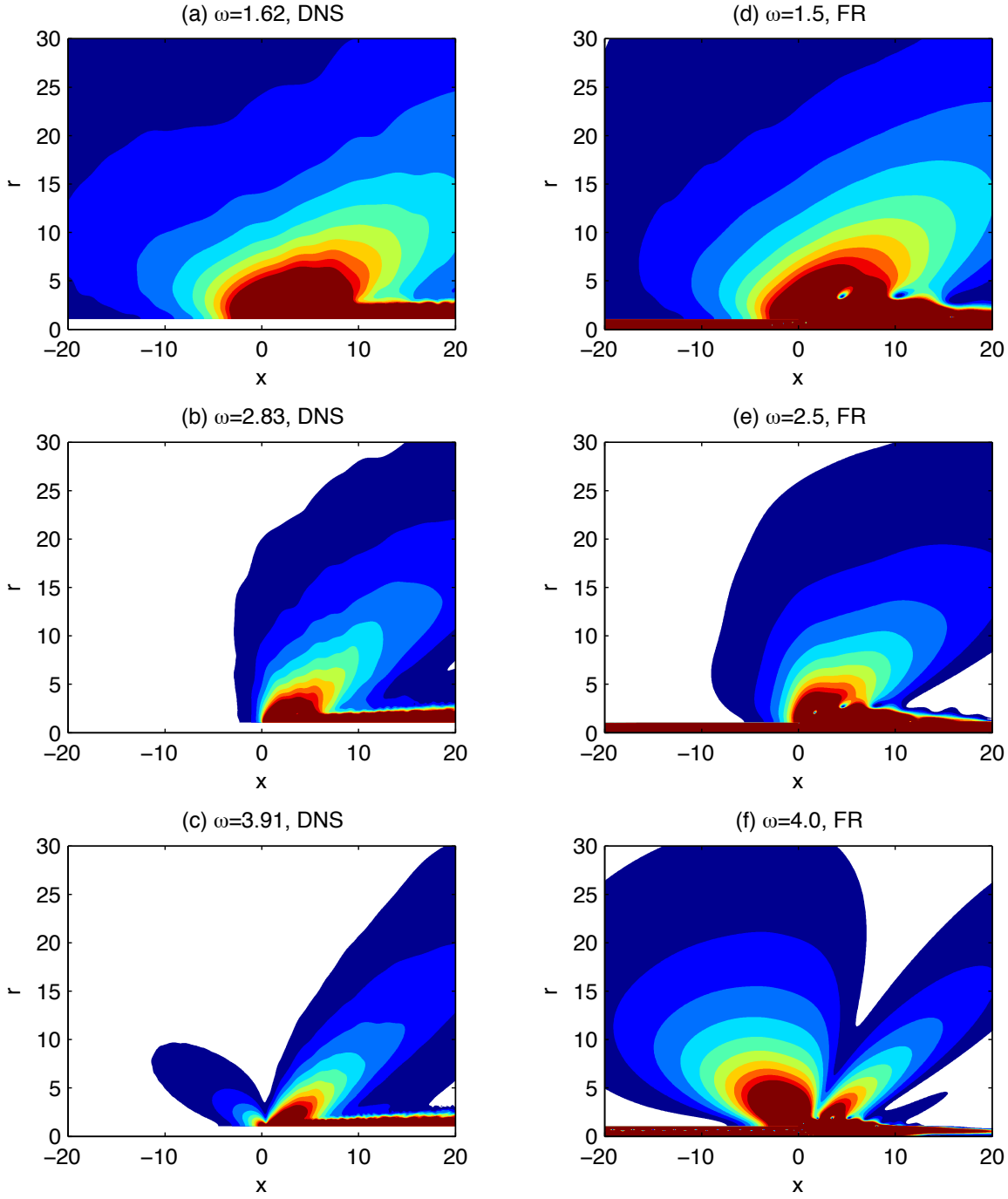

Figure 7. Comparison between global frequency response modes and temporal Fourier modes extracted from the DNS (axisymmetric perturbations) in the far field. The amplitude of acoustic density perturbations is shown in a linear color scale. The data presented in (*b*,*c*) is identical to those of figures 9 (*a*,*b*) in Ref. 1.

The acoustic far-field results are then compared to DNS data in figure 7. As in figure 5, the DNS data is obtained from a temporal Fourier transform of axisymmetric fluctuations of pressure. Note again that the frequencies are not identical, but close. The amplitude of density fluctuations in the far field is shown using a linear color scale. It appears that the linear frequency response reproduces very well the acoustic

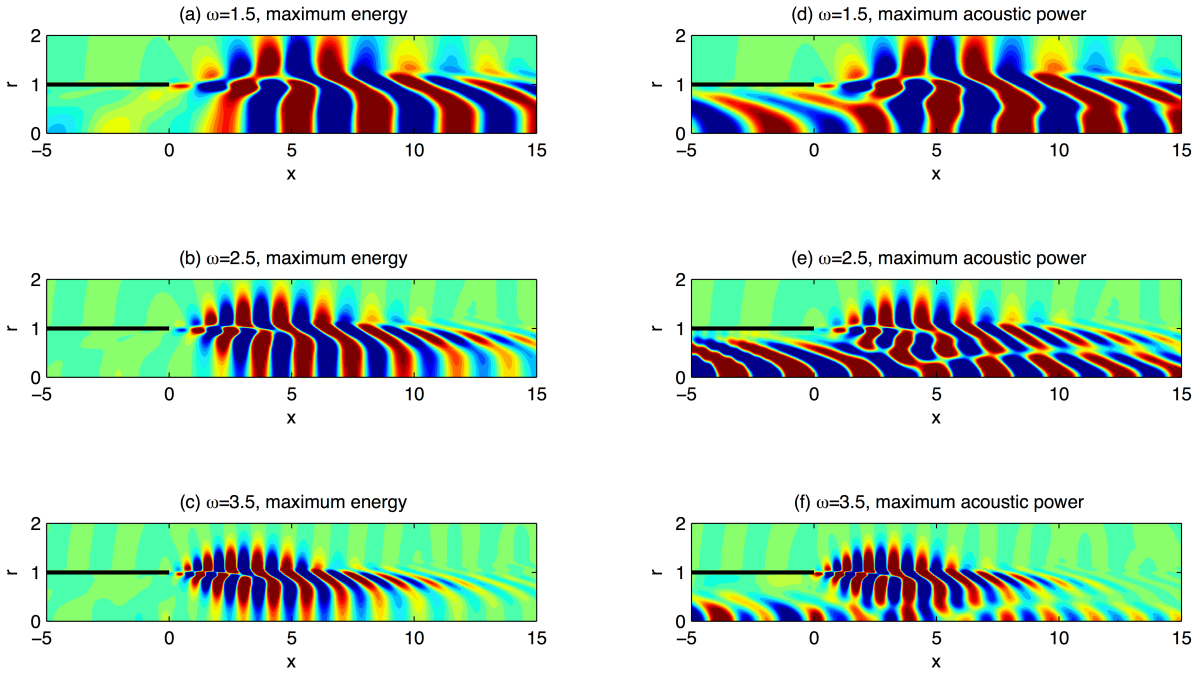

Figure 8. Snapshots of the near-field frequency response wavpackets (axial momentum perturbations). *a,b,c*: optimization with respect to the integrated energy (5); *d,e,f*: optimization with respect to the radiated acoustic power (6). Contour levels are chosen as appropriate to visualize the wavepacket structures.

directivity characteristics measured in the DNS, particularly at the lower frequencies $\omega = 1.5$ and 2.5. The beam pattern is retrieved with the correct angle and correct outward decay rate. At the high frequency value $\omega = 4$, the upstream lobe that is weak in the DNS is found to be dominant in the FR solution, as already mentioned in the discussion of figure 5. The reasons for this difference between FR and DNS behavior are not clear at present. In principle, direct sound that is forced inside the pipe and then refracts into the free far field may occur in either of the two computations; however, it seems implausible that refraction would cause an upstream radiation from the nozzle.

IV.B. Maximum acoustic radiation response

Optimal flow forcing for maximal acoustic far-field radiation, in the sense of the pseudo-norm $\mathcal{F}$ (equation 6), has only been computed for three frequencies $\omega = 1.5$, 2.5 and 3.5 at present. Only a short and rather preliminary discussion can be offered in this section.

The gain, defined as the acoustic power $\mathcal{F}$ of the flow response divided by the energy $\mathcal{E}$ of the volume forcing inside the pipe, is found to increase monotonically with frequency. The values are $(\omega, \sigma) = (1.5,\ 7.6),\ (2.5,\ 20.2)$ and $(3.5,\ 81.7)$. This trend is consistent with a similar study performed on a model turbulent mean flow in an outer fluid at rest.[18]

The acoustic far field of these "loudest" modes is displayed in figure 6 (*d,e,f*) alongside the results discussed in the previous section. The comparison reveals that the acoustic radiation at frequencies $\omega = 1.5$ and 2.5 are virtually identical, whether the optimization is based on the near-field or far-field response. This observation is reassuring in the sense that the FR results appear to be fairly universal and robust with respect to details of the definition of optimality. The results obtained for a model mean flow displayed similar agreement.[18] The higher-frequency case $\omega = 3.5$ in figure 6 does show some sensitivity to the optimization objective. The upstream acoustic lobe, which has been discussed before as an exaggerated feature in the FR results, is found to be even more intense in the case of maximal acoustic power. The downstream beam, which compares favorably with the DNS results, is still present, but very weak compared to the upstream-radiated intensity.

The near-field flow response obtained with the two different optimization objectives are compared in figure 8. Axial momentum perturbations are shown in the flow region near the nozzle. If the acoustic

far-field in both scenarios is quite similar, the instability wavepackets in the near-field present one clear difference: while the maximum-energy flow response modes start out as a pure local shear-layer mode at the nozzle, forced only in the immediate vicinity of the nozzle lip, the maximum-acoustic flow response modes include a strong center-mode component already inside the pipe, which continues seamlessly as a jet-column mode in the free jet. The shear-layer wavepacket is still present, and it does not seem to be affected by the added jet-column perturbations.

V. Conclusion

A linear frequency response analysis has been presented for a compressible, subsonic jet with coflow. Optimal forcing distributions inside a long nozzle pipe have been identified with respect to two distinct optimization objectives: first, the total (integrated) energy of the flow response wavepacket has been maximized; second, the acoustic power that is radiated into the far field has been used as a measure. A fully global formalism has been used, in combination with highly accurate discretization schemes that allow high-fidelity computations of the acoustic field. Both the near-field and the far-field results compare favorably with Fourier-transformed DNS reference data. Coherent perturbation structures in the free jet and inside the pipe, obtained from the DNS, bear a strong resemblance to the frequency response wavepackets, the latter computed as linear perturbations in the turbulent mean flow.

If maximum perturbation energy gain is the optimization objective, the near-field wavepacket is composed only of shear-layer instability perturbations inside the potential core. These transition smoothly towards jet-column perturbations downstream of the potential core. Optimization on the basis of radiated acoustic power yields near-field wavepackets that include a significant component of jet-column perturbations already inside the pipe and in the potential core. The directivity of the associated acoustic far field, however, is only weakly affected by these differences in the near field at. The acoustic radiation measured in the DNS compares well with the present results. The most notable difference is the presence of a strong upstream radiation in the linear frequency response computations at frequencies $\omega \gtrsim 3$. This upstream radiation is more marked in the case when acoustic power is maximized.

The frequency response solutions have also been compared to near-field results obtained from integration of the linear parabolized stability equations (PSE). Some noticeable differences are observed in the features of the wavepackets, particularly in the region of stable decay downstream of the potential core. These differences must be seen as errors of the PSE approximation. It should be noted in this context that one PSE run requires a computation time of less than one CPU minute, whereas the present frequency response computations require $\mathcal{O}(1000)$ CPU hours each. The main advantages of the global frequency response analysis over linear PSE computations are (i) the inclusion of the acoustic far field; (ii) the optimization framework that is inherent in the FR approach, and the flexibility in the choice of an optimization objective; (iii) the fully global character, which in the jet noise problem principally helps to account for nozzle effects.

The results presented in this paper hold much information for further analysis that has not yet been fully exploited. For instance, the question is raised which role the jet column mode plays in noise generation in the present configuration. Most importantly, we believe that the results demonstrate a great potential of the employed method for future progress in the understanding of aeroacoustic sound generation in a variety of shear flows.

Acknowledgments

The present work has immensely benefitted from the many contributions by Patrick Huerre and Peter Schmid during the course of XG's PhD work. Financial support from the EADS Foundation and from the DGA is gratefully acknowledged. Calculations were performed using HPC resources provided through GENCI Grant No. 2012-026451.

References

[1]Sandberg, R., Sandham, N., and Suponitsky, V., "DNS of fully turbulent jet flows in flight conditions including a canonical nozzle," AIAA Paper 2011–2918, 2011.

[2]Sandberg, R., Suponitsky, V., and Sandham, N., "DNS of compressible pipe flow exiting into a coflow," *Int. J. Heat Fluid Fl.*, Vol. 35, 2012, pp. 33–44.

[3]Mollo-Christensen, E., "Work on shear layer stability and jet noise," Tech. Rep. 19620000982, NASA, 1961.

[4]Jordan, P. and Colonius, T., "Wave packets and turbulent jet noise," *Annu. Rev. Fluid Mech.*, Vol. 45, 2013, pp. 173–195.

[5]Michalke, A., "Instabilität eines kompressiblen runden Freistrahls unter Berücksichtigung des Einflusses der Strahlgrenzschichtdicke," *Z. Flugwiss.*, Vol. 19, 1971, pp. 319–328.

[6]Crighton, D. and Gaster, M., "Stability of slowly diverging jet flow," *J. Fluid Mech.*, Vol. 77, 1976, pp. 397–413.

[7]Bertolotti, F., Herbert, T., and Spalart, P., "Linear and nonlinear stability of the Blasius boundary layer," *J. Fluid Mech.*, Vol. 242, 1992, pp. 441–474.

[8]Gudmundsson, K. and Colonius, T., "Instability wave models for the near field fluctuations of turbulent jets," *J. Fluid Mech.*, Vol. 689, 2011, pp. 97–128.

[9]Léon, O., *Étude du rayonnement acoustique des instabilités hydrodynamiques de jets double-flux avec les équations de stabilité parabolisées (PSE)*, Ph.D. thesis, ONERA, Toulouse, France, 2012.

[10]Cheung, L. and Lele, S., "Linear and nonlinear processes in two-dimensional mixing layer dynamics and sound radiation," *J. Fluid Mech.*, Vol. 625, 3 2009, pp. 321–351.

[11]Rodriguez, D., Samanta, A., Cavalieri, A., Colonius, T., and Jordan, P., "Parabolized stability equation models for predicting large-scale mixing noise of turbulent round jets," AIAA Paper 2011–2838, 2011.

[12]Trefethen, L., Trefethen, A., Reddy, S., and Driscoll, T., "Hydrodynamic stability without eigenvalues," *Science*, Vol. 261, 1993, pp. 578.

[13]Schmid, P. and Henningson, D., *Stability and transition in shear flows*, Vol. 142, Springer, 2001.

[14]Monokrousos, A., Akervik, E., Brandt, L., and Henningson, D., "Global three-dimensional optimal disturbances in the Blasius boundary-layer flow using time-steppers," *J. Fluid Mech.*, Vol. 650, 2010, pp. 181.

[15]Sipp, D. and Marquet, O., "Characterization of noise amplifiers with global singular modes: the case of the leading-edge flat-plate boundary layer," *Theoretical and Computational Fluid Dynamics*, 2012.

[16]Garnaud, X., Lesshafft, L., Schmid, P., and Huerre, P., "The preferred mode of incompressible jets: linear frequency response analysis," *J. Fluid Mech.*, Vol. 716, 2013, pp. 189–202.

[17]Nichols, J. and Lele, S., "Non-normal global modes of high-speed jets," *International Journal of Spray and Combustion Dynamics*, Vol. 3, No. 4, 2011, pp. 285–302.

[18]Garnaud, X., *Modes, transient dynamics and forced response of circular jets*, Ph.D. thesis, École Polytechnique, Palaiseau, France, 2012.

[19]Poinsot, T. and Lele, S., "Boundary conditions for direct simulations of compressible viscous flows," *J. Comput. Phys.*, Vol. 101, No. 1, 1992, pp. 104.

[20]Berland, J., Bogey, C., Marsden, O., and Bailly, C., "High-order, low dispersive and low dissipative explicit schemes for multiple-scale and boundary problems," *Journal of Computational Physics*, Vol. 224, No. 2, 2007, pp. 637 – 662.

[21]Chu, B.-T., "On the energy transfer to small disturbances in fluid flow (Part i)," *Acta Mechanica*, Vol. 1, 1965, pp. 215–234.

[22]Hanifi, A., Schmid, P., and Henningson, D., "Transient growth in compressible boundary layer flow," *Phys. Fluids*, Vol. 8, No. 3, 1996, pp. 826.

[23]Fosas de Pando, M., Sipp, D., and Schmid, P., "Efficient evaluation of the direct and adjoint linearized dynamics from compressible flow solvers," *J. Comp. Phys.*, Vol. 231, 2012, pp. 7739–7755.

[24]Salgado, A. and Sandham, N., "Viscous Instability of a Compressible Round Jet," Tech. Rep. AFM-07/01, University of Southampton, 2007.

[25]Andersson, P., Henningson, D., and Hanifi, A., "On a stabilization procedure for the parabolic stability equations," *J. Eng. Math.*, Vol. 33, 1998, pp. 311–332.

[26]Lesshafft, L. and Huerre, P., "Linear impulse response in hot round jets," *Phys. Fluids*, Vol. 19, 2007, pp. 024102.

[27]Sinayoko, S., Agarwal, A., and Sandberg, R., "Physical sources of sound in laminar and turbulent jets," AIAA Paper 2011–2916, 2011.

Theoretical and Applied Mechanics Letters 5 (2015) 126–128

Contents lists available at ScienceDirect

Theoretical and Applied Mechanics Letters

journal homepage: www.elsevier.com/locate/taml

Letter

Linear global stability of a confined plume

Lutz Lesshafft

Laboratoire d'Hydrodynamique, CNRS-École polytechnique, Palaiseau, France

ARTICLE INFO

Article history:
Received 19 July 2014
Received in revised form
7 January 2015
Accepted 2 February 2015
Available online 8 May 2015
*This article belongs to the Fluid Mechanics

Keywords:
Plume
Linear instability
Laminar flow stability
Buoyancy-driven instability
Bifurcation and symmetry breaking

ABSTRACT

A linear stability analysis is performed for a plume flow inside a cylinder of aspect ratio 1. The configuration is identical to that used by Lopez and Marques (2013) for their direct numerical simulation study. It is found that the first bifurcation, which leads to a periodic axisymmetric flow state, is accurately predicted by linear analysis: both the critical Rayleigh number and the global frequency are consistent with the reported DNS results. It is further shown that pressure feedback drives the global mode, rather than absolute instability.

Localized heating on a horizontal surface entrains a buoyancy-driven plume flow in the fluid above. Plumes are very common in the oceans and in the atmosphere, and they are of great importance to transport and mixing processes [1]. Unconfined by fluid boundaries or by strong stratification, plumes represent a class of open shear flows. Plumes within a confined geometry represent a closed flow, which is likely to induce marked differences in the dynamics when compared to unconfined situations. Confined plumes are notably encountered in internal ventilation problems [2] and in Rayleigh–Bénard convection [3].

Lopez and Marques [4] used direct numerical simulation (DNS) for a comprehensive investigation of the dynamics of confined plumes. Their study describes several successive bifurcations, associated with symmetry breaking, for what is arguably the most basic confined plume configuration: the internal flow in a fluid-filled cylinder, induced by localized heating at the bottom wall. As the wall heating becomes more and more intense, characterized by an increasing value of the Rayleigh number, steady convection becomes dominant over diffusion for the heat transport. Beyond a first critical Rayleigh number, the steady plume flow bifurcates to a time-periodic regime, characterized by the convection of axisymmetric "puffs" along the centerline of the plume. The next bifurcation, at a higher critical value of the Rayleigh number, leads to a breaking of the axial symmetry, and further successive bifurcations lead to chaotic flow states and eventually to turbulence.

The present paper aims to investigate the first bifurcation, from a steady flow to a time-periodic limit cycle, using the tools of linear global stability analysis. Lopez and Marques describe this transition as a supercritical Hopf bifurcation, which suggests that the observed nonlinear dynamics are related to the destabilization of a linear temporal eigenmode of the steady-state system. The flow geometry as well as the governing equations are chosen exactly identical to the standard configuration in the reference DNS: the fluid is confined in a vertical cylinder of height and diameter both equal to 1. All walls are isothermal, at a constant temperature $T_0-\Delta T/2$, except at the bottom wall, where a circular spot of radius r_d is heated to a temperature $T_0+\Delta T/2$. The wall temperature varies smoothly over the radial distance $[r_\mathrm{d}, r_\mathrm{d}+r_\mathrm{w}]$ from the cylinder axis, according to expression (2.5) of Ref. [4]. As in the reference study, we choose $r_\mathrm{d} = r_\mathrm{w} = 0.125$. The nondimensional wall temperature is 0.5 in the center of the hot spot, and -0.5 everywhere outside the heated area.

The governing equations are cast in the Boussinesq approximation, written in nondimensional form identically to Ref. [4] as

$$(\partial_t + \boldsymbol{u}\cdot\nabla)\boldsymbol{u} = -\nabla p + \nabla^2\boldsymbol{u} + \sigma^{-1}Ra\,T\boldsymbol{e}_z, \tag{1}$$

$$(\partial_t + \boldsymbol{u}\cdot\nabla)T = \sigma^{-1}\nabla^2 T, \qquad \nabla\cdot\boldsymbol{u} = 0. \tag{2}$$

The nondimensional parameters of the problem are the Rayleigh number $Ra = \alpha g d^3 \Delta T \kappa^{-1}\nu^{-1}$ and the Prandtl number $\sigma = \nu/\kappa$. All symbols are standard notation (see Ref. [4]). The Rayleigh number is proportional to the dimensional temperature difference, and may be interpreted as representing the intensity of the heating.

E-mail address: lutz.lesshafft@ladhyx.polytechnique.fr.

http://dx.doi.org/10.1016/j.taml.2015.05.001

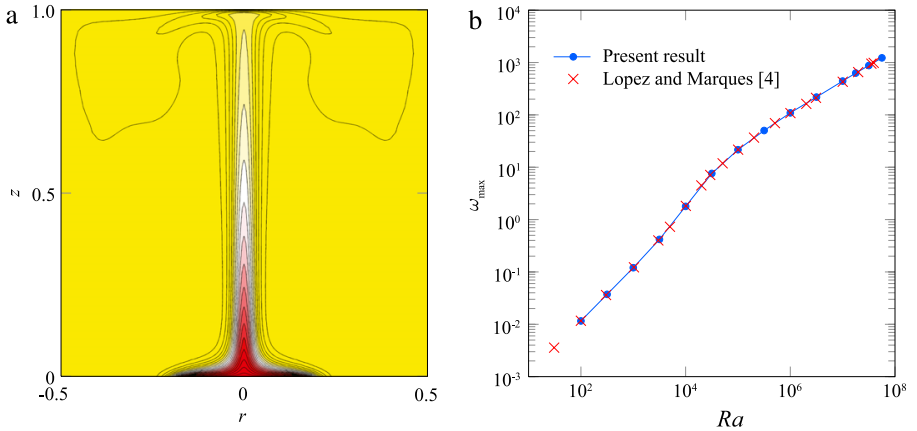

Fig. 1. (Color online) (a) Temperature distribution in the steady base flow at $Ra = 10^7$. Twenty contour levels between $T_{min} = -0.5$ and $T_{max} = 0.5$ are shown. (b) Maximum vertical velocity w_{max} of the steady base flow, as a function of Rayleigh number. Blue line and dots: present results; red crosses: results reported by Lopez and Marques [4], rescaled by a factor $\sigma = 7$.

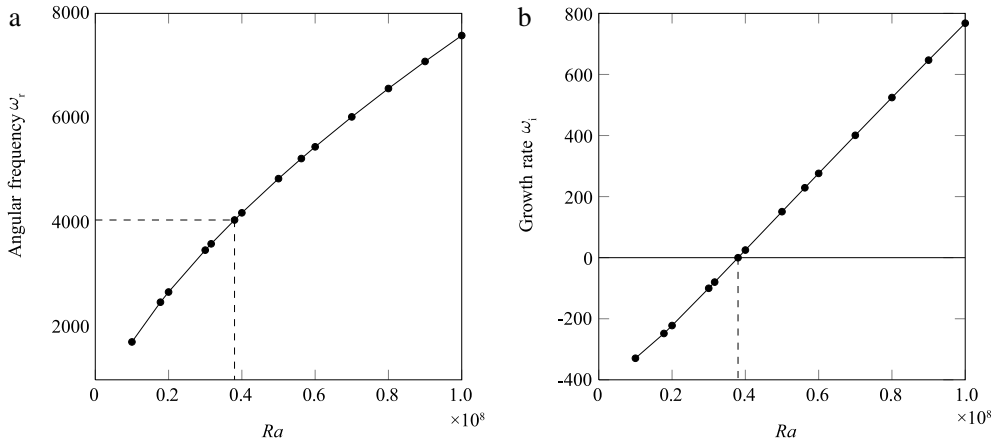

Fig. 2. Linear instability eigenvalue as a function of Rayleigh number. (a) Angular frequency (real part). (b) Temporal growth rate (imaginary part).

In a first step, base flow states are computed as exact steady solutions of the nonlinear equations (1) and (2). In a second step, the same equations are linearized around the base flow, and temporal eigenmodes of this linear system are extracted. Both numerical procedures are performed using a finite element method as implemented in the FreeFEM++ package (http://www.freefem.org). A Newton–Raphson method is employed to identify the steady base flow for a given setting of σ and Ra. All results presented herein pertain to $\sigma = 7$, consistent with the standard case of Ref. [4]. The temperature distribution of the base flow at $Ra = 10^7$ is represented in Fig. 1(a). It appears to be indeed identical to the result of Lopez and Marques [4] (their Fig. 3(a), same colormap). The associated velocity fields are also consistent, provided that the values reported in Ref. [4] are divided by the Prandtl number, $\sigma = 7$, as plotted in Fig. 1(b). It seems that the time scaling in Ref. [4] is based on thermal diffusivity, whereas a viscous scale is used here. The accuracy of the present base flow results has been verified through independent time-resolved simulations with the software package Gerris [5].

Temporal eigenmodes of the linearized form of Eqs. (1) and (2) are sought in the form $\boldsymbol{u}'(r,\theta,z,t) = \hat{\boldsymbol{u}}(r,z)\exp(\mathrm{i}m\theta - \mathrm{i}\omega t)$, and accordingly for perturbations T' and p'. The eigenvalue is the complex frequency $\omega = \omega_r + \mathrm{i}\omega_i$, where ω_i represents the temporal growth rate. It is found that all eigenmodes are stable ($\omega_i < 0$) at Rayleigh numbers below the critical value $Ra_c = 3.801 \times 10^7$. At Rayleigh numbers $Ra > Ra_c$, one axisymmetric instability mode ($m = 0$) becomes unstable, while helical modes ($|m| \geqslant 1$) remain stable at least up to $Ra = 10^8$. The angular frequency and growth rate of this unstable global mode are displayed as functions of Rayleigh number in Fig. 2. The critical value for onset of linear global instability is to be compared to the value reported in Ref. [4], $Ra = 3.854 \times 10^7$, at which self-excited axisymmetric perturbations are observed in the nonlinear simulations. The global angular frequency of the limit cycle in the simulations is approximately $\tilde{\omega}_g = 28500$ in terms of the diffusive time scale, or $\omega_g = \tilde{\omega}_g/\sigma \approx 4070$ when rescaled to the viscous time scale used in the present study. This latter value matches within 0.5% accuracy the frequency $\omega_r = 4050$ that linear instability analysis predicts at the critical Rayleigh number (see Fig. 2(a)).

Lopez and Marques [4] point out that the oscillation period of the nonlinear limit cycle corresponds to the propagation time of a vortex ring along the axis of the plume. The vortex then impacts the top wall, causing a pressure perturbation, which in turn triggers the formation of a new vortex ring near the bottom wall. Al-

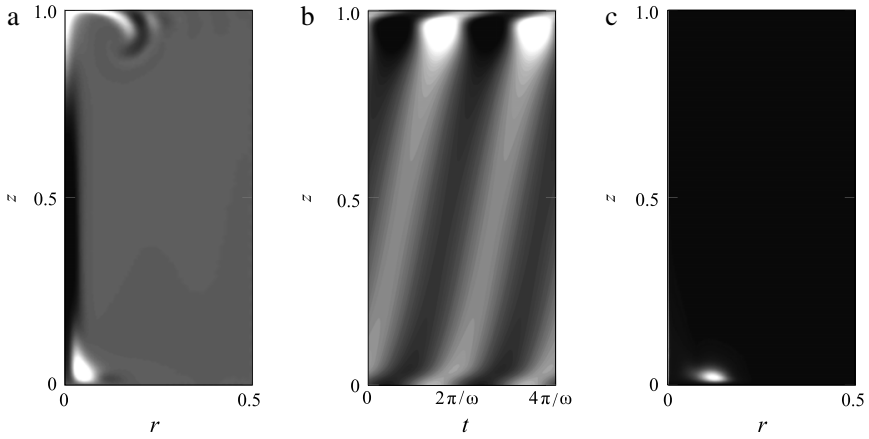

Fig. 3. Linear perturbation eigenfunctions of the unstable mode at the critical Rayleigh number $Ra = 3.801 \times 10^7$. (a) Temperature perturbation (snapshot). (b) Pressure perturbation at $r = 0.1$ as a function of z and time. Two oscillation periods are shown. (c) Structural sensitivity. White is positive, black is negative (or zero in plot (c)).

though the roll-up of a vortex ring is a strongly nonlinear event, it is remarkable how the linear eigenmode reproduces the same qualitative behavior. Figure 3(a) displays the linear temperature perturbation at one instance during the cycle. It resembles very much the nonlinear snapshots shown in Fig. 10 of Ref. [4]. The propagation time of disturbances is visualized in the space–time diagram in Fig. 3(b), which shows pressure perturbations along the vertical z, at a fixed radial station $r = 0.1$, as a function of time. A pressure maximum (minimum) near the top wall coincides precisely with a maximum (minimum) at the bottom wall, which then propagates upward. The picture suggests the presence of a pressure feedback, similar to what is observed for instance in cavity flows [6]. Figure 3(c) finally shows the structural sensitivity of the unstable eigenmode, in the sense of Giannetti and Luchini [7]. This quantity is computed as the local product of the norms of the direct eigenfunction and its adjoint. The structural sensitivity of the unstable eigenmode is seen to be significant only in the vicinity of the hot spot near the bottom wall. This observation suggests that this flow region is of particular importance for the destabilization of the eigenmode. It is plausible that the strong pressure fluctuations generated at the top boundary, where the vorticity impinges on the wall, induce perturbations in the receptive flow region near the hot spot at the bottom. Synchronized communication between these two flow regions establishes a feedback loop that seems to be the root cause for the observed instability.

It is classically assumed that global instability may either be linked to pressure feedback, as described here, or to the presence of local absolute instability [8]. A local analysis has been performed for the base flow at the critical setting $Ra = 3.801 \times 10^7$, confirming that the flow at this setting is convectively unstable everywhere. Absolute instability therefore does not provide the global instability mechanism. All these observations support the interpretation that the vertical confinement leads to pressure feedback that induces a global instability. It is remarkable that such a seemingly nonlinear scenario is captured with high quantitative accuracy by a linear analysis.

Acknowledgments

The author sincerely thanks Gaétan Lerisson at LadHyX for his generous help with the Gerris simulations. Financial support for this work was provided by the Agence Nationale de la Recherche under the "Cool Jazz" project.

References

[1] P. Linden, Convection in the environment, in: Perspectives in Fluid Dynamics: A Collective Introduction to Current Research, 2000, pp. 289–345.
[2] P. Linden, The fluid mechanics of natural ventilation, Annu. Rev. Fluid Mech. 31 (1999) 201–238. http://dx.doi.org/10.1146/annurev.fluid.31.1.201.
[3] S. Grossmann, D. Lohse, Fluctuations in turbulent Rayleigh–Bénard convection: the role of plumes, Phys. Fluids 16 (2004) 4462–4472. http://dx.doi.org/10.1063/1.1807751.
[4] J.M. Lopez, F. Marques, Instability of plumes driven by localized heating, J. Fluid Mech. 736 (2013) 616–640. http://dx.doi.org/10.1017/jfm.2013.537.
[5] S. Popinet, Gerris: a tree-based adaptive solver for the incompressible Euler equations in complex geometries, J. Comput. Phys. 190 (2003) 572–600. http://dx.doi.org/10.1016/S0021-9991(03)00298-5.
[6] E. Åkervik, J. Hœpffner, U. Ehrenstein, D. Henningson, Optimal growth, model reduction and control in a separated boundary-layer flow using global eigenmodes, J. Fluid Mech. 579 (2007) 305–314. http://dx.doi.org/10.1017/S0022112007005496.
[7] F. Giannetti, P. Luchini, Structural sensitivity of the first instability of the cylinder wake, J. Fluid Mech. 581 (2007) 167–197. http://dx.doi.org/10.1017/S0022112007005654.
[8] P. Huerre, P. Monkewitz, Local and global instabilities in spatially developing flows, Annu. Rev. Fluid Mech. 22 (1990) 473–537. http://dx.doi.org/10.1146/annurev.fl.22.010190.002353.

J. Fluid Mech. (2015), *vol.* 780, *pp.* 344–369. © Cambridge University Press 2015
doi:10.1017/jfm.2015.478

Local linear stability of laminar axisymmetric plumes

R. V. K. Chakravarthy[1], L. Lesshafft[1,†] and P. Huerre[1]

[1]Laboratoire d'Hydrodynamique, CNRS/École polytechnique, 91128 Palaiseau CEDEX, France

(Received 30 January 2015; revised 21 May 2015; accepted 10 August 2015)

The temporal and spatiotemporal stability of thermal plumes is investigated for laminar velocity and temperature profiles, under the Boussinesq approximation, in the far self-similar region as well as in the region close to a finite-size inlet. In the self-similar case, Prandtl and Grashof numbers are systematically varied, and azimuthal wavenumbers $m = 0$, 1 and 2 are considered. In the temporal analysis, helical modes of $m = 1$ are found to be dominant throughout the unstable parameter space, with few exceptions. Axisymmetric modes typically present smaller growth rates, but they may dominate at very low Prandtl and Grashof numbers. Double-helical modes of $m = 2$ are unstable over a very restricted range of parameters. Only the helical $m = 1$ mode is found to ever become absolutely unstable, whereas $m = 0$ and $m = 2$ modes are at most convectively unstable. In a temporal setting, an analysis of the perturbation energy growth identifies buoyancy- and shear-related mechanisms as the two potentially destabilizing flow ingredients. Buoyancy is demonstrated to be important at low Grashof numbers and long wavelengths, whereas classical shear mechanisms are dominant at high Grashof numbers and shorter wavelengths. The physical mechanism of destabilization through the effect of buoyancy is investigated, and an interpretation is proposed. In the near-source region, both axisymmetric and helical modes may be unstable in a temporal sense over a significant range of wavenumbers. However, absolute instability is again only found for helical $m = 1$ modes.

Key words: absolute/convective instability, buoyancy-driven instability, plumes/thermals

1. Introduction

The present paper investigates the local stability properties of round laminar plumes under the Boussinesq approximation. With these premises, the analysis pertains to physical situations where viscous forces are significant, and where density variations are sufficiently small. Examples of such situations are magma flows, saline jets, convective CO_2 transport in water, under-ice convection and algae suspensions (see Thorpe 2005; Lombardi *et al.* 2011; Nadal *et al.* 2011, and references therein).

The velocity field of a steady plume resembles that of a jet, with the fundamental difference that a jet emerges from a nozzle with a given amount of streamwise momentum, which merely diffuses radially as the fluid convects downstream, whereas

† Email address for correspondence: lesshafft@ladhyx.polytechnique.fr

the buoyancy in a plume flow continues to generate vertical momentum at any streamwise station. With regard to unsteady dynamics, buoyancy may provide new mechanisms of perturbation growth in addition to the well-known shear instabilities that are present in jets.

Mollendorf & Gebhart (1973) investigated the spatial stability of a self-similar plume, although in a simplified framework where buoyancy effects were accounted for by adding a small forcing parameter to a non-buoyant jet analysis, thereby avoiding the solution of the coupled system of temperature and momentum equations. A spatial analysis was performed for Prandtl numbers $Pr = 2$ and 6.7. Weak buoyancy was observed to destabilize helical perturbations, with azimuthal wavenumber $m = 1$, but no instability was found for axisymmetric perturbations ($m = 0$). These conclusions were confirmed by the spatial analysis of Wakitani (1980), who solved the fully coupled Boussinesq equations for settings with Prandtl numbers $Pr = 0.7$ and 2, and over a range of Grashof numbers. The observation of stable axisymmetric and unstable helical perturbations is consistent with the instability properties of fully developed non-buoyant jets (Batchelor & Gill 1962).

The first temporal analysis of axisymmetric plumes was performed by Riley & Tveitereid (1984). Their investigation was limited to $Pr = 1$, and the results were congruous with the earlier spatial studies. By resorting to the perturbation kinetic energy equation, it was demonstrated that the instability at low Grashof numbers is mainly driven by buoyancy effects. The absence of a lower branch of the neutral instability curve, i.e. a lower limit on unstable wavenumbers, was attributed to the locally parallel flow assumption. A subsequent non-parallel spatial stability analysis (Tveitereid & Riley 1992) did indeed yield such a lower limit. However, the absolute or convective nature of the instability in all these laminar base flows has never been established, and the pertinence of a spatial analysis therefore remains to be proven.

There is ample experimental and numerical evidence for oscillator behaviour in plumes and in related flows, suggesting the presence of absolute instability. The large majority of those settings, however, involve strong density differences outside the realm of validity of the Boussinesq approximation. Subbarao & Cantwell (1992) as well as Cetegen & Kasper (1996) observed self-sustained axisymmetric oscillations in their experiments with helium jets in air. Similar self-excited behaviour has been documented for planar plumes (Cetegen, Dong & Soteriou 1998) and diffusion flames (Maxworthy 1999). Jiang & Luo (2000*a*,*b*) numerically studied the instability dynamics of thermal plumes and of diffusion flames, and they examined the role of buoyancy and baroclinic torque in the vorticity equation in order to explain the occurrence of self-sustained oscillations. Hattori *et al.* (2013) identified an instability of the boundary layer over a heated plate as the cause of sinuous oscillations in the rising planar plume. Satti & Agrawal (2004, 2006*a*,*b*) performed a series of experimental and numerical studies on helium–air mixture injected into pure air. Their results indicate that such jets transition from oscillator- to amplifier-type behaviour as gravity is reduced. However, Lesshafft *et al.* (2006) found oscillator behaviour in light jets in the absence of gravity. For the case of a confined plume inside a cylindrical container, driven by an extended heat source in the bottom wall, Lopez & Marques (2013) documented a succession of bifurcations, through direct numerical simulation, leading from steady laminar flow to turbulence. The first of these bifurcations gives rise to a regular formation of axisymmetric vortices.

Despite all these experimental and numerical studies of intrinsic plume dynamics, the linear global stability of plumes appears to never have been investigated so far. The absolute/convective character of local instability has only been examined by

Lombardi *et al.* (2011) for the case of a planar plume in a stratified environment. The present study extends that analysis to round plumes, without the effect of background stratification, over a large range of Grashof and Prandtl numbers and for azimuthal wavenumbers between 0 and 2. The Boussinesq approximation is employed in order to exclude the effect of the density ratio as an additional parameter.

The paper presents instability results for two different types of base flows: a general self-similar set of velocity and temperature profiles, typical for the flow field far away from a buoyancy source (§ 2), and one specific case of a 'forced' plume close to an inlet (§ 3), which may also be characterized as a buoyant jet. Within each of these sections, the base flow is described first, the linear stability problem is posed, and then the results of temporal and absolute/convective analysis are documented. The physical discussion focuses principally on the temporal instability modes of the self-similar base flow (§ 2.3). Conclusions are summarized in § 4.

2. Self-similar plume

2.1. *Base flow*

A quiescent incompressible fluid is considered, characterized by its temperature T_∞, density ρ_∞, kinematic viscosity ν, volumetric expansion coefficient α, thermal diffusivity κ and conductivity K. All fluid properties are assumed to be independent of temperature. A point source of heat flux Q is introduced into this quiescent medium. Buoyancy then induces a flow in the positive z-direction, opposite to the gravity $-g\boldsymbol{e}_z$.

The governing equations for primitive flow variables are written in the Boussinesq approximation (Tritton 1988):

$$\boldsymbol{\nabla}\cdot\boldsymbol{u}=0, \tag{2.1a}$$

$$\frac{\mathrm{D}\boldsymbol{u}}{\mathrm{D}t}=-\frac{\boldsymbol{\nabla}p}{\rho_\infty}+\nu\nabla^2\boldsymbol{u}-\frac{(\rho-\rho_\infty)g}{\rho_\infty}\boldsymbol{e}_z, \tag{2.1b}$$

$$\frac{\mathrm{D}T}{\mathrm{D}t}=\kappa\nabla^2T, \tag{2.1c}$$

$$\frac{\rho-\rho_\infty}{\rho_\infty}=-\alpha(T-T_\infty). \tag{2.1d}$$

The pressure p includes the hydrostatic correction for $\rho_\infty gz$. Under a boundary-layer type approximation of slow streamwise variations, the steady self-similar base flow is governed by

$$\frac{\partial(ru_z)}{\partial z}+\frac{\partial(ru_r)}{\partial r}=0, \tag{2.2a}$$

$$u_z\frac{\partial u_z}{\partial z}+u_r\frac{\partial u_r}{\partial r}=g\alpha(T-T_\infty)+\frac{\nu}{r}\frac{\partial}{\partial r}\left(r\frac{\partial u_z}{\partial r}\right), \tag{2.2b}$$

$$u_z\frac{\partial}{\partial z}(T-T_\infty)+u_r\frac{\partial}{\partial r}(T-T_\infty)=\frac{\kappa}{r}\frac{\partial}{\partial r}\left[r\frac{\partial}{\partial r}(T-T_\infty)\right], \tag{2.2c}$$

with boundary conditions

$$u_r=\frac{\partial u_z}{\partial r}=\frac{\partial}{\partial r}(T-T_\infty)=0\quad\text{for } r=0, \tag{2.3a}$$

$$u_r,\,u_z,\,(T-T_\infty)\to 0\quad\text{for } r\to\infty. \tag{2.3b}$$

Following Yih (1988), the similarity variables are chosen to be

$$\left.\begin{aligned} \psi &= \nu z f(\eta), \\ T - T_\infty &= \frac{Q}{Kz} h(\eta), \\ \eta &= \frac{r}{z^{1/2}} \left[\frac{\alpha g Q}{K\nu^2}\right]^{1/4}, \end{aligned}\right\} \tag{2.4}$$

where ψ is a streamfunction defined by

$$u_z = \frac{1}{r}\frac{\partial \psi}{\partial r}, \quad u_r = -\frac{1}{r}\frac{\partial \psi}{\partial z}. \tag{2.5a,b}$$

Substituting these variables into (2.2*a*)–(2.2*c*), one obtains

$$\left[\eta \left(\frac{f'}{\eta}\right)'\right]' = -\eta h - f\left[\frac{f'}{\eta}\right]', \tag{2.6}$$

$$\eta h' + Prfh = 0, \tag{2.7}$$

where the prime denotes differentiation with respect to η, and the Prandtl number is defined as $Pr = \nu/\kappa$. The boundary conditions (2.3) become

$$h', f, (f'/\eta)' = 0 \quad \text{for } \eta = 0, \tag{2.8a}$$

$$h, f'/\eta \to 0 \quad \text{for } \eta \to \infty. \tag{2.8b}$$

With the above choice of variables for the similarity transformation, the following scales for length, velocity and temperature have been adopted:

$$R(z) = z^{1/2}\left(\frac{K\nu^2}{\alpha g Q}\right)^{1/4}, \tag{2.9a}$$

$$U = \left(\frac{\alpha g Q}{K}\right)^{1/2}, \tag{2.9b}$$

$$\Theta(z) = Q/Kz, \tag{2.9c}$$

where $R(z)$ defines a measure of the local plume radius. With these scales, the Grashof number is defined as

$$Gr = \frac{g\alpha\Theta(z)R^3(z)}{\nu^2} = \left(\frac{\alpha g Q z^2}{K\nu^2}\right)^{1/4}. \tag{2.10}$$

From (2.4), (2.5) and (2.9), one obtains

$$u_z = U\overline{U}_z = U\frac{f'(\eta)}{\eta}, \tag{2.11}$$

$$u_r = U\overline{U}_r = U\frac{1}{Gr}\left(\frac{f'(\eta)}{2} - \frac{f(\eta)}{\eta}\right), \tag{2.12}$$

$$T - T_\infty = \Theta\overline{T} = \Theta(z)h(\eta). \tag{2.13}$$

Symbols with an overbar denote non-dimensional base flow quantities.

In order to have a unique solution, conservation of the heat flux at any axial location z is imposed. Furthermore, due to the self-similarity assumption, some

boundary conditions in (2.8) are seen to become redundant. The following conditions are retained:

$$f'/\eta \to 0, \quad \text{as } \eta \to \infty, \tag{2.14a}$$

$$f,\ (f'/\eta)' = 0, \quad \text{at } \eta = 0, \tag{2.14b}$$

$$\int_0^\infty f' h \, \mathrm{d}\eta = 1/(2\pi Pr). \tag{2.14c}$$

The base flow for any given Prandtl number can be derived by solving (2.6), (2.7) and (2.14). A closed-form solution to these equations is known only for $Pr = 1$ and 2 (Brand & Lahey 1967; Yih 1988). For all other values, the solution must be constructed numerically as follows (Worster 1986). Guessed values for $f'(\eta)/\eta$ and for h are prescribed at $\eta = 0$, and the equations are integrated outward using a Runge–Kutta algorithm. The guessed values for $f'(\eta)/\eta$ and h at $\eta = 0$ are improved based on the errors incurred in satisfying the boundary conditions (2.14*a*,*c*). The resulting base flow profiles at Prandtl numbers between 0.1 and 10 are shown in figure 1. As Pr increases, both the temperature and the velocity mixing layers become thinner, measured by their vorticity thickness (see solid symbols in figure 1*d*). Yet, remarkably, the maximum value of the shear decreases at the same time (see open symbols in figure 1*d*).

2.2. *Formulation of the linear stability problem*

In the context of local stability analysis, the base flow is assumed to be locally parallel, i.e. the radial velocity u_r given by (2.12) is neglected, and perturbations are assumed to be of the form

$$(\tilde{u}_r, \tilde{u}_\theta, \tilde{u}_z, \tilde{P}, \tilde{T}) = \left[\hat{A}(\eta), \hat{B}(\eta), \hat{C}(\eta), \hat{P}(\eta), \hat{T}(\eta)\right] \mathrm{e}^{\mathrm{i}(kz+m\theta-\omega t)} + \text{c.c.} \tag{2.15}$$

As in any local stability analysis, the locally parallel assumption can be taken as valid as long as the Grashof number is sufficiently large. The limitations of this assumption are critically discussed by Crighton & Gaster (1976) in the context of jets. The axial wavenumber k, which in the following will simply be referred to as the wavenumber, as well as the frequency ω may take on complex values ($\omega = \omega_r + \mathrm{i}\omega_i$), whereas the azimuthal wavenumber m is an integer. The non-dimensional, linearized equations that govern the perturbations are obtained as

$$\eta\hat{A}' + \hat{A} + \mathrm{i}m\hat{B} + \mathrm{i}\eta k\hat{C} = 0, \tag{2.16a}$$

$$\mathrm{i}(k\overline{U}_z - \omega)\hat{A} = -\hat{P}' + \frac{1}{Gr}\left(\hat{A}'' + \frac{\hat{A}'}{\eta} - \left(k^2 + \frac{m^2+1}{\eta^2}\right)\hat{A} - \frac{2\mathrm{i}m\hat{B}}{\eta^2}\right), \tag{2.16b}$$

$$\mathrm{i}(k\overline{U}_z - \omega)\hat{B} = -\frac{\mathrm{i}m\hat{P}'}{\eta} + \frac{1}{Gr}\left(\hat{B}'' + \frac{\hat{B}'}{\eta} - \left(k^2 + \frac{m^2+1}{\eta^2}\right)\hat{B} + \frac{2\mathrm{i}m\hat{A}}{\eta^2}\right), \tag{2.16c}$$

$$\mathrm{i}(k\overline{U}_z - \omega)\hat{C} + \overline{U}_z'\hat{A} = -\mathrm{i}k\hat{P} + \frac{\hat{T}}{Gr} + \frac{1}{Gr}\left(\hat{C}'' + \frac{\hat{C}'}{\eta} - \left(k^2 + \frac{m^2}{\eta^2}\right)\hat{C}\right), \tag{2.16d}$$

$$\mathrm{i}(k\overline{U}_z - \omega)\hat{T} + \overline{T}'\hat{A} = \frac{1}{PrGr}\left(\hat{T}'' + \frac{\hat{T}'}{\eta} - \left(k^2 + \frac{m^2}{\eta^2}\right)\hat{T}\right), \tag{2.16e}$$

where $\overline{U}_z$ and $\overline{T}$ are defined in (2.11) and (2.13).

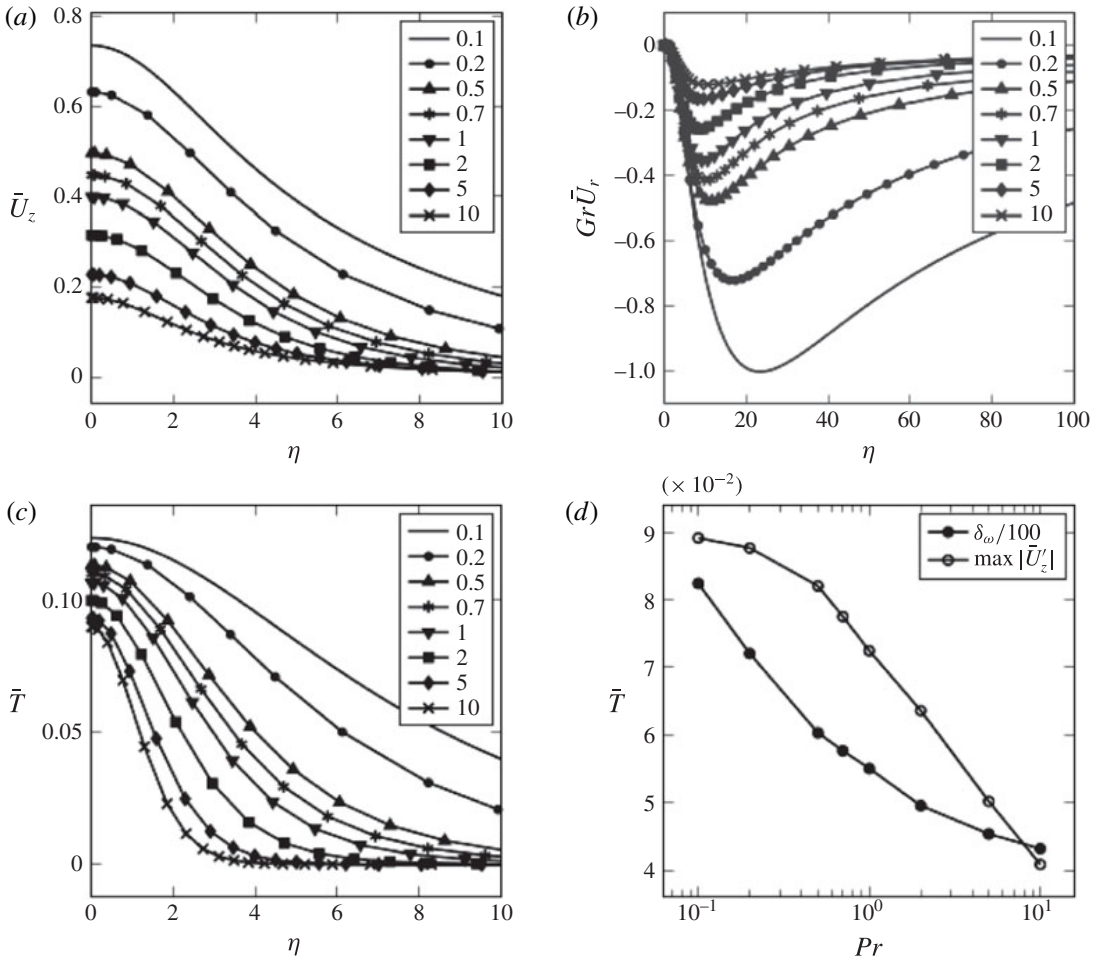

FIGURE 1. Self-similar base flow profiles, computed from (2.11)–(2.13) for various Prandtl numbers as specified in the legend. (*a*) Axial velocity; (*b*) radial velocity; (*c*) temperature; (*d*) vorticity thickness δ_ω of the velocity shear layer (scaled by a factor $1/100$), and maximum value of the velocity gradient.

In the limit $\eta \to \infty$, all perturbations vanish. The boundary conditions on the axis depend on m (Khorrami, Malik & Ash 1989):

$$\text{For } m = 0: \quad \hat{A}(0) = \hat{B}(0) = 0,\ \hat{C}'(0) = \hat{P}'(0) = \hat{T}'(0) = 0, \tag{2.17}$$

$$\text{for } m = \pm 1: \quad \hat{A}(0) \pm \mathrm{i}\hat{B}(0) = 0,\ \hat{A}'(0) = 0,\ \hat{C}(0) = \hat{P}(0) = \hat{T}(0) = 0, \tag{2.18}$$

$$\text{for } |m| > 1: \quad \hat{A}(0) = \hat{B}(0) = \hat{C}(0) = \hat{P}(0) = \hat{T}(0) = 0, \tag{2.19}$$

$$\text{for all } m: \quad \hat{A}(\infty) = \hat{B}(\infty) = \hat{C}(\infty) = \hat{P}(\infty) = \hat{T}(\infty) = 0. \tag{2.20}$$

Equations (2.16) are solved numerically as an eigenvalue problem in ω for given values of k, and for a set of parameters (Pr, Gr, m). The problem is discretized using Chebyshev collocation on a finite interval $0 \leqslant \eta \leqslant \eta_\infty$. The value of η_∞ is prescribed to be at least 5000, and up to 50 000 for very low values of k and Gr. The domain is discretized with 300–350 points for all the cases considered here and the points are distributed using a mapping function (equation (52) in Khorrami *et al.* 1989), which clusters the points close to the axis. Convergence with respect

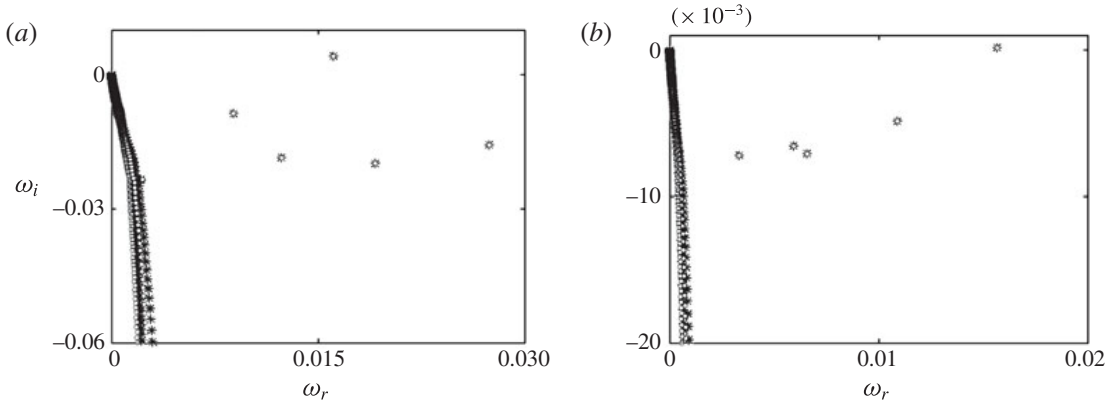

FIGURE 2. Eigenvalue spectrum for the base flow at Prandtl number of 2 for two different resolutions where asterisk markers correspond to 300 discretization points while open circles correspond to 350 points: (*a*) $m = 1$, $Gr = 70$, $k = 0.12$; (*b*) $m = 0$, $Gr = 100$, $k = 0.05$.

to resolution and domain size has been verified. In all cases, at most one unstable discrete eigenmode could be identified, i.e. all other eigenmodes appear to belong to the continuous spectrum. The convergence of the method is demonstrated in figure 2 for two different parameters as an example.

2.3. *Temporal analysis*

2.3.1. *Results*

Temporal analysis is performed on the self-similar base flow for Prandtl number values between 0.1 and 10, and for a range of Grashof numbers between 0.1 and 50 000. Azimuthal wavenumbers $m = 0$, 1, 2 are considered for each (Gr, Pr) combination, and the axial wavenumber k is varied such as to cover the entire unstable range. The principal result from these computations is a set of neutral stability curves, traced in figure 3, representing contour lines of zero growth rate. At nearly all Prandtl and Grashof numbers, the domain of instability of the helical $m = 1$ mode contains the other two modes. An exception to this rule is observed at $Pr \leqslant 0.2$, where instability sets in for axisymmetric $m = 0$ modes at slightly lower Grashof numbers than for $m = 1$ modes. Double-helical $m = 2$ modes are found to be unstable only over quite restricted parameter ranges; higher azimuthal wavenumbers are therefore not considered in this study. For $Pr \geqslant 5$, the double-helical mode is stable at all locations in the k–Gr plane, and therefore there is no neutral curve to be shown for these Prandtl numbers in figure 3.

Another important observation from figure 3 is that the unstable range of wavenumbers in general has no finite lower limit, at least within the considered range of k. As the present numerical method requires k to be finite, a minimum value of 10^{-3} is used. In other words, the neutral curve for $m = 1$ in most cases has no lower branch, and it appears as if instability prevails even in the limit $k \to 0$, for Grashof numbers above a critical value Gr_c that is a function of the Prandtl number. Values of Gr_c, as a function of Pr, are reported in figure 4 for all m. In the absence of a lower branch, Gr_c is taken to be the critical value for $k = 10^{-3}$. The slight precedence of $m = 0$ over $m = 1$ at very low Prandtl numbers is visible in figure 4. Above $Pr = 0.2$, the self-similar plume will always first become unstable to helical perturbations as the Grashof number increases.

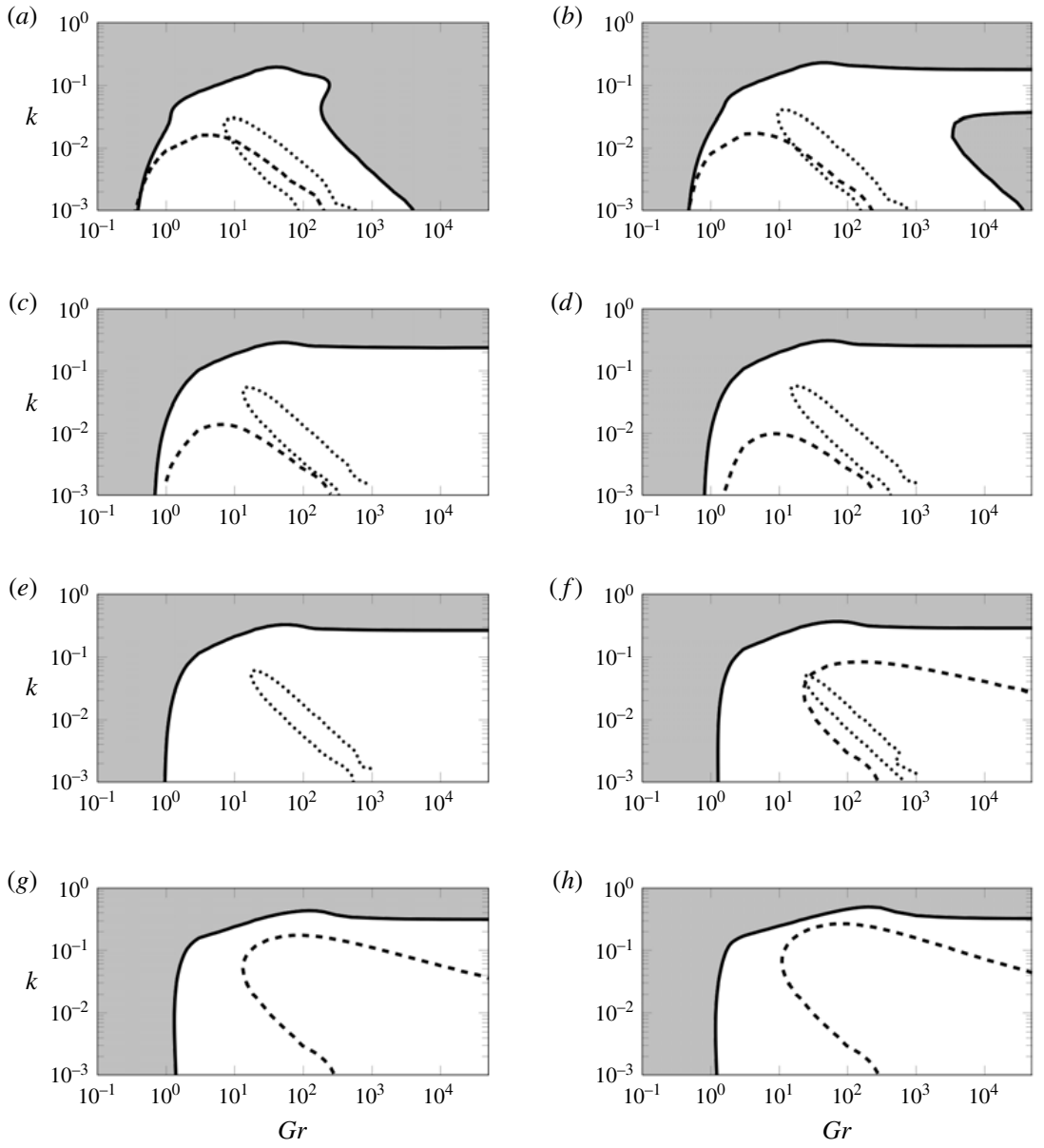

FIGURE 3. Neutral curves for azimuthal wavenumbers $m = 0$ (dashed), $m = 1$ (solid) and $m = 2$ (dotted) at various Prandtl numbers. Shaded regions indicate the parameter space over which the flow is stable to $m = 1$ perturbations: (*a*) $Pr = 0.1$; (*b*) $Pr = 0.2$; (*c*) $Pr = 0.5$; (*d*) $Pr = 0.7$; (*e*) $Pr = 1$; (*f*) $Pr = 2$; (*g*) $Pr = 5$; (*h*) $Pr = 10$.

The neutral curve for $m = 0$ modes in figure 3 shows a peculiar behaviour near a Prandtl number of unity. No unstable axisymmetric mode is found at $Pr = 1$, and the unstable ranges of Gr and k are very different for Prandtl numbers above and below $Pr = 1$. We associate this change with an observation in the context of an asymptotic expansion for large radial distances η. Such a study was attempted, but as it remained inconclusive, it is not presented here in detail. However, it can be reported that the analytically obtained solution for the potentially unstable $m = 0$ mode contains a factor $(Pr - 1)^{-1}$. The present numerical results suggest that this factor indeed causes a

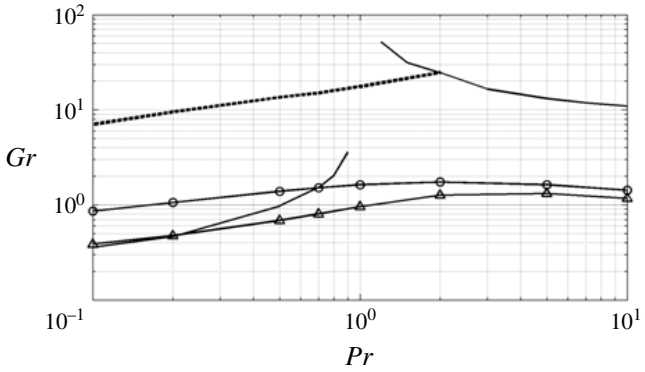

FIGURE 4. Critical Grashof number Gr_c for onset of temporal instability, as a function of Prandtl number Pr, for azimuthal wavenumbers $m = 0$ (solid), $m = 1$ (solid with triangular markers) and $m = 2$ (dashed). The solid line with circular markers denotes the transition from convective to absolute instability for $m = 1$, which will be discussed in § 2.4.

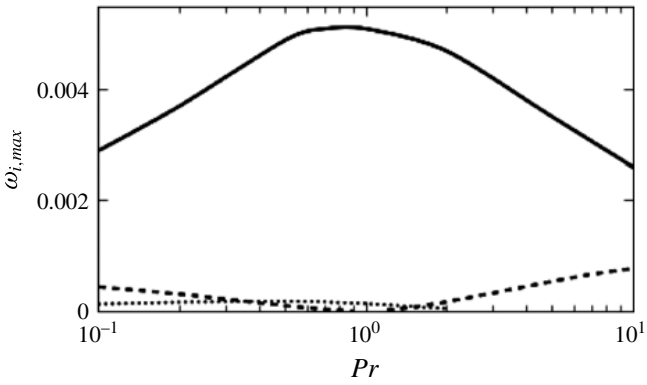

FIGURE 5. Maximum growth rate $\omega_{i,max}$, as a function of Prandtl number Pr, for azimuthal wavenumbers $m = 0$ (dashed), $m = 1$ (solid) and $m = 2$ (dotted).

singularity at $Pr = 1$, separating two regimes of distinct character. The $m = 0$ mode is found to be always stable in the limit $Gr \to \infty$, which implies that the mode is stable to shear mechanisms. This is consistent with the Rayleigh criterion (Batchelor & Gill 1962), which states that, for shear instability to exist in an axisymmetric inviscid non-buoyant flow, the relation

$$\eta_0 \left[\frac{\eta_0 \overline{U}'}{m^2 + k^2 \eta_0^2} \right]' = 0 \tag{2.21}$$

must be satisfied for some point $\eta_0 \in (0, \eta_\infty)$. For the base flow under consideration, expression (2.21) is not satisfied anywhere for the $m = 0$ mode. Therefore, instability is excluded in the inviscid (large Gr) limit by the Rayleigh criterion.

The $m = 1$ mode may be unstable over the largest range of parameters, but nothing has been said so far about the strength of the instability. Figure 5 compares the maximum values $\omega_{i,max}$ reached by the growth rate over all wavenumbers and Grashof

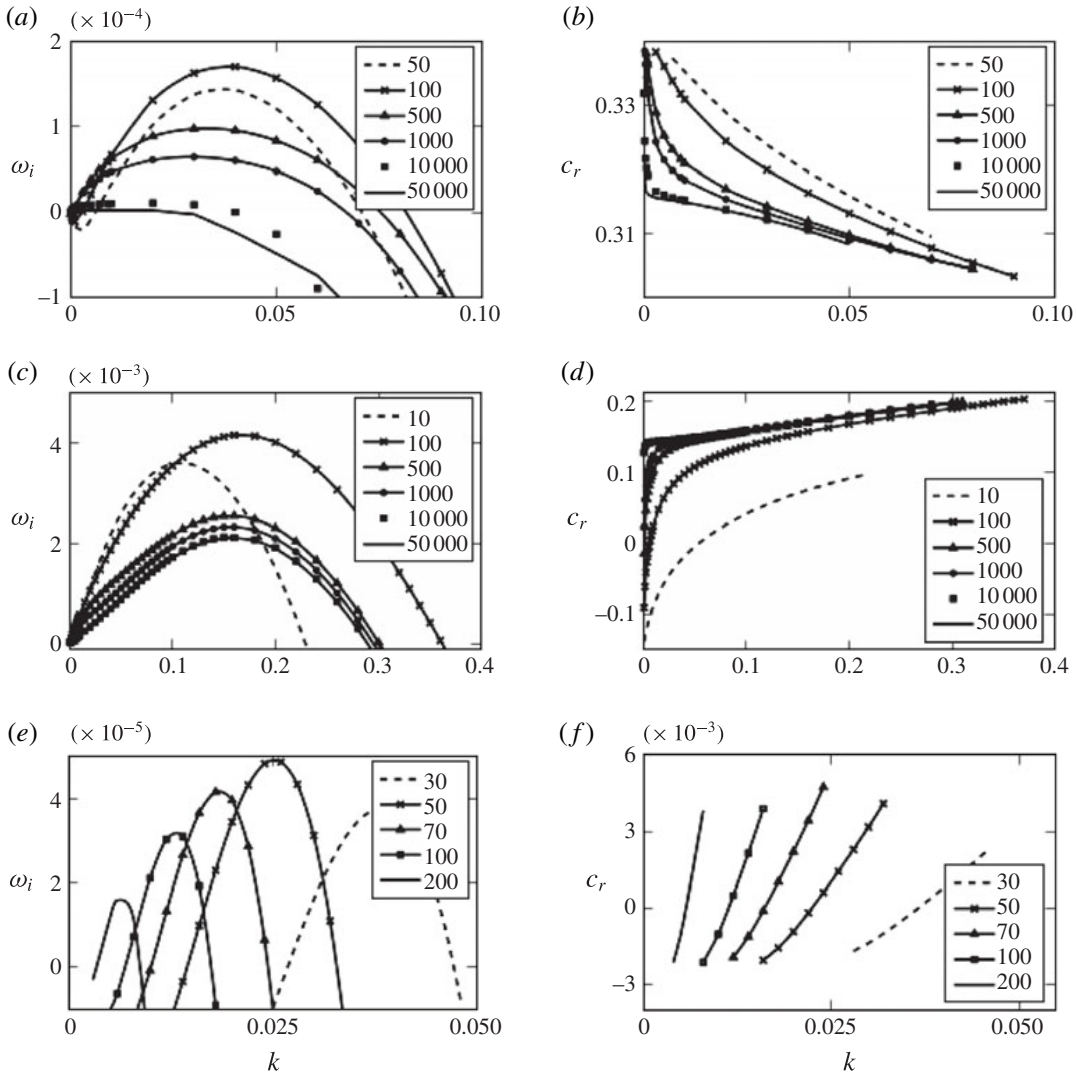

FIGURE 6. Variations of growth rate ω_i and phase velocity c_r with wavenumber k at a Prandtl number of 2 for various azimuthal wavenumbers m and for Grashof numbers indicated in the legend: (*a*,*b*) $m = 0$; (*c*,*d*) $m = 1$; (*e*,*f*) $m = 2$.

numbers, at $m = 0$, 1 and 2, for different Prandtl numbers Pr. Clearly, the $m = 1$ mode also dominates by this measure. The overall maximum is reached at $Pr = 1$, where the axisymmetric mode vanishes. A more detailed comparison is given for $Pr = 2$ in figure 6. Plots to the left show the variations of the growth rate ω_i with k for various values of Gr and for all m; diagrams to the right show the corresponding phase velocities $c_r = \omega_r/k$. The growth rates are consistently largest for $m = 1$ and smallest for $m = 2$.

The phase velocities display several characteristic trends. All axisymmetric modes (figure 6*b*) have phase velocities approximately equal to the base flow centreline velocity $\overline{U}(\eta = 0) = 0.315$ (see figure 1*a*). Unstable helical modes at high Grashof number ($m = 1$, figure 6*d*) display lower phase velocities, corresponding to base flow velocities in the shear layer. The values of c_r at $Gr = 50\,000$ are in fact within 1 % of

the base flow velocity $\overline{U}(\eta_0)$ at the radial station η_0 where the Rayleigh criterion (2.21) is fulfilled, indicating that, in this limit, the instability is predominantly shear-driven. Remarkably, at low values of k and Gr, the phase velocity for $m = 1$ drops sharply and even becomes negative. We do not have a clear explanation for this behaviour at present. Unstable $m = 2$ modes (figure 6*f*) have phase velocities near zero.

2.3.2. *Perturbation energy analysis*

A useful characterization of the various physical mechanisms that affect the stability of the base flow can be inferred from the perturbation energy equation. Following the procedure outlined by Nachtsheim (1963) and adopting the notation of Riley & Tveitereid (1984), the following equations are obtained:

$$2\omega_i \int_0^\lambda \langle \mathrm{KE} \rangle \, \mathrm{d}z = \int_0^\lambda \langle M_u \rangle \, \mathrm{d}z + \int_0^\lambda \langle B \rangle \, \mathrm{d}z - \int_0^\lambda \langle D_u \rangle \, \mathrm{d}z, \tag{2.22}$$

$$2\omega_i \int_0^\lambda \langle \mathrm{TE} \rangle \, \mathrm{d}z = \int_0^\lambda \langle M_t \rangle \, \mathrm{d}z - \int_0^\lambda \langle D_t \rangle \, \mathrm{d}z, \tag{2.23}$$

where

$$\left.\begin{gathered} \mathrm{KE} = \frac{\tilde{u}_r^2 + \tilde{u}_\theta^2 + \tilde{u}_z^2}{2}, \quad \mathrm{TE} = \frac{\tilde{T}^2}{2}, \\ M_u = -(\overline{U}_z)' \tilde{u}_r \tilde{u}_z, \quad B = \frac{\tilde{u}_z \tilde{T}}{Gr}, \quad M_t = -\overline{T}' \tilde{u}_r \tilde{T}, \\ D_u = \frac{\tilde{\chi} \cdot \tilde{\chi}}{Gr}, \quad D_t = \frac{\boldsymbol{\nabla} T \cdot \boldsymbol{\nabla} T}{PrGr}, \\ \langle (\,) \rangle = \int_0^\infty (\,) \eta \, \mathrm{d}\eta, \quad \tilde{\chi} = \boldsymbol{\nabla} \times \tilde{\boldsymbol{u}}, \quad \tilde{\boldsymbol{u}} = (\tilde{u}_r, \tilde{u}_\theta, \tilde{u}_z), \end{gathered}\right\} \tag{2.24}$$

and $\lambda = 2\pi/k$ is the perturbation wavelength. While KE is the perturbation kinetic energy, note that TE only represents an *ad hoc* temperature norm; it is not rigorously defined as the thermal perturbation energy. The quantities D_u and D_t, which represent the dissipation terms associated with viscous and thermal diffusion respectively, are positive definite. The only terms that may give rise to a positive growth rate are therefore M_u, M_t and B. The symbol M_u stands for the work of Reynolds stresses, i.e. shear-related instability mechanisms, B denotes the work of buoyancy, and M_t represents the convective transfer of thermal energy between base flow and perturbations. All these production terms may take on positive or negative values.

In order to compute the various terms in (2.22) and (2.23), the equations are cast in terms of complex eigenfunctions, leading to

$$2\omega_i \langle \mathscr{K} \rangle = \langle \mathscr{M}_u \rangle + \langle \mathscr{B} \rangle - \langle \mathscr{D}_u \rangle, \tag{2.25}$$

$$2\omega_i \langle \mathscr{T} \rangle = \langle \mathscr{M}_t \rangle - \langle \mathscr{D}_t \rangle, \tag{2.26}$$

with

$$\mathscr{K} = \frac{1}{2}(\hat{A}^* \hat{A} + \hat{B}^* \hat{B} + \hat{C}^* \hat{C}), \quad \mathscr{M}_u = -\frac{\overline{U}_z'}{2}(\hat{A}^* \hat{C} + \hat{A} \hat{C}^*), \quad \mathscr{B} = \frac{1}{2Gr}(\hat{C}^* \hat{T} + \hat{C} \hat{T}^*), \tag{2.27a–c}$$

$$\mathscr{D}_u = \frac{1}{Gr}\left[\frac{m^2|\hat{C}|^2}{\eta^2} + k^2|\hat{B}|^2 - \frac{km}{\eta}(\hat{B}^*\hat{C} + \hat{B}\hat{C}^*) + k^2|\hat{A}|^2 + |\hat{C}'|^2 \right.$$
$$- \mathrm{i}k(-\hat{A}^*\hat{C}' + \hat{A}\hat{C}'^*) + \frac{|\hat{B}|^2}{\eta^2} + |\hat{B}'|^2 + \frac{|\hat{A}|^2}{\eta^2} + \frac{\hat{B}^*\hat{B}' + \hat{B}\hat{B}'^*}{\eta}$$
$$\left. - \mathrm{i}m\frac{\hat{A}\hat{B}'^* - \hat{A}^*\hat{B}'}{\eta} - \mathrm{i}\frac{\hat{A}\hat{B}^* - \hat{A}^*\hat{B}}{\eta^2}\right], \tag{2.27d}$$

$$\mathscr{T} = \frac{|\hat{T}|^2}{2}, \quad \mathscr{M}_t = -\overline{T}'\frac{\hat{A}^*\hat{C} + \hat{A}\hat{C}^*}{2}, \quad \mathscr{D}_t = \frac{1}{PrGr}\left[|\hat{T}'|^2 + \left(k^2 + \frac{m^2}{\eta^2}\right)|\hat{T}|^2\right]. \tag{2.27e–g}$$

An asterisk denotes the complex conjugate. Riley & Tveitereid (1984) gave identical expressions for the special case $m = 1$. A typographical error in their expression for $\mathscr{B}$ is corrected above.

Based on the kinetic energy equation (2.25), the separate contributions of buoyancy, shear and viscosity to the flow instability can be quantified. Viscosity is always stabilizing in the present context and will not be further considered. The relative importance of buoyancy and shear for the helical mode instability in the (Gr, k) plane is indicated in figure 7 by the contour lines $\langle\mathscr{B}\rangle/\langle\mathscr{M}_u\rangle = \{0.2, 5\}$. Clearly, buoyancy-related effects dominate at low Grashof numbers, and shear effects dominate at high Grashof numbers. This is expressed in (2.27a–c) by the scaling $\mathscr{B} \sim Gr^{-1}$. The shear-dominated character of the instability at high Grashof numbers is consistent with the accurate prediction of a critical point in η_0, from the Rayleigh criterion (2.21), as observed in § 2.3.1. Figure 7 shows that buoyancy effects gain importance as the wavenumber is lowered. Markers in figure 7 indicate the (Gr, k) combination at which the highest growth rate is reached, as reported in figure 5. Invariably, this combination is found in a region where buoyancy and shear contributions are of similar importance.

Figure 8 compares eigenfunction shapes of two representative modes in the buoyancy-dominated and shear-dominated regimes, respectively, for a Prandtl number $Pr = 2$. The shear mode (thin lines) has significant amplitudes only inside the plume, with peaks in several quantities at the critical point $\eta_0 = 3.2$, whereas the buoyancy mode (thick lines) spreads over a much larger radial distance.

Figure 7 indicates that a higher Prandtl number favours a stronger dominance of buoyancy contributions to the instability at low and moderate Grashof numbers. This trend may be partially ascribed to a base flow effect, as the base flow shear reduces with increasing Pr (see figure 1d). In addition, the thermal dissipation of temperature perturbations is decreased (2.27e–g), which should lead to an increase in $\langle\mathscr{B}\rangle$ (2.27a–c).

In the high Grashof number regime, the unstable range of wavenumbers increases steadily with Pr, as seen in figures 3 and 7. This is easily understood from the fact that the vorticity thickness of the base flow decreases monotonically with the Prandtl number, as thinner shear layers are unstable to a larger band of wavenumbers. However, the complete stabilization at $Pr = 0.1$ cannot be explained from obvious shear instability arguments. The variations in growth rate with wavenumber, at $m = 1$ and for various Prandtl number values, are shown in figure 9. The trends for $Pr \geqslant 1$ are fully consistent with classical results for non-buoyant inviscid shear layers: the unstable range of k grows with increasing Pr, because the vorticity thickness shrinks;

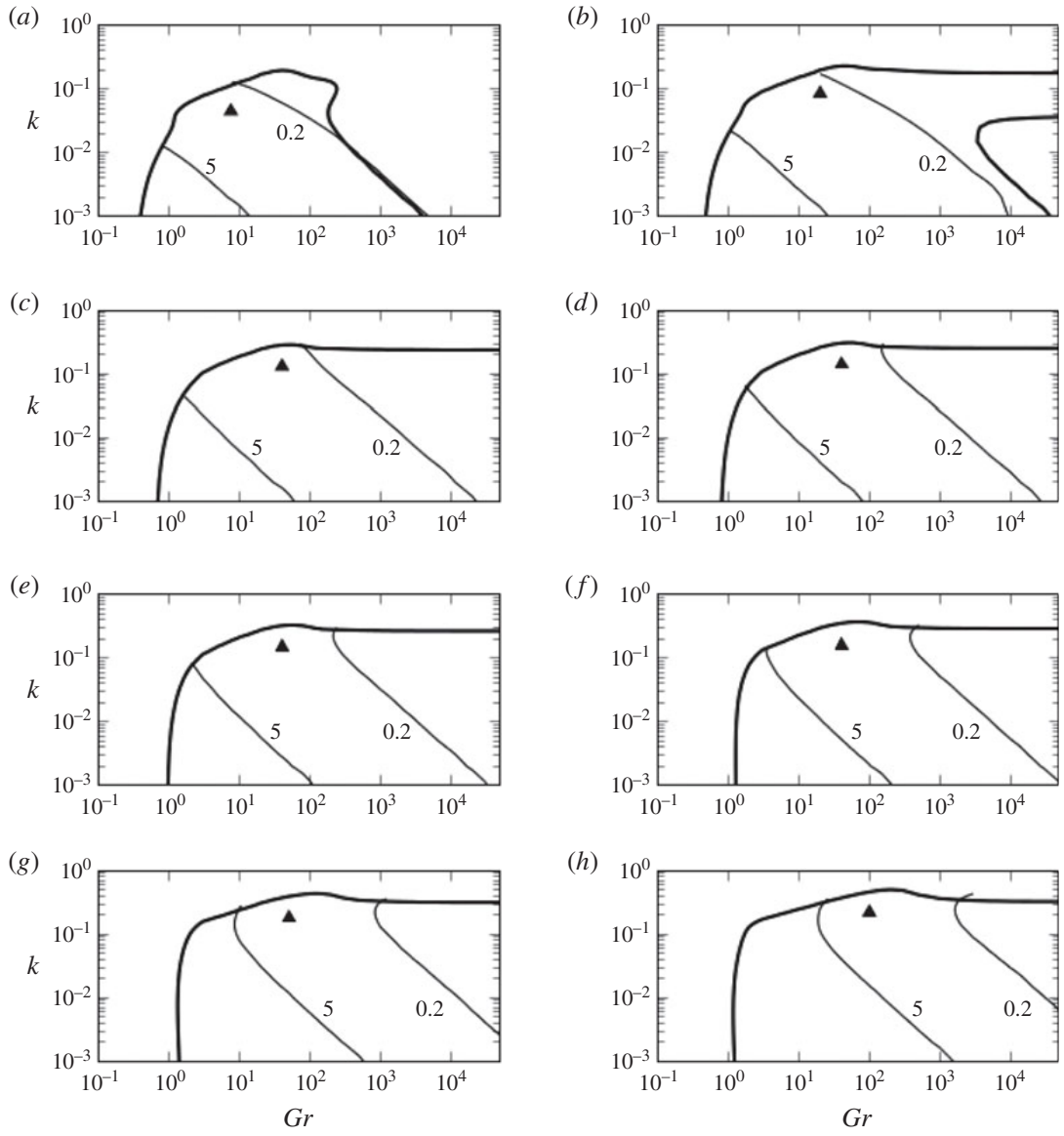

FIGURE 7. Neutral curves for $m=1$ mode instability (thick lines), alongside contour lines $\langle\mathscr{B}\rangle/\langle\mathscr{M}_u\rangle = \{0.2, 5\}$ (thin lines), at various Prandtl numbers. Triangles mark the point of maximum growth rate $\omega_{i,max}$: (*a*) $Pr=0.1$; (*b*) $Pr=0.2$; (*c*) $Pr=0.5$; (*d*) $Pr=0.7$; (*e*) $Pr=1$; (*f*) $Pr=2$; (*g*) $Pr=5$; (*h*) $Pr=10$.

the maximum growth rate diminishes with increasing Pr, because the maximum velocity gradient of the base flow decreases. Yet the latter trend is reversed for $Pr<1$, and lower Prandtl numbers stabilize the flow. It is observed, but not shown here, that the Reynolds stress $u_z'u_r'$ eigenfunction decreases in amplitude at low Prandtl numbers.

Both the $m=0$ and the $m=2$ modes are stable in the inviscid limit of high Grashof numbers (figure 3). According to (2.27*a*–*c*), the buoyant energy production term vanishes as Gr grows large, and the only potential source of instability is the shear term $\mathscr{M}_u$. However, the Rayleigh criterion (2.21) for a cylindrical geometry predicts that all self-similar base flows in the present study are stable with respect

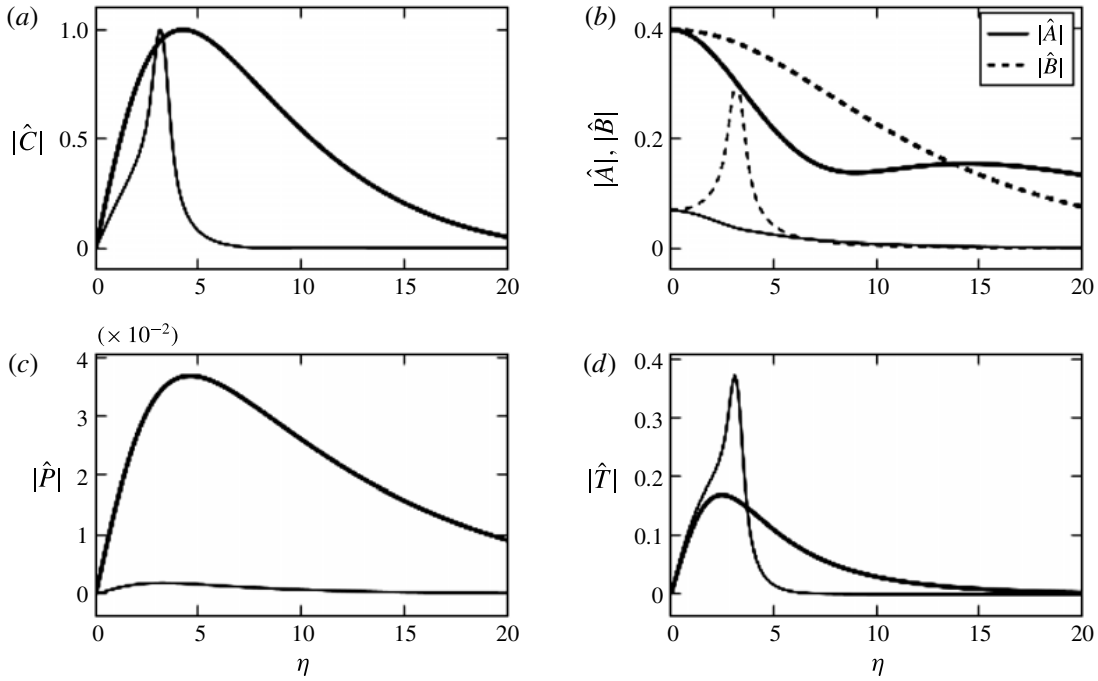

FIGURE 8. Unstable eigenfunctions (absolute values) for $m = 1$, $k = 0.1$ and $Pr = 2$. Thick lines: buoyancy-dominated regime $Gr = 5$; thin lines: shear-dominated regime $Gr = 50\,000$. The eigenfunctions are normalized with respect to their maximum in the axial velocity.

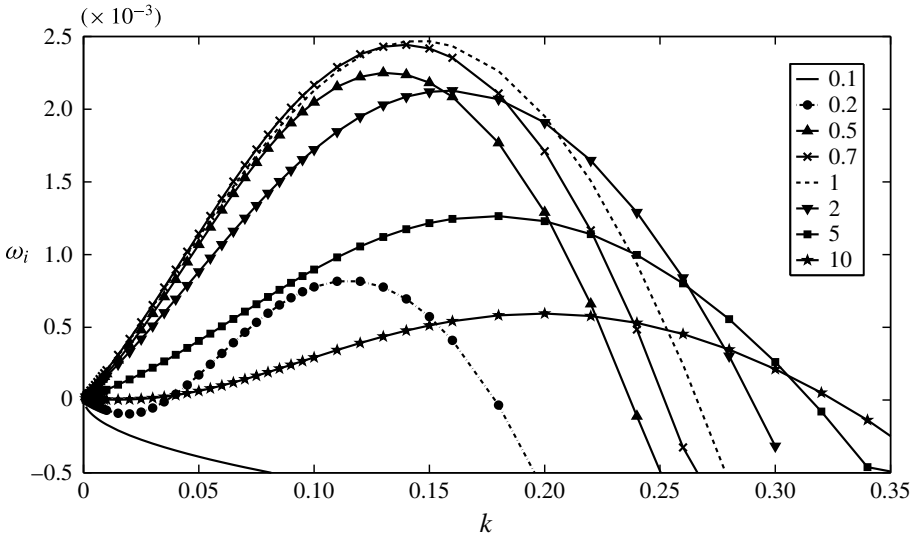

FIGURE 9. Growth rate as a function of wavenumber, for $m = 1$, various Prandtl numbers as indicated in the legend, and $Gr = 50\,000$.

to $m = 0$ perturbations in the inviscid limit. It is confirmed numerically that the term $\langle \mathscr{M}_u \rangle$ takes on negative values for $m = 0$ under all conditions. Any growth of axisymmetric perturbations must be attributed to buoyancy effects.

Shear-related instability of $m = 2$ perturbations cannot be categorically ruled out on the basis of the Rayleigh criterion; however, earlier studies (Batchelor & Gill 1962;

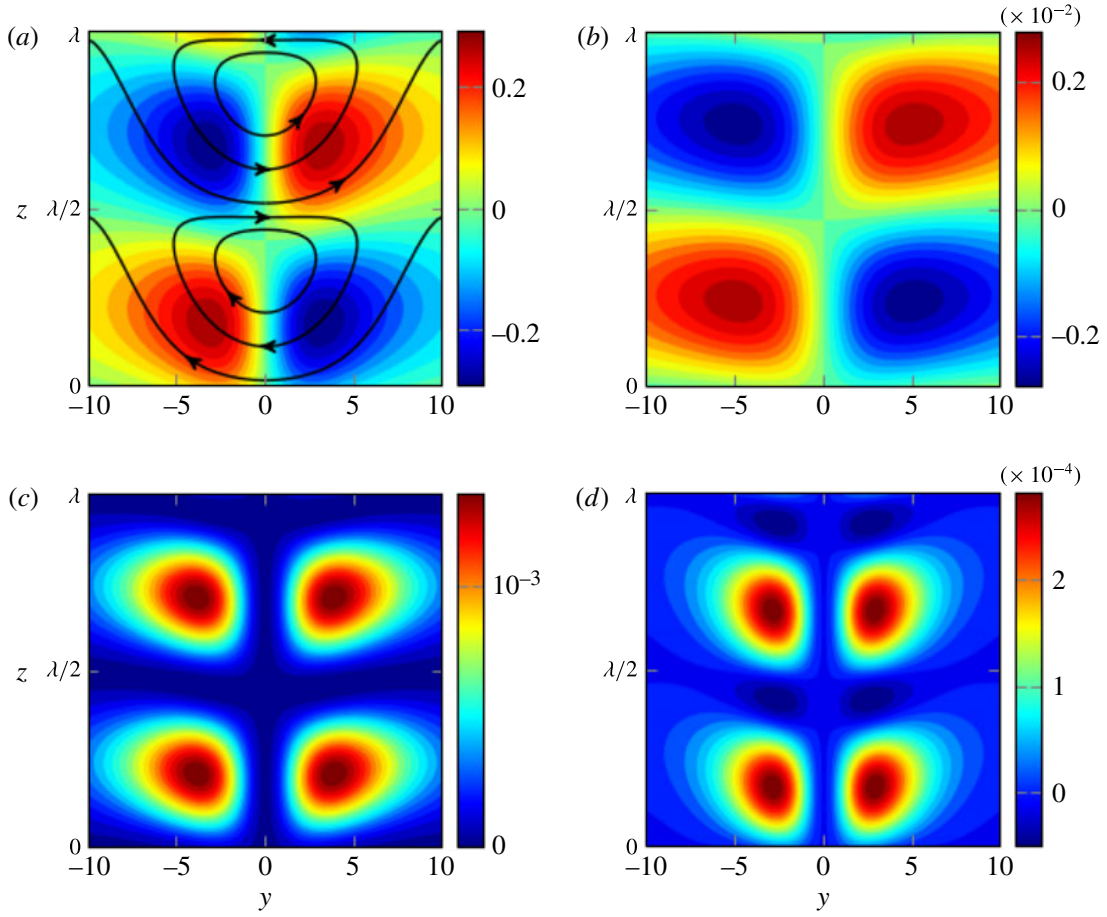

FIGURE 10. (Colour online) Helical $m=1$ eigenmode for parameters $Pr=1$, $Gr=5$ and $k=0.01$. All quantities are shown in a Cartesian plane, with the centreline of the plume at $y=0$. (*a*) Perturbation isotherms and perturbation streamlines; (*b*) perturbation axial velocity; (*c*) buoyancy work B; (*d*) shear-related work M_u.

Mollendorf & Gebhart 1973) on non-buoyant and weakly buoyant jets have found $m=2$ modes to be stable in such flows in the presence of viscosity. Comparison of $\langle \mathscr{M}_u \rangle$ and $\langle \mathscr{B} \rangle$ in the present calculations consistently identifies the buoyant term as the dominant contributor to $m=2$ instability.

2.3.3. *Buoyancy-driven instability mechanism*

While the shear-driven instability at high Grashof numbers is among the most classical phenomena described in the literature (see Drazin & Reid 2004), the buoyancy-driven instability that prevails in the low Grashof number regime deserves some further attention. Insights into the physical mechanisms are sought from an examination of the instability eigenfunctions.

Figure 10 presents contour plots of some relevant perturbation quantities for the case $m=1$, $Pr=1$, $Gr=5$ and $k=0.01$. A Cartesian (y, z) plane is shown for convenience, where y is identical with the radial coordinate η at positive values, and $y=0$ is the centreline of the plume. Perturbation streamlines are superposed on temperature perturbation contours in figure 10(*a*). Note that the true streamlines in an $m=1$ geometry are three-dimensional; for the purpose of our argument, the

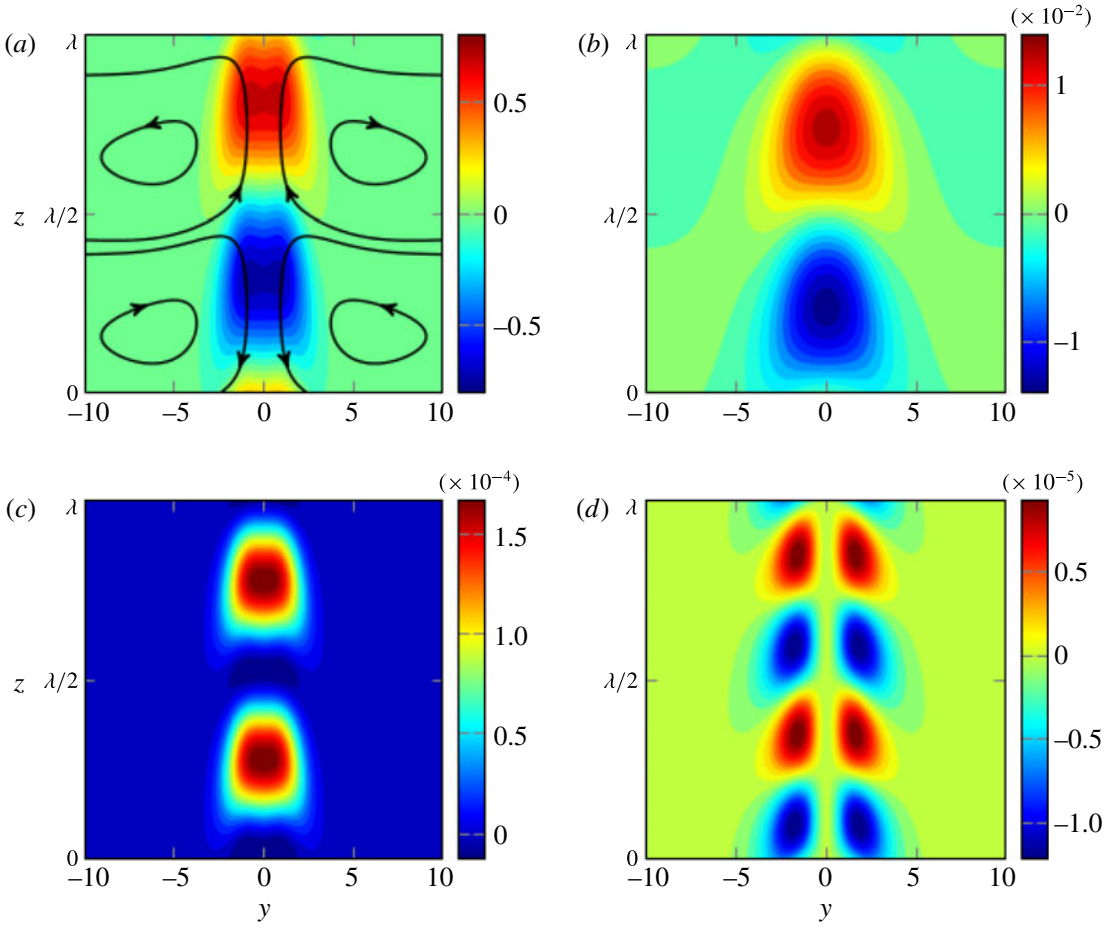

FIGURE 11. (Colour online) Axisymmetric $m = 0$ eigenmode for parameters $Pr = 10$, $Gr = 50$ and $k = 0.1$. All quantities are shown in a Cartesian plane, with the centreline of the plume at $y = 0$. (*a*) Perturbation isotherms and perturbation streamlines; (*b*) perturbation axial velocity; (*c*) buoyancy work B; (*d*) shear-related work M_u.

azimuthal velocity component may be safely ignored, as it does not contribute to the convection of base flow quantities. It is clear from figure 10(*a*) that the perturbation velocity convects hotter fluid from the centreline, where the base flow temperature is maximum, into the regions of positive perturbation temperature. We may therefore interpret this temperature perturbation as an effect of the velocity perturbation. In turn, this temperature perturbation induces a vertical motion (figure 10*b*) that reinforces the circulating flow in the sense of the streamlines. This action of buoyancy therefore constitutes a positive feedback on the fluid motion, providing a plausible scenario for an instability mechanism. Figure 10(*c*) demonstrates that the resulting buoyancy work B is indeed positive everywhere for the chosen parameter combination, i.e. the phase relation between $\tilde{T}$ and $\tilde{u}_z$ is such that the feedback mechanism is destabilizing at every point in space. The shear-related work M_u is visualized in figure 10(*d*). Its net contribution is clearly positive, and therefore destabilizing, but the amplitudes are lower than those of the buoyancy work by a factor of around 5.

A similar situation for an unstable $m = 0$ mode is shown in figure 11. Parameters $Pr = 10$, $Gr = 50$ and $k = 0.1$ are chosen, corresponding to a comparatively strong axisymmetric instability. The perturbation streamlines show the presence of

counter-rotating toroidal vortices. These vortices deform the column of hot fluid, thus leading to positive and negative values of the temperature perturbation along the axis, which in turn drive the vertical convection. Stationary vortices would lead to maximum temperature perturbation at the hyperbolic points, whereas buoyant acceleration would be most efficient with the temperature maxima just between two hyperbolic points. In the case shown in figure 11, the position of temperature maxima is between these two extremes; by virtue of this compromise, temperature perturbations grow due to convection of base flow temperature, and at the same time they drive the convection rolls.

2.4. *Absolute/convective analysis*

Everyday observations, for example in cigarette smoke (van Dyke 1982, figure 107), suggest that laminar plumes may spontaneously bifurcate to a state of periodic oscillations. Such behaviour is usually linked to an absolute instability of the steady flow state. The possibility of absolute instability, in parameter regimes defined by m, Gr and Pr, is investigated in this section.

The absolute instability mode in a given base flow profile (§ 2.1) is identified by tracking a saddle point of the complex-valued function $k(\omega)$, according to the Briggs–Bers criterion (see Huerre & Monkewitz 1985). This analysis turns out to be very delicate in the present flow case, and the following procedure is found to yield the most accurate results: values of ω are computed on a grid of complex k values in an area of interest in the k-plane. The group velocity v_g associated with these modes is obtained as detailed in Lesshafft & Marquet (2010). The saddle point, characterized by zero group velocity, is then identified through successive mesh refinements. A convergence criterion $|v_g| < 10^{-4}$ is used for all results presented here. The absolute instability mode is characterized by its complex frequency ω_0 and its complex wavenumber k_0. If the growth rate $\omega_{0,i}$ is positive, the flow is absolutely unstable.

Absolute instability is found to occur at Grashof numbers above a critical value, $Gr > Gr_{ca}$, which depends on the Prandtl number. The absolute mode is always found to be of the helical type ($m = 1$). Indeed, no convective–absolute transition is observed for any other azimuthal modes over the investigated parameter range. The variation of the critical Grashof number $Gr_{ca}(Pr)$ is presented in figure 4 (circles). Its value is close to unity at all Prandtl numbers.

The variations of ω_0 and k_0 with Grashof number at $Pr = 1$ are shown in figure 12. Transition from convective to absolute instability (sign change in $\omega_{0,i}$) takes place at $Gr_{ca} = 1.627$, and the flow remains absolutely unstable at all $Gr > Gr_{ca}$. As the Grashof number is proportional to the square root of vertical distance (2.10), this transition station will typically be located close to the source. However, both ω_0 and k_0 asymptote to zero as the Grashof number tends to infinity. Very small values of ω and k correspond to perturbations that are quasi-steady in time and quasi-constant in z, and such perturbation modes are difficult to track numerically. The analysis is therefore limited to Grashof number values below 1000.

The near-zero asymptotic variations of both ω_0 and k_0 are rather peculiar, and require a validation. In particular, it must be ascertained that no other undetected saddle point might dominate the long-time dynamics. Three-dimensional time-resolved direct numerical simulations are therefore performed, using the linear evolution equations for perturbations of a parallel base flow. The code of Deloncle (2007) has been adapted to the present problem; typical simulations run over 2000 time

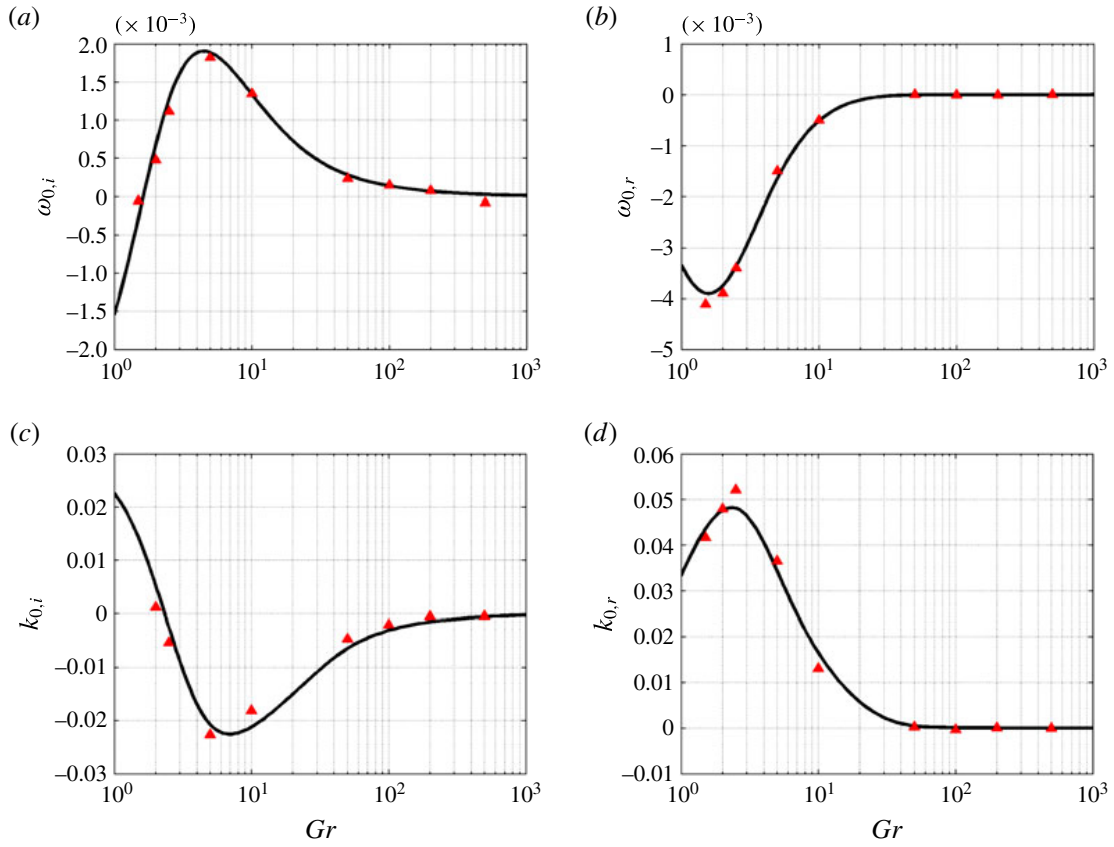

FIGURE 12. (Colour online) Variations of ω_0: (*a*) $\omega_{0,i}$; (*b*) $\omega_{0,r}$ and k_0: (*c*) $k_{0,i}$; (*d*) $k_{0,r}$ as a function of Grashof number at a Prandtl number of unity. Results obtained from eigenvalue problems (——) and from direct numerical simulation of the linear impulse response (▲).

steps on 10^8 grid points. Starting from an initial impulse, the long-time perturbation wavepacket is computed, and the absolute mode is recovered from a spatiotemporal Fourier transform (Delbende, Chomaz & Huerre 1998). The (ω_0, k_0) values obtained with this procedure, represented as triangles in figure 12, clearly validate the results found from direct solution of eigenvalue problems. The eigenvalue procedure is significantly cheaper, and more accurate.

Variations of the absolute growth rate $\omega_{0,i}$ with Grashof number at various Prandtl numbers are displayed in figure 13. The qualitative features do not vary significantly with Pr; in all cases, absolute instability sets in at a Grashof number around 1, and the maximum growth rate is reached shortly after. The overall maximum of $\omega_{0,i}$ is found at $Pr = 1$. The spatial distribution of the eigenfunction for the absolutely unstable $m = 1$ helical mode at absolute wavenumber k_0 is shown in figure 14 for two different Grashof numbers at $Pr = 1$. It is seen that the phase relation between the temperature and velocity perturbations strongly resembles the temporal results shown in figure 10, indicating a similar mechanism for destabilization of the absolute mode. Note that in order to show this correlation between velocity and temperature perturbation clearly, the imaginary part $k_{0,i}$ is set to zero. However, as the imaginary part of k_0 only contributes to the amplitude, the arguments about the phase continue to hold for the actual case of $k_{0,i} \neq 0$.

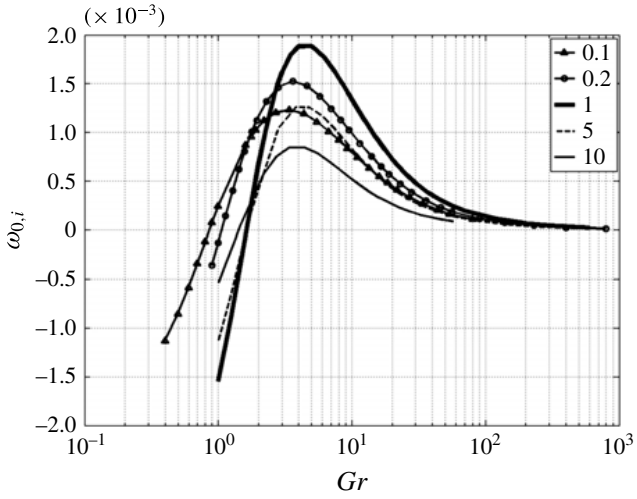

FIGURE 13. Absolute variations in growth rate $\omega_{0,i}(Gr)$ at various Prandtl numbers Pr given in the legend.

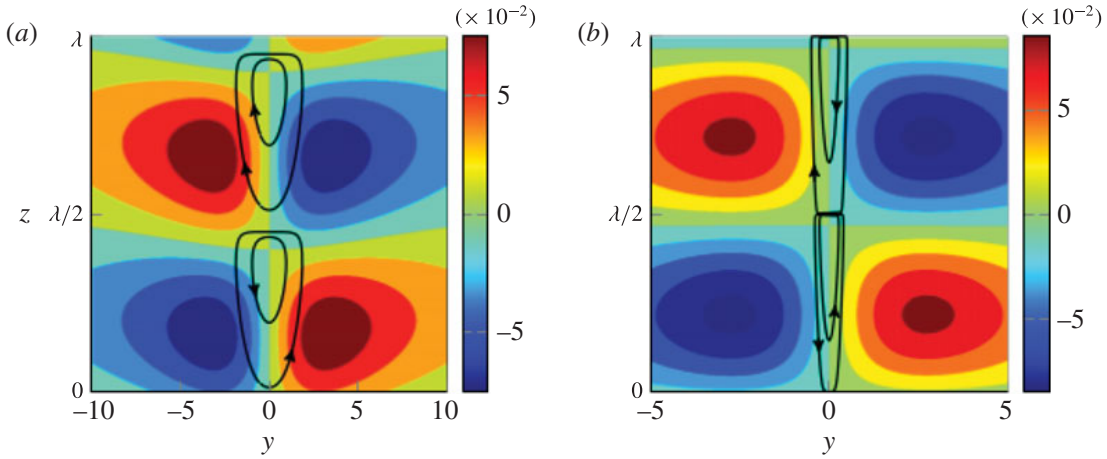

FIGURE 14. (Colour online) Perturbation isotherms and perturbation streamlines for helical $m=1$ eigenmode for $Pr=1$ at the absolute wavenumber k_0 at two different Grashof numbers: (*a*) $Pr=1$, $Gr=4$ and (*b*) $Pr=1$, $Gr=100$. All quantities are shown in a Cartesian plane, with the centreline of the plume at $y=0$.

We surmise that this quasi-steady absolute mode is the local trace of a non-oscillatory global instability mode. If this is the case, then the spatially developing plume is expected to first bifurcate to a new steady flow state that breaks the axial symmetry; in analogy to axisymmetric wakes (Pier 2008; Meliga, Sipp & Chomaz 2010), the result would be a deflected steady flow, which may exhibit secondary oscillatory instabilities. This scenario remains to be confirmed in future studies.

3. Plume near a finite-sized inlet

3.1. *Base flow*

The self-similar base flows investigated in the preceding section represent laminar plumes far away from the buoyancy source. However, as it has been found that the

convective–absolute transition takes place at low Grashof number, i.e. close to the source, the global dynamics are likely to be determined in the near-source region. The defining characteristic of the self-similar flow regime is its generality; upstream of this region, the base flow profiles depend on the specific form of the buoyancy source. Such a source may be a heated body, a jet of light fluid, a flame, or other, and any such configuration would require an individual analysis. In this section, the particular case of hot fluid issuing from a circular orifice is examined. The fluid is injected at $z=0$ with finite momentum; the initial flow near the orifice is therefore a buoyant jet, characterized by a thin shear layer at $z=0$. With increasing distance from the orifice, the velocity profiles are more and more dominated by the momentum that is induced by buoyancy, and the influence of the inlet condition is lost. The self-similar profile shapes of § 2.1 are asymptotically recovered.

Specifically, the following flow configuration is considered: a fluid is injected with a prescribed velocity $u(r)$ and temperature $T(r)$ from an inlet of radius R into a quiescent ambient at temperature T_∞ and density ρ_∞. Non-dimensionalizing the governing equations (2.1) with the centreline axial velocity at the inlet U_c and centreline temperature difference $(T_c - T_\infty)$ at the inlet, one obtains

$$\boldsymbol{\nabla}\cdot\boldsymbol{u}=0, \tag{3.1a}$$

$$\frac{\mathrm{D}\boldsymbol{u}}{\mathrm{D}t}=-\boldsymbol{\nabla}p+\frac{1}{Re}\nabla^2\boldsymbol{u}+Ri(T-T_\infty)\boldsymbol{e}_z, \tag{3.1b}$$

$$\frac{\mathrm{D}T}{\mathrm{D}t}=\frac{1}{PrRe}\nabla^2 T, \tag{3.1c}$$

where Richardson number $Ri = g\alpha R(T_c - T_\infty)/U_c^2$ and $Re = U_c R/\nu$. These are related to the Grashof number from § 2 as $Gr = RiRe^2$. All quantities are made non-dimensional with U_c as the velocity scale, R as the length scale and $(T_c - T_\infty)$ as the temperature scale. The base flow is computed by a Newton–Raphson method, using finite elements as implemented in FreeFEM++ (Garnaud *et al.* 2013), on a domain of size 20×200 in the radial and streamwise directions. Analytic inflow profiles of the form

$$u(r, z=0) = T(r, z=0) - T_\infty = \mathrm{sech}^{20}\left[20\times r^{20}\right], \quad r\leqslant 2, \tag{3.2a}$$

$$u(r, z=0) = T(r, z=0) - T_\infty = 0, \quad r>2. \tag{3.2b}$$

are prescribed at $z=0$, which give a momentum thickness of the shear layer and the thermal mixing layer that is $1/46$ of the orifice radius. At the lateral boundary, vertical velocity is set to zero and temperature is set to T_∞, while a Neumann condition for the radial velocity allows an entrainment influx. Stress-free boundary conditions are imposed at the outlet, and axial symmetry is enforced at $r=0$. Domain convergence is verified on a grid of dimension 50×300.

A single configuration is presented here, with parameters $Pr = 1$, $Re = 100$ and $Ri = 1$. The base flow is documented in figure 15(*a–d*), which shows axial velocity and temperature as a function of r at several streamwise positions, as well as the streamwise development of the centreline values. The asymptotic behaviour of the latter characterizes the approach towards the self-similar solution. It is stressed again that all following results pertain to the very specific case that is considered here as an example.

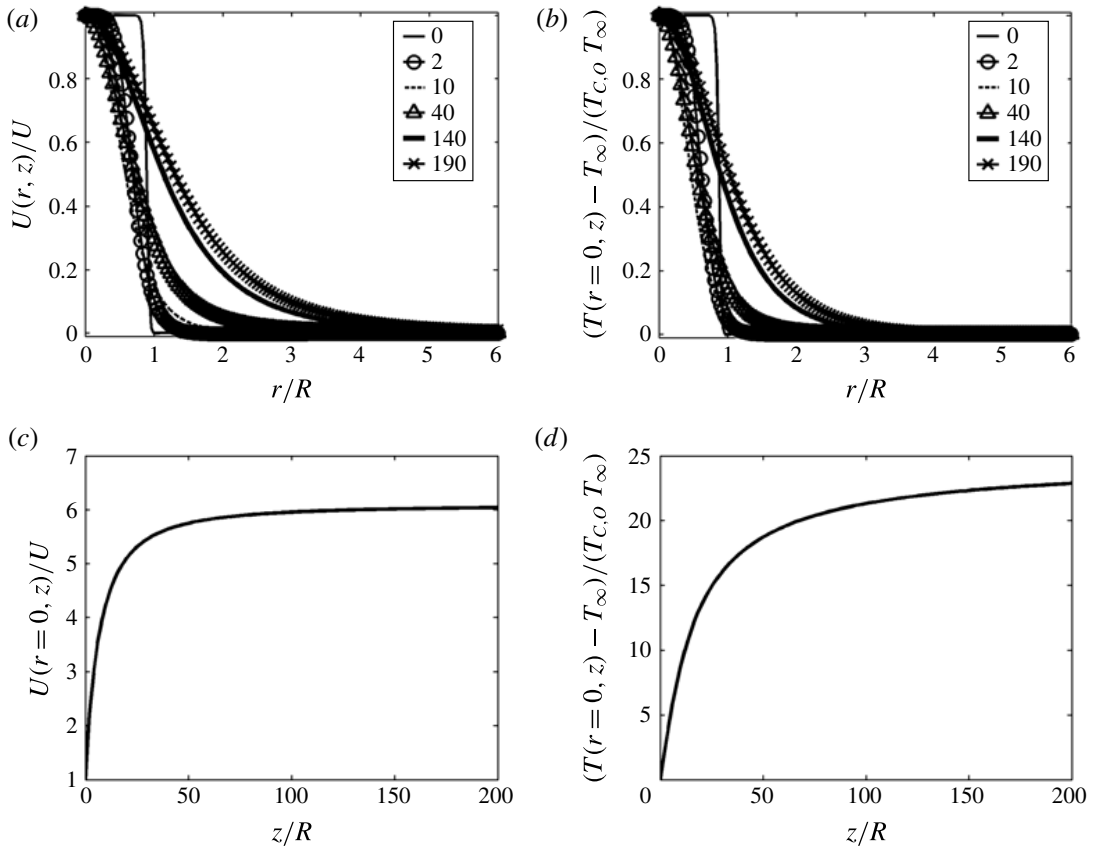

FIGURE 15. Velocity and temperature evolution of the base flow. (*a*) Radial profiles of axial velocity at various streamwise positions indicated in the legend; (*b*) corresponding radial profiles of temperature; (*c*) streamwise development of centreline velocity; (*d*) streamwise development of centreline temperature.

3.2. *Temporal analysis*

The linearized instability equations for a local analysis are identical to (2.16), with the substitutions $\eta \to r$, $Gr \to Re$ in the viscous and thermal diffusion terms, and $Gr^{-1} \to Ri$ in the buoyancy term.

The temporal growth rates as functions of real-valued k are plotted in figure 16 for several vertical positions. Unlike in the self-similar flow, where the helical $m=1$ mode is clearly dominant, axisymmetric and helical modes present similar growth rates in the near-inlet region. The axisymmetric mode then stabilizes rapidly with increasing distance from the inlet. At large distance z, the results are fully consistent with those obtained earlier for the self-similar region: the $m=1$ growth rates at $z=190$ from figure 16 match the corresponding values from the self-similar analysis, at $Gr=630$ and appropriately rescaled, within 1 %.

3.3. *Absolute/convective analysis*

Absolute frequency and wavenumber, as functions of the vertical distance z, are displayed in figure 17 for the helical $m=1$ mode. Also in the present case of a spatially developing base flow with thin initial shear layer, axisymmetric perturbations are found to never become absolutely unstable, just like in the self-similar analysis

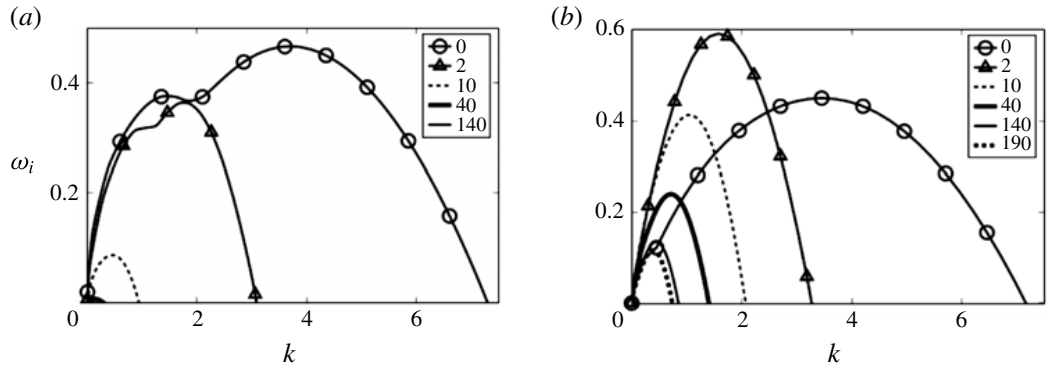

FIGURE 16. Temporal growth rate $\omega_i(k)$ for (*a*) $m = 0$, (*b*) $m = 1$ at various streamwise locations z given in the legend, for the spatially evolving base flow shown in figure 15(*a*).

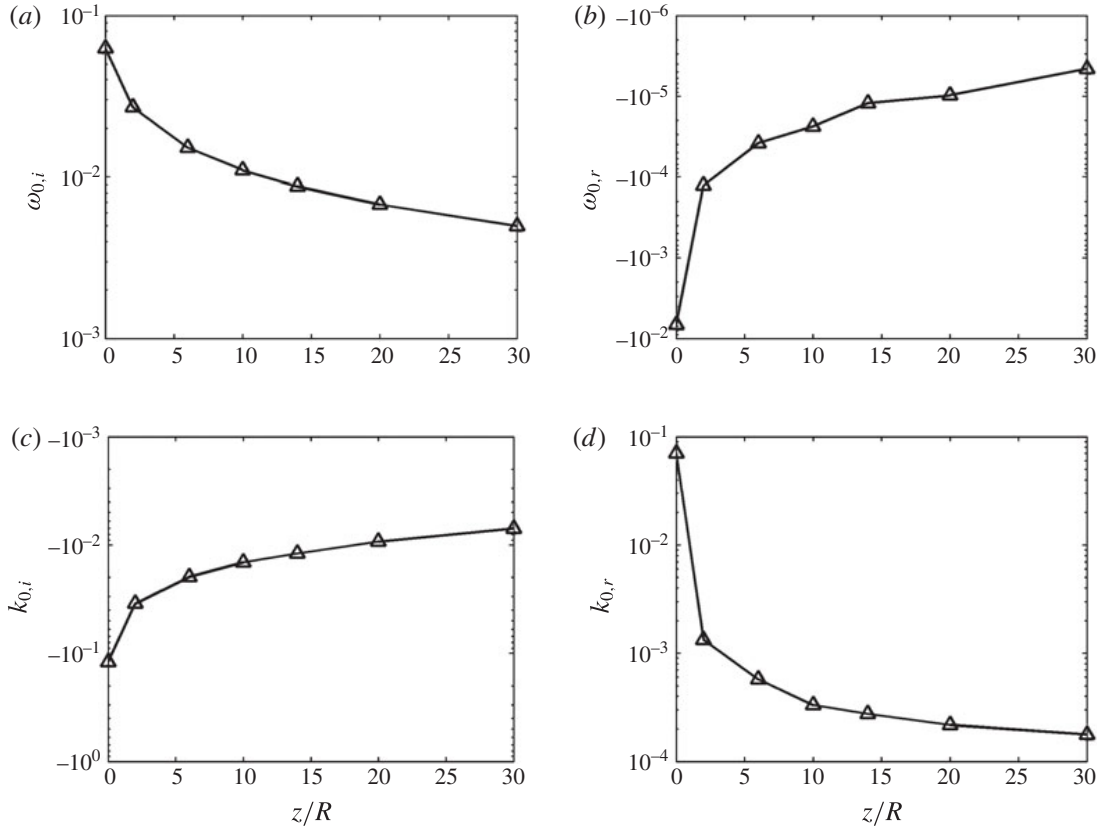

FIGURE 17. Variation of absolute frequency ω_0: (*a*) $\omega_{0,i}$; (*b*) $\omega_{0,r}$ and wavenumber k_0: (*c*) $k_{0,i}$; (*d*) $k_{0,r}$ with streamwise distance.

of § 2.4. However, the helical mode is seen to be absolutely unstable everywhere along z, starting from the inlet. The values of ω_0 and k_0 are again very small, especially at larger distances from the inlet. Saddle points could be reliably identified only down to $z = 40$, due to numerical difficulties that arise when ω_0 and k_0 tend to zero.

All absolute/convective instability results presented herein are markedly different from what is typically found in jet flows (Lesshafft & Huerre 2007). If the present

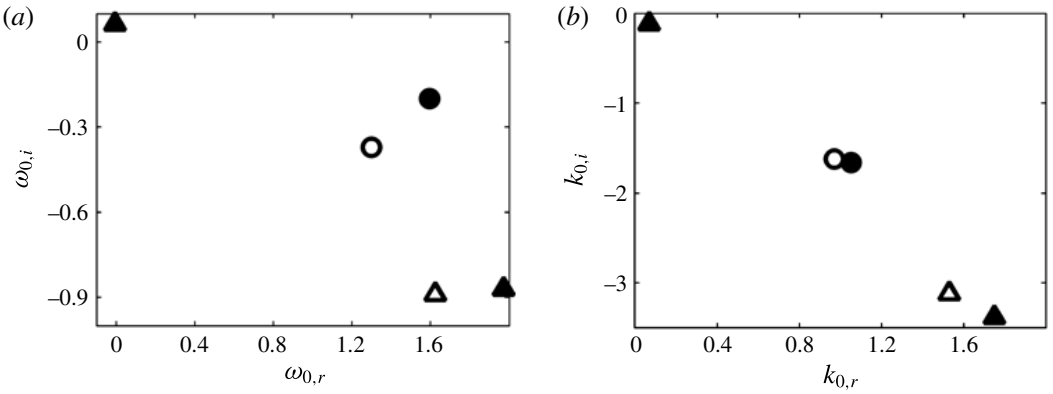

FIGURE 18. Saddle point locations computed for the evolving base flow at the inlet ($z=0$), with parameters $Ri=1$, $Pr=1$ and $Re=100$: (a) in the complex ω-plane; (b) in the complex k-plane. Filled symbols: with buoyancy; open symbols: without buoyancy. Circles: $m=0$ (axisymmetric); triangles: $m=1$ (helical).

analysis is consistent with classical jet results, the described helical absolute instability must arise from the Boussinesq-type buoyancy term. The saddle point represented in figure 17 is the most unstable one, which therefore dominates the long-time behaviour of the linear impulse response, but other saddle points arise as well. Several such saddle points in the complex ω- and k-planes are displayed in figure 18. Open symbols represent saddle points of the inlet profile if buoyancy is completely removed. The addition of buoyancy (filled symbols) shifts the positions of these points moderately, but most importantly it creates a new saddle point, with higher absolute growth rate than all others, that has no counterpart in the non-buoyant case. This is the saddle point that has been described above, the one that causes absolute instability in the plume; it follows that the occurrence of this absolute instability is conditioned by the presence of buoyancy.

4. Conclusions

The local linear stability of laminar plumes has been investigated, first in full detail in the self-similar region far away from the buoyancy source, then for one particular setting in the vicinity of an orifice from which exits a hot fluid with imposed initial momentum. The temporal stability properties as well as the absolute instability modes have been documented over a wide range of Grashof and Prandtl numbers, under the Boussinesq approximation, and the physical origin of the flow instability has been discussed. Shear and buoyancy are the two ingredients that may give rise to instability. With rare exceptions, helical perturbation modes ($m=1$) have been found to dominate the temporal instability properties of the self-similar flow under all conditions. It has been shown for these modes that buoyancy effects drive the instability at low Grashof numbers and wavenumbers, whereas shear effects are prevalent in the high Grashof number and wavenumber regime. The strongest temporal instability is found at intermediate parameters, where the two effects are of comparable strength. For axisymmetric perturbations, the Rayleigh criterion precludes an instability of the self-similar flow profiles by shear mechanisms alone; therefore a destabilization through buoyancy effects is necessarily involved whenever an $m=0$ mode becomes unstable.

Interpretations for the physical mechanisms behind buoyancy-driven instability in plumes have been proposed, both for $m = 0$ and $m = 1$ perturbations, based on the observed eigenfunction shapes. Temperature perturbations induce vortical structures through buoyancy, which in turn convect the base flow temperature. Instability arises if the temperature perturbations and the convection rolls cooperate constructively.

Instability persists down to Grashof number values near unity. However, as instability appears to set in at inaccessibly low values of k, the critical value of the Grashof number could not be determined unambiguously for most Prandtl numbers. It cannot be excluded that zero-wavenumber perturbations are unstable in the limit of zero Grashof number. Yet this question is quite irrelevant for practical purposes, as the parallel base flow hypothesis is not valid at low Grashof numbers and long wavelengths.

Absolute instability arises in all self-similar profiles above a critical Grashof number close to unity. The absolute mode is always of the $m = 1$ type; absolute instability of axisymmetric perturbations has not been observed at any parameter setting in the present investigation. The dominant absolute instability mode is linked to a saddle point of the dispersion relation that only exists due to the buoyancy term in the governing equations; it vanishes if the buoyancy term is removed. However, both the frequency and the wavenumber of the absolute mode are nearly zero, which characterizes this mode as being quasi-steady and quasi-constant in the vertical flow direction. An *ad hoc* interpretation of this result, which will have to be confirmed in future studies, is that this absolute mode is associated with a non-oscillatory global instability of the spatially developing plume. Such an instability is expected to provoke a first bifurcation that leads to a non-axisymmetric steady flow state.

Classical theory predicts that the dynamics of globally unstable flows is dominated by the local properties near the transition station from convective to absolute instability. The results obtained for self-similar plumes suggest that this transition station indeed lies far upstream (at small local Grashof number), where the parallel flow hypothesis may not be well justified. This consideration motivated the investigation of the flow region near a finite-sized inlet. The principal conclusions from this extended investigation are consistent with the observations in the self-similar region. Absolute instability is found only for helical $m = 1$ perturbations, and indeed all throughout the flow domain, starting from the inlet, with very small values of the absolute frequency and wavenumber. The temporal analysis shows that axisymmetric perturbations, although convective, exhibit similarly strong growth rates as their helical counterparts in the jet-like region very close to the inlet. The self-similar behaviour is recovered at a far distance from the inlet.

The dominance of helical modes in the jet-like region, where the shear layer is thin compared to the inlet radius, contrasts with the absolute instability of axisymmetric perturbations in non-buoyant light jets (Monkewitz & Sohn 1988). Experiments as well as numerical simulations of plumes with strong density differences, e.g. Subbarao & Cantwell (1992), Satti & Agrawal (2004) and Jiang & Luo (2000*b*), also show evidence of axisymmetric self-excited instability structures. A major difference between those settings and the present investigation lies in the use of the Boussinesq approximation in this paper, which is valid only for small density variations. In particular, the Boussinesq approximation eliminates the baroclinic torque term from the dispersion relation, which has been shown to be responsible for the occurrence of absolute instability in light jets by Lesshafft & Huerre (2007). We hope to be able to report soon on our ongoing investigation about the influence of the density ratio on the instability characteristics of plumes.

Acknowledgement

R.V.K.C. is supported by a PhD fellowship from École Polytechnique.

REFERENCES

BATCHELOR, G. K. & GILL, A. E. 1962 Analysis of the stability of axisymmetric jets. *J. Fluid Mech.* **14**, 529–551.

BRAND, R. S. & LAHEY, F. J. 1967 The heated laminar vertical jet. *J. Fluid Mech.* **29** (2), 305–315.

CETEGEN, B. M., DONG, Y. & SOTERIOU, M. C. 1998 Experiments on stability and oscillatory behaviour of planar buoyant plumes. *Phys. Fluids* **10** (7), 1658–1665.

CETEGEN, B. M. & KASPER, K. D. 1996 Experiments on the oscillatory behavior of buoyant plumes of helium and helium-air mixtures. *Phys. Fluids* **8** (11), 2974–2984.

CRIGHTON, D. G. & GASTER, M. 1976 Stability of slowly diverging jet flow. *J. Fluid Mech.* **77** (02), 397–413.

DELBENDE, I., CHOMAZ, J.-M. & HUERRE, P. 1998 Absolute/convective instabilities in the batchelor vortex: a numerical study of the linear impulse response. *J. Fluid Mech.* **355**, 229–254.

DELONCLE, A. 2007 Three dimensional instabilities in stratified fluids. PhD thesis, Ecole Polytechnique, Palaiseau, France.

DRAZIN, P. G. & REID, W. H. 2004 *Hydrodynamic Stability*. Cambridge University Press.

VAN DYKE, D. 1982 *An Album of Fluid Motion. p. figure 107*. Parabolic Press.

GARNAUD, X., LESSHAFFT, L., SCHMID, P. J. & HUERRE, P. 2013 Modal and transient dynamics of jet flows. *Phys. Fluids* **25** (4), 044103.

HATTORI, T., BARTOS, N., NORRIS, S. E., KIRKPATRICK, M. P. & ARMFIELD, S. W. 2013 Simulation and analysis of puffing instability in the near field of pure thermal planar plumes. *Intl J. Therm. Sci.* **69**, 1–13.

HUERRE, P. & MONKEWITZ, P. A. 1985 Absolute and convective instabilities in free shear layers. *J. Fluid Mech.* **159**, 151–168.

JIANG, X. & LUO, K. H. 2000*a* Combustion-induced buoyancy effects of an axisymmetric reactive plume. *Proc. Combust. Inst.* **28** (2), 1989–1995.

JIANG, X. & LUO, K. H. 2000*b* Direct numerical simulation of the puffing phenomenon of an axisymmetric thermal plume. *Theoret. Comput. Fluid Dynamics* **14**, 55–74.

KHORRAMI, M. R., MALIK, M. R. & ASH, R. L. 1989 Application of spectral collocation techniques to the stability of swirling flows. *J. Comput. Phys.* **81**, 206–229.

LESSHAFFT, L. & HUERRE, P. 2007 Linear impulse response in hot round jets. *Phys. Fluids* **19** (2), 024102.

LESSHAFFT, L., HUERRE, P., SAGAUT, P. & TERRACOL, M. 2006 Nonlinear global modes in hot jets. *J. Fluid Mech.* **554**, 393–409.

LESSHAFFT, L. & MARQUET, O. 2010 Optimal velocity and density profiles for the onset of absolute instability in jets. *J. Fluid Mech.* **662**, 398–408.

LOMBARDI, M., CAULFIELD, C. P., COSSU, C., PESCI, A. I. & GOLDSTEIN, R. E. 2011 Growth and instability of a laminar plume in a strongly stratified environment. *J. Fluid Mech.* **671**, 184–206.

LOPEZ, J. M. & MARQUES, F. 2013 Instability of plumes driven by localized heating. *J. Fluid Mech.* **736**, 616–640.

MAXWORTHY, T. 1999 The flickering candle: transition to a global oscillation in a thermal plume. *J. Fluid Mech.* **390**, 297–323.

MELIGA, P., SIPP, D. & CHOMAZ, J.-M. 2010 Effect of compressibility on the global stability of axisymmetric wake flows. *J. Fluid Mech.* **660**, 499–526.

MOLLENDORF, J. C. & GEBHART, B. 1973 An experimental and numerical study of the viscous stability of a round laminar vertical jet with and without thermal buoyancy for symmetric and asymmetric perturbations. *J. Fluid Mech.* **61** (2), 367–399.

MONKEWITZ, P. & SOHN, K. 1988 Absolute instability in hot jets. *AIAA* **26**, 911–916.

NACHTSHEIM, P. R. 1963 Stability of free-convection boundary layer flows. *NACA Tech. Rep.* TN D-2089.

NADAL, F., MEUNIER, P., POULIGNY, B. & LAURICHESSE, E. 2011 Stationary plume induced by carbon dioxide dissolution. *J. Fluid Mech.* **719**, 203–229.

PIER, B. 2008 Local and global instabilities in the wake of a sphere. *J. Fluid Mech.* **603**, 39–61.

RILEY, D. S. & TVEITEREID, M. 1984 On the stability of an axisymmetric plume in a uniform flow. *J. Fluid Mech.* **142**, 171–186.

SATTI, R. P. & AGRAWAL, A. K. 2004 Numerical analysis of flow evolution in a helium jet injected into ambient air. *ASME* **2**, 1267–1276.

SATTI, R. P. & AGRAWAL, A. K. 2006*a* Computational analysis of gravitational effects in low-density gas jets. *AIAA* **44** (7), 1505–1515.

SATTI, R. P. & AGRAWAL, A. K. 2006*b* Flow structure in the near-field of buoyant low-density gas jets. *Intl J. Heat Fluid Flow* **27** (2), 336–347.

SUBBARAO, E. R. & CANTWELL, B. J. 1992 Investigation of a co-flowing buoyant jet: experiments on the effect of Reynolds number and Richardson number. *J. Fluid Mech.* **245**, 69–90.

THORPE, S. A. 2005 *The Turbulent Ocean*. Cambridge University Press.

TRITTON, D. J. 1988 *Physical Fluid Dynamics*. Clarendon.

TVEITEREID, M. & RILEY, D. S. 1992 Nonparallel flow stability of an axisymmetric buoyant plume in a coflowing uniform stream. *Phys. Fluids* A **4** (10), 2151–2161.

WAKITANI, S. 1980 The stability of a natural convection flow above a point heat source. *J. Phys. Soc. Japan* **49** (6), 2392–2399.

WORSTER, M. G. 1986 The axisymmetric laminar plume: asymptotic solution for large Prandtl number. *Stud. Appl. Maths* **75**, 139–152.

YIH, C. S. 1988 *Fluid Mechanics*. West River Press.

Identifying the active flow regions that drive linear and nonlinear instabilities

Olivier Marquet[1] **& Lutz Lesshafft**[2]

[1]ONERA/DAFE, 8 rue des Vertugadins, 92190 Meudon, France
[2]Laboratoire d'Hydrodynamique, CNRS/École polytechnique, 91128 Palaiseau, France

(Preliminary version, 14 July 2015)

A new framework for the analysis of unstable oscillator flows is explored. In linear settings, temporally growing perturbations in a non-parallel flow represent unstable eigenmodes of the linear flow operator. In nonlinear settings, self-sustained periodic oscillations of finite amplitude are commonly described as nonlinear global modes. In both cases the flow dynamics may be qualified as being *endogenous*, as opposed to the exogenous behaviour of amplifier flows driven by external forcing. This paper introduces the *endogeneity* concept, a specific definition of the sensitivity of the global frequency and growth rate with respect to variations of the flow operator. The endogeneity, defined both in linear and nonlinear settings, characterizes the contribution of localized flow regions to the global eigendynamics. It is calculated in a simple manner as the local point-wise inner product between the time derivative of the direct flow state and an adjoint mode. This study demonstrates for two canonical examples, the Ginzburg–Landau equation and the wake of a circular cylinder, how an analysis based on the endogeneity may be used for a physical discussion of the mechanisms that drive a global instability. The results are shown to be consistent with earlier 'wavemaker' definitions found in the literature, but the present formalism enables a more detailed discussion: a clear distinction is made between oscillation frequency and growth rate, and individual contributions from the various terms of the flow operator can be isolated and separately discussed. In particular, in the context of nonlinear saturated oscillations in the cylinder wake, such an analysis allows to discriminate between the quasi-linear dynamics of fluctuations around a time-averaged mean flow on one hand and the effect of harmonic interactions on the other hand; the results elucidate why a linear analysis of the mean flow in this particular case provides accurate predictions of the nonlinear dynamics.

1. Introduction

Global instability in flows denotes the possibility of a spontaneous bifurcation from a steady flow state to a time-periodic state of synchronised oscillations in the entire flow field. A commonly observed scenario is that of a supercritical Hopf bifurcation, where linearly unstable perturbations of small amplitude first experience exponential growth, until nonlinear effects lead to amplitude saturation. The final time-periodic flow state is named a nonlinear global mode (Huerre & Monkewitz 1990); the exponentially growing small-amplitude perturbations in the early stage of the bifurcation correspond to eigenmodes of the linearized flow operator, traditionally called linear global modes. The attribute *global* is used here to designate an analysis that resolves all non-homogeneous flow directions, as opposed to a *local* Ansatz, which implies the approximation of locally parallel flow.

Nonlinear global modes are usually obtained as asymptotic oscillatory states from time-resolved numerical simulations, whereas linear global mode analysis requires the solution

of linear eigenvalue problems. Complex eigenvalues represent the temporal growth rate and the oscillation frequency; the associated eigenfunctions characterize the spatial distribution of fluctuation amplitude and phase. Linear global mode analysis is now routinely applied to two- and three-dimensional flow configurations. Beyond the primary question whether or not perturbations at small amplitude are unstable, a physical discussion of linear global modes is usually centered around two questions: (i) what are the physical mechanisms that give rise to unstable growth, and (ii) by what means can instability be reduced or enhanced? The first of these questions addresses the endogenous (or intrinsic) flow behaviour, the second question concerns the control of those dynamics through exogenous (or extrinsic) manipulation.

Huerre & Monkewitz (1990) describe the conceptual notion of a 'wavemaker' (a word first used by Monkewitz 1990) as the region where instability waves are intrinsically generated in globally unstable flows. The interpretation by Koch (1985) of global instability in a wake already uses the same principal idea. Chomaz *et al.* (1991) derive a formal criterion for the global frequency selection in the context of the linear Ginzburg–Landau equation, based on the local absolute instability properties. Their formalism is rooted in a WKBJ approximation of instability wavepackets developing in a weakly non-parallel open flow. Within this approximation, local instability waves with upstream- and downstream-oriented group velocity emanate from a streamwise station, the 'wavemaker' location, where the two mode branches can be matched by means of a non-physical analytic continuation of the dispersion relation, defined as a function of a complex spatial x-coordinate. Such intrinsically generated waves grow and decay as they propagate. While the localized 'wavemaker' selects the frequency and drives the global instability mode, it is in general not characterized by large oscillation amplitudes. The spatial separation of the region where waves are generated and the region where they reach their maximal amplitude is caused by convective instability mechanisms in a local sense, or by the non-normality of the linear Navier–Stokes operator in a global sense (Cossu & Chomaz 1997).

A quantitative theory of frequency selection in *nonlinear* systems, still based on the assumption of slow streamwise flow development and for the Ginzburg–Landau model equation, has been proposed by Couairon & Chomaz (1997) and by Pier *et al.* (1998). These studies draw on the theory of front dynamics (van Saarlos 1988, 1989), leading to the simple criterion that the nonlinear global mode frequency is given to first order by the absolute frequency at the upstream boundary of a (locally) absolutely unstable flow region of finite extent. Subsequent applications to wake flows (Pier & Huerre 2001; Pier 2002; Chomaz 2003) suggest that the accuracy of this criterion is only limited by the non-parallelism of the base flow over the distance of amplitude saturation. The transition from (upstream) convective to (downstream) absolute instability marks the 'wavemaker' location within the framework of this nonlinear model.

Linear global modes in non-parallel flows may now be computed directly, without the need for the hypothesis of slow streamwise development. However, the notion of a cause-and-effect relation between different streamwise regions is lost along with this approximation, and the localisation of a 'wavemaker' region within a global structure must be accomplished through new criteria. The *sensitivity* of the linear eigenvalue (frequency and growth rate) with respect to localized changes of the flow operator provides the appropriate concepts for a formal definition of a global 'wavemaker'. Yet the sensitivity problem may be posed in several ways, depending on the physical premise of what 'drives' an instability.

Giannetti & Luchini (2007) provide a discussion of the cylinder wake instability based on the structural sensitivity of the unstable linear eigenmode. The structural sensitivity,

in their definition, quantifies how an eigenvalue is affected by the introduction of localized forcing of a given perturbation quantity, proportional in strength to the same or another perturbation quantity. It thereby provides a measure in every point in space for the effect of internal feedback between perturbations. Giannetti & Luchini (2007) conjecture that those regions where an altered coupling induces the strongest change of the eigenvalue must also be the most significant regions for the action of internal feedback mechanisms that underpin the genuine eigenmode dynamics. At present, this formalism is arguably the most commonly accepted definition of the 'wavemaker' in a global analysis framework. The concept is quite naturally extended to nonlinear global modes by way of Floquet theory (Luchini *et al.* 2008). However, one inconvenience of this approach is that it does not distinguish between frequency and growth rate, as the Cauchy–Schwarz theorem is invoked in order to define an upper bound for the drift of the *modulus* of the eigenvalue. Another stems from the large number of feedback relations between the various flow quantities that may prove to be significant. The formalism does not allow to single out the influence of specific terms in the flow equations.

Marquet *et al.* (2008) investigate the sensitivity of the linear cylinder wake instability with respect to localized modifications of the base flow. As far as linear instability is linked to the interaction between perturbations and the base flow, it may be argued that such an analysis is well suited to identify the principal flow regions where instability originates. The formalism distinguishes between frequency and growth rate, yet it is clearly cast in the form of a *control* problem. The question how an instability mode is affected by *exogenous* alterations, be it alterations of the internal feedback (Giannetti & Luchini 2007) or of the base flow (Marquet *et al.* 2008), is conceptually different from the question how its *endogenous* dynamics come into being.

The objective of the present paper is to propose a variant of the sensitivity problem for linear as well as nonlinear global modes that identifies more directly those endogenous eigendynamics. For the sake of comparison and validation, these concepts are demonstrated for the two traditional test settings used in the literature on wavemakers: the one-dimensional Ginzburg–Landau equation and the two-dimensional cylinder wake. It is hoped that the formalism will be useful for the analysis of physical instability phenomena in a wide range of applications.

The paper is organised as follows. Section 2 documents linear and nonlinear global mode results for the Ginzburg–Landau equation and for the cylinder wake. This section does not contain genuinely new results, but rather serves as a repertory and review. The configurations discussed here are used in the following as examples in order to demonstrate the proposed formalism. The endogeneity concept is introduced for linear settings in §3, and its application for the analysis of linear global modes is demonstrated for the two example configurations. The extension of the formalism to fully nonlinear situations is laid out in §4. Conclusions are given in §5. An appendix addresses the implications of general inner products for the analysis.

2. Linear, nonlinear, direct and adjoint global modes

The evolution equation of a flow variable $\mathbf{q}(\mathbf{x}, t)$ is considered in the general form

$$\mathcal{B}\,\partial_t \mathbf{q} = \mathcal{N}(\mathbf{q})\,, \tag{2.1}$$

where $\mathcal{N}$ is a nonlinear operator, and $\mathcal{B}$ is an operator of very simple structure that indicates on which component of $\mathbf{q}$ the time derivative applies. In what follows, it will always be assumed that $\mathcal{B}$ is self-adjoint.

A base flow $\mathbf{q}_b$ is a steady solution of the nonlinear equation, $\mathcal{N}(\mathbf{q}_b) = 0$. The linear stability of such a steady base flow is investigated by superposing small-amplitude time-dependent perturbations $\mathbf{q}'$. The dynamics of these perturbations is governed by the linear equation

$$\mathcal{B}\,\partial_t \mathbf{q}' = \mathcal{L}_{\mathbf{q}_b}\mathbf{q}'\,, \tag{2.2}$$

where the linear operator $\mathcal{L}_{\mathbf{q}_b}$ is obtained as the linearisation of $\mathcal{N}$ around the base flow: $\mathcal{N}(\mathbf{q}_b + \epsilon\mathbf{q}') = \mathcal{N}(\mathbf{q}_b) + \epsilon\mathcal{L}_{\mathbf{q}_b}\mathbf{q}'$. Eigenvalues λ_j and associated eigenfunctions $\boldsymbol{\phi}_j(\mathbf{x})$ of $\mathcal{L}_{\mathbf{q}_b}$ are obtained as solutions of the eigenvalue problem

$$\lambda_j\,\mathcal{B}\,\boldsymbol{\phi}_j = \mathcal{L}_{\mathbf{q}_b}\boldsymbol{\phi}_j\,. \tag{2.3}$$

The eigenmodes $\mathbf{q}'_j(\mathbf{x},t) = \boldsymbol{\phi}_j(\mathbf{x})\exp(\lambda_j t)$ form a complete basis for the range of $\mathcal{L}_{\mathbf{q}_b}$. In physical terms, the real and imaginary parts of a complex eigenvalue represent temporal growth rate σ and frequency ω of a linear eigenmode. The convention $\lambda = \sigma - \mathrm{i}\omega$ is adopted here, i.e. the frequency is given by the negative imaginary part of λ.

For the purpose of deriving an adjoint equation associated with the direct equation (2.2), the following inner product of vector-valued functions is introduced:

$$\{\boldsymbol{f}(\mathbf{x},t),\boldsymbol{g}(\mathbf{x},t)\} = \int_0^T\!\!\int_\Omega \boldsymbol{f}^*(\mathbf{x},t)\cdot\boldsymbol{g}(\mathbf{x},t)\,\mathrm{d}\mathbf{x}\,\mathrm{d}t\,, \tag{2.4}$$

where the star denotes the complex conjugate. The adjoint linear operator $\mathcal{L}^\dagger_{\mathbf{q}_b}$ is then derived by requiring

$$\left\{\mathbf{q}^\dagger, \mathcal{B}\,\partial_t\mathbf{q}' - \mathcal{L}_{\mathbf{q}_b}\mathbf{q}'\right\} = \left\{-\mathcal{B}\,\partial_t\mathbf{q}^\dagger - \mathcal{L}^\dagger_{\mathbf{q}_b}\mathbf{q}^\dagger, \mathbf{q}'\right\}. \tag{2.5}$$

The adjoint equation associated with (2.2) is thus found as

$$-\mathcal{B}\,\partial_t\mathbf{q}^\dagger = \mathcal{L}^\dagger_{\mathbf{q}_b}\mathbf{q}^\dagger\,. \tag{2.6}$$

The linear adjoint operator has eigenmodes $\mathbf{q}^\dagger_j(\mathbf{x},t) = \boldsymbol{\phi}^\dagger_j(\mathbf{x})\exp(\lambda^*_j t)$. Adjoint eigenvalues λ^*_j are the complex conjugate values of the corresponding direct eigenvalues λ_j. Adjoint eigenfunctions $\boldsymbol{\phi}^\dagger_j(\mathbf{x})$ satisfy

$$\lambda^*_j\,\mathcal{B}\,\boldsymbol{\phi}^\dagger_j = \mathcal{L}^\dagger_{\mathbf{q}_b}\boldsymbol{\phi}^\dagger_j\,. \tag{2.7}$$

The direct and adjoint eigenfunctions form biorthogonal sets,

$$\langle\boldsymbol{\phi}^\dagger_j, \mathcal{B}\boldsymbol{\phi}_k\rangle = \delta_{jk}\,, \tag{2.8}$$

with respect to the purely spatial inner product

$$\langle\boldsymbol{f}(\mathbf{x}),\boldsymbol{g}(\mathbf{x})\rangle = \int_\Omega \boldsymbol{f}^*(\mathbf{x})\cdot\boldsymbol{g}(\mathbf{x})\,\mathrm{d}\mathbf{x}\,. \tag{2.9}$$

In the definition of Huerre & Monkewitz (1990), a *nonlinear* global mode is a time-periodic solution of the nonlinear evolution equation (2.1), denoted here by $\mathbf{q}_0(\boldsymbol{x},t)$. In the examples considered in the present investigation, such a nonlinear global mode is the limit-cycle solution that is reached as the result of amplitude saturation of an initially growing linear eigenmode. The nonlinear global mode has a real-valued global frequency $\omega_g = 2\pi/T$, with T being the cycle period.

The linear stability of this time-periodic solution is investigated by considering the temporal evolution of small perturbations $\mathbf{q}'(\mathbf{x},t)$, governed by the linear equation

$$\mathcal{B}\,\partial_t\mathbf{q}'(\boldsymbol{x},t) = \mathcal{L}_{\mathbf{q}_0(t)}\,\mathbf{q}'(\boldsymbol{x},t)\,. \tag{2.10}$$

The tangential linear operator $\mathcal{L}_{\mathbf{q}_0(t)}$ is obtained by linearizing the nonlinear operator $\mathcal{N}$ around the time-periodic solution $\mathbf{q}_0(t)$. As $\mathcal{L}_{\mathbf{q}_0(t)}$ is also time-periodic, a fundamental set of solutions to (2.10) is given by $\boldsymbol{\psi}_j(\mathbf{x},t)\exp(\zeta_j t)$ (see Iooss & Joseph 1997). The Floquet modes $\boldsymbol{\psi}_j(\mathbf{x},t)$ are T-periodic in time, and the associated Floquet multipliers $\exp(\zeta_j T)$ characterize the temporal growth or decay of a mode over one cycle period. The real part of ζ_j is in fact the Lyapunov exponent, the imaginary part of ζ_j corresponds to a variation of the fundamental frequency.

An interesting property is that the time derivative of the time-periodic solution, $\partial_t\mathbf{q}_0$, is a neutral Floquet mode of the autonomous periodic operator $\mathcal{L}_{\mathbf{q}_0(t)}$. This property results from the phase invariance of the time-periodic solution. Both $\mathbf{q}_0(\mathbf{x},t)$ and $\mathbf{q}_0(\mathbf{x},t+\delta t)$ represent T-periodic solutions of the nonlinear equation (2.1), therefore their difference $\delta\mathbf{q} = \mathbf{q}_0(\mathbf{x},t+\delta t) - \mathbf{q}_0(\mathbf{x},t)$ is T-periodic as well. A Taylor expansion for small δt gives $\delta\mathbf{q} = \partial_t\mathbf{q}_0(\mathbf{x},t)\delta t$. It follows that $\partial_t\mathbf{q}_0(\mathbf{x},t)$ is a T-periodic solution of (2.10), and is therefore a *neutral* Floquet mode:

$$\boldsymbol{\psi}_1(\mathbf{x},t) = \partial_t\mathbf{q}_0(\mathbf{x},t)\,, \quad \zeta_1 = 0\,. \tag{2.11}$$

An adjoint tangential operator $\mathcal{L}^\dagger_{\mathbf{q}_0(t)}$ can also be defined by requiring

$$\big\{ -\mathcal{B}\,\partial_t\mathbf{q}^\dagger - \mathcal{L}^\dagger_{\mathbf{q}_0(t)}\mathbf{q}^\dagger, \mathbf{q}'\big\} = \big\{\mathbf{q}^\dagger, \mathcal{B}\,\partial_t\mathbf{q}' - \mathcal{L}_{\mathbf{q}_0(t)}\mathbf{q}'\big\}\,, \tag{2.12}$$

from where follows the adjoint equation associated with (2.10),

$$-\mathcal{B}\,\partial_t\mathbf{q}^\dagger(\mathbf{x},t) = \mathcal{L}^\dagger_{\mathbf{q}_0(t)}\mathbf{q}^\dagger(\mathbf{x},t)\,. \tag{2.13}$$

The linear operator $\mathcal{L}^\dagger_{\mathbf{q}_0(t)}$ is also T-periodic. Equation (2.13) has fundamental solutions in the form of adjoint Floquet modes $\boldsymbol{\psi}^\dagger_j(\mathbf{x},t)\exp(\zeta^*_j t)$. The sets $\boldsymbol{\psi}^\dagger_j$ and $\boldsymbol{\psi}_k$ are again biorthogonal, with respect to the spatio-temporal inner product (2.4), such that with a suitable normalisation they fulfill

$$\{\boldsymbol{\psi}^\dagger_j, \mathcal{B}\boldsymbol{\psi}_k\} = \delta_{jk}\,. \tag{2.14}$$

Only the adjoint Floquet mode $\boldsymbol{\psi}^\dagger_1$ associated with the neutral Floquet mode $\boldsymbol{\psi}_1$ and $\zeta_1 = 0$ will be used in the following analysis.

2.1. *Ginzburg–Landau equation*

The Ginzburg–Landau equation has often served as a simple model for flow instability dynamics (Huerre 2000). Its scalar state variable $q(x,t)$ only depends on one spatial coordinate, yet its dispersion relation permits a double branch point that allows to distinguish between absolutely and convectively unstable situations, analogous to open shear flows. The nonlinear Ginzburg–Landau equation is used here in the form

$$\partial_t q = \mathcal{N}(q) = -U\partial_x q + \mu(x)q + \gamma\partial_{xx}q - \beta|q|^2 q\,. \tag{2.15}$$

The operator $\mathcal{B}$, in the general notation (2.1), in this case is simply the identity, and the operator $\mathcal{N}$ is given by the right-hand side in (2.15). It is composed of terms representing convection, linear reactive sources, diffusion, and cubic nonlinearity. Following Cossu & Chomaz (1997), constant convection and diffusion parameters are chosen, $U = 6$ and $\gamma = 1 - i$, while a parabolic variation of the reactive parameter is prescribed as

$$\mu(x) = \mu_0 + 0.5\mu_2 x^2\,. \tag{2.16}$$

Different values of μ_0 will be used in the following, while $\mu_2 = -0.1$ is maintained throughout. This variation yields a strong local stability of the system far from $x = 0$.

All following calculations are performed on an interval $x \in [-40, 40]$, and in all cases the fluctuation amplitudes are indeed negligibly small at the numerical boundaries. The nonlinearity parameter is chosen as $\beta = 1 - \mathrm{i}$, except when linear situations $\beta = 0$ are considered.

2.1.1. *Linear Ginzburg–Landau*

Note that the zero state $q \equiv 0$ is a steady solution of the nonlinear Ginzburg–Landau equation (2.15). Linearisation around that state yields the linear Ginzburg–Landau equation

$$\partial_t q = \mathcal{L}q = -U\partial_x q + \mu(x)q + \gamma\partial_{xx}q\,, \tag{2.17}$$

which is equivalent to (2.15) with $\beta = 0$. A subscript 0 could be attached to $\mathcal{L}$, denoting the zero base state, but this will be omitted in the following. The associated adjoint operator is obtained as

$$\mathcal{L}^\dagger q^\dagger = U\partial_x q^\dagger + \mu(x)q^\dagger + \gamma^*\partial_{xx}q^\dagger\,. \tag{2.18}$$

As derived by Chomaz *et al.* (1987), the leading eigenmodes of the direct problem $\lambda\phi = \mathcal{L}\phi$ and of the adjoint problem $\lambda^*\phi^\dagger = \mathcal{L}^\dagger\phi^\dagger$ are found as

$$\lambda = \mu_0 - \frac{U^2}{4\gamma} - \sqrt{\frac{-\mu_2\gamma}{2}}\,, \tag{2.19}$$

$$\phi(x) = \exp\left(\frac{Ux}{2\gamma} - \sqrt{\frac{-\mu_2}{2\gamma}}\frac{x^2}{2}\right)\,, \tag{2.20}$$

$$\phi^\dagger(x) = \exp\left(-\frac{Ux}{2\gamma^*} - \sqrt{\frac{-\mu_2}{2\gamma^*}}\frac{x^2}{2}\right)\,. \tag{2.21}$$

For fixed values of U, γ and μ_2, the real-valued parameter μ_0 completely determines the eigenvalue, but it has no influence on the eigenfunction shape. The direct and adjoint eigenfunctions are shown in figure 1. Their maxima are located at $x = 8.6$ and $x = -8.6$, respectively. According to Cossu & Chomaz (1997), global instability arises when $\mu_0 > \mu_c$, with a critical value

$$\mu_c = \frac{U^2}{4|\gamma|^2} + \left|\sqrt{\frac{-\mu_2\gamma}{2}}\right|\cos\left(\frac{\arg\,\gamma}{2}\right)\,. \tag{2.22}$$

The local instability properties are given by Chomaz *et al.* (1988). The model is locally stable wherever $\mu(x) < 0$, convectively unstable for $0 < \mu(x) < U^2/4|\gamma|^2$ and absolutely unstable for $\mu(x) > U^2/4|\gamma|^2$. The extent of these regions depends on the value of μ_0.

2.1.2. *Nonlinear Ginzburg–Landau*

Pier *et al.* (1998) report that the Hopf bifurcation in a nonlinear Ginzburg–Landau system is supercritical. Nonlinear global instability therefore follows from linear global instability, $\mu_0 > \mu_c$, and the nonlinear global mode emerges after saturation of the growing linear global mode. A strongly supercritical setting is considered here, with $\mu_0 = 2\mu_c$.

The direct nonlinear global mode is computed by time-stepping (2.15), starting from the linear global mode shape (2.20) as an initial perturbation at low amplitude, until an asymptotic time-periodic state q_0 is reached. The linearisation of Equation (2.15) around the oscillating state q_0 is accomplished as detailed in Hwang (2015). The nonlinear term $\beta|q|^2q$ is properly linearized by augmenting the complex state variable with its complex conjugate, i.e. writing out the nonlinear and linear equations in terms of state vectors $(q, q^*)^T$. In the present study, the direct linear equation is in fact never needed, except

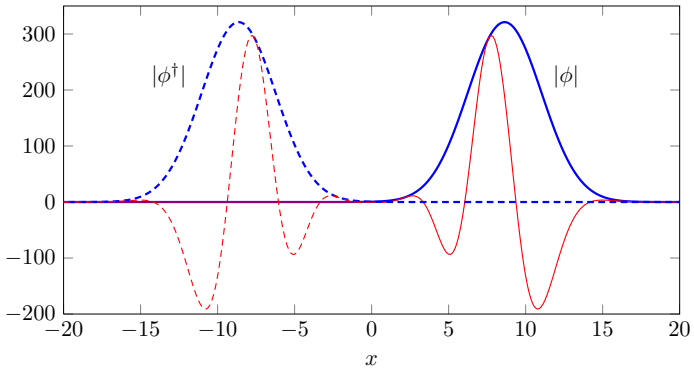

FIGURE 1. Direct and adjoint eigenfunctions (2.20, 2.21) of the linear Ginzburg–Landau equation. Absolute values are shown as thick blue lines, real parts as thin red lines. Solid lines represent the direct mode, dashed lines represent the adjoint mode. The scaling is such that $\langle \phi^\dagger, \phi \rangle = 1$.

for the derivation of the adjoint linear equation,

$$-\partial_t q^\dagger - U\partial_x q^\dagger - \mu q^\dagger - \gamma^* \partial_{xx} q^\dagger - 2\beta^* |q_0(t)|^2 q^\dagger + \beta^* q_0^2(t) q^{\dagger *} = 0\,. \tag{2.23}$$

With the known time-periodic solution $q_0(t)$, this equation is numerically integrated backward in time, until convergence towards a periodic solution $q_1^\dagger$ is reached. The existence of such an asymptotic solution is guaranteed, because this is the adjoint Floquet mode associated with the neutral direct Floquet mode q_1, defined as the time-derivative of the nonlinear time periodic solution $q_1 = \partial_t q_0$. Details on Floquet theory can be found in Iooss & Joseph (1997).

A Crank–Nicolson scheme is used for the time integration of the nonlinear direct and the associated linear adjoint problem. The use of upwinding finite-difference stencils (seven points) for the spatial discretisation of the direct problem, and downwinding for the adjoint problem, is essential in order to achieve the required numerical accuracy.

Figure 2(a) shows the nonlinear global mode q_0 as it is recovered after transients have disappeared. The amplitude envelope has the emblematic shape of an 'elephant' mode (Pier *et al.* 1998), with a sharp upstream wavefront and a softer downstream decay. According to WKBJ theory, the front should be situated at the upstream boundary of the absolutely unstable region in x. In the present case, absolute instability prevails in the interval $x \in [-10, 10]$, and the foot of the front is indeed placed around $x = -10$. The adjoint Floquet mode, represented in figure 2(b), has significant amplitudes only upstream of the direct wavepacket, with a maximum near $x = -13$.

It is to be noted that the nonlinear global mode of the Ginzburg–Landau equation only contains one single frequency, because the nonlinear term is of such a form that it does not generate harmonics. As a result, the time signal in each point shows pure sinusoidal oscillations with zero mean. This property proves to be very convenient for all further discussion, whereas the harmonics and the non-zero mean oscillations that are characteristic for the nonlinear dynamics of the Navier–Stokes equations add further complexity to the analysis (see §4.4).

2.2. *Two-dimensional cylinder wake*

The wake of a cylinder is the most commonly used example of an oscillator-type shear flow. The critical Reynolds number for onset of self-sustained vortex shedding, $Re_c = 47$ according to the experiments by Provansal *et al.* (1987), has been repeatedly recovered

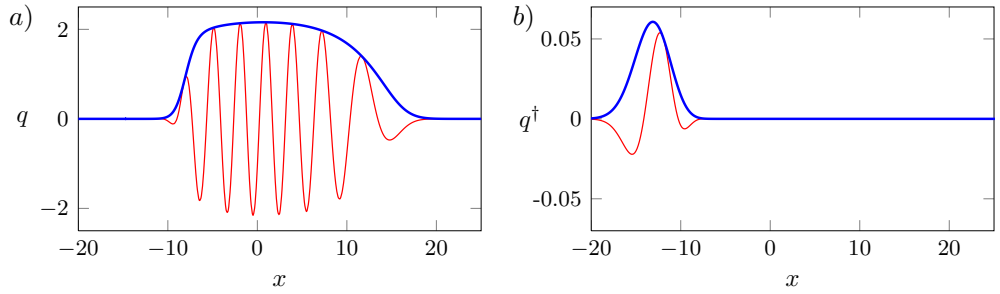

FIGURE 2. *a*) Direct nonlinear global mode of the Ginzburg–Landau equation, with parameters as given in the text. Thick blue line: amplitude envelope; thin red line: snapshot of the real part of q. *b*) Associated neutral adjoint Floquet mode. Same line styles as in *a*.

with high precision as the critical value for the onset of linear global instability (see for instance Barkley 2006; Sipp & Lebedev 2007). Furthermore, the nonlinear global instability of wakes is rather accurately predicted by local theory (Pier 2002; Chomaz 2003). The cylinder wake has been chosen to illustrate the sensitivity studies by Giannetti & Luchini (2007), by Marquet *et al.* (2008), by Luchini *et al.* (2008) and by Luchini & Bottaro (2014). The case at $Re = 80$, well above the instability threshold, is considered in the present study.

In the general notation (2.1), the state vector $\mathbf{q} = (\boldsymbol{u}, p)$ now gathers the velocity vector and the pressure field, which together satisfy the incompressible Navier-Stokes equations, and the operators $\mathcal{B}$ and $\mathcal{N}$ are defined by

$$\mathcal{B} = \begin{pmatrix} \mathcal{I} & 0 \\ 0 & 0 \end{pmatrix}, \quad \mathcal{N}(\mathbf{q}) = \begin{pmatrix} -(\mathbf{u}\cdot\boldsymbol{\nabla})\mathbf{u} - \boldsymbol{\nabla}p + Re^{-1}\boldsymbol{\Delta}\mathbf{u} \\ \boldsymbol{\nabla}\cdot\mathbf{u} \end{pmatrix}. \tag{2.24}$$

2.2.1. *Linear instability of the cylinder wake*

The cylinder wake problem permits a non-trivial steady solution $\mathbf{q}_b = (\mathbf{u}_b, p_b)$, satisfying $\mathcal{N}(\mathbf{q}_b) = \mathbf{0}$, which will serve as a base flow. Linear perturbations $\mathbf{q}' = (\mathbf{u}', p')$ developing on this base flow are governed by the linear equations (2.2) with

$$\mathcal{L}_{\mathbf{q}_b}\mathbf{q}' = \begin{pmatrix} -(\mathbf{u}_b\cdot\boldsymbol{\nabla})\mathbf{u}' - (\mathbf{u}'\cdot\boldsymbol{\nabla})\mathbf{u}_b + Re^{-1}\boldsymbol{\Delta}\mathbf{u}' - \boldsymbol{\nabla}p' \\ \boldsymbol{\nabla}\cdot\mathbf{u}' \end{pmatrix}. \tag{2.25}$$

Eigenmodes of this linear operator are obtained numerically as described in Sipp & Lebedev (2007). Only one unstable mode is found for $Re = 80$, with an eigenvalue $\lambda = \sigma - \mathrm{i}\omega = 0.1018 - 0.7852\mathrm{i}$. The streamwise velocity of the real part of this mode is shown in figure 3(a). The black line represents the stagnation-point streamline of the base flow, demarcating the recirculation region. The streamwise velocity $u^\dagger$ of the associated adjoint eigenmode is displayed in figure 3(b). As discussed in detail by Giannetti & Luchini (2007), Marquet *et al.* (2008) and others, the direct and adjoint eigenmode are localized upstream and downstream of the recirculation region, respectively.

2.2.2. *Nonlinear instability of the cylinder wake*

As the growing linear eigenmode reaches finite amplitude levels, the nonlinear terms become significant and the cylinder wake settles into a saturated periodically oscillating state, the Bénard–von Kármán vortex street. This time-periodic solution $\mathbf{q}_0(\mathbf{x}, t)$ is obtained numerically by time-marching the nonlinear equations with a semi-implicit second-order temporal discretisation, and a spatial discretisation identical to the one used for the eigenvalue problem. At each temporal iteration, an unsteady Stokes problem is

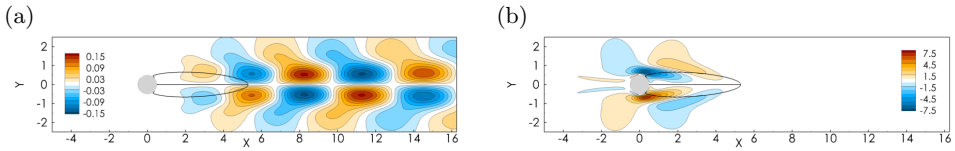

FIGURE 3. Unstable linear eigenmode of the cylinder wake at $Re = 80$. The real frequency is $\omega_r = 0.785$, and the temporal growth rate is $\omega_i = 0.102$. a) streamwise velocity perturbations u of the direct eigenmode; b) adjoint streamwise velocity perturbations $u^\dagger$ of the associated adjoint mode.The black line indicates the recirculation region in the steady flow.

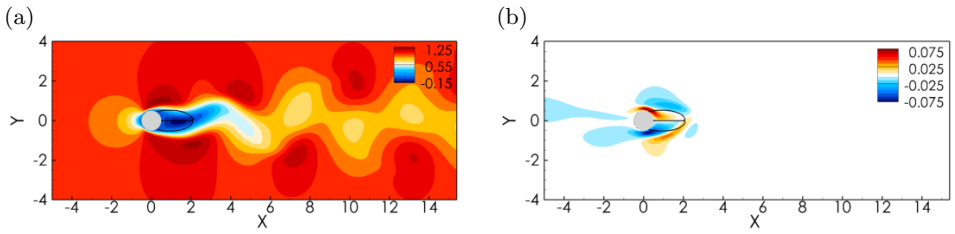

FIGURE 4. Nonlinear global mode of the cylinder wake at $Re = 80$: a) total streamwise velocity $U + u$; b) adjoint streamwise velocity perturbations $u^\dagger$ of the associated adjoint Floquet mode. Both snapshots are taken at the same instant. The black line indicates the recirculation region in the mean flow.

solved with a preconditionned Uzawa algorithm (see Cuvelier *et al.* 1986) implemented in the FreeFem++ software. At $Re = 80$, the global frequency is found to be $\omega_g = 0.9957$, which is to be compared to the frequency of the linear eigenmode, $\omega = 0.7852$. The nonlinear correction to the global frequency is significant in this supercritical setting. A snapshot of the total streamwise velocity of the nonlinear global mode is shown in figure 4(a), where the black line now represents the stagnation-point streamline contour of the time-averaged flow. In the same way as discussed in §2.1.2 for the nonlinear Ginzburg–Landau equation, see (2.13, 2.23), an adjoint mode associated with the neutral Floquet mode of the nonlinear periodic state can be obtained by backward time-stepping of the adjoint tangential equation. Its streamwise velocity component $u^\dagger$ is shown in figure 4(b), taken at the same instant as the direct flow field in figure 4(a).

3. Active flow regions in linear global modes

3.1. *Sensitivity of the eigenvalue*

The sensitivity of an eigenvalue measures how this value varies in response to changes of the operator. In the present context, only *linear* sensitivities are considered, i.e. all variations are assumed to be infinitesimally small. If the original linear equation (2.2) has eigenmodes that satisfy $\lambda_j \mathcal{B}\boldsymbol{\phi}_j = \mathcal{L}\boldsymbol{\phi}_j$, a small perturbation $\epsilon\delta\mathcal{L}$ of the operator leads to a perturbed eigenvalue problem,

$$(\lambda_j + \epsilon\delta\lambda_j)\mathcal{B}(\boldsymbol{\phi}_j + \epsilon\delta\boldsymbol{\phi}_j) = (\mathcal{L} + \epsilon\delta\mathcal{L})(\boldsymbol{\phi}_j + \epsilon\delta\boldsymbol{\phi}_j)\,, \tag{3.1}$$

which at order ϵ can be rearranged to give

$$(\lambda_j\mathcal{B} - \mathcal{L})\,\delta\boldsymbol{\phi}_j = -\delta\lambda_j\mathcal{B}\boldsymbol{\phi}_j + \delta\mathcal{L}\,\boldsymbol{\phi}_j\,. \tag{3.2}$$

The Fredholm alternative states that this inhomogeneous problem in $\delta\boldsymbol{\phi}_j$ has a solution if and only if the right-hand side term is orthogonal to the nullspace of the left-hand side operator, i.e. $\langle\boldsymbol{\phi}_j^\dagger, -\delta\lambda_j\mathcal{B}\boldsymbol{\phi}_j + \delta\mathcal{L}\,\boldsymbol{\phi}_j\rangle = 0$. If the direct and adjoint modes are normalized

such that $\langle \boldsymbol{\phi}_j^\dagger \, , \, \mathcal{B}\boldsymbol{\phi}_j \rangle = 1$, this condition leads to

$$\delta\lambda_j = \langle \boldsymbol{\phi}_j^\dagger \, , \, \delta\mathcal{L}\, \boldsymbol{\phi}_j \rangle \, . \tag{3.3}$$

On the basis of (3.3), Giannetti & Luchini (2007) consider spatially localized perturbations of the operator,

$$\delta\mathcal{L} = \delta(\mathbf{x} - \mathbf{x}_0)\, \mathcal{C}_0 \, , \tag{3.4}$$

where $\mathcal{C}_0$ represents some artificially added coupling between the various flow variables at the location $\mathbf{x}_0$. If $\boldsymbol{\phi}_j(\mathbf{x}_0)$ and $\boldsymbol{\phi}_j^\dagger(\mathbf{x}_0)$ are understood to be vectors containing the n flow variable values at $\mathbf{x}_0$ ($n = 1$ for the Ginzburg–Landau equation and $n = 3$ for the cylinder wake), then $\mathcal{C}_0$ is represented by an $n \times n$ matrix, C_0, and the eigenvalue variation is obtained from (3.3) as

$$\delta\lambda_j\big|_{\mathbf{x}_0} = \boldsymbol{\phi}_j^{\dagger\star}(\mathbf{x}_0) \cdot \mathsf{C}_0 \cdot \boldsymbol{\phi}_j(\mathbf{x}_0) \, . \tag{3.5}$$

Taking the norm of C_0 to be unity without loss of generality, application of the Cauchy–Schwarz theorem yields an upper bound for the modulus of the eigenvalue variation, induced by an operator variation at $\mathbf{x}_0$ (Giannetti & Luchini 2007):

$$|\delta\lambda_j|_{\mathbf{x}_0} \leqslant \|\boldsymbol{\phi}_j^\dagger(\mathbf{x}_0)\| \, \|\boldsymbol{\phi}_j(\mathbf{x}_0)\| \, . \tag{3.6}$$

Marquet *et al.* (2008) define the operator variation in (3.3) specifically as being due to variations δU of the base flow, $\delta\mathcal{L} = (\nabla_U \mathcal{L})\, \delta U$. This definition allows to quantify how a given small modification of the base flow, localized or distributed, alters the frequency ω and the growth rate σ. Both approaches represent the mathematical formulation of a well-posed question, based on different interpretations of what constitutes a 'wavemaker': in the case of Giannetti & Luchini (2007), it is the localized 'internal feedback' between perturbations, whereas in the case of Marquet *et al.* (2008) it is the feeding of perturbation growth on base flow energy. In both approaches, the answer is sought by probing the system with *exogenous* modifications of the operator structure.

3.2. *Endogeneity analysis of linear global modes*

With the question in mind how a localized region in the flow contributes to the global dynamics, we note that the admittance of any arbitrary operator $\mathcal{C}_0$ in (3.4) may be too general for the purpose of identifying the specific interactions that are inherent in the linear Navier–Stokes operator. Retaining the idea of considering the sensitivity of the eigenvalue with respect to *localized* changes of the operator, we stipulate that those changes preserve the local *structure* of the operator. This naturally leads to choosing

$$\delta\mathcal{L} = \delta(\mathbf{x} - \mathbf{x}_0)\, \mathcal{L} \, . \tag{3.7}$$

The variation of the operator at $\mathbf{x}_0$ is chosen to be proportional to the original operator itself in that same location. The sensitivity with respect to such variations quantifies directly how much the eigendynamics in a given point in space contribute to the frequency and to the growth rate; it is therefore suitable for an investigation of the *endogenous* global dynamics. We call this specific sensitivity

$$E(\mathbf{x}) = \boldsymbol{\phi}_j^{\dagger\star}(\mathbf{x}) \cdot \big(\mathcal{L}\boldsymbol{\phi}_j\big)\,(\mathbf{x}) \tag{3.8}$$

the *endogeneity* of the eigenmode $(\lambda_j, \boldsymbol{\phi}_j)$. Its computation is straightforward if the direct and adjoint eigenmodes as well as the operator are available. The dot-product in (3.8) again only denotes the scalar multiplication of two vectors containing the various state variables in one point in space.

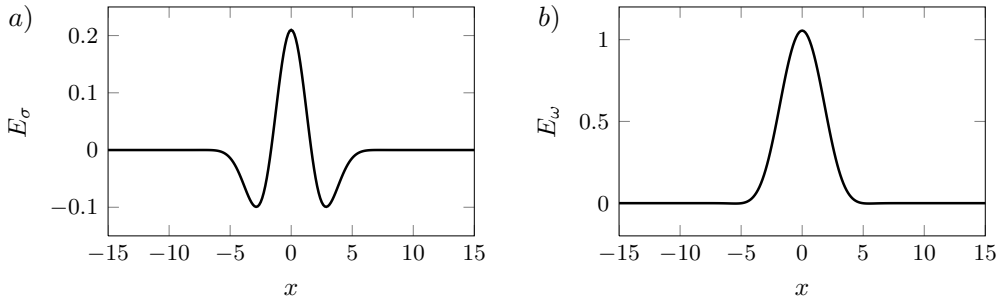

FIGURE 5. Endogeneity distribution of the leading linear Ginzburg–Landau eigenmode. (a) real part E_σ, related to growth rate, (*b*) negative imaginary part E_ω, related to frequency.

An essential property of the endogeneity is that its integral over $\mathbf{x}$ is equal to the eigenvalue λ_j:

$$\int_\Omega E(\mathbf{x})\mathrm{d}\mathbf{x} = \int_\Omega \boldsymbol{\phi}_j^{\dagger\star} \cdot \left(\mathcal{L}\boldsymbol{\phi}_j\right) \mathrm{d}\mathbf{x} = \langle \boldsymbol{\phi}_j^\dagger \,,\, \mathcal{L}\boldsymbol{\phi}_j \rangle = \langle \boldsymbol{\phi}_j^\dagger \,,\, \lambda_j \mathcal{B}\boldsymbol{\phi}_j \rangle = \lambda_j \,. \tag{3.9}$$

It is important to note that, while any spatial distribution can be normalised to yield any integral scalar value, the endogeneity is the unique quantity that represents *local* contributions to the eigenvalue. For instance, the endogeneity allows to exclude any point in space from the integration, and the result reflects how the eigenvalue is altered due to the missing local contribution.

An endogeneity-based analysis clearly distinguishes between the promotion of unstable growth, contained in the real part of $E(\mathbf{x})$, and the frequency selection, given by the negative imaginary part. For the sake of clarity, let

$$E_\sigma(\mathbf{x}) = \Re\left[E(\mathbf{x})\right] \text{ and } E_\omega(\mathbf{x}) = -\Im\left[E(\mathbf{x})\right] \tag{3.10}$$

be defined, such that $E(\mathbf{x}) = E_\sigma(\mathbf{x}) - \mathrm{i}E_\omega(\mathbf{x})$, analogous to $\lambda = \sigma - \mathrm{i}\omega$. The distinction between these two components is of great importance for a physical discussion, and the following examples will show that E_σ and E_ω in general present quite different spatial structures. Furthermore, with the definition (3.8) it is straightforward to decompose the operator $\mathcal{L}$, for instance into convection, diffusion and other terms, and to examine the individual contributions of these separate parts. Such a decomposition will be discussed in §3.4 for the cylinder wake.

3.3. *Example 1: linear Ginzburg–Landau equation*

The endogeneity formalism is first applied to the global instability modes shown in figure 1, with the parameters as given in § 2.1.1. Choosing $\mu_0 = \mu_c$, as defined by (2.22), the system is marginally unstable in a global sense. The endogeneity is found by multiplying $\phi^{\dagger *}$ with $\mathcal{L}\phi$ in every point x, where the eigenfunctions $\phi(x)$ and $\phi^\dagger(x)$ are given analytically by (2.20, 2.21), and the operator $\mathcal{L}$ is written out in (2.17).

Both parts of the endogeneity, E_σ and E_ω, are shown in figure 5: both are even functions, with their maximum values at $x = 0$. The integral of $E(x)$ is exactly equal to the associated eigenvalue, $\lambda = -4.398\mathrm{i}$. In the $E_\sigma(x)$ distribution, shown in figure 5(a), negative and positive regions exactly counterbalance each other, totalling a zero growth rate. The largest contribution to both the frequency selection and the growth rate stems from the region around $x = 0$, not from regions where the magnitude of either the direct or adjoint eigenmodes is large (compare to figure 1).

This result is compared to the saddle point criterion given by Chomaz *et al.* (1991). In

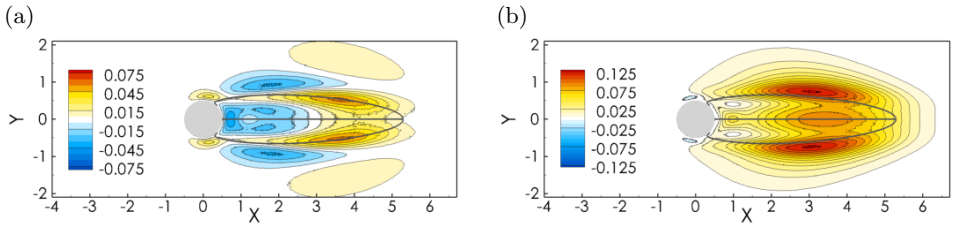

FIGURE 6. Endogeneity distribution of the linear cylinder wake instability. *a*) $E_\sigma(\mathbf{x})$, related to growth rate; *b*) $E_\omega(\mathbf{x})$, related to frequency. The spatial integral of E_σ equals the growth rate $\sigma = 0.102$, the spatial integral of E_ω equals the frequency $\omega = 0.785$.

their model, the 'wavemaker' location is defined by a saddle point of the local absolute frequency ω_0 in the complex x plane, $\partial_x \omega_0 = 0$. In the present case, one finds $\omega_0(x) = i\mu(x) - iU^2/4\gamma$, and therefore $\partial_x \omega_0 = i\partial_x \mu$, with a single saddle point precisely at $x = 0$. The 'wavemaker' location according to the criterion of Chomaz *et al.* (1991) is identical with the *maximally endogenous* location in this example. But whereas their WKBJ-based criterion identifies a singular location, the endogeneity quantifies contributions to the growth rate and the frequency from any point in the domain, thereby characterizing a distributed 'wavemaker'.

3.4. *Example 2: unstable linear global mode of the cylinder wake*

The endogeneity of the unstable linear eigenmode $\boldsymbol{\phi}$ of the cylinder wake, displayed in figure 3(a), is now examined. It is readily computed by point-wise multiplication of the complex conjugate of the adjoint eigenmode $\boldsymbol{\phi}^\dagger$, displayed in figure 3(b), with $\mathcal{L}\boldsymbol{\phi}$ where the definition of $\mathcal{L}$ is given in (2.25). As the divergence of perturbation velocity is zero in every point, the continuity equation along with the adjoint pressure $p^\dagger$ vanishes from the endogeneity definition, and one is left with

$$E(\mathbf{x}) = -\mathbf{u}^{\dagger *} \cdot [(\mathbf{u}_b \cdot \nabla)\mathbf{u}] - \mathbf{u}^{\dagger *} \cdot [(\mathbf{u} \cdot \nabla)\mathbf{u}_b] - \mathbf{u}^{\dagger *} \cdot \nabla p + Re^{-1}\, \mathbf{u}^{\dagger *} \cdot \Delta \mathbf{u}\,, \qquad (3.11)$$

where again it is understood that the left-hand side is to be evaluated in every point $\mathbf{x}$, such that all vectors only contain two scalar elements (x- and y-components). The endogeneity of the linear cylinder-wake instability mode is displayed in figure 6. The distribution of $E_\sigma(\mathbf{x})$, depicted in figure 6(a), shows where the temporal growth rate is generated, whereas $E_\omega(\mathbf{x})$, shown in figure 6(b), indicates how the various flow regions influence the global frequency selection.

A few general conclusions can be inferred from figure 6. Mainly, it is observed that the endogeneity (real and imaginary parts) is concentrated around the shear layers of the separation region, delimited in the figures by black lines. The frequency selection is clearly concentrated in two symmetric maximum locations. This part of the endogeneity resembles the quantity displayed by Giannetti & Luchini (2007) in their figure 17. The distribution of $E_\sigma(\mathbf{x})$ however bears a more faceted structure. Some regions are positive, contributing to global instability, others are negative, thus stabilising the eigenmode. The entire flow downstream of the separation region has practically no influence on frequency and growth rate, consistent with the conclusions of Giannetti & Luchini (2007) and Marquet *et al.* (2008).

A more insightful analysis of physical mechanisms may be based on a decomposition of the endogeneity into contributions from the various left-hand side terms in (3.11). In the given order, these terms account for the effects of base flow convection; production through base flow shear; pressure forces and diffusion. Their spatial distributions (real parts only, reflecting contributions to the growth rate) are shown in figure 7. The effect

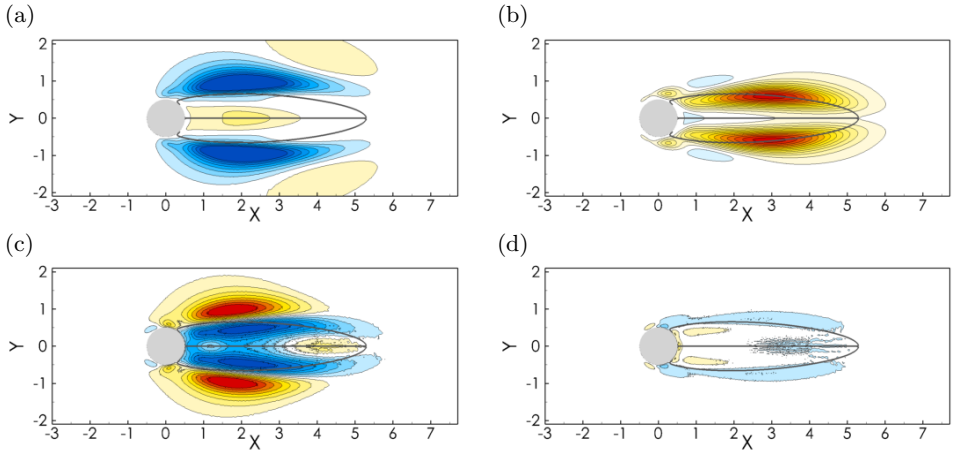

FIGURE 7. Real parts of the individual endogeneity terms in (3.11) (from left to right). *a*) Convection by the base flow; *b*) production through base flow shear; *c*) pressure forces; *d*) diffusion. The sum of these contributions gives $E_\sigma(\mathbf{x})$, shown in figure 6*a*. The same color scale is used here.

of convection by the base flow is dominantly stabilising (figure 7*a*). In the outer vicinity of the separation bubble, the downstream convection of perturbations counteracts their capacity of *in situ* growth, and renders the instability more convective. Inside the recirculation region, the upstream convection has the opposite effect. The production term (figure 7*b*) provides the principal source of global unstable growth.

The workings of pressure forces are not as obvious to interpret in physical terms, and their integrated net contribution to E_σ and E_ω is exactly zero in an incompressible setting. Since the adjoint velocity field is divergence-free, $\nabla \cdot \mathbf{u}^\dagger = 0$, it is easily found that

$$\int_\Omega \mathbf{u}^\dagger \cdot \nabla p \, \mathrm{d}\mathbf{x} = -\int_\Omega (\nabla \cdot \mathbf{u}^\dagger)\, p \, \mathrm{d}\mathbf{x} = 0 \tag{3.12}$$

Yet this term contributes strongly to the local values of the overall endogeneity. Tentatively, it may be argued that the role of the perturbation pressure gradient is to enforce the continuity condition, thereby causing a perturbation volume flux across the shear layer. As the instability perturbations tend to shorten the length of the separation bubble (manifest in the nonlinear mean flow), the stagnation-point streamline is forced toward the symmetry line, lessening the convective effect outside the bubble, and enhancing it inside.

The diffusion term is globally stabilizing, although inside the separation bubble near the cylinder it provokes a weak destabilisation. This seems to be the consequence of viscous transport of perturbation velocity into the shear layer. However low the amplitude of the diffusive contribution, it is crucial for accurately determining the instability threshold. The Reynolds number is expected to have two distinct effects on the instability. First, the stabilizing effect of the perturbation diffusion should weaken when the Reynolds number is increased. This is confirmed in figure 8(a), which shows the trends of the convection, production and diffusion contributions to the growth rate, as functions of the Reynolds number. The stabilizing diffusion effect lessens with increasing Reynolds number. Secondly, the steady base flow is influenced by the Reynolds number, affecting the instability mechanism via the production and convection terms. Individually, these contributions appear to be dominant, but with opposite effects on the growth rate. As

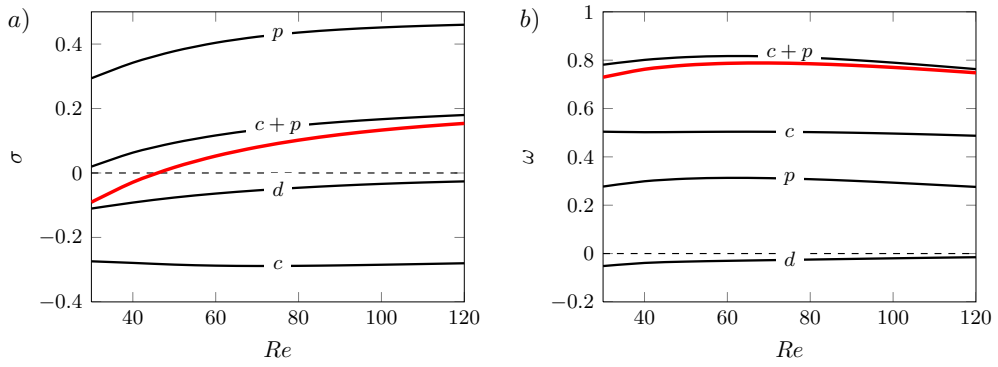

FIGURE 8. Net contributions of individual terms in the endogeneity definition (3.11), (*a*) to the linear growth rate, and (*b*) to the global frequency, as a function of the Reynolds number *Re*. Convection (-*c*-), production (-*p*-) and diffusion (-*d*-) contributions are shown, as well as the sum of convection and production ($c+p$) and the total values of σ and ω (thick red lines). The pressure gradient contribution is zero for all Reynolds numbers.

the Reynolds number is increased, the destabilisation by the production term overcomes the stabilisation by the convection term. The *combined* effect of these competing terms, represented by a line marked $c+p$ in figure 8(a), is then comparable in strength to the diffusion effect. On the other hand, the role of the diffusion in the frequency selection is all but negligible, as seen in figure 8(b). As for the growth rate, the dominant contributors are the production and convection terms. Both contribute here to increase the frequency. Their combined effect ($c+p$) gives a good prediction of the linear frequency (red line), especially at high Reynolds number.

4. Active flow regions in nonlinear global modes

4.1. *Sensitivity of the global frequency*

The general sensitivity formulation for nonlinear time-periodic oscillations of a bifurcated flow state adopted here is similar to the analysis by Luchini *et al.* (2008), with some variations in the notation. Consider a nonlinear global mode $\mathbf{q}_0(\mathbf{x},t)$, time-periodic solution of (2.1), with fundamental frequency ω_g. In order to make the frequency explicitly visible in the equation, the time variable is rescaled as $\tau=\omega_g t$, such that $\mathbf{q}_0(\mathbf{x},\tau)$ is 2π-periodic in τ and satisfies

$$\omega_g\,\mathcal{B}\,\partial_\tau\mathbf{q}_0=\mathcal{N}(\mathbf{q}_0)\,. \tag{4.1}$$

Just as in the linear case of §3.1, small variations of the left-hand side operator cause variations of the solution, including its frequency:

$$(\omega_g+\epsilon\delta\omega_g)\,\mathcal{B}\,\partial_\tau(\mathbf{q}_0+\epsilon\delta\mathbf{q}_0)=(\mathcal{N}+\epsilon\delta\mathcal{N})(\mathbf{q}_0+\epsilon\delta\mathbf{q}_0)\,. \tag{4.2}$$

With the introduction of the tangential linear operator $\mathcal{L}_{\mathbf{q}_0(t)}$ and its neutral Floquet mode $\boldsymbol{\psi}_1=\partial_\tau\mathbf{q}_0$, defined in (2.10, 2.11), variations are governed at order ϵ by the relation

$$(\omega_g\mathcal{B}-\mathcal{L}_{\mathbf{q}_0(t)})\,\delta\boldsymbol{\psi}_1=-\delta\omega_g\,\mathcal{B}\,\boldsymbol{\psi}_1+\delta\mathcal{N}(\mathbf{q}_0)\,, \tag{4.3}$$

The Fredholm alternative can be written out with the aid of the neutral adjoint Floquet mode $\boldsymbol{\psi}_1^\dagger$ (see §2), normalised to give $\{\boldsymbol{\psi}_1^\dagger,\mathcal{B}\boldsymbol{\psi}_1\}=1$, which leads to

$$\delta\omega_g=\left\{\boldsymbol{\psi}_1^\dagger,\delta\mathcal{N}(\mathbf{q}_0)\right\}. \tag{4.4}$$

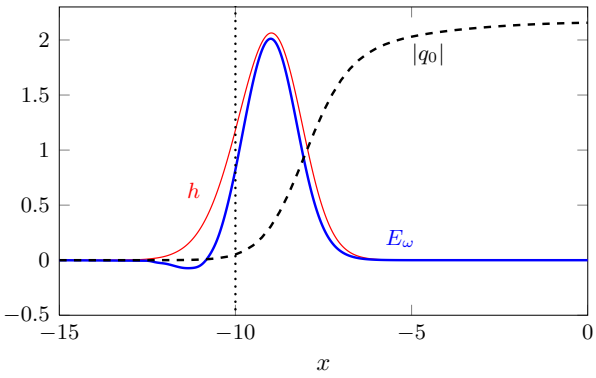

FIGURE 9. Endogeneity E_ω (thick blue line) of the nonlinear global mode of the Ginzburg—Landau equation, as shown in figure 2, compared with the quantity $h(x)$ (thin red line), which is obtained with the formalism described by Hwang (2015) according to (4.7). The dotted line marks the location x_{ca}, and the dashed line traces the envelope shape of the nonlinear global mode.

If $\boldsymbol{\psi}_1^\dagger$ is known, then the impact of any small operator variation $\delta\mathcal{N}$ on the global frequency can be immediately evaluated from (4.4). In practice, $\boldsymbol{\psi}_1^\dagger$ is obtained in the following way: first, the nonlinear equation is numerically integrated by time-stepping until the periodic nonlinear global mode regime is fully attained. Then the (linear) adjoint tangential equation is stepped backwards in time, starting from an arbitrary initialization, over as many cycles of the nonlinear global mode as necessary. During this backward-in-time integration, the adjoint solution converges asymptotically towards the sought-after neutral mode.

4.2. *Endogeneity analysis of nonlinear global modes*

Analogously to the linear case in § 3.2, the endogeneity of a nonlinear global mode is defined by considering variations of the nonlinear operator that preserve its structure but are localized in space, and also in time, since the nonlinear operator is time-dependent,

$$\delta\mathcal{N} = \delta(\mathbf{x}-\mathbf{x}_0)\delta(\tau-\tau_0)\mathcal{N}\,. \tag{4.5}$$

The inner product in (4.4) involves integration in $\mathbf{x}$ as well as in τ. Integration over the Dirac functions yields the expression for the influence of spatio-temporal variations in the operator on the frequency selection,

$$E_\omega(\mathbf{x},\tau) = \Re\left[\boldsymbol{\psi}_1^{\dagger *}(\mathbf{x},\tau)\cdot\mathcal{N}(\mathbf{q}_0(\mathbf{x},\tau))\right]. \tag{4.6}$$

Only the frequency selection in nonlinear global modes is considered at present, because it is assumed here that both quantities, in practice, are obtained from a flow solver in the form of real-valued variables. The scaled time τ denotes the temporal phase within an oscillation cycle.

4.3. *Example 1: the nonlinear Ginzburg–Landau equation*

The nonlinear global mode and its neutral adjoint Floquet mode of the Ginzburg–Landau equation (figure 2) have been discussed in §2.1.2. The associated endogeneity, according to (4.6), is shown in figure 9. It is noted that the endogeneity is independent of τ in the present case of the Ginzburg–Landau equation.

The E_ω distribution is nonzero in a narrow region around $x=-9$, and its integral in

x and over one period $0 \leqslant \tau \leqslant 2\pi$ is exactly equal to the global frequency, $\omega_g = 3.70$. According to Pier *et al.* (1998), the global frequency of a nonlinear Ginzburg–Landau system with slowly varying coefficients is selected at the location x_{ca}, where the local instability changes from upstream convective to downstream absolute. In the limit of marginal global instability, the global frequency is then predicted to correspond to the absolute frequency at x_{ca}. In the present example, one finds $x_{ca} = -10$, and the absolute frequency at this location is $\omega_0(x_{ca}) = 4.50$. The chosen parameter configuration (see §2.1) is strongly globally unstable, and the parameter μ varies significantly in x around x_{ca}, therefore the present case does not respect the limiting assumptions of Pier *et al.* (1998), and the frequency prediction is quite inaccurate as a result. The endogeneity however provides a clear and accurate picture of the frequency selection process. The maximum contribution to the global frequency is found at $x = -9$, indeed not far from the 'wavemaker' location x_{ca} as defined by Pier *et al.* (1998).

The present results may be compared to the structural sensitivity of nonlinear global modes as defined by Hwang (2015), who adapted the formulation of Luchini *et al.* (2008) to analyze nonlinear global modes of the Ginzburg–Landau equation. According to Hwang (2015), worst-case variations of the global frequency due to added 'closed-loop perturbations' (synonymous to 'internal feedback'), written in the notation of this paper, are characterized by the spatial distribution

$$h(x) = \left| \frac{q_0^*(x)\, \psi_1^\dagger(x)}{N} \right|, \quad \text{with} \quad N = \int_0^T \int_{-\infty}^{\infty} (\psi_1^{\dagger *}\, q_0 - \psi_1^\dagger\, q_0^*)\, \mathrm{d}x\, \mathrm{d}t\,. \tag{4.7}$$

Figure 9 compares this distribution, multiplied with $2\omega_g$ for consistent scaling, with the endogeneity E_ω. The two curves are very similar, and in particular the position of their maxima is identical. Again it is pointed out that the analysis of Hwang (2015), in contrast to the endogeneity formalism, considers modifications of the operator that do not preserve its original structure.

In conclusion, just as in the linear analysis of §3.2, the results obtained from the nonlinear endogeneity analysis are consistent with the 'wavemaker' definition from classical asymptotic theory, but they go further in a quantitative description of the dynamics, because the endogeneity fully accounts for the effects of non-parallelism and supercriticality. It is also consistent with recent formulations that describe the structural sensitivity, but it reveals the endogenous dynamics that are specific to the operator under consideration.

4.4. *Example 2: Nonlinear frequency selection in the cylinder wake*

The endogeneity of the time-periodic flows developing in the wake of the circular cylinder, described in §2.2.2, is explicitly obtained as

$$E_\omega(\mathbf{x}, \tau) = \mathbf{u}_1^\dagger \cdot \left[-(\mathbf{u}_0 \cdot \nabla)\mathbf{u}_0 - \nabla p_0 + Re^{-1} \Delta \mathbf{u}_0 \right], \tag{4.8}$$

where $\mathbf{q}_0(\mathbf{x}, \tau) = (\mathbf{u}_0, p_0)$ is the 2π-periodic nonlinear solution and $\mathbf{u}_1^\dagger$ is the velocity component of the 2π-periodic solution of the linear adjoint equation.

The spatio-temporal endogeneity (4.8) is integrated over one oscillation cycle, and the result, shown in figure 10, demonstrates that the endogenous region resembles a front, localized around $x = 2$. Similarly to the earlier observations in the context of the Ginzburg-Landau equation, the endogenous region of the nonlinear global mode in the cylinder wake is located further upstream than that of its linear counterpart (compare to figure 6b). The separation line of the recirculation regions both in the base flow and in the time-averaged mean flow are depicted by grey and black lines, respectively, in figure 10. Interestingly, the endogenous region of the nonlinear global mode appears to

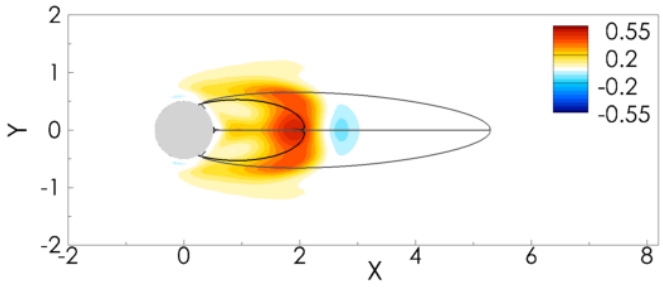

FIGURE 10. Time-integrated endogeneity $E_\omega(\mathbf{x})$ of the nonlinear global mode in the cylinder wake at $Re = 80$. The nonlinear frequency is $\omega_g = 0.995$. The black (resp. grey) lines indicate the recirculation region in the time-averaged mean flow (resp. base flow).

be supported by the recirculation region in the mean flow, as opposed to the base flow. This observation suggests that further investigation of the nonlinear dynamics should focus on the analysis of fluctuations around the mean flow state.

To this aim, the nonlinear global mode state is first decomposed as $\mathbf{q}_0 = \bar{\boldsymbol{q}} + \mathbf{q}'$ into a time-averaged component $\bar{\boldsymbol{q}} = (\bar{\boldsymbol{u}}, \bar{p})^T$ and a zero-mean fluctuation component $\mathbf{q}' = (\mathbf{u}', p')^T$. Introducing this decomposition into the Navier-Stokes operator (2.24), and time-averaging over one oscillation cycle, one obtains the steady nonlinear equations that govern the mean flow,

$$(\bar{\boldsymbol{u}} \cdot \nabla)\bar{\boldsymbol{u}} + \nabla\bar{p} - Re^{-1}\Delta\bar{\boldsymbol{u}} = -\overline{(\boldsymbol{u'} \cdot \nabla)\boldsymbol{u'}}, \tag{4.9}$$

$$\nabla \cdot \bar{\boldsymbol{u}} = 0\,. \tag{4.10}$$

By subtraction, the unsteady nonlinear equations for the fluctuations are obtained as

$$\omega_g\,\partial_\tau \boldsymbol{u'} + (\bar{\boldsymbol{u}} \cdot \nabla)\boldsymbol{u'} + (\boldsymbol{u'} \cdot \nabla)\bar{\boldsymbol{u}} + \nabla p' - Re^{-1}\Delta\boldsymbol{u'} = -(\boldsymbol{u'} \cdot \boldsymbol{\nabla})\boldsymbol{u'} + \overline{(\boldsymbol{u'} \cdot \boldsymbol{\nabla})\boldsymbol{u'}}, \tag{4.11}$$

$$\nabla \cdot \boldsymbol{u'} = 0\,. \tag{4.12}$$

The right-hand side forcing terms both in (4.9) and in (4.11) arise from the nonlinear interaction of fluctuations. The temporal mean of $(\boldsymbol{u'}\cdot\boldsymbol{\nabla})\boldsymbol{u'}$ forces the mean flow, whereas its zero-mean fluctuation forces the flow fluctuations. At small amplitudes of $\boldsymbol{u'}$, these terms are negligible, such that the steady and unsteady equations reduce to the base flow and linear perturbation equations. By contrast, when a linear eigenmode experiences exponential growth and reaches finite amplitude levels, the effect of the forcing terms in (4.9) and (4.11) will become significant. The right-hand side in (4.9) drives the base flow towards the mean flow. The right-hand side in (4.11) modifies the dynamics of the fundamental oscillations at frequency ω_g, and it generates harmonic components at integer multiples of ω_g. Thus the effect of nonlinearity on the frequency selection can be attributed to two distinct origins. The first is a nonlinear deformation of the mean flow, which in turn modifies the left-hand side linear operator in (4.11). The second one is the nonlinear interaction of fluctuation harmonics, induced by the right-hand side forcing term in (4.11).

The endogeneity definition (4.8) is now expanded in terms of mean flow and fluctuation

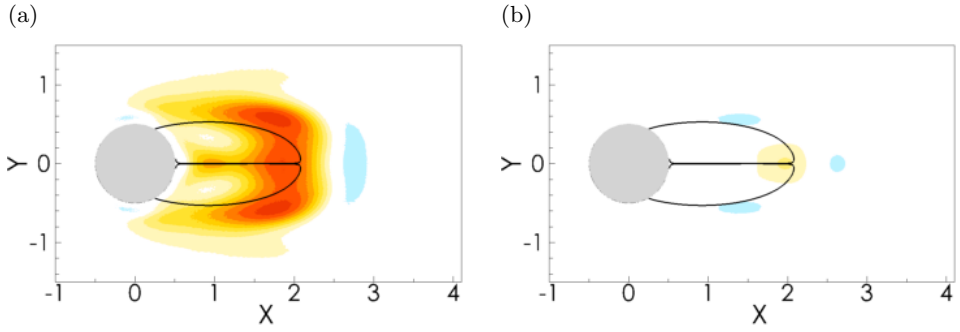

FIGURE 11. Contributions to the time-integrated endogeneity of the nonlinear global mode. (a) Quasi-linear dynamics around the mean flow defined by (4.15) and (b) interaction between high harmonical components defined by (4.15). The color bar shown in figure 10 is also used here. The black line indicates the recirculating flow region in the mean flow. $Re = 80$.

components. With this decomposition, as developed above, one obtains

$$\begin{aligned} E_\omega(\mathbf{x},\tau) = \mathbf{u}^\dagger \cdot \Big[&- (\bar{\boldsymbol{u}}\cdot\nabla)\bar{\boldsymbol{u}} - \nabla\bar{p} + Re^{-1}\Delta\bar{\boldsymbol{u}} - \overline{(\mathbf{u}'\cdot\nabla)\mathbf{u}'}\Big] \\ + \mathbf{u}^\dagger \cdot \Big[&- (\overline{\mathbf{u}}\cdot\nabla)\mathbf{u}' - (\mathbf{u}'\cdot\nabla)\overline{\mathbf{u}} - \nabla p' + Re^{-1}\Delta\mathbf{u}'\Big] \\ + \mathbf{u}^\dagger \cdot \Big[&- (\mathbf{u}'\cdot\nabla)\mathbf{u}' + \overline{(\mathbf{u}'\cdot\nabla)\mathbf{u}'}\Big]. \end{aligned} \tag{4.13}$$

The first line in the above equation vanishes because the expression in square brackets is the momentum equation for the mean flow (4.9. By further splitting the adjoint velocity into mean and fluctuation components, denoted $\overline{\boldsymbol{u}}^\dagger$ and $\boldsymbol{u}^{\dagger\prime}$ respectively, the time-integrated endogeneity simplifies to

$$\int_0^{2\pi} E_\omega(\mathbf{x},\tau)\, d\tau = \int_0^{2\pi} E_m(\mathbf{x},\tau)\, d\tau + \int_0^{2\pi} E_h(\mathbf{x},\tau)\, d\tau\,, \tag{4.14}$$

with

$$E_m(\mathbf{x},\tau) = \boldsymbol{u}^{\dagger\prime}\cdot\left(-(\overline{\mathbf{u}}\cdot\nabla)\mathbf{u}' - (\mathbf{u}'\cdot\nabla)\overline{\mathbf{u}} - \nabla p' + Re^{-1}\Delta\mathbf{u}'\right), \tag{4.15}$$

$$E_h(\mathbf{x},\tau) = \boldsymbol{u}^{\dagger\prime}\cdot\left(-(\mathbf{u}'\cdot\nabla)\mathbf{u}' + \overline{(\mathbf{u}'\cdot\nabla)\mathbf{u}'}\right), \tag{4.16}$$

All contributions involving the mean adjoint velocity vanish. The component $E_m(\boldsymbol{x},\tau)$ highlights spatial regions where the quasi-linear dynamics around the mean flow contribute to the frequency selection, whereas $E_h(\boldsymbol{x},\tau)$ identifies regions where the interaction of harmonic components influences the global frequency.

The time-integrated components E_m and E_h, for the nonlinear global mode in the cylinder wake at $Re = 80$, are shown in figure 11. The sum of these two contributions, according to (4.14), gives the time-integrated frequency endogeneity displayed in figure 11. In the present configuration, the frequency selection process is clearly dominated by the quasi-linear dynamics around the mean flow, whereas harmonic interactions contributes only very weakly. The total contributions

$$\omega_m = \int_\Omega\int_0^{2\pi} E_m(\mathbf{x},\tau)\, d\tau\, d\boldsymbol{x}\,, \quad \omega_h = \int_\Omega\int_0^{2\pi} E_h(\mathbf{x},\tau)\, d\tau\, d\boldsymbol{x}\,, \tag{4.17}$$

are reported in table 1 for various values of the Reynolds number. For all values of the Reynolds number investigated in this study, the contribution ω_m of the quasi-linear mean flow dynamics to the global frequency is greater than 97%.

Re	ω	ω_g	$\omega_m(\%)$	$\omega_h(\%)$
50	0.7676	0.8159	0.8087 (99.1)	0.0072 (0.9)
75	0.7742	0.9726	0.9543 (98.1)	0.0182 (1.9)
80	0.7852	0.9957	0.9768(98.1)	0.0189(1.9)
100	0.7553	1.0703	1.0493 (98.0)	0.0210 (2.0)
125	0.7246	1.1382	1.1127 (97.7)	0.0255 (2.3)
150	0.6896	1.1922	1.1596 (97.2)	0.0325 (2.8)

TABLE 1. Endogeneity-based decomposition of the nonlinear global mode frequency, for various values of the Reynolds number Re. Linear eigenmode frequency ω of the base flow; nonlinear global mode frequency ω_g; contributions to ω_g from quasi-linear dynamics in the mean flow (ω_m) and from harmonic interaction (ω_h), as defined by (4.17).

This result explains a posteriori why a global stability analysis of the time-averaged flow accurately predicts the frequency of the time-periodic vortex shedding in the cylinder wake (Barkley 2006). Mantic-Lugo *et al.* (2014) recently proposed a self-consistent nonlinear model based on the marginal stability of the mean flow, which accurately determines both the mean flow and the frequency of the vortex shedding in the cylinder wake. However, the influence of higher harmonics in the frequency selection of nonlinear instability is not negligible in all circumstances. Indeed, Turton *et al.* (2015) recently showed that in thermosolutal convection driven by opposite thermal and solutal gradients, oscillation frequencies of *travelling* convection waves can be predicted from stability analysis of the mean flow, but not those of *standing* waves. The application of endogeneity analysis to the thermosolutal convection problem is not attempted here, but it is expected to reveal a stronger influence of the harmonic interactions in the frequency selection of standing waves.

Finally, a decomposition of the endogeneity component (4.15) similar to the demonstration in §3.4 characterizes the contributions of the various terms to the quasi-linear dynamics. For $Re = 80$, the contributions of production and mean flow convection to the global frequency are displayed in figures 12*a,b*, and the contributions of diffusion and pressure gradient are shown in figures 12*c,d*. The production contribution is dominant, concentrated in the shear layers of the mean recirculation region. Inside this region, the action of the pressure gradient further increases the frequency. Table 2 summarizes all total contributions, ω_m^p, ω_m^c, ω_m^d, of the production, convection and diffusion terms at various Reynolds numbers . The net integral of the pressure gradient term is always identically zero. At all Reynolds numbers, the effects of diffusion and mean flow convection approximately compensate each other, and their balance is small compared to the strong contribution of the production term.

5. Conclusions

A novel sensitivity formalism has been introduced, named the endogeneity, which allows to precisely quantify the influence of each point in the flow field on the global frequency selection and on the promotion of unstable growth, both in the context of linear temporal eigenmodes and of nonlinear global modes. Its application has been demonstrated for the Ginzburg–Landau equation and for the wake of a circular cylinder, in linear as well as nonlinear settings. The results obtained have been shown to be consistent with earlier 'wavemaker' definitions, in particular the WKBJ-based saddle point criterion of Chomaz *et al.* (1991) and the structural sensitivities defined by Giannetti &

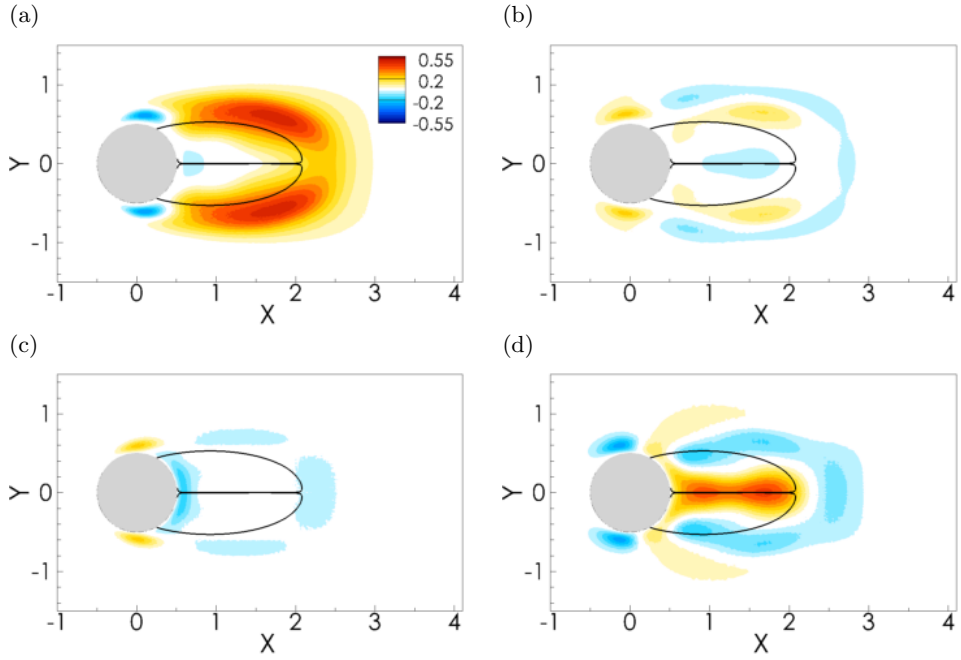

FIGURE 12. Spatial distribution of various contributions to the endogeneity of the quasi-linear mean flow dynamics: (a) production by the mean flow, (b) convection by the mean flow, (c) diffusion and (d) pressure gradient. The black line delimits the recirculation region in the mean flow.

Re	ω_m	ω_m^p	ω_m^c	ω_m^d
50	0.8087	0.9997	0.0023	−0.1933
75	0.9543	0.9435	0.1567	−0.1459
80	**0.9768**	**0.9482**	**0.1679**	**-0.1394**
100	1.0493	0.9999	0.1696	−0.1203
125	1.1127	1.0989	0.1224	−0.1087
150	1.1596	1.1721	0.0853	−0.0978
175	1.1935	1.2220	0.0604	−0.0889

TABLE 2. Decomposition of the quasi-linear contribution to the fresquency into three contributions: the production term ω_m^p, convection term ω_m^c and diffusion term ω^d in the quasi-linear mean flow dynamics.

Luchini (2007), Luchini *et al.* (2008) and Hwang (2015). The novel aspect with respect to the latter sensitivity approaches arises from the specific form of operator variations that are considered: the endogeneity characterizes the sensitivity of the eigenvalue with respect to localized operator variations that preserve the specific structure of the original operator. This sensitivity may therefore be interpreted as the *local contribution* of any point in the flow field to the global eigendynamics, in terms of frequency selection and unstable growth. Contributions to these two parts of the eigenvalue are clearly distinguished, contained separately in the real and imaginary parts of the endogeneity. Further analysis of the role of individual terms of the operator follows naturally within this framework. In particular, a decomposition of a nonlinear flow operator into time-averaged and

fluctuating parts gives insight into the role of quasi-linear dynamics developing on the mean flow versus the nonlinear interaction of harmonic fluctuation components. This latter part of the analysis, exemplified for the case of the cylinder wake, has important implications for the characterisation of nonlinear time-periodic flow states, in relation to recent investigations (Mantic-Lugo *et al.* 2014; Turton *et al.* 2015).

The authors are grateful to Patrick Huerre, Jean-Marc Chomaz and Denis Sipp for their helpful comments. Lutz Lesshafft acknowledges financial support from the Agence Nationale de la Recherche under the "Cool Jazz" project.

Appendix A. Influence of the inner product

The question may arise whether and how the choice of an inner product different from (2.9) affects the endogeneity definition. In particular, many flow problems are investigated in cylindrical coordinates, where the standard inner product includes the radial coordinate r as part of the volume element. For practical purposes, the procedure is outlined here for *discrete* eigenvalue problems, with a generalized inner product.

Let $\tilde{\boldsymbol{\phi}}_j$ be a discrete representation of the linear eigenfunction $\boldsymbol{\phi}_j$, in a discrete space where the inner product $\langle \boldsymbol{\phi}_1, \boldsymbol{\phi}_2 \rangle$ between two flow states is expressed as $\tilde{\boldsymbol{\phi}}_1^H \mathsf{Q} \tilde{\boldsymbol{\phi}}_2$. The matrix Q is typically diagonal, with real elements that represent volume elements of the mesh, and possibly any further weight functions. It will only be assumed here that Q is invertible, but even this condition can be relaxed with some additional effort.

The discrete direct and adjoint eigenvalue problems are defined by

$$-\mathrm{i}\omega_j \mathsf{B} \tilde{\boldsymbol{\phi}}_j = \mathsf{L} \tilde{\boldsymbol{\phi}}_j \,, \tag{A 1}$$

$$\mathrm{i}\omega_j^* \mathsf{Q}^{-1,H} \mathsf{B}^H \mathsf{Q}^H \tilde{\boldsymbol{\phi}}_j^\dagger = \mathsf{Q}^{-1,H} \mathsf{L}^H \mathsf{Q}^H \tilde{\boldsymbol{\phi}}_j^\dagger \,. \tag{A 2}$$

The matrix $\mathsf{Q}^{-1,H}$ on both sides of (A 2) can be omitted. It is found that $\check{\boldsymbol{\phi}}_j^\dagger = \mathsf{Q}^H \tilde{\boldsymbol{\phi}}_j^\dagger$ is the adjoint eigenvector satisfying

$$\mathrm{i}\omega_j^* \mathsf{B}^H \check{\boldsymbol{\phi}}_j^\dagger = \mathsf{L}^H \check{\boldsymbol{\phi}}_j^\dagger \,. \tag{A 3}$$

Let $\boldsymbol{\Phi}_j(\mathbf{x}_k)$ be defined as the vector $\boldsymbol{\Phi}_j(\mathbf{x}_k) = \delta(\mathbf{x} - \mathbf{x}_k) \mathsf{L} \tilde{\boldsymbol{\phi}}_j$ for convenient writing, where $\mathbf{x}_k$ denotes the discrete mesh points. The endogeneity definition, written in terms of discrete vectors and operators, is then

$$-\mathrm{i}E(\mathbf{x}_k) = \langle \phi_j^\dagger, \delta(\mathbf{x} - \mathbf{x}_k)\, \mathcal{L}\phi_j \rangle = \tilde{\boldsymbol{\phi}}_j^{\dagger H} \mathsf{Q} \boldsymbol{\Phi}_j(\mathbf{x}_k) = \check{\boldsymbol{\phi}}_j^{\dagger H} \boldsymbol{\Phi}_j(\mathbf{x}_k). \tag{A 4}$$

It follows from (A 4) that the endogeneity is invariant with respect to the choice of the inner product. This holds true also for the example of cylindrical coordinates: it seems unnecessary to account for the r factor. Without the need to specify a Q matrix, $E(\mathbf{x}_k)$ may be computed directly from the discrete adjoint eigenvector, obtained from the transpose conjugate problem (A 3). This will generally be the simplest option.

REFERENCES

Barkley, D. 2006 Linear analysis of the cylinder wake mean flow. *Europhys. Lett.* **75**, 750–756.

Chomaz, J.-M. 2003 Fully nonlinear dynamics of parallel wakes. *J. Fluid Mech.* **495**, 57–75.

Chomaz, J.-M., Huerre, P. & Redekopp, L.G. 1987 Models of hydrodynamic resonances in separated shear flows. In *Proceedings of the Sixth Symposium on Turbulent Shear Flows, Toulouse, France*, pp. 321–326.

Chomaz, J.-M., Huerre, P. & Redekopp, L.G. 1988 Bifurcations to local and global modes in spatially developing flows. *Phys. Rev. Lett.* **60**, 25–28.

Chomaz, J.-M., Huerre, P. & Redekopp, L.G. 1991 A frequency selection criterion in spatially developing flows. *Stud. Appl. Math* **84** (2), 119–144.

Cossu, C. & Chomaz, J.-M. 1997 Global measures of local convective instabilities. *Phys. Rev. Lett.* **78** (23), 4387.

Couairon, A. & Chomaz, J.-M. 1997 Absolute and convective instabilities, front velocities and global modes in nonlinear systems. *Physica D* **108**, 236–276.

Cuvelier, C., Segal, A. & Van Steenhoven, A. 1986 *Finite element methods and Navier-Stokes equations*, , vol. 22. Reidel, Dordrecht, Netherlands.

Giannetti, F. & Luchini, P. 2007 Structural sensitivity of the first instability of the cylinder wake. *J. Fluid Mech.* **581**, 167–197.

Huerre, P. 2000 Open shear flow instabilities. In *Perspectives in Fluid Dynamics* (ed. G. K. Batchelor, H. K. Moffatt & M. G. Worster), pp. 159–229. Cambridge University Press.

Huerre, P. & Monkewitz, P.A. 1990 Local and global instabilities in spatially developing flows. *Annu. Rev. Fluid Mech.* **22**, 473–537.

Hwang, Y. 2015 Structural sensitivities of soft and steep nonlinear global modes in spatially developing media. *Eur. J. Mech. B/Fluids* **49B**, special issue: "Trends in Hydrodynamic Instabilities".

Iooss, G. & Joseph, D. 1997 *Elementary stability and bifurcation theory*. Springer, New York.

Koch, W. 1985 Local instability characteristics and frequency determination of self-excited wake flows. *J. Sound Vib.* **99** (1), 53–83.

Luchini, P. & Bottaro, A. 2014 Adjoint equations in stability analysis. *Annu. Rev. Fluid Mech.* **46**, 493–517.

Luchini, P., Giannetti, F. & Pralits, J. 2008 Structural sensitivity of linear and nonlinear global modes. *AIAA Paper* **2008-4227**.

Mantic-Lugo, V., Arratia, C. & Gallaire, F. 2014 Self-consistent mean flow description of the nonlinear saturation of the vortex shedding in the cylinder wake. *Phys. Rev. Lett.* **113**, 407–417.

Marquet, O., Sipp, D. & Jacquin, L. 2008 Sensitivity analysis and passive control of cylinder flow. *J. Fluid Mech.* **615**, 221–252.

Monkewitz, P. 1990 The role of absolute and convective instability in predicting the behavior of fluid systems. *Eur. J. Mech. B/Fluids* **9**, 395–413.

Pier, B. 2002 On the frequency selection of finite-amplitude vortex shedding in the cylinder wake. *J. Fluid Mech.* **458**, 407–417.

Pier, B. & Huerre, P. 2001 Nonlinear self-sustained structures and fronts in spatially developing wake flows. *J. Fluid Mech.* **435**, 145–174.

Pier, B., Huerre, P., Chomaz, J.-M. & Couairon, A. 1998 Steep nonlinear global modes in spatially developing media. *Phys. Fluids* **10**, 2433–2435.

Provansal, M., Mathis, C. & Boyer, L. 1987 Bénard–von Kármán instability: transient and forced regimes. *J. Fluid Mech.* **182**, 1–22.

van Saarlos, W. 1988 Front propagation into unstable states: marginal stability as dynamical mechanism for velocity selection. *Phys. Rev. A* **37**, 211–229.

van Saarlos, W. 1989 Front propagation into unstable states: II. linear versus nonlinear marginal stability and rate of convergence. *Phys. Rev. A* **39**, 6367–6390.

Sipp, D. & Lebedev, A. 2007 Global stability of base- and mean-flows: a general approach and its applications to cylinder and open cavity flows. *J. Fluid Mech.* **593**, 333–358.

Turton, S. E., Tuckerman, L. S. & Barkley, D. 2015 Prediction of frequencies in thermosolutal convection from mean flows. *Phys. Rev. E* **91**, 043009.

International Journal of Heat and Fluid Flow 000 (2016) 1–9

Contents lists available at ScienceDirect

International Journal of Heat and Fluid Flow

journal homepage: www.elsevier.com/locate/ijhff

Modeling of coherent structures in a turbulent jet as global linear instability wavepackets: Theory and experiment

Onofrio Semeraro[a,*], Lutz Lesshafft[a], Vincent Jaunet[b], Peter Jordan[b]

[a] LadHyX, CNRS, École polytechnique – Palaiseau, FR
[b] Institut PPRIME, CNRS, Université de Poitiers, ENSMA – Poitiers, FR

ARTICLE INFO

Article history:
Available online xxx

Keywords:
Turbulent jet
Frequency response analysis
Linear stability analysis
Aeroacoustics

ABSTRACT

Perturbation wavepackets in a jet, induced by externally applied forcing, are computed from the linearized equations of motion. An experimentally measured mean flow serves as the base state for this linear analysis, and optimally amplified mono-frequency perturbations are identified, in the sense of maximal gain between the forcing energy input and the flow response energy. Sub-optimal orthogonal forcing/response structures are also discussed. Linear analysis results are then compared to measured perturbation wavepackets in the jet experiment. The study addresses the question to what extent the true dynamics of a turbulent jet can be represented by a model based on linear instability.

1. Introduction

Since the experiments by Mollo-Christensen (Mollo-Christensen, 1963) and by Crow & Champagne (Crow and Champagne, 1971), it has been recognized that turbulent jets exhibit large-scale vortical structures of relatively high spatial and temporal coherence. These structures are well described as wavepackets of synchronized frequency, with streamwise amplitude and phase modulations. It has furthermore been established that the dominant noise radiated from such jets is correlated with these wavepacket structures, as for instance in the numerical study by Freund (Freund, 2001). Many investigations have since been based on the idea that the coherent wavepackets in turbulent jets and other shear flows may be modeled as instability waves (e.g. Cavalieri et al., 2013; Crighton and Gaster, 1976), linear or nonlinear, that develop in some steady state, either a laminar steady solution of the Navier–Stokes equations or an empirically determined mean flow. Such a model is tempting, because it opens a way for the analysis of the perturbation dynamics and, if the model carries that far, of the sound-producing mechanisms that are responsible for the jet noise.

However, the description of wavepackets in turbulent jets as instability waves within a steady flow state requires an empirical justification. A recent review (Jordan and Colonius, 2013) cites several studies that corroborate the pertinence of such an approach. In particular, Suzuki and Colonius (2006) present sophisticated experimental measurements of near-field pressure fluctuations outside the shear layer of subsonic high Reynolds number jets, and they demonstrate that the coherent fluctuations compare well with the local k^+ instability mode characteristics. Cavalieri et al. (2012) take this approach further, by comparing PIV data obtained in the interior of a $Ma = 0.4$ jet with linear PSE instability calculations. Their study shows remarkable agreement in the development of vortical wavepackets throughout the potential core of the mean flow, for Strouhal numbers between 0.3 and 0.9. At lower Strouhal numbers, and at streamwise distances beyond the potential core, measurements and PSE predictions differ significantly.

The aim of this study is to extend the comparison between experiment and theoretical modeling to a framework of fully global linear stability analysis, named the linear frequency response. Optimization is performed in order to identify the most energy-efficient linear forcing of a jet at a given Strouhal number. New high-quality experimental data, obtained in a jet at $Ma = 0.9$ and $Re = 10^6$, is used for a detailed comparison between linear flow-response wavepackets and coherent turbulent structures. A similar investigation by Jeun et al. (2016) established good agreement between linear frequency response and LES results for a jet at nominally identical operating conditions. Linear frequency response analysis has been applied in earlier work (Garnaud et al., 2013a, 2013b) to different jet configurations. In the present paper, the formalism is applied for the first time to experimental jet data.

The paper is organized as follows. The experimental setup is described in Section 2; mean flow quantities are shown, and the main frequency-resolved PIV results are summarized. The frequency response analysis, and some details on numerical procedures, are presented in Section 3. Linear analysis results are

* Corresponding author.
E-mail address: semeraro@ladhyx.polytechnique.fr (O. Semeraro).

http://dx.doi.org/10.1016/j.ijheatfluidflow.2016.10.010
0142-727X/

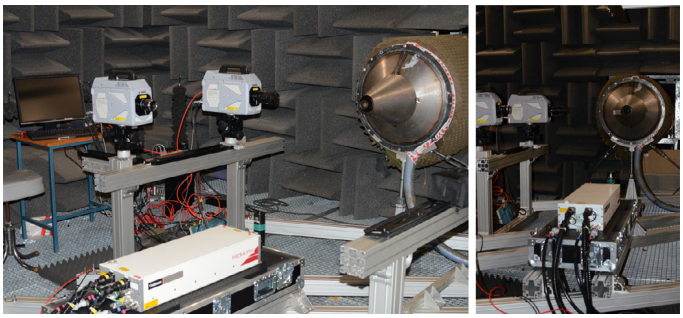

Fig. 1. The "Bruit et Vent" experimental set-up.

documented in Section 4 and compared to experimental data in Section 5.

2. Experimental setup

Experiments were conducted at the "Bruit et Vent" jet-noise facility at the CEAT, PPRIME Institute, Poitiers, France. The measurements were carried out at a Mach number ($Ma = U_j/c$, where U_j is the jet velocity and c the ambient speed of sound) equal to 0.9 in isothermal conditions. The nozzle diameter D was 0.05 m, giving a Reynolds number of $Re_D = \rho U_j D/\mu \approx 10^6$. Transition in the incoming internal boundary layer is triggered using a Carborundum strip glued on the wall upstream from the nozzle exit.

The PIV system consisted of a Photron SAZ camera and a 532 nm Continuum MESA PIV laser providing 6 mJ of light pulse energy. The system was placed on a traverse parallel to the jet axis in order to scan the jet flow field from axis location close to the nozzle up to 20 jet diameter. The camera was equipped with a 100 mm macro lens with low optical distortion, the aperture set at f#4. A photograph of the set-up in given in Fig. 1.

Two different field of views (FOV) were used during the experimental campaign. The first FOV measured the velocity field in an area of about $2D \times 2D$, and was used for axial positions from the nozzle exit up to $x = 6D$. The second FOV measured the velocity field in an area of $4D \times 4D$, and was used for more downstream locations, *i.e.* $x > 5D$. Hence, a finer spatial resolution was obtained for measurements close to the nozzle exit to ensure a good capture of the local velocity gradients. The complete measurement of the jet flow was obtained with the use of 11 acquisitions performed at various downstream locations. In between each of these locations an overlap of 20% of the FOV was set in order to control the correct alignment of the measured velocity fields. A calibration was made at all acquisition positions in order to be able to correct for both the remaining optical distortions and laser light sheet/measurement plane misalignment using a *self-calibration procedure* (Wieneke, 2005).

Both the jet flow and the surrounding air were seeded using glycerin smoke particles, whose diameter lays in the range between 1 and 2 µm, thus sufficiently small to follow the velocity fluctuations of interest in this paper. The particles formed images of 2–3 particles in diameter, and no evidence of peak-locking was found in the data set.

The image acquisition was performed at 20 kHz (10,000 PIV samples a second) at a resolution of 1024 × 1024 pixels. The time between the two laser pulses was set according to the local velocity amplitude and to the laser sheet width (which was set at 2 mm), and ranged between 4 and 5 µs. For each acquisition 42,000 image pairs were acquired.

PIV calculations were carried out using a commercial software, and a multi-pass iterative PIV algorithm with deforming interrogation area (Scarano, 2002) to account for the local mean velocity gradients. The PIV interrogation area size was set to 32 × 32 pixels for the first pass, decreased at 16 × 16 pixels for the remaining passes, with an overlap of 50% between two neighboring interrogation areas. Displacement computed were retained only the correlation peak-ratio was higher than 1.3. After each pass a Universal Outlier Detection (UOD) (Westerweel and Scarano, 2005) is applied on a 3 × 3 vector grid to avoid corrupted data and enhance the particle motion calculation. Finally, prior to the computation of the flow statistical quantities a 5-sigma filter is applied to remove the remaining outliers and they are replaced using the UOD technique.

2.1. Mean flow measurements and postprocessing

The mean flow for which all further analysis will be performed is computed from the PIV measurements through time-averaging. The axial velocity component $\overline{u}$ is presented in Fig. 2*a*, and the correlation $\overline{u'v'}$ of velocity fluctuations around the mean flow, from which the turbulent viscosity will be estimated, is shown in Fig. 2*b*. The potential core extends about six diameters downstream of the nozzle exit.

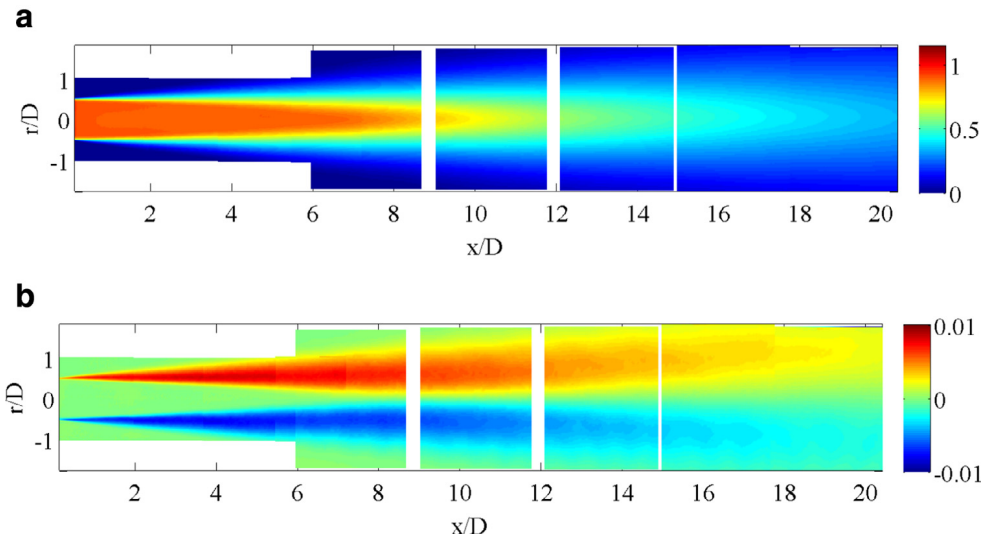

Fig. 2. PIV results: the spatial distribution of the meanflow axial velocity and the $\overline{u'v'}$ fluctuations are shown in (*a*) and (*b*), respectively.

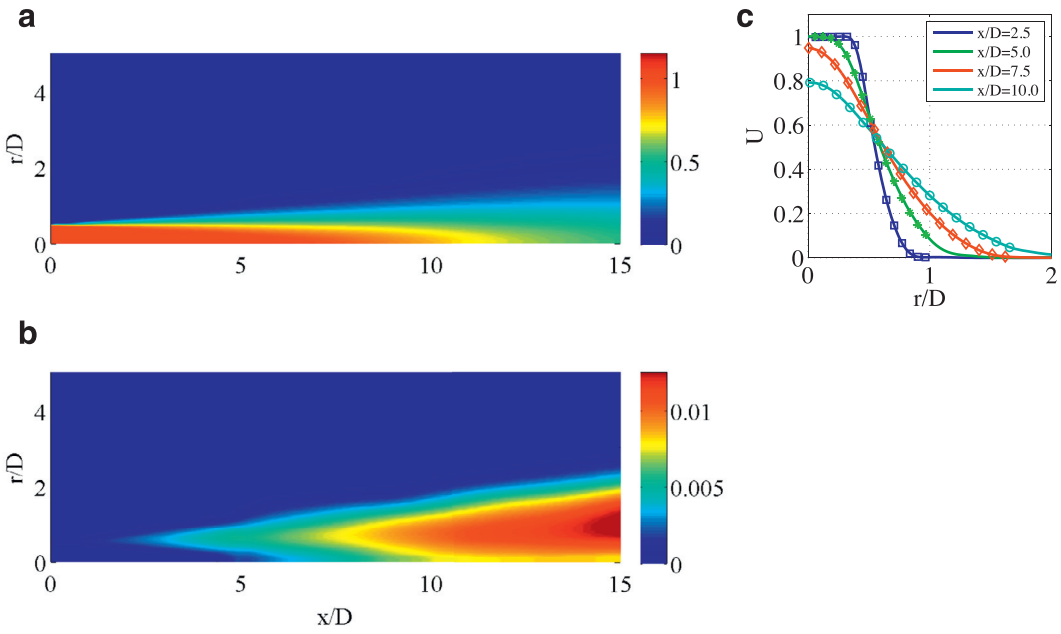

Fig. 3. (*a*) Extrapolated axial mean flow velocity $\overline{u}$ and (*b*) turbulent viscosity ν_t, obtained from processed experimental measurements. (*c*) Velocity profiles at four different x-locations; solid lines: processed mean flow as in (*a*), markers: experimental data as in Fig. 2*a*.

Smooth mean flow profiles must be constructed from this data, throughout a large numerical domain, for density, radial and axial velocity. We closely follow the procedure outlined in Gudmundsson and Colonius (2011); in particular, the mean axial velocity is extrapolated in the outer regions $r/D > 1$ and $x/D > 20$ by use of a Gaussian profile (Troutt and McLaughlin, 1982), given by

$$\frac{\overline{u}}{U_j} = \begin{cases} 1, & \text{if } r < R(x) \\ U_c(x)\exp\left(-\dfrac{(r-R(x))^2}{\delta(x)^2}\right), & \text{otherwise.} \end{cases} \tag{1}$$

$R(x)$ characterizes the radial extent of the potential core, $U_c(x)$ represents the evolution of the centerline velocity, and $\delta(x)$ marks the radial position along x where $\overline{u}(x,0) = U_c(x)/2$. Outside the streamwise interval where experimental data is available, the profile parameters $R(x)$, $U_c(x)$ and $\delta(x)$ at $x/D > 20$ are extracted from a large eddy simulation (LES) of the same setting (Brès et al., 2015; Jordan et al., 2014), and the velocity profiles for the pipe flow and the nozzle region are directly taken from this simulation as well. The LES was performed with the solver "Charles" from Cascade Technologies, and it has been shown to reproduce the reference experiment with remarkable precision.

The axial velocity component $\overline{u}$ of the final mean flow model is shown in Fig. 3*a*. Some smoothing with high-order moving-average filters (Berland et al., 2007) has been applied for reasons of numerical resolution. The agreement between the experimental data and the reconstructed mean flow model is very satisfactory, as shown in Fig. 3*c*. The maximum difference between the numerical mean flow from LES and the reconstructed experimental one is approximately 7% of the velocity $\overline{u}$ in the mixing layer at locations $x/D > 10$. Corresponding mean density variations are computed from the Crocco–Busemann relation, and the radial mean velocity $\overline{v}$ is finally obtained from the continuity equation.

3. Frequency response methodology

As the jet behaves as an amplifier of external flow perturbations, the appropriate theoretical framework for a global analysis is the *frequency response* formalism (Garnaud et al., 2013a), which is synonymously referred to as 'resolvent analysis' or 'input-output analysis' in the literature. This section provides the problem formulation and an outline of the numerical procedure.

3.1. Governing equations

The fully compressible Navier–Stokes equations are written in terms of conservative variables (ρ, ρu, ρv, ρE) in axisymmetric cylindrical coordinates (r, x). Axial and radial velocity components are denoted as u and v, respectively, ρ is the density and E the total energy. Only axisymmetric dynamics are considered, therefore all quantities are independent of the azimuthal coordinate θ, and the azimuthal velocity is always zero. The flow quantities are made non-dimensional with respect to the diameter D of the nozzle, the ambient density ρ_∞, and the jet centerline velocity U_j, measured at the nozzle exit $x = 0$. The resulting set of equations reads

$$\frac{\partial \rho}{\partial t} + \nabla(\rho \mathbf{u}) = 0, \tag{2}$$

$$\frac{\partial \rho \mathbf{u}}{\partial t} + \nabla(\rho \mathbf{u} \otimes \mathbf{u}) = -\nabla p + \nabla \boldsymbol{\tau}, \tag{3}$$

$$\frac{\partial \rho E}{\partial t} + \nabla(\rho \mathbf{u} E) = -\nabla \mathbf{h} + \nabla(\boldsymbol{\tau}\mathbf{u}). \tag{4}$$

The total energy E is defined as

$$E = \frac{T}{\gamma(\gamma-1)Ma^2} + \frac{1}{2}\mathbf{u}^T\mathbf{u}, \tag{5}$$

with $\gamma = 1.4$. The molecular stress tensor is written as $\boldsymbol{\tau}$, and the heat flux is denoted as $\mathbf{h}$. Further details and definitions are given in Sandberg (2007).

Eqs. (2)–(4) are linearized around the turbulent mean state presented in Section 2.1, in terms of fluctuation variables defined by a Reynolds decomposition, $\rho = \overline{\rho} + \rho'$, and accordingly for all other flow variables.

Turbulent viscosity. Our analysis aims at modeling the evolution of coherent fluctuation patterns ('wavepackets') in a fully turbulent

jet. Undoubtedly this evolution is affected by the action of fluctuations in the Reynolds stresses, and the question how these effects are to be accounted for in a linear model has been a topic of debate for a long time. A systematic approach has been established (Reynolds and Hussain, 1972) on the basis of a *triple decomposition*, which clearly identified the underlying closure problem. Various strategies have been employed in linear stability studies (useful discussions can be found in Meliga et al., 2012; Mettot et al., 2014), and new approaches have been presented in the recent literature (Beneddine et al., 2016; Tammisola and Juniper, 2016), but all of these still rely on empirical models and ad hoc choices.

For the present study, we opt for a comparably simple turbulent viscosity approach, based on the assumption that the unsteady RANS equations provide a suitable model for low-frequency motion in turbulent jets. The classical turbulent viscosity model, which replaces the Reynolds stresses with a diffusive term as $\overline{u'v'} = -\nu_t \partial_r \overline{u}$, has proven to yield accurate results for the steady mean flow of round jets (Pope, 2000). Here we extend the application of this model to the coherent fluctuations. The turbulent viscosity ν_t is taken to be a function of the coordinates x and r, and it is directly obtained from the experimental measurements as

$$\nu_t = -\frac{\overline{u'v'}}{\partial_r \overline{u} + \epsilon}. \tag{6}$$

The original $\overline{u'v'}$ measurements are shown in Fig. 2*b*. This distribution has been smoothened and extrapolated in a similar fashion as the axial mean flow velocity. Since the mean shear $\partial_r \overline{u}$ decays to zero outside the jet, the fraction in Eq. (6) is regularized with a value $\epsilon = 10^{-4}$. The resulting distribution of ν_t, shown in Fig. 3*c*, is then added to the molecular viscosity in the linear perturbation equations. Note that ν_t itself is not considered to be a perturbed quantity, as this would require additional modeling assumptions.

3.2. Computation of optimal forcing/response structures

Following our initial hypothesis, the harmonic component is obtained as the solution of an optimally forced problem (Garnaud et al., 2013a). The discretized state vector is denoted as $\mathbf{q} \in \mathbb{C}^n$, where n is the total number of degrees of freedom, describing the amplitude and phase of all fluctuation variables in every point of the numerical domain. The domain lies in the (r, x) plane, and all quantities are taken to be invariant in the azimuthal direction.

The linear perturbation equations are expressed in compact form as

$$\frac{\mathrm{d}\mathbf{q}}{\mathrm{d}t} - \mathbf{L}\mathbf{q} = \mathbf{B}\hat{\mathbf{f}} e^{i\omega t}. \tag{7}$$

On the right-hand side, the system is driven by harmonic forcing $\hat{\mathbf{f}}$ at frequency ω. The operator $\mathbf{B}$ represents a weight function, which is used here in order to place constraints on the forcing. By setting $\mathbf{B}$ to zero everywhere outside the inlet pipe, the forcing is restricted to the pipe interior. This choice is motivated by the observation that the jet dynamics are particularly sensitive to details of the flow upstream of the nozzle, and to the development of the pipe boundary layer in particular (Brès et al., 2015).

Introducing the ansatz $\mathbf{q} = \hat{\mathbf{q}} e^{i\omega t}$, Eq. (7) can be rewritten as the following input-output system

$$\hat{\mathbf{q}} = (i\omega - \mathbf{L})^{-1}\mathbf{B}\hat{\mathbf{f}} = \mathbf{R}(\omega)\mathbf{B}\hat{\mathbf{f}}, \tag{8}$$

where the resolvent operator $\mathbf{R}(\omega)$ plays the role of a transfer function at a given frequency ω. The forcing $\hat{\mathbf{f}}$ is the unknown of our system: it is defined such that the ratio between the energy of the frequency response and the energy of the forcing input is maximized, *i.e.*

$$\sigma^2_{max} = \max_{\hat{f}} \frac{\|\hat{\mathbf{q}}\|^2_Q}{\|\hat{\mathbf{f}}\|^2_Q} = \max_{\hat{f}} \left(\frac{\hat{\mathbf{f}}^\dagger \mathbf{B}^\dagger \mathbf{R}^\dagger \mathbf{Q} \mathbf{R} \mathbf{B} \hat{\mathbf{f}}}{\hat{\mathbf{f}}^\dagger \mathbf{Q} \hat{\mathbf{f}}} \right), \tag{9}$$

where the †-superscript indicates the Hermitian transpose. The real positive-definite matrix $\mathbf{Q}$ represents the norm (see Hanifi et al., 1996)

$$\|\hat{\mathbf{q}}\|^2_Q = \int_\Omega \left(\rho_0 \hat{\mathbf{u}}^2 + \frac{p_0}{\rho_0} |\hat{\rho}|^2 + \frac{\rho_0^2}{\gamma^2(\gamma-1)Ma^4 p_0} |\hat{T}|^2 \right) r \,\mathrm{d}r \,\mathrm{d}x. \tag{10}$$

The optimal forcing $\hat{\mathbf{f}}$ and associated gain $\sigma^2_{\max}$ at frequency ω are recovered as the leading eigenvalue/eigenvector pair of the operator

$$\mathbf{C} = \mathbf{Q}^{-1}\mathbf{B}^\dagger \mathbf{R}^\dagger(\omega)\mathbf{Q}\mathbf{R}(\omega)\mathbf{B}, \tag{11}$$

according to the Rayleigh quotient in Eq. (9). This maximum-gain forcing/response pair will be named the *optimal* mode in the following. All subsequent eigenmodes of $\mathbf{C}$ are orthogonal among each other with respect to the scalar product defined by $\mathbf{Q}$, and they can be ordered according to their real eigenvalues (gains). These forcing/response pairs will be named *sub-optimal* modes.

The global frequency response analysis describes an externally forced system, and as such it is closely related to the PSE and to the local spatial stability approaches that were used in earlier studies (Cavalieri et al., 2012; Suzuki and Colonius, 2006). In contrast to these, the present formalism fully accounts for non-parallelism, and it does not restrict the flow response to locally exponential behavior. The model hypothesis is that the most observable structures in the jet response to stochastic forcing, as measured in the experiment, will correspond to the most amplified wavepackets, as identified in the linear analysis. The acoustic radiation that is associated with near-field wavepackets is obtained as part of the flow response to the applied forcing.

3.3. Numerical methods

Due to the large dimensions of the discrete linear system, the optimization problem is solved by power iteration, which involves alternate time-stepping of the direct and adjoint perturbation equations. High-order explicit finite difference schemes (Berland et al., 2007) are used to resolve spatial derivatives. Time integration is performed with a fourth-order Runge–Kutta algorithm. Symmetry boundary conditions are imposed at $r = 0$, and convective boundary conditions and sponge regions are used on all other boundaries.

Convergence tests. The numerical domain extends over the interval $x = [-18.5D, 21D]$ in the streamwise direction, and over $r = [0, 22D]$ in the radial direction. It is discretized with $(N_r, N_x) = (330, 625)$ points, concentrated near the nozzle tip with minimum spacings $\Delta x = 0.015$ and $\Delta r = 0.011$. Grid convergence has been verified by varying the resolution and the point distribution; three examples are reported in Table 1, labeled as cases A, B and C0 for the case $St = 0.4$. The level of convergence is estimated based on the maximum amplification rate $\sigma_{\max}$. In all these test runs, in

Table 1
Convergence test configurations, run for $St = 0.4$.

	$\Delta x_{\min}$	$\Delta r_{\min}$	T_{opt}	$\sigma_{\max}$
case A	0.020	0.015	60	386.77
case B	0.015	0.015	60	391.90
case C0	0.015	0.011	60	394.77
case C1	0.015	0.011	50	392.14
case C2	0.015	0.011	70	395.13

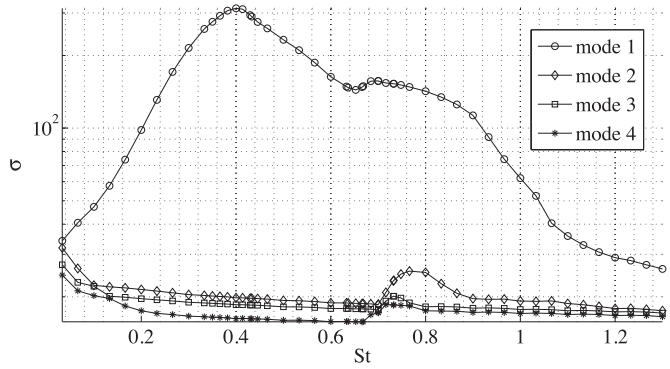

Fig. 4. Amplification rate σ, as a function of the Strouhal number, for the four most amplified modes. The maximum amplification rate is attained at $St = 0.4$. Another local maximum is found around $St = 0.7$ in all four curves.

contrast to the results presented in detail in the following section, the forcing support was not restricted to the pipe interior, and the values of $\sigma_{\max}$ are higher as a result.

The amplification rate is also affected by the time horizon T_{opt} over which the optimization is carried out. For all results presented in the following section, direct and adjoint time integration is always performed with a time step $\Delta t \approx 0.01$ over $T_{opt} = 60$ nondimensional units; this time horizon corresponds roughly to twice the convection time along the centerline between the nozzle lip and the sponge region. The comparison between cases C0, C1 and C2 (Table 1) demonstrates very good convergence. The four most amplified forcing/response pairs are computed at each Strouhal number, using a Krylov space of dimension $N_k = 15$.

In order to test the robustness of the results with respect to details of the mean flow, the same computations have also been performed at $St = 0.4$ on the mean flow obtained from LES (Brès et al., 2015). Some discrepancies in the flow response arise downstream of the potential core, where indeed the LES and experimental mean flows differ. However, amplification rates and forcing structures are found to be in very good agreement for both mean flows.

4. Near-field and far-field results of the frequency response analysis

The amplification gain σ is shown as a function of the Strouhal number St in Fig. 4 for the optimal mode and the first three sub-optimal modes. The overall maximum gain is attained at $St = 0.4$. This value is consistent with previous studies of jets without co-flow: for instance, Crow and Champagne (1971) report a maximum forcing response at $St = 0.3$ in their experiments; Garnaud et al. (2013a) find the maximum gain around $St = 0.45$ in an incompressible jet, and they show this value to be quite insensitive with respect to the Reynolds number and to the restrictions imposed on the forcing support.

Near its maximum, the gain of the optimal mode is more than one order of magnitude larger than that of all others. The sub-optimal modes exhibit gain values that are comparable among each other over the entire range of Strouhal numbers shown in Fig. 4. The clear dominance of the optimal over the sub-optimal modes is in contrast with the observations of Jeun et al. (2016), who found little separation between these in a $Ma = 0.9$ jet. The mean flow fields used in the present study and in Ref. (Jeun et al., 2016) are believed to be very similar (Jordan et al., 2014). However, a different norm is used, no Reynolds-stress model is included, and forcing is applied throughout the free-jet region in Ref. (Jeun et al., 2016).

In Fig. 5, the axial velocity component of the optimal forcing, restricted to the pipe interior, is shown alongside the associated response wavepackets for six values of the Strouhal number. The forcing structures are consistently composed of two elements: a plane acoustic wave that travels downstream, and slim vortical structures at the pipe wall that are tilted against the flow direction. The latter structures, which were also identified in incompressible settings (Garnaud et al., 2013a), resemble optimal perturbations in wall-bounded flows that exploit the Orr mechanism. Such tilted structures rotate as they convect, thereby extracting energy from the mean flow, until they are aligned with the mean flow velocity gradient.

Close to the nozzle, the flow response in the free jet is clearly dominated by a vigorous shear instability. As the mean flow spreads quickly, the perturbations invade the entire jet column. In the fully developed downstream region of the jet, all perturbations eventually decay. Low frequencies sustain spatial growth over a longer streamwise interval, consistent with the local stability properties of a spreading jet (Garnaud et al., 2013a). Indeed, all optimal response wavepackets resemble each other, except that with growing Strouhal number the characteristic length scales become shorter, affecting both the carrier wavelength and the envelope length.

A peculiar non-monotonic behavior is observed in Fig. 4 in all gain curves around $St = 0.7$. In the optimal mode case (Fig. 5), this coincides with a change in the forcing structure: at Strouhal numbers between 0.7 and 0.8, the acoustic component of the forcing appears to shift from a plane to an oblique wave pattern, as the half-length of an acoustic wave becomes comparable to the pipe diameter. We hypothesize that these oblique waves in the pipe increase the efficiency of the jet forcing.

Sub-optimal forcing structures and associated flow response wavepackets are presented in Fig. 6. The Strouhal number is 0.4 in all cases, and singular modes $n = 2, 3, 4$ are shown, from top to bottom. The spatial distributions in all three cases are quite distinct from the one of the optimal mode in Fig. 5; in particular, the forcing amplitude peaks in the center of the pipe, although it presents again oblique near-wall structures reminiscent of Orr-type forcing, and the wavelength corresponds to a convective (non-acoustic) phase velocity. The forcing structures of the $n = 2$ and 4 modes bear a strong resemblance, but mode 4 displays an additional phase change in the radial direction, suggesting that these modes are of the same family, with different radial wavenumbers. The same observation is true for the associated response wavepackets. It is less obvious how the $n = 3$ mode may relate to the two others, although it still exhibits similar qualitative features. All three sub-optimal modes excite perturbations on the jet centerline, with no discernible shear-type signature. The wavelength of the sub-optimal response modes in the potential core is significantly larger than that of the shear-related optimal mode, and their phase velocities are positive (directed downstream) throughout the near field, including the pipe.

The *acoustic far field* of the flow response wavepackets is finally visualized in Fig. 7, for the optimal mode at $St = 0.4$ and 0.64. Snapshots of the density perturbation field are shown, with a color scale that resolves the low acoustic amplitudes away from the jet. The sound waves seem to emanate either from the near-nozzle region, where hydrodynamic perturbations grow exponentially, or perhaps directly from the nozzle. A double-beam pattern forms at $St = 0.4$, whereas a single beam is found at $St = 0.64$. Similarly marked directivity patterns are characteristic for the acoustic fields of the optimally forced wavepackets, also at other Strouhal number values.

5. Comparison with the experiment

The linear model results can be compared to experimental measurements, provided that the *axisymmetric* fluctuation component

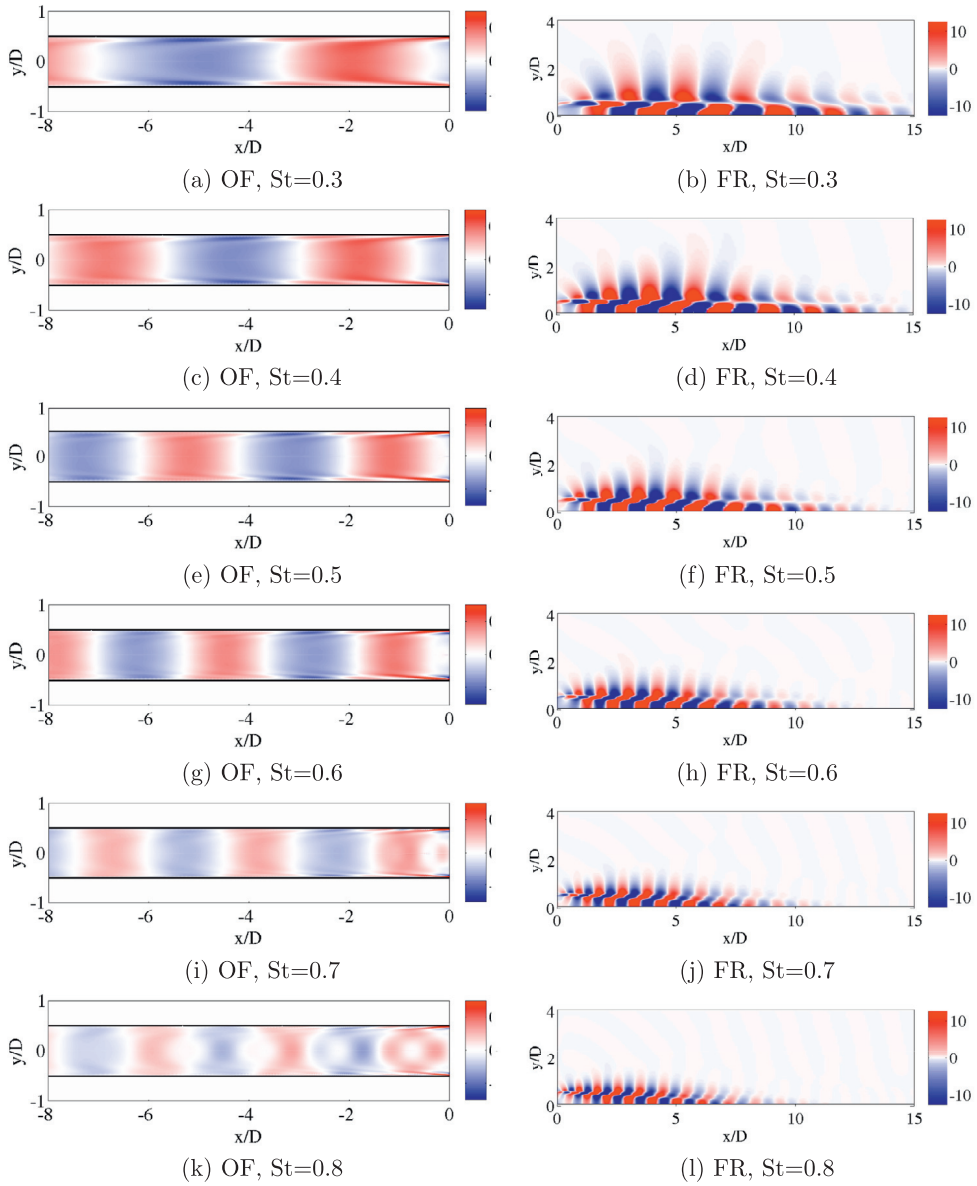

Fig. 5. Optimal forcing (OF) and flow response (FR) structures for various Strouhal numbers. The axial velocity component is shown. The forcing is restricted to the interior of the pipe.

in the experiment can be isolated. A reasonably easy way to do this is to only regard fluctuations of the axial velocity on the jet centerline; in a Fourier decomposition into azimuthal modes, only the axisymmetric mode is non-zero in this velocity component. The centerline velocity fluctuations are readily extracted from the PIV data, and a temporal FFT is performed. The results are presented in Fig. 8*a* as logarithmic color contours of the power spectral density (PSD) in the $x - St$ plane.

Corresponding centerline data, obtained from the frequency response analysis, are shown in Fig. 8*b* for comparison. The resemblance between the experimental data and the linear model results is not particularly convincing at this point. The linear frequency response appears to underpredict the amplitudes at low Strouhal number, and it does not seem to reproduce a certain anomaly that is found in the experimental spectrum at $St = 0.45$. However, all these differences may be due to the amplitude normalization of the frequency response results. In Fig. 8*b*, it is assumed that the forcing energy input is identical at every Strouhal number, which is certainly not the case in the experiment. Furthermore, the time-resolved PIV measurements in the range $2.2 \leq x \leq 3.8$ are affected by optical distortions, which explains an irregularity in the contours in Fig. 8*a*.

A more pertinent comparison can be made for individual Strouhal numbers. Fig. 9 compares experimental and linear model PSD data for eight values of St between 0.1 and 0.8. As the amplitude in the linear model is an arbitrary constant, the frequency response (FR) curves may be vertically shifted for an eyeball fit with the reference data. PIV results in the region $2 \leq x \leq 4.5$ are excluded from these plots. In order to give a more complete picture, LES data (Brès et al., 2015) are also included.

The linear model fails to capture the experimentally observed wavepackets at low Strouhal numbers, $St \leq 0.2$. At $St = 0.3$, the initial phase of exponential growth in the LES results is fairly well reproduced, although only over a short streamwise distance. The reference data shows atypical behavior at $St = 0.4$, which again is not reproduced by the linear analysis. At Strouhal numbers between 0.5 and 0.8, however, the linear predictions compare favorably with experiment and LES over the first three diameters. A sometimes

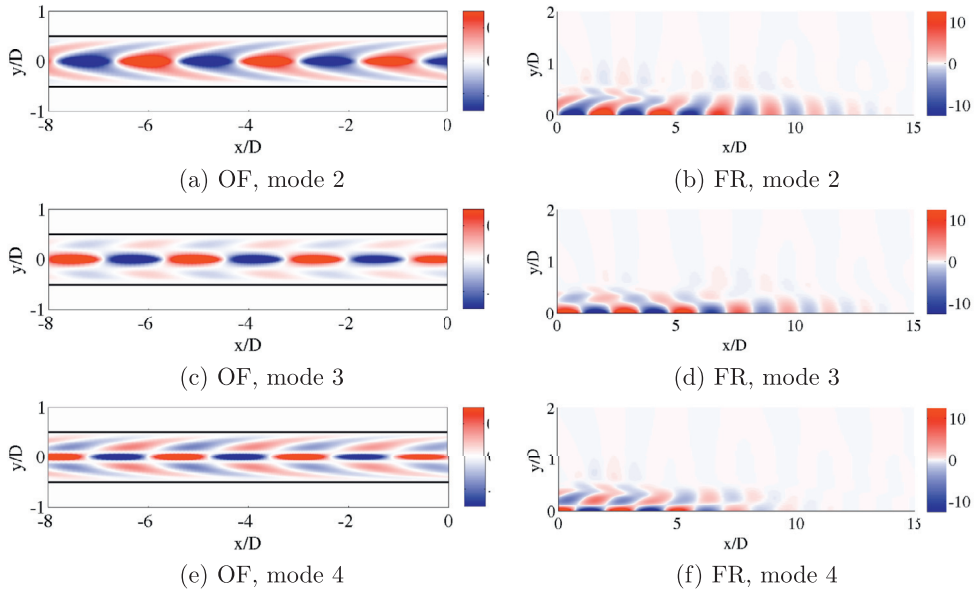

Fig. 6. Sub-optimal forcing (OF) and flow response (FR) structures for $St = 0.4$ and modes 2, 3 and 4. The axial velocity component is shown. The forcing is restricted to the interior of the pipe.

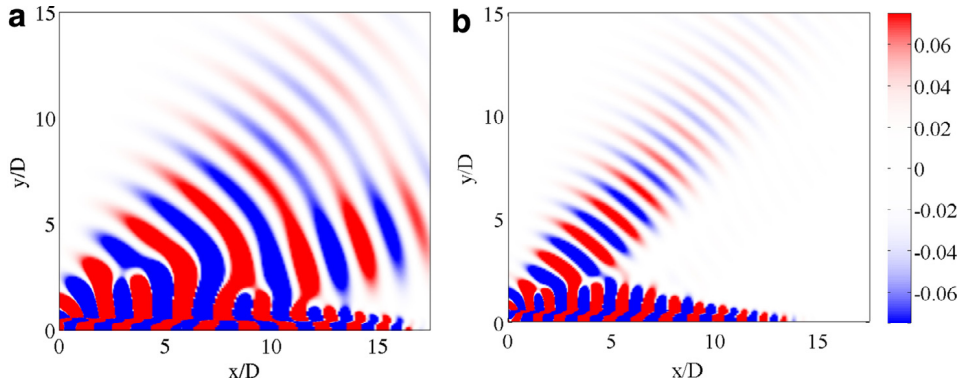

Fig. 7. Density fluctuations of the flow response to optimal forcing at (*a*) $St = 0.4$, and (*b*) $St = 0.64$.

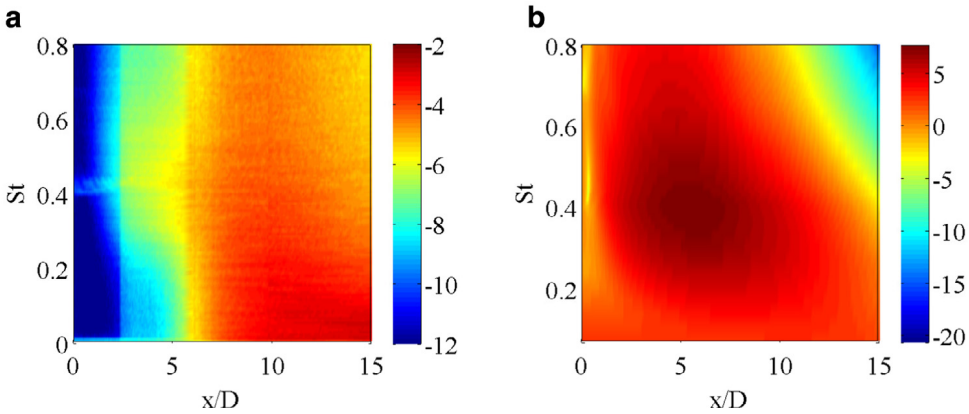

Fig. 8. Hydrodynamic near field: power spectral density of axial velocity fluctuations on the jet centerline. *(a)* PIV measurements; *(b)* linear frequency response results (axisymmetric mode). A logarithmic scale is used in both figures.

irregular curve shape may seem surprising, but is easily explained by the fact that only centerline values are plotted here, whereas the fluctuations near the nozzle exit are concentrated in the shear layer.

Far-field acoustic data is found from the microphone array measurements, taken at 16 azimuthal positions around the jet, at a radial distance of 14.2 jet diameters, and at axial positions between $x = -4$ and 39. A cylindrical surface is considered. Averaging over all azimuthal positions yields a good approximation of the instantaneous axisymmetric sound component, which is then Fourier-transformed in time. The results are shown in Fig. 10*a* as a function of Strouhal number and radiation angle. The angle with the jet

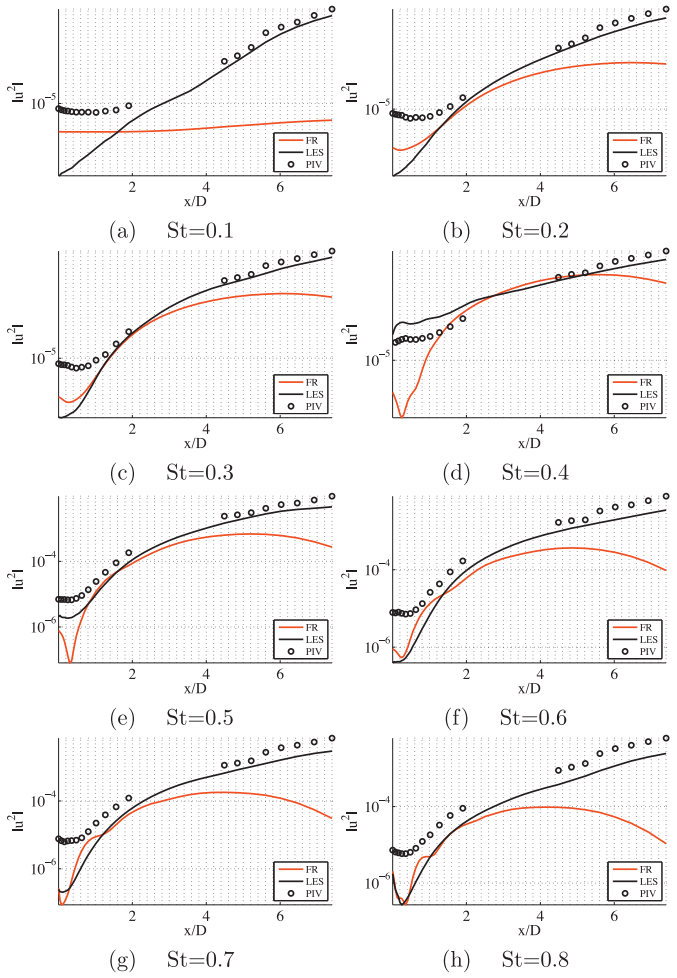

Fig. 9. Power spectrum density (PSD) of the axial momentum fluctuation velocity u' on the centerline as a function of x/D, at various Strouhal numbers, for three different datasets: i) linear frequency response (red, solid line); ii) LES data (black, solid line); iii) PIV data (markers). (For interpretation of the references to colour in this figure legend, the reader is referred to the web version of this article.)

axis, measured from the nozzle exit $x = 0$, is simply obtained by rescaling the axial coordinate; the reported values are not scaled with respect to the distance from the nozzle. In experiments at Mach numbers between 0.35 and 0.6 (Cavalieri et al., 2012), the sound emission associated with the axisymmetric wavepackets is dominant at low angles, below 25°; the present data confirm this trend also at $Ma = 0.9$. Higher-order azimuthal modes (not considered here) radiate preferably at higher polar angles.

Corresponding data from the linear frequency response analysis are plotted in Fig. 10*b* for comparison. It must be noted that the comparison between experiment and linear model again suffers from the arbitrary normalization of the linear results, and a uniform forcing norm of unity has been used in order to generate this figure. As a result, absolute contour values cannot be expected to agree between Fig. 10*a* and *b*, but the directivity patterns at individual Strouhal numbers can be compared. Both in the experiment and in the linear analysis, one dominant beam is identified at $St < 0.8$, and in both cases its angle increases slowly with Strouhal number. At $St = 0.8$, the maximum radiation is found around an angle of 50° in the linear model, whereas it is closer to 40° in the experiment. Above $St = 0.8$, a strong additional acoustic lobe appears in the linear results, radiating in the direction perpendicular to the jet, and even upstream. This lobe however is absent in the experiment. Precisely the same behavior was observed by Garnaud et al. (2013b), who obtained strong upstream radiation in the linear frequency response of a jet at high Strouhal numbers, which was not at all present in the reference DNS.

6. Conclusions

A linear frequency response analysis has been performed, for the first time, on a turbulent jet mean flow obtained from experiments. The jet operates at $Ma = 0.9$ and $Re = 10^6$. The linear analysis allowed to identify the optimal forcing mode over a range of Strouhal numbers, $0.1 \leq St \leq 1.2$, as well as the three following sub-optimal forcing modes, together with the associated flow response. Detailed hydrodynamic near-field and some acoustic far-field results have been documented, and they have been compared to experimental data. Near-field results from a companion LES study (Brès et al., 2015) were included in order to complement the comparison in flow regions where the experimental data was incomplete. The dominant linear mode has been found to agree reasonably well with the nonlinear reference data in the region close to the nozzle, where the linear approximation is valid, at Strouhal numbers between 0.3 and 0.8. The particular value $St = 0.4$ is an exception: here, experimental and LES data both display markedly different trends than at other Strouhal values, and this phenomenon has been described in full detail in recent studies (Schmidt et al., 2016) to be the manifestation of 'trapped acoustic modes'. Remarkably, no such trapped modes seem to play a dominant role in the present analysis.

The failure of a linear instability model based on the optimals to predict the flow dynamics at low Strouhal numbers, and several

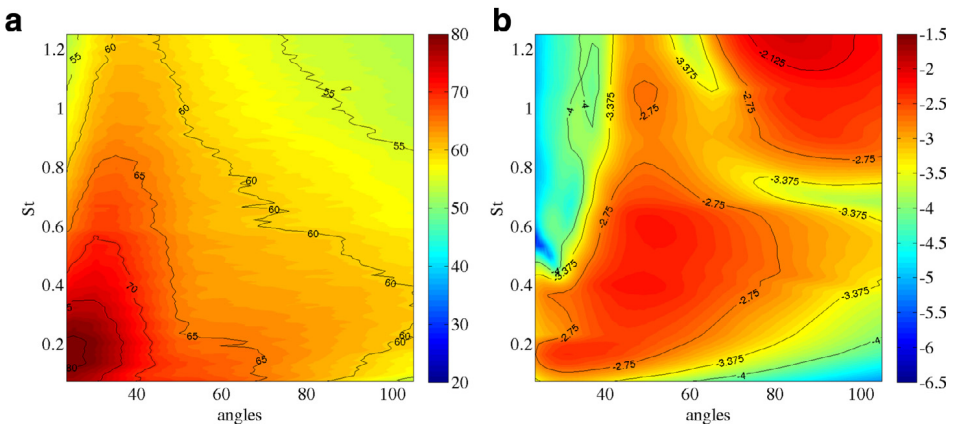

Fig. 10. Acoustic far field: power spectral density of acoustic waves outside the jet. *(a)* microphone pressure measurements (azimuthal average), scaled as dB/Hz; *(b)* linear frequency response results (axisymmetric mode), scaled with respect to unit energy forcing input at each Strouhal number.

diameters downstream of the nozzle, is consistent with previous studies that used PSE or linearized Euler simulations (Baqui et al., 2015; Cavalieri et al., 2013). However, recent results suggest that it might be possible to overcome some of these limitations within the linear frequency response formalism (Beneddine et al., 2016; Semeraro et al., 2016).

The branch of optimal modes exhibits forcing structures that are clearly composed of two distinct components: an acoustic wave (plane for $St < 0.7$ and oblique for $St > 0.7$) and oblique vortical waves near the pipe wall that draw their efficiency from the Orr mechanism. Both components trigger a shear instability in the potential core region of the jet, which provides the mechanism for strong spatial growth of perturbations. The resulting wavepackets are of the same kind as those obtained, for instance, by Crighton and Gaster (1976), or from PSE (Cavalieri et al., 2013). It is noted that the relative strength of acoustic versus vortical forcing components necessarily depends on the norm that is used to measure the input energy. The frequency response formalism involves several choices that affect the results, such as the localization of the forcing, the choice of the norm and the modeling of Reynolds stresses.

A recent frequency response analysis of a $Ma = 0.4$ jet (Semeraro et al., 2016), where turbulent viscosity is not accounted for and no localization restriction is imposed on the forcing, identifies very similar forcing structures of the optimal mode as found in the present results. The sub-optimal modes differ significantly however: without localization, both the sub-optimal forcing and the response structures reside inside the shear layer of the free jet. The present choice to restrict the forcing to the nozzle pipe allowed to identify the influence of the upstream flow system onto the free-jet dynamics (Brès et al., 2015). The first three sub-optimals in this case carry their maximum amplitude on the centerline of the pipe, and their radial structure suggests that they belong to one family, hierarchically ordered by a radial wavenumber. These centerline perturbations appear to drive jet-column instability modes in the free jet, which inherit the radial structure from the forcing modes. It is interesting to note that all shear-layer instability dynamics seems to be contained in the optimal forcing, whereas it is absent in the subsequent sub-optimals. The frequency response formalism, together with the localized forcing, cleanly separates shear-layer and jet-column dynamics inside the potential core.

A rather strong separation has been noted between the optimal gain value and that of the highest sub-optimal, at least over the relevant interval $0.2 \leq St \leq 1$. The present results in this respect differ from the findings of Jeun et al. (2016). These differences are attributed to the localization assumption, the turbulent viscosity model and the choice of the optimization norm.

Finally, only a preliminary description of acoustic radiation has been provided in this study. The comparison between linear analysis and experiment is limited to the qualitative directivity of the sound emission associated with the axisymmetric mode obtained at individual Strouhal numbers, as the available data does not allow to define a consistent scaling of the amplitude for the linear results. It can be concluded that the optimally forced linear wavepackets emit sound in a beam pattern that resembles the experimental measurements. However, the dominant beam angle in the linear model is larger by approximately 10° than in the experiment, and a strong additional acoustic lobe around 90° arises at $St > 0.8$, which is absent in the experimental data. Similar discrepancies were observed in the frequency response analysis of a DNS mean flow (Garnaud et al., 2013b). Notwithstanding, the overall agreement in the present case is clearly encouraging for further investigations into the linear modeling of jet dynamics and aeroacoustics. New experiments are under way that will facilitate a quantitative comparison of acoustic measurements with linear frequency response calculations.

Acknowledgments

The authors are grateful to Dr. Guillaume Brès for making his LES database available. This work was supported by the Agence Nationale de la Recherche (ANR) under the "Cool Jazz" project, grant number ANR-12-BS09-0024. All instability calculations were performed using HPC resources of TGCC and CINES under the allocation 2015-2a6451 made by GENCI. The LES study was performed at Cascade Technologies, with support from the NAVAIR SBIR project, under the supervision of Dr. John T. Spyropoulos. The main LES calculations were carried out on DoD HPC systems in ERDC DSRC.

References

Baqui, Y.B., Agarwal, A., Cavalieri, A.V., Sinayoko, S., 2015. A coherence-matched linear source mechanism for subsonic jet noise. J. Fluid Mech. 776, 235–267.
Beneddine, S., Sipp, D., Arnault, A., Dandois, J., Lesshafft, L., 2016. Conditions for validity of mean flow stability analysis. J. Fluid Mech. 798, 485–504.
Berland, J., Bogey, C., Marsden, O., Bailly, C., 2007. High-order, low dispersive and low dissipative explicit schemes for multiple-scale and boundary problems. J. Comput. Phys. 224 (2), 637–662.
Brès, G.A., Jaunet, J., Le Rallic, M., Jordan, P., Colonius, T., Lele, S.K., 2015. Large eddy simulation for jet noise: the importance of getting the boundary layer right. In: 21st AIAA/CEAS Aeroacoustics Conference, p. 2535.
Cavalieri, A.V., Jordan, P., Colonius, T., Gervais, Y., 2012. Axisymmetric superdirectivity in subsonic jets. J. Fluid Mech. 704, 388–420.
Cavalieri, A.V., Rodríguez, D., Jordan, P., Colonius, T., Gervais, Y., 2013. Wavepackets in the velocity field of turbulent jets. J. Fluid Mech. 730, 559–592.
Crighton, D., Gaster, M., 1976. Stability of slowly diverging jet flow. J. Fluid Mech. 77 (02), 397–413.
Crow, S.C., Champagne, F., 1971. Orderly structure in jet turbulence. J. Fluid Mech. 48 (03), 547–591.
Freund, J.B., 2001. Noise sources in a low-Reynolds-number turbulent jet at Mach 0.9. J. Fluid Mech. 438, 277–305.
Garnaud, X., Lesshafft, L., Schmid, P., Huerre, P., 2013a. The preferred mode of incompressible jets: linear frequency response analysis. J. Fluid Mech. 716, 189–202.
Garnaud, X., Sandberg, R.D., Lesshafft, L., 2013b. Global response to forcing in a subsonic jet: instability wavepackets and acoustic radiation. AIAA Paper 2232, 2013.
Gudmundsson, K., Colonius, T., 2011. Instability wave models for the near-field fluctuations of turbulent jets. J. Fluid Mech. 689, 97–128.
Hanifi, A., Schmid, P.J., Henningson, D.S., 1996. Transient growth in compressible boundary layer flow. Phys. Fluids (1994-present) 8 (3), 826–837.
Jeun, J., Nichols, J.W., Jovanović, M.R., 2016. Input-output analysis of high-speed axisymmetric isothermal jet noise. Phy. Fluids (1994-present) 28 (4), 047101.
Jordan, P., Colonius, T., 2013. Wave packets and turbulent jet noise. Annu. Rev. Fluid Mech. 45, 173–195.
Jordan, P., Colonius, T., Brès, G., Zhang, M., Towne, A., Lele, S., 2014. Modeling intermittent wavepackets and their radiated sound in a turbulent jet. In: Proceedings of the Summer Program, p. 241.
Meliga, P., Pujals, G., Serre, E., 2012. Sensitivity of 2-d turbulent flow past a D-shaped cylinder using global stability. Phys. Fluids (1994-present) 24 (6), 061701.
Mettot, C., Sipp, D., Bézard, H., 2014. Quasi-laminar stability and sensitivity analyses for turbulent flows: prediction of low-frequency unsteadiness and passive control. Phys. Fluids (1994-present) 26 (4), 045112.
Mollo-Christensen, E., 1963. Measurements of Near Field Pressure of Subsonic Jets. Technical Report. DTIC Document.
Pope, S.B., 2000. Turbulent Flows. Cambridge University Press.
Reynolds, W., Hussain, A., 1972. The mechanics of an organized wave in turbulent shear flow. Part 3. Theoretical models and comparisons with experiments. J. Fluid Mech. 54 (02), 263–288.
Sandberg, R. D., 2007. Governing equations for a new compressible Navier-Stokes solver in general cylindrical coordinates. Monograph No. AFM-07/07, School of Engineering Sciences, University of Southampton.
Scarano, F., 2002. Iterative image deformation methods in piv. Meas. Sci. Tech. 13, R1–R19.
Schmidt, O., Towne, A., Colonius, T., Jordan, P., Jaunet, V., Cavalieri, A.V., Brès, G.A., 2016. Super-and multi-directive acoustic radiation by linear global modes of a turbulent jet. In: 22nd AIAA/CEAS Aeroacoustics Conference, p. 2808.
Semeraro, O., Jaunet, V., Jordan, P., Cavalieri, A.V., Lesshafft, L., 2016. Stochastic and harmonic optimal forcing in subsonic jets. In: 22nd AIAA/CEAS Aeroacoustics Conference, p. 2935.
Suzuki, T., Colonius, T., 2006. Instability waves in a subsonic round jet detected using a near-field phased microphone array. J. Fluid Mech. 565, 197–226.
Tammisola, O., Juniper, M., 2016. Coherent structures in a swirl injector at Re= 4800 by nonlinear simulations and linear global modes. J. Fluid Mech. 792, 620–657.
Troutt, T., McLaughlin, D., 1982. Experiments on the flow and acoustic properties of a moderate-Reynolds-number supersonic jet. J. Fluid Mech. 116, 123–156.
Westerweel, J., Scarano, F., 2005. Universal outlier detection for piv data. Exp. Fluids 39 (6), 1096–1100.
Wieneke, B., 2005. Stereo-piv using self-calibration on particle images. Exp. Fluids 39, 267–280.

Aeroacoustics Conferences
30 May - 1 June, 2016, Lyon, France
22nd AIAA/CEAS Aeroacoustics Conference

AIAA-2016
22nd AIAA/CEAS Aeroacoustics Conference and Exhibit

Stochastic and harmonic optimal forcing in subsonic jets

Onofrio Semeraro*, Vincent Jaunet†, Peter Jordan‡, André V. G. Cavalieri§ and Lutz Lesshafft¶

Coherent fluctuations in a turbulent jet at $Ma = 0.4$ and $Re = 4.6 \times 10^5$ are analysed by combining experiments and linear stability analysis. Following the work by Dergham et al,[1] we explore the connection between singular modes of the resolvent operator and the measured covariance, within the framework introduced by Farrell and Ioannou.[2]

Instantaneous velocity fields are measured by means of time-resolved, stereoscopic PIV, in the radial-azimuthal plane at different locations along the streamwise direction. Proper orthogonal decomposition of the cross-spectral density covariance is applied for extracting coherent wavepackets, at a given frequency. The mean flow field is used for the linear stability analysis. We compute the singular value decomposition of the linear resolvent operator, derived from the fully compressible Navier-Stokes equations, in order to identify the optimal harmonic forcing and the associated linear flow response.

The analysis shows a remarkable agreement between the modal structures computed by linear analysis and the wavepackets extracted by statistical analysis of experimental measurements. These results suggest that the stochastic framework may help in shedding light on the structure of the non-linear forcing responsible for the wavepackets as observed in experiments.

I. Introduction

Much evidence has been produced in recent years that the fluctuation dynamics in the potential core of subsonic turbulent jets sustain coherent wavepackets.[3] Within a range of moderate Strouhal numbers, and in a flow region near the jet nozzle, the structure of these wavepackets has been found to be rather well predicted by means of local instability analysis,[4] by PSE[5] or by global analysis.[6] It is not clear at present why the agreement is limited to the near-nozzle region and to a certain band of Strouhal numbers. Indeed, it is not quite clear either why within these limits the agreement is pertinent: it appears to be a bold proposition that the coherence of fluctuations in a turbulent jet should resemble harmonically forced linear perturbations evolving in a quasi-laminar mean flow. The principal objective of the present study is to justify and validate the relevance of harmonically forced structures for the stochastic jet dynamics, on the basis of the theory developed by Farrell & Ioannou.[2]

In particular, accounting for the stochastic nature of fluctuations in jets is likely to be an important prerequisite for successful jet noise modelling. With regard to the noise that is generated by coherent wavepackets, linear models fail to give reliable predictions at present. On the one hand, the directivity pattern measured in direct numerical simulations of a low Reynolds number jet could be reasonably well

*Postdoctoral fellow, LadHyX, CNRS – École polytechnique, Palaiseau, France
†Postdoctoral fellow, Institute PPrime, University of Poitiers, Poitiers, France
‡Research Scientist, Institute PPrime, University of Poitiers, Poitiers, France
§Divisão de Engenharia Aeronáutica, Instituto Tecnológico de Aeronáutica, São José dos Campos, SP, Brazil
¶Research Scientist, LadHyX, CNRS – École polytechnique, Palaiseau, France

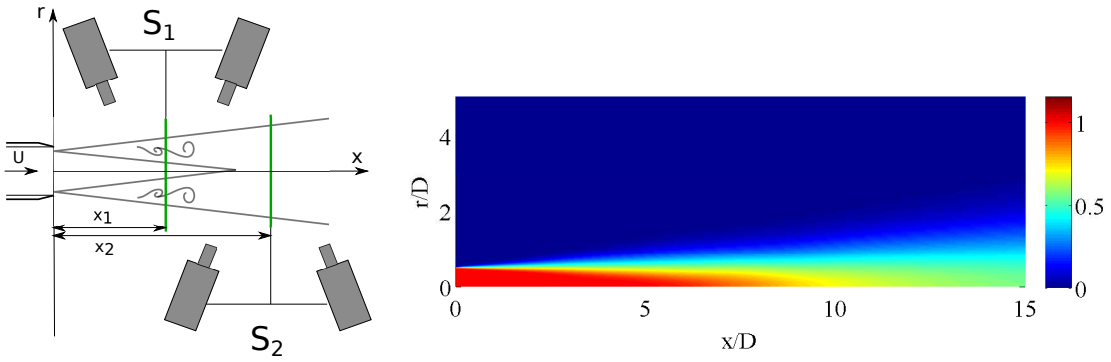

Figure 1. A schematic of the experimental setup is sketched on the left. On the right, the streamwise component of the meanflow is shown. The experiment operates at $Ma = 0.4$, corresponding to Reynolds number $Re_D \approx 4.6 \times 10^5$.

reproduced by singular modes of the resolvent operator,[6] and encouraging agreement has been found also for cases at high Reynolds number.[7,8] On the other hand, the absolute intensity of the sound field appears to elude linear modelling in terms of harmonic flow forcing. Baqui *et al.*[9] showed for high Reynolds number jets that the expected sound radiation from coherent wavepackets, computed from time-integration of the linear Euler equations, is significantly weaker than what is observed experimentally. In the same study, and in full agreement with earlier work,[10] the authors demonstrate that "jitter", or stochasticity, in a wavepacket is capable of greatly increasing its acoustic output.

In the present study, a well-documented jet configuration with Mach number $Ma = 0.4$ and Reynolds number $Re = 460\,000$ is revisited.[5] Its mean flow, as measured experimentally, is taken as a basis for the computation of the linear flow response to harmonic forcing, represented by singular modes of the resolvent operator at specific Strouhal numbers. This formalism identifies the optimal harmonic forcing, in the sense of maximum gain between the norms of forcing input and flow response output, as well as ordered orthogonal sub-optimal input-output pairs. The characteristics of these linear structures, which arise under perfectly harmonic and coherent flow conditions, are documented and discussed. A theroretical framework for stochastic dynamics[2] is then exploited in order to link these harmonic structures to the flow response to white-noise forcing, which is assumed to be provided by nonlinear turbulent dynamics.[1,11]

New experimental data allow to compute the two-point covariance of velocity fluctuations in the near field of the jet, within and beyond the potential core. POD wavepackets educed from this experimental data will be compared directly to the linear model results, in order to assess the applicability of the linear theory.

The remainder of the paper is organized as follows. In Sec. II, we provide the details of the experimental setup and the numerical tools used for the present analysis. The Sec. III describes the theoretical background and the results of the current investigation. The resolvent operator analysis is described in Sec. III.A, while the results are presented in Sec. III.A.2. In Sec. III.B, we introduce the stochastic framework by comparing it with the resolvent analysis; the link between the two approaches is stated. Finally, numerical results are compared with the experimental modal analysis in Sec. III.C.

II. Experimental and numerical setup

II.A. Experimental setup

Experiments were conducted at the "Bruit et Vent" jet-noise facility of the PPRIME Institute, Poitiers, France. The measurements were carried out at Mach number ($Ma = U_j/c$, where U_j is the jet velocity and c the ambient speed of sound) equal to 0.4 in isothermal conditions. These conditions are the same as used by Cavalieri *et al.*[5] The nozzle diameter D is 0.05m, giving a Reynolds number $Re = \rho U_j D/\mu = 4.6 \times 10^5$. The Strouhal number is defined as $St = \omega D/(2\pi U_j)$, where ω is the frequency.

Since we focus on low-order azimuthal Fourier modes and their two-point statistics, a dual-plane, time-

resolved, stereoscopic PIV system was used. The setup consisted of two synchronised TR-SPIV systems that could be moved independently, measuring instantaneous flow fields in the (r, θ) plane. The arrangement of the two systems allows the two measurement planes to be either coplanar or axially separated. The axial positions of the measurement planes were: $x_1 \in [1D, 8D]$ and $x_2 \in [x_1, 8D]$ in increments of $0.5D$, where x_1 refers to the axial position of the upstream system (S1) and x_2 to that of the downstream system (S2). For example, at a fixed position of S_1 at $x_1/D = 1$, the second system was successively positioned at $x_2/D = \{1, 1.5, 2..., 8\}$, and for each (x_1, x_2) couple an acquisition was performed. Hence, a complete set of pairs of instantaneous velocity fields was collected and two-point information was then retrieved for varying reference points and separations. A schematic of the setup is shown in figure 1.

The image acquisition was performed at 10kHz (5000 PIV samples per second), giving a maximum resolved Strouhal number of $St = 0.9$. The instantaneous velocity fields were interpolated onto a polar grid of 64 points in the radial direction and 64 points in the azimuth for $r/D < 0.8$, using a bi-cubic interpolation method. The spatial resolution of the interpolated field has been chosen to match the original one in order to avoid any loss of information. A more detailed description of the setup together with a validation of the results is given in Jaunet *et al.*[12]

II.B. Mean flow data

The mean flow used for the stability analysis described in the next section is shown in Fig. 1. The axial (streamwise) velocity component is shown. The present results are in excellent agreement with previous measurements by Cavalieri *et al.*;[5] therefore, the same mean flow as used by the aforementioned authors is adopted here. With respect to the original data, the velocity profile is further extended in the region far downstream ($x/D > 15$) and along the radial direction by means of self-similar solutions.[13] Moreover, we extrapolated the velocity field in the pipe – fully turbulent – from the data collected in the vicinity of nozzle. The resulting axial velocity field is used for computing the remaining quantities; temperature and density distributions are approximated from the Crocco-Busemann relation, and the radial velocity is recovered from the continuity equation.

II.C. Governing equations

The stability analysis is performed by solving the compressible Navier–Stokes equations linearised around the mean flow. The equations are cast in conservative variables $(\rho, \rho\mathbf{u}, \rho E)$ in cylindrical coordinates (r, θ, x). The reference length is taken to be the diameter of the nozzle D; the reference velocity is chosen as the centreline velocity U_j at the pipe exit at $x = 0$, and the ambient density is ρ_∞. The set of nonlinear equations in total variables reads

$$\frac{\partial \rho}{\partial t} + \nabla(\rho \mathbf{u}) = 0, \tag{1}$$

$$\frac{\partial \rho \mathbf{u}}{\partial t} + \nabla(\rho \mathbf{u} \otimes \mathbf{u}) = -\nabla p + \nabla \tau, \tag{2}$$

$$\frac{\partial \rho E}{\partial t} + \nabla(\rho \mathbf{u} E) = -\nabla \mathbf{h} + \nabla(\tau \mathbf{u}), \tag{3}$$

where ρ is density, $\mathbf{u}$ is velocity and E is the total energy, defined as

$$E = \frac{T}{[\gamma(\gamma - 1)Ma^2]} + \frac{1}{2}\mathbf{u}^T\mathbf{u}, \tag{4}$$

with $\gamma = 1.4$. The molecular stress tensor is τ, and the heat flux is denoted as $\mathbf{h}$. The reference quantities are used for the non-dimensionalisation of the equations. We refer to the technical report by[14] for a detailed formulation of each of the terms appearing in the equations.

The equations are linearised by introducing a triple decomposition[15] of the flow variables; for instance, the total velocity is decomposed as

$$\mathbf{u} = \bar{\mathbf{U}} + \tilde{\mathbf{u}} + \mathbf{u}', \tag{5}$$

where $\bar{\mathbf{U}}$ represents the time-averaged mean flow, and the remaining terms are fluctuations. The further analysis focusses on coherent fluctuations $\tilde{\mathbf{u}}$, whereas $\mathbf{u}'$ denotes the incoherent part of the turbulent spectrum. Within the framework of Reynolds & Hussain,[15] we adopt the 'quasi-laminar' approach: the molecular viscosity is computed using Sutherland's law, and turbulent viscosity is not accounted for in the equations that govern fluctuations.

In the following, coherent fluctuations $\tilde{\mathbf{u}}$ are modelled to obey the linearised Navier–Stokes equations. The analysis of these large-scale fluctuations through linear or nonlinear *ansätze* has been the object of numerous recent investigations on their role in the generation of jet noise.[3]

II.D. Numerical method

The Navier–Stokes equations in cylindrical coordinates are solved by means of numerical simulation. An axisymmetric geometry is considered. Spatial derivatives are discretised by means of high-order explicit finite-difference schemes[16] on a non-uniform cartesian grid. The discrete mesh consists of $[Nr, Nx] = [300, 700]$ grid points distributed on a non-uniform Cartesian grid, concentrated near the nozzle lip with minimum spacings $\Delta x = 0.02$ and $\Delta r = 0.005$. The domain extends in the streamwise direction over the interval $x/D = [-10.5,\ 22.75]$, and over $r/D = [0,\ 12.5]$ in the radial direction. Symmetry boundary conditions are imposed at $r = 0$. Characteristic boundary conditions in combination with a sponge region are applied along all other boundaries.

Time integration is performed with a fourth-order Runge–Kutta algorithm, with $\Delta t \approx 0.005$. More details on the numerical method are given in Garnaud.[17]

III. Harmonic and stochastic optimal forcing

The spatial discretisation allows to write the system in a compact discrete form. The linear flow response to a forcing input can be written as

$$\frac{\partial \mathbf{q}}{\partial t} = \mathbf{A}\mathbf{q} + \mathbf{f}, \tag{6}$$

where the state vector $\mathbf{q} = (\tilde{\rho}, \tilde{\mathbf{u}}_x, \tilde{\mathbf{u}}_r, \tilde{E})$ contains the fluctuation quantities of density, streamwise and radial velocity, and total energy. The flow forcing is given by the vector $\mathbf{f}$; the matrix $\mathbf{A}$ represents the Navier–Stokes operator, linearised around the mean flow, after boundary conditions are applied. The forcing enables the analysis of the system from an input-output perspective. Two possible choices are explored:

1. time-harmonic forcing at fixed frequency, using resolvent analysis,
2. stochastic noise input, characterised by *empirical orthogonal functions* (EOF).

In the following, the two approaches are introduced and compared from a theoretical point of view; numerical and experimental results are discussed.

III.A. Harmonic forcing

The input-output behaviour of the linear system 6, forced at frequency ω, is analyzed by introducing the forcing *ansatz* $\mathbf{f} = \hat{\mathbf{f}} e^{i\omega t}$. The time-asymptotic flow response will be of the form $\mathbf{q} = \hat{\mathbf{q}} e^{i\omega t}$, and the spatial structure of fluctuations around the mean flow is obtained as

$$\hat{\mathbf{q}} = (i\omega - \mathbf{A})^{-1} \hat{\mathbf{f}} = \mathbf{R}(\omega)\, \hat{\mathbf{f}}. \tag{7}$$

The operator $\mathbf{R}(\omega) = (i\omega - \mathbf{A})^{-1}$ is named the resolvent operator at frequency ω. A singular-value decomposition (SVD) of the resolvent operator identifies the optimal forcing structure $\hat{\mathbf{f}}$ that produces the most energetic flow response $\hat{\mathbf{q}}$, i.e. the maximum energy gain between input and output. This optimal forcing is given by the leading *right singular mode*; the associated flow response is the corresponding *left singular mode*, and the singular value represents the square root of the energy gain that is achieved between forcing

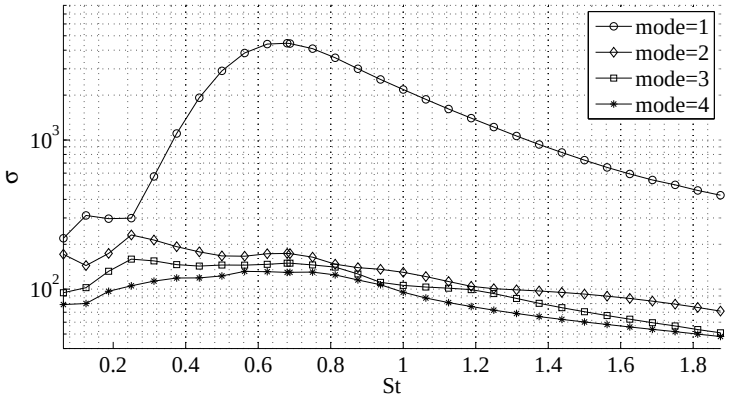

Figure 2. Gain curves as a function of the Strouhal number St; the curves are obtained by means of a resolvent analysis (see Sec. III.A). The optimal and three suboptimal branches are shown.

input and flow response. Suboptimal forcing-response pairs are given by subsequent singular modes. These modes, which are all mutually orthogonal, are readily ordered according to their gain.

Such analysis of the resolvent operator has been applied in recent years to boundary layers,[18,19] to incompressible[20] and compressible jets,[6,7] and to the backward-facing step,[21] to name just a few examples.

III.A.1. Optimisation procedure

The resolvent operator $\mathbf{R}(\omega)$ is built from the linearised, fully compressible Navier–Stokes equations. Due to the large dimension of the discrete linear system, the optimisation problem is solved by power iteration. This procedure involves alternate time-stepping of the direct and adjoint perturbation equations, with the energy norm[22] defined as

$$\|\hat{\mathbf{q}}\|^2 = \int_\Omega \left(\rho_0 \hat{\mathbf{u}}^2 + \frac{p_0}{\rho_0} |\hat{\rho}|^2 + \frac{\rho_0^2}{\gamma^2 (\gamma - 1) Ma^4 p_0} |\hat{T}|^2 \right) r \, \mathrm{d}r \, \mathrm{d}x \,. \tag{8}$$

As a result of this optimisation, we obtain the optimal forcing and maximum amplification rate at a given frequency, corresponding to the leading right singular mode and the singular value of the SVD, respectively. The frequency response is computed by solving the linear system forced by the computed forcing, at the prescribed frequency ω.

The first four singular modes are computed as a function of the Strouhal number, using a Krylov space of dimension $N_{kr} = 10$. The final time of integration for the direct and adjoint simulations is $T = 80$. All parameters were tested and found to provide reliable results at resonable computational cost. The numerical implementation invokes the SLEPC library for the solution of large scale sparse eigenvalue problems.[23] Further details on the implementation are given in Garnaud *et al.*[17]

III.A.2. Singular modes of the resolvent operator

Fig. 2 displays the energy amplification rate σ as a function of the Strouhal number. Three suboptimal branches are shown in the same figure. For values $St > 0.25$, the gain of the optimal branch is consistently well above the suboptimal ones; the maximum amplification rate is found to occur at $St = 0.68$. At this Strouhal number, the maximum amplification is about one order of magnitude larger than the first suboptimal.

The optimal forcing structures at $St = [0.25, 0.50, 0.68, 0.81]$ are displayed in the left column of Fig. 3. The optimal forcing in all cases is localised upstream of the nozzle: elongated structures are distributed all throughout the pipe, with maximum amplitude near the wall and towards the nozzle exit, and tilted against the gradient of the shear. These structures resemble the typical shape of optimal perturbations in

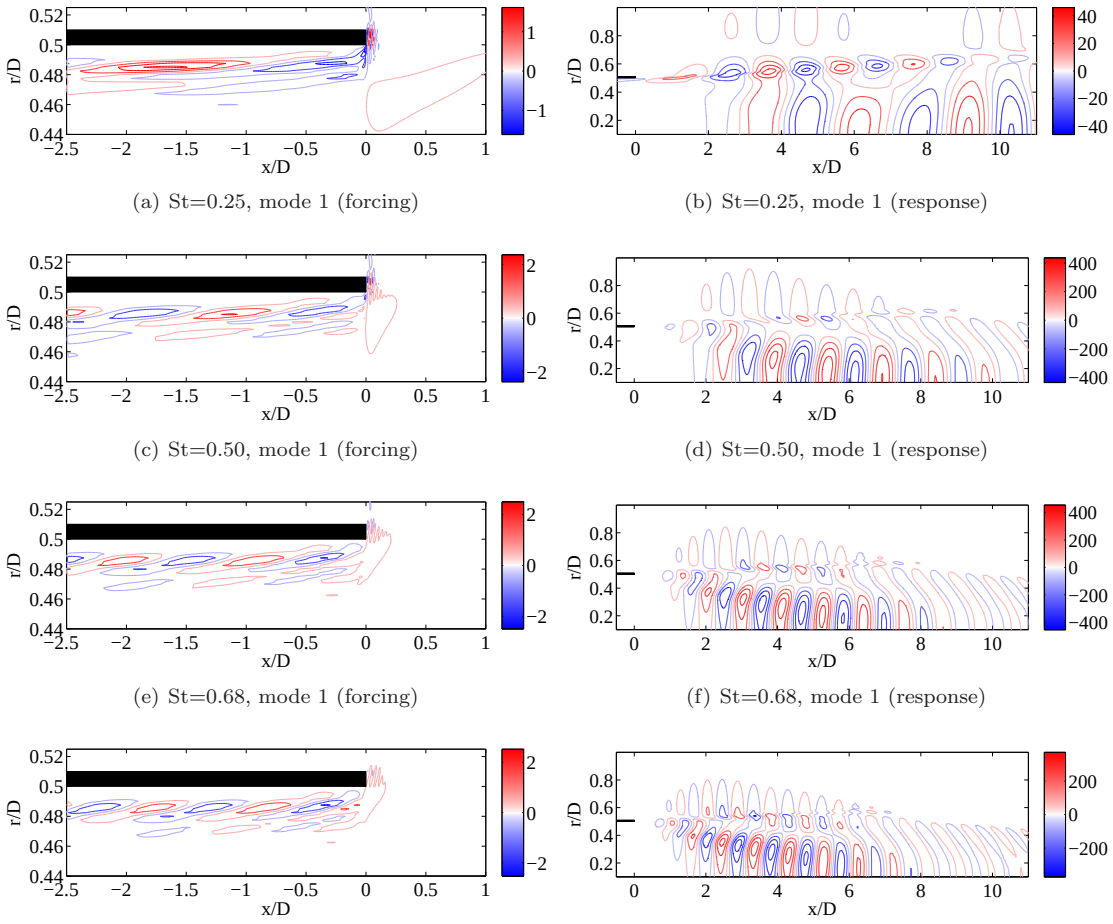

(a) St=0.25, mode 1 (forcing)

(b) St=0.25, mode 1 (response)

(c) St=0.50, mode 1 (forcing)

(d) St=0.50, mode 1 (response)

(e) St=0.68, mode 1 (forcing)

(f) St=0.68, mode 1 (response)

(g) St=0.81, mode 1 (forcing)

(h) St=0.81, mode 1 (response)

Figure 3. Optimal forcing and response mode pairs for St = [0.25, 0.50, 0.68, 0.81]. The streamwise velocity component is shown with 10 contour levels; blue and red contours indicate negative and positive levels, respectively.

wall-bounded flows (Orr-mechanism[18]), as observed in previous investigations.[6,20] As the Strouhal number increases, the features of the optimal forcing are preserved, but the streamwise wavelength progressively shortens; this behaviour can be observed by comparing the structures of the four optimal forcing structures shown in Fig. 3.

At $St < 0.25$, the amplification rates of the four different branches take on comparable values, and a crossing between the first two branches is observed. This low-St range is characterised by strongly elongated streamwise structures. At the same time, the optimal forcing includes patterns that extend outside of the pipe. Yet, the most amplified forcing structures are those that develop along the pipe wall for the optimal and the first suboptimal (not shown).

Associated near-field response wavepackets are shown in the right column of Fig. 3. The flow response feeds on shear instability, with support inside the shear layer and in the jet column inside the potential core. All optimal response wavepackets display a similar spatial development, with reduced length scales as the Strouhal number increases. Note that, as the Stouhal number increases, the perturbation decay in the fully developed downstream region quickens. This behaviour is consistent with the local stability properties:[20] low frequencies sustain spatial growth over a longer streamwise interval.

Suboptimal forcing and response structures are shown in Fig. 4 at the maximally amplified Strouhal

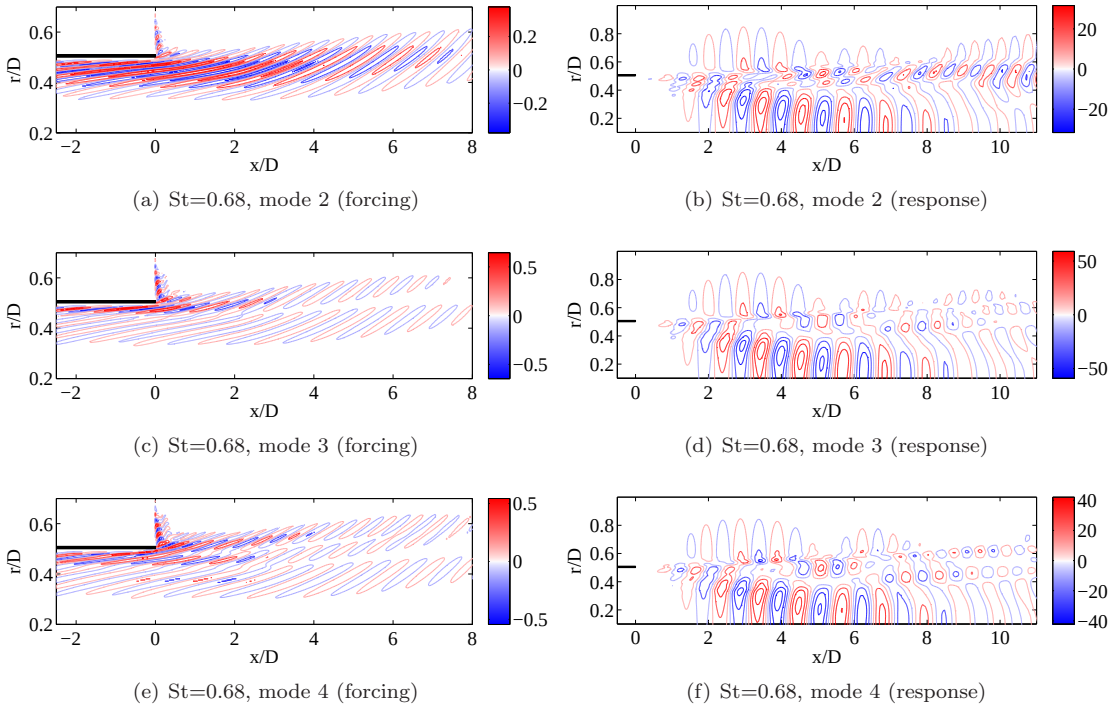

(a) St=0.68, mode 2 (forcing)

(b) St=0.68, mode 2 (response)

(c) St=0.68, mode 3 (forcing)

(d) St=0.68, mode 3 (response)

(e) St=0.68, mode 4 (forcing)

(f) St=0.68, mode 4 (response)

Figure 4. Three suboptimal forcing and response mode pairs at $St = 0.68$. The streamwise velocity component is shown with 10 contour levels; blue and red contours indicate negative and positive levels, respectively.

number 0.68. Also the suboptimal forcing structures are oriented against the gradient of the mean velocity. In contrast to the optimal forcing, the support of suboptimals extends well into the shear layer of the free jet. This is particularly evident for the second mode. All forcing structures share common features but appear to be hierarchically ordered by a radial wavenumber. The suboptimal flow response modes resemble the optimal wavepackets in that the maximum fluctuation amplitude is located inside the jet column in the potential core. Inside the shear layer, the radial signature of the forcing carries over to the response structure (compare Fig. 4*d* and Fig. 4*f*). As the Strouhal number increases, not shown in Fig. 4, the suboptimal modes retain their basic features, but the streamwise wavelength and the wavepacket envelope shortens.

III.B. Stochastic forcing

Incoherent noise input into equation 6 may be modelled by a forcing of the form $\mathbf{f}(\mathbf{x},t) = \mathbf{F}(\mathbf{x})\mathbf{w}(t)$. The vector $\mathbf{w}(t)$ contains random scalar elements with zero mean, $\langle \mathbf{w}(t) = 0 \rangle$, with all components uncorrelated in time, $\langle w_i(t)\, w_j(t') \rangle = \delta_{ij}\delta(t-t')$. The matrix $\mathbf{F}$ characterises the spatial distribution of the forcing; each column of $\mathbf{F}$ is multiplied with one scalar component of $\mathbf{w}(t)$. If $\mathbf{F}$ is a unitary matrix, $\mathbf{F}^H\mathbf{F} = \mathbf{I}$, the forcing is uncorrelated also in space.

Under these assumptions, $\mathbf{q}$ is now a stochastic state variable; all further analysis focuses on the covariance of $\mathbf{q}$. The covariance matrix is defined as

$$\mathbf{P}_{\mathbf{qq}} = \mathcal{E}[\mathbf{q}\mathbf{q}^H], \tag{9}$$

where the vector $\mathbf{q}$ is the flow state at any given time, $\mathbf{q}^H$ is its transpose conjugate and $\mathcal{E}$ denotes the expected value operator. $\mathbf{P}_{\mathbf{qq}}$ is a square matrix, with dimensions corresponding to the spatial degrees of freedom. Similarly, a covariance matrix for the forcing input is defined, $\mathbf{P}_{\mathbf{ww}} = \mathcal{E}[\mathbf{w}\mathbf{w}^H]$. By introducing the solution of the system 6 in the covariance Eq. 9, if the forcing is uncorrelated in time, we can write the

covariance in time-domain as

$$\mathbf{P_{qq}} = \int_0^\tau e^{\mathbf{A}(t-\tau)}\mathbf{F}\mathbf{P_{ww}}\mathbf{F}^H e^{\mathbf{A}^\dagger(t-\tau)}\mathrm{d}\tau. \tag{10}$$

It can be shown[2] that the covariance converges to a statistically steady state that is a solution of the Lyapunov equation

$$\mathbf{A}\mathbf{P_{qq}} + \mathbf{P_{qq}}\mathbf{A}^H + \mathbf{F}\mathbf{P_{ww}}\mathbf{F}^H = 0, \tag{11}$$

in the long-time limit $\tau \to \infty$. The covariance $\mathbf{P_{qq}}$ is called the *Gramian* of the system. The orthogonal eigenmodes of $\mathbf{P_{qq}}$ are referred to as *empirical orthogonal functions* (EOFs)[2] or proper orthogonal modes (PODs) of the Gramian . The eigenmodes of the dual Gramian $\mathbf{P_{ww}}$ represent the forcing structures that optimally excite the EOFs.[1]

In order to compute the EOFs, the Gramian $\mathbf{P_{qq}}$ needs to be constructed. The direct solution of the Lyapunov equation is feasible only if small dynamical systems are considered; indeed, for a number of degrees of freedom N, the storage requirement is of order N^2 and the computational costs of order N^3, regardless of the numerical technique adopted. Therefore, for systems with $N > 10^3$, alternative strategies are necessary. In particular, we can approximate the Gramian by means of the integral definition given in Eq. 10. In this case, the Gramian is computed by collecting snapshots from a linearised simulation, stochastically forced with noise uncorrelated in space and time. The integral is approximated by means of discrete quadrature in time-domain; this technique is often referred to as the *snapshot method*.[24] Equivalently, it has been demonstrated by Dergham *et al.*[1] that these matrices may be very well approximated in frequency-domain, in the basis of the optimal forcing and associated response modes obtained from the resolvent operator analysis, described in the previous subsection. This property is briefly discussed in the next paragraph as it provides the theoretical link between the resolvent modes and the stochastic framework.

III.B.1. Relation between harmonic and stochastic approach

The covariance matrix $\mathbf{P_{qq}}$ can be rewritten in frequency domain as follows

$$\begin{aligned}\mathbf{P_{qq}} &= \frac{1}{4\pi^2}\mathcal{E}\int\int_{-\infty}^{\infty}\hat{\mathbf{q}}(\omega_1)\hat{\mathbf{q}}^{\mathbf{H}}(\omega_2)e^{i(\omega_1-\omega_2)t}d\omega_1 d\omega_2 \\ &= \frac{1}{4\pi^2}\mathcal{E}\int_{-\infty}^{\infty}\hat{\mathbf{q}}(\omega)\hat{\mathbf{q}}^{\mathbf{H}}(\omega)d\omega = \frac{1}{4\pi^2}\int_{-\infty}^{\infty}\hat{\mathbf{P}}_{\hat{\mathbf{q}}\hat{\mathbf{q}}}(\omega)d\omega,\end{aligned} \tag{12}$$

where the covariance matrix $\hat{\mathbf{P}}_{\hat{\mathbf{q}}\hat{\mathbf{q}}}(\omega)$ is defined as

$$\hat{\mathbf{P}}_{\hat{\mathbf{q}}\hat{\mathbf{q}}}(\omega) = \mathcal{E}[\hat{\mathbf{q}}(\omega)\hat{\mathbf{q}}^H(\omega)]. \tag{13}$$

Thus, the time-domain covariance can be constructed from the frequency-domain covariances, estimated at each frequency ω; these covariances are called the *cross-spectral densities* and can be evaluated for both the inputs and the outputs. Remarkably, they provide an interesting link with the resolvent modes. If the flow state is expressed with the resolvent operator as $\hat{\mathbf{q}} = \mathbf{R}(\omega)\hat{\mathbf{f}}$, the cross-spectral density matrix $\hat{\mathbf{P}}_{\hat{\mathbf{q}}\hat{\mathbf{q}}}$ and the resolvent operator are related as

$$\begin{aligned}\hat{\mathbf{P}}_{\hat{\mathbf{q}}\hat{\mathbf{q}}} &= \mathcal{E}[\mathbf{R}(\omega)\mathbf{F}\mathbf{w}(\omega)\mathbf{w}^H(\omega)\mathbf{F}^H\mathbf{R}^H(\omega)] \\ &= \mathbf{R}(\omega)\mathbf{F}\mathcal{E}[\mathbf{w}(\omega)\mathbf{w}^H(\omega)]\mathbf{F}^H\mathbf{R}^H(\omega) = \mathbf{R}(\omega)\mathbf{F}\hat{\mathbf{P}}_{\hat{\mathbf{w}}\hat{\mathbf{w}}}\mathbf{F}^H\mathbf{R}^H(\omega).\end{aligned} \tag{14}$$

In the special case of perfectly uncorrelated forcing, the relation $\mathbf{F}\hat{\mathbf{P}}_{\hat{\mathbf{w}}\hat{\mathbf{w}}}\mathbf{F}^H = \mathbf{I}$ holds. By considering the singular mode decomposition of the resolvent operator $\mathbf{R} = \mathbf{U}\mathbf{\Sigma}\mathbf{V}$ and plugging it into Eq. 14, we finally obtain

$$\hat{\mathbf{P}}_{\hat{\mathbf{q}}\hat{\mathbf{q}}} = \mathbf{R}(\omega)\mathbf{R}^H(\omega) = \mathbf{U}\mathbf{\Sigma}\mathbf{V}\mathbf{V}^H\mathbf{\Sigma}^H\mathbf{U}^H = \mathbf{U}\mathbf{\Sigma}^2\mathbf{U}^H. \tag{15}$$

Therefore, the eigenmodes of the cross-spectral density matrix, written for the state responses at a given frequency ω, correspond to the singular response modes of the resolvent if the system is forced by white-noise forcing.

In the next section, the resolvent modes obtained by numerical simulation are compared with the eigenmodes of the cross-spectral matrix obtained from the experimental dataset.

III.C. Comparison between numerical and experimental results

Starting from the PIV data, we compute the cross-spectral density matrix $\hat{\mathbf{P}}(\omega)$ as the Fourier transform of the time-domain cross-correlation function

$$\hat{\mathbf{P}}(\omega, \mathbf{x}, \mathbf{x}') = \frac{1}{2\pi} \int \left(\int \mathbf{u}_x(\mathbf{x}, t) \mathbf{u}_x(\mathbf{x}', t-\tau) dt \right) e^{-i\omega\tau} d\tau, \tag{16}$$

where $\mathbf{x} = (x, r)$. We consider the axisymmetric component $m = 0$ of the streamwise velocity $\mathbf{u}_x$. Following the theoretical background, the coherent features of the cross-spectral density matrix can be extracted by means of an eigenvalue decomposition

$$\hat{\mathbf{P}}_r(\omega, \mathbf{x}, \mathbf{x}')\phi = \lambda_\omega \phi, \tag{17}$$

where λ_ω indicate the eigenvalues, while ϕ is the set of related eigenvectors. Note that the kernel $\hat{\mathbf{P}}_r(\omega, \mathbf{x}, \mathbf{x}')$ is given by

$$\hat{\mathbf{P}}_r(\omega, \mathbf{x}, \mathbf{x}') = \hat{\mathbf{P}}(\omega, \mathbf{x}, \mathbf{x}')\sqrt{rr'}, \tag{18}$$

where r and r' are the radii of the x and y points. This scaling ensures that $\hat{\mathbf{P}}_r$ is Hermitian. The final EOFs are rescaled by a spatial factor $r^{-\frac{1}{2}}$ along the radial direction. In practice, note that it is rather difficult to obtain an Hermitian $\hat{\mathbf{P}}_r$ from the experiments and negative eigenvalues are usually discarded.

The measurements are performed at $N_x = 15$ points along the streamwise direction, spanning the interval $x/D = 1, 1.5, ..., 8$. Along the radial direction, the resolution is $N_r = 64$, for $r/D < 0.8$. These values lead to matrices of dimension N^2, where $N = N_r \cdot N_x = 960$. An eigenvalue decomposition is performed for each frequency ω.

Before discussing the results, it is important to stress two aspects. First, the theoretical development relies on the assumption that the forcing is uncorrelated in space and time, i.e. it is white-noise. If the forcing is *coloured*, the covariances are still Hermitian, but the exact relation between resolvent modes and eigenmodes of the CSD does not hold anymore. Second, the CSD computed from experimental data are based only on the streamwise velocity component, while the numerical resolvent modes are based on all the components of the forced system. Discrepancies between the two set of the data discussed in the next section may result from these differences.

III.C.1. Discussion

In Fig. 5 the EOF modes obtained from the experimental cross-spectral density matrices are compared with the optimal frequency response at the same Strouhal numbers already discussed in Sec. III.A.2, i.e. $St = [0.25, 0.50, 0.68, 0.81]$. The modulus of the streamwise velocity component is plotted, normalised with respect to the energy norm. At Strouhal numbers above 0.25, the agreement between the experimental and model results is indeed remarkable. In particular, for $St = [0.50, 0.68, 0.81]$, the linear model correctly predicts the region of maximum amplitude of the wavepackets and the spatial distribution of the coherent structure within the potential core. The streamwise extent is well reproduced for modes close to the maximum gain at $St = 0.68$. Note also that structures above the critical layer, $r/D > 0.5$, appear in both the numerical and experimental results. However, some discrepancies are noted. For instance, the EOF mode educed from the experiments at $St = 0.81$ displays a more compact structure in the downstream region. We attribute this discrepancy to the hypothesis of white-noise forcing underlying the linear analysis.

The scenario is quite different at low Strouhal number, as can be observed by comparing Fig. 5*a* and *b*. In particular, the linear model predicts a stronger amplification in the shear layer, while the structure observed in the experiment develops mostly along the centerline for $x/D > 6$. The limitation of linear models in reproducing the experimental behaviour of the wavepackets at low Strouhal numbers has been already observed in past investigations (see for instance[25]). This limitation may be related to the comparable gain values of the optimal with respect to the suboptimal structures at low Strouhal, as already observed in Fig 2.

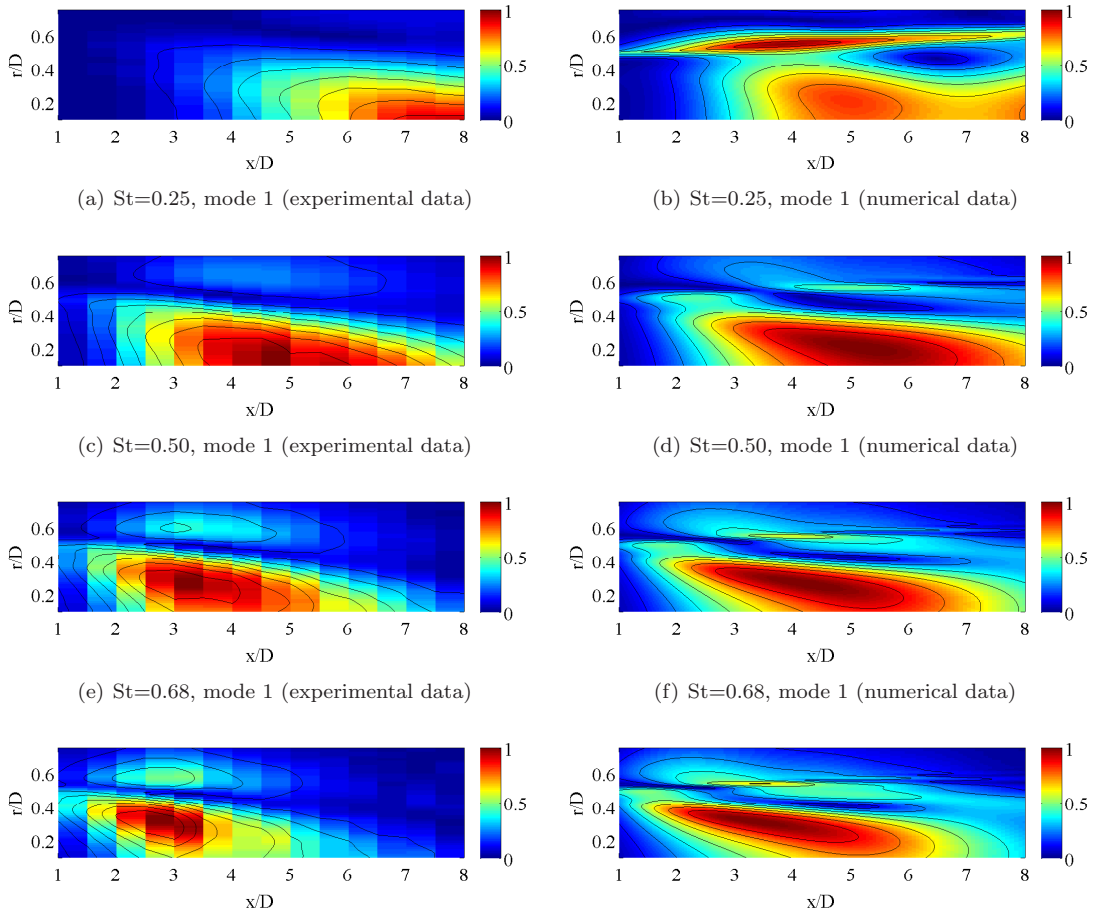

(a) St=0.25, mode 1 (experimental data)

(b) St=0.25, mode 1 (numerical data)

(c) St=0.50, mode 1 (experimental data)

(d) St=0.50, mode 1 (numerical data)

(e) St=0.68, mode 1 (experimental data)

(f) St=0.68, mode 1 (numerical data)

(g) St=0.81, mode 1 (experimental data)

(h) St=0.81, mode 1 (numerical data)

Figure 5. In the left column, the EOFs of the cross-spectral matrix, based on experimental measurements, are shown for Strouhal numbers $St = [0.25, 0.50, 0.68, 0.81]$. In the right column, the optimal response modes at the same St are shown, as obtained from the linear numerical simulations. in all cases, the contours represent the spatial distribution of the modulus of the streamwise component.

In Fig. 6, the linear flow response to suboptimal forcing modes is shown for the maximum of the optimal gain curve, $St = 0.68$. The response structure of the second mode, obtained from the numerical simulation, still agrees well with its experimental counterpart. The same general features observed for the optimal modes can be noted here. For higher-order modes, the agreement progressively diminishes.

In order to assess the range of validity of these comparisons, the following metric is introduced:

$$c = \frac{\langle \tilde{\mathbf{u}}_x^E, \tilde{\mathbf{u}}_x^N \rangle}{\sqrt{(\langle \tilde{\mathbf{u}}_x^E, \tilde{\mathbf{u}}_x^E \rangle \cdot \langle \tilde{\mathbf{u}}_x^N, \tilde{\mathbf{u}}_x^N \rangle)}}, \tag{19}$$

representing an inner product between the numerical and the experimental modal structures, indicated with the superscripts $(\cdot)^N$ and $(\cdot)^E$, respectively. The inner product is computed as the energy integral, scaled with the denominator of Eq. 19. Values of the inner product close to unity indicate good agreement between the modal structures. Note that only the streamwise component $\tilde{\mathbf{u}}_x$ is used for this comparison and the numerical data have been interpolated onto the coarser grid of the experimental results.

In Fig. 7, the metric c is plotted as a function of St for the four branches of optimal and suboptimal modes. Good quantitative agreement is achieved for $St > 0.3$. In this range of St, a good match is found also

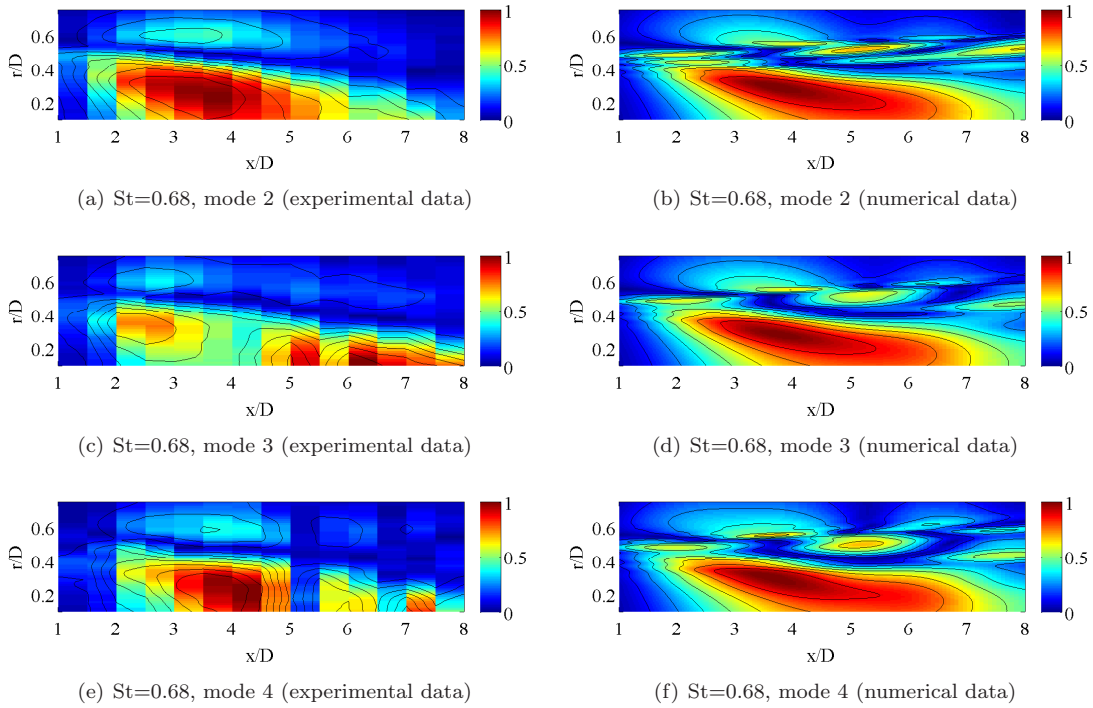

(a) St=0.68, mode 2 (experimental data)

(b) St=0.68, mode 2 (numerical data)

(c) St=0.68, mode 3 (experimental data)

(d) St=0.68, mode 3 (numerical data)

(e) St=0.68, mode 4 (experimental data)

(f) St=0.68, mode 4 (numerical data)

Figure 6. In the left column, the second, the third and the fourth modes computed as eigenvectors of the cross-spectral matrix are shown; the results are based on experimental measurements at Strouhal number $St = 0.68$. In the right column, the corresponding response modes, computed from the linear resolvent, are shown at the same St for the first three suboptimals. In all cases, the contours trace the spatial distribution of the modulus of the streamwise velocity fluctuation.

for the second mode. Lower-order modes are in good agreement when considering higher Strouhal numbers, namely $St \geq 0.5$. Note that this is the range of Strouhal numbers where the highest gain values are found in the linear analysis. At low Strouhal numbers, good agreement between the numerical and the experimental results persists in some cases, in particular for the suboptimal branches. The trend of c as a function of St for the leading branch is less clear.

IV. Conclusions

A linear frequency response analysis was performed on a turbulent jet mean flow. The mean flow is obtained from experiments operating at $Ma = 0.4$ and $Re = 4.6 \times 10^5$. The linear analysis was performed in the range of Strouhal numbers $0.05 < St < 1.85$; the optimal branch and three suboptimal branches were analysed. The features of the optimal and suboptimal forcing and the associated harmonic responses have been documented. The linear model results were then compared to experimental data obtained by high-resolution stereoscopic-PIV of flow fluctuations measured in the radial-azimuthal plane at several locations along the streamwise direction. Coherent wavepackets were identified in the form of eigenmodes (EOFs) of the cross-spectral densities matrices at different frequencies, in the range $0.01 < St < 0.9$.

Remarkable agreement between the experimental and numerical model results has been observed. Leading singular modes of the resolvent operator and EOFs computed from the experimental data bear a strong resemblance at Strouhal numbers above 0.3, whereas modes of suboptimal branches tend to show better agreement at low Strouhal numbers. These findings demonstrate that the stochastic framework of Farrell & Ioannou[2] provides valuable tools for the analysis of wavepacket dynamics in jets at high Reynolds number, in particular with regard to the role of nonlinear ingredients in the forcing of linear structures.

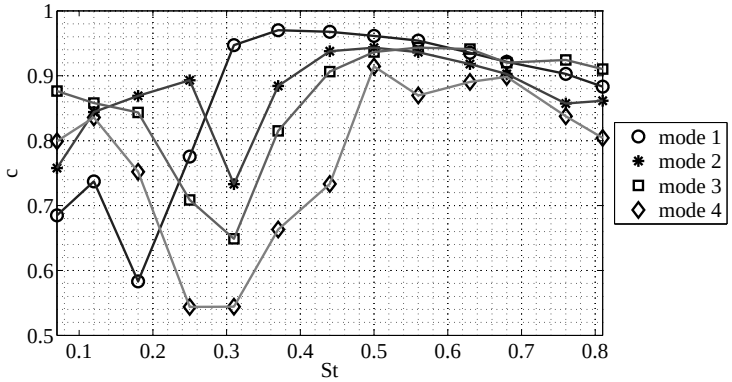

Figure 7. Inner product between the eigenvectors of the cross-spectral density matrices, obtained from the experimental measurements, and the corresponding linear resolvent modes, as a function of Strouhal number. Good agreement between experimental measurements and linear model is indicated by values close to 1.

Acknowledgements This work was supported by the Agence Nationale de la Recherche (ANR) under the *Cool Jazz* project, grant number ANR-12-BS09-0024. All instability calculations were performed using HPC resources of TGCC and CINES under the allocation x2016-2a6451 made by GENCI.

References

[1]Dergham, G., Sipp, D., and Robinet, J.-C., "Stochastic dynamics and model reduction of amplifier flows: the backward facing step flow," *Journal of Fluid Mechanics*, Vol. 719, 2013, pp. 406–430.

[2]Farrell, B. F. and Ioannou, P. J., "Stochastic forcing of the linearized Navier–Stokes equations," *Physics of Fluids A: Fluid Dynamics (1989-1993)*, Vol. 5, No. 11, 1993, pp. 2600–2609.

[3]Jordan, P. and Colonius, T., "Wave packets and turbulent jet noise," *Annual Review of Fluid Mechanics*, Vol. 45, 2013, pp. 173–195.

[4]Suzuki, T. and Colonius, T., "Instability waves in a subsonic round jet detected using a near-field phased microphone array," *Journal of Fluid Mechanics*, Vol. 565, 2006, pp. 197–226.

[5]Cavalieri, A. V., Rodríguez, D., Jordan, P., Colonius, T., and Gervais, Y., "Wavepackets in the velocity field of turbulent jets," *Journal of Fluid Mechanics*, Vol. 730, 2013, pp. 559–592.

[6]Garnaud, X., Sandberg, R. D., and Lesshafft, L., "Global response to forcing in a subsonic jet: instability wavepackets and acoustic radiation," *AIAA paper*, Vol. 2013–4633, 2013.

[7]Jeun, J., Nichols, J., and Jovanović, M., "Input-output analysis of high-speed axisymmetric isothermal jet noise," *Phys. Fluids*, Vol. 28, 2016, pp. 047101.

[8]Wan, Z., Yang, H., Zhang, X., and Sun, D., "Instability waves and aerodynamic noise in a subsonic transitional turbulent jet," *Eur. J. Mech. B/Fluids*, Vol. 57, 2016, pp. 192–203.

[9]Baqui, Y. B., Agarwal, A., Cavalieri, A. V., and Sinayoko, S., "A coherence-matched linear source mechanism for subsonic jet noise," *Journal of Fluid Mechanics*, Vol. 776, 2015, pp. 235–267.

[10]Kerhervé, F., Jordan, P., Cavalieri, A., Delville, J., Bogey, C., and Juvé, D., "Educing the source mechanism associated with downstream radiation in subsonic jets," *Journal of Fluid Mechanics*, Vol. 710, 2012, pp. 606–640.

[11]McKeon, B. and Sharma, A., "A critical-layer framework for turbulent pipe flow," *Journal of Fluid Mechanics*, Vol. 658, 2010, pp. 336–382.

[12]Jaunet, V., Jordan, P., and Cavalieri, A. V. G., "Two-point coherence of wavepackets in turbulent jets," 2016.

[13]Pope, S. B., *Turbulent flows*, Cambridge university press, 2000.

[14]Sandberg, R. D., "Governing equations for a new compressible Navier-Stokes solver in general cylindrical coordinates," *Monograph No. AFM-07/07, School of Engineering Sciences, University of Southampton*, 2007.

[15]Reynolds, W. and Hussain, A., "The mechanics of an organized wave in turbulent shear flow. Part 3. Theoretical models and comparisons with experiments," *Journal of Fluid Mechanics*, Vol. 54, No. 02, 1972, pp. 263–288.

[16]Berland, J., Bogey, C., Marsden, O., and Bailly, C., "High-order, low dispersive and low dissipative explicit schemes for multiple-scale and boundary problems," *Journal of Computational Physics*, Vol. 224, No. 2, 2007, pp. 637–662.

[17]Garnaud, X., *Modes, transient dynamics and forced response of circular jets*, Ph.D. thesis, Ecole Polytechnique X, 2012.

[18]Monokrousos, A., Åkervik, E., Brandt, L., and Henningson, D. S., "Global three-dimensional optimal disturbances in the Blasius boundary-layer flow using time-steppers," *Journal of Fluid Mechanics*, Vol. 650, 2010, pp. 181–214.

[19]Sipp, D. and Marquet, O., "Characterization of noise amplifiers with global singular modes: the case of the leading-edge flat-plate boundary layer," *Theoretical and Computational Fluid Dynamics*, Vol. 27, No. 5, 2013, pp. 617–635.

[20]Garnaud, X., Lesshafft, L., Schmid, P., and Huerre, P., "The preferred mode of incompressible jets: linear frequency response analysis," *Journal of Fluid Mechanics*, Vol. 716, 2013, pp. 189–202.

[21]Boujo, E. and Gallaire, F., "Sensitivity and open-loop control of stochastic response in a noise amplifier flow: the backward-facing step," *Journal of Fluid Mechanics*, Vol. 762, 2015, pp. 361–392.

[22]Hanifi, A., Schmid, P. J., and Henningson, D. S., "Transient growth in compressible boundary layer flow," *Physics of Fluids (1994-present)*, Vol. 8, No. 3, 1996, pp. 826–837.

[23]Hernandez, V., Roman, J. E., and Vidal, V., "SLEPc: A scalable and flexible toolkit for the solution of eigenvalue problems," *ACM Transactions on Mathematical Software (TOMS)*, Vol. 31, No. 3, 2005, pp. 351–362.

[24]Sirovich, L., "Turbulence and the dynamics of coherent structures. Part I: Coherent structures," *Quarterly of applied mathematics*, Vol. 45, No. 3, 1987, pp. 561–571.

[25]Lesshafft, L., Semeraro, O., Jaunet, V., and Jordan, P., "Modeling of coherent structures in a turbulent jet as global linear instability wavepackets: theory and experiment," 2015.

J. Fluid Mech. (2017), *vol.* 820, *pp.* 187–207. © Cambridge University Press 2017
doi:10.1017/jfm.2017.203

Global instability of low-density jets

W. Coenen[1,2,†], L. Lesshafft[3], X. Garnaud[3,‡] and A. Sevilla[1]

[1]Grupo de Mecánica de Fluidos, Universidad Carlos III de Madrid, Av. Universidad 30, 28911 Leganés (Madrid), Spain

[2]Department of Mechanical and Aerospace Engineering, University of California San Diego, 9500 Gilman Dr., La Jolla, CA 92093-0411, USA

[3]Laboratoire d'Hydrodynamique (LadHyX), École polytechnique – CNRS, 91128 Palaiseau, France

(Received 4 January 2016; revised 28 March 2017; accepted 29 March 2017; first published online 5 May 2017)

The global stability of laminar axisymmetric low-density jets is investigated in the low Mach number approximation. The linear modal dynamics is found to be characterised by two features: a stable arc branch of eigenmodes and an isolated eigenmode. Both features are studied in detail, revealing that, whereas the former is highly sensitive to numerical domain size and its existence can be linked to spurious feedback from the outflow boundary, the latter is the physical eigenmode that is responsible for the appearance of self-sustained oscillations in low-density jets observed in experiments at low Mach numbers. In contrast to previous local spatio-temporal stability analyses, the present global analysis permits, for the first time, the determination of the critical conditions for the onset of global instability, as well the frequency of the associated oscillations, without additional hypotheses, yielding predictions in fair agreement with previous experimental observations. It is shown that under the conditions of those experiments, viscosity variation with composition, as well as buoyancy, only have a small effect on the onset of instability.

Key words: instability, jets

1. Introduction

Submerged jets become globally unstable, achieving a self-sustained oscillatory state, when their density is sufficiently smaller than that of their surroundings, as clearly evidenced by many experimental, theoretical and numerical studies. The phenomenon was first recognised thanks to the pioneering work of Monkewitz & Sohn (1988), who demonstrated the existence of a region of local absolute instability close to the injector of a turbulent heated jet by means of a quasi-parallel linear stability analysis. The global transition has been experimentally characterised in detail both for hot jets (Monkewitz *et al.* 1990) and for light jets, where the density difference is due to the injection of fluid of smaller molecular weight than that of the ambient (Kyle & Sreenivasan 1993; Hallberg & Strykowski 2006), and also by means of a number

† Email address for correspondence: wicoenen@ucsd.edu
‡ Present address: Safran Tech, Rue des Jeunes Bois, 78772, Magny-Les-Hameaux, France.

of local stability analyses which accounted for the origin of the phenomenon with increasing detail (Jendoubi & Strykowski 1994; Lesshafft & Huerre 2007; Coenen, Sevilla & Sánchez 2008; Lesshafft & Marquet 2010; Coenen & Sevilla 2012). These studies have been complemented by direct numerical simulations (Lesshafft, Huerre & Sagaut 2007) that unambiguously demonstrated the link between the existence of locally absolutely unstable regions in the near field of low-density jets and the onset of global self-sustained oscillations.

Recently, several global linear stability analyses of submerged jet configurations, avoiding the quasi-parallel approximation, have been performed thanks to the availability of sufficient computational power and the development of appropriate numerical techniques. Nichols & Lele (2011*a*) pioneered the use of a global approach to study hot and cold compressible jets. Garnaud *et al.* (2013*a*,*b*) considered the case of constant-density incompressible jets, revealing that global modes are strongly affected by the domain length and the numerical discretisation, while the frequency response is robust and explains the origin of the preferred mode in globally stable jets. In contrast with the case of constant-density jets, the important experiments of Hallberg & Strykowski (2006) strongly suggest the existence of an isolated eigenmode responsible for the global transition for sufficiently low values of the Reynolds number. Isolated eigenmodes in low-density jets have indeed been detected by Nichols & Lele (2010) for supersonic cases, and by Qadri (2014) for a low Mach number configuration.

The main objective of the present work is to provide a detailed characterisation of the global stability properties of light He/N_2 laminar jets in the low Mach number limit, by means of modal and frequency response analyses. Two key questions addressed are whether there exists an isolated eigenmode that explains the experimentally observed transition in low-density jets, and what are the differences between the global stability properties of constant-density and low-density jets.

The paper begins with the mathematical formulation in § 2. In § 3 we study a slowly developing globally stable jet, followed by an analysis of a rapidly spreading helium jet in § 4. Finally, concluding remarks are given in § 5.

2. Formulation

We consider an axisymmetric laminar low-density He/N_2 jet, discharging with a constant flow rate Q^* from an injector pipe with radius R^* into an ambient of N_2. The ratio of the density ρ_j^* of the jet and the ambient density $\rho_{N_2}^*$ is given by $S = W_j^*/W_{N_2}^*$. Here $W_j^* = [Y_j/W_{He}^* + (1 - Y_j)/W_{N_2}^*]^{-1}$ is the mean molecular weight of the jet mixture, determined by the initial mass fraction Y_j of He. In other terms, to obtain a jet with jet-to-ambient density ratio S, an initial mass fraction $Y_j = (S^{-1} - 1)/(W_{N_2}^*/W_{He}^* - 1)$ of He is injected. The viscosity μ_j^* of the jet can be related to μ_{He}^* and $\mu_{N_2}^*$ through Hirschfelder, Curtiss & Bird's law (see Coenen & Sevilla 2012, (2.11)). Note that in the formulation dimensional quantities are indicated with an asterisk *. The jet exit values ρ_j^*, μ_j^* are used as scales for the dimensionless density ρ and viscosity μ, whereas the jet radius R is used as the characteristic length scale, yielding the dimensionless cylindrical coordinate system (x, r). The velocity field $\boldsymbol{u} = (u, v)$ is non-dimensionalised with the mean velocity $U_m^* = 4Q^*/(\pi R^{*2})$. All flow quantities are taken to be independent of the azimuth ϕ throughout this study; only axisymmetric perturbations are considered.

The Reynolds number of the jet is assumed to be large, $Re = \rho_j^* U_m^* R^*/\mu_j^* \gg 1$, resulting in a slender jet flow. The importance of buoyancy effects can be estimated

through the Richardson number $Ri = (\rho^*_{N_2} - \rho^*_j)g^*R^*/(\rho^*_j U^{*2}_m)$. For comparison with experiments, it is useful to write this as $Ri = Gr/Re^2$, where $Gr = \rho^*_j(\rho^*_{N_2} - \rho^*_j)g^*R^{*3}/\mu^{*2}_j = (1/S-1)g^*R^{*3}/\nu^*_j$ is a Grashof number. The latter only depends on the injector radius and the properties of the gas mixture, which usually do not vary within the same experimental campaign. For simplicity, we will neglect buoyancy effects, i.e. we will assume $Ri \ll 1$, except for the comparison with experiments in § 4.2. Furthermore, for the description of the resulting jet flow it is assumed that the characteristic jet velocity U^*_m is much smaller than the ambient speed of sound, so that the simplifications associated with the low Mach number approximation (Williams 1985; Nichols, Schmid & Riley 2007) can be applied. This implies that the density variations in the jet are only due to variations in molecular weight, and are not related to pressure variations. It also means that if the jet discharges with the same temperature as the ambient, the flow will remain isothermal everywhere, and the energy equation is not needed in the description. Furthermore, in the low Mach number limit, the viscous stress term that is proportional to the second coefficient of viscosity can be incorporated in the definition of the variable p. This p represents the pressure difference from the unperturbed ambient distribution, scaled with the characteristic dynamic pressure $\rho^*_j U^{*2}_m$. The jet is then effectively described by the continuity, momentum conservation and species conservation equations,

$$\frac{\partial \rho}{\partial t} + \boldsymbol{\nabla}\cdot(\rho \boldsymbol{u}) = 0, \tag{2.1}$$

$$\rho\left(\frac{\partial \boldsymbol{u}}{\partial t} + \boldsymbol{u}\cdot\boldsymbol{\nabla}\boldsymbol{u}\right) = -\boldsymbol{\nabla}p + \frac{1}{Re}\nabla^2\boldsymbol{u} + Ri\frac{1-S\rho}{1-S}\boldsymbol{e}_x, \tag{2.2}$$

$$\rho\left(\frac{\partial Y}{\partial t} + \boldsymbol{u}\cdot\boldsymbol{\nabla}Y\right) = \frac{1}{Re\,Sc}\boldsymbol{\nabla}\cdot(\rho\boldsymbol{\nabla}Y), \tag{2.3}$$

together with the relation between the mass fraction Y of He and the density ρ of the jet,

$$Y = Y_j(1/\rho - S)/(1-S). \tag{2.4}$$

In (2.3) the Schmidt number $Sc = \mu^*_j/(\rho^*_j\mathcal{D}^*)$ is based on the values of the viscosity and density at the jet exit. For example, the two density ratios used in the present work, $S = 0.143$ and $S = 0.5$, correspond to Schmidt numbers $Sc = 1.69$ and $Sc = 0.49$, respectively. For simplicity, the variation of the viscosity with the composition is not taken into account in the conservation equations (2.1)–(2.3), and is thus neglected in the results, except for the comparison with experiments of § 4.2, where its influence is studied separately. To the latter aim, the viscous term in (2.2) is written as $Re^{-1}\boldsymbol{\nabla}\cdot[\mu(\boldsymbol{\nabla}\boldsymbol{u} + \boldsymbol{\nabla}\boldsymbol{u}^{\mathrm{T}})]$ and Hirschfelder's law (see Coenen & Sevilla 2012, (2.11)) is used to relate the dimensionless viscosity $\mu = \mu^*/\mu^*_j$ to the mass fraction Y.

2.1. *Base flow*

As a base state for the linear stability analysis, a steady solution $(\bar{u}, \bar{v}, \bar{p}, \bar{\rho})$ of the low Mach number Navier–Stokes equations (2.1)–(2.3) is employed. The flow domain under consideration is depicted in figure 1. In order to mimic experimental conditions, a short injector pipe of length x_p is included, bounded by a wall Γ_w of thickness 0.02 that ends on a 5.7° knife edge. At the pipe inlet Γ_i a velocity profile $\bar{u}_i(r)$ is imposed,

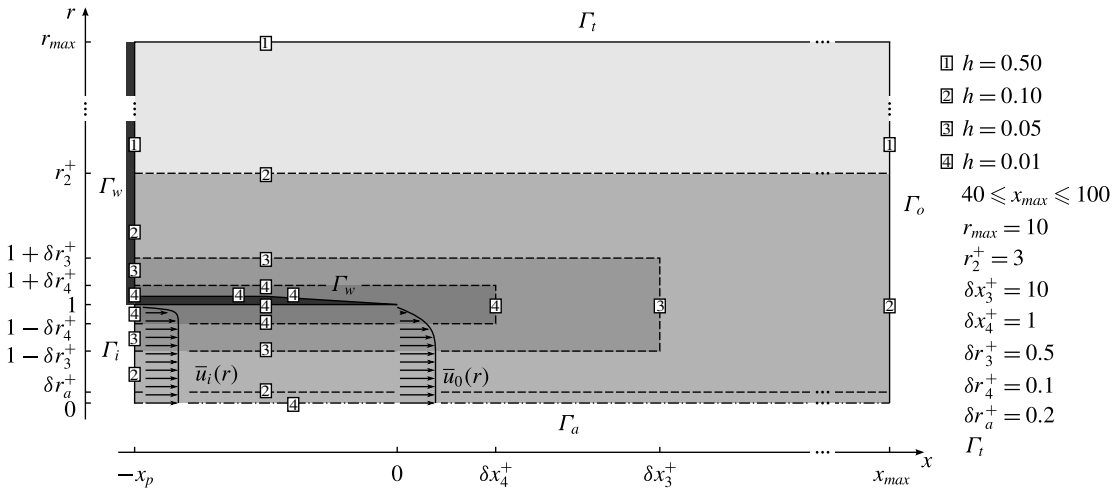

FIGURE 1. Schematic representation of the numerical domain. The boxed numbers on the boundaries indicate the level of refinement through the distance h between discretisation points. The areas with different grid resolutions that are obtained in this manner are indicated by the grey shading.

taken from a collection of profiles that is obtained by solving the laminar boundary-layer equations in a circular pipe (see Coenen & Sevilla 2012, § 2.1.1). Because the flow in the short injector pipe of the domain will further develop, the velocity profile $\bar{u}_i(r)$ at the inlet must be carefully chosen to obtain a certain desired velocity profile $\bar{u}_0(r)$ at the jet exit plane. We will characterise the latter profile through the inverse of its dimensionless momentum thickness D/θ_0, defined by

$$\theta_0 = \int_0^\infty \frac{\bar{u}_0(r)}{\bar{u}_0(0)} \left[1 - \frac{\bar{u}_0(r)}{\bar{u}_0(0)}\right] \mathrm{d}r, \tag{2.5}$$

and scaled with the jet diameter $D=2R$ for consistency with Hallberg & Strykowski (2006). For the computations of the results of the present work a pipe length $x_p=3$ was used, with the exception of the transition points with $D/\theta_0>30$ of figure 12, for which a pipe length $x_p=1.5$ was used. It was verified that larger values of x_p did not affect the results. The remaining boundaries of the flow domain are the axis Γ_a, the lateral boundary Γ_t and the downstream outlet boundary Γ_o, as labelled in figure 1. Stress-free boundary conditions are imposed on the latter two. Because the jet entrains fluid through the lateral boundary, the density at that boundary must be fixed to $1/S$ to obtain the desired jet-to-ambient density ratio. The radial extent of the domain was set to $r_{max}=10$, and it was checked that larger values did not change the results. The downstream extent x_{max} does not influence the computation of the base flow, but it does affect various results of the stability analysis, as will be explained in detail in §§ 3 and 4; values in the range $40\leqslant x_{max}\leqslant 100$ were used. To summarise, the boundary conditions for the base flow are

$$\bar{u}-\bar{u}_i=\bar{v}=\bar{\rho}-1=0 \quad \text{on } \Gamma_i, \tag{2.6}$$

$$\bar{u}=\bar{v}=\boldsymbol{n}\cdot\boldsymbol{\nabla}\bar{\rho}=0 \quad \text{on } \Gamma_w, \tag{2.7}$$

$$\bar{\rho}-\frac{1}{S}=-\bar{p}\boldsymbol{n}+\frac{1}{Re}\boldsymbol{n}\cdot\boldsymbol{\nabla}\begin{pmatrix}\bar{u}\\ \bar{v}\end{pmatrix}=0 \quad \text{on } \Gamma_t \tag{2.8}$$

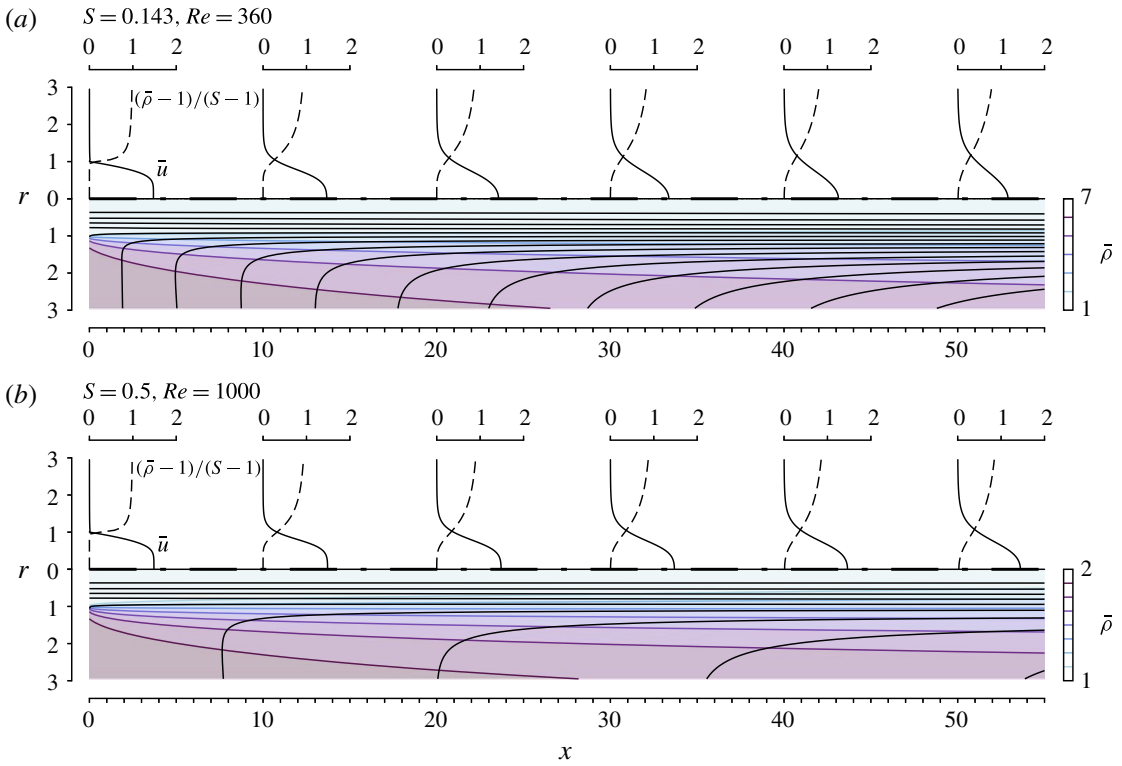

FIGURE 2. (Colour online) Radial profiles of axial velocity $\bar{u}$ and rescaled density $(\bar{\rho}-1)/(S-1)$ at $x=0, 10, 20, 30, 40, 50$, together with streamlines and contours of the density field $\bar{\rho}$, for (*a*) $S=0.143$, $Re=360$, $D/\theta_0=24.3$ and (*b*) $S=0.5$, $Re=1000$, $D/\theta_0=24.3$.

$$-\bar{p}\boldsymbol{n}+\frac{1}{Re}\boldsymbol{n}\cdot\boldsymbol{\nabla}\begin{pmatrix}\bar{u}\\ \bar{v}\end{pmatrix}=0 \quad \text{on } \Gamma_o, \tag{2.9}$$

$$\bar{v}=\partial_r\bar{u}=\partial_r\bar{\rho}=0 \quad \text{on } \Gamma_a, \tag{2.10}$$

where $\boldsymbol{n}$ is the outward normal vector on the boundary.

The governing equations are discretised using Taylor–Hood elements, quadratic (P2) for the density and velocity, and linear (P1) for the pressure, to satisfy the Ladyzenskaja–Babuška–Brezzi condition. The refinement of the unstructured mesh is controlled through the distance h between discretisation points on the boundaries of the domain and on auxiliary lines, as indicated in figure 1. It was checked that the results were converged with respect to further mesh refinements. The steady base flow is computed using a Newton–Raphson method and the FreeFem++ software (Hecht 2012). Figure 2 shows the resulting base flow for the two cases that will be studied in detail in §§ 3 and 4: $S=0.143$, $Re=360$, $D/\theta_0=24.3$ and $S=0.5$, $Re=1000$, $D/\theta_0=24.3$.

2.2. *Direct eigenmodes*

All experimental and numerical evidence indicates that the global instability in light jets gives rise to axisymmetric flow oscillations, and the present analysis therefore is restricted to axisymmetric disturbances. All flow quantities are independent of the azimuthal coordinate, and the azimuthal velocity is always zero. Small

unsteady axisymmetric perturbations are introduced into the steady base flow as $(u,\ v,\ \rho,\ p) = (\bar{u},\ \bar{v},\ \bar{\rho},\ \bar{p}) + \varepsilon(u',\ v',\ \rho',\ p')$. The evolution of these perturbations (primed quantities) is then governed to leading order by the equations (2.1)–(2.4), linearised around the base flow,

$$\boldsymbol{\nabla}\cdot\boldsymbol{u}' = -\frac{1}{Re\,Sc}\boldsymbol{\nabla}\cdot\left(\frac{1}{\bar{\rho}}\boldsymbol{\nabla}\rho' - \frac{\rho'}{\bar{\rho}^2}\boldsymbol{\nabla}\bar{\rho}\right), \tag{2.11}$$

$$\frac{\partial \boldsymbol{u}'}{\partial t} + \bar{\boldsymbol{u}}\cdot\boldsymbol{\nabla}\boldsymbol{u}' + \boldsymbol{u}'\cdot\boldsymbol{\nabla}\bar{\boldsymbol{u}} + \frac{\rho'}{\bar{\rho}}\bar{\boldsymbol{u}}\cdot\boldsymbol{\nabla}\bar{\boldsymbol{u}} = -\frac{1}{\bar{\rho}}\boldsymbol{\nabla}p' + \frac{1}{Re}\frac{1}{\bar{\rho}}\nabla^2\boldsymbol{u}' - Ri\frac{S}{1-S}\frac{\rho'}{\bar{\rho}}\boldsymbol{e}_x, \tag{2.12}$$

$$\frac{\partial \rho'}{\partial t} + \bar{\boldsymbol{u}}\cdot\boldsymbol{\nabla}\rho' + \boldsymbol{u}'\cdot\boldsymbol{\nabla}\bar{\rho} - \frac{\rho'}{\bar{\rho}}\bar{\boldsymbol{u}}\cdot\boldsymbol{\nabla}\bar{\rho} = -\frac{1}{Re\,Sc}\bar{\rho}\boldsymbol{\nabla}\cdot\left(\frac{1}{\bar{\rho}}\boldsymbol{\nabla}\rho' - \frac{\rho'}{\bar{\rho}}\boldsymbol{\nabla}\bar{\rho}\right). \tag{2.13}$$

Assuming temporal normal-mode solutions

$$(u',\ v',\ \rho',\ p') = (\hat{u},\ \hat{v},\ \hat{\rho},\ \hat{p})\mathrm{e}^{-i\omega t}, \tag{2.14}$$

the linearised equations can be written in the form of a generalised eigenvalue problem

$$-i\omega\mathcal{B}\hat{\boldsymbol{q}} = \mathcal{L}\hat{\boldsymbol{q}}, \tag{2.15}$$

where $\hat{\boldsymbol{q}}(r,x) = [\hat{u}(r,x),\ \hat{v}(r,x),\ \hat{\rho}(r,x),\ \hat{p}(r,x)]^{\mathrm{T}}$ is the vector-valued eigenfunction that contains all perturbation quantities. For what follows, let $\tilde{\boldsymbol{q}}$, $\boldsymbol{L}$ and $\boldsymbol{B}$ be understood to be the eigenvector and the matrices of the discretised eigenvalue problem, $-i\omega\boldsymbol{B}\tilde{\boldsymbol{q}} = \boldsymbol{L}\tilde{\boldsymbol{q}}$, that is to be solved numerically.

The following boundary conditions are imposed for the perturbation variables (boundary labels as given in figure 1):

$$\hat{u} = \hat{v} = 0 \quad \text{on } \Gamma_i,\ \Gamma_w, \tag{2.16}$$

$$-\hat{p}\boldsymbol{n} + \frac{1}{Re}\boldsymbol{n}\cdot\boldsymbol{\nabla}\begin{pmatrix}\hat{u}\\ \hat{v}\end{pmatrix} = 0 \quad \text{on } \Gamma_t,\ \Gamma_o, \tag{2.17}$$

$$\hat{v} = \partial_r\hat{u} = 0 \quad \text{on } \Gamma_a. \tag{2.18}$$

The discrete system matrices $\boldsymbol{L}$ and $\boldsymbol{B}$ are constructed with a finite element formalism in FreeFEM++, analogous to the incompressible computations by Garnaud *et al.* (2013*a*), using P2 elements for $\hat{\rho}$, $\hat{u}$, $\hat{v}$ and P1 elements for $\hat{p}$. These matrices are then exported to Matlab for the solution of the eigenvalue problem, by use of the ARPACK library, and for all further post-processing. The eigenvalue computation involves an LU decomposition for inversion of the shifted system.

2.3. *Adjoint eigenmodes*

The physical discussion of eigenmode dynamics in § 4 will be based on the structural sensitivity formalism proposed by Giannetti & Luchini (2007). Such an analysis requires the computation of the adjoint discrete eigenvector $\tilde{\boldsymbol{q}}^\dagger$ associated with a given eigenvalue ω of the direct problem (2.15). The form of the adjoint eigenvalue problem, of which $\tilde{\boldsymbol{q}}^\dagger$ is a solution, depends on the definition of an inner product. Let the inner product between two perturbation states $\hat{\boldsymbol{q}}_1$ and $\hat{\boldsymbol{q}}_2$ be defined as the standard spatial integral in cylindrical coordinates,

$$\langle\hat{\boldsymbol{q}}_1,\ \hat{\boldsymbol{q}}_2\rangle = \int_\Omega (\hat{u}_1^*\hat{u}_2 + \hat{v}_1^*\hat{v}_2 + \hat{\rho}_1^*\hat{\rho}_2 + \hat{p}_1^*\hat{p}_2)r\,\mathrm{d}r\,\mathrm{d}x = \tilde{\boldsymbol{q}}_1^H\boldsymbol{Q}\tilde{\boldsymbol{q}}_2. \tag{2.19}$$

Again, the symbols $\hat{\boldsymbol{q}}_{1,2}$ are meant to represent the continuous spatial distribution of perturbations, whereas $\tilde{\boldsymbol{q}}_{1,2}$ represent the discretised form, containing all N degrees of freedom of the discrete problem. The $N \times N$ matrix $\boldsymbol{Q}$ contains the metric coefficients for a given spatial discretisation, reflecting the area size of the individual mesh elements as well as the weight factor r from the integral. It is a diagonal, positive definite Hermitian matrix.

With this definition, the discrete adjoint eigenvalue problem is found to be

$$\mathrm{i}\omega^{\dagger}\boldsymbol{Q}^{-1}\boldsymbol{B}^{H}\boldsymbol{Q}\tilde{\boldsymbol{q}}^{\dagger} = \boldsymbol{Q}^{-1}\boldsymbol{L}^{H}\boldsymbol{Q}\tilde{\boldsymbol{q}}^{\dagger}. \tag{2.20}$$

Each adjoint eigenvalue $\omega^{\dagger}$ is the complex conjugate of an associated direct eigenvalue ω.

For the presentation of results in §§ 3 and 4, direct eigenvectors are always normalised such that

$$\|\tilde{\boldsymbol{q}}\|^2 = \tilde{\boldsymbol{q}}^{H}\boldsymbol{Q}\tilde{\boldsymbol{q}} = 1, \tag{2.21}$$

whereupon the associated adjoint eigenvectors are normalised according to

$$\tilde{\boldsymbol{q}}^{\dagger H}\boldsymbol{Q}\boldsymbol{B}\tilde{\boldsymbol{q}} = 1. \tag{2.22}$$

2.4. *Eigenvalue sensitivity*

The sensitivity of an eigenvalue measures how much the eigenvalue is affected by variations of the associated operator. According to the procedure proposed by Giannetti & Luchini (2007), a spatial map of the sensitivity of ω with respect to 'internal feedback' interactions can be obtained by measuring the local overlap between the direct and adjoint eigenfunctions. The idea is to introduce small variations into the system matrix $\boldsymbol{L}$ that modify the coupling between perturbation variables at a given point in space. Several choices are possible to estimate the effect of such modifications in the local structure of the operator on the eigenvalue. We adopt here the original formulation chosen by Giannetti & Luchini (2007), which provides an upper-bound estimation of the eigenvalue drift due to modified velocity–velocity coupling. The formulation is slightly altered to include the density. It is convenient to first define the $3 \times N$ matrix $\boldsymbol{U}_{x_i}$ that extracts from a vector $\tilde{\boldsymbol{q}}$ the velocity components and density $[\hat{u}(\boldsymbol{x}_i), \hat{v}(\boldsymbol{x}_i), \hat{\rho}(\boldsymbol{x}_i)]^{\mathrm{T}} = \boldsymbol{U}_{x_i}\tilde{\boldsymbol{q}}$ at a given discretisation point $\boldsymbol{x}_i$. Following the derivation in Giannetti & Luchini (2007), the structural sensitivity in the present context is then characterised by the scalar quantity

$$\lambda(\boldsymbol{x}_i) = \|\boldsymbol{U}_{x_i}\boldsymbol{Q}\tilde{\boldsymbol{q}}^{\dagger}\|\,\|\boldsymbol{U}_{x_i}\tilde{\boldsymbol{q}}\|. \tag{2.23}$$

Giannetti & Luchini (2007) argue that flow regions with a large value of λ influence strongly the eigenvalue selection, and thus represent the 'core' or 'wavemaker' of the eigenmode. Additional information can be obtained by analysing the components of the structural sensitivity tensor $\boldsymbol{S}(\boldsymbol{x}_i) = \boldsymbol{U}_{x_i}\boldsymbol{Q}\tilde{\boldsymbol{q}}^{\dagger}(\boldsymbol{U}_{x_i}\tilde{\boldsymbol{q}})^{H}$, which represent how changes in the feedback from axial velocity, radial velocity and density into the axial momentum, radial momentum and species conservation equation can affect the eigenvalue (see, for example, Qadri, Chandler & Juniper 2015). Note that the Frobenius norm of $\boldsymbol{S}$ is equal to the structural sensitivity λ. It is noted that the choice to only include the density and velocity in (2.23) is rather arbitrary. The quantity λ could just as well

be based on momentum, vorticity or combinations thereof, if such a choice appeared physically more sensible.

Marquet, Sipp & Jacquin (2008) developed the theoretical framework to assess the sensitivity of a global eigenmode to arbitrary (not necessarily solution of the Navier–Stokes equations) modifications of the base flow. In the present work we will use this concept to study how modifications in the base flow velocity $\bar{\boldsymbol{u}} = (\bar{u}, \bar{v})$ affect the growth rate ω_i:

$$\nabla_{\bar{\boldsymbol{u}}}\omega_i = (\nabla_{\bar{u}}\omega_i, \nabla_{\bar{v}}\omega_i) = \mathrm{Re}[-\nabla(\hat{\boldsymbol{u}})^H \cdot \hat{\boldsymbol{u}}^\dagger + \nabla\hat{\boldsymbol{u}}^\dagger \cdot \hat{\boldsymbol{u}}^*], \tag{2.24}$$

where $\hat{\boldsymbol{u}}$ and $\hat{\boldsymbol{u}}^\dagger$ contain the velocity components of the direct and adjoint eigenmodes.

2.5. *Pseudospectrum*

As Trefethen & Embree (2005) note in their preface, 'eigenvalues might be meaningful in theory, but they [can] not always be trusted on a computer'. This remark is highly pertinent for the present study: the linearised Navier–Stokes operator is known to be non-normal (see the review by Chomaz 2005), and this property has important implications for the sensitivity of eigenmodes with respect to details of the discretisation and to finite precision arithmetics. In the study of non-normal dynamics, the pseudospectrum provides a very valuable basis for physical discussion.

According to Trefethen & Embree (2005), the ϵ-pseudospectrum can be defined in at least three equivalent ways. For the purpose of the present study, we will adopt the definition that a given complex frequency ω is an ϵ-pseudoeigenvalue of the linear flow equations if

$$\|(\mathrm{i}\omega\boldsymbol{B} + \boldsymbol{L})^{-1}\| = \epsilon^{-1}. \tag{2.25}$$

The operator $(\mathrm{i}\omega\boldsymbol{B} + \boldsymbol{L})^{-1}$ is the resolvent of $\boldsymbol{L}$, and its spectral norm is given by its largest singular value σ. In physical terms, the largest singular value represents the optimal gain that can be achieved when forcing the system at frequency ω. We obtain $\epsilon^{-1} = \sigma$ as the leading singular value in the same way as Garnaud *et al.* (2013*b*).

3. Analysis of a slowly developing stable jet: the arc branch

The first case to be investigated is a jet of Reynolds number $Re = 1000$ and density ratio $S = 0.5$. A shear layer thickness given by $D/\theta_0 = 24.3$ is measured at the nozzle exit. While $Re = 1000$ may seem to be a low value for a jet, in laminar conditions it yields a very slow viscous spreading, as can be seen in figure 2(*b*).

The eigenvalue spectrum for this setting is shown in figure 3, where different panels contain results obtained with different numerical box lengths x_{max} between 40 and 100. The radial extent in all cases is $r_{max} = 10$. The dominant feature of the spectrum is an upper arching branch of eigenvalues, named the arc branch in the following. Eigenvalues are distributed along it with an even spacing in the real frequency. All eigenvalues are confined to the stable half-plane of ω, but in the case of the shortest box length, $x_{max} = 40$, the arc branch nearly crosses into the unstable domain. Clearly, convergence with respect to the box length x_{max} is not achieved. This is consistent with the analysis of constant-density jets by Garnaud *et al.* (2013*a*), who argue that a further increase of x_{max} is not guaranteed to ever lead to convergence. It seems unreasonable anyway to assume that the linear dynamics more than 100 radii downstream of the nozzle, in a hypothetical steady flow, should have any physical relevance.

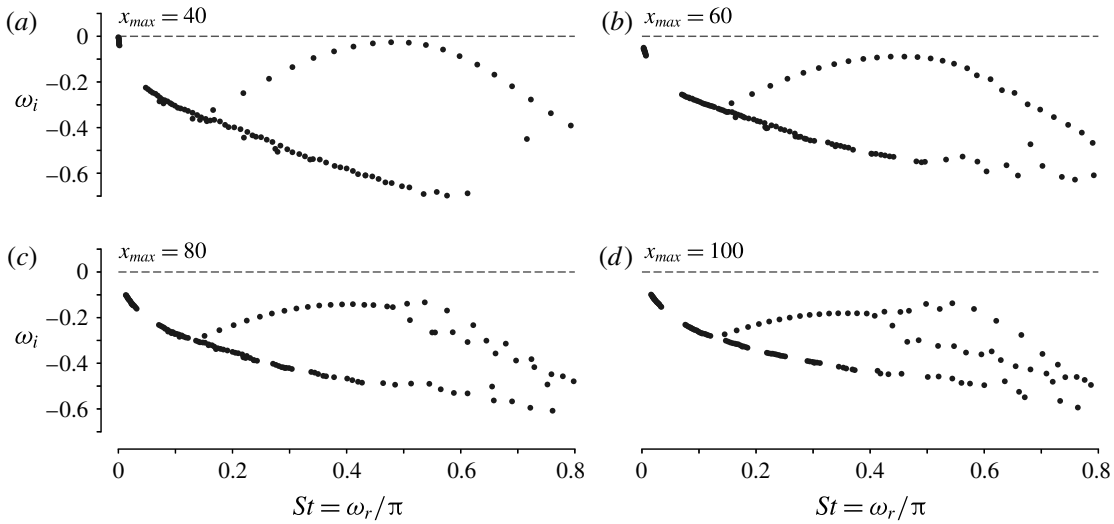

FIGURE 3. Eigenvalue spectra of a jet at $Re = 1000$, $S = 0.5$ and $D/\theta_0 = 24.3$, obtained in numerical domains of different length.

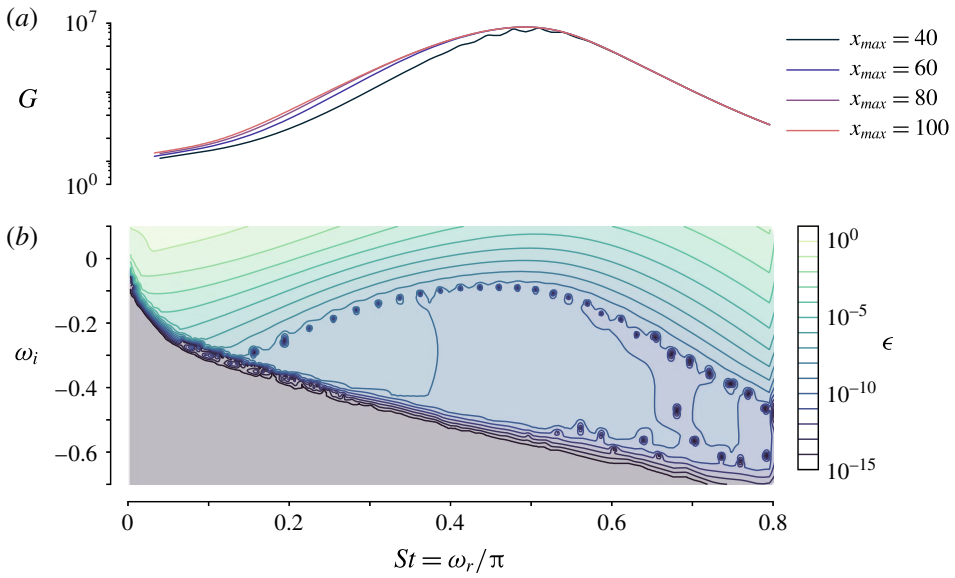

FIGURE 4. (Colour online) Forcing response of a jet at $Re = 1000$, $S = 0.5$ and $D/\theta_0 = 24.3$. (*a*) Optimal gain as a function of real forcing frequency. Different colours denote results obtained in numerical domains of different lengths, as indicated in the legend. (*b*) Pseudospectrum, represented as the inverse of the optimal gain for complex forcing frequencies, $\epsilon = \sigma^{-1}(\omega)$. The case $x_{max} = 60$ is represented.

A lower branch of densely packed eigenvalues is also observed. These modes have been discussed by Garnaud *et al.* (2013*a*), and they will not be investigated in more depth in this paper.

If the entire spectrum of a flow is stable, its dynamics in a noisy environment is determined by the response to external forcing. The linear frequency response of the present jet is represented in figure 4(*a*) by the optimal energy gain as a function of real forcing frequency (see § 2.5), as calculated in numerical domains of different

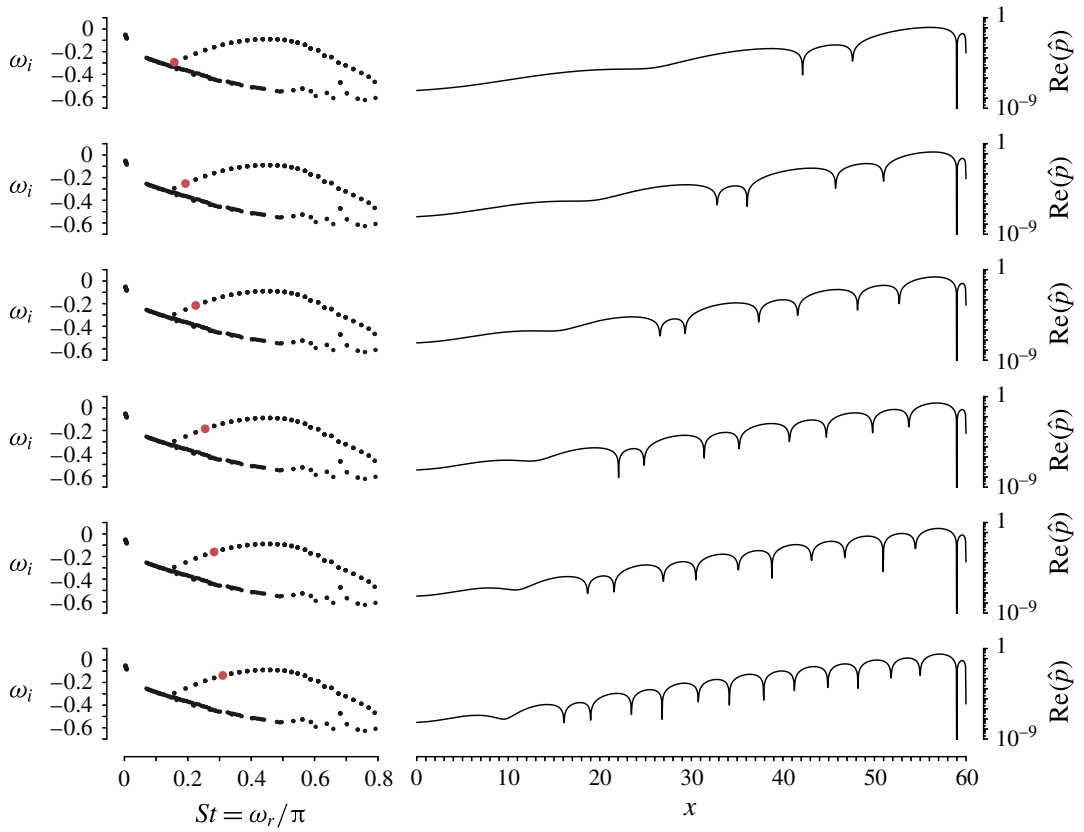

FIGURE 5. Pressure eigenfunction along $r = 1$ for several modes of the arc branch for $S = 0.5$, $Re = 1000$ and $D/\theta_0 = 24.3$, with a numerical domain length $x_{max} = 60$.

length. The gain curve is clearly affected by domain truncation in the case of the shortest box length, $x_{max} = 40$, but all curves obtained with larger domains are seen to be in close agreement. The maximum gain is reached at $\omega_r = 1.55$, corresponding to a value of the Strouhal number based on the jet diameter $St = \omega_r/\pi = 0.49$. It is remarkable that the forced (exogenous) dynamics is well converged with respect to the box length, while the unforced (endogenous) dynamics is not. Note also that the maximum gain, $O(10^7)$, is very large compared to that of the constant-density setting, $O(10^2)$, investigated by Garnaud *et al.* (2013*b*), for the same value of the Reynolds number. The main difference between the two configurations lies in the choice of the base state, which in the case of Garnaud *et al.* (2013*b*) was a model mean flow with constant density.

The full pseudospectrum of the slowly developing jet is shown in figure 4(*b*). Two observations are pointed out: firstly, the arc branch is seen to align approximately with a pseudospectrum contour (here with a value of approximately 10^{-8}); secondly, the pseudospectrum variations below the arc branch are markedly different from those above the branch. Below the arc branch, the pseudospectrum indeed is nearly constant, compared to the strong variations in the upper part of the domain.

For a physical interpretation, eigenfunctions of the first six arc branch modes are represented in figure 5 by their pressure component along the nozzle lip line, $r = 1$, as a function of x. Absolute real values $|\mathrm{Re}(\hat{p})|$ are plotted in logarithmic scale, and the phase is adjusted such that $\mathrm{Re}(\hat{p})$ is zero at $x = 59$ in all cases. The eigenfunctions

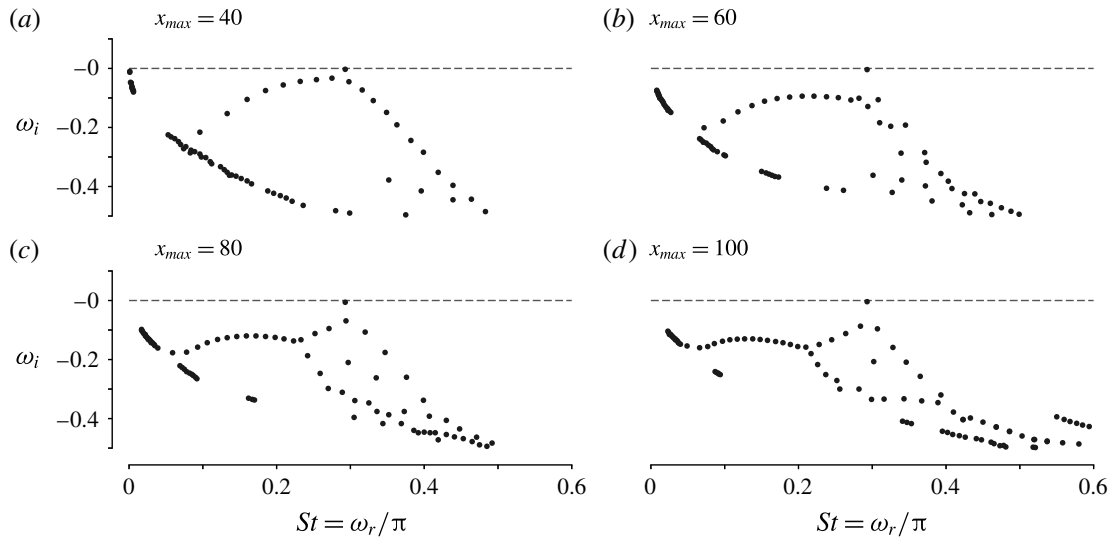

FIGURE 6. Eigenvalue spectra of a jet at $Re = 360$, $S = 0.143$ and $D/\theta_0 = 24.3$, obtained in numerical domains of different length.

take the form of wavepackets; their particularity lies in the fact that each mode fits an integer number of wavelengths inside the numerical domain. Only the first six eigenfunctions are shown, but the same characteristic applies to all arc branch modes. The number of wavelengths increases steadily as one moves along the arc branch from low to higher real frequency values. This observation suggests that the arc branch is composed of box modes, similar to resonance modes in a pipe of finite length, a conjecture that deserves future investigation.

4. Analysis of a rapidly spreading pure helium jet

A jet with parameters $S = 0.143$ (pure helium), $D/\theta_0 = 24.3$ and $Re = 360$ is considered next. The strong density contrast is certain to result in absolute instability close to the nozzle (Coenen & Sevilla 2012), and the low value of the Reynolds number leads to a fast viscous spreading of the jet base flow, as seen in figure 2(*a*).

The eigenvalue spectrum for this setting is shown in figure 6, where different panels again contain results obtained with different numerical box lengths x_{max} between 40 and 100. The radial extent still is maintained at $r_{max} = 10$. One single eigenvalue $\omega = 0.9197 - 0.0042\mathrm{i}$, very near marginal instability, is identically obtained (within $|\Delta\omega| = 0.0015$) independently of x_{max}. This eigenmode, indeed the only one that seems to be converged with respect to box size, will be denoted here as the isolated mode.

An arc branch can be discerned, similar to the one described in § 3. In the spectrum of the shortest numerical box, figure 6(*a*), the eigenvalues along this branch are still evenly distributed. With larger box lengths, this regularity persists at low frequencies, but breaks down in the vicinity of the isolated mode. The pattern observed here resembles the 'zipper phenomenon', described by Heaton, Nichols & Schmid (2009) and Nichols & Lele (2011*b*).

4.1. *The isolated mode*

The fact that the isolated mode is robust with respect to x_{max} indicates that it must be quite distinct from the arc branch modes described earlier. A first characterisation

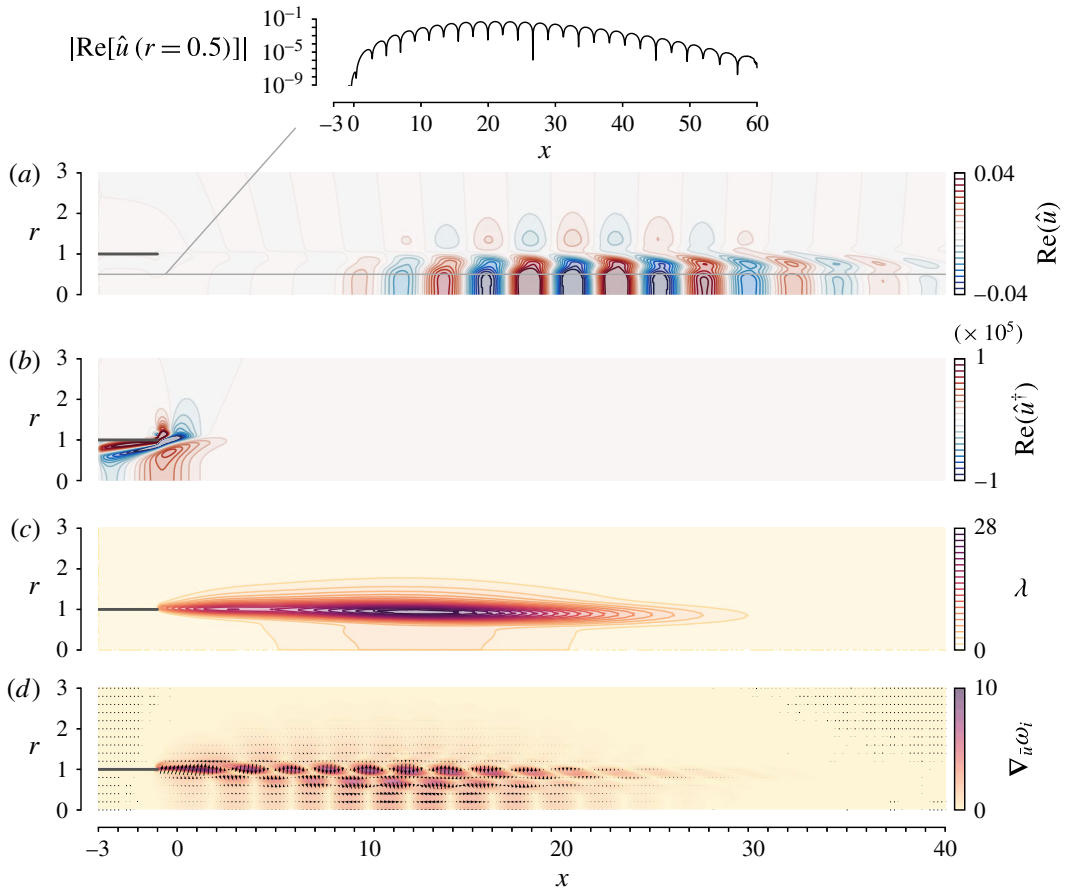

FIGURE 7. (Colour online) (*a*) Spatial structure of the eigenfunction of axial velocity $\hat{u}$ corresponding to the most unstable eigenmode for $S = 0.143$, $Re = 360$, $D/\theta_0 = 24.3$, together with $|\mathrm{Re}(\hat{u})|$ along $r = 0.5$. (*b*) Spatial structure of the adjoint eigenmode associated with the direct mode shown in (*a*). (*c*) Structural sensitivity λ, as defined by (2.23). (*d*) Sensitivity $\nabla_{\bar{\boldsymbol{u}}}\omega_i = (\nabla_{\bar{u}}\omega_i, \nabla_{\bar{v}}\omega_i)$ of the growth rate to modifications of the base flow.

of this mode is attempted by inspecting its spatial eigenfunction, shown in figure 7. Note that the results that are shown were obtained with $x_{max} = 60$, although for clarity only a fraction of the domain (up to $x = 40$ and $r = 3$) is shown. The top frame (*a*) represents a snapshot of the axial velocity perturbation. Quite in contrast with the arc branch modes in figure 5, the region of significant eigenfunction amplitude is found to be well contained in the centre of the domain. This is seen even clearer when looking at the inset where the modulus of the perturbation values along a line $r = 0.5$ is plotted in logarithmic scale. At the inflow and at the outflow boundaries, the perturbations are at least five orders of magnitude smaller than at their maximum location.

A numerical solution of the associated discrete adjoint eigenvalue problem retrieves the complex conjugate counterparts of the direct eigenvalues, as shown in figure 6, with high accuracy (arc branch and isolated mode). The adjoint eigenfunction of the isolated mode is displayed in figure 7(*b*). It is strongly localised around the nozzle edge, marking this region as being the most receptive to initial perturbations for triggering the direct eigenmode.

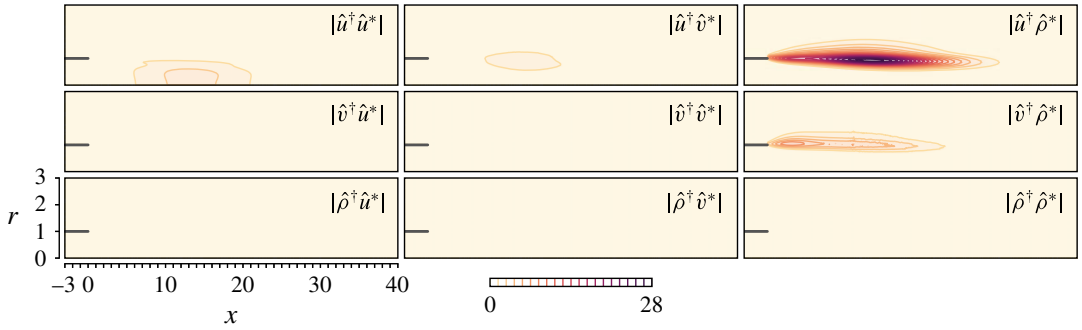

FIGURE 8. (Colour online) Absolute value of the components of the structural sensitivity tensor $\boldsymbol{S}$ corresponding to the most unstable eigenmode for $S = 0.143$, $Re = 360$, $D/\theta_0 = 24.3$.

Direct and adjoint eigenmodes may then be multiplied, according to (2.23), in order to estimate the flow region in which local feedback mechanisms contribute most to the existence of the global eigenmode. This quantity λ is represented in figure 7(*c*). A well-localised maximum is found around $x = 13$, concentrated near the lower part of the shear layer; the potential core is also highlighted. Comparing the individual components of the sensitivity tensor $\boldsymbol{S}$, shown in figure 8, reveals that feedback proportional to the density perturbation ρ' into the axial and – to a lesser degree – radial momentum equations forms the strongest contribution to changes in the eigenvalue. Note that it does not tell us whether these changes are stabilizing or destabilizing. From inspection of the stability equations (2.11)–(2.13) at zero Richardson number, we can thus draw the conclusion that the convection term $\bar{\boldsymbol{u}} \cdot \boldsymbol{\nabla}\bar{\boldsymbol{u}}$ to which ρ' is proportional plays a highly important role for the growth rate and frequency of the isolated eigenmode that is responsible for the self-sustained global oscillations in low-density jets. The fact that the feedback has a stronger effect in the axial momentum equation than in the radial momentum equation can easily be explained by remembering that the slenderness of this moderately large Reynolds number jet flow implies that $\bar{u} \gg \bar{v}$ and consequently $\bar{u}\partial\bar{u}/\partial x \gg \bar{u}\partial\bar{v}/\partial x$.

It is tempting, but hardly pertinent, to try to relate the spatial distribution of the structural sensitivity to a supposed jet-column character of the eigenmode. The distinction between jet-column and shear layer modes is meaningful in the context of a local analysis. A physical examination of the active instability mechanisms in the isolated mode should ideally be based on the role of the baroclinic torque, following the local analysis of Lesshafft & Huerre (2007). However, it is not clear how the structural sensitivity could be exploited for such a discussion.

It is noted from figure 7 that the shapes of the direct and adjoint eigenmodes, as well as their pointwise product, compare well with the results of Qadri (2014), shown in his figure 4.1. Recently, Qadri *et al.* (2015) have analysed self-sustained oscillations in lifted diffusion flames. In their configuration, fuel with a density 7 times smaller than that of the ambient is injected at a Reynolds number, based on the present scales, of approximately 500, with a moderately steep velocity profile, $D/\theta_0 = 25$. Given the similarities with the present set-up, it is not surprising that there are also many similarities between their 'mode A' and the isolated eigenmode under consideration here. For example, the structural sensitivity component with the strongest contribution in their work is that associated with changes in the mixture fraction feedback into the axial momentum equation (figure 6 of Qadri *et al.* (2015)).

Upstream of the diffusion flame, in the isothermal jet zone where the sensitivity of their mode A peaks, the mixture fraction is equivalent to the density, so that their strongest sensitivity component is in fact the analogue of $\hat{u}^\dagger\hat{\rho}^*$ in the present analysis, which has indeed been shown to be the strongest contributor to the structural sensitivity (figure 8). We would like to point out, however, that the low-density jet region in Qadri *et al.* (2015) is bounded by a diffusion flame downstream, and is thus not a canonical jet configuration.

Figure 7(*d*) shows the sensitivity of the growth rate of the global mode to arbitrary modifications of the base flow. The magnitude $[(\nabla_{\bar{u}}\omega_i)^2 + (\nabla_{\bar{v}}\omega_i)^2]^{1/2}$ is indicated by the colour, whereas the arrows indicate the direction $(\nabla_{\bar{u}}\omega_i, \nabla_{\bar{v}}\omega_i)$ in which the base flow has to be modified to achieve a positive increment in the growth rate, i.e. to destabilize the global mode. The results are in line with those observed by Tammisola (2012) for unconfined wake flows, i.e. a region of high sensitivity just downstream of the injector, followed by on oscillatory pattern in a region that stretches from approximately 5 to 20 radii downstream of the injector. This sensitivity measure can be further separated in two parts: the sensitivity to changes in the base flow advection and the sensitivity to changes in the energy extraction from base flow gradients ('production'). It was found (not shown in the figure) that the contribution of the production part corresponds to the region of high sensitivity adjacent to the nozzle, while the advection part dominates in the second region of high sensitivity farther downstream. A change in the velocity profiles just downstream of the injector in the direction indicated by $(\nabla_{\bar{u}}\omega_i, \nabla_{\bar{v}}\omega_i)$ would cause a thinning of the shear layer, increasing the streamwise velocity gradient while bringing together the inflection points of the density and velocity profiles. From a local stability point of view (Lesshafft & Marquet 2010; Coenen & Sevilla 2012), it is not surprising that such a change would cause a destabilisation of the flow.

If the isolated mode is not the result of non-local pressure feedback, which in the present setting could only arise from spurious effects at the outflow boundary, then it is expected to be linked to the presence of local absolute instability. According to previous studies, for instance Lesshafft *et al.* (2007), global instability in jets requires an absolutely unstable region of finite extent adjacent to the nozzle exit. To confirm the absolute character of the local instability near the nozzle in the present base flow, a local spatio-temporal stability analysis has been performed. To that aim, at each downstream position x, the basic flow is assumed to be locally parallel, with radial profiles of velocity $\bar{\boldsymbol{u}}(r) = (\bar{u}(r), 0)$ and density $\bar{\rho}(r)$; small perturbations are introduced as normal modes $[\hat{u}_l(r), \mathrm{i}\hat{v}_l(r), \hat{p}_l(r), \hat{\rho}_l(r)]\exp[\mathrm{i}(kx - \omega t)]$, with complex axial wavenumber $k = k_r + \mathrm{i}k_i$ and complex angular frequency $\omega = \omega_r + \mathrm{i}\omega_i$. Here k, ω, and t are non-dimensionalised using R^* and U_m^*. Substitution of the normal modes into the equations of motion, linearised around the steady base flow, yields a system of ordinary differential equations that, together with appropriate boundary conditions, provides a generalised eigenvalue problem (see, for instance, Coenen & Sevilla 2012), to be interpreted as a dispersion relation $D(k, \omega; Re, S, D/\theta_0, \ldots, \bar{u}, \bar{v}, \bar{p}, \bar{\rho}) = 0$ between k and ω. Here we are concerned with the absolute or convective character of the instability. Therefore we need to find the spatio-temporal instability modes with zero group velocity, i.e. modes for which $\mathrm{d}\omega/\mathrm{d}k = 0$. The growth rate $\omega_{0,i}$ of these is called the absolute growth rate and determines whether the instability is convective, $\omega_{0,i} < 0$, or absolute, $\omega_{0,i} > 0$. The condition $\mathrm{d}\omega/\mathrm{d}k = 0$ is equivalent to the existence of a double root, or saddle point, in the complex k-plane, $\partial D/\partial k|_{k=k_0} = 0$. Among all the saddle points that may exist, only the one with the largest value of $\omega_{0,i}$, while satisfying the Briggs–Bers criterion, determines the large-time impulse response of the

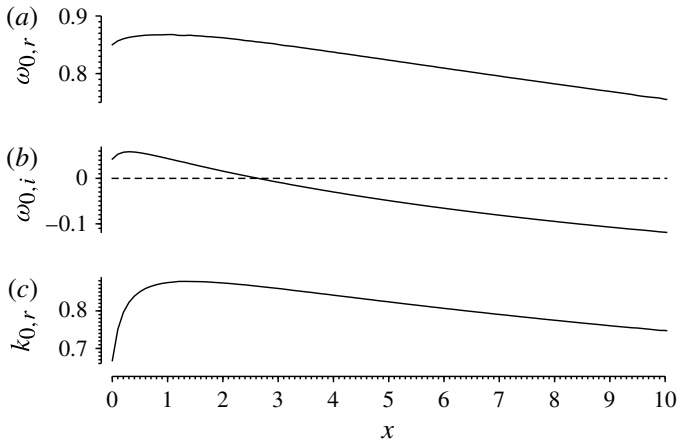

FIGURE 9. Results of a local stability analysis for the case $S = 0.143$, $Re = 360$, $D/\theta_0 = 24.3$.

flow (see, for instance, Huerre 2000, and references therein). The numerical method used to determine $(\omega_{0,i}, k_{0,i})$ is described in Coenen & Sevilla (2012).

Figure 9 shows the streamwise variation of $\omega_{0,r}$, $\omega_{0,i}$, and $k_{0,r}$. Absolute instability prevails over the interval $0 \leqslant x \leqslant 2.6$. Couairon & Chomaz (1999) and Lesshafft *et al.* (2006) showed that when an absolutely unstable region is bounded by the jet outlet, the length x_{AC} of this region needs to be sufficiently large for the global mode to be triggered. Coenen & Sevilla (2012) used the criterion $x_{AC} = C/\sqrt{\omega_i(x=0)}$ (Chomaz, Huerre & Redekopp 1988; Couairon & Chomaz 1999) that contains a free parameter C. They found that $C = 0.85$ gave good agreement with the experimental observations of Hallberg & Strykowski (2006). The same criterion would predict here that the length of the absolutely unstable region must be 4 radii. In figure 9 we can observe that for this globally marginally stable flow, this length is approximately 3 radii. From the spatially oscillating structure of the global mode of figure 7(*a*), we can also estimate a wavenumber $k = 1.4$, to be compared with the value $0.7 \simeq k_{0,r} \simeq 0.9$ in the absolutely unstable region of figure 9(*c*). The frequency of the global mode for this case is $\omega_r = 0.91$, whereas the local stability analysis results in a frequency that ranges from 0.85 to 0.87. The discrepancies between the two analyses can be attributed to the rapid spatial development of the flow (see figure 2*a*) that violates the parallel flow hypothesis on which the local analysis is based. An clear example of this was found recently by Moreno-Boza *et al.* (2016) when studying buoyancy-driven flickering in diffusion flames.

As the current value $S = 0.143$ already represents the case of pure helium, in figure 10 the Reynolds number is varied in order to demonstrate its influence on the isolated eigenvalue. Indeed, the growth rate ω_i is found to increase steadily with the Reynolds number, crossing into the unstable half-plane before $Re = 380$, while the Strouhal number remains almost constant over the plotted interval of Re.

The pseudospectrum of the $Re = 360$ helium jet is presented in figure 11 for a complete comparison with the $Re = 1000$ case in the previous section. Most features are shared by both configurations, in particular the distinct variations of the energy gain in the regions above and below the arc branch. The response to forcing at real frequency is well converged in the case of the $Re = 360$ jet at all x_{max} settings. The most prominent difference with respect to the $Re = 1000$ case is a sharp resonance

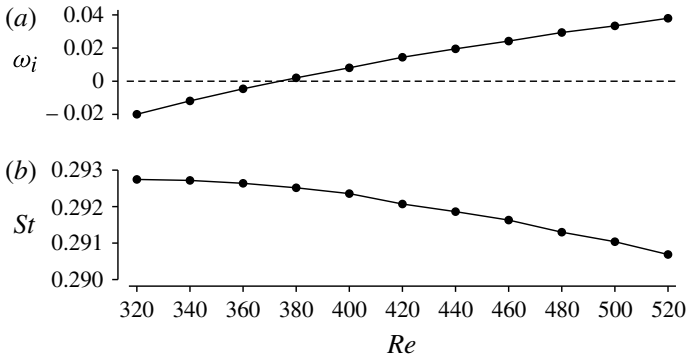

FIGURE 10. Evolution of the isolated mode with the Reynolds number for a pure helium jet ($S = 0.143$) and $D/\theta_0 = 24.3$.

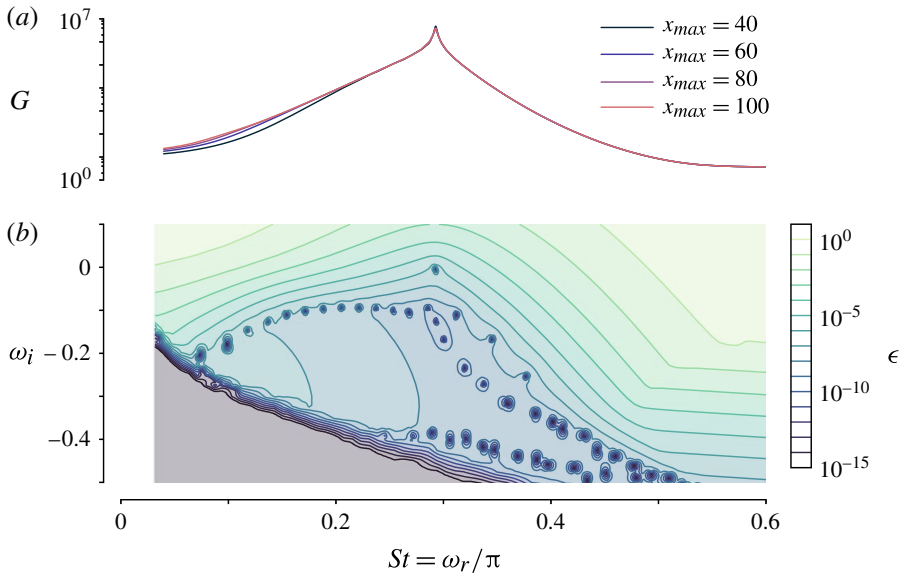

FIGURE 11. (Colour online) Forcing response of a jet at $Re = 360$, $S = 0.143$ and $D/\theta_0 = 24.3$. (*a*) Optimal gain as a function of real forcing frequency. Different colours denote results obtained in numerical domains of different lengths, as indicated in the legend. (*b*) Pseudospectrum, computed as the inverse of the optimal gain for complex forcing frequencies. The case $x_{max} = 60$ is represented.

peak in the energy gain near the frequency of the isolated mode. The gain remains finite, because the isolated mode is still slightly stable. The discussion of the arc branch provided in § 3 remains valid in all aspects in the present configuration.

4.2. *Comparison with the experiment*

The pure helium jet at $Re = 360$ discussed in § 4 has been characterised as being nearly marginally stable. By tracking the values of the control parameters Re and D/θ_0 for which the growth rate of the isolated mode ω_i is zero, a neutral curve can be constructed. In figure 12(*a*), such neutral curves in the Re–D/θ_0 plane are presented for pure helium jets ($S = 0.143$). The solid circles correspond to the results of the global mode analysis without taking into account buoyancy effects. To the left of the

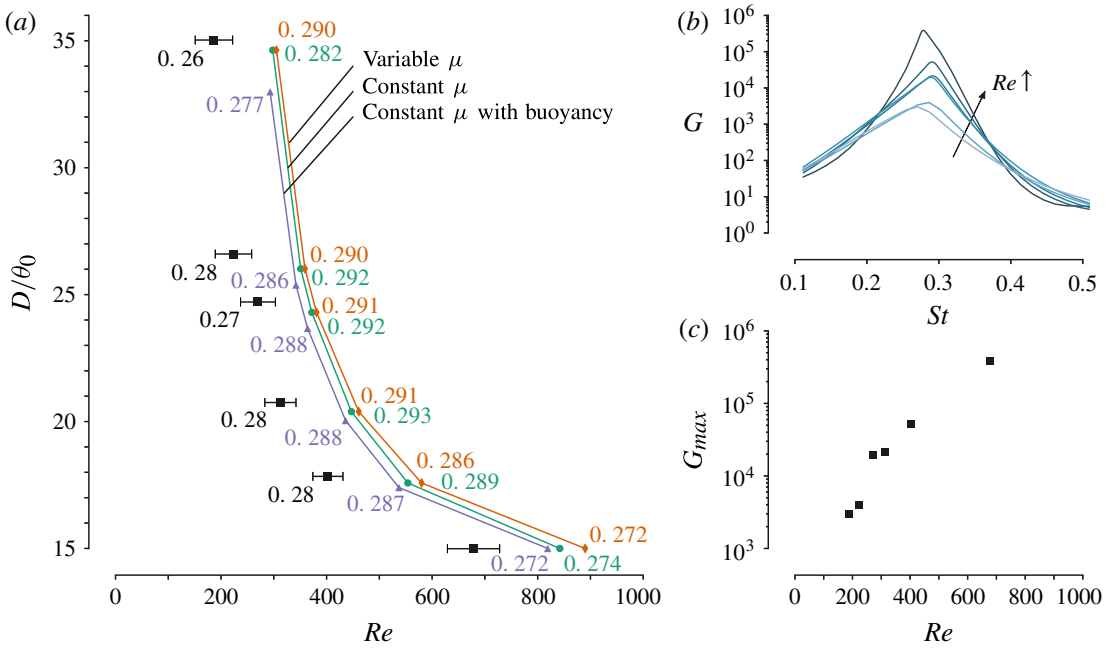

FIGURE 12. (Colour online) (*a*) Comparison with the experimental results of Hallberg & Strykowski (2006) for the onset of global instability in a pure He jet ($S = 0.143$). The experimental results are indicated with solid squares and error bars, whereas the predictions based on the global mode analysis of the present work are indicated by the solid circles. The addition of gravitational effects in the analysis results in the transition points indicated by the solid triangles, and taking into account the variation of viscosity with composition results in the solid diamonds. The numbers next to the transition points indicate the Strouhal numbers corresponding to the oscillating mode of the jet. (*b*) Frequency response computed for conditions of the experimentally observed transition points. (*c*) The maximum optimal gain for the experimentally observed transition points.

transition points the jet is globally stable ($\omega_i < 0$) whereas to the right it is globally unstable ($\omega_i > 0$). These results are compared with the experimental measurements of Hallberg & Strykowski (2006), indicated in figure 12(*a*) as squares with error bars. Care has been taken to convert the experimentally obtained critical Reynolds numbers, based on the centreline velocity, to Reynolds numbers based on the mean velocity. Fair agreement is found between the experimental and the linear neutral curves, but essentially the latter is shifted towards higher Reynolds numbers; in other words, the onset of global instability in the linear calculations is delayed with respect to the experimental observations.

Values next to the transition points in figure 12(*a*) indicate the Strouhal numbers near criticality. In the global mode calculations, the Strouhal number St is directly given by the frequency ω_r of the marginally stable eigenmode, whereas in the experiments, it was obtained by measuring the frequency of the self-sustained oscillations under slightly supercritical conditions. It can be observed that the agreement between the two is rather good, with relative differences smaller than 10 %.

In an effort to explain the offset between the critical curve given by the stability analysis and the experimental evidence, we assessed the influence of buoyancy. Strictly speaking, while estimating the importance of the latter, the characteristic length scale

that should be used in the construction of the Richardson number is not the radius R^*, but the development length of the jet, of order ReR^*. This modified Richardson number can be written as Gr/Re. In the experiments of Hallberg & Strykowski (2006) the Grashof number for the pure helium jet ($S = 0.143$) is $Gr = 138$, and the marginal Reynolds numbers lie in the range 200–700. We can therefore expect that buoyancy has a non-negligible effect in the experiments. Recomputing the critical curve with the inclusion of the buoyancy term, with $Gr = 138$, we obtained the solid triangles of figure 12(*a*). Indeed, adding buoyancy destabilises the jet, and slightly improves the agreement with the experimental data. Nevertheless, its influence is not sufficiently strong to explain the offset between the stability analysis and the experiments.

A second physical aspect whose influence has been investigated is the variation of viscosity with composition. The viscosity of air is 11 % lower than that of helium, so that a small effect on the molecular transport can be expected, changing both the base flow and the stability properties. Figure 12(*a*) shows that there is indeed a small shift of the transition curve (solid diamonds). The variable viscosity is seen to have a slightly stabilising influence. This seems counterintuitive, as a lower viscosity in the flow field due to variations with the composition would result in an higher local effective Reynolds number, and would therefore be expected to destabilize the flow. Nevertheless, subtle changes in the base flow profiles may just as well counteract this, eventually causing a net stabilization. A more detailed study may be interesting in flows where variations of the viscosity are stronger, such as heated jets or diffusion flames.

In figure 12(*b*) we show the frequency response computed at the transition points of Hallberg & Strykowski (2006). Because these points are located to the left of the transition curve obtained with the global mode stability analysis, the jet is globally stable under these conditions. Nevertheless, the optimal gain is seen to be very high, $O(10^3–10^6)$, in a narrow band around the frequency associated with the global mode (see also the discussion of figure 11). This means that small perturbations that act as a forcing to the jet may suffer very strong amplifications that may sustain a nonlinear global oscillation of the jet at the frequency of maximum amplification. In an experiment this could cause a shift in the observed critical value of the bifurcation parameter. Applying this hypothesis to the present analysis would mean that, if both the incoming noise and the necessary amplification threshold to sustain a nonlinear oscillation were constant over all experimental conditions, the computed frequency response at the experimental transition points should have values that are of the same order of magnitude. Nevertheless, figure 12(*b*) shows that this is not the case here. In fact, the maximum gain is seen to be larger for the experimental conditions corresponding to higher Reynolds numbers (and lower D/θ_0). It must be mentioned that these results correspond to the optimal forcing, whose spatial structure varies from case to case, and might be very different from realistic noise present under experimental conditions. To rule out this variability the computations were repeated for a fixed spatial forcing distribution (a uniform distribution in the injection pipe), yielding similar results (not shown here) to the ones of figure 12(*b*), but with generally lower values of the gain.

Finally, it is worth mentioning that, as the sensitivity to base flow modifications of figure 7(*d*) shows, small changes in the region just downstream of the injector have a strong influence on the growth rate of the global instability. Although care has been taken to mimic the experimental set-up of Hallberg & Strykowski (2006), some details, such as the exact nozzle shape and the sharpness of the nozzle lip, are hard to account for, and may as well play a role in the discrepancy between experiment and linear theory.

5. Conclusions

The present work gives, for the first time, a detailed account of the linear global stability of low-density jets. By making use of the low Mach number approximation, all dynamic effects of density variations in the limit of zero Mach number are retained, while avoiding the numerically challenging necessity to resolve acoustic wave propagation.

We have found that when the spatial development of the jet flow is sufficiently fast ($Re = 360$ and $S = 0.143$), an isolated eigenvalue dominates the global eigenvalue spectrum. This mode has been shown to arise from the presence of absolute instability in light jets, documented in numerous earlier studies (e.g. Monkewitz & Sohn 1988; Lesshafft & Huerre 2007; Coenen & Sevilla 2012). It is this mode that causes global instability in light jets at low Mach numbers. It has been found to converge without much effort in our numerical calculations, in particular with respect to the domain size. The structural sensitivity of this mode is concentrated in a confined region close to the nozzle; according to Giannetti & Luchini (2007), it is sufficient to resolve this flow region in order to accurately compute the eigenvalue.

Unlike previous local stability analyses (e.g. Coenen & Sevilla 2012), in which the length of the absolutely unstable region that is necessary to trigger a global mode introduces an unknown parameter in the problem, the isolated global eigenmode is able the determine the critical conditions for the onset of global instability in terms of the governing flow parameters without any additional hypotheses. This has been employed to link the isolated mode to the supercritical Hopf bifurcation that was observed in the helium jet experiments by Hallberg & Strykowski (2006): the neutral curves for the onset of instability, in the experiments and in the present linear analysis match, within reasonable accuracy, and the predicted Strouhal numbers agree within ten per cent with the experimentally reported values at onset. The bifurcation in the experiments takes place in situations that are characterised as slightly subcritical in the linear framework. An additional destabilisation due to buoyancy effects has been demonstrated to be insufficient in order to explain this offset. Including the variation of viscosity with composition has been shown to have a small stabilising effect, and is thus also ruled out as an essential ingredient to explain the discrepancy. An inspection of the pseudospectrum however indicates that small perturbations may suffer a very strong amplification in the slightly stable regime. According to linear theory, experimental low-level noise might therefore be amplified and observed as sustained coherent wavepackets. A dedicated detailed study is required to assess this hypothesis, for example by comparing with direct numerical simulations with a controlled low-level forcing.

A second feature of the global eigenvalue spectra of low-density jets is a branch of eigenvalues, called the arc branch, that, when the spatial development of the jet flow is sufficiently slow ($Re = 1000$, $S = 0.5$) may dominate the spectrum, hindering the detection of the isolated mode. This arc branch is found to be highly sensitive to the numerical domain size, consistent with numerous existing studies of jets (Nichols & Lele 2011*a*; Garnaud *et al.* 2013*a*) and boundary layers (Ehrenstein & Gallaire 2005, 2008; Åkervik *et al.* 2008). The present results suggest, for the first time, that these eigenmodes are not only affected by domain truncation, but that their very existence is dependent on spurious feedback from the outflow boundary. Two observations support this conjecture: first, the arc branch aligns approximately with isocontours of the pseudospectrum, suggesting a link between a given level of exogenous energy input and the occurrence of arc branch modes; second, the associated eigenfunctions display an integer number of wavelengths between inflow and outflow, suggesting a

resonance condition. A more detailed study to prove this conjecture is currently being carried out, but lies out of the scope of the present work.

Acknowledgements

L.L. acknowledges financial support from ANR under the Cool Jazz project and from DGA under contract LADX2331. W.C. and A.S. were supported by the Spanish MICINN under project DPI2014-59292-C3-1-P and DPI2015-71901-REDT.

REFERENCES

ÅKERVIK, E., EHRENSTEIN, U., GALLAIRE, F. & HENNINGSON, D. S. 2008 Global two-dimensional stability measures of the flat plate boundary-layer flow. *Eur. J. Mech. (*B*/Fluids)* **27** (5), 501–513.

CHOMAZ, J.-M. 2005 Global instabilities in spatially developing flows: non-normality and nonlinearity. *Annu. Rev. Fluid Mech.* **37**, 357–392.

CHOMAZ, J.-M., HUERRE, P. & REDEKOPP, L. G. 1988 Bifurcations to local and global modes in spatially developing flows. *Phys. Rev. Lett.* **60**, 25–28.

COENEN, W. & SEVILLA, A. 2012 The structure of the absolutely unstable regions in the near field of low-density jets. *J. Fluid Mech.* **713**, 123–149.

COENEN, W., SEVILLA, A. & SÁNCHEZ, A. 2008 Absolute instability of light jets emerging from circular injector tubes. *Phys. Fluids* **20**, 074104.

COUAIRON, A. & CHOMAZ, J.-M. 1999 Fully nonlinear global modes in slowly varying flows. *Phys. Fluids* **11**, 3688–3703.

EHRENSTEIN, U. & GALLAIRE, F. 2005 On two-dimensional temporal modes in spatially evolving open flows: the flat-plate boundary layer. *J. Fluid Mech.* **536**, 209–218.

EHRENSTEIN, U. & GALLAIRE, F. 2008 Two-dimensional global low-frequency oscillations in a separating boundary-layer flow. *J. Fluid Mech.* **614**, 315–327.

GARNAUD, X., LESSHAFFT, L., SCHMID, P. J. & HUERRE, P. 2013*a* Modal and transient dynamics of jet flows. *Phys. Fluids* **25**, 044103.

GARNAUD, X., LESSHAFFT, L., SCHMID, P. J. & HUERRE, P. 2013*b* The preferred mode of incompressible jets: linear frequency response analysis. *J. Fluid Mech.* **716**, 189–202.

GIANNETTI, F. & LUCHINI, P. 2007 Structural sensitivity of the first instability of the cylinder wake. *J. Fluid Mech.* **581**, 167–197.

HALLBERG, M. P. & STRYKOWSKI, P. J. 2006 On the universality of global modes in low-density axisymmetric jets. *J. Fluid Mech.* **569**, 493–507.

HEATON, C. J., NICHOLS, J. W. & SCHMID, P. J. 2009 Global linear stability of the non-parallel batchelor vortex. *J. Fluid Mech.* **629**, 139–160.

HECHT, F. 2012 New development in freefem++. *J. Numer. Math.* **20** (3–4), 251–265.

HIRSCHFELDER, J. O., CURTISS, C. F. & BIRD, R. B. 1954 *Molecular Theory of Gases and Liquids*. Wiley.

HUERRE, P. 2000 Open shear flow instabilities. In *Perspectives in Fluid Dynamics* (ed. G. Batchelor, K. Moffatt & G. Worster), pp. 159–229. Cambridge University Press.

JENDOUBI, S. & STRYKOWSKI, P. J. 1994 Absolute and convective instability of axisymmetric jets with external flow. *Phys. Fluids* **6**, 3000–3009.

KYLE, D. M. & SREENIVASAN, K. R. 1993 The instability and breakdown of a round variable-density jet. *J. Fluid Mech.* **249**, 619–664.

LESSHAFFT, L. & HUERRE, P. 2007 Linear impulse response in hot round jets. *Phys. Fluids* **19**, 024102.

LESSHAFFT, L., HUERRE, P. & SAGAUT, P. 2007 Frequency selection in globally unstable round jets. *Phys. Fluids* **19** (5), 054108.

LESSHAFFT, L., HUERRE, P., SAGAUT, P. & TERRACOL, M. 2006 Nonlinear global modes in hot jets. *J. Fluid Mech.* **554**, 393–409.

LESSHAFFT, L. & MARQUET, O. 2010 Optimal velocity and density profiles for the onset of absolute instability in jets. *J. Fluid Mech.* **662**, 398–408.

MARQUET, O., SIPP, D. & JACQUIN, L. 2008 Sensitivity analysis and passive control of cylinder flow. *J. Fluid Mech.* **615**, 221–252.

MONKEWITZ, P. A., BECHERT, D. W., BARSIKOW, B. & LEHMANN, B. 1990 Self-excited oscillations and mixing in a heated round jet. *J. Fluid Mech.* **213** (-1), 611.

MONKEWITZ, P. A. & SOHN, K. D. 1988 Absolute instability in hot jets. *AIAA J.* **28**, 911–916.

MORENO-BOZA, D., COENEN, W., SEVILLA, A., SANCHEZ, A. L. & LIÑÁN, A. 2016 Diffusion-flame flickering as a hydrodynamic global mode. *J. Fluid Mech.* **798**, 997–1014.

NICHOLS, J. W. & LELE, S. K. 2010 Global mode analysis of turbulent high-speed jets. *Annual Research Briefs 2010*. Center for Turbulence Research. Stanford University.

NICHOLS, J. W. & LELE, S. K. 2011*a* Global modes and transient response of a cold supersonic jet. *J. Fluid Mech.* **669**, 225–241.

NICHOLS, J. W. & LELE, S. K. 2011*b* Non-normal global modes of high-speed jets. *Int. J. Spray Combust* **3** (4), 285–302.

NICHOLS, J. W., SCHMID, P. J. & RILEY, J. J. 2007 Self-sustained oscillations in variable-density round jets. *J. Fluid Mech.* **609**, 275–284.

QADRI, U. A. 2014 Global stability and control of swirling jets and flames. PhD thesis, University of Cambridge.

QADRI, U. A., CHANDLER, G. J. & JUNIPER, M. P. 2015 Self-sustained hydrodynamic oscillations in lifted jet diffusion flames: origin and control. *J. Fluid Mech.* **775**, 201–222.

TAMMISOLA, O. 2012 Oscillatory sensitivity patterns for global modes in wakes. *J. Fluid Mech.* **701**, 251–277.

TREFETHEN, L. N. & EMBREE, M. 2005 *Spectra and Pseudospectra: The Behavior of Nonnormal Matrices and Operators*. Princeton University Press.

WILLIAMS, F. A. 1985 *Combustion Theory*, 2nd edn. Benjamin Cummings.

PHYSICAL REVIEW FLUIDS **2**, 113904 (2017)

Time-delayed feedback technique for suppressing instabilities in time-periodic flow

Léopold Shaabani-Ardali,[1,2,*] Denis Sipp,[2] and Lutz Lesshafft[1]
[1]*LadHyX, École polytechnique–CNRS, 91120 Palaiseau, France*
[2]*DAAA, ONERA, Université Paris-Saclay, F-92190 Meudon, France*
(Received 6 February 2017; published 17 November 2017)

A numerical method is presented that allows to compute time-periodic flow states, even in the presence of hydrodynamic instabilities. The method is based on filtering nonharmonic components by way of delayed feedback control, as introduced by Pyragas [Phys. Lett. A **170**, 421 (1992)]. Its use in flow problems is demonstrated here for the case of a periodically forced laminar jet, subject to a subharmonic instability that gives rise to vortex pairing. The optimal choice of the filter gain, which is a free parameter in the stabilization procedure, is investigated in the context of a low-dimensional model problem, and it is shown that this model predicts well the filter performance in the high-dimensional flow system. Vortex pairing in the jet is efficiently suppressed, so that the unstable periodic flow state in response to harmonic forcing is accurately retrieved. The procedure is straightforward to implement inside any standard flow solver. Memory requirements for the delayed feedback control can be significantly reduced by means of time interpolation between checkpoints. Finally, the method is extended for the treatment of periodic problems where the frequency is not known *a priori*. This procedure is demonstrated for a three-dimensional cubic lid-driven cavity in supercritical conditions.

DOI: 10.1103/PhysRevFluids.2.113904

I. INTRODUCTION

Any analysis of linear flow instability first requires the definition of an unperturbed basic flow state. An obvious problem is that such flow states, if indeed they are unstable, cannot be recovered as asymptotic solutions by simple time stepping. In the context of *steady* flow, several methods exist that allow the computation of unstable steady states. Newton-Raphson iteration [1] and recursive projection [2,3] are efficient in many such configurations, although they may require deep modifications of numerical flow solvers, and their convergence is often problematic. A robust alternative, which furthermore is convenient to integrate into an existing time-stepping simulation code, has been proposed by Åkervik *et al.* [4] under the name of "selective frequency damping" (SFD). This technique has since been used for a wide variety of steady flow configurations.

Time-periodic flows constitute a distinct class of instability problems, and interest in the computation of periodic states is furthermore not limited to the purpose of instability analysis. Examples include vortex shedding in shear flows [5], pulsating flow in blood vessels [6], and complex flow in turbomachines [7].

Even when a flow settles into an asymptotically stable time-periodic state in the long-time limit, its computation by time stepping may be costly if long transient dynamics prevail. This difficulty can be overcome by use of the "harmonic balance" technique [8,9], which consists in the simultaneous computation of all or many temporal Fourier components of a given periodicity. A pseudotime is typically employed in order to make all Fourier components converge. This approach is widely used today both in fundamental and in applied contexts. Several improvements of the method address specific issues: if the fundamental period is not known *a priori,* a "gradient-based variable time period" algorithm [10–13] allows us to identify it as an additional unknown of the problem; if the

*leopold.shaabani-ardali@ladhyx.polytechnique.fr

flow is simultaneously forced at several frequencies, the method can be generalized [14]. Some strategies for control and shape optimization have also been devised on this basis [15].

Yet time-periodic flows may sustain hydrodynamic instabilities. In particular, the growth of *subharmonic* perturbations is observed in many such cases. Prominent examples are the pairing of vortices in shear flows [16] and the parametric subharmonic instability (PSI) of internal waves in stratified media [17]. Such instabilities may arise from linear dynamics, tractable in the framework of Floquet theory, or from nonlinear effects, as in the case of PSI. It may be possible to retrieve unstable periodic states through harmonic balance, as long as no harmonics of the fundamental flow frequency are involved in the instability, but to the best of our knowledge, this has never been attempted. Shooting methods have been designed to this effect [18,19], and these have been used successfully in the context of some flow problems [20,21]. However, their implementation requires a considerable overhead around a given flow solver.

The objective of this study is to present an easy-to-implement filtering technique, similar in spirit to the SFD method [4] used for steady flow, that allows the exact computation of time-periodic orbits in stable as well as unstable situations. To this end, an artificial forcing is added to the Navier-Stokes equations, which is required to leave the dynamics of the fundamental flow frequency and of all its higher harmonics unaffected, such that the simulation converges in time towards a periodic solution of the unforced equations. A *delayed feedback control* [22] achieves this objective. Such time-delay filters have been extensively used in the context of controlling chaotic dynamics in systems with a low number of degrees of freedom. In a recent study [23], a similar technique is applied in a high-dimensional flow problem, in order to suppress spatio-temporal asymmetries in wakes. In the present paper, the use of time-delayed feedback for flow stabilization is explored.

The phenomenon of vortex pairing in an axisymmetrically forced jet is chosen to illustrate the procedure. It is demonstrated how the artificial damping efficiently suppresses the growth of subharmonic perturbations, and thereby the onset of vortex pairing, so that unstable periodic solutions of the Navier-Stokes equations can be obtained. The feedback optimally eliminates subharmonic components, letting the fundamental and its harmonic components unaffected, while all nonharmonic frequencies experience damping. We will show that in weakly stable settings, the feedback can be used to accelerate the convergence towards the asymptotic state. However, this method, due to the full period storage, can be memory-consuming; to severely reduce the memory requirements, we will show how spline interpolation between checkpoints in time can be used, without affecting much the convergence properties of the algorithm.

When flow periodicity arises from intrinsic dynamics, as opposed to external forcing, the period length of the asymptotic state is not known *a priori*. We will show that the stabilization method for such cases can be extended to identify the period length through iterative adjustment, as will be demonstrated for a cubic lid-driven cavity. Due to their broad range of application, cavities are well-studied flow systems, which can sustain several types of instabilities [24]. A configuration is chosen that is known to give rise to coexisting limit cycles and intermittently chaotic dynamics [25–27].

The paper is organized as follows. The jet flow example is introduced in Sec. II, and the occurrence of vortex pairing in the absence of artificial damping is discussed. The stabilization method is presented in Sec. III. A single free parameter needs to be chosen; its optimal value is found in the context of a simple model problem. Section IV documents the performance of the technique for an unstable vortex street, with a discussion of the optimal parameter choice. It is further shown how the same technique accelerates the convergence in stable situations, and how the memory requirements may be reduced through check pointing and interpolation. Details on the simulation technique are provided here. Section V extends the stabilization procedure to periodic flows with an unknown period.

II. AN EXAMPLE OF SUBHARMONIC INSTABILITY: VORTEX PAIRING IN JETS

Axisymmetric harmonic forcing at the nozzle of a laminar round jet excites, over a wide range of frequencies, a shear instability of the steady flow state, leading to exponential growth of the perturbation amplitude along the axial direction. As the amplitude reaches nonlinear levels, the

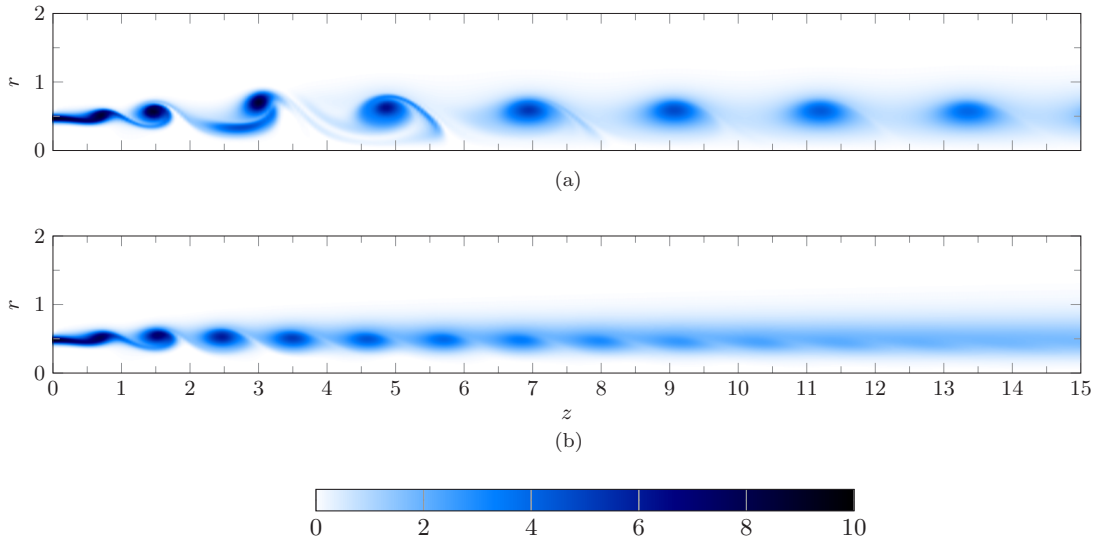

FIG. 1. Vorticity snapshots of paired and unpaired states, obtained without stabilization for two different parameter settings. The paired state (a) was obtained at Re = 2000 and St = 0.6 while the unpaired state (b) was obtained at Re = 1300 and St = 0.6. Reynolds and Strouhal numbers are defined in Sec. IV A.

shear layer rolls up into a regular street of vortex rings, which form and convect at the frequency of the applied forcing. Depending on flow parameters and forcing frequency (more details are given in Sec. IV A), these vortices may undergo subsequent pairing [28], and if the ambient flow is sufficiently quiet and the harmonic forcing is well-controlled, this pairing takes place in a perfectly regular fashion. The numerical method is detailed in Sec. IV A.

In cases where pairing occurs, two neighboring vortices merge into one, such that the passage frequency of vortices downstream of the pairing location is exactly half that of the imposed forcing. If the forcing is characterized by the time period T, such that $\omega_f = 2\pi/T$, the "paired state" is globally $2T$-periodic (T-periodic upstream of the pairing and $2T$-periodic downstream). The velocity field of a paired state will be denoted $\mathbf{u}^p$. An example, obtained by direct numerical simulation, is shown in Fig. 1(a).

Another case at different parameter settings, where no pairing is found to occur, is shown in Fig. 1(b). Vortices roll up close to the nozzle and advect downstream, until they are dissipated by viscosity. Such a flow state is (globally) T-periodic and will be called hereafter an "unpaired state." Its velocity field will be denoted $\mathbf{u}^u$.

The purpose of this study is to show how, for each paired state, a corresponding unpaired state can be recovered, defining two valid periodic solutions of the Navier-Stokes equations at the same parameter setting.

III. SUBHARMONIC STABILIZATION

In this section, after a brief presentation of filtering techniques (Sec. III A), a simple model problem is introduced in order to determine the coefficients of a time-delayed feedback—here an additional term added to the momentum equation—so that the forced Navier–Stokes simulation converges towards a T-periodic state.

A. Time-delayed feedback

A fully synchronized paired state can be decomposed into components that are T-periodic and those that are only $2T$-periodic,

$$\mathbf{u}^p(\mathbf{x},t) = \sum_n \mathbf{u}_n^T(\mathbf{x})\,\exp(in\omega_f t) + \sum_n \mathbf{u}_n^{2T}(\mathbf{x})\,\exp\left(i\frac{2n+1}{2}\omega_f t\right), \quad \text{with}$$
$$n = 0,\pm1,\pm2,\ldots,\pm N. \tag{1a}$$

An unpaired state, in contrast, is purely T-periodic,

$$\mathbf{u}^u(\mathbf{x},t) = \sum_n \mathbf{u}_n^T(\mathbf{x})\,\exp(in\omega_f t). \tag{1b}$$

The objective is to design a filter that will damp all $2T$-periodic components under the second sum in Eq. (1a), while leaving any T-periodic flow state unaffected. Of course, this filter should also lead to a stable global system.

A first approach might be to consider a standard linear band-stop filter H that cuts around the subharmonic frequency $\omega_f/2$ (i.e., gain $|H(\omega_f/2)| \ll 1$), while preserving the steady component and the fundamental frequency: $H(0) = H(\omega_f) = 1$. However, in order to achieve such characteristics, a very high-order filter is needed: in logarithmic scale, $\omega_f/2$ and ω_f are apart by only $\log(2) = 0.69$, whereas the gains are separated by $-\log[|H(\omega_f/2)|] \gg 1$. This filter would be cumbersome to implement, and it would require a careful stability and pole placement analysis, as described, for example, by Aström and Murray [29] or by Doyle *et al.* [30]. Furthermore, such a filter could not satisfy all requirements: the gain at $\omega_f/2$ cannot be strictly zero, and no constraint can be imposed on the higher $2T$-periodic harmonics $(\pm\frac{3}{2}\omega_f, \pm\frac{5}{2}\omega_f, \ldots)$.

A better approach, that will be adopted here, is to use time-delayed feedback (TDF), as described by Pyragas [22]. When the flow at time t is compared with the flow at time $t - T$, components of period T and of period $2T$ are cleanly distinguished.

The $2T$-periodic components in a paired state (1a), which are the target of artificial damping, are thus isolated as

$$\mathbf{u}^p(\mathbf{x},t) - \mathbf{u}^p(\mathbf{x},t-T) = 2\sum_n \mathbf{u}_n^{2T}(\mathbf{x})\,\exp\left(i\frac{2n+1}{2}\omega_f t\right), \tag{2}$$

whereas a T-periodic unpaired state satisfies

$$\mathbf{u}^u(\mathbf{x},t) - \mathbf{u}^u(\mathbf{x},t-T) = 0. \tag{3}$$

Then adding a forcing term of the form

$$\mathbf{f} = -\lambda[\mathbf{u}(t) - \mathbf{u}(t-T)] \tag{4}$$

to the right-hand side of (12) allows us to control $2T$-periodic fluctuations without any forcing on T-periodic dynamics. In this framework, λ is a forcing parameter that needs to be prescribed (see Sec. III B).

The Laplace transform of this forcing term is

$$\mathcal{L}\{f\} = -\lambda(1 - e^{-\omega T})\mathcal{L}\{u\}, \tag{5}$$

so that its gain for a given frequency ω is found as

$$\frac{\|\mathcal{L}\{f\}\|}{\|\mathcal{L}\{u\}\|}(i\omega) = \lambda\sqrt{2 - 2\cos(\omega T)}. \tag{6}$$

The resulting transfer function is plotted in Fig. 2. The time-delayed feedback damps all frequencies that are not harmonics of ω_f, with maximum effect on the subharmonic frequency $\omega_f/2$ and on its

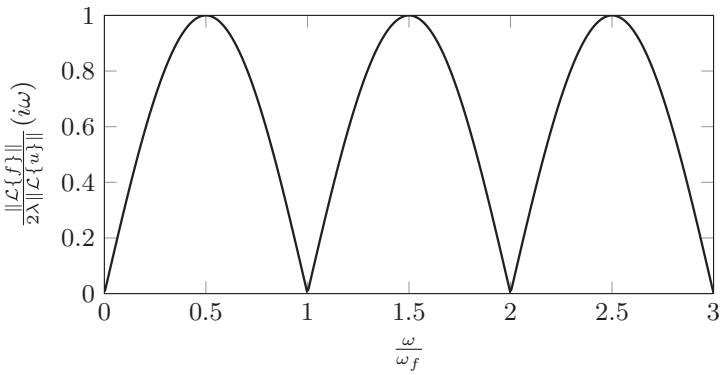

FIG. 2. Gain of the delayed feedback transfer function.

odd harmonics $(n + 1/2)\omega_f$. It is neutral with respect to the mean flow, the fundamental frequency ω_f, and its harmonics $n\omega_f$.

If the forced system converges towards a T-periodic unpaired state, the forcing will vanish, such that the recovered state is a consistent solution of the unforced Navier-Stokes equations.

B. Choice of the feedback parameter λ

At first glance, it might be expected from (6) that larger values of λ will always lead to more efficient nonharmonic damping. This however is not the case, similar to what has been demonstrated in the context of low-dimensional chaotic systems [22].

In order to guide the choice of the feedback parameter λ for the present purpose, a model problem is proposed. The dynamics of a two-frequency oscillator is considered,

$$\frac{d}{dt}\begin{pmatrix} x^s \\ \tilde{x}^s \\ x^h \\ \tilde{x}^h \end{pmatrix} = \begin{pmatrix} 0 & \frac{\omega_f}{2} & 0 & 0 \\ -\frac{\omega_f}{2} & 0 & 0 & 0 \\ 0 & 0 & 0 & \omega_f \\ 0 & 0 & -\omega_f & 0 \end{pmatrix}\begin{pmatrix} x^s \\ \tilde{x}^s \\ x^h \\ \tilde{x}^h \end{pmatrix} - \lambda\begin{pmatrix} x^s(t) - x^s(t-T) \\ \tilde{x}^s(t) - \tilde{x}^s(t-T) \\ x^h(t) - x^h(t-T) \\ \tilde{x}^h(t) - \tilde{x}^h(t-T) \end{pmatrix}, \tag{7}$$

with $T = 2\pi/\omega_f$ the period of the fundamental mode. Unlike the flow problem, the two frequencies ω_f and $\frac{1}{2}\omega_f$ in this model are uncoupled. After nondimensionalization, $\omega_f t \to t$ and $\lambda/\omega_f \to \lambda$, the system can be diagonalized as

$$\frac{d}{dt}\begin{pmatrix} y^s \\ \tilde{y}^s \\ y^h \\ \tilde{y}^h \end{pmatrix} = \begin{pmatrix} \frac{i}{2} & 0 & 0 & 0 \\ 0 & -\frac{i}{2} & 0 & 0 \\ 0 & 0 & i & 0 \\ 0 & 0 & 0 & -i \end{pmatrix}\begin{pmatrix} y^s \\ \tilde{y}^s \\ y^h \\ \tilde{y}^h \end{pmatrix} - \lambda\begin{pmatrix} y^s(t) - y^s(t-2\pi) \\ \tilde{y}^s(t) - \tilde{y}^s(t-2\pi) \\ y^h(t) - y^h(t-2\pi) \\ \tilde{y}^h(t) - \tilde{y}^h(t-2\pi) \end{pmatrix}. \tag{8}$$

In a general linear problem with time-delayed feedback, the eigenvalues are not found in closed form, and their number is infinite [31]. In contrast, exact eigensolutions of the uncoupled problem (8) can be found analytically. Introducing exponential modes, the following system is obtained:

$$y^s \propto e^{\alpha^s t} \Rightarrow \alpha^s = \frac{i}{2} - \lambda\left(1 - e^{-2\pi\alpha^s}\right), \tag{9a}$$

$$\tilde{y}^s \propto e^{\tilde{\alpha}^s t} \Rightarrow \tilde{\alpha}^s = -\frac{i}{2} - \lambda\left(1 - e^{-2\pi\tilde{\alpha}^s}\right), \tag{9b}$$

$$y^h \propto e^{\alpha^h t} \Rightarrow \alpha^h = i - \lambda\left(1 - e^{-2\pi\alpha^h}\right), \tag{9c}$$

$$\tilde{y}^h \propto e^{\tilde{\alpha}^h t} \Rightarrow \tilde{\alpha}^h = -i - \lambda\left(1 - e^{-2\pi\tilde{\alpha}^h}\right). \tag{9d}$$

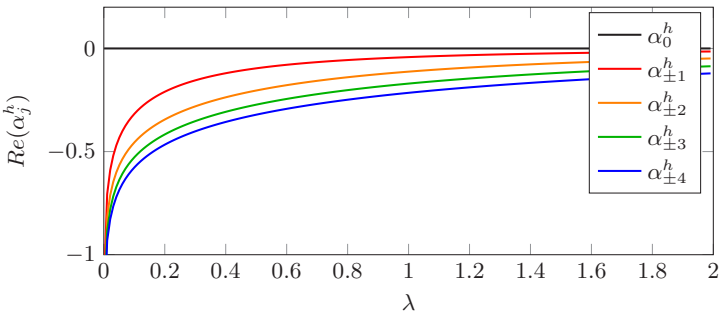

FIG. 3. Real part of eigenvalues α_j^h for $-4 \leqslant j \leqslant 4$, pertaining to fundamental oscillations, as functions of λ. It is found numerically that α_j^h and α_{-j}^h always have the same real part. The system is neutrally stable for any value of λ, with the neutral mode $\alpha_0^h = i$.

As long as real values are chosen for λ, the solutions of Eqs. (9a)–(9d) come in complex conjugate pairs, $\tilde{\alpha}^s = \bar{\alpha}^s$ and $\tilde{\alpha}^h = \bar{\alpha}^h$. It is therefore sufficient to consider Eqs. (9a) and (9c) and their closed-form solutions:

$$\alpha_j^s = \frac{i}{2} - \lambda + \frac{1}{2\pi} W_j(-2\pi\lambda e^{2\pi\lambda}), \tag{10a}$$

$$\alpha_j^h = i - \lambda + \frac{1}{2\pi} W_j(2\pi\lambda e^{2\pi\lambda}), \quad j \in \mathbb{Z}. \tag{10b}$$

W_j denotes the jth branch of the Lambert W function, which is the inverse relation of the complex function $z \mapsto ze^z$ [32]. An infinite number of solutions of Eqs. [(9a) and (9c)] exists, each corresponding to individual branches of the Lambert function. In particular, W_0 gives $\alpha_0^h = i$ for any value of λ, preserving the harmonic dynamics. For the purpose of flow stabilization, only the real part of the α values is of interest, as these govern the growth or decay of fluctuations. If, for a given λ, there exists at least one j such that the real part of α_j^s or of α_j^h is positive, then the system is unstable. Therefore, λ must meet two criteria:

(1) It should provide the most efficient damping in the subharmonic component equation (9a). For a given λ, it is always sufficient to consider the least stable mode among all possible solutions, i.e., the mode α_j^s with the largest real part in Eq. (10a). The optimal value of λ leads to maximal decay in the least stable mode.

(2) At the same time, λ must not create any instability in the fundamental equation (9c); the real part of α_j^h must be negative for every $j \in \mathbb{Z}$. While the neutral fundamental mode $\alpha_0^h = i$ exists irrespective of λ, it must not be dominated by any unstable mode.

In order to identify the optimal λ according to these requirements, the following result is demonstrated in the Appendix: if, for a given value of λ, Eqs. (9a) or (9c) has unstable solutions, the branch j on which this solution lies is such that

$$|j| < 2\lambda + 1. \tag{11}$$

As will be seen later, optimal subharmonic damping is found to be achieved within the range $0 < \lambda < 2$; consequently, the stability of the fundamental component must be ascertained for this range of λ, and the branches $-4 \leqslant j \leqslant 4$ are to be considered.

Figure 3 shows that no fundamental modes on these branches are unstable for any value of λ. As expected, the neutral eigenvalue $\alpha_0^h = i$ is always recovered, which is consistent with the premise that the applied forcing does not modify the fundamental dynamics. Therefore, the stability requirement for the fundamental modes (criterion 2) does not restrict the choice of λ.

Figure 4 demonstrates that the subharmonic modes on branches $-2 \leqslant j \leqslant 2$ experience damping for any value of λ. The same is observed for branches $|j| = 3,4$. Therefore, all the subharmonic modes are stable. The least stable modes among these correspond to $j = 0$ and $j = -1$. The real

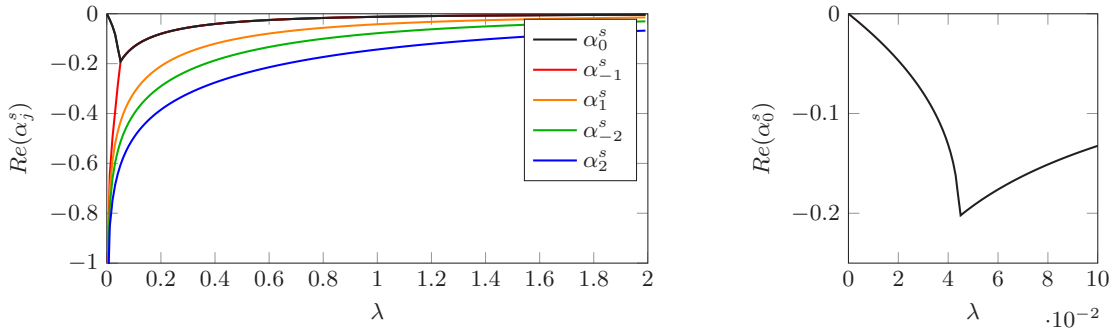

FIG. 4. Real part of eigenvalues α_j^s, pertaining to subharmonic oscillations, as functions of λ. On the left, eigenvalues for $-2 \leqslant j \leqslant 2$; on the right, zoom on small λ values only for $j = 0$. All these eigenvalues are stable, but least so for the $j = 0$ branch. Higher eigenvalues than those shown are even more stable.

parts of α_0^s and α_{-1}^s are identical for $\lambda > 0.04432$. This is identified as the optimal λ value, as it provides the strongest stabilization of α_0^s.

It is now examined whether the damped value $\alpha_0^s = -0.203 + 0.501i$ is still the least stable across all j branches. It is demonstrated in the Appendix that, if such a mode exists, it must stem from a branch j such that $|j| < 1 + (1 + e^{2\pi 0.203})\lambda$. For $\lambda < 2$, this criterion restricts the search interval to $-10 \leqslant j \leqslant 10$. It can be reported that α_0^s is indeed the least stable eigenvalue of the stabilized system. Consequently, $\lambda = 0.04432$ is the optimal value of the damping parameter, leading to a system where the maximum subharmonic growth rate is -0.203.

IV. STABILIZED VORTEX STREET

In this section, the TDF technique presented in Sec. III is applied to the case of vortex pairing. The configuration and the numerical code used in this article (Sec. III A) are first described in more detail. Then, in Sec. IV B, it is demonstrated that adding a time-delayed feedback makes a Navier-Stokes simulation converge towards the unstable unpaired state when initialized with the natural paired state. In Sec. IV C, it is confirmed that the simple model problem provides the optimal coefficient in the present vortex pairing case. Finally, in Sec. IV D, the technique is shown to also provide an efficient means to accelerate convergence in the case of a stable unpaired state.

A. Simulation method

Direct numerical simulations were carried out using NEK5000 [33], an incompressible spectral element code. An axisymmetric laminar jet is described in cylindrical coordinates (z,r), z being the main flow direction and r being the radial distance from the jet axis. The flow is assumed to be governed by the incompressible Navier-Stokes equations with zero azimuthal velocity, written in dimensionless form as

$$\frac{\partial \mathbf{u}}{\partial t} + (\mathbf{u} \cdot \nabla)\mathbf{u} = -\nabla p + \frac{1}{\mathrm{Re}}\Delta \mathbf{u}, \quad \nabla \cdot \mathbf{u} = 0. \tag{12}$$

The velocity $\mathbf{u}$ has axial and radial components u and v, and p denotes pressure. The jet diameter D and the inlet centerline velocity U_0 are used to render the flow problem nondimensional, defining the Reynolds number as $\mathrm{Re} = U_0 D/\nu$, with ν the kinematic viscosity. The computational domain extends over 15×5 diameters in the axial and radial directions, respectively, and it is discretized with 6600 spectral elements, each containing 64 mesh points. Mesh convergence has been validated by comparing results for different spectral polynomial orders ($n = 4, 6, 8$, and 10; 8 being the standard). Boundary conditions are specified as follows.

(1) In the inlet plane, $z = 0$, a hyperbolic-tangent velocity profile is imposed. In dimensionless form, its amplitude is modulated in time as

$$\mathbf{u}(r,t) = \frac{1}{2}\left\{1 - \tanh\left[\frac{1}{4\theta_0}\left(r - \frac{1}{4r}\right)\right]\right\}[1 + A\cos(\omega_f t)]\mathbf{e_z}, \tag{13}$$

where $A = 0.05$ is the forcing amplitude of the jet, $\theta_0 = 0.025$ is the initial dimensionless mixing layer thickness and ω_f is the axial forcing frequency. The periodic nature of the flow is imposed with the periodic inlet forcing, similar as in Jacobs and Durbin [34]. The forcing period is given by $T = 2\pi/\omega_f$, and the Strouhal number is defined as $\mathrm{St} = \omega_f D/(2\pi U_0)$.

(2) On the centerline of the jet, $r = 0$, axisymmetric boundary conditions are imposed,

$$\frac{\partial u}{\partial r} = v = \frac{\partial p}{\partial r} = 0. \tag{14}$$

(3) In the outlet plane, $z = 15$, and on the lateral boundary, $r = 5$, a stress-free outflow condition is applied:

$$-p\mathbf{n} + \frac{1}{\mathrm{Re}}(\nabla\mathbf{u})\mathbf{n} = 0. \tag{15}$$

The flow configuration is thus characterized by the Reynolds number Re, the Strouhal number St, the dimensionless mixing layer thickness θ_0, and the forcing amplitude A.

B. Computation of an unstable unpaired state

The stabilization technique described in Sec. III A is now applied, by adding a time-delayed feedback term

$$\mathbf{f}(t) = -\lambda\omega_f[\mathbf{u}(t) - \mathbf{u}(t - T)] \tag{16}$$

to the right-hand side of the Navier-Stokes equations (12). The parameter setting $\mathrm{Re} = 2000$ and $\mathrm{St} = 0.6$ has previously been found to exhibit synchronized vortex pairing in the absence of stabilization [Fig. 1(a)] and will serve as example case. The action of the feedback is measured by tracing a norm of nonharmonic (in the sense of non-T-periodic) fluctuations, defined as

$$e(t) = \frac{1}{2}\sqrt{\int_z\int_r r\,\|\mathbf{u}(t) - \mathbf{u}(t - T)\|^2\,dr\,dz}. \tag{17}$$

This quantity measures the residual during the stabilization process.

The simulation is started at $t = 0$ from the paired state represented in Fig. 1(a), and the optimal value $\lambda = 0.04432$ as identified in Sec. III B is used first. Feedback is switched on at $t = T$, because one flow period needs to be recorded before the TDF term can be evaluated. The evolution of $e(t)$ is plotted in Fig. 5; four phases in the stabilization process can be distinguished.

During the first phase, the applied forcing quenches the $2T$-periodic paired vortices. The distinct vortex structures downstream of the pairing location are thus replaced by a diffuse band of vorticity, as seen by comparing Figs. 6(a) and 6(c). The magnitude of the nonharmonic component, $\|\mathbf{u}(t) - \mathbf{u}(t - T)\|$, which is proportional to the magnitude of the instantaneous forcing, is displayed in Fig. 6(d): the forcing at this stage is active in the entire paired region, but not in the region of initial vortex roll-up. This behavior is typical for $0 < t < 5T$, when the decay of the nonharmonic component is fastest, according to Fig. 5. This stage of the stabilization process is conceptually similar to the subharmonic damping in the model problem of Sec. III B. However, the damping rate observed in the jet is smaller than predicted by the model. This may be explained by the inherent positive subharmonic growth in the jet, which the damping has to overcome, whereas no such growth was assumed in the model problem.

During the following phase, the flow domain is gradually repopulated by a street of unpaired vortices, essentially by convection, as shown in Fig. 6(e). This interpretation is consistent with the

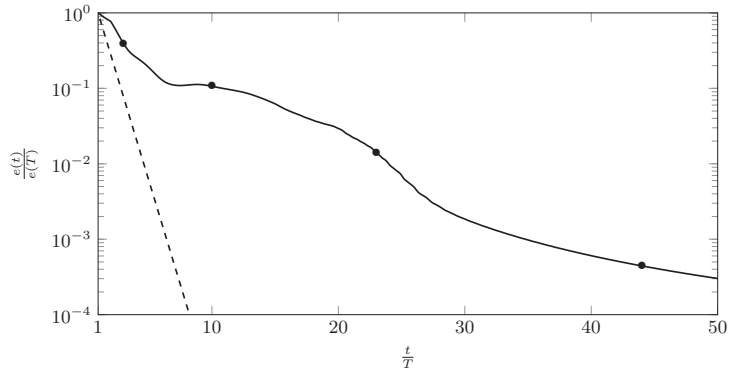

FIG. 5. Evolution of the residual norm $e(t)$ [Eq. (17)], in a jet simulation with $\mathrm{Re} = 2000$, $\mathrm{St} = 0.6$, and $\lambda = 0.04432$. Dashed line: decay rate found in the model problem. Markers indicate the instances of snapshots shown in Fig. 6.

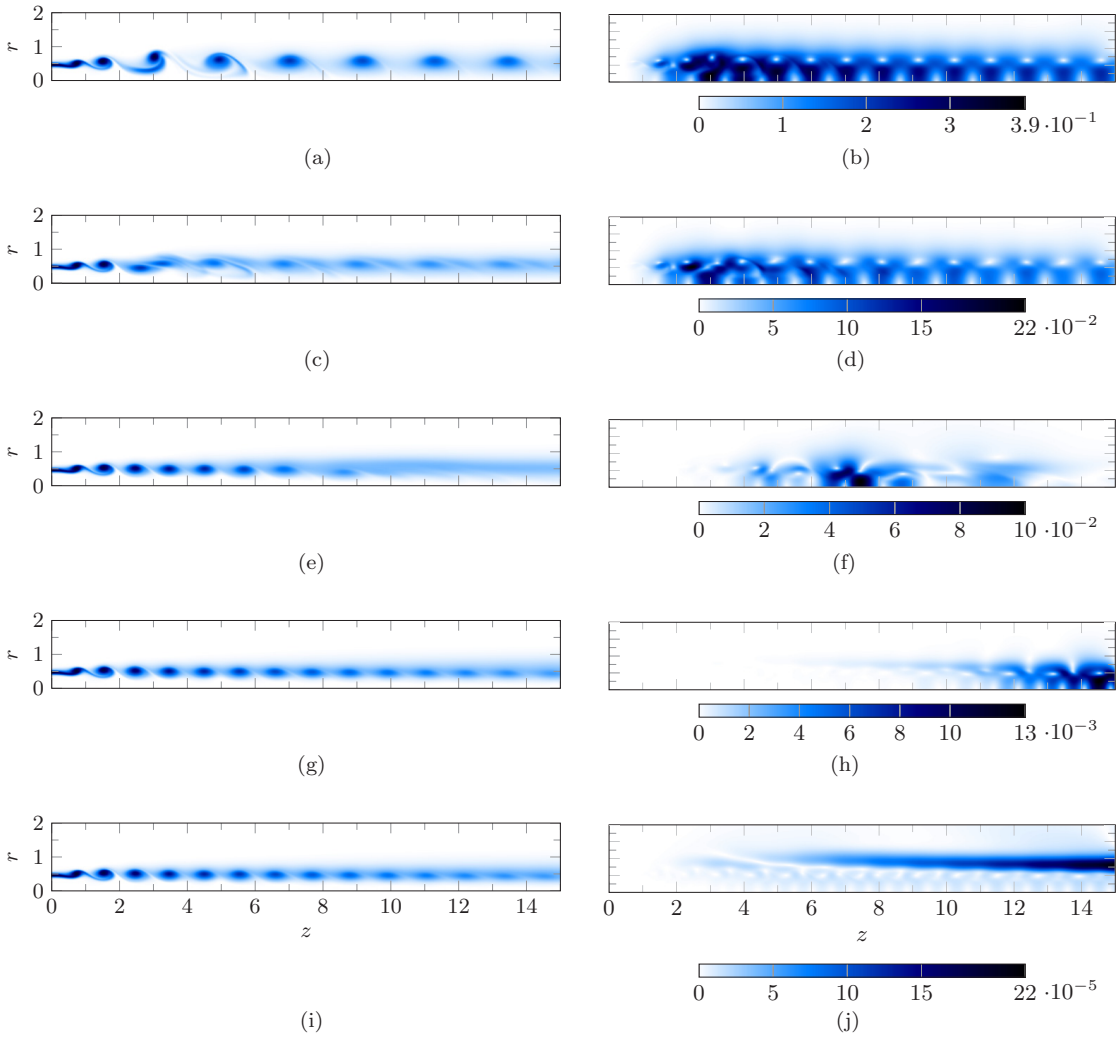

FIG. 6. Vorticity (left) and nonharmonic component magnitude $\|\mathbf{u}(t) - \mathbf{u}(t - T)\|$ (right) represented at $t = T$ (a)-(b), $3T$ (c)-(d), $10T$ (e)-(f), $23T$ (g)-(h) and $44T$ (i)-(j) for $\lambda_{\mathrm{opt}} = 0.04432$. The vorticity colorbar is in Fig. 1(b).

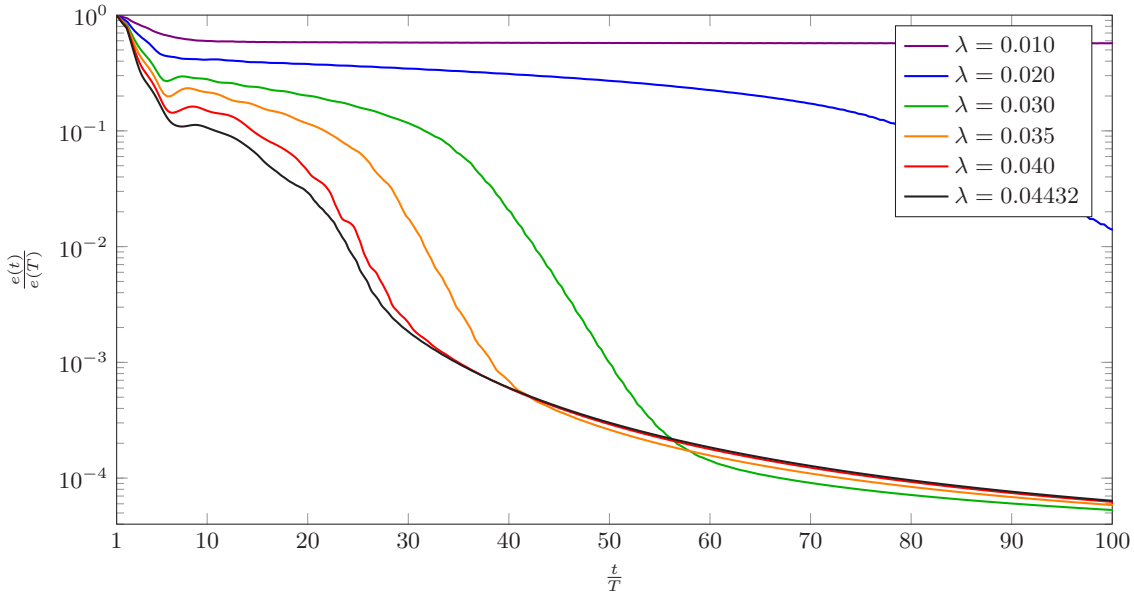

(a)

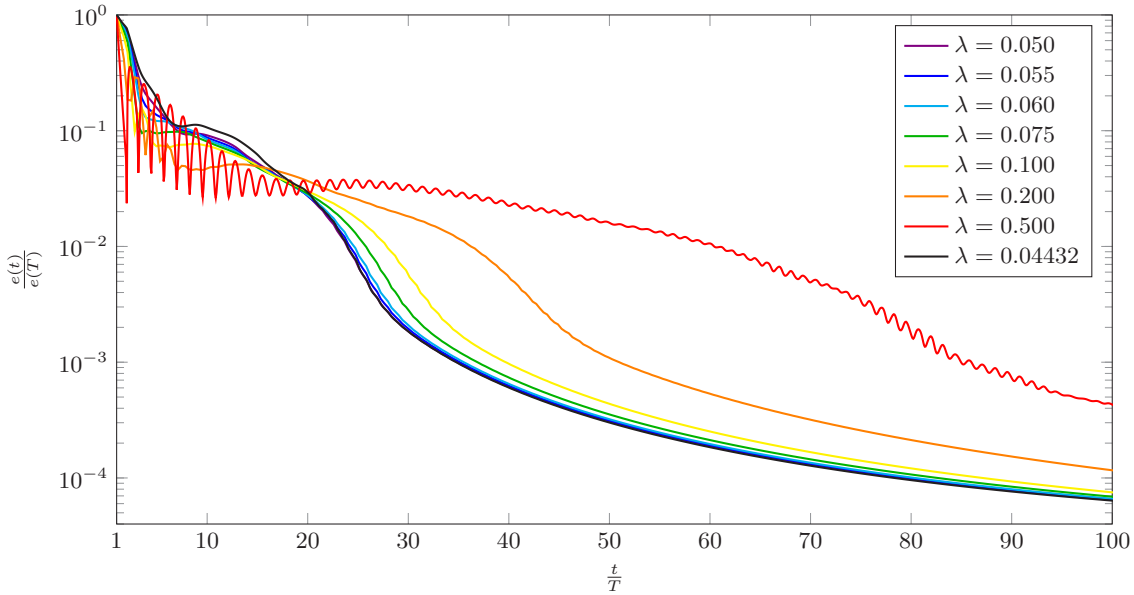

(b)

FIG. 7. Residual norm as a function of time for several values of $\lambda : \lambda \leqslant 0.0432$ (a) and $\lambda \geqslant 0.0432$ (b). Curves for $\lambda = 0.0425, 0.0475$ are omitted for clarity. At values of λ larger than 0.5, the convergence is increasingly ill-behaved, displaying huge oscillating behavior, and results are not reported.

map in Fig. 6(f), where nonharmonic fluctuations are seen to be concentrated around the trailing end of the emerging vortex array. This behavior dominates the plateau region around $t = 10T$ in Fig. 5.

The third phase begins as the unpaired vortex street reaches the downstream end of the domain, when the flow visually appears to have reached a periodic state, displayed in Fig. 6(g). The nonharmonic fluctuations at the trailing end of the vortex street leave the domain at this point, as seen in Fig. 6(h), and this leads to a second sudden drop in the residual norm $e(t)$ in Fig. 5.

In the final phase, the flow is globally synchronized, and no visible difference between subsequent periods is observed anymore. Fig. 6(i) shows the flow state at $t = 44T$. The residual norm continues to slowly decay in time as residual fluctuations are suppressed. These fluctuations are located far

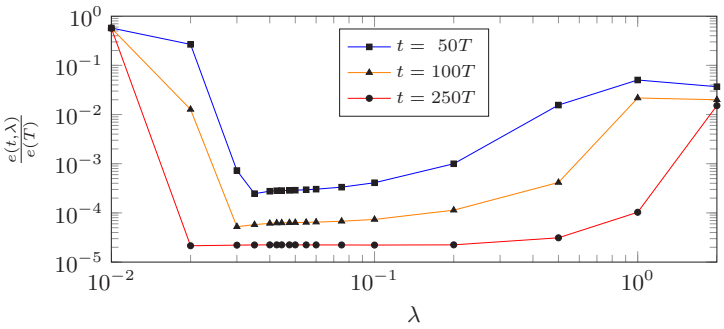

FIG. 8. Residual norm $e(t)$ at $t = 50T$, $100T$, and $250T$ as a function of λ.

from the jet inlet [see Fig. 6(j)], and they do not present any spatial structure that can be associated with vortex pairing.

C. Validation of the optimality of the feedback parameter λ

In the preceding section, λ has been prescribed as the optimal value derived in the context of a model problem. The optimality for the present flow problem is now to be assessed. The simulation from Sec. IV B is repeated, over a time horizon of $250T$, with 16 different values of λ between 0.01 and 2. The time evolution of $e(t)$ is documented in Figs. 7(a) and 7(b) for each value $0.01 \leqslant \lambda \leqslant 0.5$. Larger values give poor results and are not reported.

Comparable results are achieved with $0.03 \leqslant \lambda \leqslant 0.2$; all curves in this range display the same characteristic phases of convergence, albeit with different efficiencies over short times. The long-time residual $e(t \gg T)$ is seen in Fig. 8 to be insensitive to the choice of λ within these limits. However, an optimal λ value may be identified that induces the fastest convergence towards the final phase, i.e., the λ for which the end of the third phase defined in Sec. IV B is reached in the shortest time. Figures 7(a) and 7(b) show that the optimal value in this sense, among all values tried, is indeed $\lambda = 0.04432$, the one obtained in Sec. III B.

D. Convergence acceleration in a stable setting

In the context of steady flows, selective frequency damping is effective in stabilizing unstable settings, but it also provides accelerated convergence towards a steady state in weakly stable situations [4]. Time-delayed feedback may achieve the same for weakly stable periodic flow. The case of a jet at $\mathrm{Re} = 1300$, forced at $\mathrm{St} = 0.6$, is chosen for a demonstration. The stable periodic solution in this setting is the unpaired state presented in Fig. 1(b). This case is close to the onset of a pairing instability, as the same configuration with $\mathrm{Re} = 1400$ settles into a stable paired state. Convergence of the final periodic unpaired state at $\mathrm{Re} = 1300$ is slow as a consequence.

A converged steady laminar state without inflow forcing is chosen as initial condition, and harmonic inflow forcing (13) is started at $t = 0$. Simulations are then performed with and without time-delayed feedback; the nonharmonic component norm $e(t)$ is plotted as a function of time for both runs in Fig. 9.

Without damping, pairing sets in quickly several diameters downstream of the inlet. The paired vortex is then convected downstream, while repeated pairing takes place at almost the same location, such that the global norm of non-T-periodic components continue to grow (dashed line in Fig. 9). This growth ends at $t = 14T$, when the first paired ring reaches the outlet, as can be seen in Figs. 10(a) and 10(b). Subsequently, $e(t)$ decays as the pairing location moves slowly downstream. At the end of the simulation, at $t = 200T$, pairing still takes place near the downstream end of the domain, as shown in Figs. 10(c) and 10(d). Evacuation of the transient pairing through convection is a very slow process in this setting.

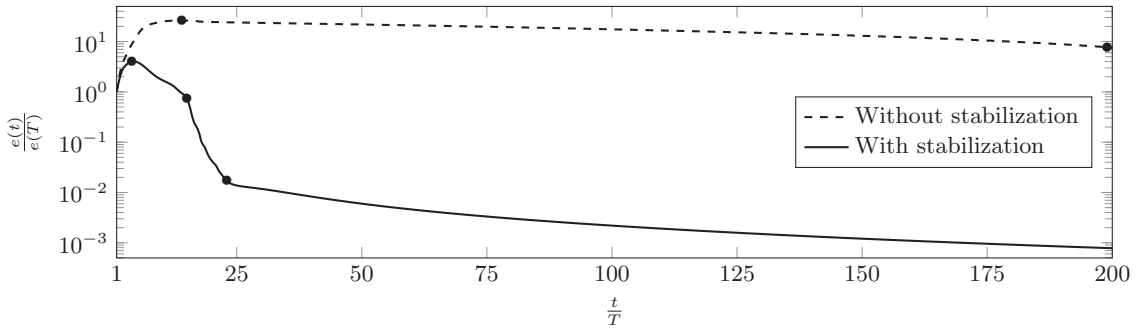

FIG. 9. Evolution of the residual norm $e(t)$ with and without stabilization applied. The different time steps defined in Sec. IV D are reported.

In the presence of time-delay feedback, pairing is never observed, and the convergence is significantly accelerated. According to Fig. 9, subharmonic fluctuations are reduced to residual levels within 20 forcing periods, which corresponds to the convection time of vortices through the domain. Snapshots of vorticity and of nonharmonic components are shown in Fig. 11 for three notable instances, as marked in Fig. 9.

E. Reducing the memory requirements through time interpolation

The TDF method described so far, although easy to implement, needs the storage of one full flow period, which can be resource-intensive, especially in the case of three-dimensional simulations. A remedy may be to store all flow variables and their time derivatives only at N equispaced instants over one period, and to approximate all intermediate time steps through interpolation.

A first interpolation technique could rely on Fourier methods, since the converged flow is T-periodic. However, since the algorithm is based on the damping of *nonperiodic* components, accurate reconstruction of these component precludes the use of Fourier series.

A spline interpolation is tried instead: each period is composed of $N_{\Delta t}$ time steps, and N equispaced time steps of the previous running period are stored in memory, i.e., one time step every $N_{\Delta t}/N$ time steps. The time derivative $\mathbf{u}_t$ of the velocity at each time step, computed with a centered-difference scheme, is also stored. Then, to reconstruct the flow at $t-T$, if $t_i \leqslant t-T \leqslant t_{i+1}$, with

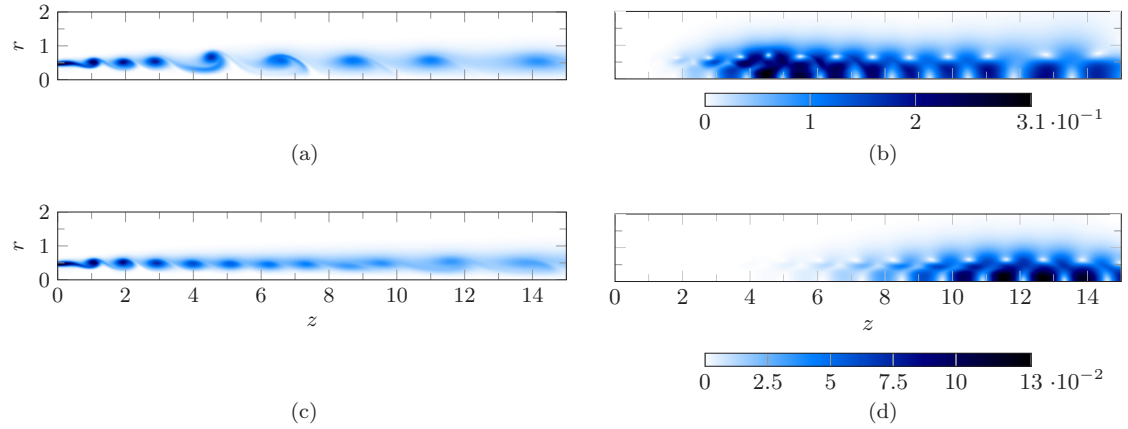

FIG. 10. Vorticity (left) and nonharmonic component magnitude $\|\mathbf{u}(t)-\mathbf{u}(t-T)\|$ (right) without time-delayed feedback applied represented at $t=14T$ (a)-(b) and $200T$ (c)-(d). The vorticity colorbar is in Fig. 1(b).

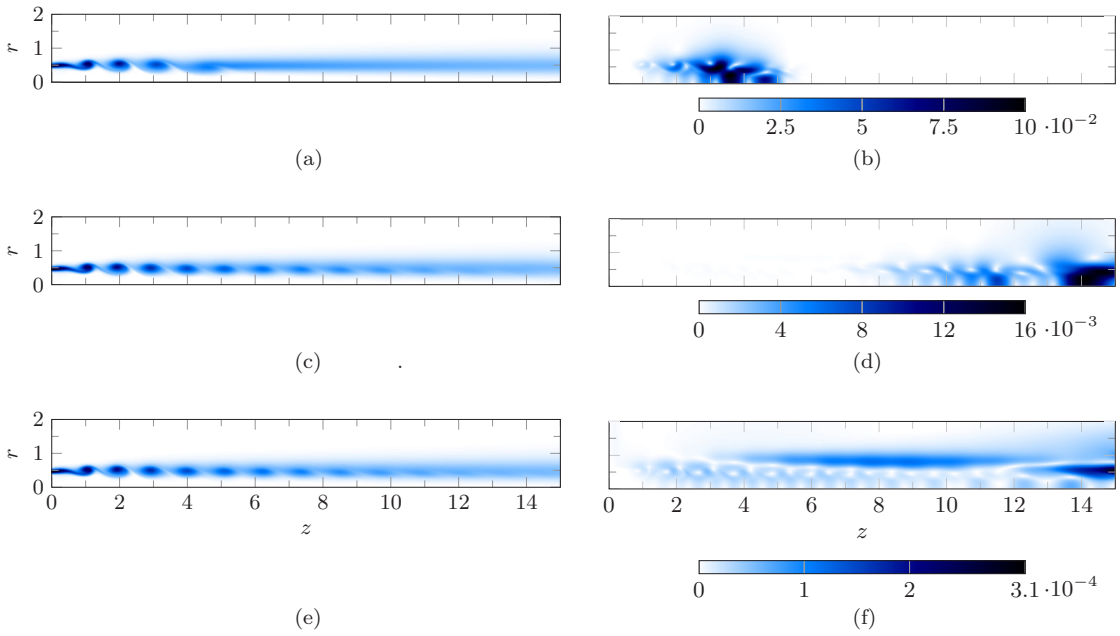

FIG. 11. Vorticity (left) and nonharmonic component magnitude $\|\mathbf{u}(t) - \mathbf{u}(t-T)\|$ (right) with time-delayed feedback applied represented at $t = 4T$ (a)-(b), $15T$ (c)-(d) and $23T$ (e)-(f). The vorticity colorbar is in Fig. 1(b).

t_i and t_{i+1} time steps where the flow is stored, the following spline interpolation formula is used:

$$\tilde{\mathbf{u}}(r,z,t-T) = (1-t')^2(1+2t')\mathbf{u}(r,z,t_i) + t'(1-t')^2\frac{T}{N}\mathbf{u}_t(r,z,t_i) + t'^2(3-2t')\mathbf{u}(r,z,t_{i+1}) + t'^2(t'-1)\frac{T}{N}\mathbf{u}_t(r,z,t_{i+1}), \tag{18}$$

with the normalized time

$$t' = \frac{t-T-t_i}{t_{i+1}-t_i}. \tag{19}$$

This interpolation technique yields interpolated values, continuous up to the first time-derivative, that match the true velocity and acceleration at every checkpoint. Therefore, the forcing used in the Navier-Stokes equations (12) is now taken as

$$\tilde{\mathbf{f}}(t) = -\lambda\omega_f[\mathbf{u}(t) - \tilde{\mathbf{u}}(t-T)]. \tag{20}$$

In traditional check-pointing techniques, such as the one used in direct-adjoint optimization schemes ([35,36]), a new simulation is run from the checkpoint to avoid errors from interpolation. This strategy cannot be applied in the present case, due to endless interdependency between periods: the time-delayed feedback at $t-T$ requires the knowledge of the flow at $t-2T$, which in turn depends on the flow state at $t-3T$, and so forth.

The reconstruction technique has been evaluated for the paired jet case at $\mathrm{Re} = 2000$ and $\mathrm{St} = 0.60$. Each period of the flow is composed of 1000 time steps, with $\Delta t = 5/3 \times 10^{-3}$. Four cases have been investigated and compared to the results obtained without interpolation: $N = 50, 20, 10,$ and 5. These cases respectively need 10, 25, 50, and 100 times less memory than the full-storage method (as memory is needed for the flow and its derivative).

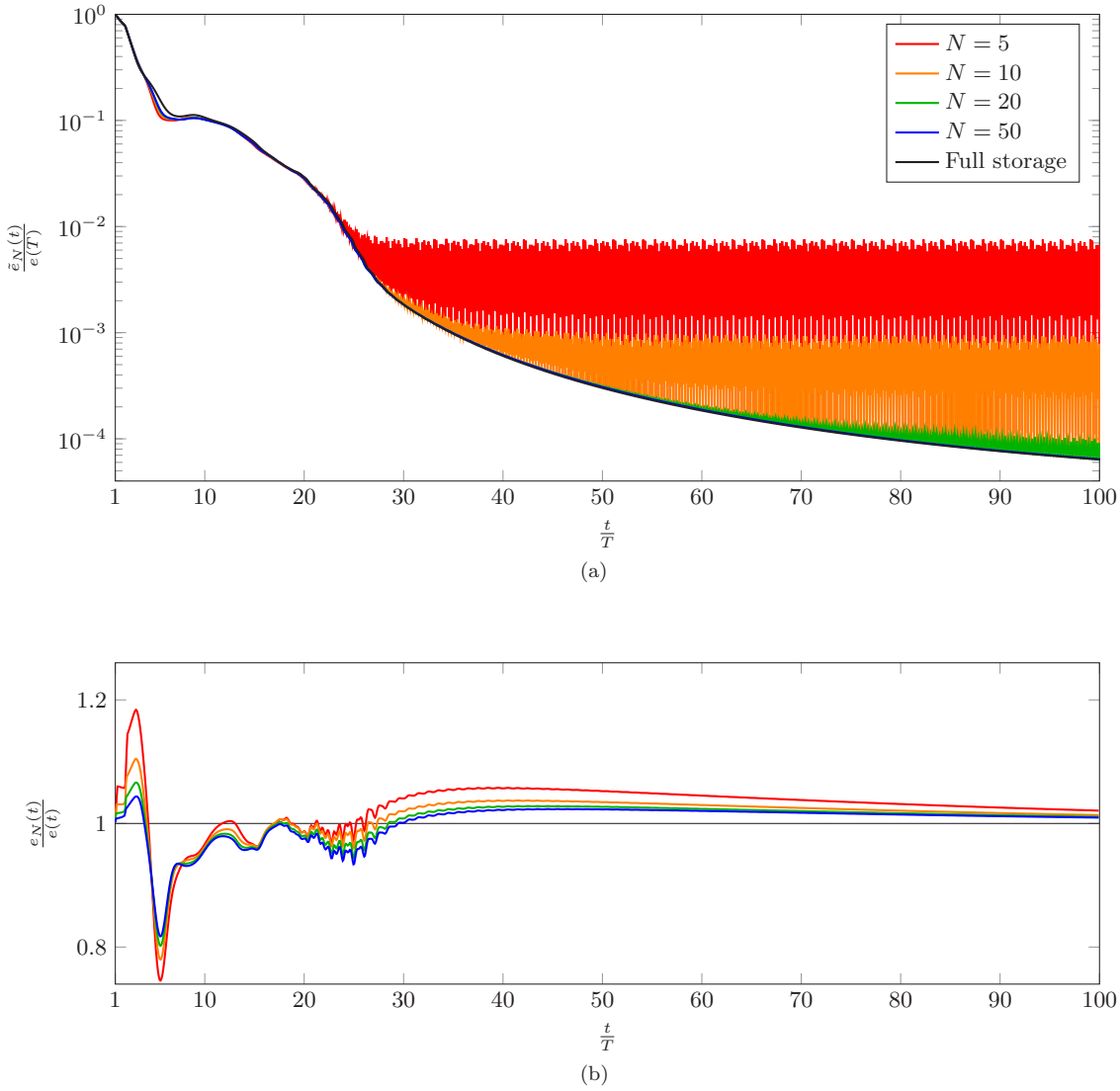

FIG. 12. Convergence analysis of the stabilization procedure with interpolation, for different storage requirements N: (a) residual norm based on the interpolated velocity $\tilde{e}_N(t)$ as a function of time for different N and comparison to full-storage residual $e(t)$ and (b) ratio between the exact residual $e_N(t)$ and the residual obtained with full storage $e(t)$ as a function of time for different N. For $N = 5$, 10 and 20, $\tilde{E}_N$ is defined as the maximum peak of $\tilde{e}_N(t)$ when the residual starts oscillating. For $N = 50$, no oscillations of $\tilde{e}_N(t)$ are observed.

In order to evaluate the convergence performance of the algorithm for various values of N, two residuals are used. The first one, denoted $\tilde{e}_N(t)$, is based on the interpolated velocity $\tilde{\mathbf{u}}$ at $t - T$:

$$\tilde{e}_N(t) = \frac{1}{2}\sqrt{\int_z \int_r r \|\mathbf{u}(t) - \tilde{\mathbf{u}}(t - T)\|^2 \, dr \, dz}. \tag{21}$$

The second one, denoted $e_N(t)$, is based on the true velocity $\mathbf{u}$ at $t - T$, as defined in Eq. (17). $\tilde{e}_N(t)$ is the only available residual when interpolation is applied in general, whereas $e_N(t)$ is the true residual, which is normally unknown. For each N, the evolution of each of these two residuals is compared to the evolution of the residual $e(t)$ obtained with the full-storage version (see Sec. IV B).

The convergence results with the interpolated residual $\tilde{e}_N(t)$ are depicted in Fig. 12(a). In every case, the residual first decreases in the same way as the uninterpolated stabilized flow. However,

TABLE I. Maximum normalized error between the interpolated and the real flow as a function of N for a fully stabilized unpaired flow at Re = 2000 and St = 0.60.

N	50	20	10	5
$\frac{\max_t \|\mathbf{u}(t)-\tilde{\mathbf{u}}(t)\|}{e(T)}$	3.6×10^{-6}	1.3×10^{-4}	1.5×10^{-3}	1.1×10^{-2}

for $N < 50$, the residual starts to oscillate at a critical residual threshold. These oscillations have a maximum peak value $\tilde{E}_N$, which depends on N, and they descend in *all* cases to the same residual level E that is found in the full-storage solution (black line). The oscillation period corresponds to the interpolation period T/N. It is found that at the precise instants where snapshots are stored, the residual $\tilde{e}_N(t)$ is of the same order as the reference residual E.

In order to understand the meaning of this residual peak $\tilde{E}_N$, the maximum error between the interpolated and the real flow field as a function of t and N has been computed for the stabilized unpaired case. This maximum error occurs at $t = (t_i + t_{i+1})/2$ and is listed in Table I. For each N, the values obtained are of the same order as $\tilde{E}_N$ from Fig. 12(a). For $N = 50$, the value 3.6×10^{-6} is one order of magnitude smaller than $\min_t \tilde{e}_{50}(t) = 6 \times 10^{-5}$, which explains why oscillations are not encountered in this case. The residual from the interpolated velocity $\tilde{e}_N(t)$ can then be understood as the sum of two components: the non-T-periodic component of the flow $e_N(t)$ and the interpolation error of the flow at $t - T$. At large times, the interpolation error component seems to dominate the interpolated residual $\tilde{e}_N(t)$. We will now prove this statement and show that interpolation does not affect the overall precision of the reconstructed flow.

For this, Fig. 12(b) displays the evolution of the ratio between the residual $e_N(t)$ computed with the exact flow field for each interpolation level N and the residual $e(t)$ from the full-storage reference case. For $t > 30T$, in the final phase of stabilization [see Fig. 12(a)], the exact residual with interpolation $e_N(t)$ is only slightly above the residual from full-storage calculations. As N increases, the interpolation improves and $e_N(t)$ approaches the reference value. It is found that the stabilized flow state obtained with checkpointing, even for $N = 5$, is about as accurate as the full-storage solution, despite large residual values $\tilde{e}(t)$ between checkpoints. When interpolation is used and only $\tilde{e}_N(t)$ is available, the convergence of the algorithm should therefore be assessed only at times t that correspond to checkpoints at $t - T$.

V. STABILIZATION OF LIMIT CYCLES UNKNOWN FREQUENCIES: THE LID DRIVEN CAVITY EXAMPLE

When the frequency of the limit cycle is not known *a priori*, unlike the jet example, some techniques have been developed in the harmonic balance technique to overcome this issue, such as the Gradient-Based Variable Time Period [10–13]. This technique is based on considering the residual as a function of not only t but also T, and to choose T as an extremum of this residual. This method, based in their case on gradient computations, can easily be transposed to our stabilization procedure:

(1) A starting guess T_g of the period T_0 of the limit cycle is required.

(2) TDF is then applied with this T_g. Both the term $\mathbf{u}(t - T_g)$ and the dimensional λ depend on T_g; see Eq. (16).

(3) At $t = t_1$, when initial transients are stabilized, i.e., when $e(t_1, T_g)$ is small enough (for instance, $e(t_1, T_g) < 0.01\|\mathbf{u}(t_1)\|$), a new value for T_g is identified as the minimum

$$T_g = \underset{T' \in [0.8T_g; 1.2T_g]}{\arg\min} \; e(t_1, T'), \tag{22}$$

with the residual $e(t, T)$ as defined in Eq. (17). This global search, almost inexpensive since $\mathbf{u}(t)$ and $\mathbf{u}(t - T')$ are already stored, is restricted to $[0.8T_g; 1.2T_g]$ in order to avoid abrupt variations of T_g.

(4) The stabilization procedure is applied again with the new T_g over a time horizon equal to T_g.

TABLE II. Review of the critical Reynolds number and frequency of the linear unstable mode at Re_c for the cubic lid-driven cavity.

	Feldman and Gelfgat ([25])	Kuhlmann and Albensoeder ([26])	Loiseau *et al.* ([27])
Re_c	1914.0	1919.5	1914.0
ω_c	0.575	0.586	0.585

(5) The global search is regularly carried out at $t_{i+1} = t_i + T_g$.

We prefer performing regular global searches for T_g instead of calculating $\partial e/\partial T$, because the full storage of the past period allows us to perform a cheap and quick optimization over a full range of T_g values ($[0.8T_g; 1.2T_g]$) and because of the superior robustness provided by global methods compared to local methods.

As the limit-cycle frequency in the forced jet is prescribed by the applied forcing, it would be contrived to treat it as an unknown. The flow in a three-dimensional cubic lid-driven cavity is chosen instead for a demonstration. It has been shown that the steady solution of such a flow, above a critical Reynolds Re_c, is no longer stable [25–27], and that it bifurcates towards a limit cycle in a slightly subcritical fashion [26]. The bifurcated state is unsteady and, close to Re_c, it evolves at the frequency ω_c predicted by linear stability theory. Critical Reynolds number and frequency are listed in Table II. However, as shown in Refs. [26,27], this limit cycle is not stable since it experiences *intermittent chaos*: short bursts occur that destabilize the cycle before disappearing. Therefore, without applying any stabilization technique, it cannot be expected that this cycle will converge naturally.

These simulations have been carried out again with NEK5000, on the same mesh as used in Ref. [27]. The driving velocity and the cube side length are used to nondimensionalize the problem. A Reynolds number of 1930, above the critical limit, is chosen. At this Reynolds number, the limit-cycle frequency is kept unchanged at $\omega_0 = 0.585$ ([27]). The time step was fixed to $\Delta t = 2.0 \times 10^{-3}$. In this study, all time steps have been stored (the method described in Sec. IV E was not applied). At $t = 0$, the cavity is at rest: $\mathbf{u}(t = 0) = \mathbf{0}$.

To understand the performance of the algorithm, several cases have been investigated:

(1) With no forcing.

(2) With forcing applied at the fixed frequency of the limit cycle, $\omega_0 = 0.585$.

(3) With variable-frequency forcing applied, starting from an initial guess. Five estimated values have been tried: $\omega_g = 0.50, 0.55, 0.60, 0.65$, and 0.585. The frequency interval covered is $\omega_0 \pm 15\%$.

The results are reported in Fig. 13. First, it can be stated that the method works for every ω_g studied: the convergence is improved by at least two orders of magnitude compared to the time stepping without stabilization. Moreover, the convergence of the flow and ω is achieved whatever ω_g studied, which shows the robustness of the technique. Convergence is achieved in about $25T_0$ whatever ω_g, which is the same physical time needed for the case with fixed ω_0 to settle. Therefore, the frequency search does not augment significantly the computational cost. However, contrary to the unpaired jet, the decrease of the residual is not monotonic, which can be linked to the fact that the cavity flow is not receptive to $\omega_0/2$ perturbations but to other frequencies [27].

VI. CONCLUSION

A time-delayed feedback method, introduced by Pyragas [22] in the context of ODEs with few degrees of freedom, has been applied to a flow problem for the purpose of computing unstable time-periodic states. It has been demonstrated that spontaneous vortex pairing in a harmonically forced jet is efficiently suppressed by this method, such that an unpaired vortex street, synchronized at the frequency of the prescribed inflow forcing, is recovered. In this final converged flow state, the stabilizing feedback term vanishes, and the recovered state is therefore a true solution of the flow equations, uncompromised by artificial damping. The one free numerical parameter for this procedure has been chosen based on a simple model problem, where the optimal value could be

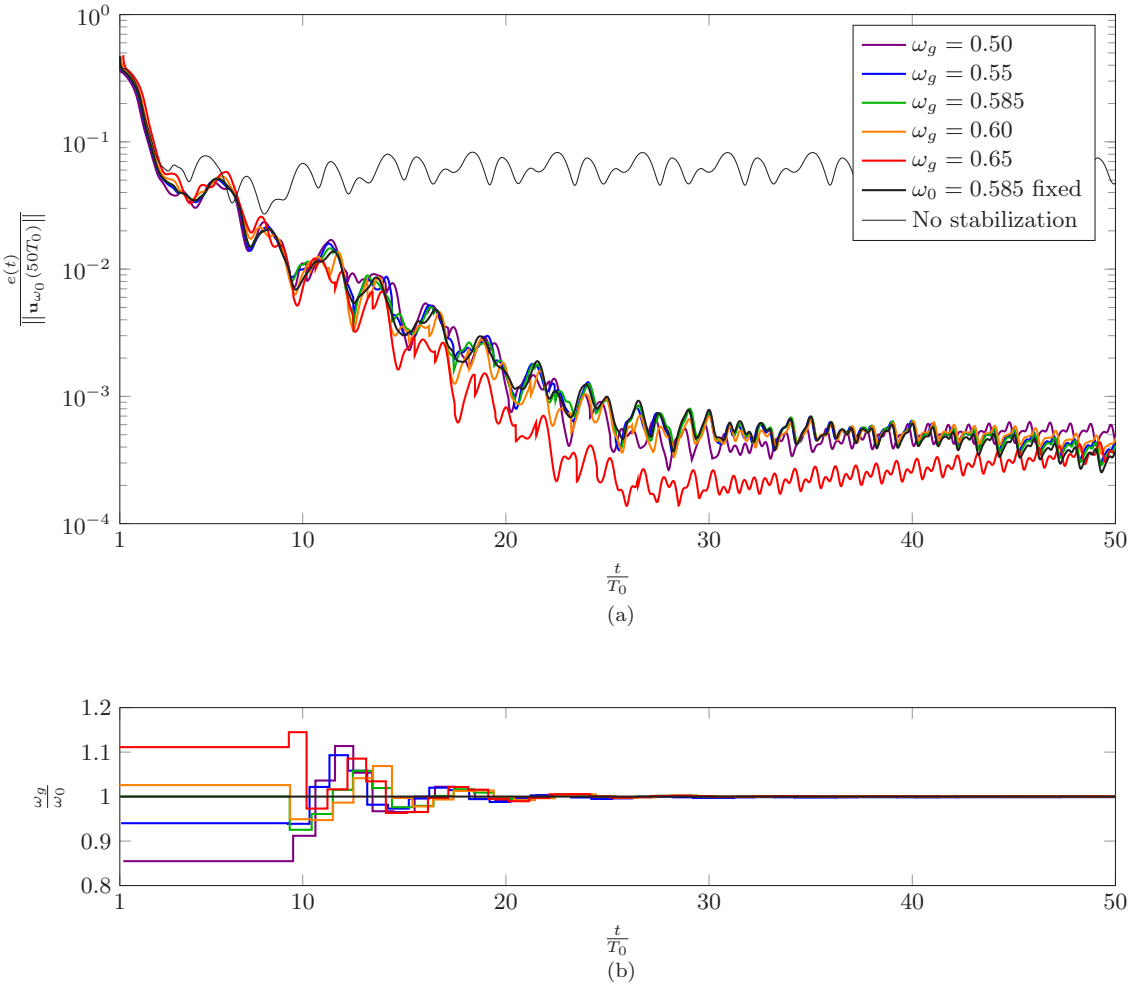

FIG. 13. Convergence analysis of the lid-driven cavity: (a) norm of the residual component as a function of time for the different cases studied normalized with the total velocity norm at $t = 50T_0$ for the fixed ω_0 case and (b) evolution of the global frequency guess for each case as a function of time.

determined analytically. It has then been found that the same value provides optimal convergence also in the jet calculations.

The same technique has been shown to be useful also in weakly stable situations, where uncontrolled time stepping converges towards a T-periodic state, but only slowly so. Artificial damping through time-delay feedback greatly increases the rate of convergence in this case.

The described method is very easy to implement with a given flow solver, as it requires only the addition of a simple source term, as well as the storage of one full cycle of the flow. The latter aspect may be memory resource-intensive. An interpolation method has been proposed in order to overcome this limitation. In the jet example, the storage requirement could thus be reduced by a factor 100, without significant loss of accuracy, and at negligible additional cost.

The suppression of vortex pairing in the present example enables a stability analysis of the recovered unpaired state, and the results of such analysis will be reported in a forthcoming study.

The time-delayed feedback method has finally been adapted to stabilize limit cycles in unforced flows, where the frequency is not known *a priori*. This was demonstrated for a lid-driven cubic cavity case with intermittent chaos. The procedure has been found to be very effective, enabling limit-cycle stabilization at the correct frequency. The iteration identification of the limit-cycle frequency, as

an additional unknown, did not lead to prolonged simulations in the cavity example. As in the harmonically forced jet, the recovered state is a true solution of the flow equations.

ACKNOWLEDGMENTS

We gratefully acknowledge valuable discussions with Olivier Marquet. We thank Holly Johnson for her help with NEK5000 and Jean-Christophe Loiseau for suggesting the lid-driven cubic cavity as a test case and for providing his NEK5000 mesh. This work was granted access to the HPC resources of TGCC under the allocation Grant No. 2016-2a6451 made by GENCI, and it benefited from financial support of the DGA under Grant No. 2015.60.0004.00.470.75.01.

APPENDIX: STABILITY OF SOLUTIONS TO EQS. (9a) AND (9c)

Consider the equation

$$\alpha = ki - \lambda(1 - e^{-2\pi\alpha}), \tag{A1}$$

with both k and λ having positive real values. Solutions [32] are found as

$$\alpha_j = ki - \lambda + \frac{1}{2\pi} W_j(2\pi\lambda e^{2\pi(\lambda - ik)}), \quad j \in \mathbb{Z}. \tag{A2}$$

The jth solution involves the jth branch W_j of the Lambert function. Assuming that there exists a branch W_j such that $\mathrm{Re}(\alpha_j) > \beta$ for a given λ, the triangular inequality, applied to Eq. (A1), guarantees

$$|\alpha_j| \leqslant |ki| + \lambda|1 - e^{-2\pi\alpha_j}| \leqslant k + (1 + e^{-2\pi\beta})\lambda. \tag{A3}$$

The imaginary part of (A2) is evaluated as

$$\mathrm{Im}(\alpha_j) = k + \frac{1}{2\pi}\mathrm{Im}[W_j(2\pi\lambda e^{2\pi(\lambda - ik)})]. \tag{A4}$$

Positive and negative integer values of j need to be considered separately.

1. Case $j > 0$

In this case, from [32], as $\mathrm{Im}[W_j(z)] > 0$ for all complex number z and $k > 0$:

$$|\mathrm{Im}(\alpha_j)| = k + \frac{1}{2\pi}\mathrm{Im}[W_j(2\pi\lambda e^{2\pi(\lambda - ik)})], \tag{A5}$$

so that, as $|\alpha_j| \geqslant |\mathrm{Im}(\alpha_j)|$:

$$|\alpha_j| \geqslant k + \frac{1}{2\pi}\mathrm{Im}[W_j(2\pi\lambda e^{2\pi(\lambda - ik)})]. \tag{A6}$$

Therefore, combining (A3) and (A6):

$$\mathrm{Im}[W_j(2\pi\lambda e^{2\pi(\lambda - ik)})] \leqslant 2\pi(1 + e^{-2\pi\beta})\lambda. \tag{A7}$$

From the properties of the Lambert function [32], and because $j > 0$, $\mathrm{Im}[W_j(z)] > 2\pi(j - 1)$ for all complex z. Therefore a necessary condition for $\mathrm{Re}(\alpha_j) > \beta$ with $j > 0$ is

$$|j| < 1 + (1 + e^{-2\pi\beta})\lambda. \tag{A8}$$

2. Case $j < 0$

In this case, from [32], as $\mathrm{Im}[W_j(z)] < 0$ for all complex number z and $k > 0$:

$$|\mathrm{Im}(\alpha_j)| = k - \frac{1}{2\pi}\mathrm{Im}[W_j(2\pi\lambda e^{2\pi(\lambda - ik)})], \tag{A9}$$

so that, as $|\alpha_j| \geqslant |\mathrm{Im}(\alpha_j)|$,

$$|\alpha_j| \geqslant k - \frac{1}{2\pi}\mathrm{Im}[W_j(2\pi\lambda e^{2\pi(\lambda - ik)})]. \tag{A10}$$

Therefore, combining (A3) and (A10):

$$-\mathrm{Im}[W_j(2\pi\lambda e^{2\pi(\lambda - ik)})] \leqslant 2\pi(1 + e^{-2\pi\beta})\lambda. \tag{A11}$$

From the properties of the Lambert function [32], and because $j < 0$, $\mathrm{Im}[W_j(z)] < 2\pi(j+1)$ for all complex z. Therefore a necessary condition for $\mathrm{Re}(\alpha_j) > \beta$ with $j < 0$ is

$$|j| < 1 + (1 + e^{-2\pi\beta})\lambda. \tag{A12}$$

3. Conclusion

The two cases $j \lesseqgtr 0$ leads to the same conclusion, which is also valid for $j = 0$. Therefore, for a given λ, any mode α_j such that $\mathrm{Re}(\alpha_j) > \beta$ must derive from branches W_j with

$$|j| < 1 + (1 + e^{-2\pi\beta})\lambda. \tag{A13}$$

This criterion is strict and holds for any value of k.

In particular, for a given λ, the unstable modes, if they exist, must derive from branches W_j with $|j| < 1 + 2\lambda$.

[1] D. Sipp and A. Lebedev, Global stability of base and mean flows: A general approach and its applications to cylinder and open cavity flows, J. Fluid Mech. **593**, 333 (2007).

[2] G. M. Shroff and H. B. Keller, Stabilization of unstable procedures: The recursive projection method, SIAM J. Numer. Anal. **30**, 1099 (1993).

[3] M. S. Campobasso and M. B. Giles, Stabilization of a linear flow solver for turbomachinery aeroelasticity using recursive projection method, AIAA J. **42**, 1765 (2004).

[4] E. Åkervik, L. Brandt, D. S. Henningson, J. Hœpffner, O. Marxen, and P. Schlatter, Steady solutions of the Navier-Stokes equations by selective frequency damping, Phys. Fluids **18**, 068102 (2006).

[5] R. D. Henderson and D. Barkley, Secondary instability in the wake of a circular cylinder, Phys. Fluids **8**, 1683 (1996).

[6] S. J. Sherwin and H. M. Blackburn, Three-dimensional instabilities and transition of steady and pulsatile axisymmetric stenotic flows, J. Fluid Mech. **533**, 297 (2005).

[7] Fr. Sicot, G. Dufour, and N. Gourdain, A time-domain harmonic balance method for rotor/stator interactions, J. Turbomachinery **134**, 011001 (2012).

[8] K. C. Hall, J. P. Thomas, and W. S. Clark, Computation of unsteady nonlinear flows in cascades using a harmonic balance technique, AIAA J. **40**, 879 (2002).

[9] J. P. Thomas, E. H. Dowell, and K. C. Hall, Nonlinear inviscid aerodynamic effects on transonic divergence, flutter, and limit-cycle oscillations, AIAA J. **40**, 638 (2002).

[10] M. McMullen, A. Jameson, and J. J. Alonso, Application of a non-linear frequency domain solver to the Euler and Navier–Stokes equations, in *40th AIAA Aerospace Sciences Meeting & Exhibit* (AIAA, Reston, VA, 2002), AIAA paper 2002-0120.

[11] M. A. Spiker, J. P. Thomas, K. C. Hall, R. E. Kielb, and E. H. Dowell, Modeling cylinder flow vortex shedding with enforced motion using a harmonic balance approach, in *47th AIAA/ASME/ASCE/AHS/ASC Structures, Structural Dynamics, and Materials Conference* (AIAA, Reston, VA, 2006), AIAA paper 2006-1965.

[12] A. K. Gopinath and A. Jameson, Application of the time spectral method to periodic unsteady vortex shedding, in *44th AIAA Aerospace Sciences Meeting and Exhibit* (AIAA, Reston, VA, 2006), AIAA paper 2006-449.

[13] M. McMullen, A. Jameson, and J. Alonso, Demonstration of nonlinear frequency domain methods, AIAA J. **44**, 1428 (2006).
[14] K. Ekici and K. C. Hall, Nonlinear frequency-domain analysis of unsteady flows in turbomachinery with multiple excitation frequencies, AIAA J. **46**, 1912 (2008).
[15] S. Nadarajah and A. Jameson, Optimum shape design for unsteady three-dimensional viscous flows using a nonlinear frequency-domain method, J. Aircraft **44**, 1513 (2007).
[16] K. B. M. Q. Zaman and A. K. M. F. Hussain, Vortex pairing in a circular jet under controlled excitation. Part 1. General jet response, J. Fluid Mech. **101**, 449 (1980).
[17] B. Bourget, T. Dauxois, S. Joubaud, and P. Odier, Experimental study of parametric subharmonic instability for internal plane waves, J. Fluid Mech. **723**, 1 (2013).
[18] D. Roose, K. Lust, A. Champneys, and A. Spence, A Newton-Picard shooting method for computing periodic solutions of large-scale dynamical systems, Chaos Solitions Fractals **5**, 1913 (1995).
[19] K. Lust and D. Roose, An adaptive Newton–Picard algorithm with subspace iteration for computing periodic solutions, SIAM J. Sci. Comput. **19**, 1188 (1998).
[20] J. Sánchez, M. Net, B. Garcıa-Archilla, and C. Simó, Newton-Krylov continuation of periodic orbits for Navier-Stokes flows, J. Comput. Phys. **201**, 13 (2004).
[21] J. Sánchez and M. Net, On the multiple shooting continuation of periodic orbits by Newton-Krylov methods, Int. J. Bifurcation Chaos **20**, 43 (2010).
[22] K. Pyragas, Continuous control of chaos by self-controlling feedback, Phys. Lett. A **170**, 421 (1992).
[23] D. Jallas, O. Marquet, and D. Fabre, Linear and nonlinear perturbation analysis of the symmetry breaking in time-periodic propulsive wakes, Phys. Rev. E **95**, 063111 (2017).
[24] P. N. Shankar and M. D. Deshpande, Fluid mechanics in the driven cavity, Annu. Rev. Fluid Mech. **32**, 93 (2000).
[25] Y. Feldman and A. Yu. Gelfgat, Oscillatory instability of a three-dimensional lid-driven flow in a cube, Phys. Fluids **22**, 093602 (2010).
[26] H. C. Kuhlmann and S. Albensoeder, Stability of the steady three-dimensional lid-driven flow in a cube and the supercritical flow dynamics, Phys. Fluids **26**, 024104 (2014).
[27] J.-C. Loiseau, J.-C. Robinet, and E. Leriche, Intermittency and transition to chaos in the cubical lid-driven cavity flow, Fluid Dyn. Res. **48**, 061421 (2016).
[28] C.-M. Ho and P. Huerre, Perturbed free shear layers, Annu. Rev. Fluid Mech. **16**, 365 (1984).
[29] K. J. Åström and R. M. Murray, *Feedback Systems: An Introduction for Scientists and Engineers* (Princeton University Press, Princeton, 2008).
[30] J. C. Doyle, B. A. Francis, and A. R. Tannenbaum, *Feedback Control Theory* (Macmillan, New York, 1992).
[31] W. Michiels and S.-I. Niculescu, *Stability and Stabilization of Time-Delay Systems, Advances in Design and Control* (Society for Industrial and Applied Mathematics, Philadelphia, 2007).
[32] R. M. Corless, G. H. Gonnet, D. E. G. Hare, D. J. Jeffrey, and D. E. Knuth, On the Lambert W function, Adv. Comput. Math. **5**, 329 (1996).
[33] NEK5000 Version 1.0 rc1/SVN r1094, Argonne National Laboratory, Illinois, available https://nek5000.mcs.anl.gov.
[34] R. G. Jacobs and P. A. Durbin, Simulations of bypass transition, J. Fluid Mech. **428**, 185 (2001).
[35] P. J Schmid, Nonmodal stability theory, Annu. Rev. Fluid Mech. **39**, 129 (2007).
[36] M. Hinze, A. Walther, and J. Sternberg, An optimal memory-reduced procedure for calculating adjoints of the instationary Navier-Stokes equations, Optimal Control Appl. Methods **27**, 19 (2006).

J. Fluid Mech. (2018), *vol.* 835, *pp.* 654–673.
doi:10.1017/jfm.2017.764

Global stability of buoyant jets and plumes

R. V. K. Chakravarthy[1], L. Lesshafft[1,†] and P. Huerre[1]

[1]Laboratoire d'Hydrodynamique, CNRS/École Polytechnique 91128 Palaiseau, France

(Received 8 April 2017; revised 13 September 2017; accepted 18 October 2017)

The linear global stability of laminar buoyant jets and plumes is investigated under the low-Mach-number approximation. For Richardson numbers in the range $10^{-4} \leqslant Ri \leqslant 10^{3}$ and density ratios $S = \rho_\infty/\rho_{jet}$ between 1.05 and 7, only axisymmetric perturbations are found to exhibit global instability, consistent with experimental observations in helium jets. By varying the Richardson number over seven decades, the effects of buoyancy on the base flow and on the instability dynamics are characterised, and distinct behaviour is observed in the low-Ri (jet) and in the high-Ri (plume) regimes. A sensitivity analysis indicates that different physical mechanisms are responsible for the global instability dynamics in both regimes. In buoyant jets at low Richardson number, the baroclinic torque enhances the basic shear instability, whereas buoyancy provides the dominant instability mechanism in plumes at high Richardson number. The onset of axisymmetric global instability in both regimes is consistent with the presence of absolute instability. While absolute instability also occurs for helical perturbations, it appears to be too weak or too localised to give rise to a global instability.

Key words: buoyancy-driven instability, jets, plumes/thermals

1. Introduction

Vertical injection of light fluid into a denser ambient creates a flow that either bears the characteristics of a jet, if the injected momentum is dominant over the buoyant forces, or those of a plume, if the momentum that is generated by buoyancy is dominant over the momentum that is imparted at the orifice.

The instability behaviour of jets is known to be strongly affected by density variations, even if buoyancy is not taken into account. Monkewitz & Sohn (1988) found that jets at a jet-to-ambient density ratio below 0.72 in zero gravity display absolute instability, which leads to the self-sustained formation of ring vortices at a well-defined frequency. This phenomenon has been observed experimentally (Sreenivasan, Raghu & Kyle 1989; Monkewitz *et al.* 1990; Boujemaa, Amielh & Chauve 2004; Hallberg & Strykowski 2006) and numerically (Lesshafft *et al.* 2006; Nichols, Schmid & Riley 2007). Lesshafft & Huerre (2007) established that the absolute instability arises from non-buoyant baroclinic effects. Mollendorf & Gebhart (1973) included the action of buoyancy in the form of weak forcing terms in a local instability analysis. Recently, Coenen *et al.* (2017) performed a global instability

† Email address for correspondence: lesshafft@ladhyx.polytechnique.fr

analysis for light jets in the zero-Mach-number limit, achieving good agreement with the helium jet experiments of Hallberg & Strykowski (2006). A small Richardson number in these experiments characterises buoyant effects as being small, and the global analysis confirms that their impact on the instability behaviour is negligible in this regime.

The instability of plumes, at high Richardson numbers, has received far less attention from a theoretical perspective. Wakitani (1980) and Riley & Tveitereid (1984) investigated the local instability characteristics, both temporal and spatial, of self-similar plumes within the limits of the Boussinesq approximation. Under the same assumption, Chakravarthy, Lesshafft & Huerre (2015) considered the convective/absolute nature of local instability in plumes, both in the self-similar regime far removed from the buoyancy source, and in the near-source region for one particular configuration. It was established that helical perturbations of azimuthal wavenumber $m = 1$ undergo a transition to absolute instability, due to a saddle point in the dispersion relation that is conditioned on the presence of buoyancy. However, the associated growth rates seem to be small, and their relevance for global and non-Boussinesq dynamics remains to be proved. The axisymmetric mode was found to be at most convectively unstable.

The instability of internal plumes in a confined domain appears to be a separate subject. In direct numerical simulations performed in the Boussinesq limit, Lopez & Marques (2013) document a sequence of global state bifurcations in such closed flows, occurring at successive critical Rayleigh numbers. A linear global instability analysis of the same configuration (Lesshafft 2015) suggests that at least the first of these bifurcations arises due to pressure feedback between the top and bottom solid walls.

Numerous experiments have been performed on plumes with large density differences, where the Boussinesq approximation is not justified. Subbarao & Cantwell (1992) conducted helium-air experiments, and they reported periodic axisymmetric puffing at Reynolds and Richardson numbers, Re and Ri, above critical values. Similar observations were made by Cetegen & Kasper (1996) for a larger range of Ri. A power law was obtained in the latter study that relates the puffing Strouhal number to Re and Ri. These experimental findings were corroborated by numerical simulations (Jiang & Luo 2000; Satti & Agrawal 2006) and in additional recent experiments by Bharadwaj & Das (2017). Through systematic variation of the gravity parameter, Satti & Agrawal (2006) demonstrated that the onset of self-sustained oscillations in their setting is contingent on the presence of gravity. The large majority of experiments and simulations suggest a dominant role of axisymmetric instability structures, contrary to the conclusions drawn from local instability analysis of self-similar Boussinesq plumes by Chakravarthy *et al.* (2015).

The present investigation addresses the linear instability of buoyant jets and plumes in a global and non-Boussinesq framework. The low-Mach-number approximation of McMurtry *et al.* (1986) is used in a form where density variations arise from heating of a single-species fluid. This formulation allows one to examine the stability of buoyant jets and plumes on a continuous scale provided by the Richardson number, while the density ratio as an independent parameter characterises the departure from the Boussinesq condition. Special attention will be given to the physical origin of flow instability, by means of sensitivity analysis.

A similar approach has been pursued by Bharadwaj & Das (2017) in their analysis of helium plumes. That study demonstrated close agreement between the occurrence of self-excited puffing in experiments and the onset of global linear instability. Furthermore, the linear analysis was shown to accurately predict the puffing frequency, even far from the instability threshold.

The paper is organised in the following manner. Section 2 introduces the governing equations and the numerical procedures employed for the computation of base flows and their instability characteristics in global and local frameworks. Global instability results are presented in § 3, followed by a discussion of the relevant physical mechanisms in § 4. The global results are complemented by a local absolute/convective analysis in § 5, which provides a link with the study by Chakravarthy *et al.* (2015) of local instability in Boussinesq settings. Conclusions are offered in § 6.

2. Problem formulation

2.1. *Governing equations*

A calorically perfect fluid is injected into an unstratified quiescent ambient of the same fluid at lower temperature, from a circular orifice in an adiabatic wall. In order to model a flow with strong density variations but negligible compressibility, a low-Mach-number approximation of the compressible Navier–Stokes equation is used. This approximation, which retains all the effects of variable density in the convective terms, but discards the compressible dependency of density on pressure, was introduced by McMurtry *et al.* (1986) for a study of non-buoyant jets in the limit of zero Mach number. It was then extended to include a buoyancy term by Nichols *et al.* (2007) and Chandler (2010), and their formulation is used in the present investigation. The dimensional governing equations in this approximation are given by

$$\frac{\partial \tilde{\rho}}{\partial t} + \operatorname{div}(\tilde{\rho}\tilde{\boldsymbol{u}}) = 0, \tag{2.1a}$$

$$\tilde{\rho}\frac{\mathrm{D}\tilde{\boldsymbol{u}}}{\mathrm{D}t} = -\operatorname{grad}\tilde{p} + \mu\left[\Delta\tilde{\boldsymbol{u}} + \frac{1}{3}\operatorname{grad}(\operatorname{div}\tilde{\boldsymbol{u}})\right] + g(\tilde{\rho}_\infty - \tilde{\rho})\boldsymbol{e}_z, \tag{2.1b}$$

$$\tilde{\rho}C_p\frac{\mathrm{D}\tilde{T}}{\mathrm{D}t} = \alpha\Delta\tilde{T}, \tag{2.1c}$$

$$\tilde{\rho}\mathscr{R}\tilde{T} = p_0, \tag{2.1d}$$

where $\tilde{\rho}$, $\tilde{\boldsymbol{u}}$, $\tilde{p}$, $\tilde{T}$ denote the dimensional density, velocity, pressure and temperature, $\tilde{\rho}_\infty$ is the ambient density, g is the acceleration due to gravity, α is the thermal conductivity, C_p is the specific heat, μ is the dynamic viscosity, and $\mathscr{R}$ is the specific gas constant. Note that the pressure in this formulation is split into a thermodynamic component p_0, which is constant throughout the flow, and a fluctuating hydrodynamic component $\tilde{p}$. While the continuity and momentum equations (2.1*a*) and (2.1*b*) are of the same form as in the fully compressible case, the energy equation (2.1*c*) simplifies to a simple advection–diffusion equation for temperature.

In dimensionless form, scaled with the nozzle radius R, the inlet centreline velocity $\tilde{u}_j$, the temperature difference $\tilde{T}_j - \tilde{T}_\infty$ between inflowing and ambient fluid, and the ambient density $\tilde{\rho}_\infty$, equations (2.1) become

$$\frac{\partial \rho}{\partial t} + \operatorname{div}(\rho\boldsymbol{u}) = 0, \tag{2.2a}$$

$$\rho\frac{\mathrm{D}\boldsymbol{u}}{\mathrm{D}t} = -\operatorname{grad}p + \frac{1}{ReS}\left[\Delta\boldsymbol{u} + \frac{1}{3}\operatorname{grad}(\operatorname{div}\boldsymbol{u})\right] + \frac{Ri}{S-1}(1-\rho)\boldsymbol{e}_z, \tag{2.2b}$$

$$\rho\frac{\mathrm{D}T}{\mathrm{D}t} = \frac{1}{PrReS}\Delta T. \tag{2.2c}$$

$$\rho(1 + T(S-1)) = 1. \tag{2.2d}$$

A reduced temperature $T=(\tilde{T}-\tilde{T}_\infty)/(\tilde{T}_j-\tilde{T}_\infty)$ is used, and in all further calculations, this variable is expressed in terms of ρ by use of (2.2*d*). The flow is characterised by the following parameters:

$$\text{Prandtl number} \quad Pr=\frac{\mu C_P}{\alpha}, \tag{2.3}$$

$$\text{density ratio} \quad S=\frac{\tilde{\rho}_\infty}{\tilde{\rho}_j}, \tag{2.4}$$

$$\text{Reynolds number} \quad Re=\frac{\tilde{\rho}_j\tilde{u}_j R}{\mu} \quad \text{and} \tag{2.5}$$

$$\text{Richardson number} \quad Ri=gR\frac{(\tilde{\rho}_\infty-\tilde{\rho}_j)}{\tilde{\rho}_j\tilde{u}_j^2}. \tag{2.6}$$

In the homogeneous limit $S\to 1$, the state equation (2.2*d*) prescribes $\rho\to 1$, and the system (2.2) is then identical to the Boussinesq equations used in Chakravarthy *et al.* (2015), provided $\rho-1$ is taken to be of order $S-1$; the present formulation is therefore consistent with our earlier study. A rigorous derivation of the Boussinesq equations and a discussion on the underlying assumptions may be found in Tritton (2012).

2.2. *Base flow*

In a cylindrical coordinate system (r,θ,z), the flow variables $q=(\rho,\boldsymbol{u},p,T)^{\mathrm{T}}$ are split into steady and unsteady components as

$$\boldsymbol{q}(r,\theta,z,t)=\overline{\boldsymbol{q}}(r,\theta,z)+\boldsymbol{q}'(r,\theta,z,t). \tag{2.7}$$

The numerical tools used for the construction of the base flow, as well as for the linear perturbation analysis described in § 2.3, are very similar to those employed by Coenen *et al.* (2017), except that density variations are modelled as an effect of heating, rather than species mixing. Equations (2.2) are discretised with finite elements in FreeFEM++, and a steady axisymmetric solution $\overline{\boldsymbol{q}}$ is obtained from Newton–Raphson iterations (Garnaud *et al.* 2013). The numerical domain is 80 radii long in the streamwise direction and 30 radii in the transverse direction. Iterations are performed until all flow quantities are converged to within 10^{-9} times their maximum values. At the inlet, $z=0$, boundary conditions

$$\overline{u}_z=\frac{1}{2}+\frac{1}{2}\tanh\left[\frac{5}{2}\left(\frac{1}{r}-r\right)\right], \quad \overline{u}_r=0 \quad \text{and} \quad \overline{\rho}=1-\left(1-\frac{1}{S}\right)\overline{u}_z \tag{2.8a–c}$$

are prescribed for the axial velocity $\overline{u}_z$, the radial velocity $\overline{u}_r$ and the density $\overline{\rho}$. The initial shear layer momentum thickness is 10 % of the nozzle radius. All other boundary conditions are specified as

$$\frac{1}{Re}\frac{\partial\overline{\boldsymbol{u}}}{\partial r}-\overline{p}\boldsymbol{e}_r=0, \quad \overline{\rho}=1 \quad \text{at } r=r_{max}, \tag{2.9a,b}$$

$$\frac{1}{Re}\frac{\partial\overline{\boldsymbol{u}}}{\partial z}-\overline{p}\boldsymbol{e}_z=0, \quad \frac{\partial\overline{\rho}}{\partial z}=0 \quad \text{at } z=z_{max}, \tag{2.9c,d}$$

$$\frac{\partial\overline{u}_z}{\partial r}=\overline{u}_r=\frac{\partial\overline{\rho}}{\partial r}=\frac{\partial\overline{p}}{\partial r}=0 \quad \text{at } r=0. \tag{2.9e}$$

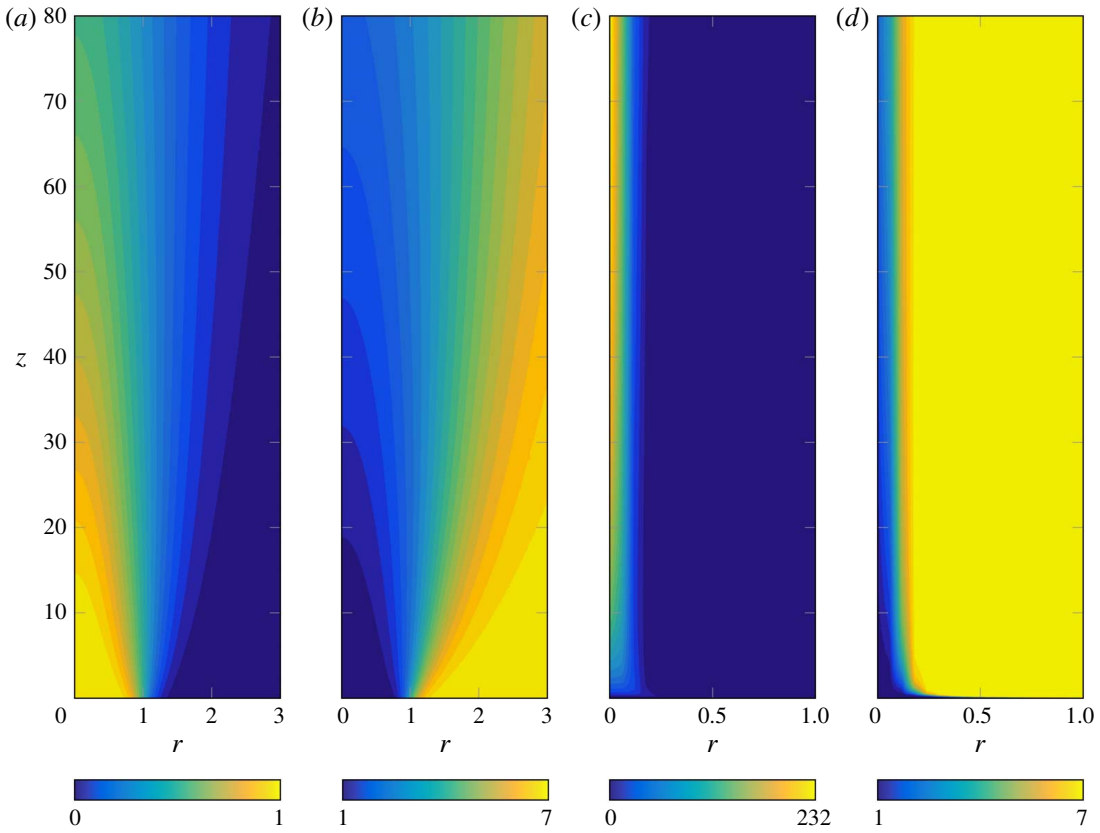

FIGURE 1. (Colour online) Axisymmetric steady base flows obtained for $Ri = 10^{-4}$ (a,b) and for $Ri = 10^{3}$ (c,d). Axial velocity (a,c) and density (b,d) are shown in the (r, z) plane.

These boundary conditions are obtained from the kinematic constraints on the axis (Khorrami, Malik & Ash 1989), and by imposing zero normal stresses at r_{max} and z_{max}, together with Dirichlet and Neumann conditions for the density.

As the objective is to characterise the role of buoyancy in the instability dynamics, the main parameters to be varied are the Richardson number and the density ratio. The ranges of parameters $10^{-4} \leqslant Ri \leqslant 10^{3}$ and $1.05 \leqslant S \leqslant 7$ will be investigated. The effect of the Reynolds number above a value of 100 is found to be weak, and a standard value of $Re = 200$ (in some cases $Re = 500$) will be used, while $Pr = 0.7$ is maintained throughout.

For a strong density ratio $S = 7$, and the two extreme values $Ri = 10^{-4}$ and $Ri = 10^{3}$, steady base flow profiles of axial velocity and density are shown in figure 1. The flow at low Ri is dominated by the momentum of the injected fluid, which diffuses radially with axial distance under the effect of viscosity. This is clearly the case of a jet, in a configuration where buoyancy has no noticeable impact on the base flow dynamics, despite the strong density variations. The flow at high Ri, in contrast, is principally driven by the buoyancy force, as the injected momentum is negligibly weak in comparison. The fluid in this case is not pushed out of the orifice, but rather pulled out by buoyancy, forming a slender rising column around the axis (note the different radial scales in figure 1). This flow is characteristic of a plume, and it is often called a ‘lazy’ plume, as the momentum at its base is much lower than that of a self-similar profile, where momentum and buoyancy are in balance.

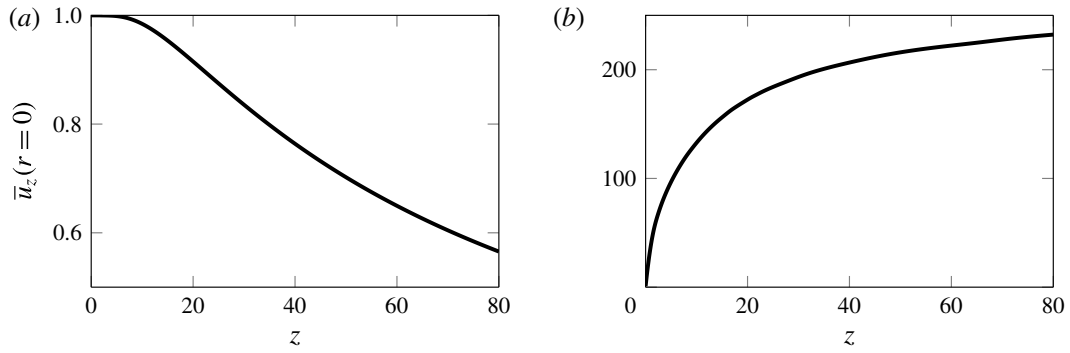

FIGURE 2. Variations of the centreline velocity along z. (*a*) $Ri = 10^{-4}$; (*b*) $Ri = 10^{3}$.

Between the two extremes shown in figure 1, the aspect of the base flow at different Richardson numbers changes gradually. Cases with $Ri < 1$ will be denoted 'buoyant jets' in the following, as opposed to 'plumes' with $Ri > 1$. Vertical variations of the centreline velocity are shown in figure 2 for the same two configurations as in figure 1. The jet, at $Ri = 10^{-4}$, exhibits a short potential core region, where the centreline velocity is constant, followed by hyperbolic decay. The plume flow, at $Ri = 10^{3}$, accelerates progressively with vertical distance from the inlet, and the centreline velocity approaches asymptotically a limit value in the self-similar regime (Yih 1988). Buoyant jets at low but finite Richardson number behave as plumes at large distances from the nozzle, when their excess momentum is sufficiently diffused. While a jet entrains ambient fluid only through momentum diffusion, entrainment into a plume tends to be much stronger due to its continuous production of axial momentum. The plume base flow presented in figure 1(*c*,*d*) is particularly marked by radial entrainment close to $z = 0$.

2.3. *Linear stability problem*

Infinitesimal perturbations of a steady base flow are sought with a global ansatz

$$[\rho', \boldsymbol{u}', p', T']^{\mathrm{T}} = [\hat{\rho}(r,z), \hat{\boldsymbol{u}}(r,z), \hat{p}(r,z), \hat{T}(r,z)]^{\mathrm{T}} \mathrm{e}^{\mathrm{i}(m\theta-\omega t)} + \mathrm{c.c.} \tag{2.10}$$

The integer m denotes the azimuthal wavenumber and $\omega = \omega_r + \mathrm{i}\omega_i$ is a complex frequency. Upon linearising the governing equations (2.2), and substitution of (2.10), the linear perturbation equations are found as

$$-\mathrm{i}\omega\hat{\rho} + \mathrm{div}_m(\hat{\rho}\,\overline{\boldsymbol{u}} + \overline{\rho}\,\hat{\boldsymbol{u}}) = 0, \tag{2.11a}$$

$$\begin{aligned} -\mathrm{i}\omega\overline{\rho}\hat{\boldsymbol{u}} + \overline{\rho}[(\mathrm{grad}_m\overline{\boldsymbol{u}})\cdot\hat{\boldsymbol{u}} + (\mathrm{grad}_m\hat{\boldsymbol{u}})\cdot\overline{\boldsymbol{u}}] + \hat{\rho}(\mathrm{grad}_m\overline{\boldsymbol{u}})\cdot\overline{\boldsymbol{u}} \\ = -\mathrm{grad}_m\hat{p} - \frac{Ri}{S-1}\hat{\rho}\boldsymbol{e}_z + \frac{1}{ReS}\left[\Delta_m\hat{\boldsymbol{u}} + \frac{1}{3}\mathrm{grad}_m(\mathrm{div}_m\hat{\boldsymbol{u}})\right], \end{aligned} \tag{2.11b}$$

$$-\mathrm{i}\omega\overline{\rho}\hat{T} + \overline{\rho}[(\mathrm{grad}_m\overline{T})\cdot\hat{\boldsymbol{u}} + (\mathrm{grad}_m\hat{T})\cdot\overline{\boldsymbol{u}}] + \hat{\rho}(\mathrm{grad}_m\overline{T})\cdot\overline{\boldsymbol{u}} = \frac{1}{PrReS}\Delta_m\hat{T}, \tag{2.11c}$$

$$\hat{\rho} + \overline{\rho}^2\hat{T}(S-1) = 0. \tag{2.11d}$$

Differential operators in the above equations are written with a subscript m in order to indicate that azimuthal derivatives are replaced with a factor im; these operators

are documented in appendix A. While the base flow is taken to be swirl free, $\overline{u}_\theta = 0$, the azimuthal perturbation velocity u'_θ may in general be non-zero. Homogeneous Dirichlet conditions are imposed on $\hat{\boldsymbol{u}}$ and $\hat{\rho}$ at the inlet, $z = 0$, and a homogeneous Neumann condition is prescribed for $\hat{p}$. On the axis, depending on the azimuthal mode considered, appropriate boundary conditions as detailed in Khorrami *et al.* (1989) and Chakravarthy *et al.* (2015) are enforced. On the outer boundaries at r_{max} and z_{max}, no-stress conditions consistent with (2.9) are used.

The system (2.11) is cast into the form of an eigenvalue problem

$$\omega B\hat{\boldsymbol{q}} = L\hat{\boldsymbol{q}}. \tag{2.12}$$

According to the ansatz (2.10), the real part of the eigenvalue, ω_r, represents the oscillation frequency while the imaginary part, ω_i, is the growth rate of the perturbation. As before, the variable $\hat{T}$ is eliminated through the equation of state (2.11*d*). So-called global eigenmodes are computed by resolving $\hat{\rho}$, $\hat{\boldsymbol{u}}$ and $\hat{p}$ in both r and z, such that spatial variations of the base flow and the perturbation quantities are accounted for without further limiting assumptions (Theofilis 2003). The eigenvalue problem (2.12) is then solved with an iterative shift-invert Arnoldi algorithm, in the same way as in Garnaud *et al.* (2013), with an accuracy close to machine precision.

In addition, a local analysis is performed in § 5, in order to identify the absolute mode in a parallel base flow (Huerre & Monkewitz 1990). Perturbations (2.10) are then Fourier-transformed in z, leading to the standard ansatz

$$[\hat{\rho}(r,z), \hat{\boldsymbol{u}}(r,z), \hat{p}(r,z), \hat{T}(r,z)]^{\mathrm{T}} = [\check{\rho}(r), \check{\boldsymbol{u}}(r), \check{p}(r), \check{T}(r)]^{\mathrm{T}} \mathrm{e}^{\mathrm{i}kz}. \tag{2.13}$$

3. Global spectra and eigenfunctions

Instability results obtained from the global formulation (2.10) are presented first for axisymmetric modes, $m = 0$, since experimental and numerical evidence suggests their leading role in the self-sustained dynamics of plumes, as discussed in § 1. A brief discussion of helical perturbations, $m = 1$, follows in § 3.2.

3.1. *Axisymmetric perturbations*

Eigenvalues ω obtained for two configurations, $Ri = 10^{-4}$ and 10^3, with otherwise identical parameters $S = 7$ and $Re = 200$, are presented in figure 3 as black symbols. These are the two extreme jet and plume cases discussed in § 2.2.

The jet, at $Ri = 10^{-4}$ (figure 3*a*), exhibits one unstable mode with $\omega = 0.558 + 0.025\mathrm{i}$. When buoyancy effects are eliminated, by setting $Ri = 0$ in the perturbation equations but still using the same base flow, eigenvalues shown as red crosses are obtained; visibly, the buoyancy term in the perturbation equations has no significant impact on the instability dynamics. This observation, as well as the overall appearance of the spectrum, is fully consistent with the non-buoyant and slightly buoyant results of Coenen *et al.* (2017), and many more details on the unstable eigenmode of pure jets are provided in their study.

The plume, at $Ri = 10^3$ (figure 3*b*), possesses five unstable modes, one being strongly dominant with $\omega = 29.4 + 11.3\mathrm{i}$. When the perturbation Richardson number is set to zero in this configuration, all unstable modes vanish from the spectrum. It can be concluded that buoyancy plays a determining role for the instability of this plume, not only by setting up the base flow, but also by the coupling of density and

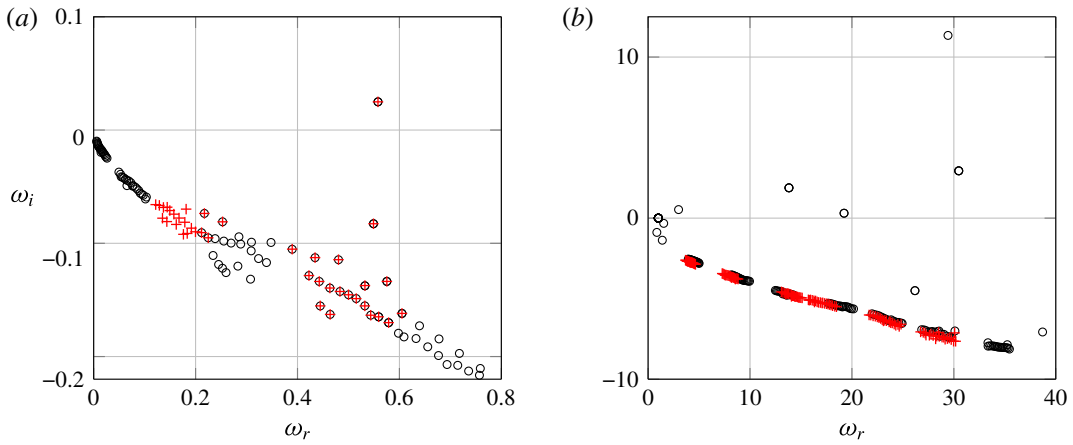

FIGURE 3. (Colour online) Global spectra of axisymmetric perturbations ($m = 0$), for the two configurations shown in figure 1. (*a*) $Ri = 10^{-4}$, jet case; (*b*) $Ri = 10^{3}$, plume case. $Re = 200$ and $S = 7$ are set identically for both cases. True eigenvalues (○) are compared to their counterparts (+) that are obtained when the buoyancy term in (2.11*b*) is removed.

velocity perturbations. It is also noted that the high-Ri plume base flow is not subject to the non-buoyant instability that affects the low-Ri jet.

Unstable eigenvalues of the plume take on significantly higher values, both in their real and in their imaginary parts, than those of the jet. This is clearly a result of the scaling with the inflow centreline velocity, which appropriately characterises a jet, but is less pertinent for 'lazy' plumes. A common scaling is employed here for the sake of consistency across the full range of Richardson number values; if only high-Ri plumes were considered, a buoyancy-based velocity scaling would be more suitable.

The distinct nature of the instability modes of the jet and the plume flows is also apparent in the shape of their eigenfunctions. Figure 4 shows the spatial distribution of the axial velocity amplitude in the dominant modes for the two respective cases. At low Richardson number, the maximum perturbation amplitude is found on the centreline, 12 radii downstream of the nozzle. Perturbations are confined inside the jet column, as documented in more detail by Coenen *et al.* (2017). In the high-Ri plume, the spatial eigenmode structure is very different: the maximum amplitude is located inside the mixing layer very close to the inflow, in the region where the density gradient in the base flow is maximal.

In the reference experiments by Cetegen & Kasper (1996) and Bharadwaj & Das (2017), a slightly different definition is chosen for the Richardson number, which corresponds to $2Ri/S$ in our nomenclature. Variations of the dominant eigenvalue in the present analysis are therefore presented as functions of Ri/S in figure 5 in order to facilitate a comparison. The baseline case, with $Re = 200$, $S = 7$ and inflow conditions (2.8), is represented by solid circles. Eigenvalues of this configuration display continuous variations both in the Strouhal number $St = \omega_r/(2\pi)$ and in the growth rate ω_i. Strouhal number values are asymptotically constant in the low-Ri/S regime, whereas they follow a power law at values $Ri/S > 0.1$. A regression fit yields the dependence $St = 0.55(Ri/S)^{0.43}$, which is in good agreement with experimental results in the range $1 \leqslant Ri/S \leqslant 250$: after conversion to the present definition of the Richardson number, the power law determined by Cetegen & Kasper (1996) in this regime is given by $St = 0.52(Ri/S)^{0.38}$ (shown as a line in figure 5*a*), and the corresponding measurements of Bharadwaj & Das (2017) for plumes from an orifice

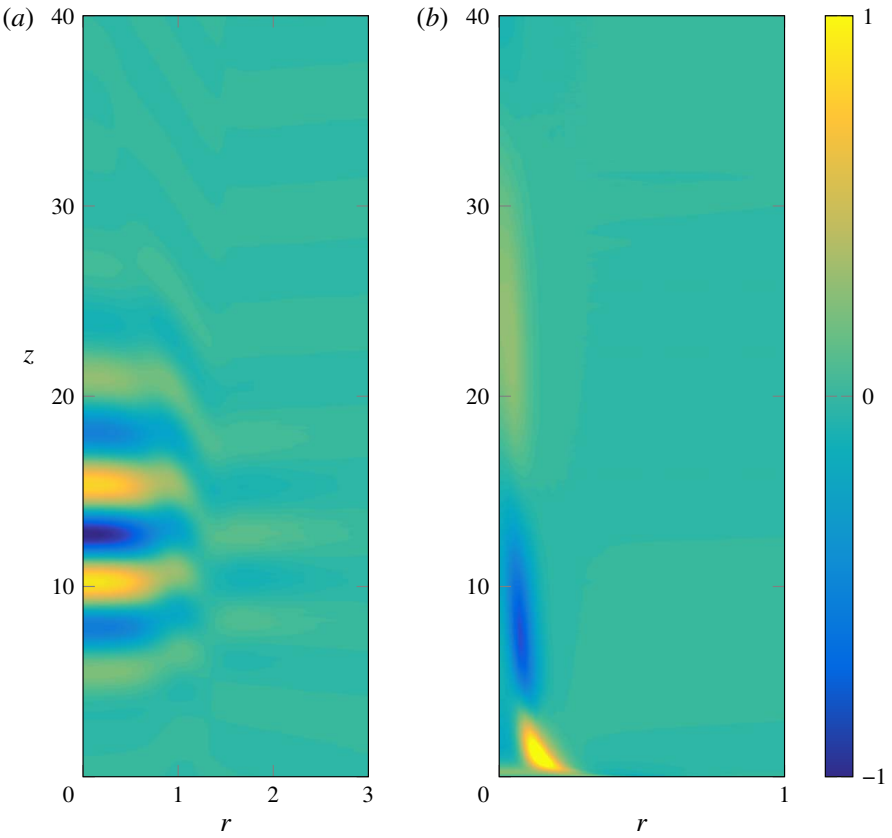

FIGURE 4. (Colour online) Spatial distributions of axial velocity eigenfunctions $\hat{u}_z$, corresponding to the most unstable modes of the two respective cases shown in figure 3. (*a*) Jet at $Ri = 10^{-4}$, $S = 7$ and $Re = 200$; (*b*) plume at $Ri = 10^{3}$, $S = 7$ and $Re = 200$.

convert to $St = 0.51(Ri/S)^{0.39}$. A different scaling, measured as $St \propto (Ri/S)^{0.28}$ for $Ri/S > 250$ by Cetegen & Kasper (1996), is outside the parameter range considered here. The growth rate in the baseline configuration, shown in figure 5(*b*), increases monotonically with Ri/S, and it is positive throughout.

Eigenvalues from three other flow configurations are included in figure 5 in order to assess the sensitivity of the instability with respect to the Reynolds number, to the density ratio and to the inlet velocity profile. With the standard profile (2.8), parameter combinations $Re = 500$, $S = 7$ (open circles) and $Re = 200$, $S = 4.5$ (squares) are chosen. The Strouhal number values in figure 5(*a*) are barely affected by these changes, and the growth rates in figure 5(*b*) follow a similar trend as in the baseline case. The less heated configuration (squares) is stable at $Ri < 0.1$, consistent with the analysis by Coenen *et al.* (2017).

Triangle symbols indicate results for a special case where $Re = 200$ and $S = 7$ are maintained, but the velocity inlet profile is changed to a parabolic pipe flow, while the density profile is still given by (2.8). This flow case is introduced in order to better approach the experimental conditions of Subbarao & Cantwell (1992) and Cetegen & Kasper (1996), where the fluid exits from a nozzle as a developed laminar pipe flow. This change in the velocity profile has barely any effect on the Strouhal number across all Ri/S values, but it does inhibit the global instability in the low-Ri/S regime. The latter is consistent with the absence of self-excited behaviour at low Ri in the

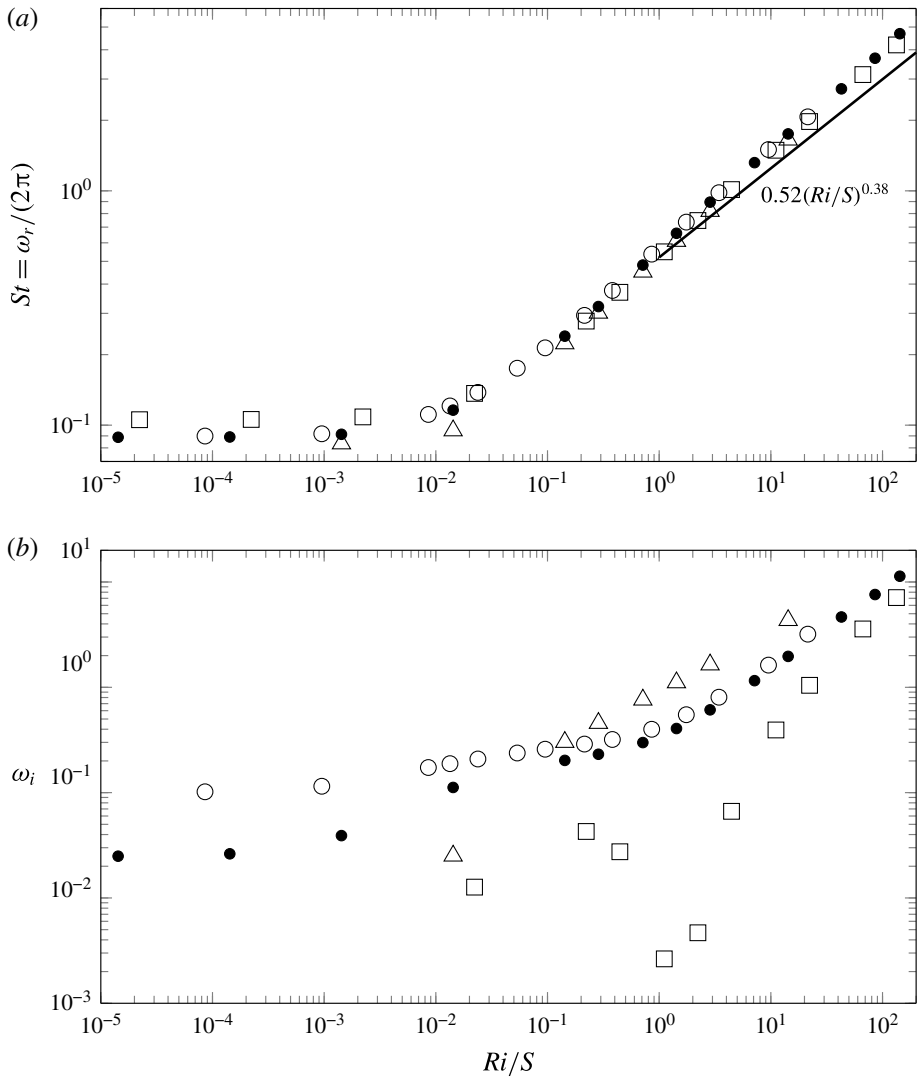

FIGURE 5. (*a*) Strouhal number and (*b*) growth rate of the global eigenvalue ω, as a function of Ri/S. Legend: (●) $Re = 200$, $S = 7$; (○) $Re = 500$, $S = 7$; (□) $Re = 200$, $S = 4.5$; (△) $Re = 200$, $S = 7$, with parabolic inlet velocity profile. All other configurations take the inlet velocity profile (2.8). (——) Power law from the Cetegen & Kasper (1996) experiments, rescaled to match the present definition of Ri.

experiments of Subbarao & Cantwell (1992) and Cetegen & Kasper (1996), and in the simulations of Satti & Agrawal (2006).

As the effect of heating enters the problem both through the density ratio S and through the Richardson number Ri, the onset of instability is examined for independent variations of these two parameters. The main results of the local (see § 5) and global instability analyses are summarised in the state diagram in the (Ri, S) plane shown in figure 6. The thin line delineates the neutral boundary separating locally convectively unstable inlet base flows (in white below the curve) from locally absolutely unstable ones (in blue and red above the curve). The thick neutral line separates the globally stable states (in white and blue below the curve) from the globally unstable states (in red above the curve). In the white area, convective

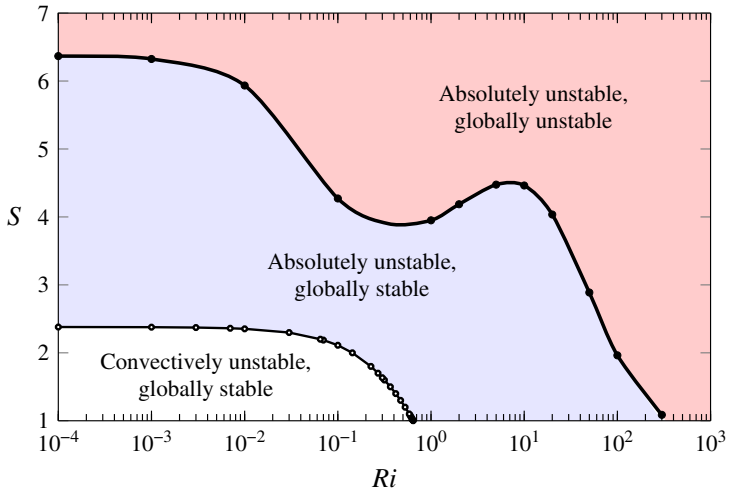

FIGURE 6. (Colour online) Instability regimes in the S–Ri plane for the axisymmetric mode at $Re = 200$. The thick line denotes the global stability boundary, and the thin line denotes the boundary between local convective and absolute instability of the inlet profile.

instability prevails, and in the blue and red areas, absolute instability prevails. Along a diagonal line in the state diagram, the flow changes from convectively unstable to absolutely unstable to globally unstable, once the absolutely unstable region is large enough. For buoyant jets (low Ri) and plumes (large Ri) the same sequence takes place as S increases at a given Ri. Note that the globally unstable domain is reached much 'sooner' for plumes than for buoyant jets. The dip in the global stability neutral curve for Ri of order unity signals a gradual shift from a shear-dominated instability to a buoyancy-dominated instability, as further discussed in § 4.

3.2. *Helical perturbations*

The local analysis of plumes in the Boussinesq limit $S \to 1$ by Chakravarthy *et al.* (2015) concluded that absolute instability only occurs for helical perturbations, $m = 1$, whereas axisymmetric perturbations in that setting were found to be only convectively unstable. Although the global instability of axisymmetric eigenmodes in non-Boussinesq situations, as documented above, appears to be fully consistent with experimental and numerical observations of self-excited behaviour, the possibility of helical global instabilities remains to be explored.

Eigenvalues pertaining to helical instability modes are displayed in figure 7 for two different calculations, both for the same physical parameter setting $S = 7$, $Ri = 1$ and $Re = 200$. One case, represented by blue unfilled circles, was computed with the same boundary conditions as all previous results. A branch of regularly spaced modes is seen to be unstable over the interval $0.8 \leqslant \omega_r \leqslant 4$. The features of this branch are very similar to several jet cases discussed by Coenen *et al.* (2017), as well as observations made in many different flow cases, especially in the boundary layer calculations by Åkervik *et al.* (2008). In a recent study (Lesshafft 2017), the occurrence of such 'arc branches' is ascribed to the presence of spurious pressure feedback from the downstream end of a truncated flow domain, and it is predicted that artificial damping near the outflow should be effective in reducing the growth rate of such unphysical modes.

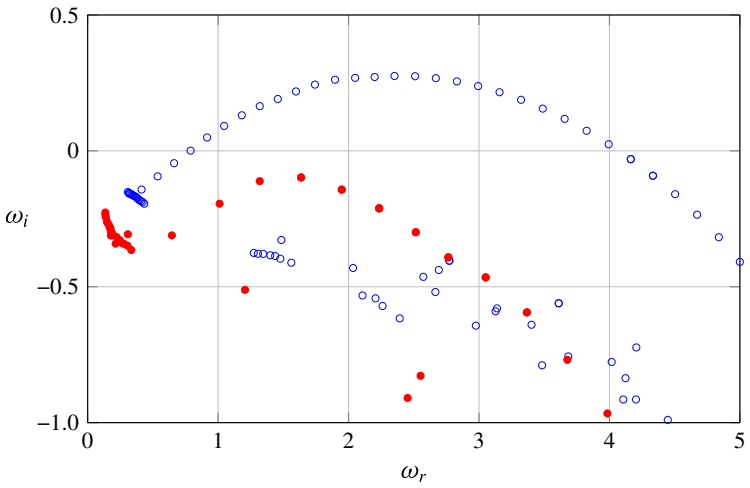

FIGURE 7. (Colour online) Global spectrum of helical perturbations ($m = 1$), for the configuration $S = 7$, $Ri = 1$ and $Re = 200$. Results from two calculations are shown: (○) without absorbing layer; (●) with absorbing layer at $z > 30$.

Indeed, if artificial damping is applied in an 'absorbing layer' (Colonius 2004) at $z > 30$, the growth rates of the arc branch modes decrease, and all modes recede to the stable half-plane if the damping is sufficiently strong. Such a case is represented by red filled circles in figure 7, where a damping term $-\lambda(z)\hat{\boldsymbol{q}}$ has been added to the right-hand side of (2.12). The damping coefficient $\lambda(z)$ ramps up from zero to 16, over the interval $30 < z < 50$, according to equation (2.4) of Chomaz (2003). No unstable helical modes are found with this boundary treatment. In contrast, the same artificial damping has no discernible effect on the unstable eigenvalues for axisymmetric perturbations shown in figure 3. This behaviour is in full agreement with the arguments of Lesshafft (2017), as $m = 0$ perturbations are locally stable in the downstream flow region, whereas $m = 1$ perturbations remain convectively unstable, as will be shown in § 5.

4. Influence of buoyant, baroclinic and shear-related mechanisms

The results discussed in § 3.1 suggest that different mechanisms drive the global instability dynamics in the low- and the high-Ri regimes. These mechanisms are investigated in the present section, on the basis of the formalism proposed by Marquet & Lesshafft (2015). This formalism is introduced here in a slightly different and weaker manner, which is sufficient for the present purpose.

A sensitivity analysis is to be performed, in order to quantify the influence of the various forces in the momentum equation onto the unstable growth of velocity perturbations. The latter are governed by the equation

$$-\mathrm{i}\omega\hat{\boldsymbol{u}} = \mathcal{C} + \mathcal{S} + \mathcal{P} + \mathcal{B} + \mathcal{V}, \tag{4.1}$$

with the right-hand-side terms

$$\mathcal{C} = -(\mathrm{grad}\,\hat{\boldsymbol{u}}) \cdot \overline{\boldsymbol{u}}, \tag{4.2a}$$

$$\mathcal{S} = -(\mathrm{grad}\,\overline{\boldsymbol{u}}) \cdot \hat{\boldsymbol{u}}, \tag{4.2b}$$

$$\mathcal{P} = -\frac{\operatorname{grad}\hat{p}}{\overline{\rho}} + \frac{\hat{\rho}\operatorname{grad}\overline{p}}{\overline{\rho}^2}, \tag{4.2c}$$

$$\mathcal{B} = -\frac{Ri}{S-1}\frac{\hat{\rho}}{\overline{\rho}^2}\boldsymbol{e}_z, \tag{4.2d}$$

$$\mathcal{V} = \frac{1}{ReS}\left[\frac{1}{\overline{\rho}}\left(\Delta\hat{\boldsymbol{u}} + \frac{\operatorname{grad}(\operatorname{div}\hat{\boldsymbol{u}})}{3}\right) - \frac{\hat{\rho}}{\overline{\rho}^2}\left(\Delta\overline{\boldsymbol{u}} + \frac{\operatorname{grad}(\operatorname{div}\overline{\boldsymbol{u}})}{3}\right)\right]. \tag{4.2e}$$

These individual terms represent the mechanisms of base flow convection $\mathcal{C}$, base flow shear $\mathcal{S}$, pressure force $\mathcal{P}$, buoyancy $\mathcal{B}$, and viscous diffusion $\mathcal{V}$. As only axisymmetric $m = 0$ perturbations are considered in this chapter, it is not necessary to append a subscript m to the differential operators.

For a better physical discussion, the pressure force can be split into a divergence-free (baroclinic) and a curl-free (barotropic) component; the former is linked to the baroclinic torque in the vorticity equation, after application of the curl operator to (4.1), whereas the latter does not affect the evolution of perturbation vorticity.

A Helmholtz decomposition is performed on the pressure force $\mathcal{P}$, such that

$$\mathcal{P} = \operatorname{curl}\mathcal{A} - \operatorname{grad}\phi, \tag{4.3}$$

where $\mathcal{A}$ and ϕ are found from

$$\mathcal{A} = \frac{1}{4\pi}(\operatorname{curl}\mathcal{P}) \otimes (1/\boldsymbol{r}), \tag{4.4a}$$

$$\phi = \frac{1}{4\pi}(\operatorname{div}\mathcal{P}) \otimes (1/\boldsymbol{r}). \tag{4.4b}$$

The operator $\otimes$ denotes a convolution over the entire volume V of the numerical domain, and $\boldsymbol{r}$ represents any position in V. This decomposition is performed numerically, such that $\mathcal{P} = \mathcal{P}_1 + \mathcal{P}_2$ is explicitly obtained, with a baroclinic component $\mathcal{P}_1$ and a barotropic component $\mathcal{P}_2$.

Further analysis is restricted to the action of shear, baroclinic and buoyant forces, because all other contributions are found to be strictly stabilising at all Richardson numbers. The dependence of an eigenvalue ω on these three components is obtained by introducing small variations into (4.1),

$$-\mathrm{i}\omega\hat{\boldsymbol{u}} = \mathcal{C} + (1+\varepsilon_S)\mathcal{S} + (1+\varepsilon_P)\mathcal{P}_1 + \mathcal{P}_2 + (1+\varepsilon_B)\mathcal{B} + \mathcal{V}, \tag{4.5}$$

from where sensitivities can be defined as

$$\partial_S\omega = \frac{\partial\omega}{\partial\varepsilon_S} = \frac{\langle\hat{\boldsymbol{q}}^\dagger, \mathcal{S}\rangle}{\langle\hat{\boldsymbol{q}}^\dagger, B\hat{\boldsymbol{q}}\rangle}, \quad \partial_P\omega = \frac{\partial\omega}{\partial\varepsilon_P} = \frac{\langle\hat{\boldsymbol{q}}^\dagger, \mathcal{P}_1\rangle}{\langle\hat{\boldsymbol{q}}^\dagger, B\hat{\boldsymbol{q}}\rangle}, \quad \partial_B\omega = \frac{\partial\omega}{\partial\varepsilon_B} = \frac{\langle\hat{\boldsymbol{q}}^\dagger, \mathcal{B}\rangle}{\langle\hat{\boldsymbol{q}}^\dagger, B\hat{\boldsymbol{q}}\rangle}. \tag{4.6a–c}$$

Note that the terms $\mathcal{S}$, $\mathcal{P}_1$ and $\mathcal{B}$ contain components of the eigenvector $\hat{\boldsymbol{q}}$, and that $\hat{\boldsymbol{q}}^\dagger$ is the associated adjoint eigenvector, defined with respect to the scalar product $\langle\cdot,\cdot\rangle$. A standard non-weighted discrete scalar product has been chosen in the present calculations, but the scalar quantities $\partial\omega$ in (4.6) are independent of this choice, as demonstrated by Marquet & Lesshafft (2015).

The sensitivities (4.6) are interpreted in the following way. An infinitesimally small positive value ε_S proportionally increases the strength of the shear-related force term, resulting in an eigenvalue variation $\delta\omega = \varepsilon_S\partial_S\omega$. If the imaginary part of

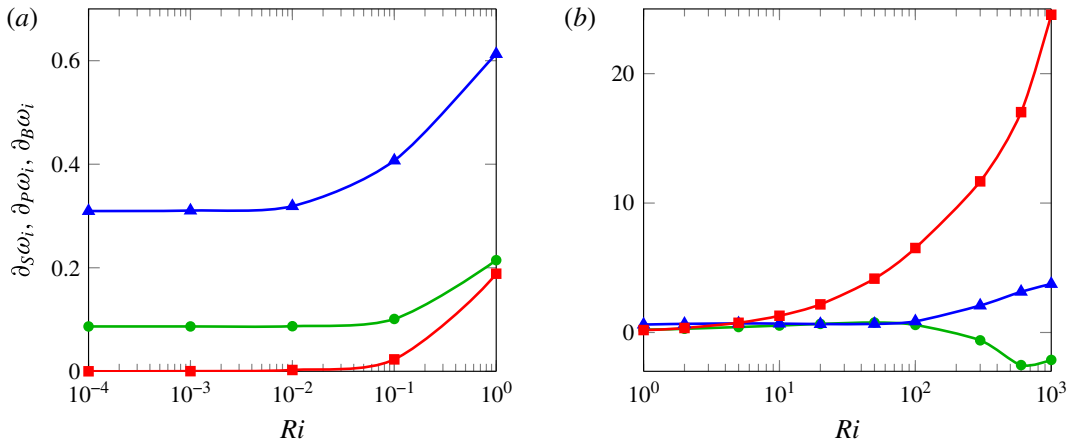

FIGURE 8. (Colour online) Sensitivity of the growth rate with respect to (▲) shear, (●) baroclinic and (■) buoyancy terms, as functions of the Richardson number, with parameters $S = 7$ and $Re = 200$.

$\partial_S\omega$ is positive, then $\mathcal{S}$ has a destabilising effect; if it is negative, then $\mathcal{S}$ acts in a stabilising way. The same reasoning applies to $\partial_P\omega$ and $\partial_B\omega$. The three sensitivities are commensurate, so that a larger absolute value of one compared to another indicates a stronger stabilising or destabilising effect.

Results from this analysis are presented in figure 8 over the full range of Ri values, for the standard setting $S = 7$ and $Re = 200$. Imaginary values of $\partial_S\omega$, $\partial_P\omega$ and $\partial_B\omega$ are shown in two separate diagrams for low and high Richardson numbers, for better readability. In the jet regime $Ri < 1$, the strongest destabilising force is due to the base flow shear. At very low Ri, the effect of buoyancy vanishes, while the baroclinic force provides a small additional destabilisation. The local analysis of Lesshafft & Huerre (2007) demonstrated that the baroclinic torque is the determining ingredient that renders a non-buoyant heated jet absolutely unstable, through co-operation with the basic shear instability. The present global results are consistent with that conclusion. In the plume regime $Ri > 1$, the buoyancy force becomes strongly destabilising, dominating all other contributions for $Ri > 5$. Shear and baroclinic effects are negligible in comparison at very high Ri; the baroclinic force even becomes stabilising above $Ri = 100$.

It is concluded that the observed global instability in the jet and plume regimes indeed involve distinct physical mechanisms. In buoyant jets at low Richardson number, the dynamics are driven by a shear instability, which is strengthened by a baroclinic force. In high-Ri plumes, the instability arises principally from buoyancy effects. These conclusions are fully consistent with the results of Bharadwaj & Das (2017), who observed that the leading eigenmode could be stabilised through artificial compensation of the baroclinic torque at low Ri, and through suppression of the buoyancy force at high Ri.

5. Local analysis

The results so far have shown a dominance of axisymmetric global instabilities, which is in stark contrast to our earlier local analysis in the $S \to 1$ Boussinesq limit (Chakravarthy *et al.* 2015), where absolute instability was found only for helical

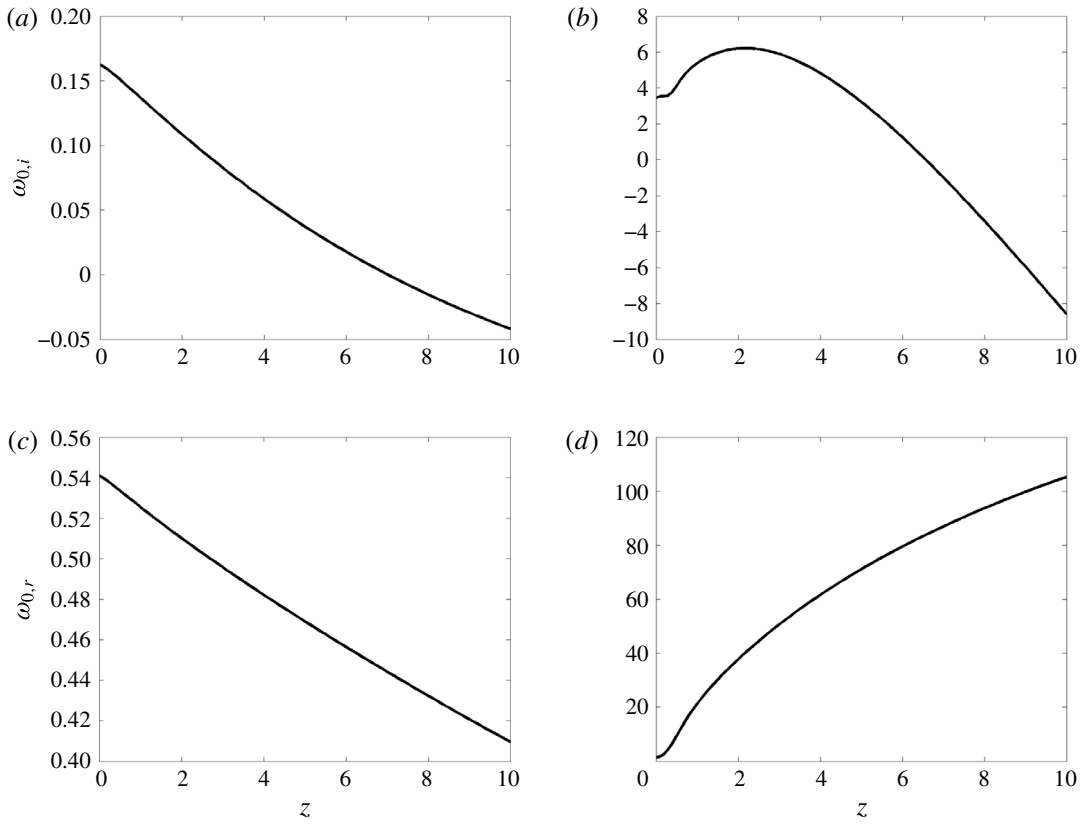

FIGURE 9. Variation of the absolute frequency ω_0 with streamwise location z for the axisymmetric mode $m = 0$ and $Ri = 10^{-4}$ (a,c) and $Ri = 10^2$ (b,d) at $S = 7$, $Re = 200$.

perturbations. The absolute/convective nature of local instability in non-Boussinesq settings is now investigated.

The same algorithm as in Chakravarthy *et al.* (2015) is used for tracking saddle points of the local dispersion relation in the complex k plane. Again, the group-velocity root-finding procedure of Lesshafft & Marquet (2010) has been found to be more efficient and robust than the classical Briggs or the cusp map methods (see Schmid & Henningson 2001).

5.1. *Axisymmetric perturbations,* $m = 0$

For the standard setting $S = 7$ and $Re = 200$, and for Richardson numbers of 10^{-4} and 10^2, variations of the absolute frequency ω_0 along the streamwise z direction are shown in figure 9. In the more extreme case $Ri = 10^3$, numerical difficulties led to unreliable results. In both configurations, the flow is found to be absolutely unstable ($\omega_{0,i} > 0$) over a streamwise interval of 6 or 7 radii downstream of the inlet. In the weakly non-parallel case of $Ri = 10^{-4}$, the real part $\omega_{0,r}$ shows moderate variations around a value of 0.5, in reasonable agreement with the global frequency $\omega_r = 0.56$ as given in figure 5(a). In the strongly non-parallel setting $Ri = 10^2$, $\omega_{0,r}$ displays a variation between 1.3 and 80 over the absolutely unstable interval. This is not inconsistent with the global frequency $\omega_r = 10.99$, but it does not provide a means of predicting ω_r at leading order.

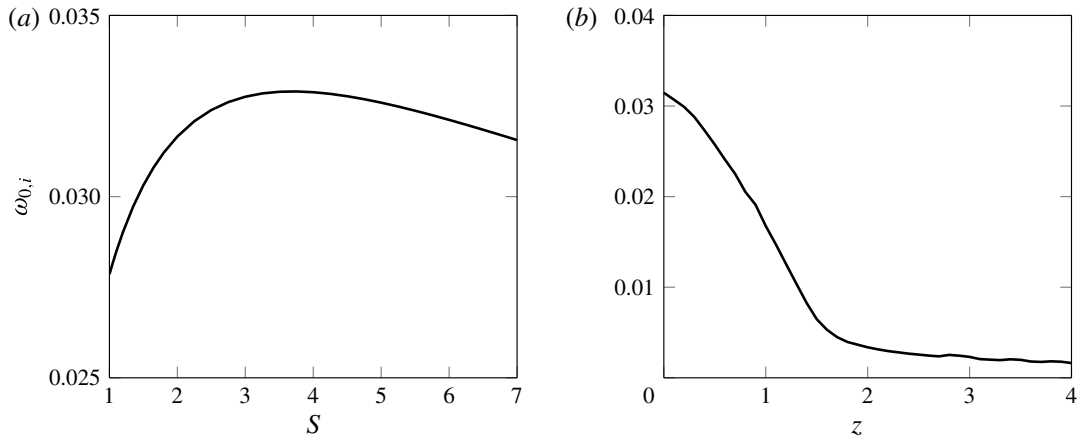

FIGURE 10. Absolute growth rate $\omega_{0,i}$ of helical perturbations, for $Re = 200$ and $Ri = 1$: (a) at the inlet, as a function of the density ratio S; (b) as a function of z, for $S = 7$.

Nonetheless, the link between local absolute and global instability of axisymmetric perturbations is very plausibly confirmed by these results, both in the low- and in the high-Richardson-number regime. The neutral curve for the onset of absolute instability in the (Ri, S) plane is reported in figure 6 for axisymmetric perturbations at $z = 0$. It is found that the transition from convective to absolute local instability at the inlet, with increasing Ri and S, occurs before global instability sets in. This is consistent with the common observation, both in model problems (Chomaz, Huerre & Redekopp 1991) and in slowly varying flow (e.g. Lesshafft, Huerre & Sagaut 2007), that absolute instability must prevail over a sufficiently long streamwise region with sufficient growth rate in order to prompt a global instability.

5.2. *Helical perturbations, $m = 1$*

The saddle point in the complex k plane that is associated with helical absolute instability in the study of Chakravarthy *et al.* (2015) is also recovered in the analysis of the present inflow profiles. The absolute growth rate $\omega_{0,i}$ for $m = 1$ perturbations at $z = 0$ is displayed in figure 10(a) as a function of S, for parameters $Ri = 1$ and $Re = 200$. A unity Richardson number is chosen here for comparison with the analysis in § 3 of Chakravarthy *et al.* (2015), but higher values of Ri lead to the same conclusions. The density ratio S characterises the departure from the Boussinesq limit, and it is seen to have a very weak effect on the growth rate $\omega_{0,i}$ of the absolute helical mode.

The spatial variation of $\omega_{0,i}$, over a short interval of z adjacent to the inlet, is shown in figure 10(b) for the highly non-Boussinesq setting $S = 7$; values beyond this streamwise region could not be obtained with sufficient confidence, due to numerical difficulties. The absolute helical growth rate at $S = 7$ displays the same qualitative characteristics as the one described in Chakravarthy *et al.* (2015) for the Boussinesq limit: the growth rate declines quickly downstream of the inlet, perhaps asymptotically tending towards zero. It is not surprising that under these conditions the weak absolute instability of $m = 1$ perturbations does not lead to a global flow destabilisation, as was found in § 3.2.

6. Conclusions

The linear instability dynamics in spatially developing buoyant jets and plumes have been investigated for a wide range of values of the Richardson number and the fluid density ratio. In the limit of zero Mach number, all variable-density effects have been taken into account in the mathematical formulation, so that configurations outside the realm of validity of the Boussinesq approximation could be considered.

Axisymmetric global instability modes have been found and documented over the entire investigated range of parameters, whereas no helical global instability could be identified. Some doubts remain only in the regime of very high Richardson number, $Ri > 100$, where spurious helical modes could not be entirely stabilised due to numerical limitations. The preponderance of axisymmetric instability is in agreement with experimental observations by Subbarao & Cantwell (1992), Cetegen & Kasper (1996) and Bharadwaj & Das (2017), who reported axisymmetric puffing in free plumes. The present global analysis furthermore reproduces the experimentally measured frequencies with satisfactory accuracy. In particular, the experimental power law $\omega_r \propto (Ri/S)^{0.38}$ has been retrieved as $\omega_r \propto (Ri/S)^{0.43}$ in the present calculations. It is noted that Bharadwaj & Das (2017) found even closer agreement from their linear analysis, which was designed to specifically model helium plumes, as opposed to thermal plumes in the present study.

The physical mechanisms behind global instability have been characterised by means of a sensitivity analysis. As proposed by Marquet & Lesshafft (2015), the sensitivity of the perturbation growth rate with respect to individual terms in the linear equations has been evaluated, which provides a quantitative measure for the stabilising or destabilising role of mechanisms represented by these terms. The main conclusion is that instability in the low-Ri jet regime is caused primarily by a shear mechanism, aided by a baroclinic force that arises from density variations, whereas the instability in the high-Ri plume regime is brought about principally by way of the buoyancy force, with a small contribution from shear. Nothing in the results indicates an abrupt switching between two distinct instability modes; the most unstable mode appears instead to vary smoothly as a function of Ri, with a gradual shift from the dominance of one mechanism to a dominance of the other.

These global results contrast with the conclusions of Chakravarthy *et al.* (2015), on the basis of local analysis in the Boussinesq limit, that the instability dynamics of self-similar plumes are dominated by helical perturbations. In particular, that earlier study showed axisymmetric perturbations to be only convectively unstable, whereas helical perturbations exhibit absolute instability, as well as larger temporal growth at real wavenumbers than axisymmetric modes. The global analysis in the present study was performed on base flows that develop from an orifice with prescribed inlet profiles, and that only relax asymptotically in the streamwise direction towards a self-similar flow solution. Close to the orifice, these base flows are markedly different from self-similar conditions, and this is the flow region where unstable axisymmetric perturbations reside in high-Ri plumes, according to the present results (see figure 4*b*). Global instability in low-Ri buoyant jets has been shown to depend on baroclinic effects, which are absent in the Boussinesq approximation. The Boussinesq framework used by Chakravarthy *et al.* (2015) is therefore inappropriate for an instability analysis in this regime.

It has finally been demonstrated, for selected configurations, that the global instability characteristics are consistent with the absolute or convective nature of local instability. All globally unstable settings in the (Ri, S) plane, with $Re = 200$, feature an absolutely unstable flow region in the vicinity of the inflow. In the examined

cases, the absolute growth rate of axisymmetric perturbations is significantly larger than that of helical perturbations, and it remains positive over a longer streamwise region. Although absolute instability also arises for helical perturbations, it appears to be too weak to set off a global instability.

It must be cautioned that the conclusions drawn from the present results may not be easily extendable to generic plume and jet flows. In particular, the instability characteristics seem to be rather sensitive to details of the inflow profiles: with similar but not identical inflow profiles, axisymmetric perturbations are absolutely unstable in the present settings, but convectively unstable in the configuration of Chakravarthy *et al.* (2015). Test calculations, documented in Chakravarthy (2015), indicate that the functional shape of the density profile has a marked influence on the local stability characteristics, even when the mixing layer thickness is matched. Subbarao & Cantwell (1992) point out, for instance, that helium release and diffusion flames create plumes with very distinct density variations, which therefore may present quite different instability dynamics. It can also not be ruled out that nonlinear effects alter the threshold of global instability (Couairon & Chomaz 1997). The influence of the Prandtl number has not been investigated in this study, but it has been shown by Lakkaraju & Alam (2007) that the instability behaviour of planar plumes undergoes qualitative changes as Pr is varied far from unity.

Acknowledgements

The authors are grateful to W. Coenen for his aid with the adjoint implementation in FreeFEM++, to O. Marquet for his contribution to the sensitivity analysis, and to Professor D. Das for precious comments on the comparison with experiments. This work has been funded by the DGA under grant no. LADX2331 and by the Agence Nationale de la Recherche under the 'Cool Jazz' project. R.V.K.C. was supported by a PhD fellowship from École Polytechnique.

Appendix A. Differential operator definitions for azimuthally decomposed field quantities

The operators for divergence, gradient, Laplacian and advection in cylindrical coordinates in equations (2.11) are written with a subscript m. This is meant to express that azimuthal derivatives of perturbations (2.10) are included in these operators in the form of terms in m, such that formally

$$\mathrm{grad}\,(\hat{\boldsymbol{u}}\,\mathrm{e}^{\mathrm{i}m\theta}) = (\mathrm{grad}_m\hat{\boldsymbol{u}})\,\mathrm{e}^{\mathrm{i}m\theta}, \tag{A 1a}$$

$$\mathrm{div}\,(\hat{\boldsymbol{u}}\,\mathrm{e}^{\mathrm{i}m\theta}) = (\mathrm{div}_m\hat{\boldsymbol{u}})\,\mathrm{e}^{\mathrm{i}m\theta}, \tag{A 1b}$$

$$\Delta(\hat{\boldsymbol{u}}\,\mathrm{e}^{\mathrm{i}m\theta}) = (\Delta_m\hat{\boldsymbol{u}})\,\mathrm{e}^{\mathrm{i}m\theta}, \tag{A 1c}$$

and accordingly for all other flow variables. All relevant terms from the (2.11) are written out below for the sake of completeness:

$$\mathrm{div}_m(\hat{\rho}\overline{\boldsymbol{u}} + \overline{\rho}\boldsymbol{u}) = \frac{1}{r}\partial_r(r\hat{\rho}\overline{u}_r + r\overline{\rho}\hat{u}_r) + \frac{\mathrm{i}m}{r}\overline{\rho}\hat{u}_\theta + \partial_z(\hat{\rho}\overline{u}_z + \overline{\rho}\hat{u}_z), \tag{A 2}$$

$$(\mathrm{grad}_m\overline{\boldsymbol{u}})\cdot\hat{\boldsymbol{u}} = [\hat{u}_r\partial_r\overline{u}_r + \hat{u}_z\partial_z\overline{u}_r]\boldsymbol{e}_r + \frac{\hat{u}_\theta\overline{u}_r}{r}\boldsymbol{e}_\theta + [\hat{u}_r\partial_r\overline{u}_z + \hat{u}_z\partial_z\overline{u}_z]\boldsymbol{e}_z, \tag{A 3}$$

$$\begin{aligned}(\mathrm{grad}_m\hat{\boldsymbol{u}})\cdot\overline{\boldsymbol{u}} \;=\; & [\overline{u}_r\partial_r\hat{u}_r + \overline{u}_z\partial_z\hat{u}_r]\boldsymbol{e}_r + [\overline{u}_r\partial_r\hat{u}_\theta + \overline{u}_z\partial_z\hat{u}_\theta]\boldsymbol{e}_\theta \\ & + [\overline{u}_r\partial_r\hat{u}_z + \overline{u}_z\partial_z\hat{u}_z]\boldsymbol{e}_z,\end{aligned} \tag{A 4}$$

$$(\mathrm{grad}_m \overline{T}) \cdot \hat{\boldsymbol{u}} = \hat{u}_r \partial_r \overline{T} + \hat{u}_z \partial_z \overline{T} \tag{A 5}$$

$$(\mathrm{grad}_m \hat{T}) \cdot \overline{\boldsymbol{u}} = \overline{u}_r \partial_r \hat{T} + \overline{u}_z \partial_z \hat{T}, \tag{A 6}$$

$$\mathrm{grad}_m \hat{p} = \partial_r \hat{p}\, \boldsymbol{e}_r + \frac{\mathrm{i}m}{r} \hat{p}\, \boldsymbol{e}_\theta + \partial_z \hat{p}\, \boldsymbol{e}_z, \tag{A 7}$$

$$\begin{aligned} \mathrm{grad}_m(\mathrm{div}_m \hat{\boldsymbol{u}}) \;=\; & \left[\partial_r \frac{\partial_r (r\hat{u}_r)}{r} - \frac{2\mathrm{i}m}{r^2} \hat{u}_\theta + \frac{\mathrm{i}m}{r} \partial_r \hat{u}_\theta + \partial_{rz} \hat{u}_z \right] \boldsymbol{e}_r \\ & + \frac{1}{r} \left[\mathrm{i}m \partial_r \hat{u}_r + \frac{\mathrm{i}m}{r} \hat{u}_r - \frac{m^2}{r} \hat{u}_\theta + \mathrm{i}m \partial_z \hat{u}_z \right] \boldsymbol{e}_\theta \\ & + \left[\partial_{rz} \hat{u}_r + \frac{\partial_z \hat{u}_r}{r} + \frac{\mathrm{i}m}{r} \partial_z \hat{u}_\theta + \partial_{zz} \hat{u}_z \right] \boldsymbol{e}_z, \end{aligned} \tag{A 8}$$

$$\begin{aligned} \Delta_m \hat{\boldsymbol{u}} \;=\; & \left[\partial_r \frac{\partial_r (r\hat{u}_r)}{r} - \frac{m^2}{r^2} \hat{u}_r + \partial_{zz} \hat{u}_r - \frac{2\mathrm{i}m}{r^2} \hat{u}_\theta \right] \boldsymbol{e}_r \\ & + \left[\partial_r \frac{\partial_r (r\hat{u}_\theta)}{r} - \frac{m^2}{r^2} \hat{u}_\theta + \partial_{zz} \hat{u}_\theta + \frac{2\mathrm{i}m}{r^2} \hat{u}_r \right] \boldsymbol{e}_\theta \\ & + \left[\frac{\partial_r (r \partial_r \hat{u}_z)}{r} - \frac{m^2}{r^2} \hat{u}_z + \partial_{zz} \hat{u}_z \right] \boldsymbol{e}_z, \end{aligned} \tag{A 9}$$

$$\Delta_m \hat{T} = \frac{\partial_r (r \partial_r \hat{T})}{r} - \frac{m^2}{r^2} \hat{T} + \partial_{zz} \hat{T}. \tag{A 10}$$

REFERENCES

Åkervik, E., Ehrenstein, U., Gallaire, F. & Henningson, D. 2008 Global two-dimensional stability measures of the flat plate boundary-layer flow. *Eur. J. Mech. (B/Fluids)* **27**, 1–13.

Bharadwaj, K. & Das, D. 2017 Global instability analysis and experiments of buoyant plumes. *J. Fluid Mech.* **832**, 97–145.

Boujemaa, S., Amielh, M. & Chauve, M. P. 2004 Analyse spatio-temporelle de jets axisymétriques d'air et d'hélium. *C. R. Méc.* **332** (11), 933–939.

Cetegen, B. M. & Kasper, K. D. 1996 Experiments on the oscillatory behavior of buoyant plumes of helium and helium-air mixtures. *Phys. Fluids* **8** (11), 2974–2984.

Chakravarthy, R. V. K. 2015 Local and global instabilities in buoyant jets and plumes. PhD thesis, École Polytechnique, Palaiseau, France.

Chakravarthy, R. V. K., Lesshafft, L. & Huerre, P. 2015 Local linear stability of laminar axisymmetric plumes. *J. Fluid Mech.* **780**, 344–369.

Chandler, G. J. 2010 Sensitivity analysis of low density jets and flames. PhD thesis, University of Cambridge, Cambridge, UK.

Chomaz, J.-M. 2003 Fully nonlinear dynamics of parallel wakes. *J. Fluid Mech.* **495**, 57–75.

Chomaz, J. M., Huerre, P. & Redekopp, L. G. 1991 A frequency selection criterion in spatially developing flows. *Stud. Appl. Maths* **84** (2), 119–144.

Coenen, W., Lesshafft, L., Garnaud, X. & Sevilla, A. 2017 Global instability of low-density jets. *J. Fluid Mech.* **820**, 187–207.

Colonius, T. 2004 Modeling artificial boundary conditions for compressible flow. *Annu. Rev. Fluid Mech.* **36**, 315–345.

Couairon, A. & Chomaz, J. M. 1997 Absolute and convective instabilities, front velocities and global modes in nonlinear systems. *Physica* D*: Nonlinear Phenomena.* **108** (3), 236–276.

GARNAUD, X., LESSHAFFT, L., SCHMID, P. J. & HUERRE, P. 2013 Modal and transient dynamics of jet flows. *Phys. Fluids* **25** (4), 044103.

HALLBERG, M. P. & STRYKOWSKI, P. J. 2006 On the universality of global modes in low-density axisymmetric jets. *J. Fluid Mech.* **569**, 493–507.

HUERRE, P. & MONKEWITZ, P. A. 1990 Local and global instabilities in spatially developing flows. *Annu. Rev. Fluid Mech.* **22** (1), 473–537.

JIANG, X. & LUO, K. H. 2000 Direct numerical simulation of the puffing phenomenon of an axisymmetric thermal plume. *Theor. Comput. Fluid Dyn.* **14**, 55–74.

KHORRAMI, M. R., MALIK, M. R. & ASH, R. L. 1989 Application of spectral collocation techniques to the stability of swirling flows. *J. Comput. Phys.* **81**, 206–229.

LAKKARAJU, R. & ALAM, M. 2007 Effects of Prandtl number and a new instability mode in a plane thermal plume. *J. Fluid Mech.* **592**, 221–231.

LESSHAFFT, L. 2015 Linear global stability of a confined plume. *Theoret. Appl. Mech. Lett.* **5** (3), 126–128.

LESSHAFFT, L. 2017 Artificial eigenmodes in truncated flow domains. Preprint, arXiv:1704.08450.

LESSHAFFT, L. & HUERRE, P. 2007 Linear impulse response in hot round jets. *Phys. Fluids* **19** (2), 024102.

LESSHAFFT, L., HUERRE, P. & SAGAUT, P. 2007 Frequency selection in globally unstable round jets. *Phys. Fluids* **19**, 054108.

LESSHAFFT, L., HUERRE, P., SAGAUT, P. & TERRACOL, M. 2006 Nonlinear global modes in hot jets. *J. Fluid Mech.* **554**, 393–409.

LESSHAFFT, L. & MARQUET, O. 2010 Optimal velocity and density profiles for the onset of absolute instability in jets. *J. Fluid Mech.* **662**, 398–408.

LOPEZ, J. M. & MARQUES, F. 2013 Instability of plumes driven by localized heating. *J. Fluid Mech.* **736**, 616–640.

MARQUET, O. & LESSHAFFT, L. 2015 Identifying the active flow regions that drive linear and nonlinear instabilities. Preprint, arXiv:1508.07620.

MCMURTRY, P. A., JOU, W. H., RILEY, J. J. & METCALFE, R. W. 1986 Direct numerical simulations of a reacting mixing layer with chemical heat release. *AIAA J.* **24** (6), 962–970.

MOLLENDORF, J. C. & GEBHART, B. 1973 An experimental and numerical study of the viscous stability of a round laminar vertical jet with and without thermal buoyancy for symmetric and asymmetric perturbations. *J. Fluid Mech.* **61** (2), 367–399.

MONKEWITZ, P. A., BECHERT, D. W., BARSIKOW, B. & LEHMANN, B. 1990 Self-excited oscillations and mixing in a heated round jet. *Phys. Fluids* **213**, 611–639.

MONKEWITZ, P. A. & SOHN, K. 1988 Absolute instability in hot jets. *AIAA J.* **26**, 911–916.

NICHOLS, J. W., SCHMID, P. J. & RILEY, J. J. 2007 Self-sustained oscillations in variable-density round jets. *J. Fluid Mech.* **582**, 341–376.

RILEY, D. S. & TVEITEREID, M. 1984 On the stability of an axisymmetric plume in a uniform flow. *J. Fluid Mech.* **142**, 171–186.

SATTI, R. P. & AGRAWAL, A. K. 2006 Computational analysis of gravitational effects in low-density gas jets. *AIAA* **44** (7), 1505–1515.

SCHMID, P. J. & HENNINGSON, D. S. 2001 *Stability and Transition in Shear Flows*, Applied Mathematical Sciences, vol. 142. Springer.

SREENIVASAN, K. R., RAGHU, S. & KYLE, D. 1989 Absolute instability in variable density round jets. *Exp. Fluids* **213**, 309–317.

SUBBARAO, E. R. & CANTWELL, B. J. 1992 Investigation of a co-flowing buoyant jet: experiments on the effect of Reynolds number and Richardson number. *J. Fluid Mech.* **245**, 69–90.

THEOFILIS, V. 2003 Advances in global linear instability analysis of nonparallel and three-dimensional flows. *Prog. Aero. Sci.* **39** (4), 249–315.

TRITTON, D. J. 2012 *Physical Fluid Dynamics*. Springer Science & Business Media.

WAKITANI, S. 1980 The stability of a natural convection flow above a point heat source. *J. Phys. Soc. Japan* **49** (6), 2392–2399.

YIH, C. S. 1988 *Fluid Mechanics*. West River Press.

Artificial eigenmodes in truncated flow domains

Lutz Lesshafft

July 16, 2018

Abstract Whenever linear eigenmodes of open flows are computed on a numerical domain that is truncated in the streamwise direction, artificial boundary conditions may give rise to spurious pressure signals that are capable of providing unwanted perturbation feedback to upstream locations. The manifestation of such feedback in the eigenmode spectrum is analysed here for two simple configurations. First, explicitly prescribed feedback in a Ginzburg–Landau model is shown to produce a spurious eigenmode branch, named the 'arc branch', that strongly resembles a characteristic family of eigenmodes typically present in open shear flow calculations. Second, corresponding mode branches in the global spectrum of an incompressible parallel jet in a truncated domain are examined. It is demonstrated that these eigenmodes of the numerical model depend on the presence of spurious forcing of a local k^+ instability wave at the inflow, caused by pressure signals that appear to be generated at the outflow. Multiple local k^+ branches result in multiple global eigenmode branches. For the particular boundary treatment chosen here, the strength of the pressure feedback from the outflow towards the inflow boundary is found to decay with the cube of the numerical domain length. It is concluded that arc-branch eigenmodes are artifacts of domain truncation, with limited value for physical analysis. It is demonstrated, for the example of a non-parallel jet, how spurious feedback may be reduced by an absorbing layer near the outflow boundary.

1 Introduction

Linear instability analysis of open flows today is commonly carried out in a so-called 'global' framework, where at least two non-homogeneous spatial directions of a steady base state are numerically resolved. In contrast to 'local' analysis, where the base state is assumed to be parallel, and unbounded in the flow direction, a global discretisation of an open flow problem in a truncated numerical domain necessitates the formulation of artificial streamwise boundary conditions for flow perturbations. The question then arises in how far such boundary conditions influence the instability dynamics of the truncated flow system.

This paper investigates the effect of spurious pressure feedback, due to domain truncation, on the eigenmode spectrum of incompressible open flow problems. The investigation is motivated by observations made in recent linear instability studies of jet flows [12, 7], where a prominent family of eigenmodes (black symbols in Fig. 1), referred to as the 'arc branch' from here on, was found to present features that suggest a resonance between the inflow and outflow boundaries. Such branches are in fact ubiquitous in many, if not all, global spectra of truncated open shear flows found in the literature: boundary layers [10, 11, 1], cylinder wakes [24, 20], jets [22, 12], plumes [4], three-dimensional boundary layers with roughness elements [19, 17] — all these and many others present similar characteristic branches of eigenvalues that are often described as being highly dependent on the type or position of outflow boundary conditions. Typically, no convergence with respect to the length of the numerical box can be attained for such modes.

Ehrenstein & Gallaire [10] remark on the resemblance between arc-branch-type global eigenmode structures obtained for a flat-plate boundary layer and spatial modes as found in a local analysis. Åkervik *et al.* [1] document the dependence of boundary layer eigenvalues on the type of outflow boundary conditions. Heaton *et al.* [13] characterise arc branch modes in the spectrum of a Batchelor vortex as artifacts, speculating that

Laboratoire d'Hydrodynamique, CNRS/École polytechnique, 91128 Palaiseau, France
E-mail: lesshafft@ladhyx.polytechnique.fr

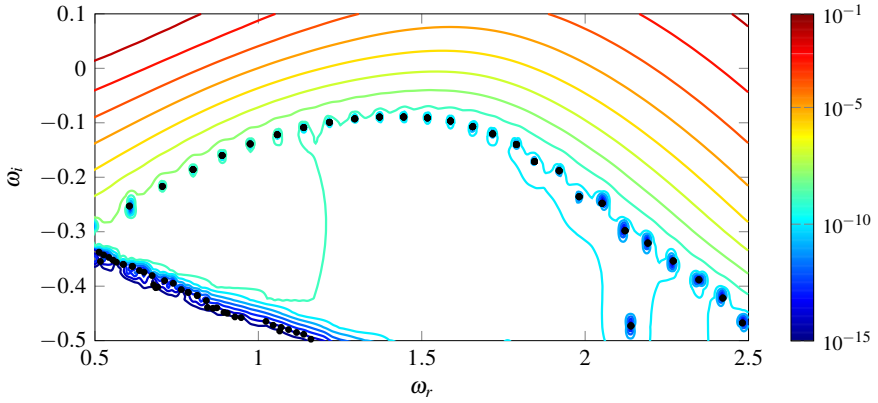

Fig. 1 Spectrum and pseudospectrum of a jet at $Re = 1000$, showing a typical arc branch. Eigenmodes are drawn as black symbols. The definition of ε values, shown as colour contours, is given in Sect. 2. The figure is made from the data of Coenen *et al.* [7].

these arise from the limited precision of their numerical scheme, not from domain truncation. Cerqueira & Sipp [3] demonstrate that such precision errors indeed lead to spurious 'quasi-eigenmodes', but that these differ from the arc branch. In their analysis, quasi-eigenmodes appear in regions of the complex frequency plane where pseudospectrum ε values [25] are very small, below approximately 10^{-12}. These modes, also visible in the lower left corner of Fig. 1, are very sensitive to the numerical scheme, to mesh refinement and to the eigenvalue shift parameter. Arc branch modes are found to be robust with respect to those details[3], but strongly dependent on the numerical domain length. Coenen *et al.*[7] show that arc branch eigenfunctions of a jet are characterised by an integer number of wavelengths between the inflow and outflow boundaries, and they suggest an analogy with acoustic modes in a pipe of finite length. This analogy implies that arc branch modes are the result of unwanted resonance between the numerical boundaries, potentially leading to a spurious instability of the numerical system. The present study expands on all these observations, and it aims at a detailed characterisation of unphysical resonance due to imperfect boundary conditions in open shear flow calculations.

The possibility that global instability in truncated systems may be brought about by spurious pressure feedback from boundary conditions was probably first described by Buell & Huerre[2]. In direct numerical simulations of perturbations in a mixing layer, unstable perturbation growth was observed at long times, in a configuration that was only convectively unstable in a local sense. Such behaviour is inconsistent with the interpretation of local convective instability, and it was demonstrated to be caused by unphysical pressure perturbations emanating from the outflow boundary, which in turn provoked the formation of vortical perturbations at the inflow boundary. Chomaz [5, section 3.2.2] interprets pressure feedback as a non-local operator variation, arguing that strong non-normality in the spectrum of convection-dominated flows is likely to induce a high sensitivity of global eigenmodes with respect to such feedback.

While the spurious generation of acoustic pressure waves from artificial boundary conditions is an important and much-discussed problem in compressible flow simulations, especially those that aim to accurately capture the acoustic radiation from shear flows [8], the question of how such artifacts may affect the global stability behaviour remains largely unexplored, both in compressible and in incompressible configurations.

The problem is approached here in the following manner. Section 2 presents a global instability analysis of the Ginzburg–Landau equation with explicit feedback from a downstream sensor to an upstream actuator, in order to examine the effect of such feedback on the eigenvalue spectrum in a controlled setting. This model study fully describes the suspected mechanism behind arc branch modes. In Sect. 3 the analysis is extended to a parallel jet flow in a finite-size numerical domain. Global eigenmodes are projected onto their local counterparts, the global pressure field is examined, and spurious feedback effects are analysed. The question how spurious feedback may be reduced in a practical manner is addressed in Sect. 4, for the example of a spatially developing jet.

2 A Ginzburg–Landau model problem

The hypothesis put forward by Coenen *et al.*[7], that the arc branch may be the manifestation of a non-physical upstream scattering of perturbations from the outflow boundary, is first investigated with the help of a simpli-

fied model. The linear Ginzburg–Landau equation is written as

$$\partial_t \psi = -U\partial_x \psi + \mu(x)\psi + \gamma\partial_{xx}\psi + f(x,\psi)\,. \tag{1}$$

The complex scalar variable $\psi(x,t)$ is a function of time t and of one single spatial coordinate x. Constant parameters $U = 6$ and $\gamma = 1 - \mathrm{i}$ are chosen *ad hoc*, whereas the coefficient μ varies linearly in x as

$$\mu(x) = \frac{U^2}{8}\left(1 - \frac{x}{20}\right). \tag{2}$$

With this particular variation of μ, the system is marginally absolutely unstable at $x = 0$, convectively unstable for $0 < x < 20$, and stable for $x > 20$, all in a local sense. Ginzburg–Landau systems of this form, with linearly decreasing $\mu(x)$ and without feedback, $f \equiv 0$, have been extensively used to model the global instability behaviour of spatially developing flows in semi-infinite domains [see for instance 9]. The instability characteristics mimic, in a very simple and qualitative manner, those of a spreading jet. However, the system (1) is not intended here to predict or reproduce the dynamics of any specific flow.

A forcing term $f(x,\psi)$ is added in (1) in order to provide an explicit closed-loop forcing between the upstream and the downstream end of the flow domain. Some aspects of closed-loop forcing in the Ginzburg–Landau equation are discussed by Chomaz [5]; in the present context, it is used to model a suspected spurious feedback in global shear flow computations. Taken to be of the form

$$f(x,\psi) = C\exp\left(-\frac{(x-x_a)^2}{0.1^2}\right)\psi(x_s), \tag{3}$$

a forcing proportional to $\psi(x_s)$ is applied in a close vicinity of x_a, such that a feedback loop is established between a (downstream) sensor location x_s and an (upstream) actuator location x_a. The complex coefficient C governs the amplitude and phase of the feedback, and the Gaussian spreading around x_a is introduced for reasons of numerical resolution.

Equation (1) is discretised on an interval $0 \leqslant x \leqslant 40$, with a step size $\Delta x = 0.1$, using an upwind-biased seven-point finite difference stencil for the spatial derivatives. A homogeneous Dirichlet boundary condition for ψ is imposed at the upstream boundary, consistent with typical jet conditions. Actuator and sensor locations are chosen close to the boundaries, at $x_a = 1$ and $x_s = 39$, where spatial derivatives are well resolved.

Temporal eigenmodes of (1) are sought in the form $\psi(x,t) = \hat{\psi}(x)\,\mathrm{e}^{-i\omega t}$. The eigenvalues of the system without feedback, $C = 0$, are known analytically to be

$$\omega_n = i\left\{\frac{U^2}{8} - \frac{U^2}{4\gamma} + \gamma^{\frac{1}{3}}\frac{U^{\frac{4}{3}}}{160^{\frac{2}{3}}}\zeta_n\right\}, \tag{4}$$

where ζ_n is the n^{th} root of the Airy function [6]. These values are represented in Fig. 2 as circles. Each frame 2(*a–d*) also displays the numerically computed eigenvalues of systems with feedback, shown as bullet symbols, for different non-zero values of the coefficient C. Already with very low-level feedback, $C = 10^{-10}$, the spectrum is clearly affected: only the leading three eigenvalues of the unforced system are recovered, and the lower part of the spectrum is replaced with two new stable branches. These branches, named *feedback branches* in the following, move upward in the complex ω plane as the feedback coefficient is increased, masking more and more of the original unforced eigenvalues. Note that those affected original eigenvalues are not merely altered by the feedback, but they rather disappear abruptly from the spectrum as they fall below the new branches.

The spectra obtained with $C = 10^{-6}$ and 10^{-2} resemble those of pure helium jets, as shown in figure 6 of [7], and those of cylinder wakes obtained by Marquet *et al.*[20, their figure 16]. The least stable original eigenvalue lies just above the feedback branches, apparently unaffected. In the strongest feedback case, $C = 10^2$, the feedback branches have merged into one, overarching the entire spectrum of the feedback-free system, which has altogether disappeared. This picture (Fig. 2*d*) resembles the spectrum of the slowly developing jet of Coenen *et al.*[7], reproduced in our Fig. 1.

The similarity between the feedback branches in the present model and the arc branch in the jet spectrum (Fig. 1) is also manifest in the pseudospectra. If feedback is thought of as a variation of the operator [5], it should be possible to relate feedback-induced eigenvalues to the pseudospectrum. The pseudospectrum is defined here by the spectral norm of the resolvent operator,

$$\partial_t \psi = \mathbf{L}\psi \quad \rightarrow \quad \|(\mathrm{i}\omega\mathbf{I} + \mathbf{L})^{-1}\| = \varepsilon^{-1}, \tag{5}$$

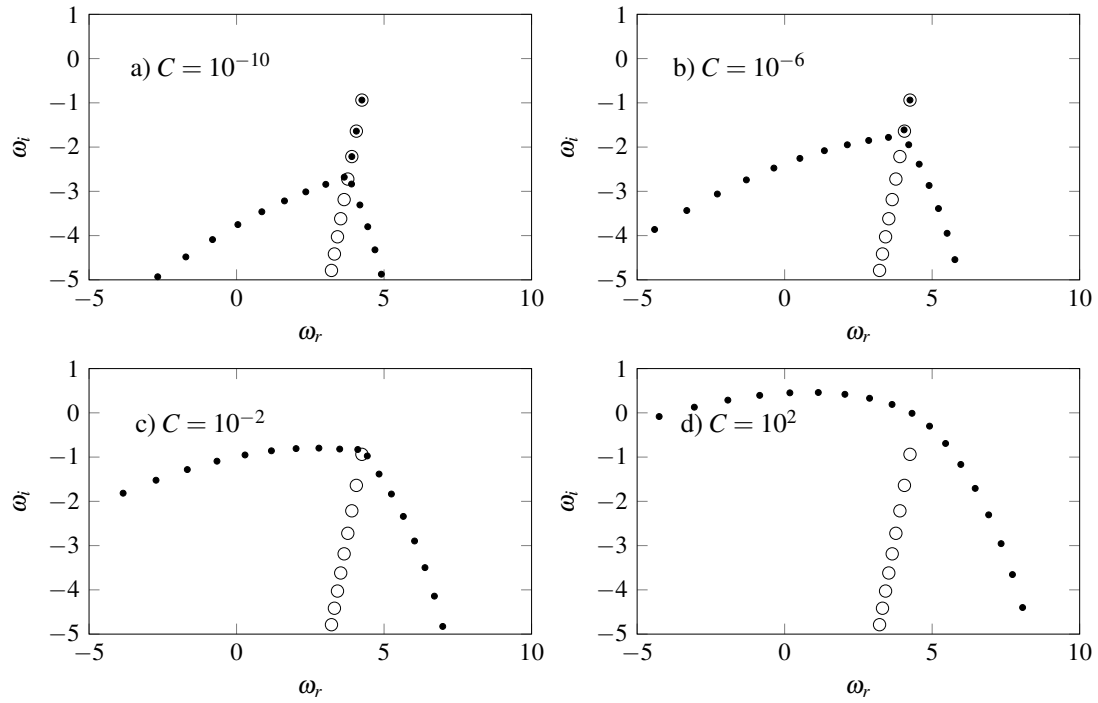

Fig. 2 Spectra of the Ginzburg–Landau equation (1) with various feedback coefficients C. Eigenvalues with closed-loop feedback (•), and analytical eigenvalues (4) of the case without feedback (○).

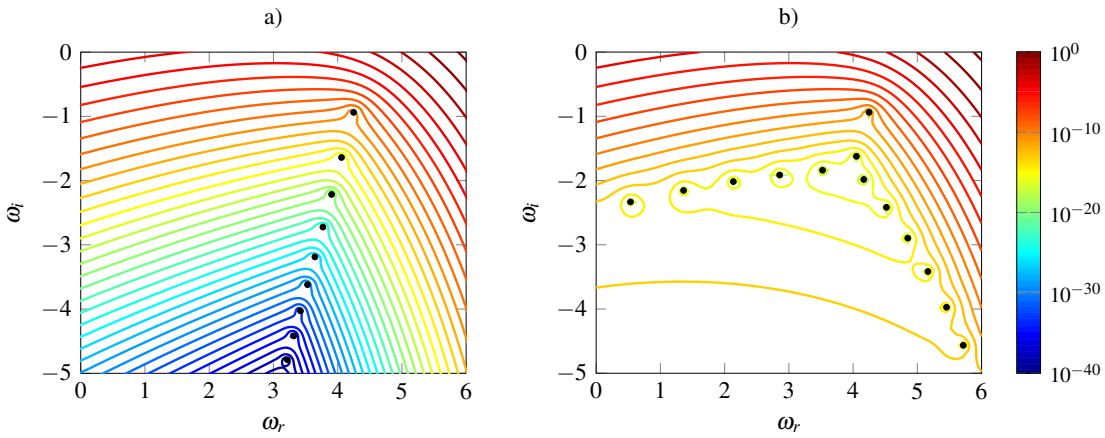

Fig. 3 Pseudospectra of the Ginzburg–Landau equation; (*a*) without feedback, $C = 0$, and (*b*) with feedback, $C = 10^{-6}$. Contours of ε, defined in (5), are represented in logarithmic colour scale.

at any complex frequency ω [25]. Pseudospectrum ε-contours of the Ginzburg–Landau equation are compared between the unforced setting with $C = 0$, Fig. 3(*a*), and the forced setting with $C = 10^{-6}$, Fig. 3(*b*). It is seen that the feedback branches align closely with an isocontour of the feedback-free pseudospectrum. This criterion also applies to all other cases displayed in Fig. 2, with different values of C, and it is fully consistent with observations made in three flow configurations [13, 3, 7]. Furthermore, the pseudospectrum of the system with feedback is identical to that of the system without feedback *above* the feedback branches, whereas the pseudospectrum is flattened, nearly constant, *below* the feedback branches. The same behaviour is found in the jet pseudospectrum shown in Fig. 1.

Finally, the discrete distribution of feedback modes along the branch is investigated. The strong feedback case $C = 10^2$ is considered for illustration. Eigenfunctions of successive feedback modes are presented in figure 4, analogous to the representation of jet results in figure 5 of [7]. The absolute value of ψ is traced in logarithmic scale as a function of x. The phase of ψ is always chosen such that the real part of ψ is zero in the

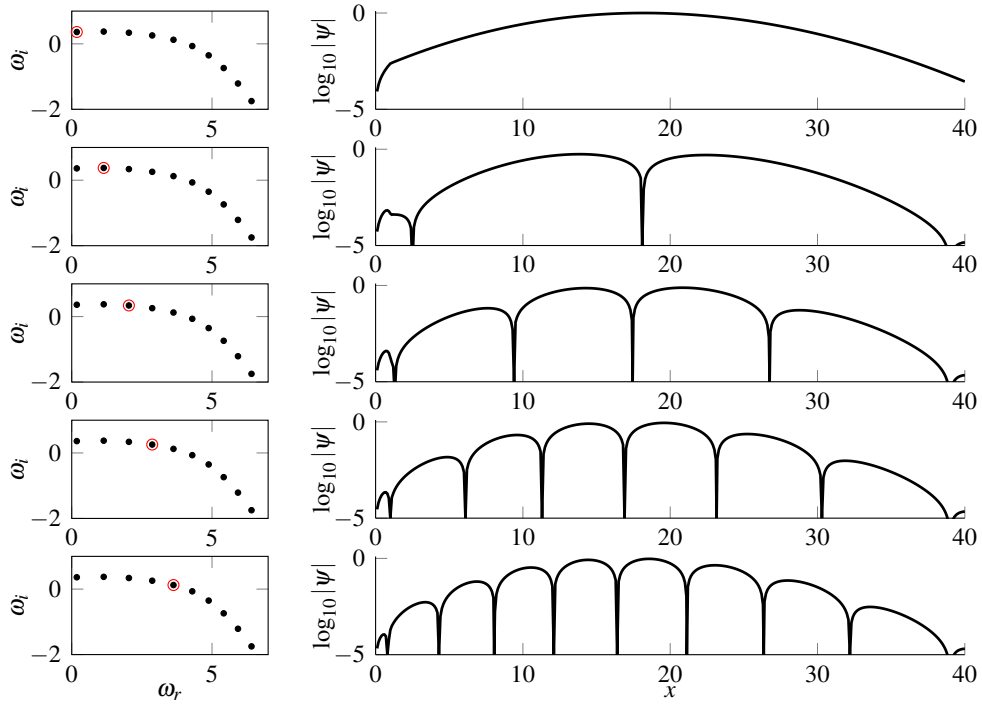

Fig. 4 Eigenfunctions of the feedback branch for $C = 10^2$. Left column: position of the eigenvalue in the spectrum; right column: corresponding eigenfunction $\log_{10}|Re(\psi)|$ along x. Zero wavelengths are present in the top frame, one in the second, and so forth up to four wavelengths in the bottom frame. The series continues further along the branch.

sensor location $x_s = 39$, with the exception of the first mode (Fig. 4*a*), which has no interior wave nodes. Only positive real frequencies are considered.

Clearly, the eigenfunctions are characterised by integer numbers of wavelengths between the actuator and sensor locations, starting from zero wavelengths in the case of the lowest real frequency (Fig. 4*a*, only amplitude variations but approximately constant phase), to one wavelength in Fig. 4(*b*), and so forth with a continuously increasing count. The series could be continued further along the entire arc branch. The present model seems to reproduce very well the characteristics of arc branch eigenfunctions, as displayed in figure 5 of [7].

The position and spacing of eigenvalues along the branch curve, fixed approximately by an isocontour of the pseudospectrum, appears to be determined by a fitting phase relation between ψ at the actuator location and the applied feedback. To further illustrate this mechanism, the phase of the feedback coefficient C is varied. Figure 5 shows the arc branch as it is obtained with values $C = 10^2$ (bullets, same as before), $C = 10^2\mathrm{i}$ (crosses), $C = -10^2$ (plus signs) and $C = -10^2\mathrm{i}$ (squares). All symbols fall onto the same curve, confirming that the position of feedback eigenmodes, which represent singularities in the pseudospectrum, is fixed by the phase of the feedback relation, such that resonance can occur between both ends of the loop.

3 A parallel jet

The effect that imperfect numerical boundary conditions can have on eigenmode computations in a two-dimensional flow domain is now investigated for the case of axisymmetric perturbations in a parallel round jet, governed by the incompressible axisymmetric Navier–Stokes equations,

$$0 = \partial_r u_r + \frac{u_r}{r} + \partial_x u_x, \tag{6a}$$

$$\partial_t u_r = -u_r\partial_r u_r - u_x\partial_x u_r - \partial_r p + \frac{1}{Re}\left(\partial_{rr}u_r + \frac{\partial_r u_r}{r} - \frac{u_r}{r^2} + \partial_{xx}u_r\right), \tag{6b}$$

$$\partial_t u_x = -u_r\partial_r u_x - u_x\partial_x u_x - \partial_x p + \frac{1}{Re}\left(\partial_{rr}u_x + \frac{\partial_r u_x}{r} + \partial_{xx}u_x\right). \tag{6c}$$

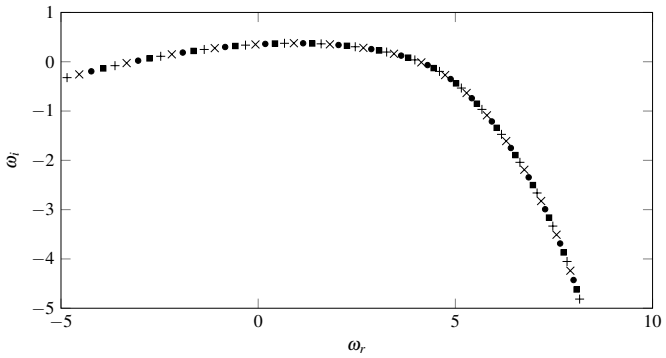

Fig. 5 Eigenvalues of the feedback branch for $|C| = 10^2$ with varying phase: (•) $C = 10^2$, (×) $C = 10^2\mathrm{i}$, (+) $C = -10^2$, (■) $C = -10^2\mathrm{i}$.

Boundary conditions are prescribed as

$$u_r = u_x = 0 \quad \text{at } x = 0, \tag{7a}$$

$$Re^{-1}\partial_x u_x - p = 0 \quad \text{at } x = x_{max}, \tag{7b}$$

$$u_r = \partial_r u_x = 0 \quad \text{at } r = 0 \text{ and } r = r_{max}. \tag{7c}$$

The stress-free outflow condition is a common and convenient choice for finite-element computations. Jet radius and centreline velocity are the dimensional length scales in this formulation, and the Reynolds number is chosen as $Re = 100$.

The advantage of using a parallel base flow profile is that the global results can be rigorously compared with local instability properties. The standard analytical model of Michalke [21] is adopted,

$$U(r) = \frac{1}{2}\left(1 + \tanh\left[\frac{1}{4\theta}\left(\frac{1}{r} - r\right)\right]\right), \tag{8}$$

and a momentum thickness $\theta = 0.1$ is chosen for this example.

The axisymmetric perturbation equations that follow from linearization of (6) about the base flow (8) are discretized with finite elements on a domain of length $x_{max} = 20$ and radial extent $r_{max} = 50$, using the FreeFEM++ software. This domain is resolved with 80 equidistant elements in x, and with 360 non-equidistant elements in r. The equations are solved for eigenmodes $[u_r, u_x, p]^T(r,x,t) = [\hat{u}_r, \hat{u}_x, \hat{p}]^T(r,x)\exp(-\mathrm{i}\omega t)$, where the eigenvalue $\omega = \omega_r + \mathrm{i}\omega_i$ contains the angular frequency ω_r and the temporal growth rate ω_i.

The global spectrum is shown in Fig. 6. It features a clean upper arc branch (red) with maximum growth rate at $\omega_1 = 1.111 - 0.052\mathrm{i}$. This mode, labelled '1', is chosen for further analysis. A lower branch (blue) is also present, from which the mode labelled '2' with $\omega_2 = 0.912 - 1.211\mathrm{i}$ will be examined. Similar lower branches are visible in wake spectra [24] and in boundary-layer calculations [1].

3.1 Projection onto local instability modes

For comparison, the corresponding local instability problem, for a domain of infinite extent $x \in (-\infty, \infty)$, is solved with a standard Chebyshev collocation technique on a staggered grid [16], using a coordinate transformation adapted for jet profiles [18]. Identical radial collocation point distributions are used in the global and local computations, such as to eliminate the need for interpolation. Consistent boundary conditions (7c) are imposed in the local problem.

Spatial local instability modes are computed for the ω values corresponding to the global modes labelled in Fig. 6. The flow is convectively unstable, with an absolute frequency $\omega_0 = 1.074 - 0.286\mathrm{i}$. Both direct and adjoint modes are solved for. The adjoint local modes represent the dual basis associated with the set of direct modes, and they serve for projecting the spatial structure of the global mode onto the local direct modes.

This projection is carried out in the following way, similar to the procedure used by Rodríguez *et al.*[23]: at a given streamwise station x, the radial variations of the global mode perturbation quantities are extracted. Since the eigenvector of the spatial local problem contains auxiliary variables $k\hat{u}_r$ and $k\hat{u}_x$ [see 18], these must also be added to the extracted slice of the global mode. This is accomplished by computing the streamwise derivative of the global $\hat{u}_r$ and $\hat{u}_x$ fields, and by augmenting the extracted vector $[\hat{u}_r, \hat{u}_x, \hat{p}]^T$ with $[-\mathrm{i}\partial_x\hat{u}_r, -\mathrm{i}\partial_x\hat{u}_x$

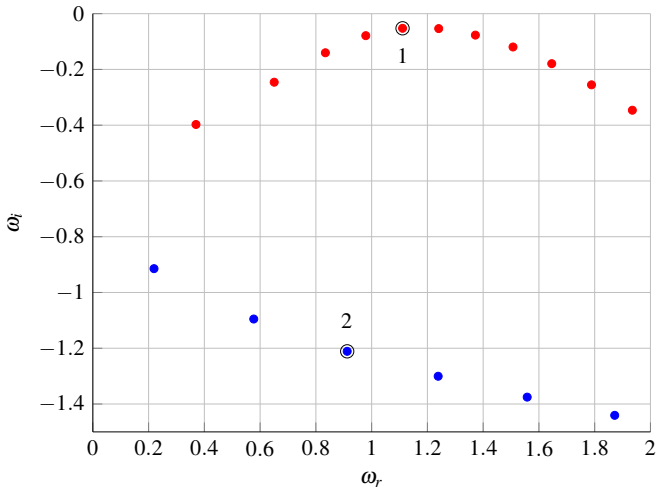

Fig. 6 Spectrum of the parallel jet in a finite domain with inflow and outflow boundary conditions. Red: arc branch; blue: lower branch. Labelled modes are discussed in the following.

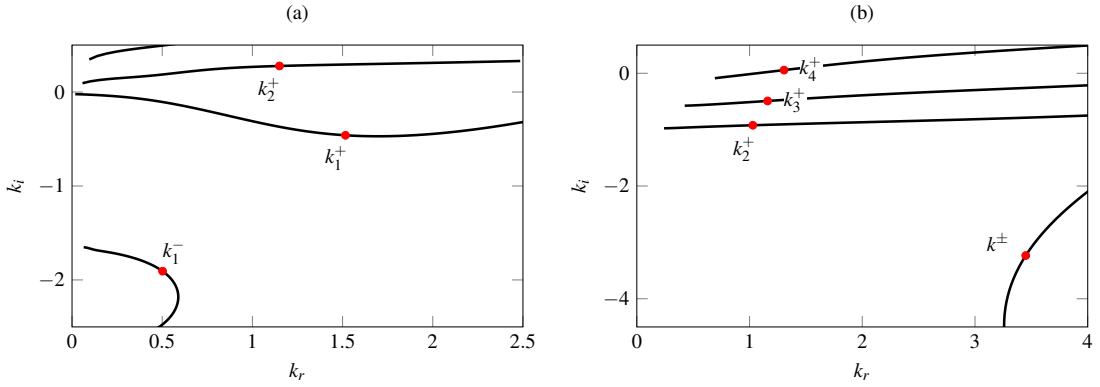

Fig. 7 Spatial eigenvalues from a local analysis of the parallel jet. Lines represent branches obtained by varying the real part of the frequency. *a*) global mode 1: $\omega = 1.111 - 0.052\mathrm{i}$; *b*) global mode 2: $\omega = 0.912 - 1.211\mathrm{i}$.

This augmented global slice is finally projected onto the local modes, via scalar multiplication with the associated adjoint modes. As usual, the adjoint modes are normalised beforehand in such a way that their scalar product with the associated direct mode is unity, whereas the direct modes are by themselves scaled to have unit norm.

The spatial local spectrum of the parallel jet profile, shown in Fig. 7 for the frequency values of global modes 1 and 2, is composed of discrete k^+ and k^- modes [15], which represent downstream- and upstream-propagating hydrodynamic perturbations inside and near the jet. The labels in Fig. 7 rank all k^+ and k^- modes according to their spatial growth rate $-k_i$.

Figure 8 displays absolute values of the projection coefficients, obtained for global mode 1, pertaining to the three dominant local modes. These are the first two k^+ modes and the first k^- mode. Blue symbols represent the k_1^+ mode (the only one displaying unstable spatial growth). Except very near the Dirichlet inlet, the streamwise variation of this local mode amplitude is perfectly exponential, with a spatial growth rate 0.4604, as measured by a regression fit over $1 \leqslant x \leqslant 19$. This value matches within 0.01% the imaginary part of the local eigenvalue. The amplitude of the global mode component $\hat{u}_x$ on the jet centerline is shown as a black line for reference.

Green symbols in Fig. 8 denote the amplitude of k_2^+, and red symbols the amplitude of k_1^-. Straight lines indicate the corresponding growth rate of the local eigenvalue for comparison. It is seen that both projections follow the amplitude variations expected from local analysis in a region close to one boundary, where their amplitude is maximal. Clearly, the k_2^+ mode originates at the upstream boundary, whereas the k_1^- mode is forced at the downstream end. Farther away from those boundaries, both projections approximately follow the slope of the dominant k_1^+ branch. This behaviour results from imperfections in the numerical projection,

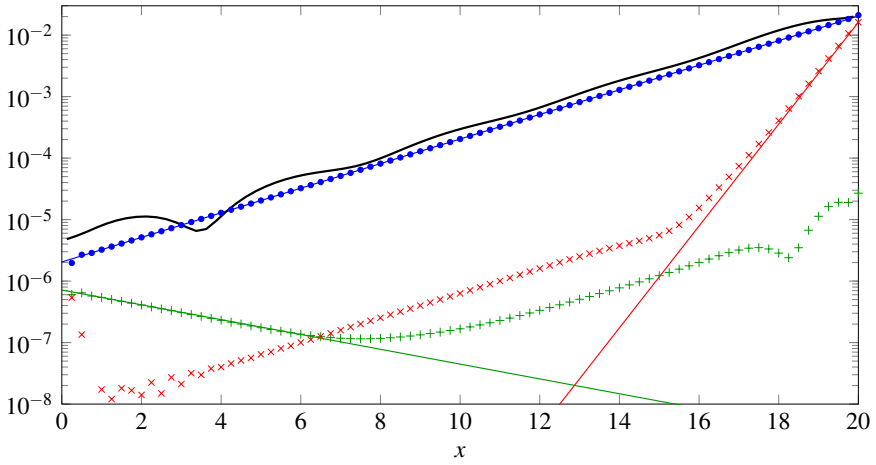

Fig. 8 Projection of global mode 1 onto spatial local modes of frequency $\omega = 1.111 - 0.052\mathrm{i}$: absolute values of the projection coefficients as functions of x. Legend: (•) k_1^+; (+) k_2^+; (×) k_1^-; (—) global mode component $\hat{u}_x(0,x)$ on axis; colored lines indicate the growth rates according to local analysis.

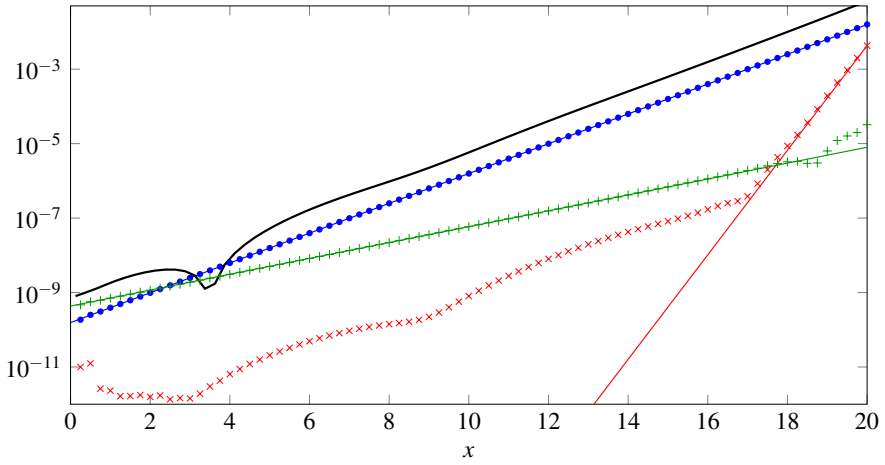

Fig. 9 Projection of global mode 2 onto spatial local modes of frequency $\omega = 0.912 - 1.211\mathrm{i}$: absolute values of the projection coefficients as functions of x. Legend: (•) k_2^+; (+) k_3^+; (×) $k^\pm$; (—) global mode component $\hat{u}_x(0,x)$ on axis; colored lines indicate the growth rates according to local analysis.

which apparently only allows a clean distinction between these local modes down to amplitude ratios around 10^{-3} in the present setup. Higher spatial resolution in the local and global computations does not improve this threshold. Note that these three modes are highly non-orthogonal, which makes their distinction numerically delicate.

Overall, local mode contributions other than from the k_1^+ mode to the global mode 1 are tractable but rather negligible. Modulations of the centerline velocity perturbation (black line in Fig. 8) are instead attributable to global pressure modes, as will be shown later on.

Very similar results are obtained for the global mode 2, for which the local mode amplitudes are displayed in Fig. 9. However, the local spectrum in this case differs from that of mode 1, as the global frequency $\omega_2 = 0.912 - 1.211\mathrm{i}$ has an imaginary part below that of the absolute frequency $\omega_0 = 1.074 - 0.286\mathrm{i}$. Therefore, in the analysis of global mode 2, the local spatial modes are selected from a spectrum where pinching of the k_1^+ and the k_1^- has already occurred (see Fig. 7*b*). In this setting, it is now the k_2^+ mode that displays the strongest downstream growth, followed by the k_3^+ mode. A mode from the mixed branch, formed from the k_1^+ and k_1^- branches after pinching, is denoted $k^\pm$.

The global mode 2, as represented by a black line in Fig. 9, is clearly dominated by the k_2^+ mode (blue bullet symbols), but the k_3^+ and $k^\pm$ modes are again discernible down to amplitudes three orders of magnitude below k_2^+. It is not clear a priori how the $k^\pm$ mode is to be interpreted, in particular with regard to its up-

or downstream propagation. However, the projection results plainly show that this mode is generated at the downstream end, from where it propagates upstream; thereby, it behaves as a mode of k^- type.

It is stressed that the analysis of spatial branches below the absolute growth rate is indeed meaningful in the present context. Spatial analysis below the absolute growth rate, i.e. after pinching has taken place, is usually said to be in violation of temporal causality, formally expressed by the fact that no integration path can be found in the complex k-plane that separates k^+ and k^- branches [14]. This argument however arises in the context of the asymptotic flow behaviour at long times, when indeed the system dynamics are determined by the absolute mode. In the same sense, a *global* system is asymptotically determined by only the most unstable eigenmode (here: global mode 1). Notwithstanding, global eigenmodes with lesser growth rate do exist, and they are observable in the transient system dynamics. The spatial local modes used in the analysis of global mode 2 are justified in the same way.

In summary, the projections onto local spatial modes demonstrate that global mode 1 is supported by a local k_1^+ mode, whereas global mode 2 relies on a k_2^+ mode. In all likelihood, the same holds true for any global mode of the arc branch (k_1^+) and of the lower branch (k_2^+). Moreover, although not shown in Fig. 6, further lower branches exist at lower growth rates $\omega_i < -1.5$, for which a match with higher local k^+ branches is anticipated. The link between the arc branch and the dominant k^+ mode has been pointed out in earlier studies [for instance 10, 1, 12]. However, the argument so far has one loose end: the presence of a local k^+ mode is contingent on it being forced upstream. The present results show that this forcing takes place immediately at the upstream boundary. The essential ingredient that can give rise to a global mode with a k^+ wave is *feedback* from downstream.

3.2 Global pressure feedback

The ellipticity of the global linear jet problem is contained in the pressure gradient and in the viscous terms. The latter will only be noticeable over distances much shorter than the numerical box length, and they are not considered in the following analysis. The pressure, as noted by Ehrenstein & Gallaire [10], obeys a Poisson equation, which in the present case of parallel flow takes the form

$$\Delta \hat{p} = -2\partial_r U \partial_x \hat{u}_r, \tag{9}$$

with homogenous Dirichlet and Neumann conditions at the upstream and lateral boundaries, respectively, and with $\hat{p} = Re^{-1}\partial_x \hat{u}_x$ at the outflow.

The following analysis is restricted to the arc branch mode labelled '1' in Fig. 6, but results for mode 2 are not fundamentally different. The pressure amplitude of mode 1 is shown in Fig. 10(a) as $\log_{10}|\hat{p}|$. Its structure is somewhat irregular in the downstream near-field region of the jet, yet the characteristic wavelength $2\pi/k_r = 4.1$ of the k_1^+ mode is apparent. The stress-free outflow boundary condition is seen to result in $\hat{p} \approx 0$, and the pressure at $r \gtrsim 5$ is essentially a superposition of fundamental solutions of the homogeneous equation $\Delta \hat{p} = 0$, with Dirichlet conditions at the inflow and outflow. These are given by

$$\hat{p}_j = \left[A_j I_0\left(\frac{j\pi}{L}r\right) + B_j K_0\left(\frac{j\pi}{L}r\right)\right]\sin\left(\frac{j\pi}{L}x\right), \quad j \in \mathbb{N}, \tag{10}$$

where I_0 and K_0 are the modified Bessel functions of the first and second kind, respectively, and $L = 20$ is the streamwise length of the numerical box. The K_0 functions are exponentially decaying in r, manifestly dominant in the present problem, whereas the I_0 functions grow exponentially in r. These only enter the global mode at very low amplitude ($A_j/B_j \ll 1$) in order to satisfy the Neumann condition at $r_{max} = 50$. Only the $\hat{p}_1$ component is clearly visible in Fig. 10a, because it experiences the slowest radial decay, but a projection confirms that at least the first five $\hat{p}_j$ components enter the pressure field with comparable global norms.

It is known from the analysis in Sect. 3.1 that the global mode involves a strong k_1^+ wave. In the present section, the complementary part is sought that may provide the upstream-reaching part of a feedback loop. Therefore, the k_1^+ component of the global mode is subtracted from the pressure field, using the already known projection coefficients shown in Fig. 8. This 'stripped' pressure field $\tilde{p}$ is presented in Fig. 10(b), as $\log_{10}|\tilde{p}|$. A remarkably clean structure is recovered, suggestive of a solution of the Laplace equation $\Delta \tilde{p} = 0$ which is forced at the outflow boundary near the jet axis. A small inhomogeneity is also observed at the inflow near the the jet axis.

Note that the local k_1^+ mode by construction represents a particular solution of (9) in a domain of infinite streamwise extent. Within the limits of the simplifying assumption that the propagating perturbations in the

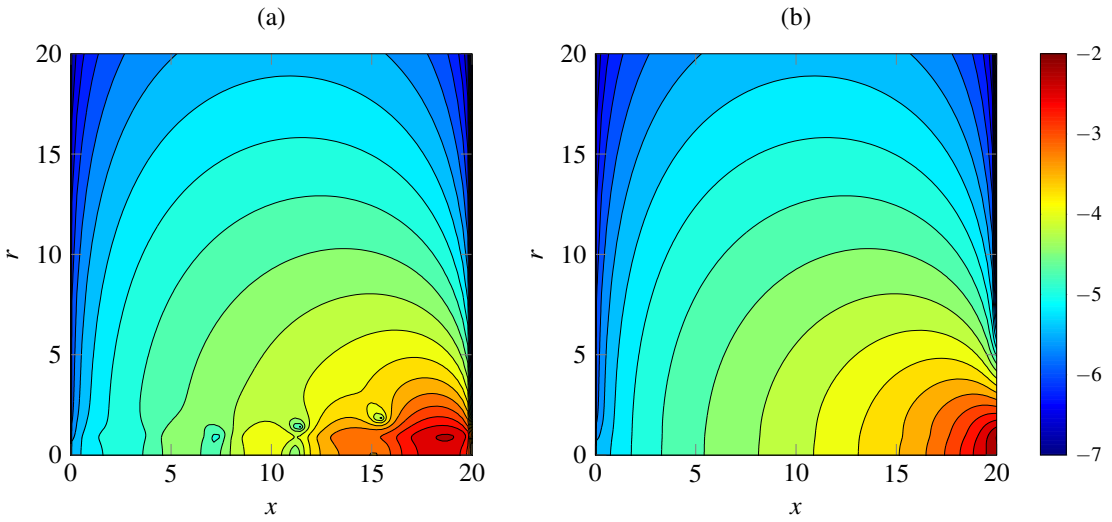

Fig. 10 Pressure perturbation fields of global mode 1. a) total pressure perturbation $\log_{10}|\hat{p}|$; b) pressure perturbation $\log_{10}|\tilde{p}|$, obtained by subtraction of the k_1^+ component.

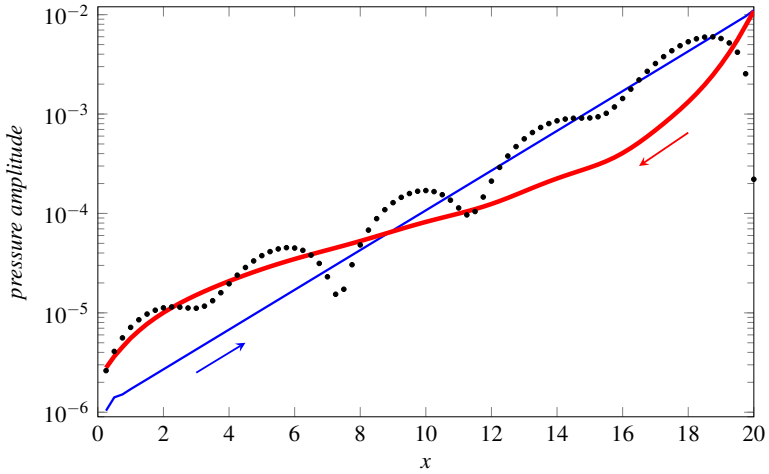

Fig. 11 Pressure signal amplitudes along x at the critical point, $r_c = 0.92$. (•) total pressure $|\hat{p}|$; (——) pressure associated with k_1^+ wave; (——) 'stripped' pressure $|\tilde{p}|$. Note that all signals are numerically zero at $x = 0$.

region of $\partial_r U \neq 0$ are indeed given by the k_1^+ mode alone, in the interior of the bounded domain, the stripped pressure field $\tilde{p}$ only needs to satisfy the inhomogeneities that arise from the boundary conditions. These inhomogeneities on both ends of the domain are thus coupled through the Laplace equation in $\tilde{p}$.

As a final plausibility check, the amplitudes of the supposed downstream-propagating and upstream-reaching components of the feedback loop are compared in Fig. 11 along a path at constant r. The radial position of the critical point of the local k_1^+ mode is chosen, $r_c = 0.92$. A thin blue line represents the pressure amplitude of the k_1^+ mode component, according to the projection carried out in Sect. 3.1, a thick red line represents the amplitude of the pressure feedback signal $\tilde{p}$, and black symbols mark the amplitude of the total pressure field $\hat{p}$. The up- and downstream branches have approximately equal amplitude at the downstream boundary, nearly cancelling each other. Near the upstream boundary, the feedback signal is larger by about a factor 3 than the k_1^+ wave — this appears reasonable in view of the assumption that the latter is forced by the former.

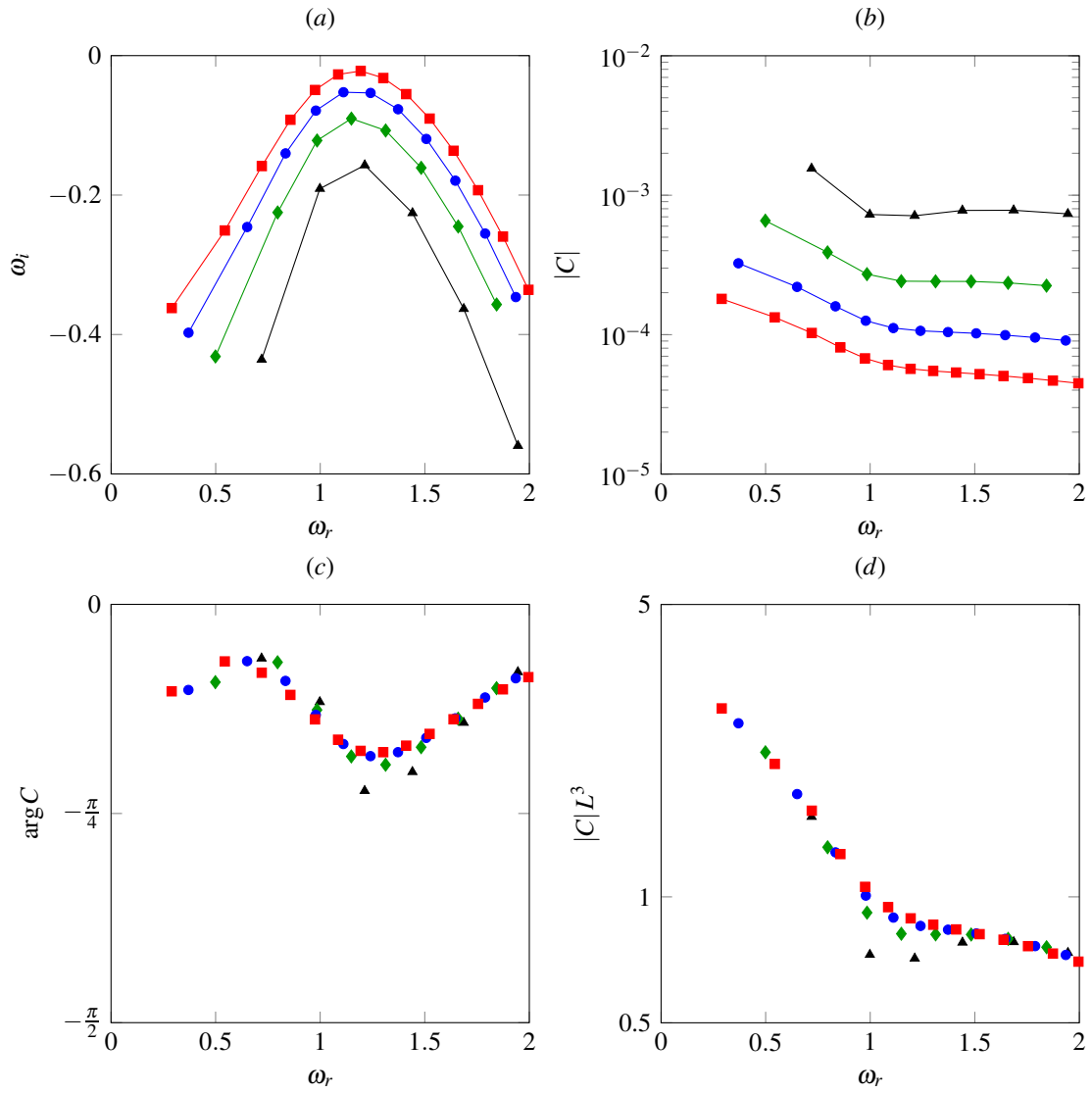

Fig. 12 Influence of the numerical box length on eigenvalues. In all figures, different symbols denote different box lengths: (■) $L = 25$; (●) $L = 20$; (♦) $L = 15$; (▲) $L = 10$. *a*) Arc branch eigenvalues. *b*) Effective reflection coefficients according to (11), absolute values. *c*) Effective reflection coefficients, phase. *d*) Effective reflection coefficients, absolute value scaled with L^3.

3.3 The influence of box length

Arc branch modes in the literature are consistently found to be sensitive to the length of the numerical box. In some instances [e.g. 12], a longer box yields eigenvalues with lower growth rates, in other instances [e.g. 10] the opposite effect is observed. If the present feedback model is correct, it should allow an estimation of the influence of the numerical box length on the arc branch growth rates.

Eigenmodes of the parallel jet (8) have been computed in numerical domains of streamwise lengths $L = 10, 15$ and 25, for comparison with the standard configuration $L = 20$; in all cases, the radial discretisation and the constant step size Δx are unchanged. Resulting modes of the arc branch are displayed in Fig. 12(*a*). As L is increased, the entire branch is seen to shift to higher growth rates, and the modes are more densely spaced.

The analysis so far suggests that a downstream-convecting k^+ mode and the elliptic pressure field are coupled in small regions near the inflow and outflow boundaries. In analogy with the Ginzburg–Landau model discussed in Sect. 2, an effective reflection coefficient C may be defined, which relates the forcing of the k^+ mode at the inflow to the k^+ amplitude at the outflow, thus lumping the narrow interaction regions into singular

actuator and sensor positions in x. The effective forcing at the Dirichlet inflow boundary is modelled as

$$-\mathrm{i}\omega\hat{q} = C\hat{q}\mathrm{e}^{\mathrm{i}kL} \quad \rightarrow \quad C = -\mathrm{i}\omega\mathrm{e}^{-\mathrm{i}kL}, \tag{11}$$

where ω is the global eigenmode frequency, and $(k,\hat{q})$ denote the relevant local k^+ mode. The coefficient C includes the effects of coupling on both ends of the domain, as well as the upstream decay of the pressure signal, seen in Fig. 11.

Numerically obtained values of C are reported in figures 12(*b*,*c*), in terms of their absolute value and their phase, for the arc branch in all four numerical domains. In each domain, the reflection coefficient decreases with real frequency, but only weakly so for frequencies larger than one. This effect may be caused by the slower radial decay of $\hat{q}$ at low frequencies, resulting in radially more extended interaction regions on both domain ends. The phase of C varies only slightly with frequency, and it is independent of box length.

If the reflection coefficients are scaled with the cube of the box length, as shown in Fig. 12(*d*), they neatly collapse onto one curve. Consequently, the effective feedback imparted by boundary reflections decreases with the domain length as L^3. This scaling factor indicates that the relevant component of the pressure signal, which couples the downstream with the upstream end of the k^+ wave, is of a *quadrupole* type (signals from monopole and dipole sources at $x = L$ would decay as L and L^2, respectively).

It is then straightforward to interpret the effect of an increased numerical box length on a given arc branch mode: if the exponential growth of the dominant k^+ mode over the added streamwise interval is larger than the algebraic decay of the upstream-reaching pressure signal, over the same added distance, then the spurious inlet forcing will increase in strength, resulting in a higher growth rate ω_i. If the k^+ mode in the added region is locally stable, then the inlet forcing will decrease, and the global growth rate will be lower as a result.

This interpretation appears to be consistent with the two cited examples: the boundary layer investigated by Ehrenstein & Gallaire [10] is locally unstable at the outflow, as confirmed by the authors, and longer domain sizes are found to result in higher global growth rates. In contrast, the rapidly spreading jet considered by Garnaud *et al.*[12] is locally stable at the outflow with respect to axisymmetric perturbations, and indeed lower global growth rates are obtained for the arc branch in longer domains. This criterion may of course be frequency-dependent: certain (complex) frequencies may be locally stable at the outflow while others are unstable, and opposite trends ought to be observed in these frequency ranges. This seems indeed to be the case in the $Re = 360$ setting of Coenen *et al.*[7].

4 Possible remedies, tested for a non-parallel jet

While the preceding analyses of the Ginzburg–Landau equation and of the parallel jet served to *characterise* the global feedback mechanism due to domain truncation, the question how such feedback may be *reduced* is addressed in this section for the example of a spatially developing jet. With this choice, the results from the previous section can be largely transferred to the new setting.

Each type of open flow may present particular problems in view of domain truncation. In favourable configurations, the numerical boundaries can be placed in stable flow regions, as for instance in a uniform flow upstream of a solid obstacle, like a cylinder. In other cases, the need for truncation may be avoided by prescribing consistent physical boundaries, like confining solid walls, which are then part of the flow configuration.

Jets belong to a more problematic category. They are created by some upstream source of momentum, and it is in general not feasible to include the entire upstream apparatus (fan, chamber, nozzle, etc.) in the calculations, which would furthermore defeat the purpose of any generic description of jet dynamics. The formulation of upstream flow and boundary conditions is therefore necessarily imperfect with respect to any flow realisation, as potentially important regions are not accounted for.

For the present study, the jet is modelled as issuing from an orifice in a solid wall, very similar to the configuration of Garnaud *et al.*[12]. Upstream of the orifice, the flow develops in a straight circular pipe, from where it exits with a fairly thin boundary layer. The base flow is computed as a steady, axisymmetric solution of the incompressible Navier–Stokes equations (6), with an inflow condition

$$U(r) = \tanh\left[\frac{5}{2}\left(\frac{1}{r} - r\right)\right] \tag{12}$$

imposed at $x = -10$. Newton–Raphson iterations are performed in order to converge to a steady flow state. The numerical domain for these base flow calculations is truncated downstream at $x_{max} = 50$ and radially at $r_{max} = 50$, where stress-free conditions are applied. The Reynolds number is set to 1000 in the free jet.

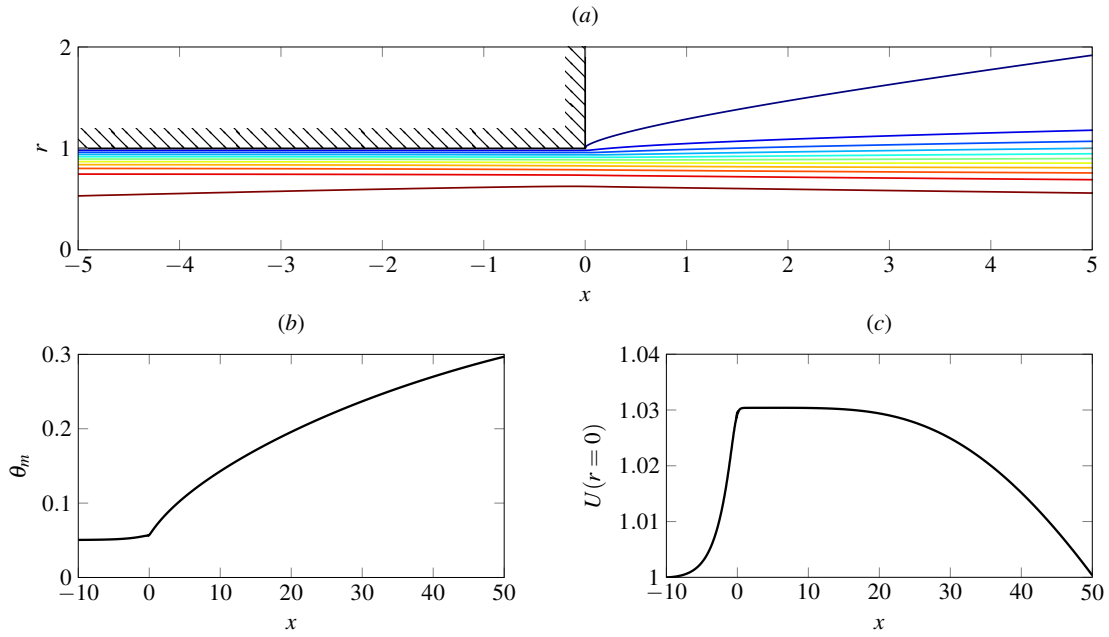

Fig. 13 Steady state of a spatially developing jet, used as a base flow in all calculations of Sect. 4. *a*) Contours of axial velocity near the orifice at $x = 0$. Contour values are distributed between 0 and 1, with constant spacing of 0.1. The base flow is computed on a larger domain, with $-10 \leqslant x \leqslant 50$ and $0 \leqslant r \leqslant 50$. *b*) Streamwise development of the shear layer momentum thickness. *c*) Streamwise development of the centreline velocity.

	x_{min}	x_{max}	upstream BC	absorbing layer
case 1	0	40	Dirichlet	no
case 2	−5	40	Dirichlet	no
case 3	−10	40	Dirichlet	no
case 4	0	40	stress-free	no
case 5	−5	40	stress-free	no
case 6	−10	40	stress-free	no
case 7	−5	40	Dirichlet	yes, $\lambda_{max} = 0.5$
case 8	−5	50	Dirichlet	yes, $\lambda_{max} = 0.75$

Table 1 Numerical configurations of the various eigenmode calculations discussed in this section.

However, in order to maintain a thin shear layer at the orifice, this value is varied exponentially inside the pipe, between $Re = 10^5$ at $x = -10$ and $Re = 10^3$ at $x \geqslant -0.2$, in the base flow calculation. The resulting flow field near the orifice at $x = 0$ is represented in Fig. 13, together with the characteristic streamwise variations of the shear layer momentum thickness θ_m and of the centreline velocity.

Eigenmode calculations are carried out on smaller domains, where portions of the base flow are cropped at the inflow, the outflow, or both, in order to probe the effect of domain truncation. All configurations are listed in table 1. The Reynolds number in these calculations is set to 1000 throughout the domain.

The influence of *upstream* truncation on eigenmodes is considered first. Figure 14a shows spectra for three different domains, with homogeneous Dirichlet conditions (7a) imposed at $x_{min} = (0, -5, -10)$, respectively. The downstream end of the numerical domain is placed at $x_{max} = 40$, where stress-free conditions (7b) are applied in all three cases. Unconverged and lower-branch eigenvalues are not shown here and in the following for clarity; the criterion for convergence is that an eigenvalue could be reproduced within three-digit accuracy using two different shift values.

It is seen from Fig. 14a that the arc branch is quite insensitive to the position of the upstream Dirichlet boundary. Even a full truncation of the upstream pipe (case 1) only results in a slight stabilisation at high frequencies. Eigenvalues obtained with pipe lengths of 5 and 10 radii (cases 2 and 3) are virtually identical. Stress-free inflow conditions (cases 4, 5 and 6, spectra shown in Fig. 14b) are found to perform less favourably. When applied at $x = 0$, these conditions give rise to global instability; the inclusion of portions of the pipe has a stabilising effect, but even with $x_{min} = -10$ the growth rates along the entire arc branch are still significantly higher than those obtained with Dirichlet conditions.

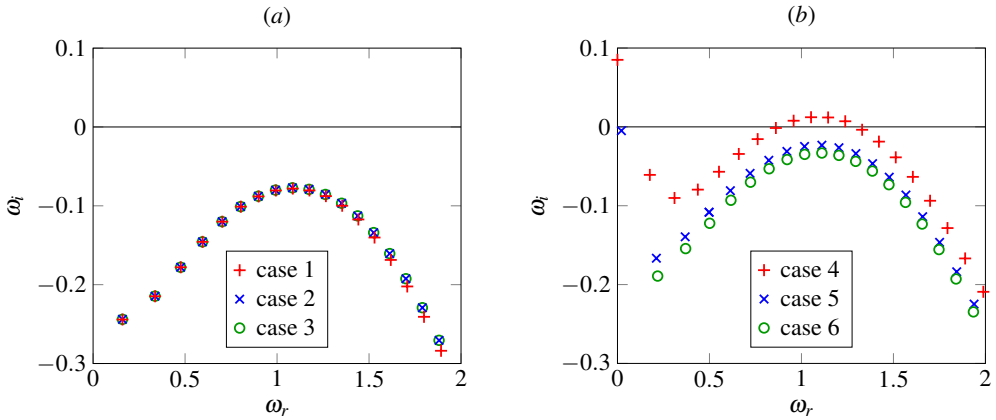

Fig. 14 Arc branch spectra obtained in calculations with (*a*) Dirichlet and (*b*) stress-free upstream boundary conditions.

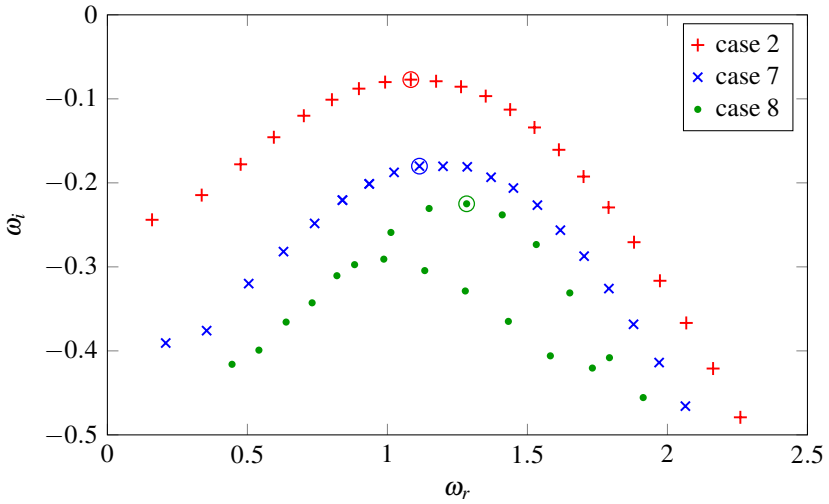

Fig. 15 Arc branch spectra obtained in calculations with (×,•) and without (+) absorbing layer. Circles mark the individual modes for which eigenfunctions are shown in Fig. 16.

It is to be expected that global pressure fluctuations induce a generation of vorticity waves at the solid corner at $x = 0$, and the independence of the eigenvalues in cases 2 and 3 (Fig. 14a) on the upstream boundary position suggests that this physical effect is dominant over spurious pressure-vorticity coupling at x_{min}. It remains to be determined to what extent the downstream boundary conditions emit spurious pressure signals, and how these may be reduced.

Garnaud *et al.* [12] tested stress-free and convective outflow conditions in an almost identical jet configuration, and found no significant difference in the resulting spectra. In the present study, the potential of *absorbing layers* [8] for a stabilisation of the arc branch is examined. To this end, an artificial damping term is added to the linear perturbation equations, with the purpose of reducing perturbation amplitudes before they reach the numerical boundary at x_{max}. If the original global eigenvalue problem is written

$$-i\omega\mathbf{B}\hat{q} = \mathbf{L}\hat{q}, \tag{13}$$

then the eigenvalue problem with absorbing layer is defined as

$$-i\omega\mathbf{B}\hat{q} = [\mathbf{L} - \lambda(x)\mathbf{B}]\,\hat{q}. \tag{14}$$

For cases 7 and 8 (see table 1), the damping parameter is prescribed as

$$\lambda(x) = \begin{cases} 0 & \text{for } x \leqslant 19, \\ 0.00625x^2 - 0.2375x + 2.25625 & \text{for } 19 < x < 21, \\ 0.025(x-20) & \text{for } x \geqslant 21. \end{cases} \tag{15}$$

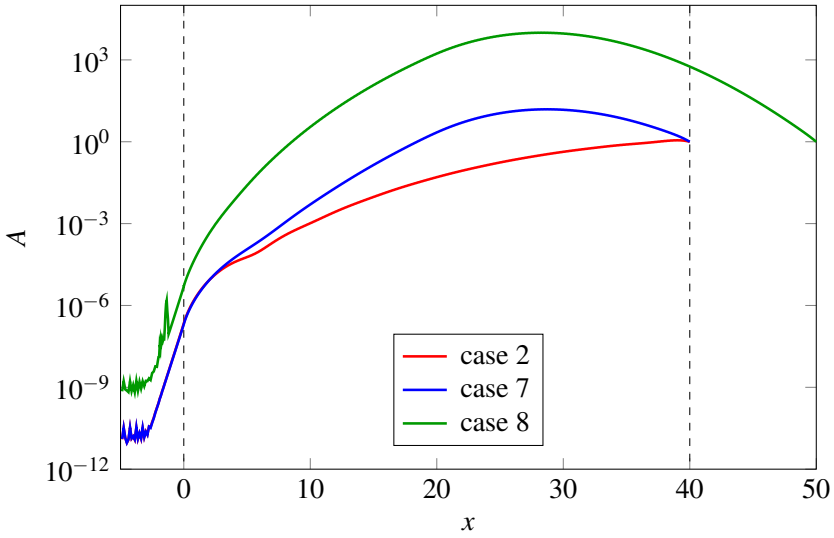

Fig. 16 Amplitude variations in x of selected eigenfunctions, as marked in Fig. 15. The amplitude is defined in Eq. (16).

This variation of λ is continuous in its first derivative, and it has maximum values 0.5 and 0.75 at $x_{max} = 40$ and $x_{max} = 50$, respectively.

The effect of absorbing layers on the eigenvalue spectrum is documented in Fig. 15. Damping in the downstream region $19 \leqslant x \leqslant 40$ (case 7) is seen to reduce the growth rates of arc branch modes significantly (compared to case 2). Eigenfunctions of selected modes, marked by circles in Fig. 15, are compared in Fig. 16. An integral amplitude measure is defined as

$$A(x) = \left[\int_0^1 \left(|\hat{u}_r|^2 + |\hat{u}_x|^2 \right) r \, \mathrm{d}r \right]^{\frac{1}{2}}, \tag{16}$$

and the amplitude curves in Fig. 16 are normalised with respect to their values at the outflow boundary for comparison. While the red curve (case 2, no absorbing layer) shows a monotonic growth of perturbation amplitude throughout the domain, similar to the parallel jet results in figures 8 and 9, the blue curve (case 7) reaches a maximum inside the absorbing layer and subsequently decays in x. Remarkably, the ratio $A(x_{max})/A(0)$ is identical in both cases, which is consistent with the interpretation of these modes as being the result of spurious feedback from the outflow, in the same way as detailed in Sect. 3 for the parallel jet. The absorbing layer reduces the gain of the k^+ hydrodynamic branch of the feedback loop, and thereby the temporal modal growth rate.

Based on the discussion in Sect. 3, stronger artificial damping of the hydrodynamic branch ought to lead to ever smaller modal growth rates; longer domains should furthermore lead to a reduced amplitude of the incident pressure signal upstream, due to its cubic decay. Both conditions are combined in case 8 (see table 1), of which results are included in figures 15 and 16. Indeed, the temporal growth rates are further reduced, and the spatial decay of the eigenfunction amplitude in the absorbing layer is more pronounced than in the case 7.

However, the shape of the arc branch in case 8 displays some differences with respect to all other cases, and similar mode patterns have been reported from jet calculations on long domains by Coenen *et al.* [7], where no artificial damping was applied. In the vicinity of the least stable mode (circled in Fig. 15), a regular spacing in ω_r is still observed, but with larger distances between consecutive modes than in cases 2 and 7. The corresponding amplitude function in Fig. 16 shows that the ratio $A(x_{max})/A(0)$ is smaller than in the two other cases, whereas the cubic decay of the reflection coefficient with box length, as described in Sect. 3, should have resulted in a larger ratio. Furthermore, stronger damping through higher values of λ, tried in test calculations that are not shown here, does not decrease the maximum growth rate much further, but it quickly leads to ill-conditioned system matrices. Case 8 seems indeed to mark an efficiency limit of absorbing layers for the stabilisation of the arc branch.

The above observations, in particular the increased spacing of modes in ω_r, suggest that pressure feedback in the strongly damped case 8 may originate from the interior of the domain, possibly from the location of the amplitude maximum. Such feedback may be spurious, in the sense of Heaton *et al.* [13], or it may be physical. This hypothesis is suggested for further examination.

5 Conclusions

A family of linear instability eigenmodes, named the arc branch, has been analysed in view of its physical or numerical origin. Branches of this type have previously been observed in a large variety of open flows. All results presented herein lead to the conclusion that arc branch modes in incompressible flow calculations are an artifact of domain truncation, due to spurious pressure feedback between numerical inflow and outflow boundaries.

A Ginzburg–Landau model was investigated first, because in this setting the effect of explicitly prescribed feedback between a downstream sensor and an upstream actuator could be examined without ambiguity. In the presence of feedback, a branch of eigenmodes was observed to arise that exhibits all typical characteristics of the arc branch described by Coenen *et al.*[7] for the example of light jets. These modes align with a contour of the pseudospectrum, spaced at regular intervals of the real frequency, and their spatial eigenfunction is characterised by an integer number of wavelengths between actuator and sensor locations. As the strength of the feedback is increased, the branch moves steadily upward to higher growth rates in the complex frequency plane. Eigenmodes of the feedback-free system that lie below the arc branch are no longer detectable. An important observation is that this arc branch in the Ginzburg–Landau equation with feedback has no counterpart in the feedback-free spectrum: these eigenmodes are not merely *affected* by the presence of feedback, indeed without it they *do not exist*.

An incompressible parallel jet in a truncated domain was examined next. No explicit feedback was prescribed in this setting, but a similar arc branch of eigenmodes was nonetheless found to dominate the spectrum. A lower branch of eigenmodes with stronger temporal decay was also described, which may correspond to subdominant branches observed in wakes and boundary layers. Both the arc-branch and the lower-branch modes in the parallel jet were shown to be composed primarily of one downstream-propagating k^+ wave, as computed from a local spatial analysis. Each of the two branches involves a different k^+ mode. This observation raises the question how a k^+ wave is generated at the upstream boundary of the numerical domain. The analogy with the Ginzburg–Landau model from Sect. 2 suggests feedback from downstream.

The most plausible mechanism for global feedback in a truncated domain is the generation of pressure perturbations due to the artificial downstream boundary condition, as described by Buell & Huerre[2]. The pressure field of the least stable arc branch mode was decomposed into one portion associated with the prominent k^+ wave, which cannot be involved in upstream feedback, and into a residual part that is essentially governed by a Laplace equation forced at the domain boundaries. The latter appears to be strongly dominated by a source region at the outflow, near the jet axis. A numerical evaluation of effective reflection coefficients, in analogy with the Ginzburg–Landau model of Sect. 2, established as a principal result that the strength of upstream feedback decays with the numerical box length to the third power. This scaling is indicative of a spurious pressure quadrupole situated at the outflow. The algebraic nature of the pressure decay allowed a prediction of the effect of box length variations on arc-branch growth rates, depending on the local stability or instability of the flow, apparently consistent with common observations. While this study has been limited to incompressible flow settings, similar mechanisms will also be present in compressible calculations, with the difference that spurious pressure signals are then propagated by a wave equation. This may in fact result in stronger feedback, as the far-field acoustic pressure only decays with the first power of the distance from the source.

Finally, possible strategies for a reduction of spurious pressure feedback have been examined for the example of a spreading jet. On the one hand, upstream boundary conditions must be chosen that minimise the unphysical conversion of pressure feedback from downstream to vortical perturbations. It has been found, in this particular flow example, that Dirichlet conditions perform much better than stress-free conditions in this regard. On the other hand, the generation of spurious pressure signals from the outflow boundary must be reduced. It has been demonstrated that artificial damping in a downstream absorbing layer provides an efficient means to achieve this. An advantage of this technique is that it is straightforward to implement in any usual open shear flow problem. It has been noted, however, that increasingly strong damping does not reduce the growth rate of the arc branch to arbitrarily low levels.

Acknowledgements Discussions with Xavier Garnaud and Wilfried Coenen greatly helped shape the ideas presented in this paper. The study was supported by the Agence Nationale de la Recherche under the Cool Jazz project, grant number ANR-12-BS09-0024.

References

1. E. Åkervik, U. Ehrenstein, F. Gallaire, and D. Henningson. Global two-dimensional stability measures of the flat plate boundary-layer flow. *Eur. J. Mech. B/Fluids*, 27:1–13, Jul 2008.
2. J.C. Buell and P. Huerre. Inflow/outflow boundary conditions and global dynamics of spatial mixing layers. *Proc. 2nd Summer Prog., Stanford Univ. Cent. Turbul. Res.*, pages 19–27, 1988.
3. S. Cerqueira and D. Sipp. Eigenvalue sensitivity, singular values and discrete frequency selection mechanism in noise amplifiers: the case of flow induced by radial wall injection. *J. Fluid Mech.*, 757:770–799, 2014.
4. R.V.K. Chakravarthy. *Local and global dynamics of buoyant jets and plumes*. PhD thesis, École polytechnique, 2015.
5. J.-M. Chomaz. Global instabilities in spatially developing flows: Non-normality and nonlinearity. *Annu. Rev. Fluid Mech.*, 37:357–392, 2005.
6. J.-M. Chomaz, P. Huerre, and L.G. Redekopp. Bifurcations to local and global modes in spatially developing flows. *Phys. Rev. Lett.*, 60:25–28, 1988.
7. W. Coenen, L. Lesshafft, X. Garnaud, and A. Sevilla. Global instability of low-density jets. *J. Fluid Mech.*, 820:187–207, 2017.
8. T. Colonius. Modeling artificial boundary conditions for compressible flow. *Annu. Rev. Fluid Mech.*, 36:315–345, 2004.
9. A. Couairon and J.-M. Chomaz. Absolute and convective instabilities, front velocities and global modes in nonlinear systems. *Physica D*, 108:236–276, 1997.
10. U. Ehrenstein and F. Gallaire. On two-dimensional temporal modes in spatially evolving open flows: the flat-plate boundary layer. *J. Fluid Mech.*, 536:209–218, Jan 2005.
11. U. Ehrenstein and F. Gallaire. Two-dimensional global low-frequency oscillations in a separating boundary-layer flow. *J. Fluid Mech.*, 614:315–327, 2008.
12. X. Garnaud, L. Lesshafft, P.J. Schmid, and P. Huerre. Modal and transient dynamics of jet flows. *Phys. Fluids*, 25:044103, Feb 2013.
13. C.J. Heaton, J.W. Nichols, and P.J. Schmid. Global linear stability of the non-parallel Batchelor vortex. *J. Fluid Mech.*, 629:139–160, 2009.
14. P. Huerre. Open shear flow instabilities. In G. K. Batchelor, H. K. Moffatt, and M. G. Worster, editors, *Perspectives in Fluid Dynamics*, pages 159–229. Cambridge University Press, 2000.
15. P. Huerre and P.A. Monkewitz. Local and global instabilities in spatially developing flows. *Annu. Rev. Fluid Mech.*, 22:473–537, 1990.
16. M.R. Khorrami. A Chebyshev spectral collocation method using a staggered grid for the stability of cylindrical flows. *Int. J. Numer. Meth. Fluids*, 12:825–833, Apr 1991.
17. H. Kurz and M. Kloker. Mechanisms of flow tripping by discrete roughness elements in a swept-wing boundary layer. *Journal of Fluid Mechanics*, 796:158–194, 2016.
18. L. Lesshafft and P. Huerre. Linear impulse response in hot round jets. *Phys. Fluids*, 19(2):024102, Jan 2007.
19. J.-C. Loiseau, J.-C. Robinet, S. Cherubini, and E. Leriche. Investigation of the roughness-induced transition: global stability analyses and direct numerical simulations. *J. Fluid Mech.*, 760:175–211, 2014.
20. O. Marquet, D. Sipp, and L. Jacquin. Sensitivity analysis and passive control of cylinder flow. *J. Fluid Mech.*, 615:221–252, Jan 2008.
21. A. Michalke. Survey on jet instability theory. *Prog. Aerospace Sci.*, 21:159–199, 1984.
22. J.W. Nichols and S.K. Lele. Global modes and transient response of a cold supersonic jet. *J. Fluid Mech.*, 669:225–241, 2011.
23. D. Rodríguez, A. V. G. Cavalieri, T. Colonius, and P. Jordan. A study of linear wavepacket models for subsonic turbulent jets using local eigenmode decomposition of PIV data. *Eur. J. Mech. B/Fluids*, 49:308–321, 2015.
24. D. Sipp and A. Lebedev. Global stability of base and mean flows: a general approach and its applications to cylinder and open cavity flows. *J. Fluid Mech.*, 593:333–358, 2007.
25. L. N. Trefethen and M. Embree. *Spectra and Pseudospectra: The Behavior of Nonnormal Matrices and Operators*. Princeton University Press, 2005. see also `http://www.cs.ox.ac.uk/projects/pseudospectra/`.

Vortex pairing in jets as a global Floquet instability: modal and transient dynamics

Léopold Shaabani-Ardali[1,2]†, Denis Sipp[2] and Lutz Lesshafft[1]

[1]LadHyX, École polytechnique–CNRS, 91120 Palaiseau, France
[2]DAAA, ONERA, Université Paris-Saclay, F-92190 Meudon, France

(Received xx; revised xx; accepted xx)

The spontaneous pairing of rolled-up vortices in a laminar jet is investigated as a global secondary instability of a time-periodic spatially developing vortex street. The growth of subharmonic perturbations, associated with vortex pairing, is analysed both in terms of modal Floquet instability and in terms of transient growth dynamics. The article has the double objective to outline a toolset for global analysis of time-periodic flows, and to leverage such an analysis for a fresh view on the vortex pairing phenomenon.

Axisymmetric direct numerical simulations (DNS) of jets with single-frequency inflow forcing are performed, in order to identify combinations of the Reynolds and Strouhal numbers for which vortex pairing is naturally observed. The same DNS calculations are then repeated with an added time-delay control term, which artificially suppresses pairing, so as to obtain time-periodic unpaired base flows for linear stability analysis. It is demonstrated that the natural occurrence of vortex pairing in nonlinear DNS coincides with a linear subharmonic Floquet instability of the underlying unpaired vortex street. However, DNS results suggest that the onset of pairing involves much stronger temporal growth of subharmonic perturbations than what is predicted by modal Floquet analysis, as well as a spatial distribution of these fast-growing perturbation structures that is inconsistent with the unstable Floquet mode. Singular value decomposition of the phase-shift operator (the operator that maps a given perturbation field to its state one flow period later) is performed for an analysis of optimal transient growth in the vortex street. Non-modal mechanisms near the jet inlet are thus found to provide a fast route towards the limit-cycle regime of established vortex pairing, in good agreement with DNS observations.

It is concluded that modal Floquet analysis accurately predicts the parameter regime where sustained vortex pairing occurs, but that the bifurcation scenario under typical conditions is dominated by transient growth phenomena.

1. Introduction

When the shear layer of a jet is subjected to low-level forcing at the nozzle, perturbations within a band of unstable frequencies are amplified as they travel downstream (Michalke 1971). When the perturbation amplitude reaches nonlinear levels, the shear layer rolls up into vortices. In the case of laminar jets, forced axisymmetrically at a single frequency, a regular street of ring vortices is formed, where the passage frequency of vortices is controlled by the nozzle forcing. It has long been observed that such vortices may, in certain parameter regimes, spontaneously undergo regular *pairing*: two neighbouring vortices then merge into one, such that a new vortex street is formed, with a periodicity that corresponds to the subharmonic of the applied forcing frequency. This

† Email address for correspondence: leopold.shaabani-ardali@ladhyx.polytechnique.fr

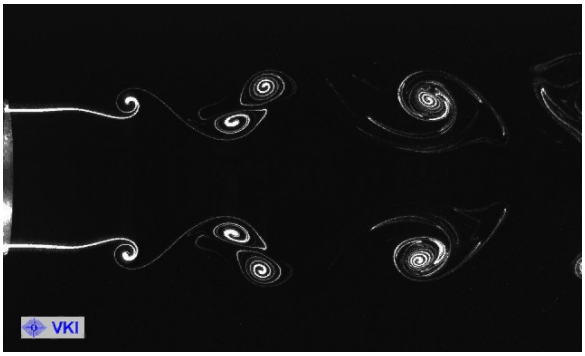

Figure 1: Experimental visualisation of pairing in a jet, snapshot of a movie by Schram (2003).

scenario is illustrated in figure 1, which shows a flow visualisation from the experiments by Schram (2003). The first systematic studies of the pairing scenario have been conducted by Zaman & Hussain (1980) and Hussain & Zaman (1980). While the merging of two vortices is clearly a nonlinear process, it remains to be clarified to what extent the occurrence of regular vortex pairing is governed by linear mechanisms, and how such linear dynamics may be properly formalised.

Numerous past studies have sought to explain the pairing phenomenon by investigating the consistency of the paired flow state itself. Monkewitz (1988) developed a theoretical framework based on weakly nonlinear interaction between the forced fundamental instability wave and its subharmonic. His formalism leads to a phase-relation criterion for subharmonic resonance, which has subsequently been validated experimentally by Husain & Hussain (1989), Raman & Rice (1991), Paschereit *et al.* (1995) and others.

A different approach consists in considering the bifurcation process from a harmonic unpaired to a subharmonic paired state. This viewpoint leads to the question whether an array of vortices convecting at the imposed forcing frequency is unstable with respect to subharmonic perturbations. In forced jets, vortex pairing occurs as a self-sustained process, and the pairing location is stationary in a spatially non-periodic flow. Therefore, the appropriate framework will have to be based on either locally absolute/convective, or fully global analysis. Brancher & Chomaz (1997) investigate the absolute nature of pairing instability in a periodic array of Stuart vortices, as a model for a rolled-up two-dimensional plane shear layer. In order to apply the notion of absolute/convective instability (Huerre & Monkewitz 1990), commonly used for steady configurations, they conduct their analysis in a co-moving frame of reference, where the vortices are stationary. By varying the concentration factor of the vortices, they show that the required backflow rate for absolute instability decreases as the vortex concentration increases. This formalism pertains to a spatially periodic array of vortices and does not account for viscous effects.

In the present study, we aim to describe the onset of vortex pairing as a secondary instability in a *global* analysis framework. As the underlying basic state, the unpaired vortex street resulting from the primary shear instability, is time-periodic, a classical Floquet formalism is employed. Modal instability as well as transient growth scenarios will be explored within this framework. Global instability analysis has become a standard approach in the context of *steady* base flows (Theofilis 2011). Linearisation of the governing flow equations around a steady base flow yields an autonomous operator; the spectrum of this operator indicates the possibility of perturbation growth in the long-time limit. However, the base flow in our case is not steady but *periodic* in time, the periodicity

being controlled by the harmonic forcing of the jet. Therefore, the global analysis method must be adapted to account for this periodicity, by use of the Floquet theorem (Floquet 1883). A global Floquet formalism has been successfully applied by Barkley & Henderson (1996) to the secondary instability of a cylinder wake around $Re = 200$ and more recently by Jallas *et al.* (2017) to a study of secondary instabilities in wake flows.

Another possible scenario for the onset of instability would be through transient growth; this phenomenon has first been described in parallel flows by Trefethen *et al.* (1993): if the linearised flow operator is non-normal, then, even though the system is stable, in the sense that at an infinite time horizon any perturbation decays towards zero, intial perturbations can be greatly amplified over a short time. For stationary jets, Nichols & Lele (2011) and Garnaud *et al.* (2013) studied this phenomenon and shown its significant role in the bifurcation. However, we aim at studying transient growth of a time-periodic jet. Several authors (Barkley *et al.* 2008; Blackburn *et al.* 2008; Arratia *et al.* 2013; Johnson *et al.* 2016) applied direct-adjoint looping in order to identify finite-time optimal perturbations in unsteady base flows. In the present paper, we use a technique that allows us to retrieve optimal perturbations based on direct time-stepping alone, and which takes full advantage of the time-periodicity of the underlying base flows.

As a prerequisite for our analysis, periodic base flow states *without* vortex pairing must be computed even in situations where such pairing arises naturally. Standard methods for the computation of periodic flow states may be based on *Newton–Picard shooting* methods, as described in Roose *et al.* (1995); Lust & Roose (1998) and applied to several flows in Sánchez *et al.* (2004); Sánchez & Net (2010). One alternative is the *harmonic balance* technique, in which several temporal Fourier components of a given periodicity are calculated simultaneously (Hall *et al.* 2002; Thomas *et al.* 2002). In a recent publication (Shaabani-Ardali *et al.* 2017), we describe how subharmonic fluctuations in time-stepping simulations can be efficiently suppressed by way of time-delayed feedback control ; this technique is employed here in order to construct the periodic base states.

The paper is organised as follows: a comprehensive literature review is provided in § 2, in order to delineate the context of our investigation. Section 3 presents a systematic study of the parameter regimes where vortex pairing is observed in direct numerical simulations (DNS) of laminar jets at moderate Reynolds numbers. Modal Floquet analysis is performed in § 4, and it is shown that the Floquet-unstable parameter regime coincides with the observation of pairing in the DNS. Non-modal transient growth dynamics are investigated in § 5, and their relevance for the bifurcation scenario is demonstrated.

2. Review of the literature on vortex pairing

2.1. *Discovery*

The pairing of vortex rings in jets was described for the first time by Becker & Massaro (1968): in jet experiments at moderate Reynolds number, acoustic single-frequency forcing was observed to give rise to regular vortex formation and subsequent pairing. Winant & Browand (1974) investigated the same phenomenon in a plane mixing layer: pairing was found to occur intermittently in these experiments, punctuated by occasional "shredding" events, *i.e.* the destruction of vortex cores by a subharmonic strain field, which interrupt the pairing process. The authors proposed a phenomenological model based on Stuart vortices. In the context of jets, Petersen (1978) examined the influence of

higher Reynolds numbers, and they inferred an argument on the basis of wave dispersion intended to predict the location of vortex pairing.

More detailed experimental investigations of vortex pairing in jets were carried out by Zaman and Hussain (Zaman & Hussain 1980; Hussain & Zaman 1980). These authors considered high Reynolds number ($Re = O(10^4)$) jets with a thin initial mixing layer, forced at a single frequency. Pairing was found to arise in two distinct frequency bands, one around $St_\theta = f\theta/U \approx 0.012$ and the other around $St_D = fD/U \approx 0.85$. These Strouhal numbers are formed with the jet exit velocity U, forcing frequency f, and either the initial shear layer thickness θ or the jet diameter D. According to their characteristic scaling, the two bands were identified with a "mixing layer mode" and a "jet column mode", respectively. In the former case, the vortices are very thin and dissipate quickly, whereas in the latter case, their radial extent is comparable to the jet radius, and their viscous dissipation takes place over a much longer travel distance. Both articles describe in much detail the vortex dynamics, their trajectories and velocities, as well as the transition to turbulence. When turbulence sets in close to the nozzle, the pairing becomes intermittent. High-quality flow visualisations of vortex pairing in jets, at Reynolds number 2300, are shown by Meynart (1983).

Vortex pairing is also a common event in *plane shear layers*. Ho & Huang (1982) found that very low-amplitude subharmonic forcing in their shear layer experiments led to a vigorous flow response in the form of regular pairing, associated with a strongly increased spreading of the mean flow. Intermittently, simultaneous coalescence of several vortices occurred, and was described as "collective interaction". Similar observations had been made in jet experiments by Kibens (1980). Ho & Huang (1982) established experimentally that spatial growth of the subharmonic component only occurs in situations where its phase velocity is equal to that of the fundamental flow perturbation.

2.2. *Interpretation in terms of wave interaction*

Prior to theoretical explanations, Arbey & Ffowcs Williams (1984) demonstrated experimentally the importance of the phase difference between fundamental and subharmonic perturbations for the onset of vortex pairing. A jet at Reynolds number 17500 was forced at moderate amplitude (about 2% of the centreline velocity) at two frequencies ω and $\omega/2$. The spatial growth of perturbations at both frequencies was found to be strongly dependent on the relative phase of the applied forcing. Thanks to a numerical model, Mankbadi (1985) argued that pairing arises when the subharmonic component acquires sufficient energy, both from the fundamental wave and from the mean flow, to become the largest-amplitude perturbation in the jet. He observed that one or more stages of subsequent pairing can occur; in his framework, the number of stages and their spatial localisation depends on the Strouhal number.

A deeper theoretical understanding of the wave interaction involved in vortex pairing was reached by Monkewitz (1988), who formulated a weakly nonlinear model for the spatial development of fundamental and subharmonic instability waves in a parallel mixing layer. This model reflects the role of the phase shift between the two waves in triggering resonance, resulting in either pairing or "shredding" of vortices. It was predicted that the fundamental wave needs to reach a critical amplitude before subharmonic perturbations may phase-lock and grow. The same conclusions are supported by the more general theory of Cheng & Chang (1992).

The model of Monkewitz (1988) was confirmed experimentally by numerous studies: in a mixing layer, Husain & Hussain (1989) showed that simultaneous forcing of a fundamental frequency and its subharmonic could either enhance or attenuate the pairing and shredding phenomena. Subsequently, detailed statistical analysis of experimental

data was performed, first for uncontrolled "natural" perturbations in a mixing layer (Hajj *et al.* 1992), then for explicitly forced fundamental and subharmonic waves in the same setup (Hajj *et al.* 1993). These two studies gave clear evidence of a parametric resonance, determined by the phase difference between both waves. Husain & Hussain (1995) carried out similar investigations of jets with a very thin shear layer, confirming that pairing was amplified for a large band of phase differences, but attenuated for a narrow band of phase differences. Moreover, these authors studied the influence of a slight frequency detuning in the subharmonic forcing, finding that the occurrence of vortex pairing depended on the instantaneous phase difference in the forcing. A parametric experimental study of pairing in jets was conducted by Raman & Rice (1991), who varied the Strouhal number, phase difference and forcing amplitude for both the fundamental and the subharmonic instability wave. Consistent with the theoretical predictions, it was shown that a critical fundamental amplitude was necessary to trigger subharmonic resonance, the growth rate being controlled by the phase difference at small forcing amplitude. When the forcing was strong enough, however, the subharmonic growth became independent of the phase difference. Paschereit *et al.* (1995) confirmed these results, and further demonstrated that the subharmonic growth draws its energy from the mean flow, whereas the fundamental wave merely acts as a catalyst. In all these studies, explicit forcing of the subharmonic wave controlled the location of vortex pairing in turbulent jets.

The modal interaction framework was used by Bradley & Ng (1989) to study interactions between more than two frequencies, or between frequencies different from the fundamental ω and its subharmonic $\omega/2$. These authors experimentally studied a jet forced either at ω and $\omega/2$ or at ω and $\omega/3$ and studied the influence of frequency, amplitude ratio and phase shift. In the ω and $\omega/3$ forcing case, they found more diverse behaviour, with collective interactions, or pairing between vortices of different sizes.

2.3. *Further developments on pairing*

2.3.1. *Chaotic behaviour*

In less controlled configurations, vortex pairing events are often observed to be irregular and intermittent. Broze & Hussain (1994, 1996) conducted jet experiments with single-frequency excitation; depending on the Strouhal number St_D and on the forcing amplitude a_f, different types of behaviour were reported, as summarised in figure 2. Regular dynamics were found to arise over large parameter regions, namely no pairing (FO regime in figure 2), stable pairing (SP) and stable double pairing (SDP), the latter referring to the occurrence of two successive stages of vortex pairing. Irregular dynamics were observed either in the mild form of "aperiodic modulations" of the first (AM) or the second pairing stage (SPMQ), or in more erratic ways, categorised as intermittency, chaos (QCA) and "nearly-periodic modulations" (NPMP).

The results of Broze & Hussain (1996) do not appear to depend significantly on the Reynolds number within their operating conditions of $11000 \leqslant Re \leqslant 90000$. Drawing on chaos theory, the authors characterised the pairing dynamics in terms of attractors. For irregular scenarios, it was demonstrated that the occurrence of pairing of two vortices is strongly influenced by previous pairing events, implying that upstream-directed feedback is involved in the subharmonic growth. This observation is fully consistent with the wave-interaction model discussed in § 2.2. Narayanan & Hussain (1997) attempted to stabilise the pairing dynamics in chaotic regimes.

2.3.2. *Pairing-related jet noise*

High-speed jets are potent sources of noise, and the role of vortex pairing as an aeroacoustic source mechanism has received much attention. Bridges & Hussain (1987)

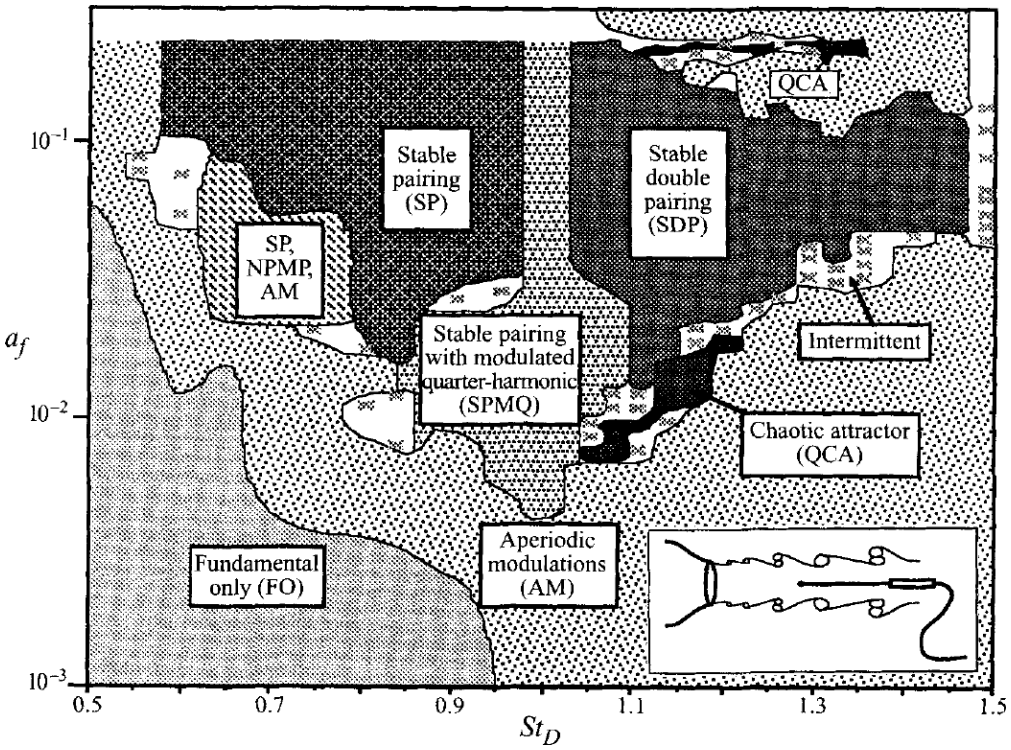

Figure 2: Pairing dynamics observed experimentally in turbulent jets at $Re = O(10^4)$, forced at a Strouhal number St_D with amplitude a_f. No subharmonic forcing is applied. From Broze & Hussain (1996).

determined that the radiated noise is dominated by pairing events only in cases where the initial shear layer is laminar; in fully turbulent jets, vortex pairing appears to be acoustically unimportant. The dominant role of vortex pairing in laminar jet noise was further analysed numerically by Bogey & Bailly (2010). A detailed description of sound generation from vortex interaction in jets was given by Inoue (2002), and model-based predictions of radiated sound levels were derived by Schram *et al.* (2005).

2.3.3. *Kinematical modelling of vortex-ring interaction*

Vortex interaction can be conveniently modelled by use of the Biot–Savart law. An account of early applications of such approaches to vortex rings is given by Shariff & Leonard (1992); these studies were largely concerned with the initial roll-up or with the collective motion of a limited number of co-axial vortices. A common representation characterises a vortex ring by its core centre position and core radius, from which a semi-analytical induction law can be derived (Saffman 1992). Contrary to vortex elements in a two-dimensional plane, axisymmetric vortex rings move at a self-induced velocity, which becomes infinitely large as the core radius approaches zero. Some simplifications arise from the assumption that the core radius is much smaller than the ring radius.

Within the limiting assumptions of inviscid flow and compact cores, such a conceptual model then yields low-dimensional systems representing the mutually induced motion of a collection of vortex rings. The "leapfrogging" interaction between two rings, when one passes through the other, corresponds to the early nonlinear stage of pairing in a jet before actual merging occurs. A model of a *plane* jet, consisting of counter-rotating vortex pairs, was studied by Tophøj & Aref (2013), who formulated a linear stability criterion for the occurrence of leapfrogging. Similarly, Borisov *et al.* (2013, 2014) derived

stability criteria for sets of two and three co-axial vortex rings, and validated these with respect to numerical simulations of viscous flow at high Reynolds number. Their work was completed by Cheng *et al.* (2015), who explicitly portrayed parameter regions in which leapfrogging could occur, depending on the Reynolds number and the aspect ratio of the vortex arrangement. Meunier *et al.* (2002) discovered a merging criterion for two co-rotating vortices in a two-dimensional plane.

2.3.4. *Pairing of helical vortices*

In several industrial applications, such as helicopter rotors or wind turbines, a wake composed of several nested helical vortices is formed (Vermeer *et al.* 2003). Further downstream, these helical vortices diffuse and can interact together as well as with the hub vortex (Delbende *et al.* 2015; Felli *et al.* 2011).

Formally, these vortices form a time-periodic three-dimensional flow, which can be regarded as a steady state in a frame of reference rotating with the blades. In addition, assuming no interaction between vortices, they diffuse slowly in the far wake, allowing for a quasi-static approximation (Selçuk *et al.* 2017*b*) when neglecting variations of the vortex structure in the axial direction. Therefore, Selçuk *et al.* (2017*a*) carried out a global stability analysis of these quasi-static states reduced to steady flows. At low pitch values, they found the existence of unstable modes that trigger leapfrogging, overtaking and eventually pairing when superposed onto the quasi-static base flow.

3. Vortex pairing in simulations at various Reynolds and Strouhal numbers

In this section, we give a general overlook of the vortex pairing phenomenon in axisymmetric laminar jets. After explaining the numerical simulation details, we show that, depending on the jet parameters and the forcing considered, vortex pairing can occur or not. When it does, we take a close look on a pairing sequence. Eventually, we finish with a parametric study to characterise its occurrence domain.

3.1. *Setup of direct numerical simulations*

Simulations were carried out using Nek5000 (Nek 5000), an incompressible spectral element code. A perfectly axisymmetric jet is described in cylindrical coordinates (z, r), z being the main flow direction and r being the radial distance from the jet axis. The flow is assumed to be governed by the incompressible axisymmetric Navier–Stokes equations with zero azimuthal velocity, written in dimensionless form as

$$\frac{\partial v}{\partial t} + v\frac{\partial v}{\partial r} + u\frac{\partial v}{\partial z} = -\frac{\partial p}{\partial r} + \frac{1}{Re}\left(\frac{1}{r}\frac{\partial}{\partial r}\left(r\frac{\partial v}{\partial r}\right) - \frac{v}{r^2} + \frac{\partial^2 v}{\partial z^2}\right), \tag{3.1a}$$

$$\frac{\partial u}{\partial t} + v\frac{\partial u}{\partial r} + u\frac{\partial u}{\partial z} = -\frac{\partial p}{\partial z} + \frac{1}{Re}\left(\frac{1}{r}\frac{\partial}{\partial r}\left(r\frac{\partial u}{\partial r}\right) + \frac{\partial^2 u}{\partial z^2}\right), \tag{3.1b}$$

$$\frac{1}{r}\frac{\partial (rv)}{\partial r} + \frac{\partial u}{\partial z} = 0, \tag{3.1c}$$

where the velocity $\mathbf{u}$ has axial and radial components u and v, and p denotes pressure. The jet diameter D and the inlet centerline velocity U_0 are used to render the flow problem nondimensional, leading to a definition of the Reynolds number as $Re = U_0 D/\nu$, with ν the kinematic viscosity. The computational domain extends, unless specified otherwise, over 40×5 diameters in the axial and radial directions, respectively, and it is discretised with 17600 spectral elements, each containing 64 mesh points.

Boundary conditions are specified as follows. In the inlet plane, $z = 0$, a hyperbolic tangent velocity profile is imposed. Its amplitude is modulated in time as

$$\mathbf{u}(z=0,r,t) = \frac{1}{2}\left\{1 - \tanh\left[\frac{1}{4\theta_0}\left(r - \frac{1}{4r}\right)\right]\right\}(1 + A\cos(\omega_f t))\,\mathbf{e}_z, \tag{3.2}$$

where A is the forcing amplitude, $\theta_0 = 0.025$ is the initial non-dimensional shear layer thickness and ω_f is the forcing frequency. The forcing period is given by $T = 2\pi/\omega_f$, and the Strouhal number is defined as $St_D = \omega_f D/(2\pi U_0)$.

On the jet centreline, axisymmetric boundary conditions are imposed as

$$\frac{\partial u}{\partial r} = v = \frac{\partial p}{\partial r} = 0 \quad \text{at } r = 0. \tag{3.3}$$

In the outlet plane, $z_{max} = 40$, and on the lateral boundary, $r_{max} = 5$, the standard outflow formulation provided by Nek5000 is employed. This prescribes a stress-free condition

$$\frac{1}{Re}\frac{\partial v}{\partial r} - p = \frac{\partial u}{\partial r} = 0 \text{ at } r = r_{max} \quad \text{and} \quad \frac{1}{Re}\frac{\partial u}{\partial z} - p = \frac{\partial v}{\partial z} = 0 \text{ at } z = z_{max}. \tag{3.4}$$

The flow configuration is thus characterised by the Reynolds number Re, the Strouhal number St_D, the initial shear layer thickness θ_0 and the forcing amplitude A. A single value $\theta_0 = 0.025$ is used throughout this study.

3.2. *Two distinct behaviours*

Depending on flow parameters and forcing Strouhal number, rolled-up vortices may spontaneously undergo subsequent pairing. In the absence of free-stream turbulence, and if the harmonic forcing is well-controlled, this pairing takes place in a perfectly regular fashion.

In cases where pairing occurs, two neighbouring vortices merge into one, such that the passage frequency of vortices downstream of the pairing location is exactly half that of the imposed forcing. An example, obtained by direct numerical simulation with parameters $Re = 2000$, $St_D = 0.6$ and $A = 5\%$, is shown in figure 3a. If the forcing is characterised by the time period T, the "paired state" is globally $2T$-periodic. The velocity field of a paired state will be denoted $\mathbf{u}^p$.

A different behaviour is observed when the Reynolds number is lowered to $Re = 1300$, as shown in figure 3b. Vortices roll up close to the nozzle and advect downstream, until they are dissipated by viscosity, but no spontaneous pairing is observed at this parameter setting. Such a flow state is globally T-periodic and will be called hereafter an "unpaired state". Its velocity field will be denoted $\mathbf{u}^u$.

When the natural time-asymptotic flow state for a given set of parameters involves pairing, it is still possible to recover an unpaired state as an alternative solution of the flow equations, by use of time-delayed feedback control (see § 4.1 and Shaabani-Ardali *et al.* (2017)). The unpaired state obtained in such a way for the previous configuration with $Re = 2000$ is shown in figure 3c. This solution is an exact solution of the Navier-Stokes equations without the time-delayed feedback.

3.3. *The dynamics of vortex pairing*

The process of the pairing of two vortices is inspected from snapshots of the vorticity, presented in figure 4, at four different phases of one pairing cycle. At $t = 0$ (figure 4a), two successive vortices, located around $z = 1$ and 2, have rolled up due to the primary shear instability. One half-cycle of the forcing period later (figure 4b), the leading vortex

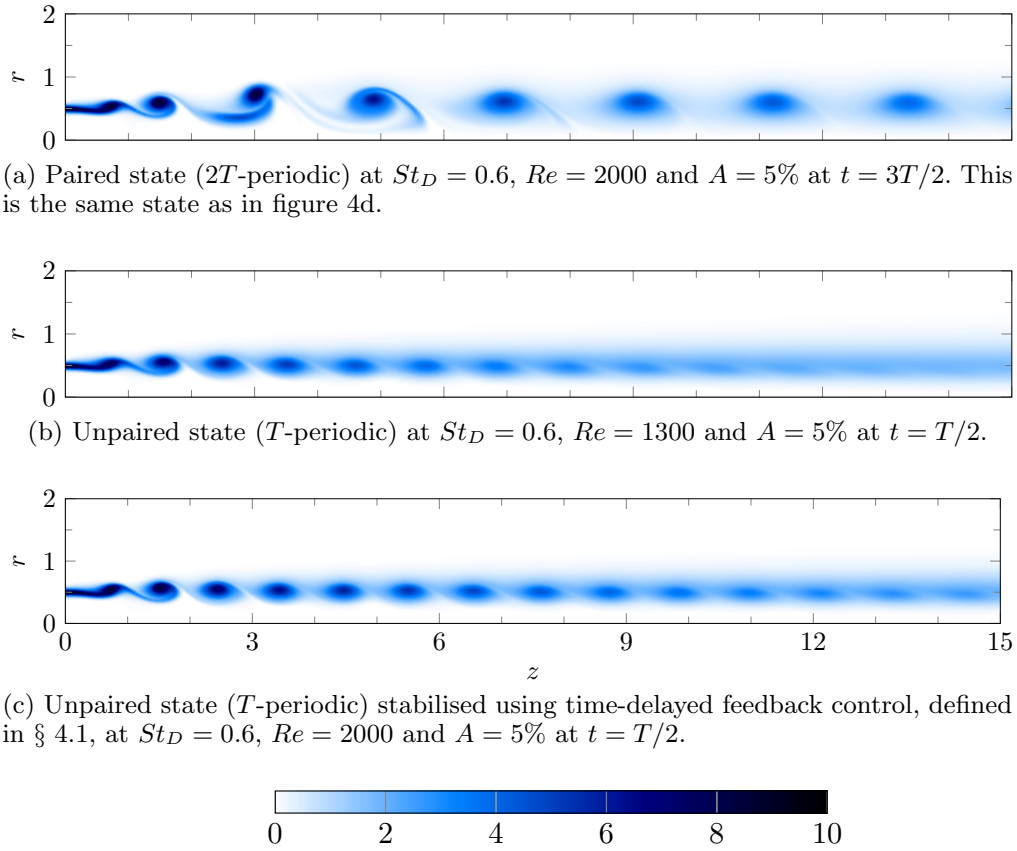

(a) Paired state ($2T$-periodic) at $St_D = 0.6$, $Re = 2000$ and $A = 5\%$ at $t = 3T/2$. This is the same state as in figure 4d.

(b) Unpaired state (T-periodic) at $St_D = 0.6$, $Re = 1300$ and $A = 5\%$ at $t = T/2$.

(c) Unpaired state (T-periodic) stabilised using time-delayed feedback control, defined in § 4.1, at $St_D = 0.6$, $Re = 2000$ and $A = 5\%$ at $t = T/2$.

Figure 3: Vorticity snapshots of the periodic paired and unpaired states, obtained naturally for two different parameter settings. Forcing amplitude, Reynolds and Strouhal numbers are defined in § 3.1.

has slightly expanded radially, while the trailing one has contracted. This movement is accompanied by a deceleration of the expanding vortex, and inversely an acceleration of the contracting vortex, through the influence of the vortex ring radius on its self-induced propulsion. The same process continues at $t = T$ (figure 4c), when the trailing vortex begins to pass through the interior of the leading vortex. At $t = 3T/2$ (figure 4d), both vortices are in the process of merging into one, which is largely achieved at the end of the cycle (figure 4a).

Conceptual arguments for the occurrence of vortex pairing in the literature are typically based on the interaction between fundamental and subharmonic fluctuations, and the possibility of energy transfer to the latter (Monkewitz 1988). Spatial energy variations of the fundamental ω_f and the subharmonic $\omega_f/2$ Fourier modes are readily extracted from the present numerical simulations. These are presented in figure 5, for the configuration $Re = 2000$, $St_D = 0.6$ and $A = 5\%$, in the form of radially integrated kinetic energy. This plot allows the distinction of various stages in the pairing process. Immediately downstream of the inlet, the fundamental mode grows from its forced initial amplitude to its peak value at $z = 1.4$. This streamwise position may be identified with the shedding of a fully formed vortex (see figure 4). The subharmonic component experiences strong exponential growth over the same interval, starting from a much lower level, as the boundary condition imposes zero amplitude at the inlet. Subharmonic growth continues down to $z = 3.1$, where figure 4(d) shows strong pairing dynamics. The energy of the

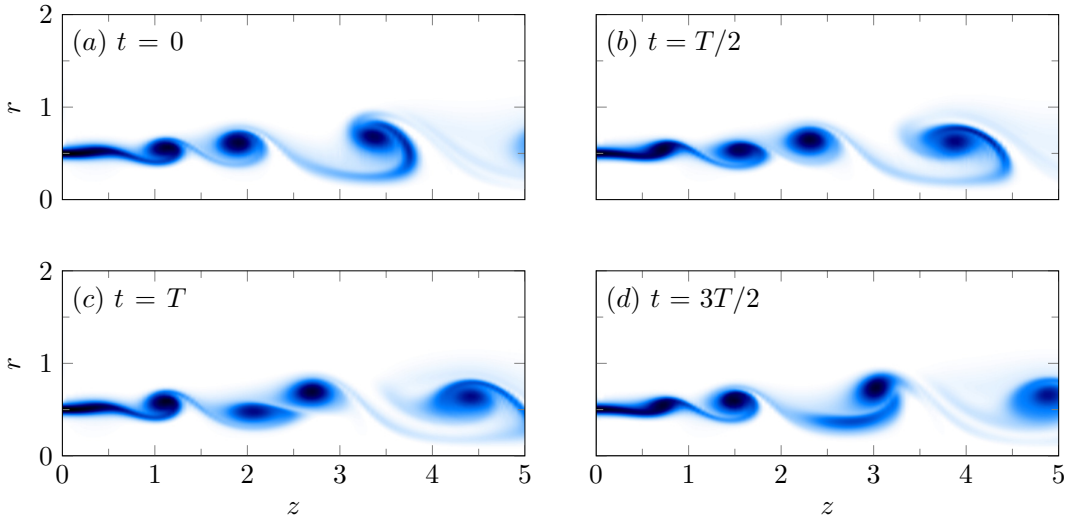

Figure 4: Vorticity snapshots of a paired case at $Re = 2000$ forced harmonically at $St_D = 0.60$ and $A = 5\%$. Only the region near the inlet is shown. The colour coding is the same as in figure 3c.

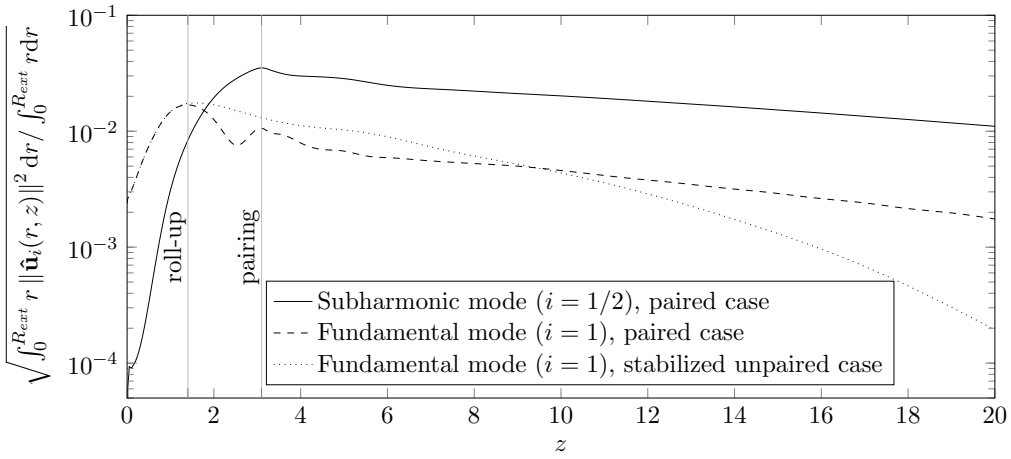

Figure 5: Total energy of the fundamental $\hat{\mathbf{u}}_1$ and subharmonic $\hat{\mathbf{u}}_{1/2}$ Fourier components in each plane $z = const.$ as a function of z at $St_D = 0.6$, $Re = 2000$ and $A = 5\%$.

fundamental mode decreases over the distance $1.4 < z < 3.1$, although a local maximum is found at the peak location of the subharmonic mode. As pairing is accomplished, at $z > 3.1$, both the fundamental and the subharmonic mode decay slowly in z, both at a similar rate, due to viscous dissipation of the convecting vortices.

Consistent with these observations, Monkewitz (1988) argued that a growth of subharmonic perturbations must be fed by energy transfer from the fundamental mode, which requires that both modes propagate at the same phase velocity. Phase velocities of fundamental and subharmonic fluctuations in the present simulation are compared in figure 6 as solid and dashed lines. The reported phase velocities are measured, for each streamwise location, at the radial distance where each respective Fourier mode has its maximum amplitude along r. The values for both modes match quite closely throughout the relevant interval upstream of the pairing location. They continue to match in the

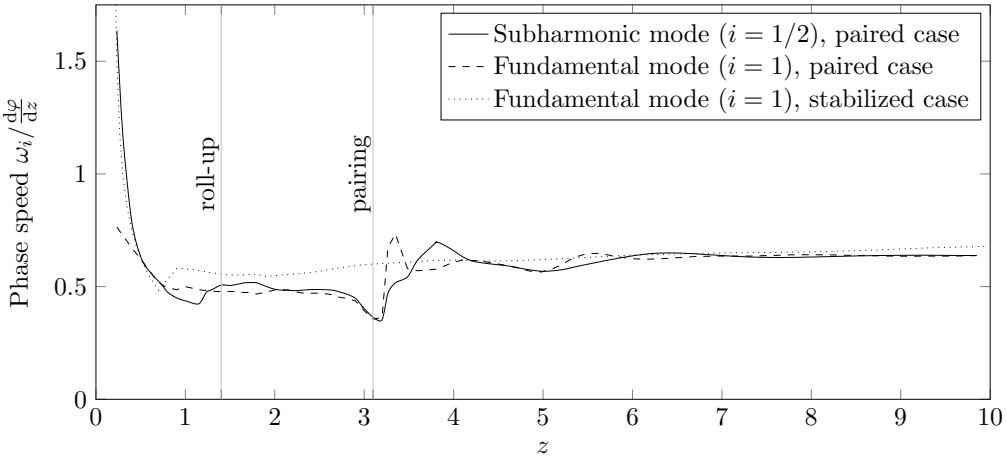

Figure 6: Phase speed along the line of maximum subharmonic mode of the subharmonic and fundamental modes of a paired jet at ($Re = 2000, St_D = 0.60$), and comparison with the phase speed of the fundamental mode along the lime of maximum fundamental mode of the corresponding stabilised (unpaired) jet. The phase of the Fourier mode is denoted as φ.

downstream region, but this is only the result of the fundamental mode being slaved to its subharmonic counterpart as a passive harmonic.

For comparison, energy and phase velocity results obtained for the fundamental mode of the corresponding stabilised (unpaired) flow are also presented in figures 5 and 6 (dotted lines), alongside the values found in the paired state. Upstream of the roll-up location, the fundamental modes show identical energy growth in both configurations. Between the roll-up and the pairing locations, the fundamental energy decay in the paired case is stronger than in the unpaired case, which again indicates that the growth of subharmonic perturbations feed on the energy of the fundamental mode. However, downstream of the pairing location, the fundamental mode in the stabilised case decays significantly faster, and at an increasing rate. This difference is also visible when one compares figures 3a and 3c: it appears that the lower frequency and the stronger circulation of the paired vortices hinders their diffusion and allow them to be sustained longer. When comparing the phase velocities in figure 6, it is seen that the unpaired fundamental mode propagates faster than its paired counterpart upstream of the pairing location, whereas their velocities are again equal in the downstream region. The discrepancy upstream of the pairing can be linked to different positions of the vortices: in the paired case, the vortices are radially more expanded than in the unpaired case, therefore moving at a slower speed. Vortex pairing does not only influence the flow downstream, but also upstream.

3.4. *Parametric study*

All simulations presented in this section were carried out on a domain with $z_{max} = 15$ in order to save computational resources. Test runs with $z_{max} = 40$ were performed for selected cases, showing no effect of domain truncation on the results presented here.

3.4.1. *Effect of Reynolds number and Strouhal number*

The effect of Reynolds and Strouhal numbers on the onset of vortex pairing is investigated first, for a fixed forcing amplitude $A = 5\%$. Direct numerical simulations were run, first in an exploratory fashion for many (Re, St_D) combinations. After an initial

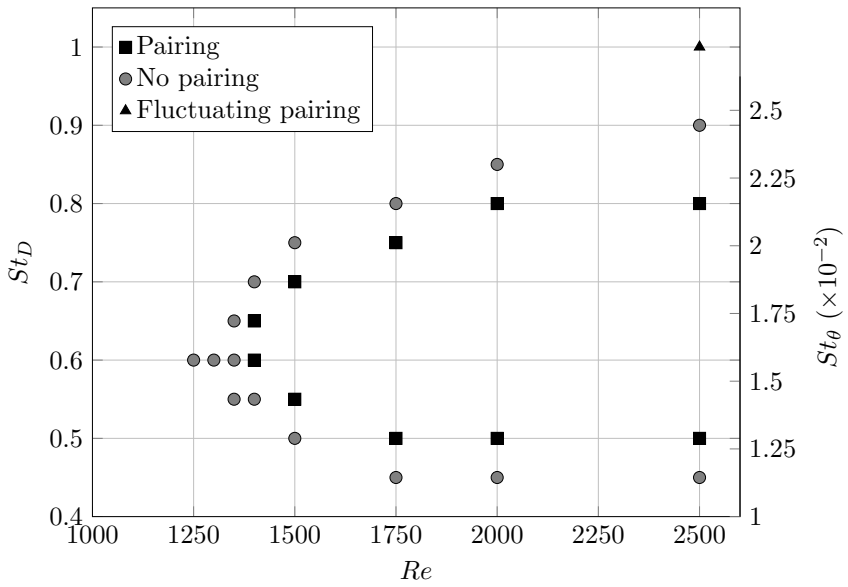

Figure 7: Occurrence of vortex pairing as a function of Reynolds number and Strouhal number for configurations with forcing amplitude $A = 5\%$ and initial shear layer thickness $\theta_0 = 0.025$. Only points near the pairing boundary are represented.

transient phase, the flow settles into an asymptotic time-periodic state. Asymptotic states that involve regular vortex pairing were found in a restricted region in the (Re, St_D) plane, and the boundary of that region was then determined more accurately by running simulations well into the asymptotic regime. Results of these simulations are mapped in figure 7. Pairing is found to occur first around a critical Reynolds number $Re_c = 1375$, for the fundamental forcing Strouhal number $St_D = 0.6$. Up to $Re = 2500$, the maximum value considered in this study, vortex pairing at asymptotic times is restricted to the band $0.5 \leqslant St_D \leqslant 0.8$. With increasing Reynolds number, the pairing becomes more vigorous, and its location gradually shifts nearer to the inlet.

Close to the instability thresholds, it becomes difficult to precisely characterise the flow behaviour, because of the long simulation times needed to achieve convergence. When the Reynolds number is about 1350, computations were run on full-length domains ($40D$), and even after several hundred forcing periods, the paired or unpaired nature of the final flow state cannot be determined. For instance, at $St_D = 0.6$, the final state for $Re = 1350$ is unpaired, for $Re = 1400$ it is paired. For intermediate values $Re = 1360$, 1372 or 1375 (close to threshold $Re_c = 1371$ predicted in § 4.4), the pairing location moves gradually downstream as time evolves, but with no indication whether it will eventually become stationary. These ambiguous data points are not displayed in figure 7.

As mentioned in § 2.1, a first parametric study of vortex pairing in terms of Reynolds and Strouhal numbers has been carried out experimentally by Zaman & Hussain (1980), for Reynolds numbers greater than 10^4 and thin initial mixing layer $\theta/D \approx 0.25\%$). They found that pairing could occur in *two* frequency bands, one characterised by a Strouhal number $St_\theta = f\theta/U$ based on the shear layer thickness, the other by a Strouhal number $St_D = fD/U$ based on the jet diameter. Pairing has been reported for St_θ around 0.012 and for $0.75 \leqslant St_D \leqslant 1.0$. With our choice of the initial shear layer thickness being 5% of the diameter, these two regimes are only weakly separated, which explains why our findings of a single band of instability at a given Reynolds is coherent; both scalings are indicated in figure 7.

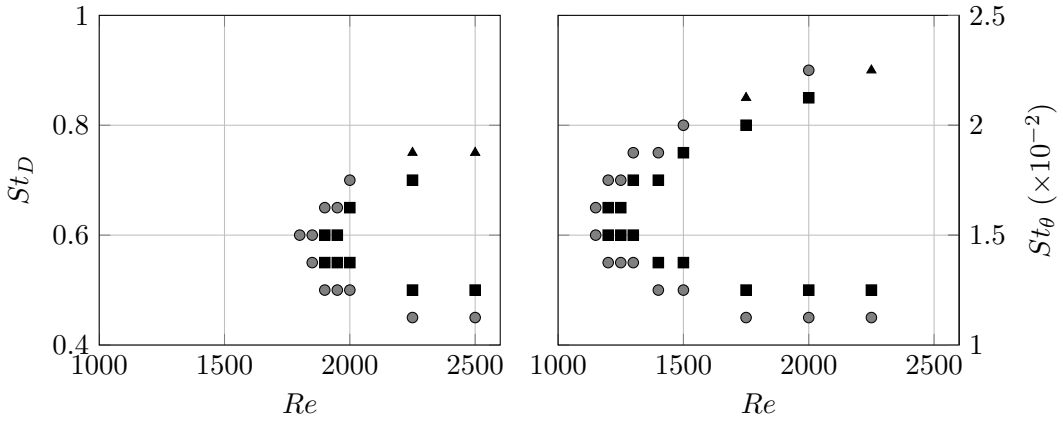

(a) $A = 1\%$. (b) $A = 10\%$.

Figure 8: Occurrence of vortex pairing as a function of the Reynolds and the Strouhal number for two different forcing amplitudes $A = 1\%$ and 10%. The same symbols as in figure 7 are used.

Again for Reynolds numbers greater than 10^4, and for a 5% forcing amplitude, Broze & Hussain (1994), found several flow regimes depending on St_D (see figure 2): no pairing for $St_D < 0.52$, aperiodic modulations and coexistence of different states (stable or modulated pairing) for $0.52 < St_D < 0.77$, stable pairing for $0.77 < St_D < 0.97$, stable pairing with quarter-harmonic modulations for $0.97 < St_D < 1.02$ and stable double pairing for $St_D > 1.02$, with some intermittent cases. The St_θ-dependance is not documented in that study. In our computations, we do not encounter such a richness of scenarios, because our inlet condition is fully laminar and time-periodic, and because our Reynolds number is one decade lower; however, the occurrence of pairing, reported in figure 7, is consistent with the experiments of Broze & Hussain (1994). Multiple stages of successive pairing are never observed in our computations, even at $St_D > 1$. This difference with respect to the experiments is certainly owing to the lower Reynolds number, as Cheng *et al.* (2015) demonstrated that viscosity inhibits pairing. However, the modulated states described by Broze & Hussain (1994) for $St_D \approx 1$ may be linked to our observation of fluctuations of the pairing position (triangle in figure 7).

Cheng *et al.* (2015) investigated numerically the leapfrogging of coaxial vortex rings. For a system of two adjacent vortices, they systematically documented the occurrence of leapfrogging as a function of Reynolds number and vortex separation. The Reynolds number, defined as the ratio of the ring vorticity over the viscosity and chosen of the order of 10^3 is related to the product between Reynolds and Strouhal numbers in our present notation. The ratio of the vortex spacing over the ring radius is related to the inverse of the Strouhal number as defined here. Cheng *et al.* found that leapfrogging occurs only above a critical Reynolds number, and for a narrow Strouhal band that increases with Reynolds number. This is consistent with our findings (figure 7), as pairing can be understood as an advanced stage of leapfrogging (figure 4).

3.4.2. *Effect of forcing amplitude*

The effect of forcing amplitude is investigated by including computations with two additional values, $A = 1\%$ and 10%. Instability maps in the (Re, St_D) plane for these configurations are displayed in figure 8a and 8b. An increase in the forcing amplitude is seen to shift the onset of pairing towards lower Reynolds number values.

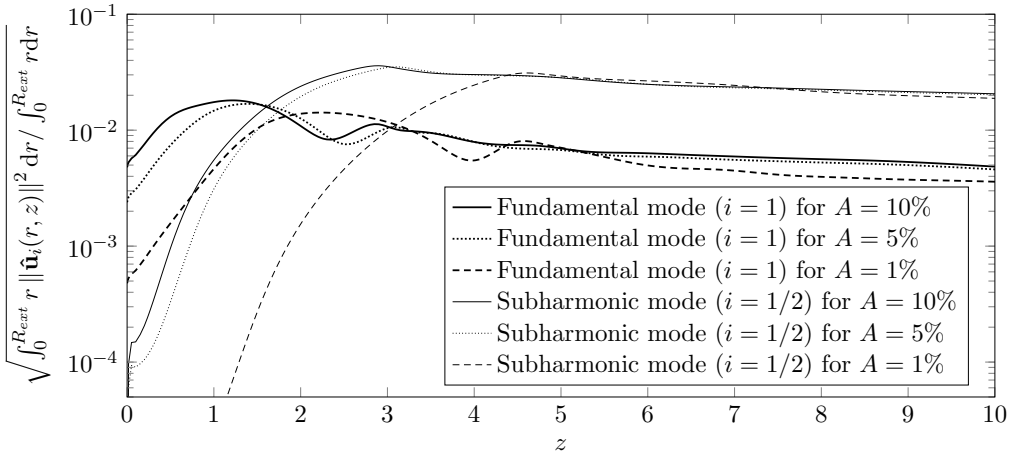

Figure 9: Total energy of the fundamental and subharmonic modes in each plane $z = const$ as a function of z at $St_D = 0.6$ and $Re = 2000$. Three values of the inlet forcing amplitude are considered, $A = 1\%$, 5% and 10%.

Another effect of increasing A is to move the roll-up and pairing locations upstream, as can be seen in figure 9. In the same way as discussed for figure 5, the energy of the fundamental mode in all cases grows from the inflow towards its maximum at the roll-up location, whereas the subharmonic mode peaks at the location of pairing. Increasing the fundamental amplitude at the inflow reduces the distance needed before roll-up, and it catalyses the subharmonic mode, inducing an earlier pairing.

However, by comparing the difference between the modes at $A = 1\%$ and 5%, and between the modes at $A = 5\%$ and 10% in figure 9, it is anticipated that a further increase in A will only marginally change the paired flow behaviour. This is consistent with Broze & Hussain (1994): as shown in figure 2, increasing the forcing amplitude above 5% does not induce significant topological changes in the final state, but below 1% forcing, no stable pairing is observed in the experiments. Raman & Rice (1991) also found that a critical minimal amplitude of the fundamental forcing was required to trigger pairing. Therefore, an expansion of the study to *lower* amplitude levels $A < 1\%$ could be of interest; however, this would require higher values of Re to be considered, rendering the assumption of laminar flow increasingly doubtful.

In their leapfrogging study of two vortex rings, Cheng *et al.* (2015) varied the vortex thickness, and thereby the vortex concentration, which is similar to varying the amplitude of forcing. Consistent with the present study, they concluded that stronger vortices undergo pairing at lower Reynolds numbers.

3.4.3. *Effect of inlet noise*

In configurations where vortex pairing does not arise intrinsically, the flow may still be receptive to low-level subharmonic extrinsic perturbations, in the sense of a "slightly damped oscillator" (Huerre & Monkewitz 1990), and exhibit vortex pairing in their presence. In the following, this receptivity is probed by imposing a random noise in addition to the fundamental forcing at the inlet, such that the inflow condition is prescribed as

$$\mathbf{u}(r,t) = \frac{1}{2}\left\{1 - \tanh\left[\frac{1}{4\theta_0}\left(r - \frac{1}{4r}\right)\right]\right\}\left(1 + A\cos\left(\omega_f t\right) + \epsilon_{noise}(t)\right)\mathbf{e_z}, \tag{3.5}$$

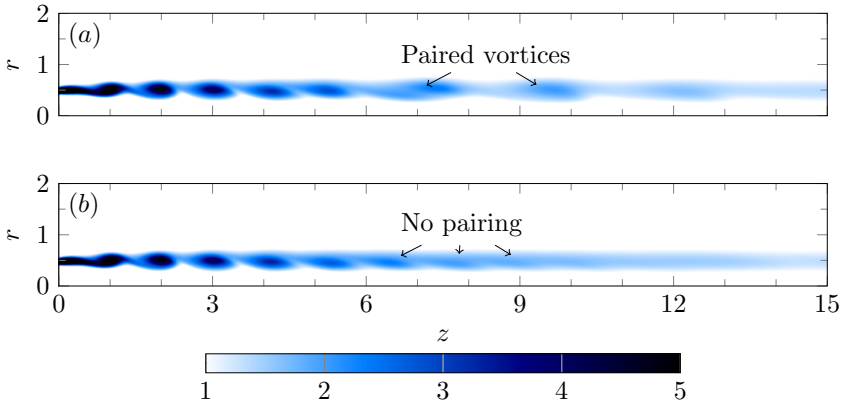

Figure 10: Vorticity snapshots at $Re = 750$, $St_D = 0.60$ and $A = 5\%$ with $A_\epsilon = 1.0\%$ taken at two different times, and both at the same phase. Pairing is intermittent, occurring in (a) and not in (b). The colorbar is rescaled compared to figure 3b, to magnify the behaviour of downstream vortices.

with ϵ_{noise} a white noise, constant in r, with a specified standard deviation. Four Reynolds number values are selected, $Re = 500$, 750, 1000 and 1300, and two values of the standard deviation $A_\epsilon = \sqrt{\langle \epsilon_{noise}, \epsilon_{noise} \rangle} = 0.1\%$ and 1% are tested. The latter are chosen such as not to exceed the level of coherent forcing A. The fundamental forcing in all cases is prescribed with $St_D = 0.6$ and $A = 5\%$.

Four distinct types of the flow response are observed:

(i)At low Reynolds number, the noise barely impacts the flow behaviour. For instance, at $Re = 500$ and for both noise levels, no significant departure from the purely harmonically forced jet is observed.

(ii)The noise induces a subharmonic modulation of the vortices, but the flow diffuses too quickly for pairing to occur, for instance in the case $Re = 750$ and $A_\epsilon = 0.1\%$.

(iii)Intermittent pairing is triggered, for instance at $Re = 1000$ and $A_\epsilon = 0.1\%$, or at $Re = 750$ and $A_\epsilon = 1.0\%$ (figure 10). In the latter case, pairing occurs far downstream, where the vortices are indistinct due to diffusion.

(iv)Continuous pairing is sustained by noise input, but its location fluctuates in time. This is observed for $Re = 1000$ with $A_\epsilon = 1\%$, and for $Re = 1300$ with $A_\epsilon = 0.1\%$ (figure 11) as well as 1.0%. As described experimentally by Ho & Huang (1982); Husain & Hussain (1989), other phenomena such as *shredding*, where one single vortex "escapes" between two successful pairing events, or *collective interaction*, where more than two vortices interact at once, can be observed, for instance in figure 12.

4. Vortex pairing as an unstable global Floquet mode

In this section, it is investigated whether the onset of vortex pairing can be described as the manifestation of a global Floquet instability of the periodic unpaired state. This unpaired state must first be computed for a given combination of flow parameters (§ 4.1). After a short reminder of Floquet theory (§ 4.2), and a presentation of the numerical implementation (§ 4.3), the linear Floquet stability of the unpaired vortex street is analysed (§ 4.4), and the instability characteristics are compared to the observations documented in the previous section.

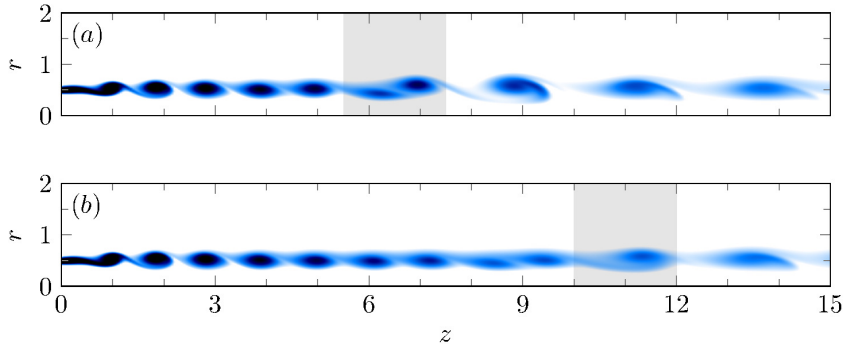

Figure 11: Vorticity snapshots at $Re = 1300$ and $St_D = 0.60$ with $A_\epsilon = 0.1\%$ taken at two different times, and both at the same phase. This shows the pairing location fluctuation, emphasised in grey, in this setup. The colorbar is in figure 10.

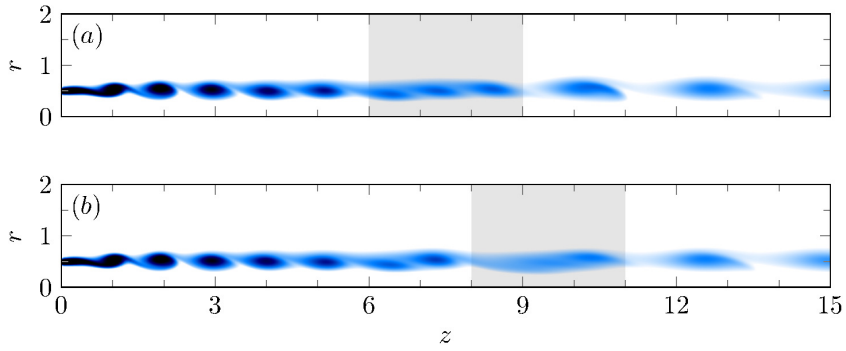

Figure 12: Vorticity snapshots at $Re = 1000$ and $St_D = 0.60$ with $A_\epsilon = 1.0\%$: (b) is taken two forcing periods after (a). The three vortices located in the shaded are on (a) merge altogether, as an example of collective interaction. The colorbar is in figure 10.

4.1. *Computation of T-periodic states without vortex pairing*

Periodic flow states are obtained through direct numerical simulation, as described in § 3.1. In order to suppress vortex pairing in configurations where it naturally arises, subharmonic fluctuations are actively damped by means of time-delayed feedback control. A short description of this method follows, for details the reader is referred to Shaabani-Ardali *et al.* (2017).

A fully synchronised *paired* state can be decomposed into one component that is T-periodic and another that is only $2T$-periodic,

$$\mathbf{u}^p(\mathbf{x},t) = \sum_n \mathbf{u}_n^T(\mathbf{x})\,\exp\left(\mathrm{i}n\omega_f t\right) + \sum_n \mathbf{u}_n^{2T}(\mathbf{x})\,\exp\left(\mathrm{i}\frac{2n+1}{2}\omega_f t\right), \qquad (4.1)$$

$$\text{with} \quad n = 0, \pm1, \pm2, \ldots, \pm N.$$

In a T-periodic *unpaired* state, the second sum is zero. Time-delayed feedback control is applied by adding a forcing term of the form

$$\mathbf{f} = -\lambda(\mathbf{u}(t) - \mathbf{u}(t-T)), \qquad (4.2)$$

to the right-hand side of the governing equations (3.1a)–(3.1c). Such forcing attenuates all $2T$-periodic fluctuations, but leaves T-periodic components unaffected. The simulations converge towards a purely T-periodic state, in which the artificial forcing term vanishes.

This solution is therefore a full solution of the Navier-Stokes equations. An example of such a stabilised unpaired state is shown in figure 3c.

The value of λ in equation (4.2) affects the convergence of the stabilisation procedure. In a previous publication (Shaabani-Ardali *et al.* 2017), it has been demonstrated that very small values of λ do not lead to convergence, as the resulting damping is insufficient to counteract the natural instability of the system. Similarly, too large values of λ result in overshooting of the damping force, which also inhibits convergence. An optimal value $\lambda = 0.0432\omega_f$ was derived from a model problem, and has been used in the present calculations.

4.2. *Floquet framework*

The Floquet stability problem for a T-periodic unpaired base flow $(\mathbf{U^u}(t), P^u(t))$ is set up by superposing small-amplitude perturbations $(\mathbf{u}', p')$, which are governed to leading order by the linear equations

$$\frac{\partial \mathbf{u}'}{\partial t} + (\mathbf{U^u}(t)\cdot\nabla)\,\mathbf{u}' + (\mathbf{u}'\cdot\nabla)\,\mathbf{U^u}(t) = -\nabla p' + \frac{1}{Re}\Delta\mathbf{u}', \qquad \nabla\cdot\mathbf{u}' = 0. \tag{4.3}$$

The following boundary conditions are implemented. In the inlet plane, the flow is unperturbed, $\mathbf{u}'(r, z = 0, t) = \mathbf{0}$. We do not allow perturbations directly at the inlet, since we consider only the behaviour of *intrinsic* perturbations. On the centreline of the jet, $r = 0$, axisymmetric boundary conditions as in the nonlinear case are imposed, $\partial_r u' = v' = \partial_r p' = 0$. In the outlet plane $z = 40$ and on the lateral boundary $r = 5$, stress-free conditions (3.4) are chosen.

The equations are written in compact form as

$$\frac{\partial \mathbf{q}'}{\partial t} = \mathcal{L}(t)\mathbf{q}', \tag{4.4}$$

where $\mathbf{q}' = (\mathbf{u}', p')$ represents the perturbation state vector.

According to Floquet theory (Floquet 1883), one may seek modal solutions of (4.4) in the form

$$\mathbf{q}'(t) = P(t)e^{At}\mathbf{q}'(0), \tag{4.5}$$

with $P(t)$ a T-periodic and A a constant matrix. Noting that

$$\mathbf{q}'(T) = e^{AT}\mathbf{q}'(0), \tag{4.6}$$

due to $P(T) = P(0) = Id$, the time-shift operator $\Phi = e^{AT}$ is introduced, such that $\mathbf{q}'(nT) = \Phi^n\mathbf{q}'(0)$. The eigenvalues μ_i of Φ are known as *Floquet multipliers*, and the associated eigenmodes v_i are the *Floquet modes* of the system (4.4). For a modal perturbation $\mathbf{q}'(0) = (\tilde{\mathbf{v}}_\mathbf{i}, \tilde{p}_i)$, the Floquet multiplier μ_i such that $\mathbf{q}'((n+1)T) = \mu_i\mathbf{q}'(nT)$ represents the complex amplitude gain over one cycle period. Therefore, the stability of the system is indicated by the modulus of μ_i: if all Floquet multipliers have a modulus lower than unity, all perturbations decay at long time and the system is stable. Floquet modes with an associated $|\mu_i| > 1$ experience exponential temporal growth.

The complex phase of a Floquet multiplier, $\arg(\mu_i)$, characterises the time-periodicity of its associated mode. At zero phase, the mode evolves with the same periodicity as the base flow, and may be qualified as being *harmonic*. A phase of $\arg(\mu_i) = \pi$, indicates that two base flow periods are needed to complete one perturbation cycle, and the mode therefore evolves as $\omega_f/2$. Such a mode is qualified as being *subharmonic*. As vortex pairing is a $2T$-periodic phenomenon, subharmonic Floquet modes are expected to arise. Floquet multiplier phases that are not integer multiples of π characterise modes with periodicities unrelated to that of the base flow.

A standard result of Floquet theory applied to the linearised Navier-Stokes equations is that the time derivative of the base flow, $(\partial_t \mathbf{U}^{\mathbf{u}}, \partial_t P^u)$, represents a neutral Floquet mode of the system, with $\mu = 1$. However, such a mode does not exist in the present problem, because it is inconsistent with the boundary conditions. While the base flow is periodically forced at the inlet boundary, according to equation (3.2), linear perturbations are prescribed to be zero there.

4.3. *Numerical implementation*

The evolution of the linearised system (4.4) is calculated using a fully implicit finite-difference time-stepping scheme of second order implemented in FreeFem++ (Hecht 2012). The mesh has the same size and resolution as the one used in the Nek5000 calculations. $P2$ finite elements are used for the velocity perturbation whereas $P1$ finite elements are used for the pressure.

In the numerical implementation of the Floquet mode calculation, only the velocity perturbation $\mathbf{u}'$ is considered. This is possible in incompressible flow, since the full state $\mathbf{q}' = (\mathbf{u}', p')$ is fully determined by $\mathbf{u}'$ alone. Therefore, the standard projection operator $P_{\mathbf{q}\to\mathbf{u}}$ from the $\mathbf{q}$-space to the $\mathbf{u}$-space can be defined, as well as its inverse $P_{\mathbf{u}\to\mathbf{q}}$. The operator $\Phi' = P_{\mathbf{q}\to\mathbf{u}} \Phi P_{\mathbf{u}\to\mathbf{q}}$ maps a given velocity perturbation to its value after one flow period. The modal stability properties of Φ' are the same as those of Φ, and Φ' will be considered in what follows.

By use of a block-Arnoldi method (Saad 2011), it is possible to construct a matrix representation of Φ' in a reduced orthonormal basis, generated by power iterations. A N_{vec}-vector block-Arnoldi is iterated over N stages, each stage consisting in time-integration of the linear flow equations over one flow period. Contrary to the standard Arnoldi algorithm, where the image of only one vector is calculated in each iteration stage, N_{vec} vectors are advanced simultaneously in the block-Arnoldi method. A value $N_{vec} = 30$ was used in all calculations presented in this section. Eigenvalues of the resulting matrix, of reduced dimension $NN_{vec} \times NN_{vec} = 750 \times 750$, may then be obtained. Concretely, the algorithm involves the following steps:

(i)An orthonormal basis of N_{vec} initial velocity perturbation vectors $\hat{\mathbf{u}}_i^0$ is built, with $i = 1, \ldots, N_{vec}$. Orthonormalisation of these vectors with respect to the energy scalar product

$$\langle \mathbf{u}, \mathbf{v} \rangle = \iint_\Omega r\mathbf{u}(r,z) \cdot \mathbf{v}(r,z) \mathrm{d}r\mathrm{d}z \tag{4.7}$$

is enforced.

(ii)At iteration $n \in [1, N-1]$, the images $\Phi\hat{\mathbf{u}}_i^{n-1}$ of each vector $\hat{\mathbf{u}}_i^{n-1}$ after one flow period are computed simultaneously by time-stepping.

(iii)The Gram–Schmidt algorithm is employed to extract and normalise the component $\hat{\mathbf{u}}_i^n$ of $\Phi'\hat{\mathbf{u}}_i^{n-1}$ for $1 \leqslant i \leqslant N_{vec}$ that is orthogonal to the already existing set of vectors $\{\hat{\mathbf{u}}_{i'}^j\}$, with $1 \leqslant i' \leqslant N_{vec}$ when $0 \leqslant j \leqslant n-1$ and $1 \leqslant i' < i$ when $j = n$. Thereby, the orthonormal basis $\{\hat{\mathbf{u}}_i^j\}$ is augmented by dimension N_{vec} in every iteration n.

(iv)In the end, after N iterations over one flow period, a fully orthonormal Krylov basis $\{\hat{\mathbf{u}}_i^0, \ldots, \hat{\mathbf{u}}_i^{N-1}\}$ and their images $\{\Phi'\hat{\mathbf{u}}_i^0, \ldots, \Phi'\hat{\mathbf{u}}_i^{N-1}\}$ after one period of time-stepping are obtained. Let R denote the matrix of this basis,

$$R = \left[\hat{\mathbf{u}}_1^0, \ldots, \hat{\mathbf{u}}_{N_{vec}}^0, \ldots, \hat{\mathbf{u}}_1^{N-1}, \ldots, \hat{\mathbf{u}}_{N_{vec}}^{N-1}\right], \tag{4.8}$$

which is of dimension $N_{dof} \times NN_{vec}$, with N_{dof} the number of degrees of freedom of the initial velocity perturbation. It is then possible to construct the projection $\tilde{\Phi}$ of the infinite-dimensional operator Φ' onto the finite-dimensional space spanned by R. $\tilde{\Phi}$ is

Re	St_D	A	N	Re	St_D	A	N	Re	St_D	A	N
500	0.60	5%	25	1750	0.60	5%	25	2000	0.85	5%	35
750	0.60	5%	25	2000	0.60	5%	25	2000	0.90	5%	40
1000	0.60	5%	25	2250	0.60	5%	25	2000	0.95	5%	40
1300	0.60	5%	25	2000	0.45	5%	25	2000	1.00	5%	40
1350	0.60	5%	25	2000	0.50	5%	25	2000	1.10	5%	45
1375	0.60	5%	25	2000	0.70	5%	30	2000	0.60	1%	25
1400	0.60	5%	25	2000	0.75	5%	35	2000	0.60	10%	25
1500	0.60	5%	25	2000	0.80	5%	35				

Table 1: Parameter combinations for which Floquet analysis is performed.

represented by the matrix

$$\tilde{\Phi}_{nN_{vec}+i,n'N_{vec}+i'} = \langle \Phi' \hat{\mathbf{u}}_{i'}^{n'}, \hat{\mathbf{u}}_i^n \rangle \quad \text{or} \quad \tilde{\Phi} = R^T M \left(\Phi' R\right), \tag{4.9}$$

with M the mass matrix associated with the scalar product (4.7).

(v)By computing the eigenvalues μ_k and eigenvectors $\boldsymbol{\alpha}^k$ of $\tilde{\Phi}$, defined such as $\dim(\boldsymbol{\alpha}^k) = NN_{vec}$, the Floquet multipliers μ_k are obtained directly, and the Floquet modes $\mathbf{v}_k$ can be reconstructed as

$$\mathbf{v}_k = \sum_{n=0}^{N-1} \sum_{i=1}^{N_{vec}} \boldsymbol{\alpha}_{nN_{vec}+i}^k \hat{\mathbf{u}}_i^n = R\boldsymbol{\alpha}^k \tag{4.10}$$

As pointed out by Saad (2011), the orthonormalisation step (*iii*) is essential for the recovery of non-dominant eigenmodes in the n^{th} iteration amidst the numerical noise on the level of round-off error.

The above algorithm is designed to maximise numerical efficiency in combination with a linear flow solver based on implicit time-stepping. As the base flow is time-dependent, a linear operator is constructed and factorised at each time step. It would not be economical to use this factorised operator for the time advancement of one single state vector; by use of the block-Arnoldi method, N_{vec} vectors can be advanced in time simultaneously, thus lowering significantly the numerical burden of constructing a high-dimensional Krylov subspace.

A minimum of $N = 25$ flow-period iterations has been used to generate the following results. This number was increased in steps of 5 as necessary in order for the dominant eigenvalue to converge to four significant digits.

The list of all examined flow configurations is given in table 1; the influence of the Reynolds number, the Strouhal number and the forcing amplitude may thus be characterised. For high values of St_D, a larger number of block-Arnoldi iterations are required in order to achieve convergence. Two competing time scales characterise the dynamics: the forcing period, which decreases with increasing St_D, and the convection time, which is constant in all cases. Therefore, a constant number of iterations at high Strouhal number corresponds to a shorter convection time.

4.4. *Floquet instability modes*

As shown in table 1, nearly all calculations have been performed for constant forcing amplitude $A = 5\%$, and with fixed values of either $St_D = 0.6$ or $Re = 2000$, in order to track the isolated influence of Strouhal and Reynolds number on the instability behaviour. In nearly all cases, one strictly subharmonic Floquet mode is identified, characterised by a negative real Floquet multiplier μ. This mode is observed to be unstable over certain

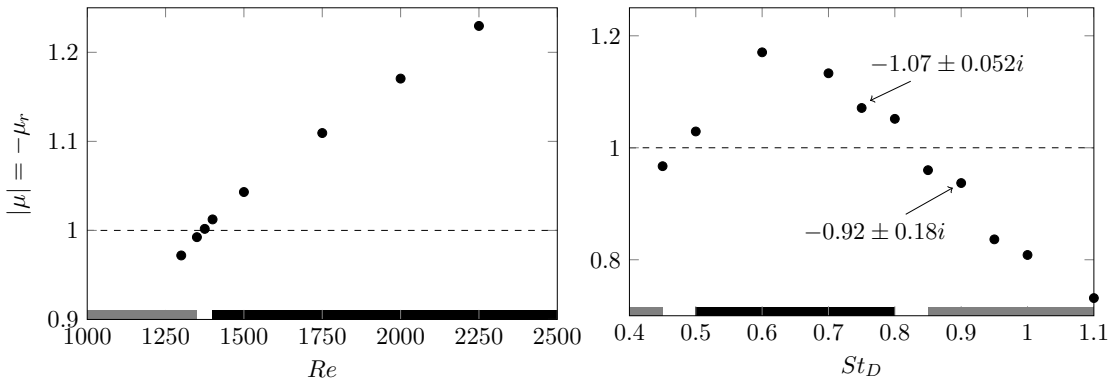

(a) $St_D = 0.6$. (b) $Re = 2000$.

Figure 13: Absolute value of the dominant subharmonic Floquet multiplier for different (Re, St_D), obtained for $A = 5\%$. When the system is unstable, the most unstable mode is always subharmonic (e.g. real negative), except for the two labeled cases in (b), where the most unstable mode is almost subharmonic. When the system is stable, the represented mode are the least stable of the subhamonic domain. Black and grey bars represent parameter regimes with and without vortex pairing, according to uncontrolled DNS (see figure 7).

ranges of St_D and Re, where μ falls below -1. The absolute value $|\mu| = -\mu$ for $St_D = 0.6$ and $A = 5\%$ is plotted as a function of Re in figure 13a: by linear interpolation of the critical Reynolds at which $\mu_c = -1$, instability in this case is found to arise for $Re \geqslant 1371$. This is to be compared to the critical band $Re \in [1350; 1400]$, above (resp. below) which sustained pairing was found to occur (resp. not to occur) in the DNS, as discussed in § 3.4.1. The paired and unpaired regimes, as identified in the DNS, are indicated in figure 13a by black and grey bars, in order to highlight the agreement with the onset of subharmonic Floquet instability.

Results for variations in St_D, at fixed values $Re = 2000$ and $A = 5\%$, are presented in the same manner in figure 13b. A finite band of subharmonically unstable Strouhal numbers is identified, again in agreement with the prevalence of vortex pairing as observed in the DNS. Two values of μ reported in this diagram are distinct from the others: at $St_D = 0.75$, the Floquet multiplier of the most unstable mode appears as a complex conjugate pair with small imaginary parts, as indicated in the figure. This mode is therefore nearly subharmonic, but not strictly so, and further iterations of the block-Arnoldi procedure do not change this result. Higher deviations from the negative real axis are found in the stable case $St_D = 0.9$. For $St_D = 0.75$, the unstable mode is slightly detuned, but the DNS does not display any irregular behaviour.

The effect of the forcing amplitude A on the instability is demonstrated for a single setting $Re = 2000$ and $St_D = 0.6$. As shown in table 2, a higher amplitude leads to stronger instability, consistent with the DNS observations discussed in §3.4.2. Vortex pairing was found to occur in all three configurations.

The spatial shape of an unstable subharmonic Floquet mode is presented in figure 14, for parameters $Re = 2000$, $St_D = 0.6$ and $A = 5\%$, associated with $\mu = -1.17$. A snapshot of perturbation vorticity is shown. Its axial wavelength corresponds to twice the spacing between vortices in the unpaired base flow, and its amplitude maximum occurs far downstream, around $z = 20$. The latter seems rather surprising, because the

Forcing amplitude	1%	5%	10%
Most unstable Floquet multiplier	$-1.06 \pm 0.069i$	-1.17	-1.19

Table 2: Evolution of the most unstable Floquet multiplier with the forcing amplitude for $Re = 2000$ and $St_D = 0.60$.

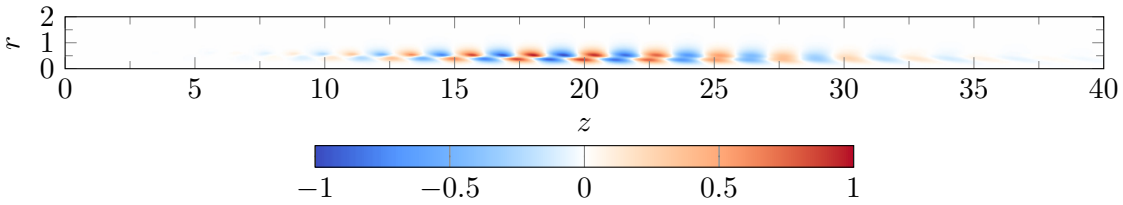

Figure 14: Vorticity component of the most unstable Floquet mode at $Re = 2000$ and $St_D = 0.60$. It peaks far downstream.

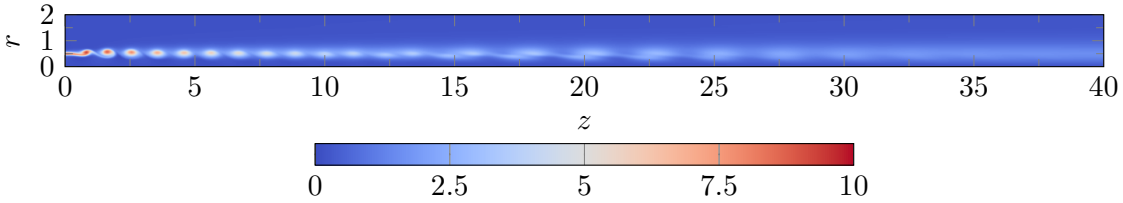

Figure 15: Vorticity snapshot of the base periodic unpaired flow at $Re = 2000$ and $St_D = 0.6$ slightly perturbed by the most unstable Floquet mode: $\mathbf{u}' = \mathbf{U}^{\mathbf{u}} + \epsilon\tilde{\mathbf{v}}_1$, with $\epsilon = 0.2$.

base flow vortices at this position are already quite diffuse, as can be seen in figure 3c. Furthermore, vortex pairing in the unstabilised flow is observed around $z = 3$.

In order to demonstrate the effect of this modal shape onto the unpaired base flow, the two are superposed, with a perturbation amplitude that is chosen *ad hoc*. The resulting vorticity field is shown in figure 15. It is seen that the perturbation indeed displaces the vortices around $z = 20$ in a fashion that indicates pairing. This pattern was also found by Selçuk *et al.* (2017*a*): the superposition of their quasistatic helical base flow and of their most unstable mode shows that their global mode shifts the helical vortices to trigger pairing.

However, in the current problem, the result from the superposition is very distinct from that of the fully developed paired state shown in figure 3a. To explain this discrepancy, it might be speculated that nonlinear adjustments could occur, or that a different, non-dominant Floquet mode could be responsible for the onset of pairing. Indeed, a second unstable mode exists at this parameter setting, characterised by a Floquet multiplier value $-1.03 \pm 0.14i$, and its vorticity distribution is given in figure 16. It displays the same spatial pattern as the first Floquet mode, but shifted several diameters further downstream, and this shift presumably accounts for its weaker growth. As this mode is not strictly subharmonic, it does not evolve precisely at $\omega_f/2$; still its growth may trigger subharmonic pairing in the nonlinear regime. However, this mode does not provide a more plausible interpretation of the observed vortex pairing much further upstream.

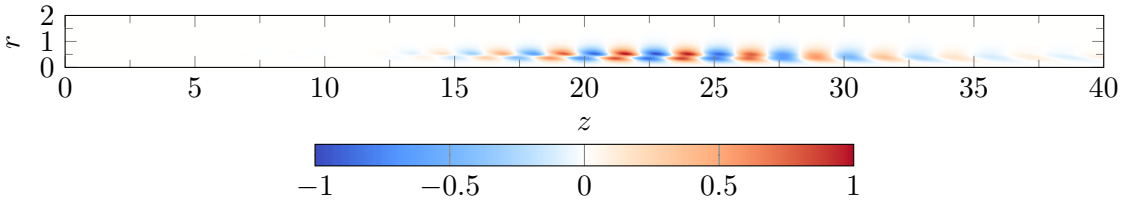

Figure 16: Real part of the vorticity component of the second most unstable Floquet mode at $Re = 2000$ and $St_D = 0.6$. Its peak is located far downstream.

5. Transient growth analysis

In this section, we show that the transient dynamics is essential to understand the bifurcation from an unpaired unstable flow to a paired flow. Indeed, it will be demonstrated that even though the stability analysis predicts in which parameter range pairing occurs, the transition from an unpaired state arises much faster and much closer to the inlet that what modal theory predicts. In contrast, transient dynamics predicts more accurately the transition rate and the perturbation structures, and it allows to explain the occurrence of intermittent phenomena in sub-critical but noisy jets shown in § 3.4.3.

5.1. *Growth of random initial perturbations*

The jet at $Re = 2000$, forced at $St_D = 0.6$ with 5% amplitude is considered throughout this section. The natural state in this case is the paired one, shown in figure 7, consistent with an unstable Floquet multiplier $\mu = -1.17$ as discussed in § 4.4. Direct numerical simulation results are presented here, which aim to show how pairing is triggered in the unstable unpaired flow.

A first simulation is performed starting from the stabilised unpaired state, displayed in figure 3c, as initial condition. Residual non-T-periodic components $(u(t) - u(t-T))/2$ in this flow state are of the order of 0.01% of the reference jet velocity.

Two additional simulations have been carried out with the same state, but with added white noise velocity perturbations, $\mathbf{u}(r, z, t = 0) = \mathbf{U^u}(r, z, t = 0) + \boldsymbol{\epsilon}(r, z)$. This noise exhibits zero spatial mean $\overline{\boldsymbol{\epsilon}} = \mathbf{0}$, and two different standard deviations $\sqrt{\overline{\boldsymbol{\epsilon}^2}} = (10^{-3}, 10^{-3})^T$ and $(10^{-4}, 10^{-4})^T$ are prescribed in the two simulations.

Non-harmonic components of the flow state at any given time are measured by a norm defined as

$$e(t) = \frac{1}{2}\sqrt{\iint \|\mathbf{u}(t) - \mathbf{u}(t-T)\|^2 r \, \mathrm{d}r \, \mathrm{d}z}. \tag{5.1}$$

The time evolution of this norm is traced in figure 17 for the three different initial conditions. While all three cases evolve into the same paired attractor state, they arrive there along different trajectories.

5.1.1. *Modal growth from very low perturbation amplitude*

Starting from the unpaired state, as it has been obtained through flow stabilisation, without any added random noise, the initial perturbation that may give rise to a growing subharmonic component is given by the residual non-T-periodicity that remained when the stabilised calculation was halted. The total vorticity after one period T is shown in figure 18a, and the magnitude of the non-T-periodic residual at the same instant is presented in figure 19a. Note that this residual is computed by comparing the state at time t with that from time $t - T$; therefore time-stepping over one period is required before the stabilisation effect can be evaluated.

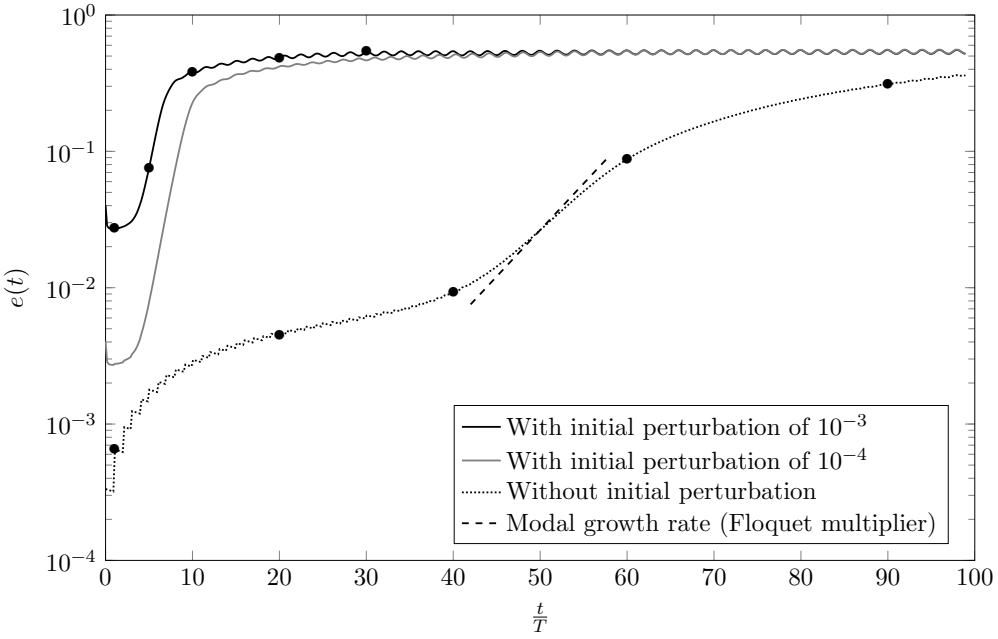

Figure 17: Growth of non-harmonic components in simulations with and without added initial noise. The modal Floquet growth rate is indicated for comparison.

Over the first forty periods, the subharmonic perturbation is dominated by a slow growth of the residual structure, but at such small amplitude that the total vorticity field in figures 18b and 18c is not noticeably affected. Then, as can be seen by comparing figures 19c and 19d with figure 14, the exponentially growing unstable Floquet mode becomes manifest. Its amplitude growth per flow period, between $t = 40T$ and $60T$, is estimated from figure 17 as a factor 1.14, to be compared to the absolute value 1.17 of the computed Floquet multiplier. The spatial structure of this perturbation, displayed in figure 20, exhibits a similar structure as the one of the corresponding Floquet mode, shown in figure 14. Beyond $t = 60T$, a nonlinear saturation of the subharmonic perturbation sets in (figure 17), accompanied by a change in its spatial shape. At $t = 90T$, as the flow approaches the asymptotic periodic regime, the maximum perturbation amplitude has moved upstream to $z \approx 10$ (figure 19e), where a pronounced pairing of vortices is observed in figure 18e. This pairing location still moves further upstream with time, until it will finally stabilise near $z = 3$, in the natural asymptotic paired state shown in figure 3a.

5.1.2. *Non-modal growth from initial white noise*

The simulations with added white noise in the initial condition (solid lines in figure 17) show a much faster convergence to the final paired flow state than the case discussed in the preceding section (dotted line in figure 17). In particular, the initial growth of $e(t)$ in these two cases is markedly stronger than that of the unstable Floquet mode.

The time development from an initial condition with $\sqrt{\overline{\boldsymbol{\epsilon}^2}} = (10^{-3}, 10^{-3})^T$ (thick solid line in figure 17) is visualised in figure 21 by successive snapshots of the total vorticity. It is seen that vortex pairing not only sets in faster than in the previous case of figure 18, but also much further upstream. Corresponding non-periodic perturbations are again displayed in figure 22: the smallest scales of the random initial condition are quickly dissipated (figure 22a), and a growing coherent perturbation structure is evident after a few period cycles (figure 22b). The maximum perturbation growth in this phase, as

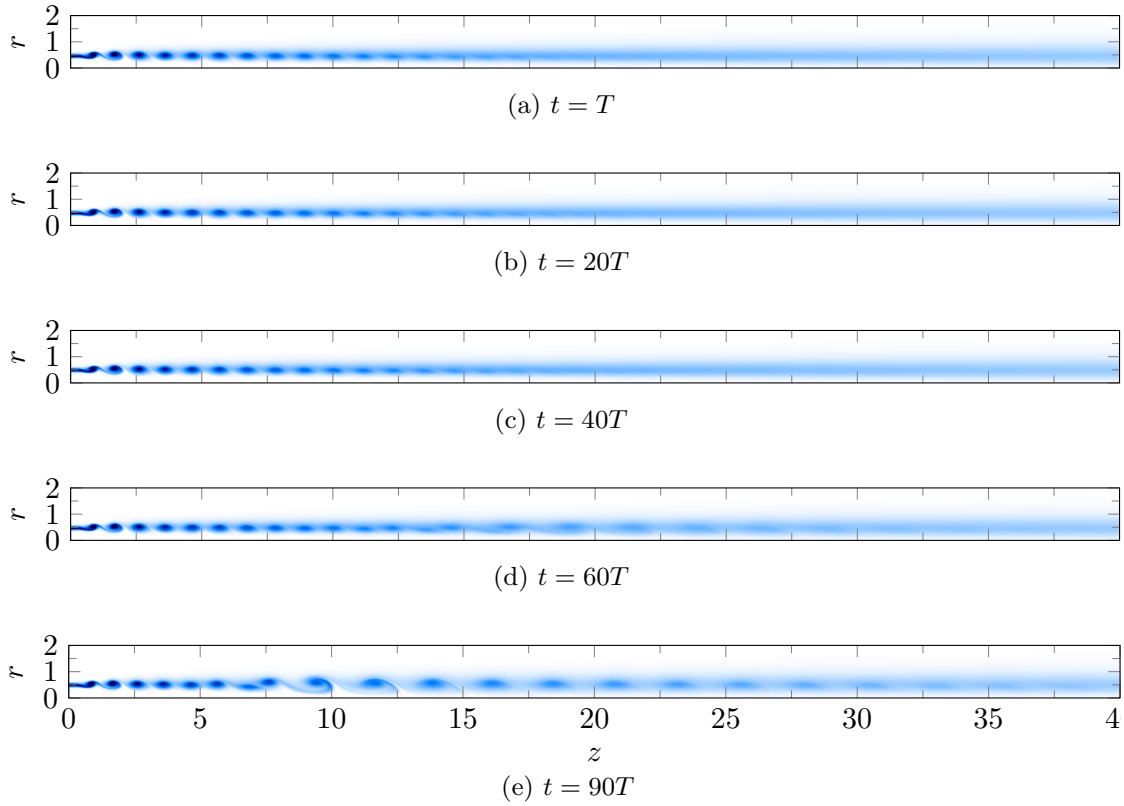

(a) $t = T$

(b) $t = 20T$

(c) $t = 40T$

(d) $t = 60T$

(e) $t = 90T$

Figure 18: Vorticity snapshots at five different instances without added initial noise. The colour coding is the same as in figure 3b.

measured from figure 17, corresponds to a factor 2.01 per period, much stronger than the modal growth factor 1.17. Persistent vortex pairing is fully established at $t = 10T$ (figure 22c); subsequently, the pairing location slowly moves upstream, and stabilises around $z = 3$.

Vorticity perturbations after five flow periods, in these simulations with added initial noise, are represented in figure 23. At this early stage, their dynamics may still be regarded as linear; however, the perturbations are now located close to the inlet, and their spatial distribution bears no resemblance with the unstable Floquet mode (figure 14). Therefore, a non-modal mechanism is expected to underpin this growth.

Simulations with a lower initial noise level of 10^{-4} show a similar behaviour, although slightly delayed (figure 17). The exponential phase is longer, since the amplitude takes more time to saturate, and the maximum growth rate is 2.16 per forcing period.

In both the "unperturbed" and "randomly perturbed cases", one should also note the absence of any sustained leapfrogging or overtaking events before pairing, contrary to what was observed by Selçuk *et al.* (2017*a*). This can be understood because the jet vortex rings are much thicker compared their helical vortices, making leapfrogging and overtaking difficult.

5.2. *Optimal linear perturbation growth over one cycle*

In order to further analyse and understand the mechanism behind the non-modal onset of vortex pairing, as observed in § 5.1.2, the *optimal* growth of subharmonic perturbations is now investigated. One cycle period T is chosen as the time horizon

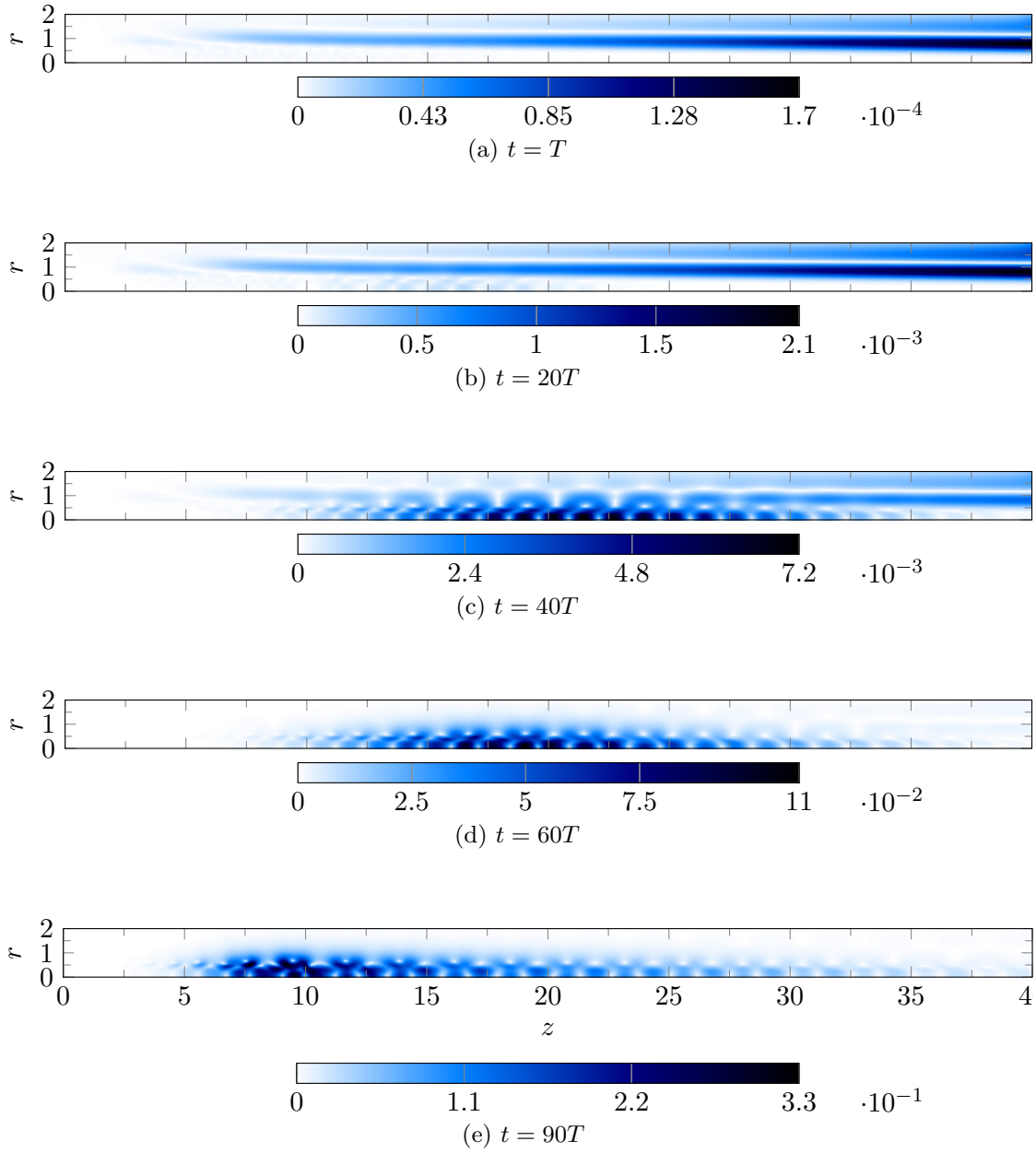

Figure 19: Perturbation magnitude $\|\mathbf{u}(t) - \mathbf{u}(t-T)\|$ at five different instances without added initial noise.

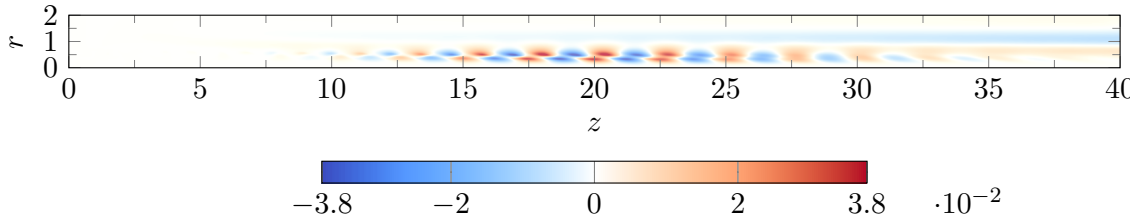

Figure 20: Vorticity field of the perturbation without any forcing applied at $t = 40T$.

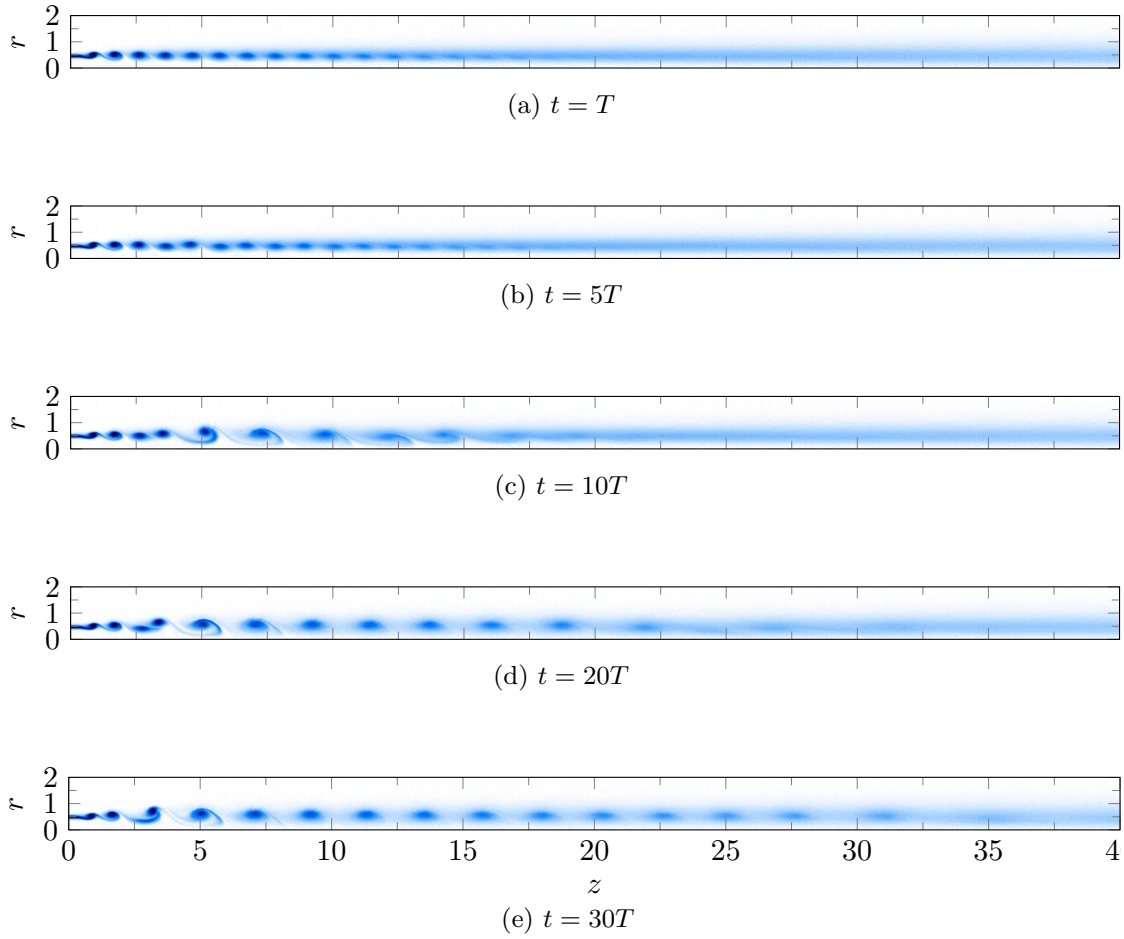

(a) $t = T$

(b) $t = 5T$

(c) $t = 10T$

(d) $t = 20T$

(e) $t = 30T$

Figure 21: Five snapshots of vorticity, evolving out of initial white noise level 10^{-3}. The colour coding is the same as in figure 3b.

over which optimisation is performed. As discussed in the context of (4.6), perturbations are propagated over one cycle by the time-shift operator Φ'. The optimal perturbation is then found as the solution to the maximisation problem

$$\|\mathbf{u}_{opt}(T)\| = \max_{\mathbf{u}'(t=0)} \frac{\|\mathbf{u}'(t=T)\|}{\|\mathbf{u}'(t=0)\|} = \max_{\mathbf{u}'(t=0)} \frac{\|\Phi'\mathbf{u}'(t=0)\|}{\|\mathbf{u}'(t=0)\|}, \tag{5.2}$$

The norm used in the following is derived from the standard real $\mathbf{u}$-scalar product in cylindrical coordinates (equation (4.7)). This scalar product defines a full norm for $\mathbf{u}$, but only a semi-norm for $\mathbf{q}$, because the separation condition is not fulfilled. The solution of the maximisation problem (5.2) is given by the norm of the operator Φ'.

To evaluate this norm, the orthonormal basis $\{\hat{\mathbf{u}}_i^n\}$ calculated in the context of modal analysis (§ 4.3) is once more exploited. Instead of maximising the norm of Φ', a infinite-dimensional operator, we maximise the norm of its projection $\tilde{\Phi}$, of finite dimension, onto this basis.

A perturbation state $\mathbf{u}'$ is projected onto $\{\hat{\mathbf{u}}_i^n\}$ as

$$\mathbf{u}' = \sum_{n=0}^{N-1} \sum_{i=1}^{N_{vec}} \boldsymbol{\beta}_{nN_{vec}+i} \hat{\mathbf{u}}_i^n + \mathbf{r}', \tag{5.3}$$

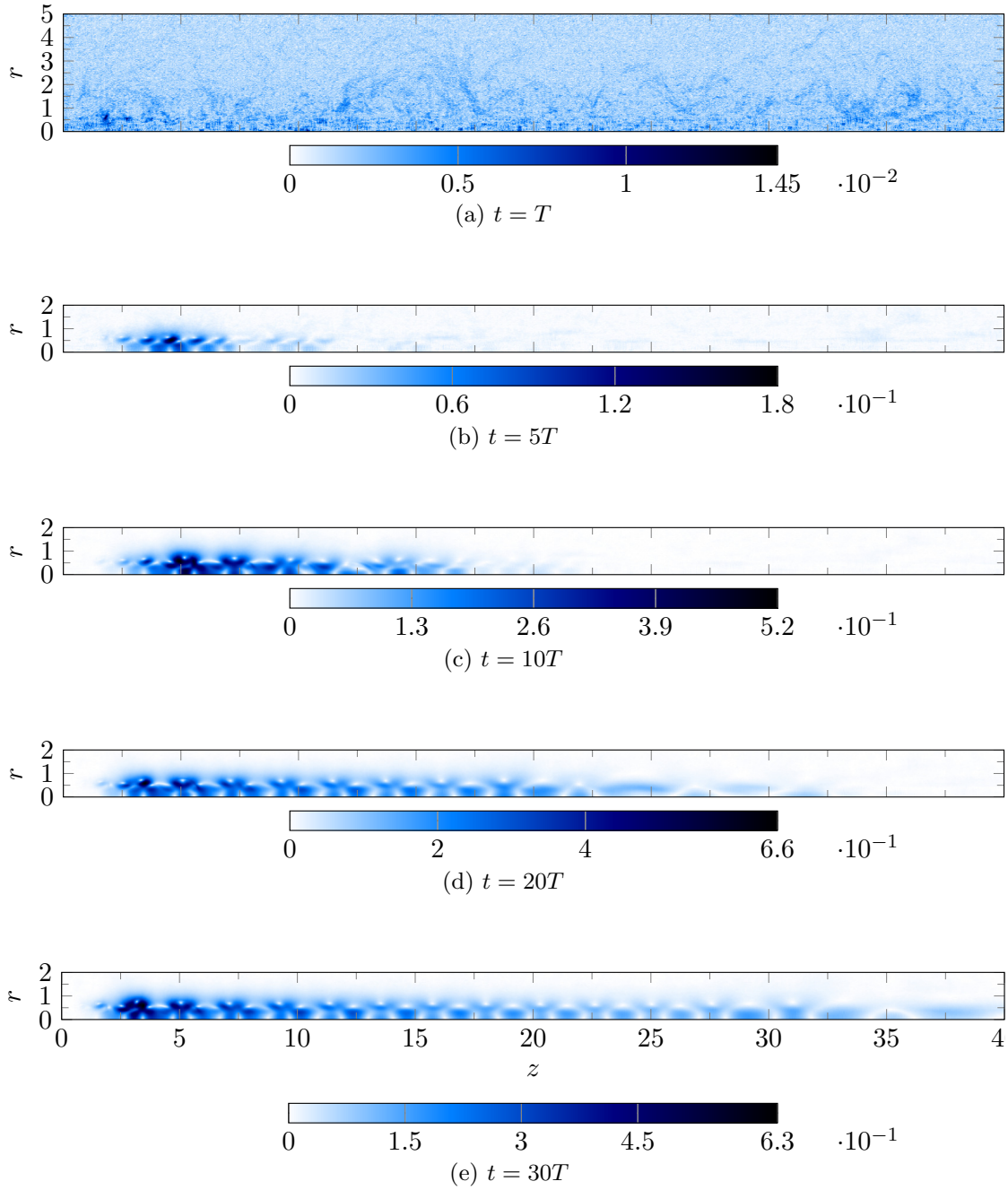

Figure 22: Perturbation magnitude $\|\mathbf{u}(t) - \mathbf{u}(t-T)\|$ at five different instances evolving out of initial white noise level 10^{-3}.

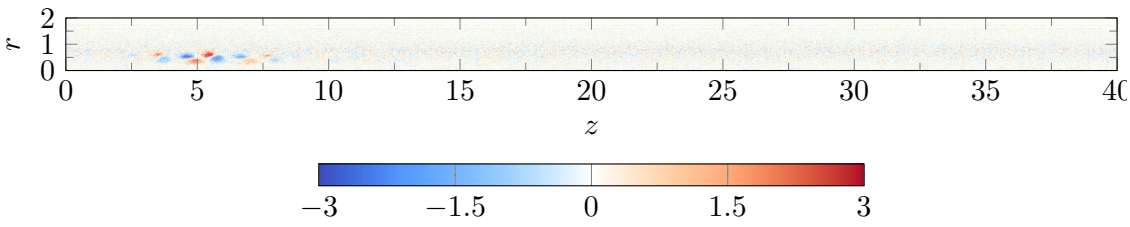

Figure 23: Vorticity field of the perturbation with random forcing (level 10^{-3}) at $t = 5T$.

$$\boldsymbol{\beta}_{nN_{vec}+i} = \langle \mathbf{u}', \hat{\mathbf{u}}_i^n \rangle \quad \text{such that} \quad \boldsymbol{\beta} = R^T M \mathbf{u}' \tag{5.4}$$

The residual $\mathbf{r}'$ is orthogonal to the basis $\{\hat{\mathbf{u}}_i^n\}$, such that $\|\mathbf{u}'\|^2 = \|\boldsymbol{\beta}\|^2 + \|\mathbf{r}'\|^2$. Therefore,

$$\boldsymbol{\Phi}'\mathbf{u}' = \sum_{n=0}^{N-1}\sum_{i=1}^{N_{vec}} \boldsymbol{\beta}_{nN_{vec}+i} \left(\boldsymbol{\Phi}'\hat{\mathbf{u}}_i^n\right) + \boldsymbol{\Phi}'\mathbf{r}' \tag{5.5}$$

$$= \sum_{n=0}^{N-1}\sum_{i=1}^{N_{vec}} \left(\tilde{\boldsymbol{\Phi}}\boldsymbol{\beta}\right)_{nN_{vec}+i} \hat{\mathbf{u}}_i^n + \boldsymbol{\Phi}'\mathbf{r}' \tag{5.6}$$

and

$$\|\boldsymbol{\Phi}'\mathbf{u}'\|^2 = \|\tilde{\boldsymbol{\Phi}}\boldsymbol{\beta}\|^2 + \|\boldsymbol{\Phi}'\mathbf{r}'\|^2 + 2\left\langle \sum_{n=0}^{N-1}\sum_{i=1}^{N_{vec}} \left(\tilde{\boldsymbol{\Phi}}\boldsymbol{\beta}\right)_{nN_{vec}+i} \hat{\mathbf{u}}_i^n, \boldsymbol{\Phi}'\mathbf{r}' \right\rangle, \tag{5.7}$$

with the norm of $\tilde{\boldsymbol{\Phi}}\boldsymbol{\beta}$ calculated in a finite-dimensional space of dimension NN_{vec}. Therefore, maximising $\|\boldsymbol{\Phi}'\mathbf{u}'\|$ is equivalent to maximising the right-hand side of the previous equation. However, the $\hat{\mathbf{u}}_i^n$-basis has not been chosen randomly: being constructed from the successive iterations of a single group of random vectors, it selects numerically the fastest-growing modes of the full system, in a similar way as power iterations (Saad 2011). These modes are then gradually excluded from the residual space of $\mathbf{r}'$, and the norm of the image of $\mathbf{r}'$ through $\boldsymbol{\Phi}'$ decreases as the number N of Krylov subspace iterations is increased. On the right-hand side of equation (5.7), the first term becomes dominant as N increases ; the second and third terms are bounded by $\|\boldsymbol{\Phi}'\mathbf{r}'\|^2$ and $\|\tilde{\boldsymbol{\Phi}}\boldsymbol{\beta}\|\|\boldsymbol{\Phi}'\mathbf{r}'\|$, respectively. Therefore, the approximation $\|\boldsymbol{\Phi}'\mathbf{u}'\| \approx \|\tilde{\boldsymbol{\Phi}}\boldsymbol{\beta}\|$ is valid for large N. This explains why, for a given value of NN_{vec}, a trade-off needs to be found between N and N_{vec}: N must be large enough to capture the salient flow dynamics, whereas N_{vec} must be sufficiently large to make the block-Arnoldi calculations computationally efficient.

The norm $\|\tilde{\boldsymbol{\Phi}}\boldsymbol{\beta}\|$ is evaluated by use of the singular value decomposition (SVD)

$$\tilde{\boldsymbol{\Phi}} = \tilde{U}\Sigma\tilde{V}^T, \tag{5.8}$$

with Σ a real positive diagonal matrix, and $\tilde{U}$ and $\tilde{V}$ real unitary matrices. Columns $\tilde{\mathbf{v}}_k$ and $\tilde{\mathbf{u}}_k$ represent forcing and response pairs in the orthonormal basis of the $\{\hat{\mathbf{u}}_i^n\}$. Σ contains the singular values ordered in descending order, such that $\tilde{\boldsymbol{\Phi}}\tilde{\mathbf{v}}_k = \sigma_k\tilde{\mathbf{u}}_k$ with $\sigma_k \geqslant \sigma_{k+1} \geqslant 0$.

Note that the Krylov base constructed in § 4.3 is orthonormal with respect to the scalar product (4.7). Therefore, the optimal initial perturbations or responses in the reduced space correspond to the optimal initial perturbations or responses in the full-state space, using the R matrix to change basis. For a given optimal initial perturbation (resp. response) $\tilde{\mathbf{v}}_k$ (resp. $\tilde{\mathbf{u}}_k$) in this reduced basis, the corresponding full-state initial perturbation velocity (resp. response velocity) $\mathbf{v}_k$ (resp. $\mathbf{u}_k$) is obtained as $\mathbf{v}_k = R\tilde{\mathbf{v}}_k$ (resp. $\mathbf{u}_k = R\tilde{\mathbf{u}}_k$). The corresponding matrices of optimal initial perturbations and responses are $V = R\tilde{V}$ and $U = R\tilde{U}$. Because of this preserved optimality, the maximum linear gain achievable over one period in the full-state is still σ_1, obtained by perturbing the velocity field at $t = 0$ with $\mathbf{v}_1$. After one period, the perturbation velocity field is given by $\mathbf{u}_1$.

This method is computationally efficient, as it is entirely based on the results already available from the modal analysis. This is in contrast with the additional computations required in a direct-adjoint approach. Moreover, with the direct-adjoint approach, the optimisation is carried out for a single time horizon T_f. In this section, only $T_f = T$ has been chosen ; however, as will be seen in the next section, this can be extended with little additional effort to any time-horizon of integer periods $T_f = nT$. Time-horizons that are

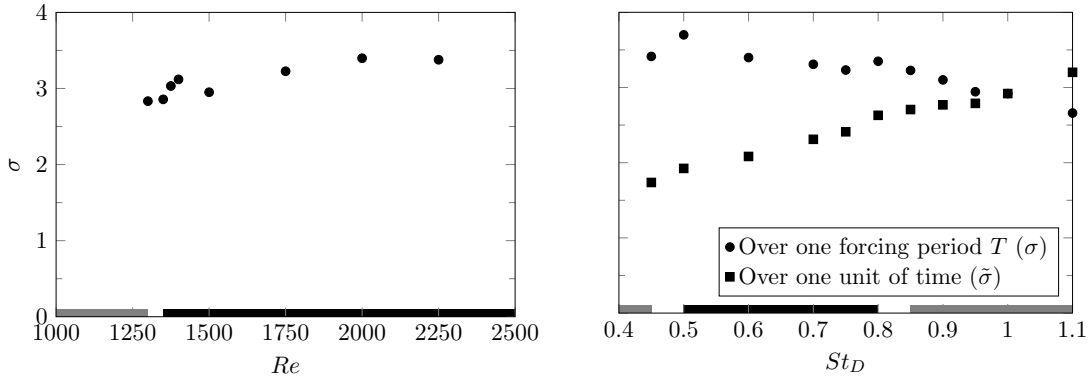

(a) $St_D = 0.6$. (b) $Re = 2000$.

Figure 24: Norm of the time-shift operator for different Reynolds and Strouhal numbers, with a 5% forcing level and a normalised momentum thickness of 5%. The grey or black domains represent the parameters values for which DNS calculations show that the "natural" solution is unpaired or paired, as shown in figure 7. In figure 24b, the leading amplification rates are also depicted rescaled over one dimensionless time unit. Additional singular values for lower Reynolds number flows are discussed in § 5.4.

Forcing amplitude	1%	5%	10%
$\|\mathbf{u}_{opt}(T)\|$	3.96	3.40	3.32

Table 3: Evolution of the optimal perturbation gain over one period with the forcing amplitude for $Re = 2000$ and $St_D = 0.60$.

not integer multiples of T, corresponding to transient phenomena within a forcing period, are not considered here.

Singular value decomposition of Φ' has been carried out for all flow configurations listed in table 1. The maximum gain values σ_1 are shown in figure 24 for fixed values of St_D and Re. Variations of σ_1 with the forcing amplitude A are given in table 3 for one setting $Re = 2000$ and $St_D = 0.6$. In all cases, the achievable transient amplification over one period is significantly higher than the maximum modal growth rate. A comparison with results of perturbed DNS flows (figure 17) is discussed in § 5.3.

At fixed Strouhal number (figure 24a), the leading singular value changes weakly as a function of Reynolds number, even as the system goes from stable to unstable. Variations of σ_1 are within 20% as the value of Re is doubled.

At fixed Reynolds number (figure 24b), variations of the Strouhal number also do not affect σ_1 in a strong way. Doubling St_D from 0.45 to 0.9 is accompanied by a 10% decrease of the maximum gain over one flow period. However, when σ_1 is rescaled to give the mean amplification over a *constant time unit*, as $\tilde{\sigma}_1 = \sigma_1 St_D$, this rescaled gain increases by more than 30% over the investigated interval of St_D. This is consistent with Broze & Hussain (1994, 1996) : in their parametric study, as shown in figure 2, they found that when the Strouhal number is increased, the jet is more prone to experience non-T- or non-$2T$-periodic behaviour (periodic or not modulations, intermittency or chaos). Our study shows that the larger the Strouhal number, the more amplified random perturbations can be over a given time unit.

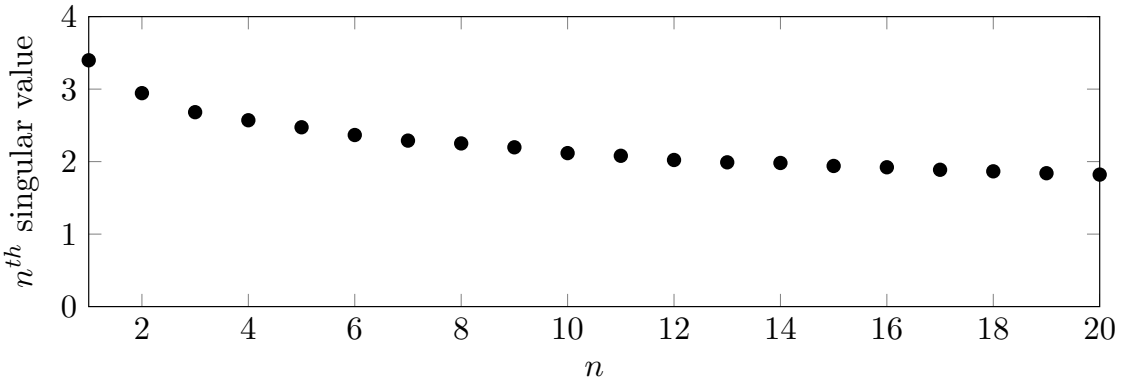

Figure 25: The twenty first singular values of Φ' for $Re = 2000$, $St_D = 0.6$ and $A = 5\%$.

With increasing forcing amplitude, the maximum gain is moderately diminished (table 3). This may indicate that the receptivity to subharmonic perturbations is larger when the shear layer is not yet fully rolled up, since increasing forcing amplitude results in a faster roll-up of vortices, as shown in figure 9. Again, this is coherent with Broze & Hussain (1994, 1996): as shown in figure 2, with larger forcing levels, except at Strouhal numbers greater than those considered in our study, the flow is less prone to non-periodic behaviour, which may be brought about by transient amplification of small disturbances.

The leading singular mode may not be the only relevant way to trigger transient growth. For the case ($Re = 2000, St_D = 0.6$), the 20 largest singular values are represented in figure 25. Indeed, a strong dominance of the optimal perturbation cannot be affirmed: the first value is 15% larger than the second, 27% larger than the third, and only 87% larger than the twentieth.

The shapes of the optimal initial perturbation and response structures are shown for the case ($Re = 2000, St_D = 0.6$) in figures 26a and 26b, respectively. In comparison with the Floquet mode discussed in § 4.4 (see figure 14), these perturbation structures are localised much closer to the inlet. Over the course of one period, the perturbation shape is largely conserved, while it is convected at the same pace as the rolled-up vortices. The manifestation of these perturbations in the total vorticity field is visualised in figure 27, where the linear optimal initial perturbation and response structures are superposed onto the periodic base state with a small amplitude of 5%. It can be observed that the optimal perturbation structures displace the vortices towards and away from the axis, in an alternating fashion. This displacement is furthermore oriented at an oblique angle, such that the distance between neighbouring vortices is modulated, thus initiating the pairing interaction.

The second singular mode pair in the same configuration, corresponding to σ_2, is displayed in figure 28. It exhibits a very similar structure as the first singular mode, the main difference being that the maximum amplitude is shifted downstream to the next vortex pair.

5.3. *Optimal linear perturbation growth over many cycles*

The technique that has been described in the previous section for optimisation over a single flow period T is easily extended in order to construct optimal perturbations for time horizons of *multiple* periods nT. Let $\mathbf{f}_n$ denote the optimal perturbation at $t = 0$ that leads to the largest possible flow response $\mathbf{r}_n$ at $t = nT$. The associated amplitude gain is then given by the norm $\|\mathbf{u}_{opt}(nT)\| = \|\mathbf{r}_n\|/\|\mathbf{f}_n\|$, which is identical to the largest

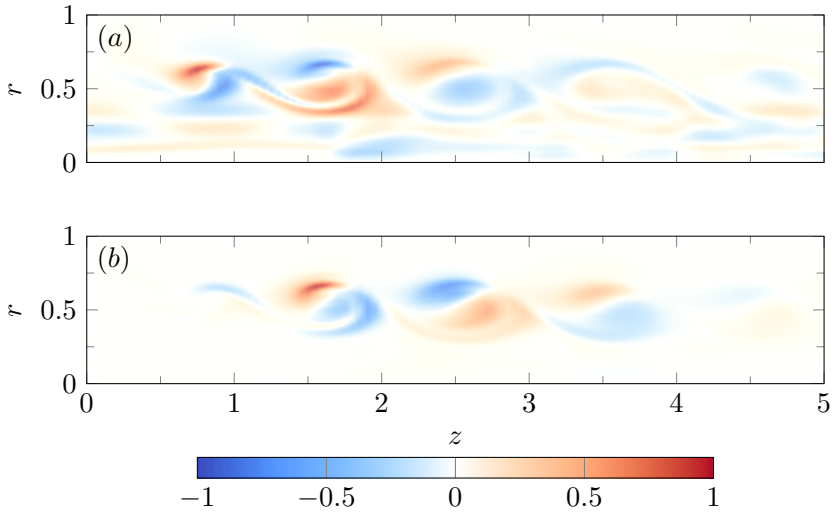

Figure 26: For $Re = 2000$ and $St_D = 0.6$, vorticity of (a) the optimal perturbation and (b) its response after one flow period. The maxima are located close to the inlet.

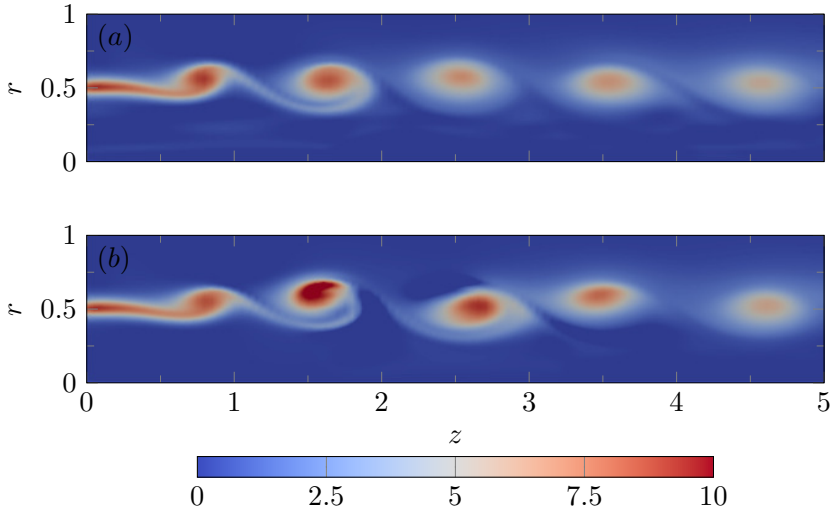

Figure 27: Superposition of the base flow and (a) the optimal perturbation, (b) the associated linear response after one flow period. The total vorticity is shown, for velocity fields $\mathbf{u}' = \mathbf{U^u} + 0.05\mathbf{u_1}$ and $\mathbf{u}' = \mathbf{U^u} + 0.05\sigma_1\mathbf{v_1}$, respectively, for the case $Re = 2000$ and $St_D = 0.6$. Both $\mathbf{u_1}$ and $\mathbf{v_1}$ have unit norm.

singular value of the nth power of the operator Φ. Substituting Φ with its approximation $\tilde{\Phi}$, the SVD of $\tilde{\Phi}^n$ is straightforward to compute.

The ensuing variation of the optimal gain with nT is traced in figure 29, alongside the perturbation growth associated with the most unstable Floquet mode (§ 4.4). Optimal perturbation at $t = 0$ enables a vigorous transient growth over short time horizons; at longer times, however, the optimal growth rate approaches that of the modal solution, given by the modulus of the dominant Floquet multiplier. This behaviour is identical to that of perturbation growth in steady base flows, which has been discussed theoretically by Trefethen & Embree (2005). In the present case, the transient non-modal growth provides a significant boost, on the order of 10^5, of the overall long-time amplitude gain. This additional factor corresponds to 73 cycle periods of modal growth.

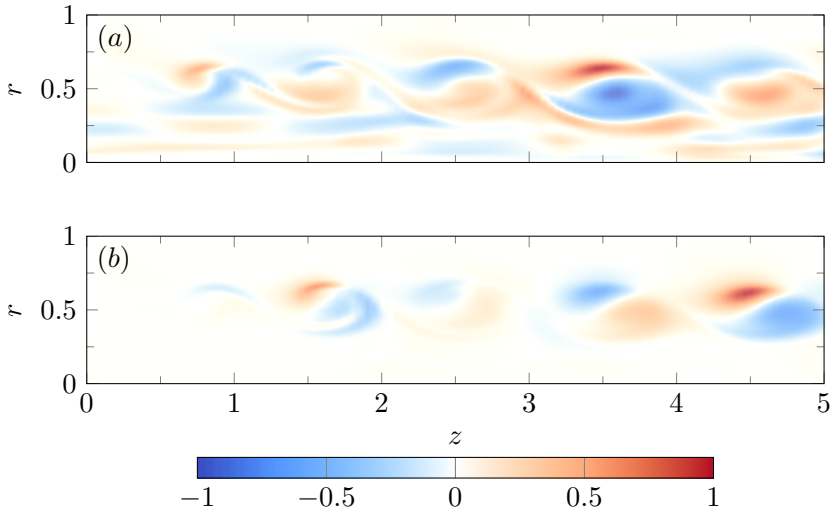

Figure 28: For $Re = 2000$ and $St_D = 0.6$, vorticity of (a) the second singular mode: (a) perturbation and (b) its response after one flow period. The maxima are located further downstream than in the optimal setting shown in figure 26.

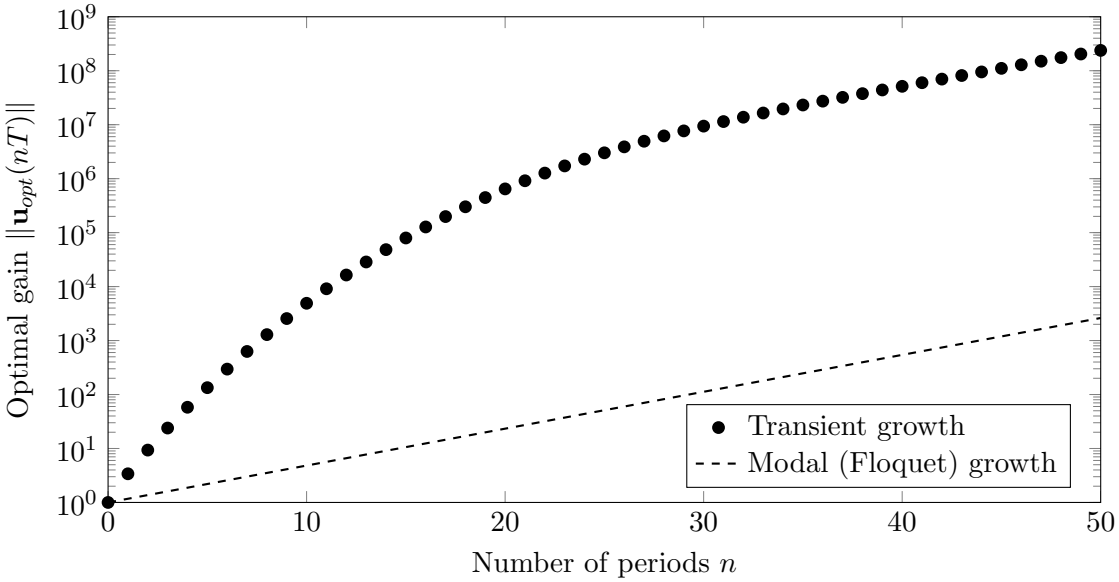

Figure 29: Transient growth gain achieved by a $(Re = 2000, St_D = 0.60)$ jet forced with 5% amplitude and comparison with modal growth.

The evolution and convergence of the optimal initial perturbation and response *structures* are examined in figure 30 in terms of projections. The scalar products of the initial perturbation and response structures obtained for any number of cycles with those at $n = 1$ and $n = 50$ are represented. It is observed that the optimal initial perturbation structure does not evolve much with time, and that the shape determined for one single period is close to optimality for all time horizons. In contrast, the shape of the optimal response changes significantly through time; the optimal response at $t = 50T$ is indeed localised at a different location than its counterpart at $t = T$. While the optimal initial perturbation structure always retains a nearly identical shape, the optimal response structure gradually shifts downstream with increasing time horizon, and eventually it

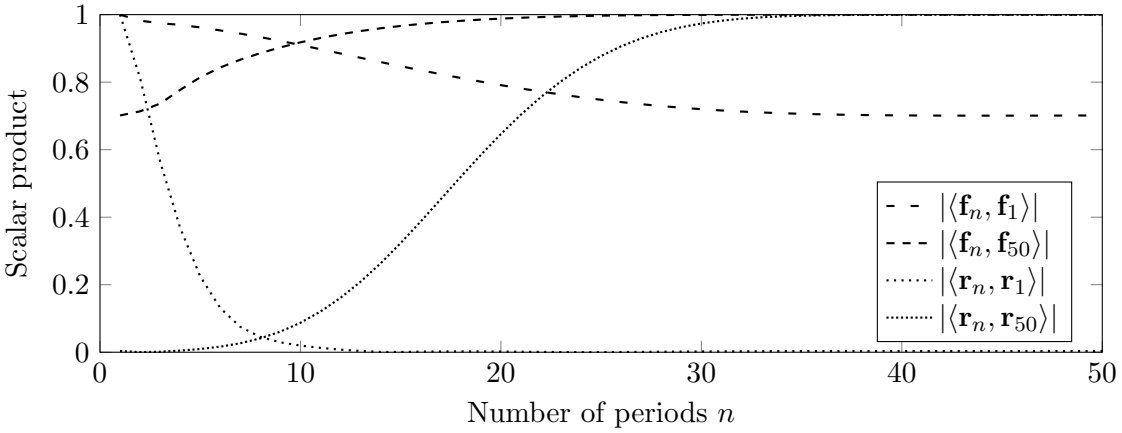

Figure 30: Projection of the optimal initial perturbation and response at time nT over the optimal initial perturbation and responses at times T and $50T$ for a jet at $Re = 2000$ and $St_D = 0.60$ forced with a 5% amplitude. While the optimal initial perturbation experiences little change, the optimal response changes drastically. All vectors considered have unit norm.

$\lvert\langle \mathbf{f}_1, \tilde{\mathbf{v}}_1 \rangle\rvert$	$\lvert\langle \mathbf{f}_{50}, \tilde{\mathbf{v}}_1 \rangle\rvert$	$\lvert\langle \mathbf{r}_1, \tilde{\mathbf{v}}_1 \rangle\rvert$	$\lvert\langle \mathbf{r}_{50}, \tilde{\mathbf{v}}_1 \rangle\rvert$
1.24×10^{-3}	1.10×10^{-5}	3.60×10^{-3}	9.9990×10^{-1}

Table 4: Scalar products (4.7) between the Floquet mode $\tilde{\mathbf{v}}_1$ and the optimal finite-time initial perturbations $\mathbf{f}_n$ and responses $\mathbf{r}_n$. All modes and perturbations have unit norm. Consistent with the notations introduced in § 5.2, $\mathbf{f}_1$ is identical to $\mathbf{v}_1$, and $\mathbf{r}_1$ to $\mathbf{u}_1$.

converges towards the structure of the Floquet mode (see figure 14). The projection values in table 4 demonstrate this convergence. It is expected on theoretical grounds (Trefethen & Embree 2005) that, at long time horizons, the optimal response structure corresponds to the dominant Floquet mode, whereas the optimal forcing is given by the associated *adjoint* mode of the time-shift operator.

The different evolution from different initial perturbations, documented in § 5.1.1 and 5.1.2 can now be interpreted in terms of the optimal perturbation results.

In the two cases that were initialised with white noise perturbations, this initial condition contained significant components of strongly amplified optimal initial perturbation modes. After approximately five periods, these structures emerged from the background noise, as may be inferred from a qualitative comparison between figures 23, 26b and 28b. However, the maximum growth observed in figure 17 for $\sqrt{\overline{\boldsymbol{\epsilon}^2}} = (10^{-3}, 10^{-3})^T$ corresponds to a factor 2.16 per period, whereas the leading singular value was determined to be 3.40 in § 5.2 for the time horizon $t = T$. Yet, the optimal growth rate decreases with time; this is shown in figure 31, which represents the marginal gain $\sigma_m(nT)$ at $t = nT$ of the nT-optimal perturbation:

$$\sigma_m(nT) = \frac{\|\mathbf{u}_{opt}[(n+1)T]\|}{\|\mathbf{u}_{opt}(nT)\|} \tag{5.9}$$

with $\|\mathbf{u}_{opt}(nT)\|$ plotted in figure 29. Therefore, the maximum growth value 2.16, ob-

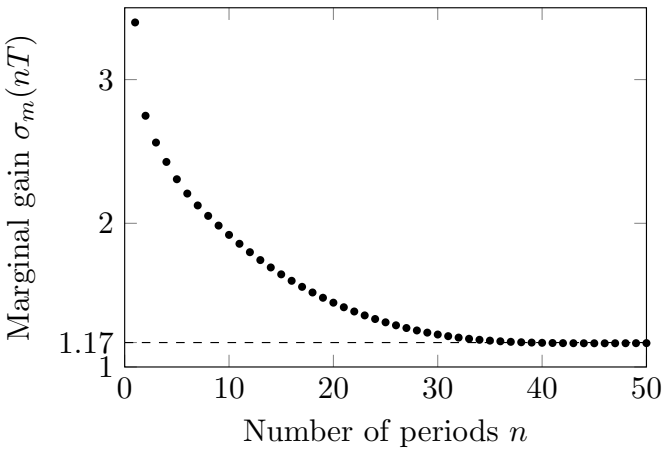

Figure 31: Marginal gain $\sigma_m(nT)$ of the optimal perturbation at the horizon time nT for $Re = 2000$, $St_D = 0.60$ and $A = 0.05$. The marginal growth rate asymptotically converges towards the modulus of the most unstable Floquet multiplier.

Reynolds number	500	750	1000	1300
Floquet multiplier	$-0.51 \pm 0.031i$	-0.64	-0.82	-0.97
Leading singular value	1.85	2.28	2.58	2.83

Table 5: For $St_D = 0.6$ and $A = 0.05$, evolution of the least stable subharmonic Floquet multiplier and of the maximum growth rate over one period as a function of Re in the stable case.

served in figure 17, is consistent with the marginal gains observed after 5 to 10 periods in figure 31.

In the case discussed in § 5.1.1, initialised without added noise, the exponential growth observed between $40T$ and $60T$ has been associated with the unstable Floquet mode. The initial perturbation (figure 19a) is spatially disjoint from optimal perturbations near the inflow. At $t = 20T$, a non-modal pairing perturbation is faintly visible in figure 19b, still in the process of transitionning towards the Floquet mode in figure 19c, the optimal linear response at long times.

Whether or not *transient* processes lead to a rapid onset of nonlinear vortex pairing depends on the energy level of oscillatory perturbations near the inflow, with appropriate wavelengths for subharmonic vortex modulation.

5.4. *Importance of transient dynamics at low Re*

In § 3.4.1, a Reynolds number threshold was determined below which pairing did no longer occur naturally. However, in § 3.4.3, it has been demonstrated that forcing a jet harmonically with a small noise level was able to trigger pairing for Reynolds numbers where pairing does not normally occur. It is now examined how this behaviour can be explained in the light of the transient growth analysis developed in the previous section. At $St_D = 0.6$ and $A = 5\%$, four Reynolds number values 1300, 1000, 750 and 500 are considered here. All these cases are modally stable, as seen in table 5. The transient growth of these cases is shown in figure 32.

Although in all cases, the gain decreases in the long term, the maximum achieved during the transient growth varies largely, between 4.5 after 6 periods for $Re = 500$, and

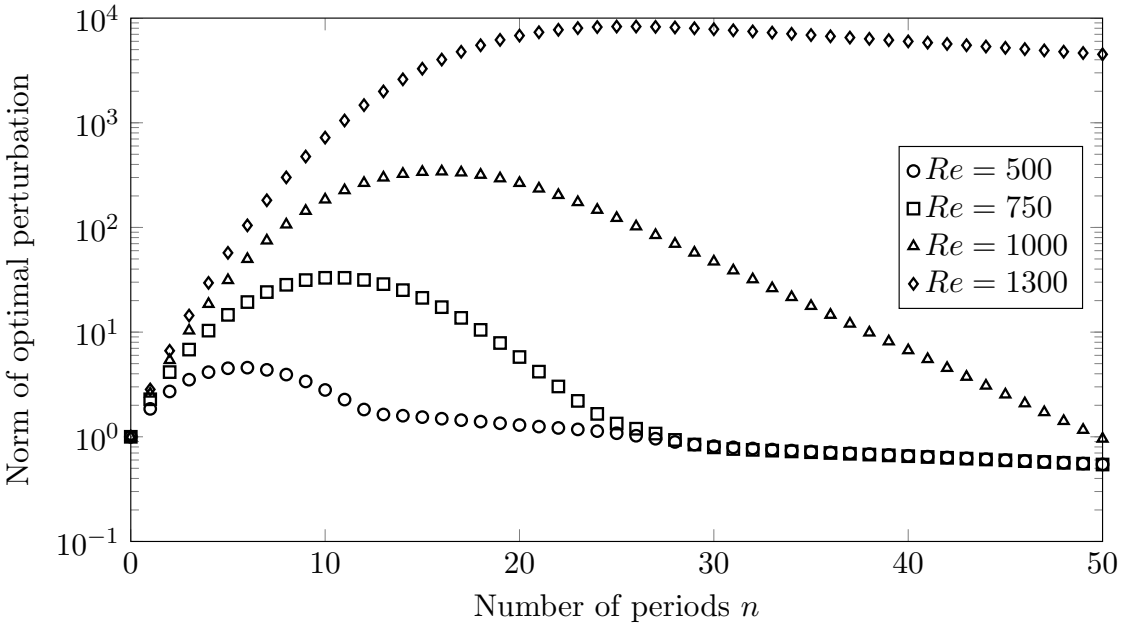

Figure 32: Transient growth gain for a jet forced at $St_D = 0.60$ with 5% amplitude at different subcritical Reynolds number values.

8.3×10^3 after 26 periods for $Re = 1300$. This change explains the different behaviour observed in § 3.4.3. At $Re = 500$, whatever the forcing level, the noise is not energetic enough to trigger pairing. On the other hand, at $Re = 1300$, even very small perturbations eventually initiate pairing via transient growth. At intermediate Reynolds numbers, the behaviour observed depends on the perturbation level.

6. Conclusion

The onset of sustained vortex pairing in the street of axisymmetric vortices in a laminar jet has been investigated by means of global instability analysis.

The numerical framework developed for this study is applicable to the instability analysis of any spatially developing time-periodic flow. It includes the computation of a strictly T-periodic base flow by means of DNS with added time-delay control (Shaabani-Ardali *et al.* 2017), the identification of dominant linear Floquet modes, and a singular value decomposition of the propagator in order to characterise non-modal transient growth phenomena. The modal and non-modal analysis are both achieved via time-stepping of the linearised flow equations, without the need for adjoint calculations, in combination with a block-Arnoldi algorithm (Saad 2011).

It has been demonstrated that self-sustained vortex pairing in a jet is the manifestation of a subharmonic linear Floquet instability of the underlying periodic vortex street. Direct numerical simulations of axisymmetric laminar jets, forced harmonically at Strouhal number St_D at the inlet, have been perfomed in order to delineate the region in the Re-St_D parameter plane where pairing in the ensuing vortex street arises spontaneously. This parameter regime has then been shown to be characterised by subharmonic Floquet instability. Furthermore, the phase velocities of fundamental and subharmonic fluctuations in the simulation results have been found to be consistent with the resonance model proposed by Monkewitz (1988). DNS results also show a strong influence of inflow forcing amplitude as well as random ambient noise on the onset of vortex pairing.

The spatial structure of the unstable linear Floquet mode, throughout the parameter regime considered in this study, reaches its maximum amplitude far downstream of the inlet, whereas the subharmonic perturbation amplitude in the nonlinear saturated paired flow state peaks a few diameters away from the inlet, where stationary vortex pairing occurs. When DNS calculations in the unstable regime are initiated with extremely low subharmonic perturbations, the Floquet mode structure and growth rate are indeed observed over a short time interval in the bifurcation process. However, when additional random noise is added to the initial condition, considerably faster subharmonic perturbation growth is observed, with spatial amplitudes concentrated near the inlet. This behaviour motivated a linear optimal perturbation analysis. It has been found that linear transient mechanisms may induce, for a standard configuration with $Re = 2000$ and $St_D = 0.6$, an additional amplitude gain of about five orders of magnitude with respect to purely modal growth. Furthermore, the spatial structure of the linear optimal perturbation response reflects the DNS observations at early times, when subharmonic perturbations may be assumed to be governed by linear dynamics.

While the asymptotic occurrence of vortex pairing is determined by modal Floquet instability, its emergence is dominated by non-modal transient growth mechanisms.

Acknowledgements

We thank Holly Johnson for her help with Nek5000 and Robin Yegavian for his help with the parallelisation of FreeFem++.

This work was granted access to the HPC resources of TGCC under the allocation Grant No. 2016-2a6451 made by GENCI, and it was financially supported by the Délégation Générale de l'Armement under Grant No. 2015.60.0004.00.470.75.01.

REFERENCES

Arbey, H. & Ffowcs Williams, J.E. 1984 Active cancellation of pure tones in an excited jet. *J. Fluid Mech.* **149**, 445–454.

Arratia, C., Caulfield, C.P. & Chomaz, J.-M. 2013 Transient perturbation growth in time-dependent mixing layers. *J. Fluid Mech.* **717**, 90–133.

Barkley, D., Blackburn, H.M. & Sherwin, S.J. 2008 Direct optimal growth analysis for timesteppers. *Int. J. Numer. Meth. Fl.* **57** (9), 1435–1458.

Barkley, D. & Henderson, R.D. 1996 Three-dimensional Floquet stability analysis of the wake of a circular cylinder. *J. Fluid Mech.* **322**, 215–241.

Becker, H.A. & Massaro, T.A. 1968 Vortex evolution in a round jet. *J. Fluid Mech.* **31** (03), 435–448.

Blackburn, H.M., Sherwin, S.J. & Barkley, D. 2008 Convective instability and transient growth in steady and pulsatile stenotic flows. *J. Fluid Mech.* **607**, 267–277.

Bogey, C. & Bailly, C. 2010 Influence of nozzle-exit boundary-layer conditions on the flow and acoustic fields of initially laminar jets. *J. Fluid Mech.* **663**, 507–538.

Borisov, A.V., Kilin, A.A. & Mamaev, I.S. 2013 The dynamics of vortex rings: Leapfrogging, choreographies and the stability problem. *Regul. Chaotic Dyn.* **18** (1-2), 33–62.

Borisov, A.V., Kilin, A.A., Mamaev, I.S. & Tenenev, V.A. 2014 The dynamics of vortex rings: leapfrogging in an ideal and viscous fluid. *Fluid Dyn. Res.* **46** (3), 031415.

Bradley, T.A. & Ng, T.T. 1989 Phase-locking in a jet forced with two frequencies. *Exp. Fluids* **7** (1), 38–48.

Brancher, P. & Chomaz, J.-M. 1997 Absolute and convective secondary instabilities in spatially periodic shear flows. *Phys. Rev. Lett.* **78** (4), 658.

Bridges, J.E. & Hussain, A.K.M.F. 1987 Roles of initial condition and vortex pairing in jet noise. *J. Sound Vib.* **117** (2), 289–311.

Broze, G. & Hussain, F. 1994 Nonlinear dynamics of forced transitional jets: periodic and chaotic attractors. *J. Fluid Mech.* **263**, 93–132.

Broze, G. & Hussain, F. 1996 Transitions to chaos in a forced jet: intermittency, tangent bifurcations and hysteresis. *J. Fluid Mech.* **311**, 37–71.

Cheng, M. & Chang, H.-C. 1992 Subharmonic instabilities of finite-amplitude monochromatic waves. *Phys. Fluids A-Fluid* **4** (3), 505–523.

Cheng, M., Lou, J. & Lim, T.T. 2015 Leapfrogging of multiple coaxial viscous vortex rings. *Phys. Fluids* **27** (3), 031702.

Delbende, I., Piton, B. & Rossi, M. 2015 Merging of two helical vortices. *Eur. J. Mech. B-Fluids* **49**, 363–372.

Felli, M., Camussi, R. & Di Felice, F. 2011 Mechanisms of evolution of the propeller wake in the transition and far fields. *J. Fluid Mech.* **682**, 5–53.

Floquet, G. 1883 Sur les équations différentielles linéaires à coefficients périodiques. *Ann. Sci. École Norm. Sup.* **12**, 47–88.

Garnaud, X., Lesshafft, L., Schmid, P.J. & Huerre, P. 2013 Modal and transient dynamics of jet flows. *Phys. Fluids* **25** (4), 044103.

Hajj, M.R., Miksad, R.W. & Powers, E.J. 1992 Subharmonic growth by parametric resonance. *J. Fluid Mech.* **236**, 385–413.

Hajj, M.R., Miksad, R.W. & Powers, E.J. 1993 Fundamental–subharmonic interaction: effect of phase relation. *J. Fluid Mech.* **256**, 403–426.

Hall, K.C., Thomas, J.P. & Clark, W.S. 2002 Computation of unsteady nonlinear flows in cascades using a harmonic balance technique. *AIAA J.* **40** (5), 879–886.

Hecht, F. 2012 New development in FreeFem++. *J. Numer. Math.* **20** (3-4), 251–265.

Ho, C.-M. & Huang, L.-S. 1982 Subharmonics and vortex merging in mixing layers. *J. Fluid Mech.* **119**, 443–473.

Huerre, P. & Monkewitz, P.A. 1990 Local and global instabilities in spatially developing flows. *Annu. Rev. Fluid Mech.* **22** (1), 473–537.

Husain, H.S. & Hussain, F. 1989 Subharmonic resonance in a shear layer. In *Advances in Turbulence 2*, pp. 96–101. Springer.

Husain, H.S. & Hussain, F. 1995 Experiments on subharmonic resonance in a shear layer. *J. Fluid Mech.* **304**, 343–372.

Hussain, A.K.M.F. & Zaman, K.B.M.Q. 1980 Vortex pairing in a circular jet under controlled excitation. Part 2. Coherent structure dynamics. *J. Fluid Mech.* **101** (03), 493–544.

Inoue, O. 2002 Sound generation by the leapfrogging between two coaxial vortex rings. *Phys. Fluids* **14** (9), 3361–3364.

Jallas, D., Marquet, O. & Fabre, D. 2017 Linear and nonlinear perturbation analysis of the symmetry breaking in time-periodic propulsive wakes. *Phys. Rev. E* **95** (6), 063111.

Johnson, H.G., Brion, V. & Jacquin, L. 2016 Crow instability: nonlinear response to the linear optimal perturbation. *J. Fluid Mech.* **795**, 652–670.

Kibens, V. 1980 Discrete noise spectrum generated by acoustically excited jet. *AIAA J.* **18** (4), 434–441.

Lust, K. & Roose, D. 1998 An adaptive Newton–Picard algorithm with subspace iteration for computing periodic solutions. *SIAM J. Sci. Comput.* **19** (4), 1188–1209.

Mankbadi, R.R. 1985 On the interaction between fundamental and subharmonic instability waves in a turbulent round jet. *J. Fluid Mech.* **160**, 385–419.

Meunier, P., Ehrenstein, U., Leweke, T. & Rossi, M. 2002 A merging criterion for two-dimensional co-rotating vortices. *Phys. Fluids* **14** (8), 2757–2766.

Meynart, R. 1983 Speckle velocimetry study of vortex pairing in a low-Re unexcited jet. *Phys. Fluids* **26** (8), 2074–2079.

Michalke, A. 1971 Instabilität eines kompressiblen runden Freistrahls unter Berücksichtigung des Einflusses der Strahlgrenzschichtdicke. *Z. Flugwiss.* **19**, 319–328, English translation: NASA Tech. Memo. 75190 (1977).

Monkewitz, P.A. 1988 Subharmonic resonance, pairing and shredding in the mixing layer. *J. Fluid Mech.* **188**, 223–252.

Narayanan, S. & Hussain, F. 1997 Chaos control in open flows–experiments in a circular jet. *AIAA Paper* (97-1822).

Nichols, J.W. & Lele, S.K. 2011 Global modes and transient response of a cold supersonic jet. *J. Fluid Mech.* **669**, 225–241.

Paschereit, C.O., Wygnanski, I. & Fiedler, H.E. 1995 Experimental investigation of subharmonic resonance in an axisymmetric jet. *J. Fluid Mech.* **283**, 365–407.

Petersen, R.A. 1978 Influence of wave dispersion on vortex pairing in a jet. *J. Fluid Mech.* **89** (03), 469–495.

Raman, G. & Rice, E.J. 1991 Axisymmetric jet forced by fundamental and subharmonic tones. *AIAA J.* **29** (7), 1114–1122.

Roose, D., Lust, K., Champneys, A. & Spence, A. 1995 A Newton-Picard shooting method for computing periodic solutions of large-scale dynamical systems. *Chaos Soliton Fract.* **5** (10), 1913–1925.

Saad, Y. 2011 *Numerical Methods for Large Eigenvalue Problems: Revised Edition*. SIAM.

Saffman, P.G. 1992 *Vortex dynamics*. Cambridge University Press.

Sánchez, J. & Net, M. 2010 On the multiple shooting continuation of periodic orbits by Newton–Krylov methods. *Int. J. Bifurcat. Chaos* **20** (01), 43–61.

Sánchez, J., Net, M., Garcia-Archilla, B. & Simó, C. 2004 Newton–Krylov continuation of periodic orbits for Navier–Stokes flows. *J. Comput. Phys.* **201** (1), 13–33.

Schram, C. 2003 Aeroacoustics of subsonic jets: prediction of the sound produced by vortex pairing based on particle image velocimetry. PhD thesis, Technische Universiteit Eindhoven.

Schram, C., Taubitz, S., Anthoine, J. & Hirschberg, A. 2005 Theoretical/empirical prediction and measurement of the sound produced by vortex pairing in a low Mach number jet. *J. Sound Vib.* **281** (1), 171–187.

Selçuk, C., Delbende, I. & Rossi, M. 2017*a* Helical vortices: linear stability analysis and nonlinear dynamics. *Fluid Dyn. Res.* **50** (1), 011411.

Selçuk, C., Delbende, I. & Rossi, M. 2017*b* Helical vortices: Quasiequilibrium states and their time evolution. *Phys. Rev. Fluids* **2** (8), 084701.

Shaabani-Ardali, L., Sipp, D. & Lesshafft, L. 2017 Time-delayed feedback technique for suppressing instabilities in time-periodic flow. *Phys. Rev. Fluids* **2** (11), 113904.

Shariff, K. & Leonard, A. 1992 Vortex rings. *Annu. Rev. Fluid Mech.* **24** (1), 235–279.

Nek 5000 Version 1.0 rc1/svn r1094, Argonne National Laboratory, Illinois. Available: `https://nek5000.mcs.anl.gov`.

Theofilis, V. 2011 Global linear instability. *Annu. Rev. Fluid Mech.* **43**, 319–352.

Thomas, J.P., Dowell, E.H. & Hall, K.C. 2002 Nonlinear inviscid aerodynamic effects on transonic divergence, flutter, and limit-cycle oscillations. *AIAA J.* **40** (4), 638–646.

Tophøj, L. & Aref, H. 2013 Instability of vortex pair leapfrogging. *Phys. Fluids* **25** (1), 014107.

Trefethen, L.N., Trefethen, A.E., Reddy, S.C. & Driscoll, T.A. 1993 Hydrodynamic stability without eigenvalues. *Science* **261** (5121), 578–584.

Trefethen, Lloyd N. & Embree, M. 2005 *Spectra and pseudospectra: the behavior of nonnormal matrices and operators*. Princeton University Press.

Vermeer, L.J., Sørensen, J.N. & Crespo, A. 2003 Wind turbine wake aerodynamics. *Prog. Aerosp. Sci.* **39** (6-7), 467–510.

Winant, C.D. & Browand, F.K. 1974 Vortex pairing: the mechanism of turbulent mixing-layer growth at moderate Reynolds number. *J. Fluid Mech.* **63** (2), 237–255.

Zaman, K.B.M.Q. & Hussain, A.K.M.F. 1980 Vortex pairing in a circular jet under controlled excitation. Part 1. General jet response. *J. Fluid Mech.* **101** (03), 449–491.

Resolvent-based modelling of coherent wavepackets in a turbulent jet

Lutz Lesshafft[1], Onofrio Semeraro[1,2], Vincent Jaunet[3], André V. G. Cavalieri[4] and Peter Jordan[3]

[1]*Laboratoire d'Hydrodynamique, CNRS / École polytechnique, 91128 Palaiseau, France*
[2]*LIMSI, CNRS / Université Paris-Saclay, Orsay, France*
[3]*Institut Pprime, CNRS / Université de Poitiers / ENSMA, 86962 Futuroscope Chasseneuil, France*
[4]*Divisão de Engenharia Aeronáutica, Instituto Tecnológico de Aeronáutica, São José dos Campos, SP, Brazil*

Coherent turbulent wavepacket structures in a jet at Reynolds number 460 000 and Mach number 0.4 are extracted from experimental measurements, and are modelled as linear fluctuations around the mean flow. The linear model is based on harmonic optimal forcing structures and their associated flow response at individual Strouhal numbers, obtained from analysis of the global linear resolvent operator. These forcing/response wavepackets ('resolvent modes') are first discussed with regard to relevant physical mechanisms that provide energy gain of flow perturbations in the jet. Modal shear instability and the non-modal Orr mechanism are identified as dominant elements, cleanly separated between the optimal and sub-optimal forcing/response pairs. A theoretical development in the framework of spectral covariance dynamics then explicates the link between linear harmonic forcing/response structures and the cross-spectral density (CSD) of stochastic turbulent fluctuations. A low-rank model of the CSD at given Strouhal number is formulated from a truncated set of linear resolvent modes. Corresponding experimental CSD matrices are constructed from extensive two-point velocity measurements. Their eigenmodes (SPOD modes) represent coherent wavepacket structures, and these are compared to their counterparts obtained from the linear model. Close agreement is demonstrated in the range of 'preferred mode' Strouhal numbers, around a value of 0.4, between the leading coherent wavepacket structures as educed from the experiment and from the linear resolvent-based model.

I. INTRODUCTION

The presence of orderly structures in many turbulent shear flows has been abundantly documented over the last fifty years; in the case of jets, such studies have largely been motivated by the need to reduce their noise generation. It was recognised early on that coherent structures in turbulent jets strongly resemble instability wavepackets, as if they were governed by linear dynamics of small-amplitude fluctuations in a time-averaged mean flow [1]. Many variants of linear analysis techniques have since been explored, in order to identify a model that may faithfully reproduce the coherent turbulence structures in jets. Based on the assumption that linear jet instability is driven by incoming disturbances from upstream, Michalke [2] computed the spatial growth of linear perturbations in parallel jet profiles, followed by the inclusion of weakly non-parallel effects by way of multiple-scales expansion [3] or parabolised stability equations (PSE, [4]), as well as fully non-parallel linear simulations with inlet forcing [5]. As discussed by Jordan & Colonius [1], all these studies successfully predict the observed spatial growth of coherent turbulence structures near the nozzle, over a dominant but restricted range of frequencies. However, the underlying theoretical model *a priori* pertains to deterministic linear perturbations developing in a steady laminar base flow, and the justification for extending it to stochastic nonlinear fluctuations around a statistical turbulent mean state has remained vague.

Laws that govern the statistical moments of turbulent flow, like average and covariance values, can be obtained by considering the linearized Navier–Stokes system subject to stochastic forcing [6]; this approach has recently evolved into the 'statistical state dynamics' framework, where stochastic forcing of higher-order statistical moments is considered [7]. Application of this framework to the aerodynamic turbulent jet problem is very promising; the interpretation, given in Ref. [7], that "turbulence in shear flow can be essentially understood as determined by quasi-linear interaction occurring directly between a spatial or temporal mean flow and perturbations", whereas "the role of nonlinearity in the dynamics of turbulence is highly restricted", is clearly born out by the empirical evidence of turbulent jet studies [1]. While most of the literature on stochastic forcing in the linearized Navier–Stokes equations, including the reviews by Schmid (Sec. 4 in [8]) and Bagheri *et al.* [9], focuses on time-domain formulations of covariance dynamics, coherence in jet turbulence has often been analysed in the frequency domain. In particular, several recent jet studies make use of *spectral proper orthogonal decomposition* (SPOD, see [10], not to be confused with [11]) as a means to extract empirical coherent structures at a given frequency from experimental or numerical flow data [4, 12, 13].

Linear instability analysis of jets in recent years has increasingly been carried out in a frequency-domain framework based on *optimal* forcing and associated flow response structures, with no limiting assumptions about the spatial development of the base state [14–20]. Forcing and response structures in this formalism are distributed throughout the interior of the flow, in contrast to the assumption of pure upstream boundary forcing made in most previous models (as cited above), and they are found as the singular modes of the global resolvent operator [8]. This global resolvent framework, also referred to as 'frequency response' [14, 21] or 'input-output' [16] analysis, has similarly been applied in the study of boundary layers [22–24], and its potential for the modelling of stochastic dynamics has been explored for backward-facing step flow [25–27]. The question at this point remains, exactly what stochastic quantities can be consistently modelled on the basis of linear resolvent analysis? Dergham *et al.* [25] use a low-rank resolvent model in order to construct approximations of time-domain POD modes, whereas Boujo & Gallaire [26] follow the arguments of Farrell & Ioannou [21] in order to estimate the frequency spectrum of the stochastic flow response to white-noise forcing. Beneddine *et al.* [27] go further and set out to model the *spatial distribution* of coherent fluctuations in the frequency domain; they demonstrate convincing agreement between the spatial structures of the optimal linear flow response and the leading SPOD mode, obtained from numerical simulations.

A formal justification for a direct comparison between optimal linear response structures and SPOD modes has subsequently been suggested in two conference papers [18, 28], and the details and conditions for their equivalence are elaborated in the recent work of Towne *et al.* [19]. On this basis, Schmidt *et al.* [20] present a detailed comparison between resolvent analysis results and SPOD modes, extracted from LES data, for high-Reynolds-number turbulent jets at Mach numbers 0.4, 0.9 and 1.5. It is found that the leading SPOD mode is well reproduced by the optimal linear flow response, at the dominant Strouhal number 0.6 for the $Ma = 0.4$ case.

The present paper revisits the same turbulent jet configuration, at Mach number 0.4 and Reynolds number 460 000, entirely based on the experimental measurements by Cavalieri *et al.* [12] and Jaunet *et al.* [29]. The latter study involved velocity measurements in cross-planes of the jet by means of two high-cadence, stereoscopic particle-image velocimetry systems that could be displaced in the streamwise direction so as to provide the cross-spectral density (CSD) of the velocity fluctuations, decomposed both in frequency and in azimuth. In this paper, SPOD modes will be educed from these experimental CSD matrices, such that they can be compared with linear predictions derived from a resolvent analysis of the experimental mean flow. The principal new

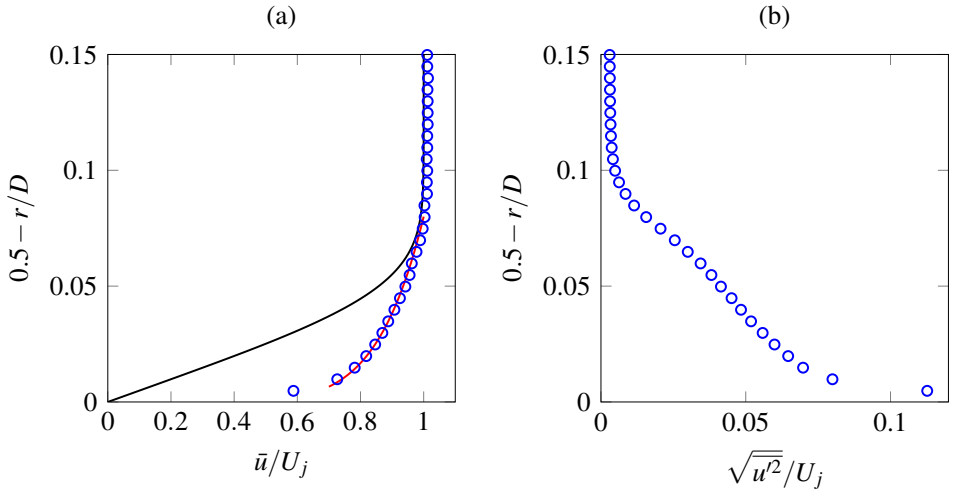

FIG. 1. Velocity profiles of the turbulent nozzle boundary layer in the jet exit plane. (a) Mean axial velocity, scaled with the centreline velocity U_j. The experimental measurements (○) are compared with the Blasius profile (—) and a fitted power law (—). (b) Measured root-mean-square velocity fluctuations. Data from Cavalieri *et al.* [12].

aspects of the present study are (i) the use of an experimental database for jet resolvent analysis, (ii) the extraction of SPOD modes from experimental jet measurements, (iii) the design of a *resolvent-based linear model* for such experimental SPOD modes, which are necessarily based on partial-state information, and (iv) a detailed discussion of the linear instability dynamics triggered by optimal and sub-optimal forcing in thin-shear-layer jets, which, by extension, underpin the spectral covariance dynamics contained in the SPOD modes. Although the results of this study are mostly consistent with those of Schmidt *et al.* [20], several quantitative as well as qualitative differences arise, with relevance for the physical interpretation in terms of instability mechanisms. These differences are attributed to the inclusion of a nozzle pipe in the present analysis. The nozzle boundary layer is identified as the most receptive flow region in the following calculations, underlining the importance of its numerical resolution, similar to recent observations in LES calculations [30].

The flow configuration, corresponding to the jet experiments, is briefly defined in Sec. II. The linear resolvent analysis, including the modal decomposition framework, the numerical implementation, and the presentation of results, is documented in Sec. III. This is followed, in Sec. IV, by a discussion of the salient linear instability mechanisms that are active in optimal and sub-optimal jet forcing. Section V presents a detailed comparison between SPOD modes from experimental data and stochastic predictions derived from the resolvent-based linear model. Our new results are then put into perspective with regard to previous modelling attempts. The paper closes, in Sec. VI, with a summary of the main conclusions.

II. FLOW CONFIGURATION

The study is based on jet experiments conducted at the *Bruit et Vent* jet-noise facility of the Pprime Institute in Poitiers. Technical details of the experimental apparatus, as well as measurement validation, are thoroughly described in past publications [12, 29].

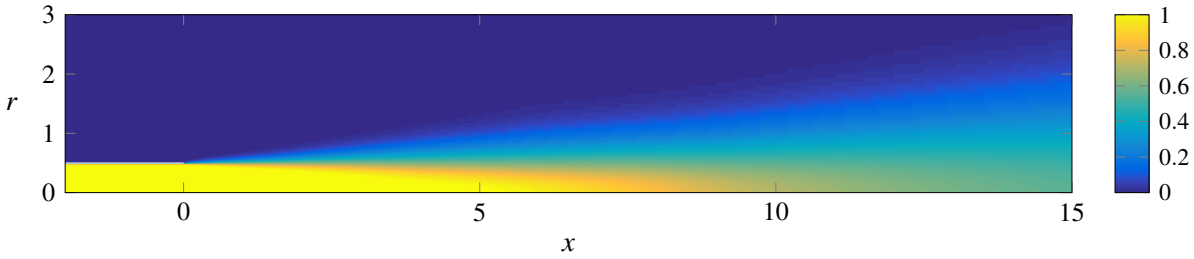

FIG. 2. Axial velocity of the mean flow, as used throughout this study. The distribution has been modelled such as to closely reproduce the experimental measurements [12]. The pipe wall is represented as a white line, and only a portion of the numerical domain is shown. The rasterisation of the colour plot corresponds to the standard numerical grid resolution (Sec. III D).

The experiments are performed on a $Ma = 0.4$ isothermal jet issuing from a convergent-straight nozzle. The Reynolds number of the jet, based on the nozzle exit diameter $D = 50$ mm and the maximum exit velocity U_j is defined as $Re = U_j D/\nu = 460\,000$, where ν is the kinematic viscosity. The Strouhal number corresponding to the dimensional frequency f is defined as $St = fD/U_j$. The transition to turbulence of the incoming boundary layer is forced using an azimuthally homogeneous carborandum strip, located at $2.8D$ upstream of the nozzle exit plane. A fully turbulent boundary layer is obtained at the exit section of the nozzle, as reported in Fig. 1, where the mean streamwise velocity and its root-mean-square fluctuation values in the interior pipe boundary layer are shown, both normalised with U_j.

Free-jet mean flow measurements from this setup are documented in Cavalieri *et al.* [12], and excellent reproducibility has been demonstrated in the more recent experiments by Jaunet *et al.* [29]. These experimental data are used to construct a parametric model of the mean flow, as described in Rodriguez *et al.* [13], providing smooth variations of axial and radial velocity, density and temperature. A self-similar solution, as described in Sec. 5.2 of Pope [31], is employed at $x > 15D$, measured from the nozzle exit, resulting in a maximum difference of 6% at $x = 15D$ between the self-similar velocity model and the PIV data. Upstream of the nozzle exit, a straight pipe is added to the numerical flow domain. The mean flow inside this pipe is taken to be parallel; the boundary layer velocity profile is approximated as being linear very near the wall, followed by a fitted power-law variation over the radial interval indicated by a red line in Fig. 1*a*, until the constant value U_j is attained. A smooth transition between the parallel nozzle flow and the spreading jet is achieved by use of a weighting function, with null derivatives on both ends, over the distance of one diameter [32]. The resulting axial velocity field, shown in Fig. 2, is used for computing temperature and density distributions by way of the Crocco–Busemann relation, and the radial velocity component is recovered from the continuity equation. The momentum thickness of the shear layer at the nozzle exit, $x = 0$, is $\delta_m/D = 0.0075$, significantly thinner than in the LES-based study by Schmidt *et al.* ([20], their figure 2b). In the free jet, the momentum thickness grows linearly with x, at a rate of $\mathrm{d}\delta_m/\mathrm{d}x \approx 0.031$.

III. LINEAR RESOLVENT ANALYSIS OF FLUCTUATIONS AROUND A MEAN FLOW

A. Governing equations

We consider the compressible Navier–Stokes equations, in terms of conservative variables $(\rho, \rho\mathbf{u}, \rho E)$, cast in axisymmetric cylindrical coordinates (x,r). In the notation of [33], these equations are

$$\frac{\partial \rho}{\partial t} + \nabla(\rho\mathbf{u}) = 0, \tag{1a}$$

$$\frac{\partial \rho\mathbf{u}}{\partial t} + \nabla(\rho\mathbf{u}\otimes\mathbf{u}) = -\nabla p + \nabla\tau, \tag{1b}$$

$$\frac{\partial \rho E}{\partial t} + \nabla(\rho\mathbf{u}E) = -\nabla\mathbf{h} + \nabla(\tau\mathbf{u}), \tag{1c}$$

where ρ is density and $\mathbf{u} = (u_x, u_r, 0)$ is the velocity vector, with axial and radial components u_x and u_r, and with zero azimuthal velocity. In our axisymmetric setting, all quantities are independent of the azimuthal coordinate θ. The total energy E is then defined as

$$E = \frac{T}{\gamma(\gamma-1)Ma^2} + \frac{1}{2}(|u_x|^2 + |u_r|^2), \tag{2}$$

with $\gamma = 1.4$ the ratio of specific heats. The tensor τ denotes the molecular stresses, and $\mathbf{h}$ is the heat flux vector. The reference length of the problem is the pipe diameter D. The reference velocity is chosen as the centreline velocity U_j at the pipe exit $x = 0$, and the reference density is set as the ambient value ρ_∞. Sutherland's law is used to calculate the viscosity, and the Prandtl number is set to $Pr = 0.72$, the standard value for air.

B. Representation as a linear input-output system

The flow variables $q = (\rho, \rho u_x, \rho u_r, \rho E)$ are decomposed into their time-averaged mean and time-dependent fluctuation components, $q(x,r,t) = \bar{q}(x,r) + q'(x,r,t)$. The governing equations (1) can then be rewritten in the form

$$\frac{\partial q'}{\partial t} - Aq' = f, \tag{3}$$

where A is the operator obtained by linearising (1) around the mean flow, and the vector f contains all remaining nonlinearities in q', i.e. the fluctuations of the generalised Reynolds stresses [34], as well as any external forcing at the boundaries of a finite-domain flow problem.

A Fourier-transform

$$q'(x,r,t) = \int_{-\infty}^{\infty} \hat{q}(x,r,\omega)e^{i\omega t}\mathrm{d}\omega, \qquad f(x,r,t) = \int_{-\infty}^{\infty} \hat{f}(x,r,\omega)e^{i\omega t}\mathrm{d}\omega, \tag{4}$$

leads to the frequency-domain system

$$\hat{q} = (i\omega I - A)^{-1}\hat{f} = R(\omega)\hat{f}, \tag{5}$$

where R is the *resolvent* operator [8]. As f contains all terms nonlinear in q', the forcing with its Fourier-transform $\hat{f}$ induces an inherent coupling between all frequencies. In order to make use of

the system (5) for the purpose of modelling, a closure assumption is required that allows a decoupling of frequencies. Following previous literature [19, 21, 27, 35], we choose to simply regard f as an anonymous forcing term, representing any incoming perturbations from the nozzle or the ambient, as well as fluctuations in the nonlinear terms of the momentum and energy equations, but without accounting for its inner structure that makes it dependent on q'. Accordingly, we neglect the dependence of $\hat{f}$ at one given frequency on $\hat{q}$ at other frequencies.

One possibility to account for a limited interaction between frequencies lies in the inclusion of turbulent dissipation through small scales in the linear operator A, in the form of turbulent viscosity. Indeed, any portion of $\hat{f}$ may be modelled as being linearly dependent on $\hat{q}$, without introducing explicit coupling between frequencies. Some empirical evidence suggests the pertinence of such modelling [36, 37], and we have used it in the past for the resolvent analysis of turbulent jets [17, 38], but the procedure requires additional modelling hypotheses and is not pursued here. All computations in this section only account for molecular viscosity at $Re = 460\,000$.

C. Modal decomposition of the resolvent operator

The following development restates the resolvent analysis formalism as it has been applied in numerous past studies, including references [14, 16–20]. It is presented here in a form that establishes our nomenclature and clarifies the influence of the chosen energy norm.

For a given frequency ω, the resolvent operator provides the mapping between any forcing structure $\hat{f}(x,r,\omega)$ and its linear flow response $\hat{q}(x,r,\omega)$. The common choice for an energy measure in compressible settings is the norm defined by Chu [39],

$$\|\hat{q}\|^2 = \iint_\Omega \left(\bar{\rho}(|u_x|^2 + |u_r|^2) + \frac{\bar{p}}{\bar{\rho}}|\hat{\rho}|^2 + \frac{\bar{\rho}^2}{\gamma^2(\gamma-1)Ma^4\bar{p}}|\hat{T}|^2 \right) r\,\mathrm{d}r\,\mathrm{d}x, \tag{6}$$

which is used in the following computations. Both the forcing and the flow response are measured in this norm, and the spatial integration in both cases is carried out over the entire numerical domain Ω, with the exception of absorbing layers near the outer boundaries (see Sec. III D). In discrete form, the norm is expressed by a Hermitian positive-definite matrix M, such that $\|\hat{q}\|^2 = \hat{q}^H M \hat{q}$, with a Cholesky factorisation $M = N^H N$. Flow forcing and response are represented by *discrete* complex-valued vectors $\hat{f}$ and $\hat{q}$ in the following

The *gain* between input and output energy is then defined as

$$\sigma^2 = \frac{\|\hat{q}\|^2}{\|\hat{f}\|^2} = \frac{\hat{f}^H R^H M R \hat{f}}{\hat{f}^H M \hat{f}} = \frac{\hat{v}^H N^{-1,H} R^H M R N^{-1} \hat{v}}{\hat{v}^H \hat{v}}, \quad \text{with } \hat{v} = N\hat{f}, \tag{7}$$

which has the form of a Rayleigh quotient, involving the Hermitian operator $N^{-1,H}R^H MRN^{-1}$. Consequently, the eigenvectors $\hat{v}_i$ of this operator are orthogonal, its eigenvalues σ_i^2 are real positive, and the largest possible energy gain of the linear flow system is given by the largest eigenvalue. The forcing structure that gives rise to an energy gain σ_i^2 is recovered as $\hat{f}_i = N^{-1}\hat{v}_i$. After normalisation, $\hat{v}_i^H \hat{v}_i = 1$, the eigenvectors $\hat{v}_i$ are the columns of the right singular matrix V of the operator

$$NRN^{-1} = U\Sigma V^H, \tag{8}$$

associated with the singular values σ_i as entries in the diagonal matrix Σ, and with the unique unitary matrix U.

	Δx_{min}	Δr_{min}	t_{max}	σ_1
case A	0.0200	0.0075	60	5117.2
case B	0.0200	0.0025	60	5256.3
case C0	0.0100	0.0025	60	5264.3
case C1	0.0100	0.0025	70	5294.4
case C2	0.0100	0.0025	75	5302.6
case C3	0.0100	0.0025	80	5306.6

TABLE I. Convergence of the optimal gain σ_1 at $St = 0.5$, as a function of grid resolution and final simulation time t_{max}. These test calculations were performed with a reduced Krylov space dimension $N_{kr} = 4$. A value $N_{kr} = 12$ is used in all following computations for an increased accuracy of sub-optimal modes.

The forcing structures $\hat{f}_i$ are the columns of a matrix $F = N^{-1}V$, and the associated flow response structures $\hat{q}_i$ form the matrix $\hat{Q} = RF$. With (8), it is found that $\hat{Q} = N^{-1}U\Sigma$, from where it follows that $\hat{Q}^H M\hat{Q} = \Sigma^2$. A normalised response matrix $Q = \hat{Q}\Sigma^{-1}$ is introduced, such that the final identities for our modal resolvent decomposition are recovered:

$$F^H MF = Q^H MQ = I, \tag{9a}$$

$$R = Q\Sigma F^H M. \tag{9b}$$

The singular values σ_i are arranged in descending order, such that the optimal energy gain is given by $\sigma_{max}^2 = \sigma_1^2$, arising for the forcing structure $\hat{f}_1$. In the inner-product space defined with the matrix M, each vector $\hat{f}_j$ represents the optimal forcing in the subspace that is orthogonal to all leading vectors $\hat{f}_i$ with $i > j$. As a convention, we will refer to a given triple $(\sigma_i, \hat{f}_i, \hat{q}_i)$ as the resolvent mode i, consisting of the i^{th} gain, forcing mode and response mode. The triple $(\sigma_1, \hat{f}_1, \hat{q}_1)$ of 'optimal gain', 'optimal forcing' and 'optimal response' is characterised by the maximum value of σ, and resolvent modes with $i > 1$ are sometimes referred to as 'sub-optimals'. Note that 'gain' in the following refers to σ, not to the *energy* gain, given by σ^2.

D. Matrix-free computation of resolvent modes

Gain values and associated forcing modes are computed by solving the reformulated eigenvalue problem

$$R^H MR\hat{f}_i = \sigma_i^2 M\hat{f}_i, \tag{10}$$

using the iterative Lanczos method that is provided by the SLEPc library [40]. A matrix-free time-stepping method is used in each iteration step, as described in detail by [32]. Time-stepping needs to be performed both for the solution of a direct system, $a = Rb$, and for the subsequent solution of an adjoint system, $a' = R^H b'$. The time horizon t_{max} of these calculations must be chosen long enough such that the final periodic flow regime is recovered with sufficient accuracy. A numerical procedure for the adjoint system is constructed according to the method of Fosas de Pando *et al.* [41], which ensures that the complete numerical encoding of the operator in (10) remains strictly Hermitian; this is an important requirement for the efficiency of the Lanczos algorithm.

The linear system (3) is discretised with explicit finite-difference schemes [42], using an 11-point stencil. Time integration is performed with a third-order Runge–Kutta algorithm, with time step $\Delta t = 2.85 \cdot 10^{-3}$. The computational domain extends along the streamwise direction over the

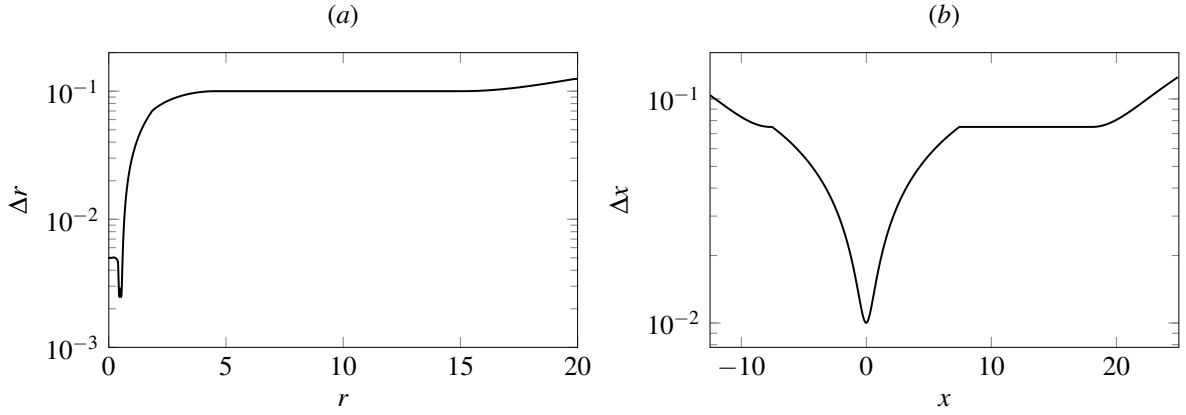

FIG. 3. Spacing of mesh points, (a) in the radial direction and (b) in the axial direction. The mesh is orthogonal.

interval $x \in [-12.5, 25]$, and from the symmetry axis $r = 0$ outwards to $r = 20$; the nozzle exit is placed at $x = 0$. The mesh that is used in all calculations presented in the following sections consists of $(N_x, N_r) = (750, 380)$ discretisation points. These points are distributed on a non-uniform Cartesian grid, with maximum resolution along the pipe walls, in the shear layer and around the nozzle lip. Figure 3 displays the axial and radial point distributions.

Symmetry boundary conditions are imposed on the jet axis by the use of ghost points: ρ, ρu_x and ρE are prescribed to be even functions in r across the axis, while ρu_r is odd. On all other boundaries, the LODI boundary conditions are applied [43], in combination with absorbing layers [44] at $r > 16$, $x < -8$ and $x > 21$.

Convergence of the optimal gain is tested with respect to the grid spacing and to the final time t_{max} of the simulations. Several results are reported in table I. For a fixed value $t_{max} = 60$, the mesh of case C0 is deemed sufficiently refined; this is the standard mesh displayed in Fig. 3. The final time is chosen by tracking the energy of time-harmonic fluctuations, in order to evaluate to what extent transient dynamics have died out. Satisfactory convergence is reached at $t_{max} = 80$, which corresponds approximately to twice the convection time of vortical structures between the nozzle exit and the downstream end of the physical domain; this value is retained for all following calculations.

For any given Strouhal number, the five leading resolvent modes are computed, using a Krylov space of dimension $N_{kr} = 12$. The Lanczos iteration is halted when the estimated residual norms of all five modes have fallen below the tolerance value $\varepsilon = 10^{-4}$ (see [40]). A typical computation for one Strouhal number requires about 12–16 wall-time hours on 192 cores of Intel Xeon E5-2690 v3 CPUs.

E. Resolvent mode results

Gain values of the five leading resolvent modes are shown in Fig. 4 as functions of the Strouhal number. Above $St = 0.3$, the optimal gain curve is well separated from the sub-optimal ones. The maximum overall gain occurs at $St = 0.7$, where σ_1 is one order of magnitude larger than σ_2.

The optimal forcing and response structures are presented in Figs. 5 and 6 for several Strouhal numbers between 0.2 and 0.7; snapshots of the real axial momentum components are shown in

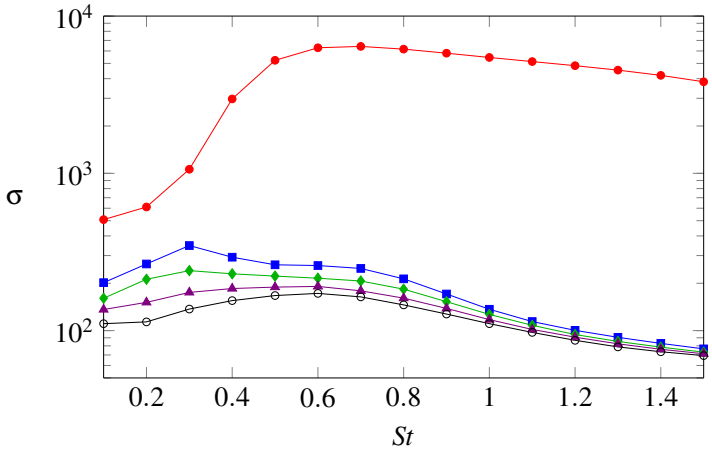

FIG. 4. The five leading resolvent gain values (● σ_1, ■ σ_2, ♦ σ_3, ▲ σ_4, ○ σ_5) as functions of Strouhal number.

all frames, with a rasterisation that corresponds to the numerical mesh. At Strouhal numbers 0.3 and above, the forcing is localised in a thin layer at the inner pipe wall, near the nozzle. The right-column frames in Fig. 5 give a magnified view of the forcing in this flow region. Elongated structures are tilted against the flow direction, in a fashion that is typical of the Orr mechanism. Similar optimal forcing structures have been identified in boundary layers [22, 23] and in past studies of incompressible as well as compressible jets [14, 15, 17]. The response structures at $St \geq 0.3$ exhibit the classical wavepacket shape associated with shear instability, with peak amplitudes inside the potential core [13, 14, 20].

The main characteristics of both the optimal forcing and the optimal response modes are similar at all Strouhal numbers above 0.2: optimal forcing acts upstream in the pipe and generates a wavepacket with amplitude growth in the potential core region of the jet. As the Strouhal number increases, the wavelength shortens, and the location of the peak amplitude moves closer to the nozzle, consistent with the interpretation of local spatial instability [2]. At low Strouhal numbers, as shown in figures 5*a* and 6*a*, different effects seem to arise: in addition to the described scenario, tilted forcing structures protrude into the free shear layer close to the nozzle, and the response wavepacket appears to be composed of two distinct regions. Along the jet axis, one local amplitude maximum occurs at $x = 5.5$, and another one at $x = 13$, far downstream of the potential core. The low-*St* optimal mode results of Schmidt *et al.* (Fig. 12*f* in [20]) show a similar pattern. As argued by those authors, the distinct mode characteristics at low Strouhal numbers are likely to be associated with a crossing or merging of mode branches, due to a lessened efficiency of the shear instability mechanism.

Sub-optimal forcing and response structures, modes 2-5, are displayed in Fig. 7 for $St = 0.7$. The forcing in all cases is again characterised by structures that are tilted against the mean flow, although these structures arise at a small radial distance away from the pipe wall, and they extend far into the free jet, with significant amplitude inside the shear region. The associated response wavepackets have their maximum amplitude far downstream of the potential core. The forcing structures display radial variations that are suggestive of orthogonal functions, with an increasing number of zero-amplitude nodes along r, and corresponding radial structures are imparted to the response wavepackets. A similar hierarchy of optimal modes has been described in Ref. [17].

Preliminary results, pertaining to the same flow configuration of the jet experiments, have been

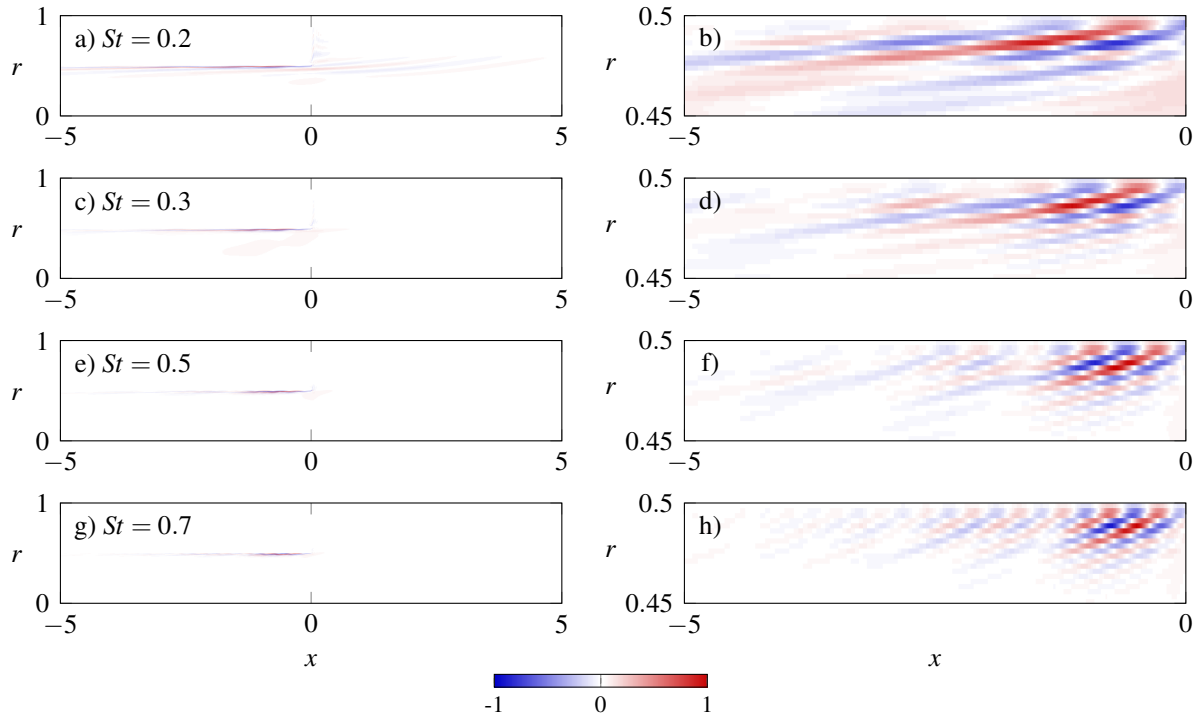

FIG. 5. Optimal forcing modes at various Strouhal numbers, associated with the response modes in Fig. 6. The real part of axial velocity forcing is represented. (a,c,e,g) Optimal forcing, plotted with aspect ratio 2. (b,d,f,h) Close-up of the pipe boundary layer, where the forcing is localised, at the same St values as in the left column. The rasterisation corresponds to the numerical mesh; each field is normalised with respect to its maximum amplitude.

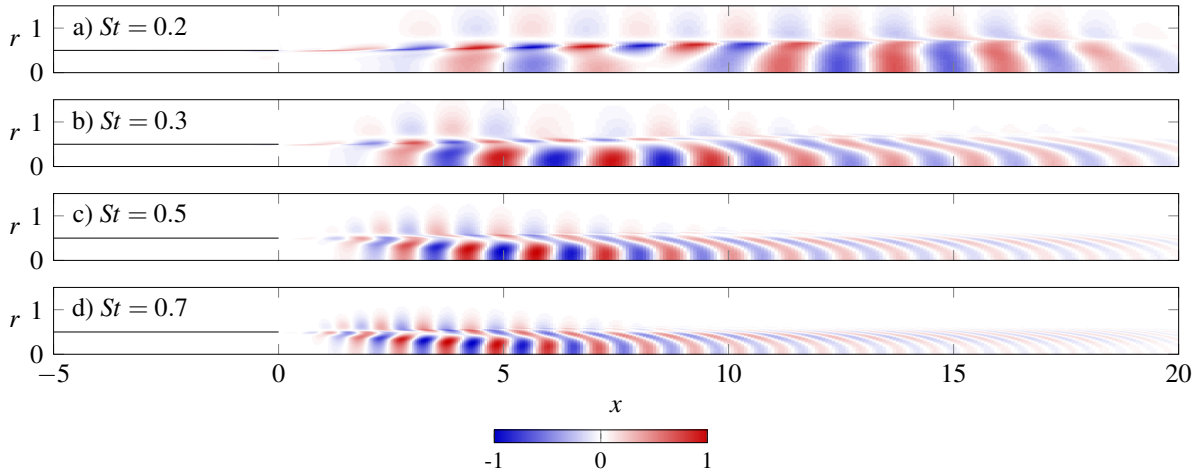

FIG. 6. Optimal response modes at various Strouhal numbers, associated with the forcing modes in Fig. 5. The real part of axial velocity perturbations is represented, with aspect ratio 1. The pipe wall is shown as a black line. Each field is normalised with respect to its maximum amplitude.

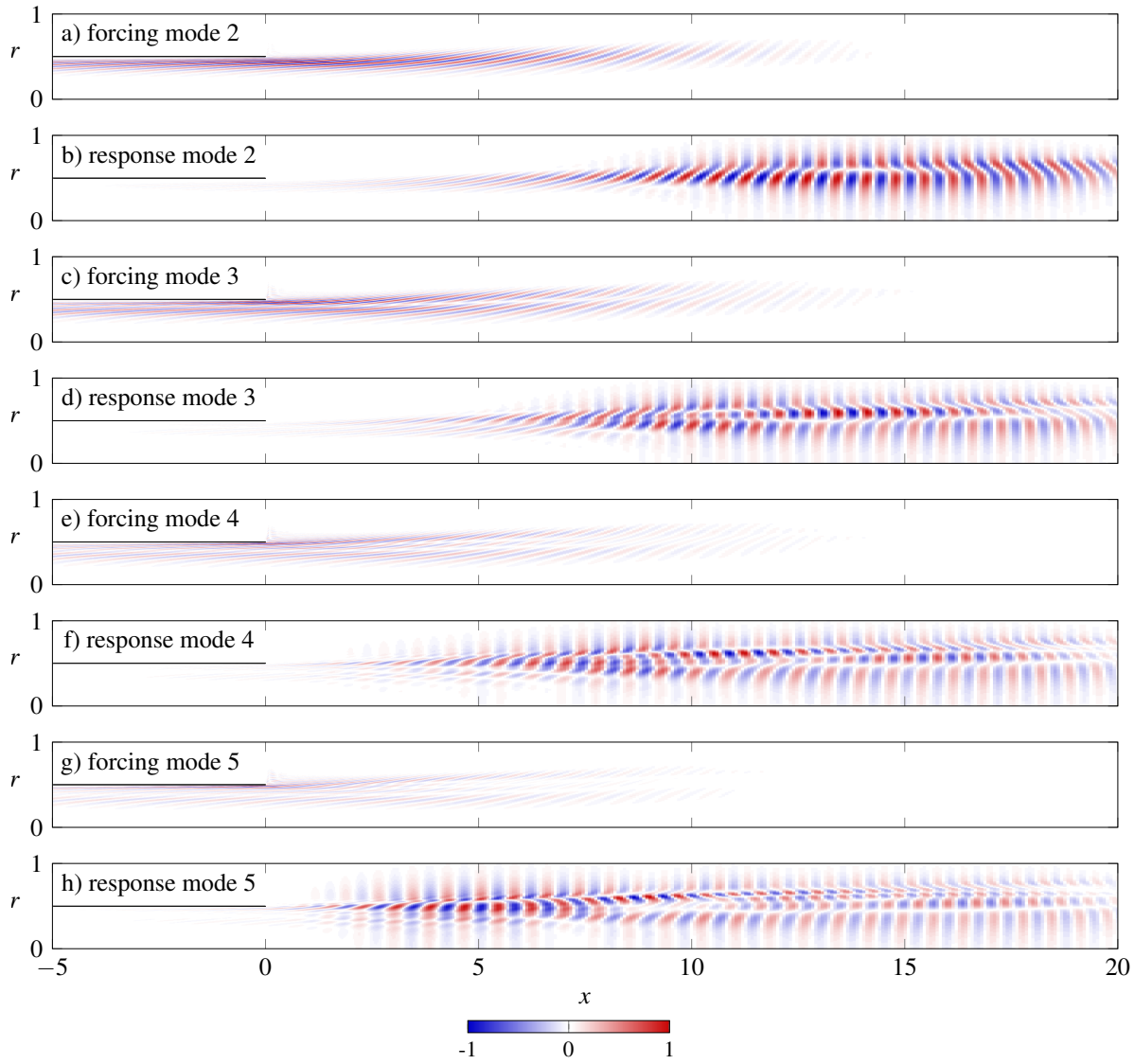

FIG. 7. Sub-optimal forcing and response modes for $St = 0.7$. The real part of axial velocity perturbations is represented. (a,c,e,g) Forcing modes; and (b,d,f,h) associated response modes. The pipe wall is shown as a black line. Each field is normalised with respect to its maximum amplitude. The aspect ratio is 2, strong magnification is required in order to visualise the fine-scale radial variations.

presented in a previous conference paper [18]. While all forcing modes in that paper are visually identical to the present results, the associated sub-optimal response modes were quite different, all bearing a strong resemblance to the optimal mode. Those earlier calculations were clearly affected by spurious numerical noise, which in all cases triggered the optimal mode sufficiently so as to overwhelm the true sub-optimal response. Non-smoothness in the base flow, as used in Ref. [18], was identified to cause this spurious effect. It has been carefully verified that forcing and response modes in the present results form orthogonal sets, with respect to our scalar product, within the accuracy imposed by the residual tolerance of the Lanczos algorithm.

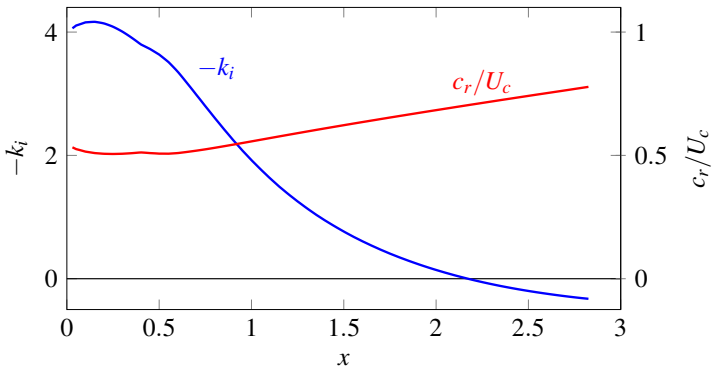

FIG. 8. Growth rate $-k_i$ and real phase velocity c_r of the local shear instability mode, and their downstream variations in the jet mean flow. The phase velocity is scaled with the local mean centreline velocity.

IV. INTERPRETATION OF OPTIMAL GROWTH MECHANISMS

The role of modal shear (Kelvin–Helmholtz) and non-modal Orr mechanisms for optimal and sub-optimal jet resolvent modes has often been invoked in the literature (see for instance [20, 45, 46]). The aim of this section is to substantiate this interpretation by use of local analysis (for shear) and a parallel model flow (for Orr).

The optimal resolvent modes (Fig. 6) strongly resemble those described by Garnaud *et al.* [14] for an incompressible turbulent jet, which have been interpreted as a constructive combination of the Orr mechanism in the pipe boundary layer and the shear mechanism in the free jet. Close to the nozzle, the optimal response modes display peak amplitudes inside the free shear layer, when measured along the radial direction. As discussed in Ref. [14], and consistent with many other studies on jet wavepackets (e.g. [13, 20]), the spatial distribution as well as the strong streamwise amplitude growth indicates a preponderant role of shear instability in the optimal forcing response. This hypothesis is easily validated by a comparison with local instability results in the near-nozzle region. In a local framework, the shear instability mechanism gives rise to a single spatial k^+ mode, which is indeed the only unstable spatial mode that can be found in the jet [47]. The downstream evolution of this k^+ eigenvalue, for $St = 0.7$ in the present jet mean flow, is displayed in Fig. 8 in terms of its spatial growth rate $-k_i$ and its real phase velocity $c_r = -\omega/k$. The latter is further scaled with the *local* centreline velocity $U_c(x)$ of the jet profile.

The local shear instability mode, for $St = 0.7$, is seen to be unstable only over the interval $0 \leq x \leq 2.17$. Downstream of this position, its eigenfunction (not shown) develops strong oscillations around $r = 0.5$, characteristic of the viscous solution in the Stokes sector above the critical point [48], and it remains numerically tractable with confidence over only a short distance further. A Reynolds number of 20 000 has been used in these local calculations, lower than in the reference experiment and in the global resolvent analysis, in order to accommodate an accurate resolution of eigenfunctions in the slightly stable regime. It can be demonstrated that results in the *unstable* regime are unaffected by this large value of *Re*. Relevant details on local spectra of compressible jets are discussed by Rodriguez *et al.* [13]; in particular, it is described how the shear layer mode, once it is stable, quickly merges into a continuous branch of oscillating modes. The same observations apply here.

Following the method of Rodriguez *et al.* [13], the optimal resolvent response wavepacket at $St = 0.7$ (Fig. 9*a*) is projected at each x onto the complete basis of local spatial eigenfunctions, by

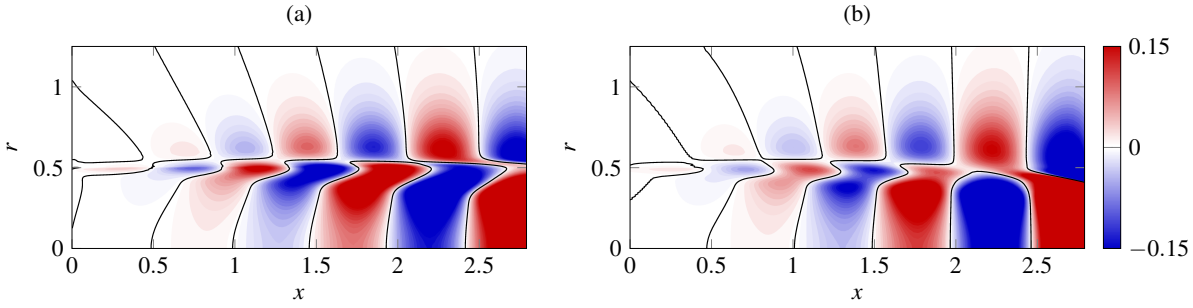

FIG. 9. Local shear instability contribution to the optimal response mode at $St = 0.7$. (a) Optimal response mode from global resolvent analysis; (b) its reconstruction from projection onto the k^+ local shear instability mode. Axial velocity fluctuations are shown over the interval in x where the local mode can be identified numerically. Both fields are normalised with respect to their amplitude maxima, but the colour scale is saturated, in order to make small-amplitude fluctuations visible. The zero contour is traced in black.

an inner product with the associated local adjoint modes. Projection coefficients are thus obtained at each x position, and the superposition of all local modes indeed fully reproduces the entire global response wavepacket. The isolated contribution of the local k^+ shear mode is shown in Fig. 9*b* over the streamwise region where this mode is identifiable without ambiguity. It is seen that this mode alone accounts rather accurately for the optimal resolvent response in the unstable interval $0 \leq x \leq 2.17$. Downstream of this region, the radial distribution of the local eigenfunction differs notably from the global result and, contrary to the discussion in Ref. [14], no other single local mode can be identified as being dominant anywhere for $x > 2.17$. The global structure in that region projects significantly onto a large number of local modes from a continuous branch, with strong non-orthogonal cancellation effects.

The second resolvent response structure (mode 2) at $St = 0.7$ (Fig. 7*b*) cannot be related to any dominant local mode anywhere along x. As perturbation growth in the resolvent mode is observed down to a streamwise station $x = 14$, it is already obvious that this behaviour is not attributable to modal growth in a local sense, since local instability at this Strouhal number is confined to $x < 2.17$. Instead, the spatial features of the response wavepacket suggest again an action of the Orr mechanism, both inside the pipe and in the jet, which feeds on energy gain from the pure convection of tilted vortical structures in a sheared base flow. Such tilted structures are generated by distributed forcing in the free shear layer (Fig. 7*a*) upstream of the response maximum. This mechanism has been described by Tissot *et al.* [45] in a different framework, where PSE and its adjoint are used to determine forcing terms that optimally match experimental results for the same jet as analysed here. A discussion in terms of local instability modes is not helpful in this case, but the sub-optimal forcing mechanism can still be characterised in the setting of a *parallel* jet flow, which will serve as a model problem in order to understand the trends obtained in the non-parallel framework.

A parallel incompressible jet is considered, defined by a Gaussian velocity profile

$$U(r) = e^{-2r^2}, \tag{11}$$

as a simple analytical model for the flow downstream of the potential core. The inflection point is located at $r = 0.5$, and the flow is locally stable at a Reynolds number $Re = 20\,000$. Axisymmetric linear perturbations are computed in a numerical domain of 10 diameters in the axial and radial directions, in response to forcing of both velocity components, which may act anywhere

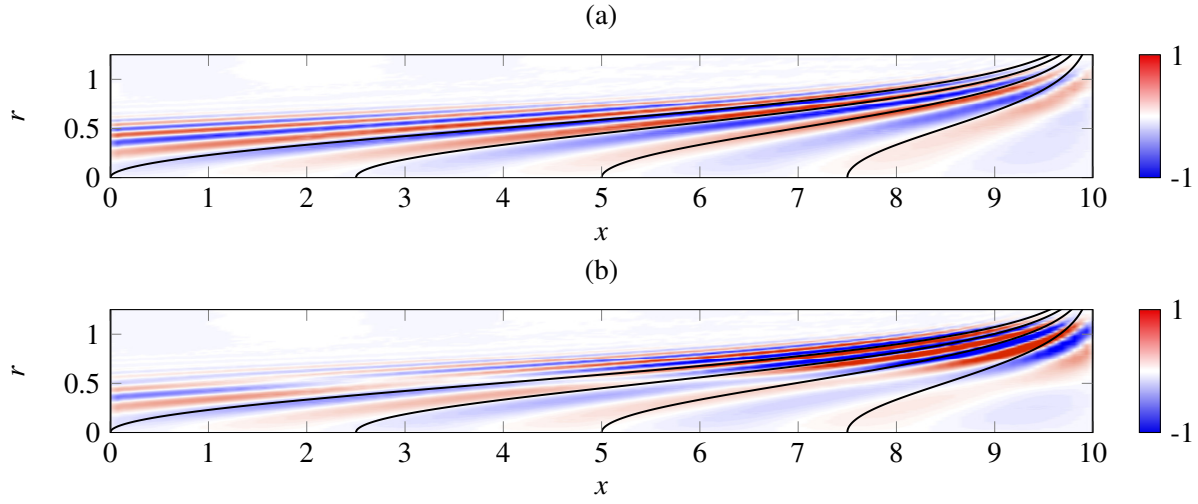

FIG. 10. Forcing mode structures in a parallel incompressible jet with Gaussian base flow profile. Kinetic energy at $x = 10$ is maximised. Streamwise velocity forcing is shown in linear colour scale. Black lines: contours that are convected into vertical lines at $x = 10$ after $\Delta t = (2.5, 5, 7.5, 10)$. a) Forcing mode 1; b) forcing mode 2.

in the domain. The numerical method of [49] is adapted for the *global* computation of optimal resolvent structures, such that the kinetic energy of the flow response at $x = 10$, integrated in r, is maximised. Thus, forcing is allowed to act throughout the flow domain, but the optimisation objective is measured only at the downstream end.

The first two forcing modes are shown in Fig. 10, for a Strouhal number $St = 1/\pi$. Tilted structures are observed, quite similar to the compressible results displayed in Fig. 7(*a,c*), and the tilting angle increases with upstream distance from the target position $x = 10$. Black curves trace material lines in the flow that are transported, through convection with the local flow velocity, into vertical lines at $x = 10$ after various time lapses. It is immediately seen that the forcing structures follow closely the local curvature of these contours, especially at far upstream positions. Along the black curves, the phase of the first forcing mode structure is approximately constant, whereas the second mode displays a sign change in the phase at the inflection point $r = 0.5$. This radial sign change provides for the orthogonality between different forcing modes, and their associated flow responses, while the streamwise variations in modes 1 and 2 are nearly identical. The third and fourth forcing modes of the parallel incompressible jet, not shown in Fig. 10, are merely characterised by additional phase changes in the radial direction. All these features are fully consistent with the sub-optimal forcing structures found for the non-parallel compressible jet (Fig. 7). The parallel jet results clearly demonstrate that an Orr-type convection mechanism is responsible for the forcing gain in this locally stable setting. From their resemblance, it is inferred that the same mechanism accounts for the gain of sub-optimal structures in the non-parallel compressible jet.

In summary, the following main interpretations of the findings in Sec. III E are proposed: (i) The optimal forcing (mode 1) targets the shear instability of the jet, leading to exponential amplitude growth along x in a finite region directly downstream of the nozzle. Forcing of this mechanism is most efficient at the upstream end of the locally unstable region. Even more efficient than direct forcing of shear-instability perturbations at the nozzle lip is the forcing of Orr structures in the inner pipe boundary layer, which experience growth before they enter the free jet (consistent with

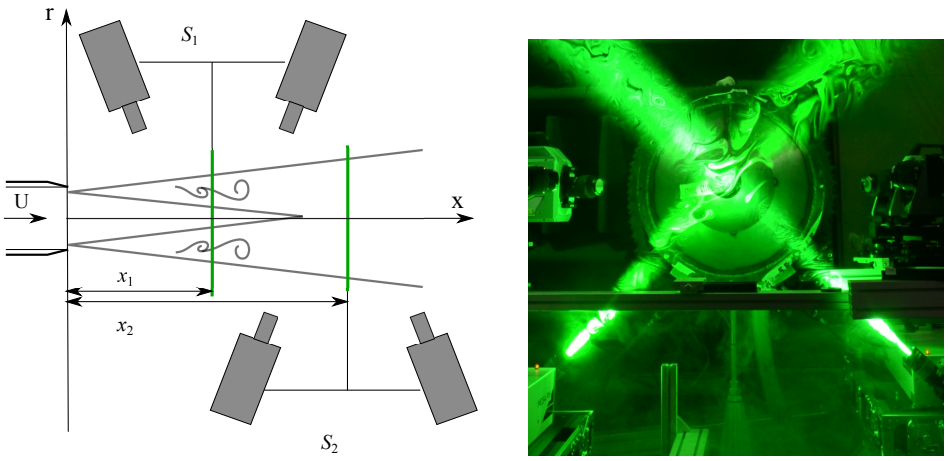

FIG. 11. (*a*) Sketch of the experimental setup, viewed from the top. The green lines represent the laser light sheets S_1 and S_2, placed at x_1 and x_2, respectively; these planes are shifted during the experiment in the range $x = [1,8]$ (see [29]). (*b*) Front view of the experiment during the PIV acquisition.

[14, 15, 17]). (ii) Sub-optimal forcing exploits the Orr mechanism in the free jet as a means of perturbation energy growth, independent of modal shear instability. Successive sub-optimal modes exhibit an increasing number of sign changes in the phase along r, which accounts for their mutual orthogonality. (iii) In our present results (Sec. III E), the above two mechanisms appear to be well separated in the optimal and sub-optimal resolvent modes at moderate Strouhal numbers. At $St = 0.2$, the shape of the optimal mode (figures 5*a* and 6*a*) suggests a mixed excitation of shear instability and free-jet Orr mechanism.

V. COHERENT STRUCTURES IN JET TURBULENCE: EXPERIMENT AND LINEAR MODEL

The resolvent analysis of Sec. III so far only describes the linear flow response to harmonic forcing input. In this section, those results will be leveraged for the modelling of coherent turbulent structures, where both the forcing f and the response q' are of a stochastic nature.

A. Extraction of SPOD modes from experimental data

The jet experiments of Jaunet *et al.* [29] provide an extensive database of synchronous PIV measurements in cross-planes at several axial positions. Two-point coherence statistics along fixed radial positions have been discussed in the first publication [29] with a focus on the streamwise coherence length; here, the same database is fully exploited for the computation of the two-dimensional cross-spectral density of axisymmetric velocity fluctuations in the (x,r) plane. To our knowledge, no experimental CSD measurements of comparable size and detail in a turbulent jet exist in the literature.

The acquisition apparatus consists of two time-resolved stereo PIV systems that can be moved independently. Both systems measure the velocity in planes orthogonal to the jet axis at either the same axial location (co-planar configuration) or at different positions. A sketch of the setup is shown in Fig. 11(a), where it is illustrated how the two PIV systems can be positioned with

respect to the nozzle. The axial positions of the measurement planes are $x_1 \in [1,8]$ and $x_2 \in [x_1,8]$ in increments of $\Delta x = 0.5$, where x_1 refers to the axial position of the upstream system (S_1) and x_2 to that of the downstream system (S_2). The instantaneous velocity fields are interpolated onto a polar grid of 32 points in the radial direction and 64 in azimuth, for $r \leq 0.8$, using a bi-cubic interpolation that guarantees a close match with the original data.

The axisymmetric component of axial velocity fluctuations is isolated by averaging each snapshot in the azimuthal direction. The cross-spectral density (CSD) matrix between all resulting $(N_x \times N_r) = (15 \times 64)$ spatial positions is then constructed using Welch's periodogram method, with data blocks of 128 time samples, overlapped by 50% (see Ref. [29] for further details). This empirically educed matrix converges statistically towards the true CSD, which is defined as the covariance of the Fourier-transformed velocity signal $\hat{y}(\mathbf{x}_i, \omega)$,

$$P_{\hat{y}\hat{y}}\big|_{ij}(\omega) = \mathscr{E}\left[\hat{y}(\mathbf{x}_i,\omega)\hat{y}^*(\mathbf{x}_j,\omega)\right]. \tag{12}$$

The "expected value" operator $\mathscr{E}$ denotes the asymptotic limit of an ensemble average. In the present calculations, for numerical reasons, each element of the CSD matrix is further scaled with a factor $\sqrt{r_i r_j}$, composed of the radial coordinates of any two points for which the correlation is computed. This procedure ensures that the resulting modified CSD matrix is strictly Hermitian [50].

Eigenvectors $\tilde{\phi}_k$ of the modified matrix are computed. These are then again rescaled in each point as $\phi_k(r,x) = \tilde{\phi}_k(r,x)r^{-0.5}$, and they are sorted in descending order of their associated eigenvalues. The structures $\phi_k(r,x)$ represent the SPOD modes, in the terminology of Picard & Delville [10], and as used in recent literature [19, 20]. Unfortunately, the same name is also used by Sieber *et al.* [11] for a different modal decomposition, which is not employed here.

The statistical convergence of SPOD modes is examined by dividing the datasets into two blocks, indicated as $i = (1,2)$, and performing the computation procedure on each subset. Each block corresponds to half of the original dataset. We use a normalized scalar product α between each mode $\phi_{i,k}$ obtained with half of the original dataset and the corresponding mode ϕ_k obtained with the complete set,

$$\alpha_{i,k} = \frac{\langle \phi_k, \phi_{i,k} \rangle}{\sqrt{||\phi_k||_2 \cdot ||\phi_{i,k}||_2}}. \tag{13}$$

The scalar quantity $\alpha_{i,k}$ is the correlation coefficient between the k^{th} mode of subset i and the corresponding mode of the full dataset. We consider modes with a correlation coefficient close to unity as being converged, showing thus that the same computation with half of the dataset leads to a very similar result.

The correlation coefficients for $St = 0.2, 0.4, 0.6$ and 0.8 are presented in Fig. 12. It is clear from these figures that the analysis is rather sensitive to the amount of data being used. The discrepancies in the higher (less energetic) modes are partially explained by differences in the order in which they emerge, depending on the data subset. However, the first two SPOD modes seem to be sufficiently correlated and can be accepted as being converged at all Strouhal numbers below $St = 0.8$. Only modes 1 and 2 will be discussed in the following, for $0.2 \leq St \leq 0.7$.

B. Resolvent-based modelling of SPOD modes

The relation between resolvent modes, as presented in Sec. III, and SPOD modes, as obtained from the experiments, is made explicit here on the basis of our earlier formulation [18]. The

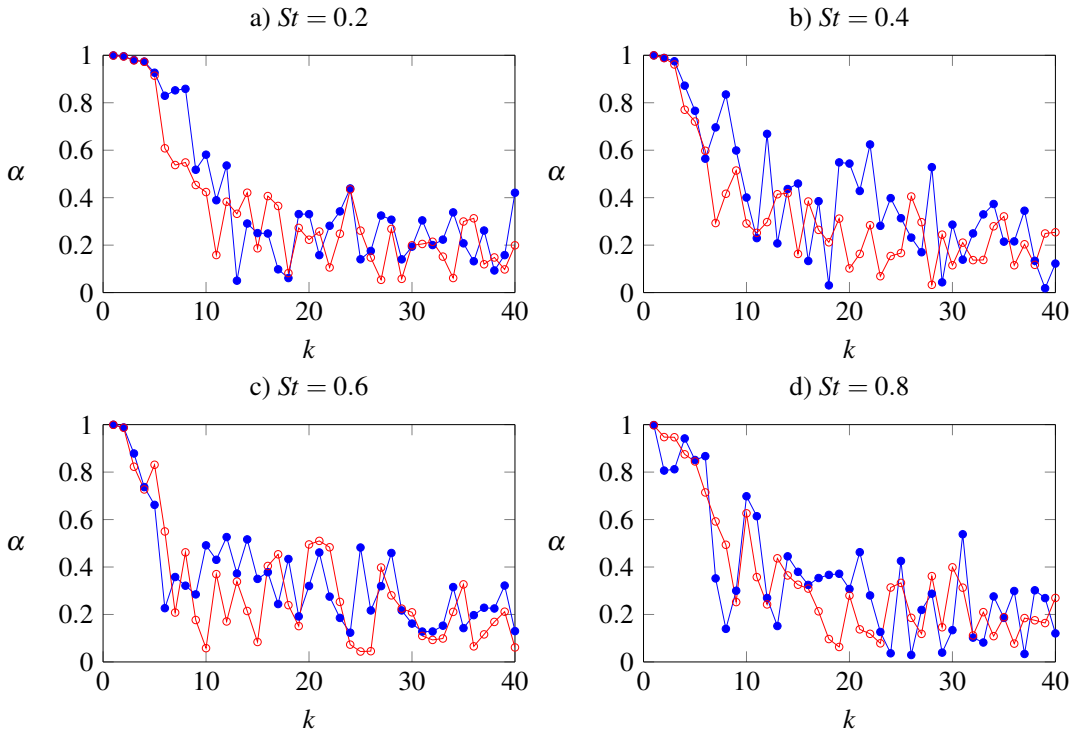

FIG. 12. Correlation coefficients α (Eq. 13), for a quantification of the statistical convergence of experimental SPOD modes. Two subsets of data are taken from the experimental acquisitions, and for each of these the SPOD modes are computed and compared: (●) $\alpha_{1,k}$ and (○) $\alpha_{2,k}$. Satisfactory convergence is observed at least for mode 1 (throughout) and for mode 2 (at $St < 0.8$).

following development is consistent with the recent work of Towne *et al.* [19] and Schmidt *et al.* [20], while using the nomenclature introduced in the previous sections.

Let $f(t)$ and $q'(t)$ represent spatial discretisations of the stochastic forcing and response, as discussed in Sec. III B. The CSD of their spectral components $\hat{f}(\omega)$ and $\hat{q}(\omega)$ is given by

$$P_{\hat{f}\hat{f}}(\omega) = \mathscr{E}\left[\hat{f}(\omega)\hat{f}^H(\omega)\right] \quad \text{and} \quad P_{\hat{q}\hat{q}}(\omega) = \mathscr{E}\left[\hat{q}(\omega)\hat{q}^H(\omega)\right]. \tag{14}$$

For the purpose of flow modelling, we consider the CSD of an experimentally observable vector $\hat{y}$ of flow quantities,

$$P_{\hat{y}\hat{y}}(\omega) = \mathscr{E}\left[\hat{y}(\omega)\hat{y}^H(\omega)\right], \quad \text{with} \quad \hat{y} = C\hat{q}. \tag{15}$$

The relation between $P_{\hat{y}\hat{y}}$ and $P_{\hat{f}\hat{f}}$ at a given frequency involves the resolvent operator; with (9b) and the definitions in Sec. III C, this relation can be written as

$$P_{\hat{y}\hat{y}} = CR\mathscr{E}\left[\hat{f}\hat{f}^H\right]R^HC^H = CQ\Sigma F^H M P_{\hat{f}\hat{f}} M F \Sigma Q^H C^H. \tag{16}$$

If the forcing $\hat{f}$ is expanded in the basis given by the columns of F, with a coefficient vector β such that $\hat{f} = F\beta$, (16) becomes

$$P_{\hat{y}\hat{y}} = CQ\Sigma P_{\beta\beta}\Sigma Q^H C^H. \tag{17}$$

We now seek the relation between eigenvectors (SPOD modes) of $P_{\hat{y}\hat{y}}$ and the resolvent response modes contained in the matrix Q. If full-state information is available, $C = I$ and $\hat{y} = \hat{q}$, one can

write

$$NP_{\hat{y}\hat{y}}N^H = NQ\Sigma P_{\beta\beta}\Sigma Q^H N^H. \tag{18}$$

Recall that the scalar product (6) is represented by the matrix $M = N^H N$. As NQ is unitary, $(NQ)^H NQ = I$, it represents the eigenvector matrix of $NP_{\hat{y}\hat{y}}N^H$, under the condition that $P_{\beta\beta}$ is a diagonal matrix. This condition signifies that the resolvent forcing modes, for a given frequency, are *uncorrelated* in the actual stochastic forcing of the system ('spatial white-noise hypothesis'). It finally follows that Q in this case is the eigenvector matrix of $P_{\hat{y}\hat{y}}M$ (the 'weighted CSD' [20]), with the diagonal elements of $P_{\beta\beta}\Sigma^2$ as associated eigenvalues.

If $\hat{y}$ represents only partial-state information, $C \neq I$, such a direct link between resolvent response modes and SPOD modes cannot be made. This is the case for the present experimental dataset. However, under the strong hypothesis $P_{\beta\beta} = I$, it is possible to construct a low-rank approximation

$$P_{\hat{y}\hat{y}} \approx C\tilde{Q}\tilde{\Sigma}^2\tilde{Q}^H C^H \tag{19}$$

of the observable CSD, where $\tilde{Q}$ and $\tilde{\Sigma}$ only contain a limited number of resolvent response modes and associated gains, as obtained from the linear analysis. The eigenvectors of (19), or equivalently the left singular vectors of $C\tilde{Q}\tilde{\Sigma}$, can then be identified and compared to those computed from the experimental data. It may be expected that the leading SPOD mode structure is well represented by such a linear model in situations where the first optimal gain σ_1 is significantly larger than σ_2: as the ratio σ_1/σ_2 tends towards infinity, the leading SPOD mode tends towards the optimal resolvent response mode $C\hat{q}_1$. At finite gain ratios however, the inclusion of several resolvent modes in $C\tilde{Q}\tilde{\Sigma}$ has the potential to improve the agreement. The comparisons provided in recent analyses of backward-facing step flow [27] and jets [19, 20] show such favourable cases of strong gain separation, as discussed in those articles.

C. Comparison between experimental and model results

It is now assessed to what extent the experimentally educed SPOD modes are accurately reproduced by the resolvent-based model. The success of this comparison depends on many factors, namely, the assumption that our forcing modes are uncorrelated in $P_{\hat{y}\hat{y}}$, the hypotheses involved in the linear resolvent analysis in Sec. III, and the accuracy of both experimental and numerical methods used.

Approximations of $P_{\hat{y}\hat{y}}$ are constructed according to the low-rank model (19). The first five resolvent modes, discussed in Sec. III E, are used to build $\tilde{Q}$ and $\tilde{\Sigma}$ (the low-rank versions of Q and Σ) at various Strouhal numbers. The matrix C selects the streamwise velocity component in the same grid points that are used in the experimental CSDs. SPOD modes are then computed as the left singular modes of the matrix $C\tilde{Q}\tilde{\Sigma}$.

The leading SPOD modes obtained from experimental data and from the resolvent-based model are compared in Fig. 13, for Strouhal numbers $St = 0.2$, 0.4, 0.6 and 0.7. Contours of their absolute value are shown, and each mode is normalised with respect to its global maximum value. The agreement between experimental (left column) and model results (right column) is remarkably good at Strouhal numbers between 0.4 and 0.7. Within this range of St, maximum SPOD amplitudes are located inside the potential core region of the jet. The maximum along r at each streamwise station follows a line that tends towards the jet axis, evocative of the "critical layer" as discussed by Tissot *et al.* [45]. At $St = 0.2$ however, the agreement between experiment and model is rather poor. While the experimental mode structure in Fig. 13*a* resembles those found at higher Strouhal numbers, but with its maximum further downstream and possibly outside the

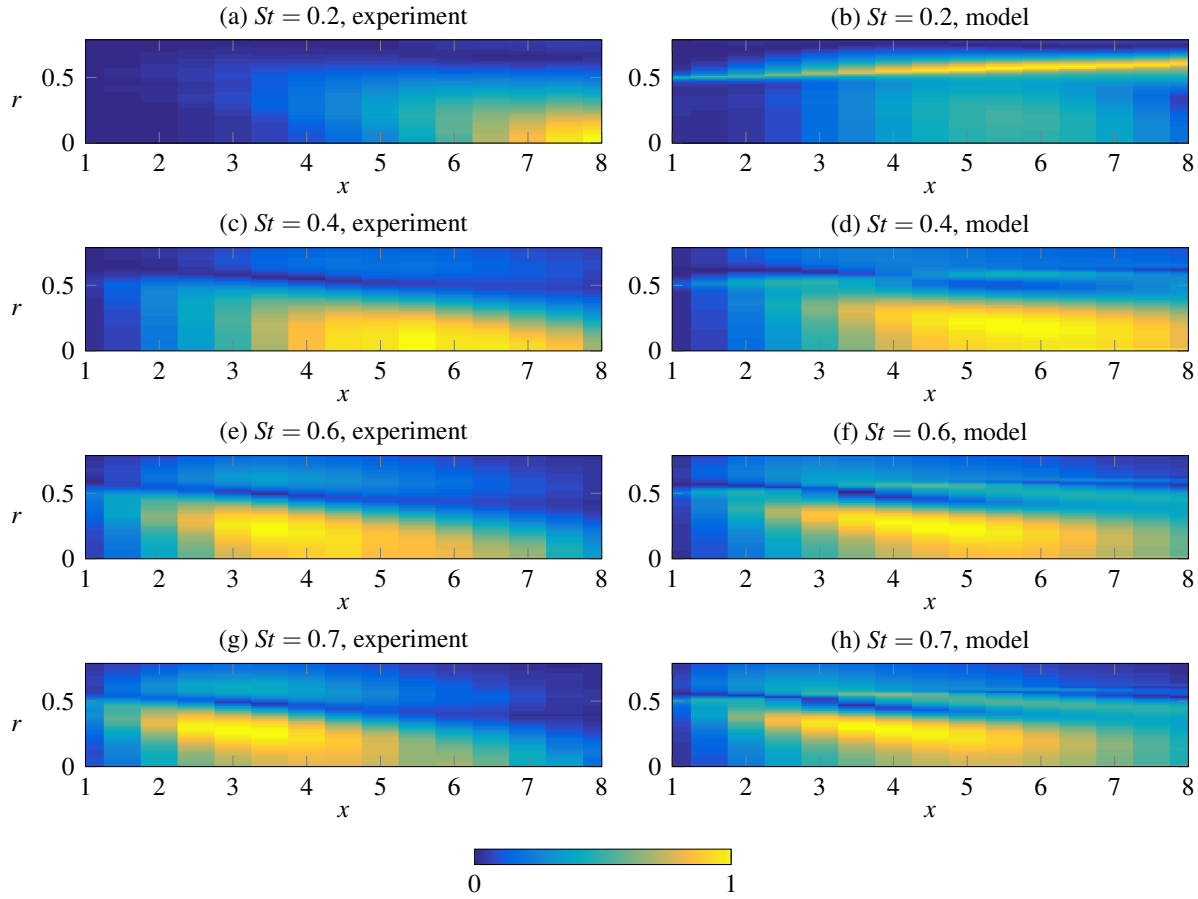

FIG. 13. Modulus of the *first* SPOD mode at $St = 0.2, 0.4, 0.6$ and 0.7, as obtained from the experimental data (left column) and from the resolvent-based model (right column). The resolution of the colour plots corresponds to the spatial grid where the CSD is defined, without interpolation.

measurement window, the resolvent-based model predicts high amplitudes in the outer portion of the shear layer (Figs. 13*b* and 6*a*).

The second SPOD modes are shown in the same manner in Fig. 14. For these modes, the comparison between experimental and model results fails at all Strouhal numbers. Mode structures obtained from the resolvent-based model have high amplitudes inside the shear layer, similar to the sub-optimal response structures shown in Fig. 7, whereas the experimentally educed structures are still characterised by maximum amplitudes near the jet axis. Inside the jet, the latter display an amplitude modulation along x with two distinct local maxima. Subsequent SPOD modes show similarly poor agreement, and they are not reported here.

Several effects may contribute to the failure of the model to capture the second SPOD mode; a rather obvious one seems to derive from the specific structure of the sub-optimal resolvent modes that are included in the low-rank operator (19). The optimal resolvent mode cannot be significantly involved in the second SPOD mode, which is orthogonal to the first one, and none of the four sub-optimal structures in Fig. 7 can be expected to reproduce spatial variations of the kind observed in the left column of Fig. 14.

Energy spectra, as given by the eigenvalues of the measured and modelled CSD matrices, are compared in Fig. 15. Their variations with Strouhal number are quite different from one another.

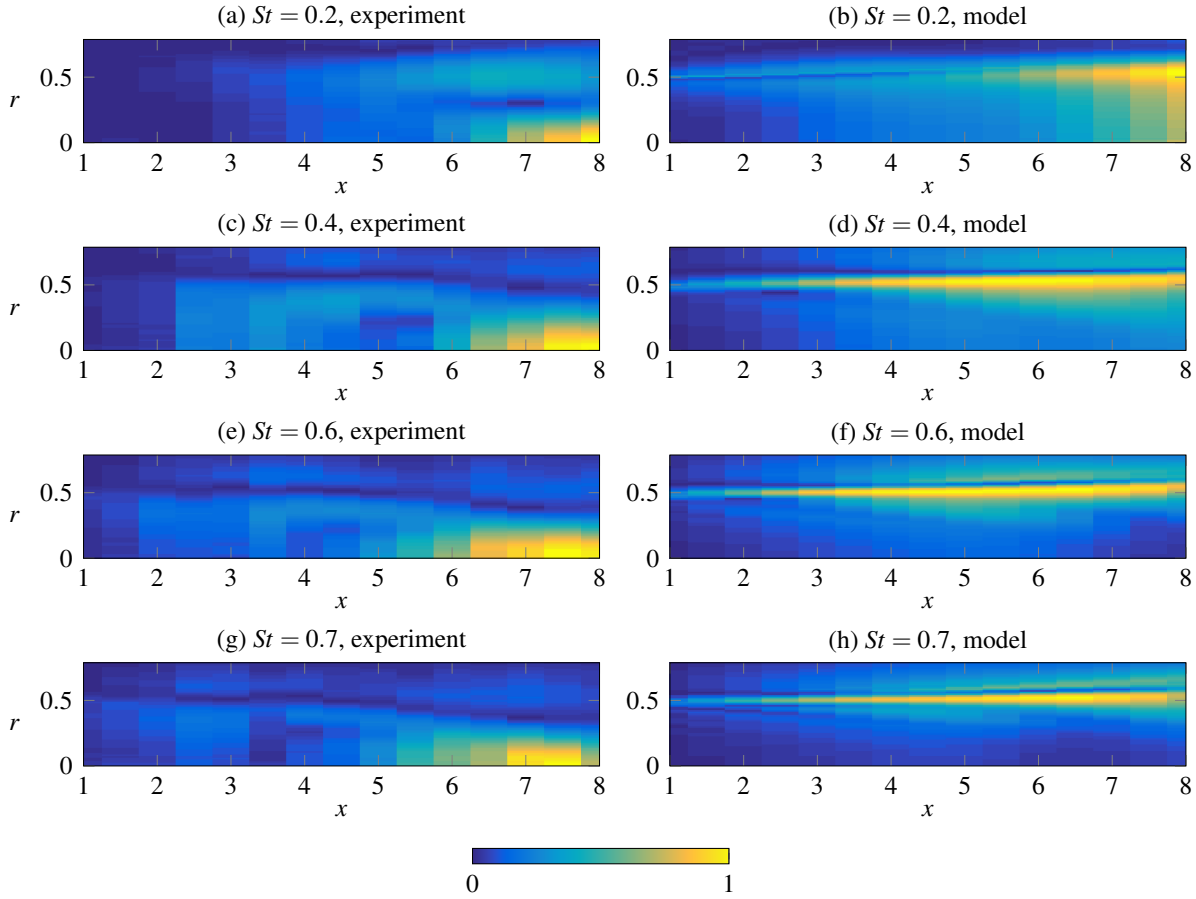

FIG. 14. Modulus of the *second* SPOD mode at $St = 0.2$, 0.4, 0.6 and 0.7, as obtained from the experimental data (left column) and from the resolvent-based model (right column). The resolution of the colour plots corresponds to the spatial grid where the CSD is defined, without interpolation.

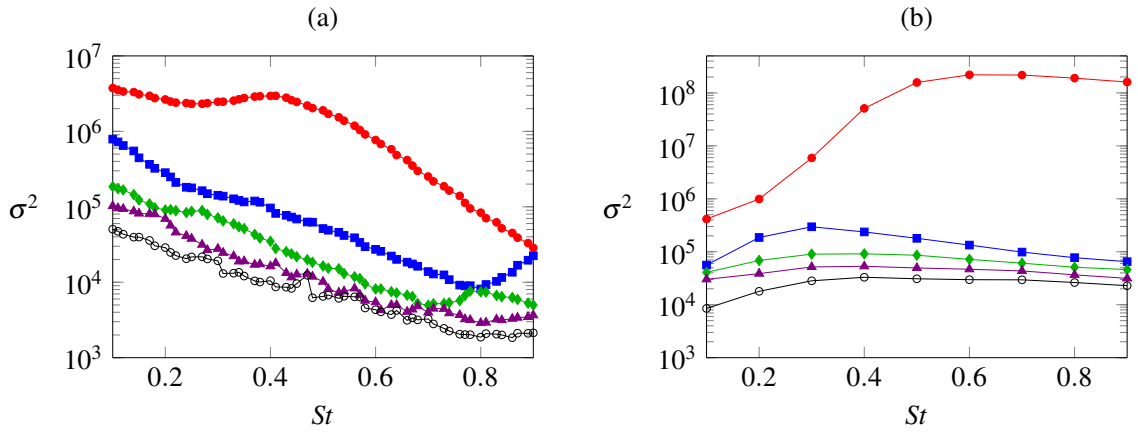

FIG. 15. The leading five CSD eigenvalue branches as functions of Strouhal number, (a) from the experiment, (b) from the resolvent-based linear model.

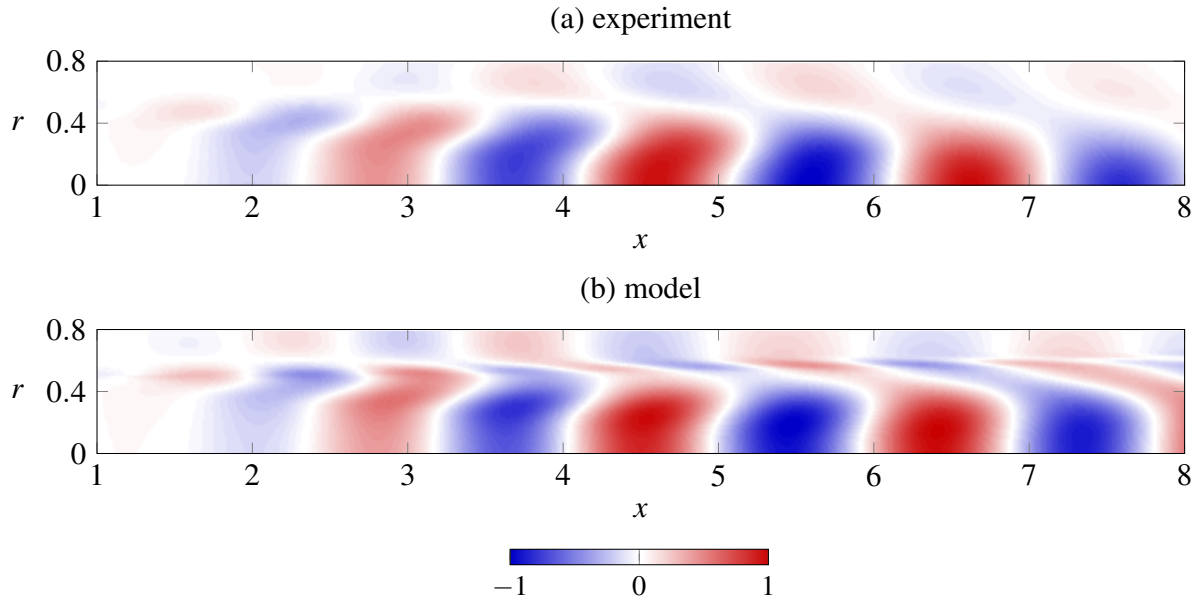

FIG. 16. Interpolated SPOD wavepackets at $St = 0.4$, (a) from the experiment, (b) from the resolvent-based linear model. Amplitude and phase are interpolated between the available data points, and the resulting real part is represented.

The dominant eigenvalue of the experimental CSD takes on its highest value at $St = 0.1$, and another local maximum arises at $St = 0.4$. The first and second eigenvalue curves are separated by a factor between 3 and 7 over the interval $0.4 \leq St \leq 0.8$, where SPOD modes in model and experiment are in good agreement. CSD eigenvalues derived from the model closely resemble the gain values shown in Fig. 4, with a slight shift of the maximum value from $St = 0.7$ to 0.6. An important source of discrepancy between the dominant branches in figures 15a and b is very likely the assumption that all resolvent forcing modes over all Strouhal numbers are contained in the Reynolds stress fluctuations with *equal amplitude*.

In order to visualise the wavepacket structure of the leading SPOD mode at $St = 0.4$, the dominant St value according to the experimental spectrum (Fig. 15a), the amplitude and the phase of this mode are interpolated onto a fine mesh. This is done both for the experimental and for the model SPOD mode, and the resulting real parts are shown in Fig. 16. Clean wavepackets are recovered, and their resemblance is even more appreciable than in the amplitude plots of Fig. 13. The model wavepacket is nearly identical to the optimal response mode (see Figs. 6b,c for $St = 0.3$, 0.5). For a more quantitative comparison, real-part oscillations of the interpolated SPOD modes are extracted along the centreline, and displayed in Fig. 17, together with their amplitude envelope. Black and red lines represent the model and the experimental data, respectively. Markers indicate the values obtained directly in the original measurement points. Experimental wavepackets are traced with their actual absolute amplitude, whereas a best-fit coefficient has been constructed, based on the interval $1 \leq x \leq 5$, for a proper scaling of the model amplitude. Good agreement is generally observed in the upstream region of exponential amplitude growth; at $St = 0.4$, the agreement is excellent down to the amplitude maximum. At lower Strouhal numbers, the model underpredicts the maximum, even by a large measure in the case of $St = 0.2$, whereas at higher Strouhal numbers, the amplitude maximum is overpredicted. Considering that a phase match is imposed in the very first position, $x = 1$, and differences therefore accumulate in the downstream

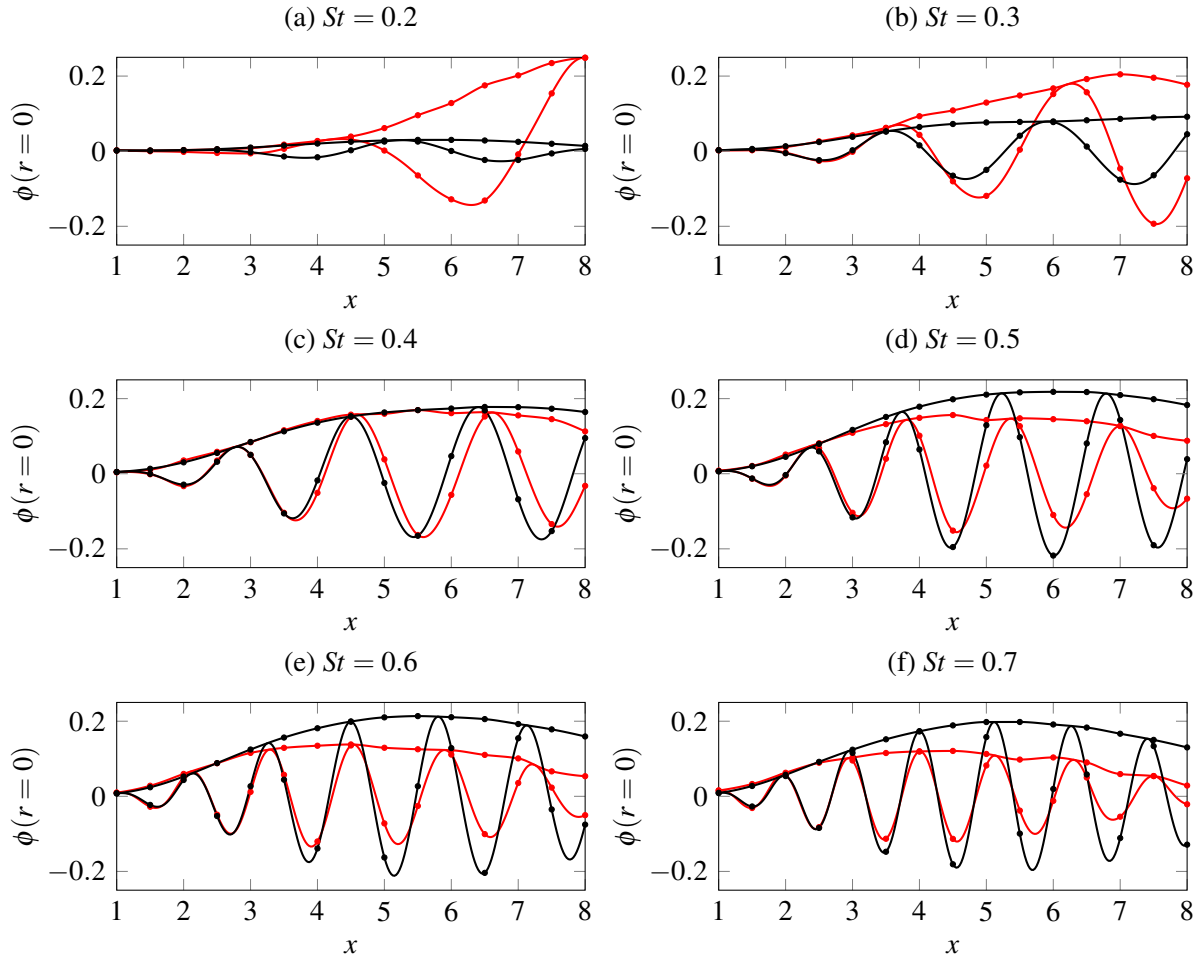

FIG. 17. Comparison between experimental (red) and model (black) SPOD wavepackets at various Strouhal numbers. Amplitude and phase variations on the centreline are interpolated between the available data points, indicated by markers. Both the amplitude envelopes and the oscillating real parts are shown.

direction, the phase prediction can be said to be satisfactory for all Strouhal numbers above 0.2. Several radial positions have been tested for the present comparison, and all have been found to give very similar agreement. The most notable difference between model and experimental results, at $St \geq 0.4$, is an underpredicted downstream attenuation of fluctuation amplitudes. This trend is clearly visible in Figs. 13, 16 and 17, and it increases with St.

D. Comparison with linear jet studies in the recent literature

The resolvent modes presented in Sec. III E and their comparison with SPOD modes in Sec. V C are, by and large, consistent with the findings of similar recent studies [14, 16, 17, 19, 20]. One striking difference with the results of Schmidt *et al.* [20] is noted in the structure of sub-optimal response modes: at Strouhal numbers above 0.2, our computations yield a clean separation between modal shear and non-modal Orr structures, whereas Schmidt *et al.* [20] observe a mixing of shear-induced wavepackets with Orr-related structures in all their sub-optimals. The associated forcing

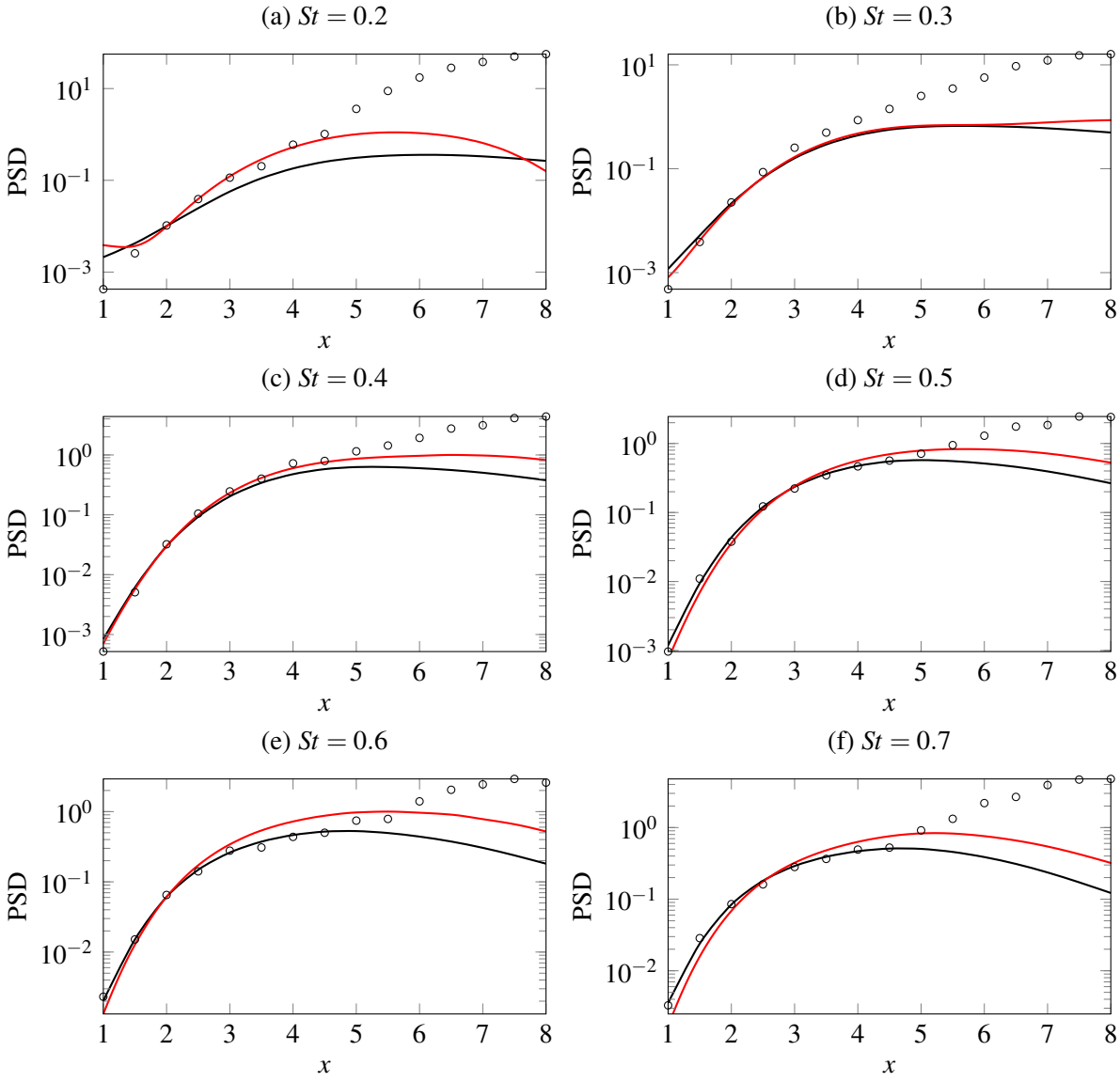

FIG. 18. Power-spectral density (PSD) along the jet centreline as a function of x at different Strouhal numbers. (○) Hot-wire measurements [12]; (—) PSE model [12]; (—) optimal response mode (present calculations).

structures, shown in Figs. 5 and 7, suggest that this difference can be attributed to the presence of a nozzle in our numerical configuration. Forcing inside the pipe is found to be particularly efficient, especially in the case of the optimal resolvent mode, which must therefore be expected to be very sensitive to the truncation of the most receptive flow region. In turn, changes in the optimal mode will affect the following sub-optimals. The localisation of optimal forcing in the present results may furthermore be linked to the observed sensitivity of LES statistics with respect to flow details in the nozzle boundary layer [30].

Numerous previous studies addressing the linear modelling of wavepackets in turbulent jets, when only *boundary forcing* at the inflow was considered, observed discrepancies in the initial amplitude growth at low Strouhal numbers, typically $St \leq 0.3$ [4, 12, 51], which play an important

role in the generation of jet noise. These differences were initially attributed either to the weakly non-parallel assumption that underlies the parabolised stability equations (PSE), or to unmodelled nonlinear effects. The limitation of PSE with regard to non-parallelism has since been ruled out by computations based on the fully non-parallel, linearised Euler equations [5]. We complete this study by revisiting the low-Strouhal discrepancy in the resolvent framework, where *volume forcing* is included as a surrogate for nonlinear effects.

Figure 18 compares the PSE and measured power-spectral density (PSD) results from Cavalieri *et al.* [12] with the kinetic energy of the optimal response modes presented in Sec. III E. All curves are extracted on the jet axis. It can be seen how, at $St = 0.2$, the resolvent mode captures the initial wavepacket growth measured in the experiment, and underpredicted by PSE, while at higher Strouhal numbers the PSE solution and resolvent mode comprise similar initial growth. The optimal forcing at $St = 0.2$ (Fig. 5a,b) involves significant contributions from inside the shear layer of the free jet, which were excluded in the models of Refs. [4, 5, 12, 51]. This volume forcing boosts the spatial growth of the response wavepacket near the nozzle. Although the high-amplitude portion of the optimal response mode is not in agreement with the experimental PSD, the initial growth is faithfully reproduced. This observation suggests that Orr-type forcing through Reynolds stresses in the free shear layer indeed contributes to perturbation growth at low Strouhal number near the nozzle.

Another much-discussed discrepancy between PSE and PSD results arises in the downstream region where linear models predict a decay in perturbation amplitude, whereas the PSD displays a marked additional growth, accompanied by a slope break in the growth rate. This peculiar behaviour of the PSD is entirely absent in the present SPOD results, in agreement with the LES-based analysis by Schmidt *et al.* [20]. This leads us to conclude that the spatio-temporal coherence, from which SPOD modes are derived, provides a sharper and more pertinent criterion for the eduction of coherent turbulent structures than the PSD, which only measures temporal coherence. As discussed by Towne *et al.* [19], the PSD may contain the trace of many SPOD modes. Figure 18 strongly suggests that sub-optimal SPOD or resolvent mode wavepackets contribute in a very significant way to the turbulent dynamics downstream of $x = 4$. The Orr-type character of our sub-optimal resolvent modes is fully consistent with the discussion of the PSD behaviour by Tissot *et al.* [45].

VI. CONCLUSIONS

Perturbation wavepackets in the mean flow of a turbulent jet have been computed in the form of resolvent modes. Nonlinear terms in the governing equations, which arise in the form of generalised Reynolds stresses, are regarded as generic forcing terms [21, 27, 35]. The five leading orthogonal forcing/response modes have been identified for several values of the Strouhal number between 0.2 and 1.5. The most amplified ("optimal") mode, over the interval $0.3 \leq St \leq 1.5$, bears the traits of a shear instability in the free jet, with strong spatial growth in the potential core. This mode arises principally from forcing in the nozzle boundary layer, which takes the shape of tilted structures indicative of the Orr mechanism, as described in our earlier studies [14, 17]. The dominant role of shear instability in the free-jet portion of the optimal resolvent mode has been demonstrated by projecting the response wavepacket onto a local k^+ shear instability mode. Subsequent ("sub-optimal") modes, with significantly lower energy gain, appear to exploit the Orr mechanism in the free jet. This interpretation is supported via an analogy with optimal forcing in a fully developed parallel jet. At low Strouhal number, $St = 0.2$, both shear and Orr mechanisms in the free jet seem to contribute to the optimal resolvent mode in a mixed fashion.

Coherent structures have then been extracted from experimental measurements, in the form of eigenvectors of the cross-spectral density, named 'spectral POD' (SPOD) modes [10, 19]. Following recent works [18, 19], it has been demonstrated that such modes should, in theory, correspond to the optimal response mode described above, under two strong conditions: (i) the corresponding optimal forcing modes are statistically *uncorrelated* among each other in the nonlinear dynamics, which are interpreted in the linear model as forcing terms; (ii) the SPOD modes are extracted from *full-state* information. As full-state information is not available from the experimental dataset, the five leading response modes were instead used to construct a low-rank model of the cross-spectral density, under the even stronger assumption that the corresponding optimal forcing structures are uncorrelated and of *equal amplitude* in the nonlinear dynamics. This procedure constitutes our resolvent-based linear model for the statistical dynamics of coherent turbulence structures, as characterised by two-point covariance.

Very good agreement has been found between the leading SPOD modes as obtained from the experiment and from the resolvent-based model, in a range of Strouhal numbers around 0.4. The leading SPOD mode of the linear model is in fact nearly identical to the optimal response wavepacket, such that the intermediate step of building a model CSD from several response structures turned out to be unimportant for the comparison with the experiment. At $St = 0.4$, the model reproduces accurately both the amplitude variations over three decades, down to at least 7 diameters behind the nozzle, and the phase variations in the experimentally educed SPOD mode. The maximum wavepacket amplitude is underpredicted at $St < 0.4$, and overpredicted at $St > 0.4$. At all Strouhal numbers between 0.2 and 0.7, the initial streamwise perturbation growth close to the nozzle is very well retrieved.

Subsequent (non-leading) SPOD modes of the experimental data and the linear model do not show satisfactory agreement. The discussion of their discrepancies may be approached from two ends: on the one hand, the linear model probably cannot replicate the experimental results because of the restricted number of basis vectors, and because the above-mentioned modelling hypotheses are too crude in order to reproduce the dynamics beyond leading order. On the other hand, the experimental measurements may be too sparse, particularly in terms of spatial resolution, in order to detect the rather fine-scale structures that the linear model predicts.

In summary, the results presented in this paper demonstrate that linear resolvent analysis, performed around the spatially developing, time-averaged mean flow, represents a valid tool for the modelling of coherent wavepacket structures in a stochastically driven turbulent jet. Only the mean flow is required for the construction of this linear model. Wavepackets arising from shear instability, which experience the strongest energy gain, could be matched between model and experiment at Strouhal numbers between 0.2 and 0.7. While these general conclusions corroborate those of the parallel study by Schmidt *et al.* [20], performed on the basis of LES data for the same flow configuration, differences are observed in the resolvent mode structures. These relate to the separation of shear and Orr mechanisms in the optimal and sub-optimal modes, and they are attributed to the inclusion of a nozzle in the present analysis.

From a final comparison with earlier PSD measurements [12], it is inferred that sub-optimal SPOD modes seem to play a determining role near and beyond the end of the potential core region. While the link between these modes and free-jet Orr-type growth mechanisms is one more time predicted by the present analysis, poor agreement is found between sub-optimal structures in model and experiment. Further progress of wavepacket modelling in high Reynolds number turbulent jets requires establishing the dynamics that dominate in the flow region downstream of the potential core, and how best to model them.

ACKNOWLEDGMENTS

This work was supported by the Agence Nationale de la Recherche under the *Cool Jazz* project, grant number ANR-12-BS09-0024, and by the Délégation Générale de l'Armement under grant number 2015.60.0004.00.470.75.01. Stability calculations were performed using HPC resources of TGCC and CINES under the allocation x2016-2a6451 made by GENCI.

[1] P. Jordan and T. Colonius, "Wave packets and turbulent jet noise," Annu. Rev. Fluid Mech. **45**, 173–195 (2013)

[2] A. Michalke, "Instability of a compressible circular free jet with consideration of the influence of the jet boundary layer thickness," Z. Flugwiss. **19**, 319–328 (1971)

[3] D. G. Crighton and M. Gaster, "Stability of slowly diverging jet flow," J. Fluid Mech. **77**, 397–413 (1976)

[4] K. Gudmundsson and T. Colonius, "Instability wave models for the near-field fluctuations of turbulent jets," J. Fluid Mech. **689**, 97–128 (2011)

[5] Y. B. Baqui, A. Agarwal, A. V. G. Cavalieri, and S. Sinayoko, "A coherence-matched linear source mechanism for subsonic jet noise," J. Fluid Mech. **776**, 235–267 (2015)

[6] B. F. Farrell and P. J. Ioannou, "Stochastic forcing of the linearized Navier–Stokes equations," Phys. Fluids A **5**, 2600–2609 (1993)

[7] B. F. Farrell and P. J. Ioannou, "Statistical state dynamics: a new perspective on turbulence in shear flow," arXiv preprint 1412.8290 (2014)

[8] P.J. Schmid, "Nonmodal stability theory," Annu. Rev. Fluid Mech. **39**, 129–162 (2007)

[9] S. Bagheri, D. S. Henningson, J. Hoepffner, and P. J. Schmid, "Input-output analysis and control design applied to a linear model of spatially developing flows," Appl. Mech. Rev. **62**, 020803 (2009)

[10] C. Picard and J. Delville, "Pressure velocity coupling in a subsonic round jet," Int. J. Heat Fluid Fl. **21**, 359–364 (2000)

[11] M. Sieber, C. O. Paschereit, and K. Oberleithner, "Spectral proper orthogonal decomposition," J. Fluid Mech. **792**, 798–828 (2016)

[12] A. V. G. Cavalieri, D. Rodriguez, P. Jordan, T. Colonius, and Y. Gervais, "Wavepackets in the velocity field of turbulent jets," J. Fluid Mech. **730**, 559–592 (2013)

[13] D. Rodriguez, A. V. G. Cavalieri, T. Colonius, and P. Jordan, "A study of linear wavepacket models for subsonic turbulent jets using local eigenmode decomposition of PIV data," Eur. J. Mech. B/Fluids **49B**, 308–321 (2015)

[14] X. Garnaud, L. Lesshafft, P. J. Schmid, and P. Huerre, "The preferred mode of incompressible jets: linear frequency response analysis," J. Fluid Mech. **716**, 189–202 (2013)

[15] X. Garnaud, R. D. Sandberg, and L. Lesshafft, "Global response to forcing in a subsonic jet: instability wavepackets and acoustic radiation," AIAA paper 2013–4633 (2013)

[16] J. Jeun, J. W. Nichols, and M. R. Jovanović, "Input-output analysis of high-speed axisymmetric isothermal jet noise," Phys. Fluids **28**, 047101 (2016)

[17] O. Semeraro, L. Lesshafft, V. Jaunet, and P. Jordan, "Modeling of coherent structures in a turbulent jet as global linear instability wavepackets: Theory and experiment," Int. J. Heat Fluid Fl. **62**, 24–32 (2016)

[18] O. Semeraro, V. Jaunet, P. Jordan, A. V. G. Cavalieri, and L. Lesshafft, "Stochastic and harmonic optimal forcing in subsonic jets," AIAA Paper 2016-2935 (2016)

[19] A. Towne, O. T. Schmidt, and T. Colonius, "Spectral proper orthogonal decomposition and its relationship to dynamic mode decomposition and resolvent analysis," J. Fluid Mech. **847**, 821–867 (2018)
[20] O. T. Schmidt, A. Towne, G. Rigas, T. Colonius, and G. A. Brès, "Spectral analysis of jet turbulence," J. Fluid Mech. **855**, 953–982 (2018)
[21] B. F. Farrell and P. J. Ioannou, "Generalized stability theory. Part I: Autonomous operators," J. Atmospheric Sci. **53**, 2025–2040 (1996)
[22] F. Alizard, S. Cherubini, and J.-C. Robinet, "Sensitivity and optimal forcing response in separated boundary layer flows," Phys. Fluids **21**, 064108 (2009)
[23] A. Monokrousos, E. Åkervik, L. Brandt, and D. S. Henningson, "Global three-dimensional optimal disturbances in the Blasius boundary-layer flow using time-steppers," J. Fluid Mech. **650**, 181–214 (2010)
[24] D. Sipp and O. Marquet, "Characterization of noise amplifiers with global singular modes: the case of the leading-edge flat-plate boundary layer," Theor. Comp. Fluid Dyn. **27**, 617–635 (2013)
[25] G. Dergham, D. Sipp, and J.-C. Robinet, "Stochastic dynamics and model reduction of amplifier flows: the backward facing step flow," J. Fluid Mech. **719**, 406–430 (2013)
[26] E. Boujo and F. Gallaire, "Sensitivity and open-loop control of stochastic response in a noise amplifier flow: the backward-facing step," J. Fluid Mech. **762**, 361–392 (2015)
[27] S. Beneddine, D. Sipp, A. Arnault, J. Dandois, and L. Lesshafft, "Conditions for validity of mean flow stability analysis," J. Fluid Mech. **798**, 485–504 (2016)
[28] A. Towne, T. Colonius, P. Jordan, A. V. G. Cavalieri, and G. A. Brès, "Stochastic and nonlinear forcing of wavepackets in a Mach 0.9 jet," AIAA Paper 2015-2217 (2015)
[29] V. Jaunet, P. Jordan, and A. V. G. Cavalieri, "Two-point coherence of wave packets in turbulent jets," Phys. Rev. Fluids **2**, 024604 (2017)
[30] G. A. Brès, P. Jordan, V. Jaunet, M. Le Rallic, A. V. G. Cavalieri, A. Towne, S. K. Lele, T. Colonius, and O. T. Schmidt, "Importance of the nozzle-exit boundary-layer state in subsonic turbulent jets," J. Fluid Mech. **851**, 83–124 (2018)
[31] S. B. Pope, *Turbulent flows* (Cambridge University Press, 2000)
[32] X. Garnaud, *Modes, transient dynamics and forced response of circular jets*, Ph.D. thesis, Ecole polytechnique (2012)
[33] R. D. Sandberg, "Governing equations for a new compressible Navier-Stokes solver in general cylindrical coordinates," Monograph No. AFM-07/07, School of Engineering Sciences, University of Southampton (2007)
[34] W. C. Reynolds and A. K. M. F. Hussain, "The mechanics of an organized wave in turbulent shear flow. Part 3. Theoretical models and comparisons with experiments," J. Fluid Mech. **54**, 263–288 (1972)
[35] B. J. McKeon and A. S. Sharma, "A critical-layer framework for turbulent pipe flow," J. Fluid Mech. **658**, 336–382 (2010)
[36] O. Tammisola and M. P. Juniper, "Coherent structures in a swirl injector at Re=4800 by nonlinear simulations and linear global modes," J. Fluid Mech. **792**, 620–657 (2016)
[37] K. Oberleithner, M. Stöhr, S. H. Im, C. M. Arndt, and A. M. Steinberg, "Formation and flame-induced suppression of the precessing vortex core in a swirl combustor: experiments and linear stability analysis," Combust. Flame **162**, 3100–3114 (2015)
[38] O. Semeraro, L. Lesshafft, and R. D. Sandberg, "Can jet noise be predicted using linear instability wavepackets?" in *Proceedings of the 5th International Conference on Jets, Wakes and Separated Flows* (Springer, 2016) pp. 413–418
[39] B.-T. Chu, "On the energy transfer to small disturbances in fluid flow (Part I)," Acta Mech. **1**, 215–234 (1965)

[40] V. Hernandez, J. E. Roman, and V. Vidal, "SLEPc: A scalable and flexible toolkit for the solution of eigenvalue problems," ACM Transactions on Mathematical Software (TOMS) **31**, 351–362 (2005)

[41] M. Fosas de Pando, D. Sipp, and P. J. Schmid, "Efficient evaluation of the direct and adjoint linearized dynamics from compressible flow solvers," J. Comput. Phys. **231**, 7739–7755 (2012)

[42] J. Berland, C. Bogey, O. Marsden, and C. Bailly, "High-order, low dispersive and low dissipative explicit schemes for multiple-scale and boundary problems," J. Comput. Phys. **224**, 637–662 (2007)

[43] T. J. Poinsot and S. K. Lele, "Boundary conditions for direct simulations of compressible viscous flows," J. Comput. Phys. **101**, 104–129 (1992)

[44] T. Colonius, "Modeling artificial boundary conditions for compressible flow," Annu. Rev. Fluid Mech. **36**, 315–345 (2004)

[45] G. Tissot, M. Zhang, F. Lajus, A. V. G. Cavalieri, P. Jordan, and T. Colonius, "Sensitivity of wavepackets in jets to non-linear effects: the role of the critical layer," J. Fluid Mech. **811**, 95–137 (2017)

[46] G. Tissot, F. Lajús, A. V. G. Cavalieri, and P. Jordan, "Wave packets and Orr mechanism in turbulent jets," Phys. Rev. Fluids **2**, 093901 (2017)

[47] L. Lesshafft and P. Huerre, "Linear impulse response in hot round jets," Phys. Fluids **19**, 024102 (2007)

[48] P. G. Drazin and W. H. Reid, *Hydrodynamic stability* (Cambridge University Press, 2004)

[49] L. Lesshafft, "Artificial eigenmodes in truncated flow domains," Theor. Comput. Fluid Dyn. **32**, 245–262 (2018)

[50] J. H. Citriniti and W. K. George, "Reconstruction of the global velocity field in the axisymmetric mixing layer utilizing the proper orthogonal decomposition," J. Fluid Mech. **418**, 137–166 (2000)

[51] D. E. Breakey, P. Jordan, A. V. G. Cavalieri, and O. Léon, "Near-field wavepackets and the far-field sound of a subsonic jet," AIAA Paper 2013-2083 (2013)